STRUCTURAL ASSESSMENT OF DAMAGED AND CFRP REPAIRED REINFORCED CONCRETE BEAMS FROM EXPERIMENTAL MODAL ANALYSIS

MOATASEM MOHAMMED FAYYADH

Thesis Submitted In Fulfilment Of The Requirements For The Degree Of Doctor Of Philosophy

FACULTY OF ENGINEERING

UNIVERSITY OF MALAYA

KUALA LUMPUR

2012

قُلْ إِنَّ صَلاَتِي وَنُسُكِي وَمَحْيَايَ وَمَمَاتِي لِلّهِ رَبِّ الْعَالَمِينَ

۝ لاَ شَرِيكَ لَهُ وَبِذَلِكَ أُمِرْتُ وَأَنَاْ أَوَّلُ الْمُسْلِمِين

سورة الأنعام

In the Name of Allâh, the Most Gracious, the Most Merciful

. . . . . .

Say (O Muhammad صلى الله عليه وسلم): "Verily, my *Salât* (prayer), my sacrifice, my living, and my dying are for Allâh, the Lord of the *'Âlamîn* (mankind, jinn and all that exists).

۝He has no partner. And of this I have been commanded, and I am the first of those who surrender (unto Him).

ABSTRACT

Many engineering structures suffer damage and deterioration with time, and need to be monitored in order to sense and predict risk of failure during its remaining service life. Damaged structures require repair work to be undertaken in order to prevent further loss of structural integrity and externally bonded Carbon Fibre Reinforced Polymer (CFRP) is one of the most widely used repair technique. In order to assess the damage and ascertain the appropriateness and effectiveness of the repaired system, various tests can be conducted on the structural element concerned. In this study, experimental modal analysis was conducted on undamaged, load induced damaged and CFRP repaired reinforced concrete beams. A total of sixteen reinforced concrete beams were cast and categorised into three groups with different loading conditions. The first group of beams were tested under a concentrated point load at mid-span to induce flexural damage while the remaining two groups for shear damage with loading positions at quarter span and close to the support.

Previous studies have used modal parameters for damage detection and the assessment of repair work, and showed that existing algorithms used for damage detection sometimes produced inaccuracies and anomalies. Thus in this study, new algorithms based on natural frequencies and mode shapes for damage detection are proposed to overcome some of the shortcomings which are related to reinforced concrete (RC) being a composite and heterogeneous material. Furthermore, the effectiveness of the CFRP sheets as flexural and shear repair system was assessed based on modal data extracted from the tests.

The results showed there was evidence of the influence of the RC composite action on the natural frequencies. By utilising the proposed algorithms in the form of damage detection indices, the type and cause of damage were identified and gave better sensitivity with

regards to damage severity. Furthermore it was also apparent that the indices were sufficiently reliable in assessing the effectiveness of the CFRP repair for both flexural and shear damage. The failure modes obtained from the CFRP repaired beams were identified as debonding when subjected to flexure, combination of flexural cracks and CFRP delamination together with a concrete layer for shear at quarter-span and a combination of shear and CFRP debonding for shear close to the support. Based on the results of this study, changes to the existing ACI equations for design of CFRP repaired beams under flexure and shear were proposed. These included modified equations for concrete and shear stirrups contribution, contribution of the external CFRP sheets and the contribution of the flexural steel. The predicted loads based on the modified form gave better agreement with the experimental results from this study.

ABSTRAK

Kebanyakan struktur kejuruteraan mengalami kerosakan dan kemerosotan mengikut peredaran masa, oleh itu ia memerlukan pemantauan bagi meramal risiko kegagalan sepanjang jangka hayat khidmat struktur tersebut. Struktur yang rosak memerlukan kerja membaik pulih bagi mengelak kegagalan yang berterusan dan pengukuhan luaran menggunakan polimer bertetulang gentian karbon (*externally bonded Carbon Fibre Reinforced Polymer* (CFRP)) adalah salah satu teknik membaik pulih yang digunakan secara meluas. Bagi menilai kerosakan dan menentukan kesesuaian dan keberkesanan sistem baik pulih, beberapa ujian telah dilakukan terhadap elemen struktur tersebut. Dalam kajian berikut "*experimental modal analysis"* dilakukan ke atas rasuk-rusuk konkrit bertetulang tidak kerosakan, rosak akibat pembebanan, dan baik pulih dengan CFRP. Sejumlah enam belas rasuk konkrit bertetulang disediakan dan dikategorikan kepada tiga kumpulan dengan keadaan beban yang berbeza. Kumpulan rasuk yang pertama diuji di bawah beban tumpu titik di tengah rentang bagi peningkatan kerosakan lenturan manakala kedua kumpulan yang lain untuk kerosakan ricih dengan lokasi beban di saper empat rentang dan berdekatan dengan sokong.

Kajian terdahulu menggunakan "*modal parameters"* bagi mengesan kerosakan dan menilai kerja pembaik pulih, menunjukkan bahawa algoritma sedia ada yang digunakan bagi mengesan kerosakan kadang kala memberi keputusan yang tidak tepat dan tidak normal. Berikutan kajian tersebut, algoritma baru berdasarkan frekuensi semulajadi dan "*mode shapes"* bagi mengesan kerosakan dicadangkan untuk mengatasi beberapa kelemahan yang berkaitan dengan konkrit bertetulang sebagai bahan komposit dan heterogen. Dengan itu,

keberkesanan CFRP sebagai sistem pembaikan lenturan dan ricih dinilai berdasarkan dari "*modal data"* yang diekstrak dari pelbagai ujian.

Keputusan menunjukkan bahawa terdapat bukti pengaruh tindakan terhadap komposit konkrit bertetulang di bawah frekuensi semulajadi. Dengan menggunakan algoritma yang dicadangkan dalam bentuk indeks pengesanan kerosakan, jenis dan punca kerosakan telah dikenal pasti dan memberi kejituan yang lebih baik berkenaan keterukan kerosakan. Selain daripada itu, ia juga jelas bahawa indeks tersebut boleh digunakan dalam menilai keberkesanan pembaikan oleh CFRP bagi kedua-dua jenis kerosakan lenturan dan ricih. Mod kegagalan diperolehi dari CFRP rasuk yang dibaik pulih dikenal pasti sebagai nyah-ikatan yang tertakluk kepada lenturan, kombinasi lenturan keretakan dan kegagalan CFRP (*delamination*) bersama dengan lapisan konkrit bagi ricih di saper empat rentang dan kombinasi – kombinasi ricihan dan nyah-ikatan CFRP, bagi ricih rapat dengan sokong. Berdasarkan keputusan kajian ini, perubahan kepada persamaan ACI sedia ada bagi reka bentuk pemulihan rasuk *CFRP (repaired beam)* di bawah lenturan dan ricih adalah dicadangkan. Ini termasuk pengubahsuaian persamaan bagi konkrit dan keberkesanan rangkai ricih, sumbangan dari CFRP dan sumbangan dari keluli lenturan. Beban kegagalan yang diramalkan berdasarkan kepada pengubah suaian ini memberi persamaan yang lebih baik dengan keputusan ujikaji kajian ini.

ACKNOWLEDGMENT

In the name of **Allah**, the most Gracious, the most Merciful. First and foremost, all thanks and praise be to **Allah** Almighty who enabled me to complete this work.

I would like to express my deepest gratitude to my supervisor **Prof. Dr. Hashim Abdul Razak** for his valuable guidance, encouragement and help throughout the preparation of this work. His esteemed opinions on my research have been extremely helpful in successfully completing my thesis.

I also would like to express my deepest gratitude for the financial assistance provided by the University of Malaya through the fellowship scheme, the research grant RG090/10AET and the PPP fund.

Also, I express my deepest appreciation to the staff of the Department of Civil Engineering and the Faculty of Engineering of the University of Malaya for their kind assistance in my work. Their help was instrumental in me reaching my research objectives on schedule.

Special thanks to my friends and colleagues for their encouragement and help to complete this thesis. Their constructive criticism, comments and suggestions were of immense benefit to me. I regard them as my own teammates for all the insightful discussions I had with them about my research.

Finally, I wish to thank the most important people in my life; my mother, father, brothers and sisters, for their unwavering support and patience throughout the duration of my studies.

Moatasem

2012

Table of Contents

LIST OF FIGURES

LIST OF TABLES

List of Symbols and Abbreviations

φ_i mode shapes vector

W_i : weightage of mode *i*

A_f : CFRP cross section area

A_{s1} : cross section area of the main steel bars

A_{s2} : cross section area of the compression steel bars

A_v : cross section area of the stirrups bar

C : curvature

c : represent undamaged case

d : beams effective depth

D: damping ratio

d: represent damaged case

d' : effective depth of the compression steel bars

EI: flexural rigidity

f : natural frequency

f_c : compressive strength

f_f : CFRP ultimate stress

f_{s1} : stress of the main steel bars

f_{s2} *:* stress of the compression steel bars

f_v : yield stress of the vertical stirrups

K: stiffness

M : mass

Mu : ultimate moment capacity

N : total number of modes

n or *i* : is mode number

s : distance between the stirrups

V: ultimate shear capacity

V_c: shear capacity taken by concrete

V_f: shear capacity taken by CFRP sheets

V_m: shear capacity taken by the mean flexural reinforcement

V_R: ultimate shear capacity of repaired beams

V_s: shear capacity taken by stirrups

ε : strain

μ : mean value

ρ_{max} : maximum steel requirement

ρ_{min} : minimum steel requirement

σ : standard deviation

ω: Eigen value

CAP: Composite Action Phenomenon

CDF : Curvature Damage Factor

CF: Contribution Factor

CFRP: Carbon Fibre Reinforced Polymer

CMP: Combined Modal Parameter

DLA: Damage Location Algorithms

DOF: Degree of Freedoms

DSA: Damage Severity Algorithms

FD: Full Deterioration

FFT: Fast Fourier Transform

FRF: Frequency Response Function

IC: Intermediate Cracks

LSI: Local Stiffness Indicator

MAC: Modal Assurance Criterion

MCDF: Modified Curvature Damage Factor

MLSI : Modified Local Stiffness Indicator

ND: No Deterioration

PD: Partial Deterioration

PWM: Proposed Weighting Method

RC: Reinforced Concrete

RF: Reduction Factor

SAE: Statistical Anomalies Elimination

SI : Stiffness Index

SRI: Stiffness Reduction Index

TFA: Transfer Function Analysis

Chapter 1: Introduction

1.1 General

Many reinforced concrete (RC) structures, when exposed to various external loads such as earthquakes, traffic, blasts and vibrations, suffer damage and deterioration over the years. RC structures can also be subjected to damage due to internal causes or material characteristics such as corrosion of reinforcement bars, segregation of concrete materials and alkali-aggregate reactions. These can seriously affect the performance of the structural elements and can even cause structural failure. RC structures need to be monitored in order to predict any defect which may become serious and may cause a failure within their service life. RC structures that suffer from serious or less serious defects i.e. progressively serious with time, require repair so as to recover what is due to deterioration and to prevent further worsening of their condition.

Modal testing is one of the vibration analysis tools providing measurements of dynamic characteristics namely natural frequency, mode shapes and modal damping which enable designing for optimal dynamic behaviour or solving structural dynamic problems in existing designs. Modal testing was first applied around 1940 in research efforts aimed at deepening understanding of aircrafts. The modern modal testing started from 1970 upon the introduction and commercially available Fast Fourier Transform (FFT) spectrum analyzer, Transfer Function Analysis (TFA) and discrete acquisition data analysis, together with the viability of increasing smaller, less expensive and more powerful digital computers to process the data. Modal testing will be used in this study for the damage assessment of RC structures. The basic idea behind this approach is that modal parameters i.e. natural

frequency, mode shape and modal damping, are functions of physical properties of a structure namely mass, damping, and stiffness. Therefore, any change in the physical properties will cause detectable changes in the modal parameters.

Traditional repair methods, for example adding of new structural elements, steel jacketing etc., have disadvantages such as adding mass to the foundations in addition to requiring intensive labour and equipment. In recent years, new structural repair techniques using externally bonded Carbon Fibre Reinforced Polymer (CFRP) sheets have become viable alternatives to the traditional methods due to their excellent characteristics such as high strength to weight ratio, corrosion resistant and fast, easy installation. The CFRP plate bonding technology was first investigated at Swiss Federal Laboratory for Material Testing and Research (EMPA) where testes on RC beams strengthening with CFRP plates started in 1984. CFRP sheets will be used in this study for repair of the damaged RC structures.

There have been many experimental and theoretical studies to assess the use of CFRP systems for repairing RC structural elements. However, the experimental approach is still based on the conventional static load test which is time consuming, has intensive equipment and labour requirements and causes major disruptions to existing use. Modal testing provides an integrated approach i.e. both local and global characteristics can be ascertained for structural assessment. Depending on accessibility to the damage elements, little or no disruption to existing use is incurred during testing works. The approach towards structural assessment work provides not only a viable but also a robust and powerful alternative to conventional techniques. Modal testing is used in this study for the assessment of RC structures repaired with CFRP sheets.

1.2 Objectives and problem statement

The study aims to investigate the damage assessment and the CFRP repair assessment of RC structures. Following are the main objectives of the study together with the corresponding problem statement.

- Investigate the influence of the composite action of RC structures on the modal frequencies. No significant research has investigated the effect of the RC element material composition on the modal parameters. The stiffness of RC elements under various loading conditions is a function of steel and concrete behaviour, and the interaction between them. Thus, an investigation of the relationship between the dynamic and static properties of RC elements should take into consideration the behaviour of each material like concrete softening in tension, compression and shear zones, and bond action between steel bars and surrounding concrete, under different loading conditions and levels.
- Identify the source of deterioration in overall stiffness which is due to either the structural element itself or the support stiffness. No significant research has been undertaken to classify the damage source using the modal parameters. The structural element can suffer deterioration due to either being exposed to extreme loading conditions or due to the deterioration of the element materials over time. On the other hand, the supports may suffer loss in stiffness over time due to the effect of wear and tear in cases when the elastic bearing is used as isolation in bridge girders and tall buildings.
- Modify and develop more sensitive and reliable damage detection algorithms based on the existing algorithms using modal parameters established from this study. As previous

studies have shown, some of the algorithms used for detecting damage severity and location in reinforced concrete structural elements were not satisfactorily accurate and thus inadequate.

- Using modal testing as an assessment tool for the effectiveness of CFRP sheet as flexural and shear repair system and verifying it based on static data. Existing studies are still based on the conventional static load test, which is time consuming, equipment and labour intensive and causes major disruptions to existing use. Moreover, no research work has investigated the CFRP repair effectiveness in flexural and shear with various parameters. In this study, the parameters considered are maximum and minimum flexural steel ratios, with and without shear stirrups, shear damage at different locations from the supports and different pre-repair damage levels.
- Evaluation of ACI-code for flexural and shear design of the RC beams repaired with CFRP sheets. Some studies have shown that ACI Code predicted lower load capacity values than the experimental results while some studies showed that ACI Code predicted higher values.

1.3 Scope of study

In this study, the investigations will be carried on reinforced concrete (RC) beams as the structural elements specimen. The damage assessment includes monitoring the health condition of the RC beams using modal testing to evaluate the degree and location of the deterioration if it exists. If there is deterioration with specific magnitude and location and it was due to the RC beam stiffness, the damaged RC beams will be repaired using CFRP sheets. After investigating the performance of the RC beams, and repairing the existing damage, repaired RC beams will be monitored to evaluate their performance in the service

conditions. Total of sixteen RC beams will be investigated and classified into groups based on the damage scenarios and design cases as shown in Figure 1.1.

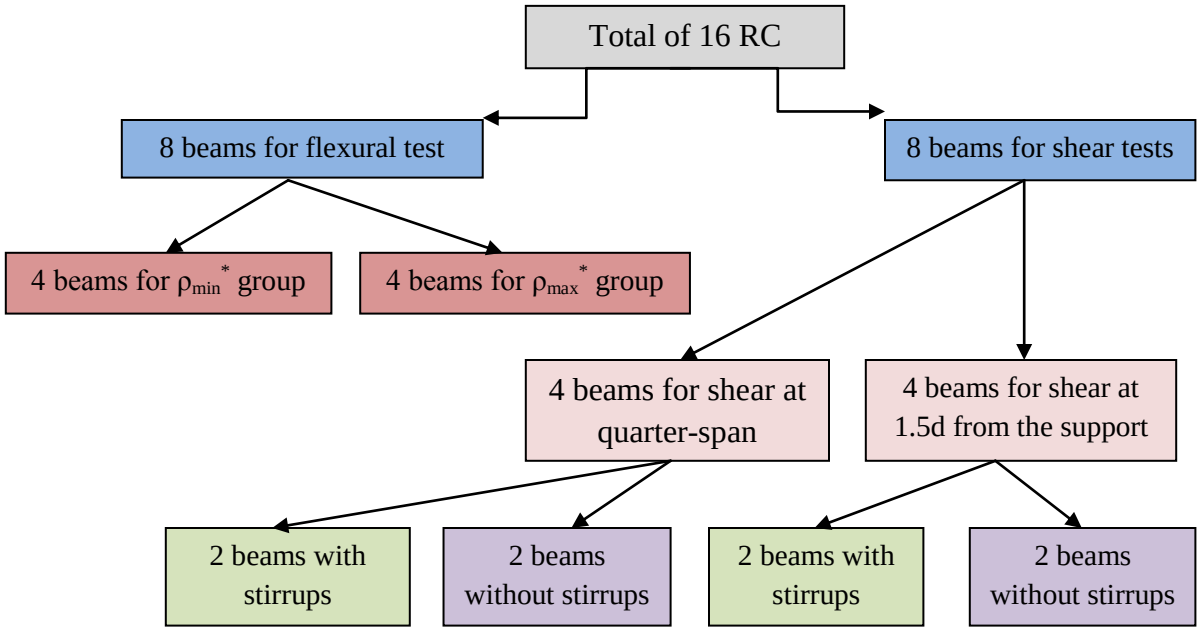

* where ρ_{min} is the minimum steel requirement and ρ_{max} is the maximum steel requirement according to code ACI-318.

Figure 1.1. Classification of the 16 RC beams used in this study

Following is the scope of the study that covers each objective.

- For the investigation of the influence of the composite action of RC structures on the modal frequencies, four damage cases are considered namely the flexural scenario with both design cases with ρ_{max} and ρ_{min}, shear scenarios with load at 1.5d from the support and at quarter-span. Static test data to be analyzed includes load against deflection, load against steel strain and residual steel strain, while dynamic data includes the modal frequencies.

- For the classification of damage type, undamaged and damaged RC beam supported on rubber bearing with various support deterioration levels i.e. no deterioration, partial deterioration and full deterioration, on both sides are used. The frequency response function, mode shape vectors and natural frequencies will be used for the evaluation.
- For modification and development of damage detection algorithms which include both damage severity and damage location algorithms, the sensitivity of the algorithms will be examined for three damage scenarios i.e. flexural, shear at 1.5d from the support and at quarter-span, and at various damage levels, starting from the first crack up to failure. The static data includes the load against deflection and the crack patterns which will be used to assess the dynamic algorithms. Moreover, the study will also propose a weighted averaging method based on mode shapes instead of normal averaging. In addition, the study will propose an elimination procedure in order to cut-off noise and anomalies that appear in the damage location algorithms.
- For the use of modal testing as an assessment tool for the effectiveness of CFRP sheets as flexural and shear repair system, various damage scenarios, design cases and pre-repair damage levels are used as shown in Figure 1.2. The modal frequencies and modal damping are used as the dynamic indicators for the evaluation of the CFRP repair effectiveness. The static data that includes the increase in the load capacity is used to assess the dynamic data. The failure modes of repaired RC beams will be discussed in detail.
- For the evaluation of the ACI Code, the comparison will be based on the ultimate capacity of the RC beams with and without externally bonded CFRP sheets. The RC beams cases mentioned in preceding paragraphs will be used for this objective.

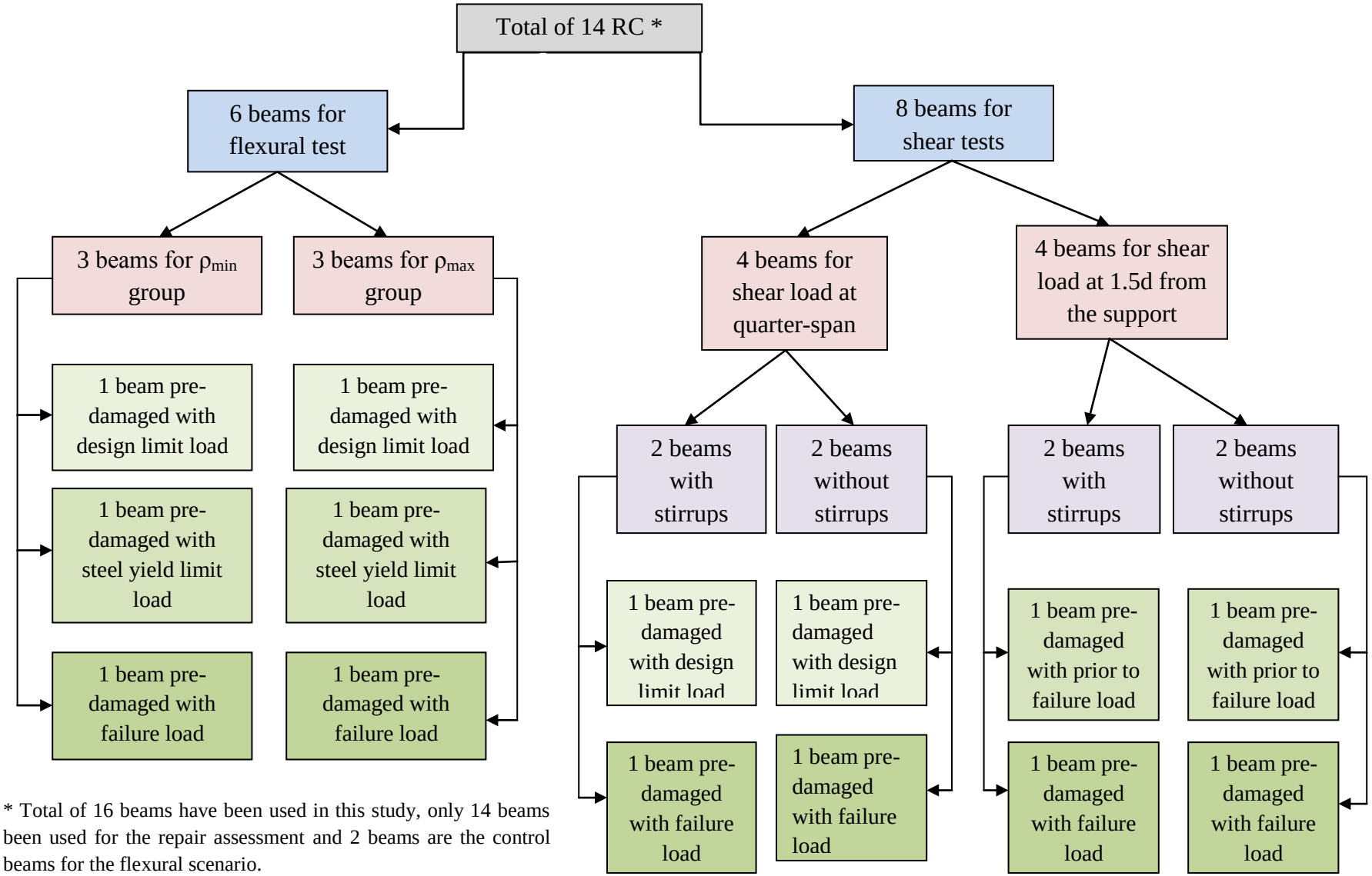

* Total of 16 beams have been used in this study, only 14 beams been used for the repair assessment and 2 beams are the control beams for the flexural scenario.

Figure 1.2. Damage scenarios, design cases and damage levels for the repair assessment

Chapter 2: Literature Review

2.1 Introduction

This chapter presents the background of the behaviour of the Reinforced Concrete (RC) material i.e. concrete and steel, at different loading and unloading conditions, in order to understand the composite action of the RC structural elements at different loading scenarios. Past and ongoing research on the support stiffness deterioration, i.e. elastic bearings for bridge girders and tall buildings, is highlighted and studies on the classification of damage source either due to the support stiffness deterioration or due to the defect of the structural element stiffness are presented. Studies on the detection of damage severity and location algorithms and procedures are presented.

Many experimental and analytical studies have been done on the strengthening of RC beams with different types of FRP. A lot of research is related to design criteria and failure modes of strengthening RC beams with FRP. This chapter presents a review on the use of the FRP plate bonding as flexural strengthening or repair system, FRP to concrete bond problems, failure modes of FRP flexural strengthening or repair system and the FRP plate as shear strengthening or repairing system and its failure modes. Moreover, the dynamic assessments of the FRP plate strengthening/repair system using modal testing are presented. Finally the equations for the calculation of the FRP plate contribution to the ultimate capacity in both flexural and shear system are covered.

2.2 Composite Actions of RC Structures

In the last two decades, investigations on the dynamic properties of structural elements have been the subject of numerous research works. The primary reason for this is the increase in awareness and interest in using dynamic testing techniques for the purposes of health monitoring and damage detection for engineering structures. The dynamic properties of any structural element are governed by the relationship of the material properties and the boundary conditions. For steel, the dynamic properties relate to steel element properties, which are assumed to be the same under different load and boundary conditions. For concrete elements, such as plain concrete, the dynamic properties are related to the behaviour of the concrete element, which will have varying behaviour under different load and boundary conditions. RC structural elements have composite effect due to the presence of different materials that form the RC elements. Therefore, in order to simplify the mechanical behaviour of RC elements, the boundary conditions are assumed to be the same under different conditions in lieu with the objective of this study.

Although many studies have been carried out in the field of mechanical behaviour of RC elements, research in this area is still ongoing due to the complexities that arise from the composite nature of the materials used (Marfia et al. 2004). Thus, any investigation on the relationship between the dynamic and static properties of RC elements should take into consideration the behaviour of each material under different conditions, the interaction between steel bar and concrete, and its influence on the overall element stiffness. When load is applied, the concrete stiffness in both tension and compression will change according to the loading levels and its behaviour under the compression or tension loading action. Cementitious materials are characterized by a softening response, which can vary depending on its strength in compression and tension. Experimental results show that these

materials exhibit brittle behaviour in tension and inelastic deformation accompanied by damage effects in compression (Marfia et al. 2004). Steel stiffness will be governed by the stress-strain relationship obtained from tensile tests. The interacting forces in the interface element between the steel and concrete elements have zero value when no load is applied but increase correspondingly when load is gradually applied to resist the slipping of the steel bar.

2.2.1 Concrete Behaviour

Concrete is a material with a hugely heterogeneous internal structure. The presence of micro-cracks in the transition zone between the cement paste and the aggregate prior to any load application can be viewed as a source of weakness in the structure of the concrete (Neville and Brooks, 1987). Some micro-cracks may develop during loading because of the difference in stiffness between the aggregate and the mortar. The gradual growth of these micro-cracks with further loading contributes to the nonlinear behaviour of concrete (Chen, 1982). Concrete can behave as either a linear or a nonlinear material depending on the nature and the level of the induced stresses. Many experimental studies on the behaviour of concrete under uniaxial and multiaxial loading have been performed in the past.

The stress-strain relationship for concrete subjected to uniaxial compression is nearly linear elastic up to about 30 percent of its maximum compressive strength (f_c). A typical curve that represents the stress-strain relationship for concrete subject to uniaxial compression is as shown in Figure 2.1. For stresses beyond this point, there is a gradual increase in curvature up to about 0.75fc to 0.9f_c, after which it bends more sharply and approaches the peak point at f_c. Beyond this peak, the stress-strain relationship has a descending trend until crushing failure occurs at some ultimate strain, ε_u, (Karsan and Jirsa, 1969). The stress level

of about 30 percent of f_c has been termed the onset of localized cracking and has been proposed as a limit of elasticity (Kotsovos and Newman, 1977).

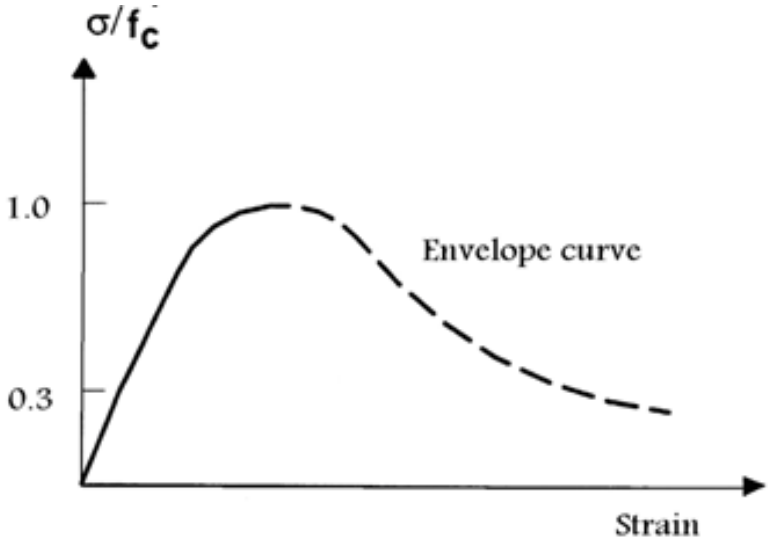

Where σ is the concrete stress and fc is the concrete compressive strength

Figure 2.1 Response of concrete to uniaxial compression (Karsan and Jirsa, 1969)

For concrete under uniaxial tensile stress, the stress-strain relationship has many similarities to that of uniaxial compression, as shown in Figure 2.2. Generally, at a stress level less than 60 percent of the tensile strength, the appearance of new micro-cracks is negligible. So, this stress level will correspond to a limit in elasticity. Beyond this level of stress, the growth of micro-cracks begins. The direction of crack propagation for uniaxial tension is transverse to the stress direction. The growth of each new crack will reduce the available load-carrying area, and this reduction causes an increase in the stresses at critical crack tips. The failure in tension is caused by a few bridging cracks rather than by a higher number of cracks, as is the case for compressive states of stress (Hughes and Chapman, 1966).

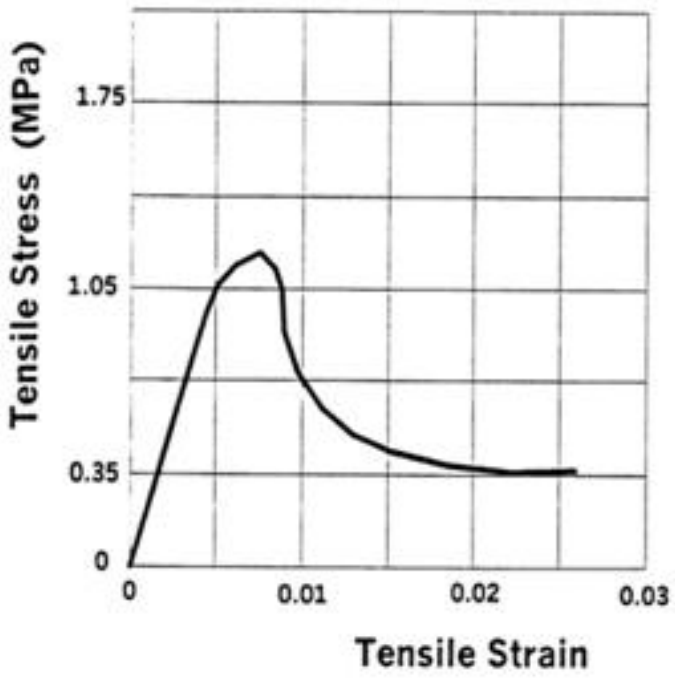

Figure 2.2 Tensile stress-strain curve of concrete (Hughes and Chapman, 1966)

Under different combinations of biaxial loading, concrete exhibits strength and stress-strain behaviour somewhat different from that under uniaxial conditions. For biaxial compression states, the maximum strength increases approximately 25 percent at a stress ratio of 0.5 and 16 percent at a stress ratio of 1.0 (Kupfer et al. 1969). Under biaxial tension, concrete exhibits a constant strength (Kupfer et al. 1969) or a slight increase in tensile strength compared to values obtained under uniaxial loading (Tasuji et al. 1978). Under biaxial compression–tension, the compressive strength decreases almost linearly as the applied tensile stress is increased.

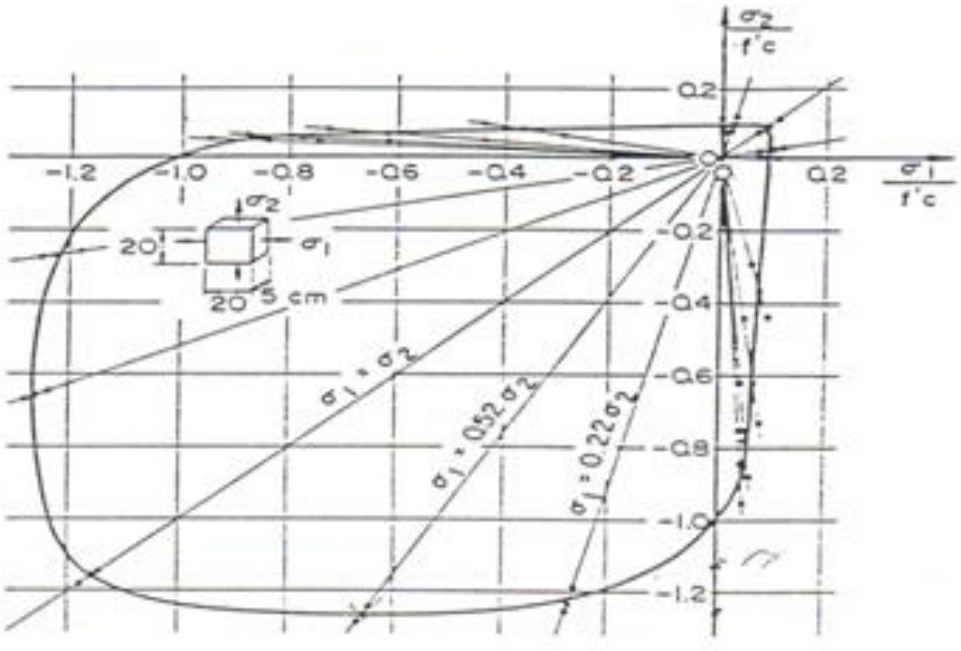

Figure 2.3 Failure envelope of concrete in biaxial stress space (Kupfer et al. 1969)

In plain and reinforced concrete structures, cracking is not a perfectly brittle phenomenon and experimental evidence shows that the tensile stresses normal to a cracking plane are gradually released as the crack width increases. For RC structures where the behaviour is characterized by the formation of many closely spaced cracks, the nature of the stress release is further complicated by the restraining effect of the reinforcing steel. After cracking, the concrete stresses drop to zero and the steel supports the full load. The concrete between the cracks, however, still carries some tensile stresses. This ability of concrete to share the tensile load with the reinforcement is termed the tension stiffening phenomenon (Chen, 1982).

The tension stiffening effect of concrete has been studied using two procedures. First, the tension portion of the concrete stress-strain curve was given a descending branch. This form of the tension-stiffening effect was first introduced by Scanlon (1971). Descending branches of many different shapes were employed, e.g., linear, bilinear, and curved shapes.

The second was to increase the steel stiffness. The additional stress in the steel represents the total tensile force carried by both the steel and the concrete between the cracks (Chen, 1982). The tension-stiffening effect plays an important role in the post-cracking behaviour (Renata and Henriette, 2008).

Several mechanisms exist by which shear is transferred across RC sections. Among these mechanisms is the shear stiffness of the un-'cracked' portion of concrete, aggregate interlocking in the crack surface (or interface shear transfer), dowel action in the reinforcement bars and the combined effect of tension in reinforcement and arching action in concrete. For the shear transfer across the cracked concrete planes crossed by reinforcement, the two major mechanisms involved are the dowel action and the aggregate interlock. Shear transfer by these two mechanisms is accompanied by slippage or relative movement of crack surfaces. In the dowel action, shear forces are partially resisted by the stiffness of reinforcing bars because slippage imposes bearing forces on the bars in the opposite direction. The aggregate inter-locking mechanism is of frictional nature. Slippage causes the irregular surfaces of the crack to separate slightly. Tensile stresses created in the steel bars by the separation of crack surfaces in turn develop into similar shear resistance (AlShaarbaf, 1990).

2.2.2 Concrete – Steel Bond Behaviour

Compared to concrete, steel is a much simpler material to represent. Its stress-strain behaviour is identical in tension and compression. The uniaxial stress-strain behaviour of reinforcement is represented by an elastic-linear work hardening model. Steel will have linear behaviour till yield. Before the yielding of steel, there is no change in steel stiffness during the unloading stage. Beyond the yield point, however, steel will exhibit nonlinear

behaviour resulting in a decrease in steel stiffness at the unloading stage (AlShaarbaf, 1990).

The fundamental role of the bond between steel and surrounding concrete through bond-slip is particularly remarkable in the cyclic behaviour of RC structures, where bond deterioration can occur due to damage caused by the load reversals. The definition of a suitable bond-slip mechanism is a widely discussed problem. The first study dates back to the sixties. Rehm (1961) showed the existence of a slip between a steel bar and concrete and the related bond action. Subsequent to this study, many experimental and numerical relationships between bond stress and slip have been proposed by Marfia et al. (2004), where the concrete – steel interface response as shown in Figure 2.4, and based on the results it was found that the tension stiffening action cannot be neglected.

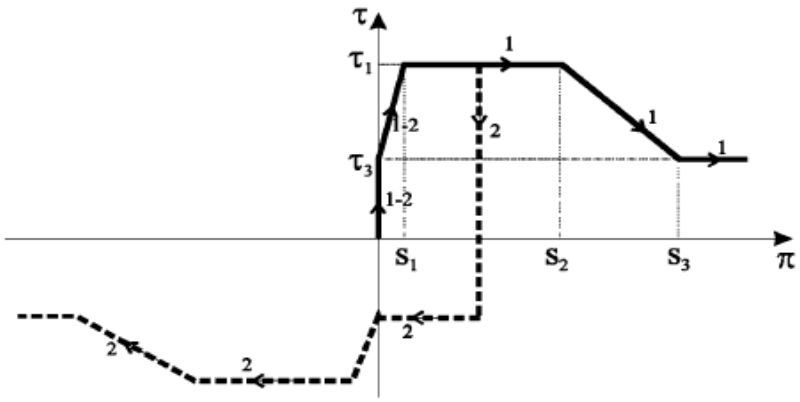

Figure 2.4. Schematic mechanical response of the concrete–steel interface (Marfia et al. 2004)

The effect of longitudinal cracks on bond behaviour was significant, for when the crack width increased two-folds, the bond strength also decreased two-folds (Lindorf et al. 2009). It is realised that the mechanical phenomena occurring at the steel–concrete interface are complex. For low values of the stress at the interface, the bond efficiency is ensured mostly by chemical adhesion; this phase can be modelled by linear elastic behaviour. For higher values of the stresses, the chemical adhesion breaks down and micro

cracks appear. When micro cracks develop into tensile cracks, tensile stress is transmitted from the steel to the concrete by means of bonding action. The stress-strain redistribution occurs along the structural elements, which in turn causes the stiffness of the element at tension zone to increase. When the applied load increases, the bonding action will increase respectively, unless slip occurs. Bonding actions are affected by many parameters, such as surrounding concrete properties and steel bar properties. Different shapes of steel bars, such as a deformed bar, will show different bonding actions compared to smooth bars, while steel bar diameters affect the interaction bonding area [Wang and Liu (2003) , Ichinose et al. (2004) , Fang et al. (2006), Wang (2009), Dahou et al. (2009), Berto et al. (2008), Haskett et al. (2008)].

2.3 Damage Identification Using Modal Parameters

Health monitoring of engineering structures has gained a lot of interest over the last few years. Many engineering structures suffer damage and deterioration when exposed to various loading and environmental changes during their lifetime. Thus, periodic inspection and testing of structural components for deterioration and damage is essential when deciding on the maintenance and repair strategies for at-risk structures. A current alternative to conventional structural testing methods is dynamic testing, which acquires modal parameters and relates these to the health status of a structure. The fundamental idea underlying the dynamic approach is that modal parameters, namely natural frequency, mode shape, and modal damping, are functions of physical properties of the structure, such as mass, damping, stiffness and the support conditions. Therefore, any change in the physical properties or support conditions will cause detectable changes in the modal parameters.

2.3.1 Support Stiffness Degradation

Several studies on the use of the modal parameters as an indicator for damage identification have been conducted. Some of these studies were concerned with issues related to use of these modal parameters in detecting the deterioration in support stiffness based on the relationship between dynamic and physical properties. Elastic bearing pads are widely used for supporting bridge girders and as base isolation of tall buildings to reduce seismic demand. The bearings are exposed to various loading conditions and environmental changes which cause deterioration of its stiffness with time. Monitoring of changes in elastic bearing stiffness is very important for ensuring timely maintenance or replacement to prevent occurrence of any serious damage to the structure. Many previous studies have used elastic bearing isolation systems to reduce seismic demand on structures, and there are numerous publications contributing to the design of these systems [Skinner et al. (1993), Naeim and Kelly (1999)]. Various types of elastic bearings have been introduced as isolation systems. A variety of isolation bearing devices have been developed and used practically for seismic design of buildings during the last 20 years in many countries. The detailed reviews on the isolation systems in bridges and buildings were reported by Kelly (1986), Buckle and Mayes (1990) and Jangid and Datta (1995). The isolation system worked by deflecting through the dynamics of the system and not by absorbing the earthquake energy (Kelly, 1997). The difference in damping of the structure and the isolation system leads to combination of motion equations and will need a complex model to analyze the system correctly (Tsai and Kelly, 1993) . The retrofit of an existing bridge by installation of bearing rubbers between the superstructure and the supporting columns was conducted by Kelly et al. (1984) and it improved the earthquake performance. The seismic response of a bridge structure with a seismic isolation

system was examined by Li (1989), Tongaonkar and Jangid (1998), Abe et al. (2000), Jangid (1996) and Adachi et al. (2000). Figure 2.5 presents the test set up used by Adachi et al. (2000). They found from the analysis that base isolation effect was present in all bridges. The isolation effectiveness was found to decrease corresponding to the increase in the flexibility of the supporting structure and vice versa.

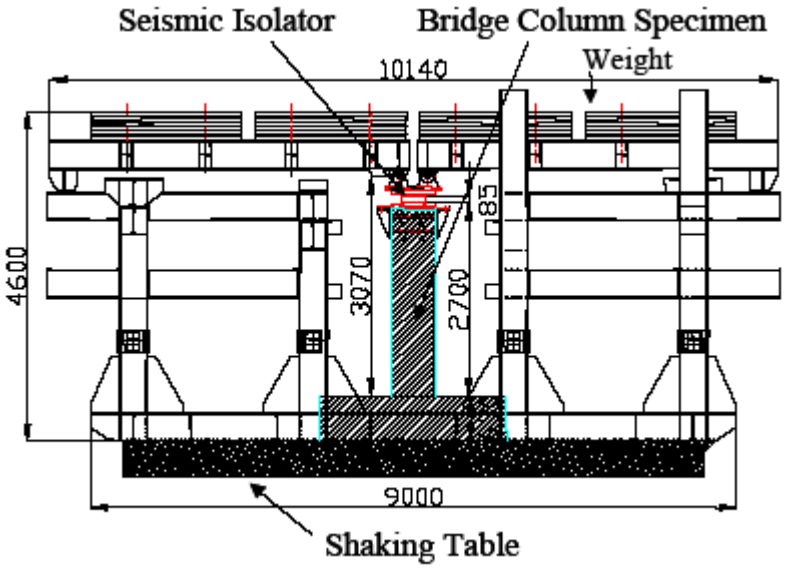

Figure 2.5. Shaking table set up (Adachi et al. 2000)

The experimental results demonstrated a substantial reduction of the seismic substructure forces in comparison to the response of the non-isolated bridge (Tsopelas et al. 1996). Isolated bridges are found to be extremely sensitive to the characteristics of the ground motion due to low redundancy and domination of the deck mode of vibration (Reinhorn et al. 1998). Force and free vibration tests were carried out on Ohito Viaduct Bridge 2, which was isolated by lead-rubber bearing (Ando et al. 1998). The frequencies were dependent on the exciting force since the amplitude reliance of equivalent stiffness isolator and the isolator stiffness were found to be dependent on the displacement

amplitude even in the linear range. A sliding type base isolation system was found to be more effective than a LRB isolation system in case a stronger earthquake affected the bridge, based on the comparison of bridge dynamic characteristics (Sugiyama, 2000). The flexibility of the bridge and reduction of the earthquake force using high damping rubber bearing was done by Iwata (2000), where bridge safety was confirmed through nonlinear dynamic analysis and a hybrid earthquake-loading test. Figure 2.6 shows the set up of the hybrid earthquake loading test.

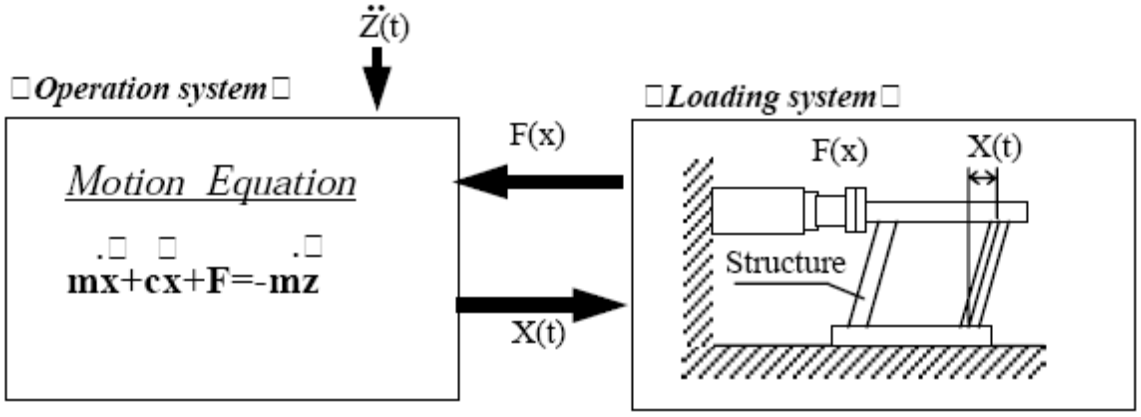

Figure 2.6. Hybrid earthquake-loading test set up (Iwata, 2000)

Some studies have also been carried out on the effect of support conditions on the dynamic properties of structures. The effect of support conditions on measured modal parameters was investigated by Wolf Jr. (1984) and Carne and Dohrmam (1998), who validated the direct relationship between the support stiffness and the measured modal parameters obtained from previous studies. The effect of the change in the support conditions, due to loading process on the vibration characteristic of rectangular plate was investigated by Souza (1994). A direct relationship was found between rubber stiffness and natural frequencies, whereby increase in rubber stiffness resulted in increase in frequency (Dai et al. 2006). All the five longitudinal natural frequencies increased corresponding to the

increase in the rubber pad stiffness and the fifth mode was the least affected by the rubber stiffness. Table 2.1 illustrated the results of the first five longitudinal natural frequencies corresponding to different rubber pads stiffness and Table 2.2 illustrated the first five transverse natural frequencies.

Carne, et al. (2007) investigated the effect of support stiffness and damping on measured modal frequencies and damping ratios using two different test models. The first model consisted of an extremely lightly damped beam that revealed changes in the measured modal frequency and damping. The second was a blade for a wind turbine, in which modal data were required to validate the analytical model of the blade. The changes in the measured modal parameters were significant and large enough that the support system was required to be taken into account when validating the analytical model of the blade. Investigation on the effect of stiffness of the supporting brace on the modal damping was done by Viola and Guidi (2009).

Table 2.1. Effect of rubber pads' stiffness on longitudinal natural frequencies (Hz) (Dai et al. 2006)

Rubber pad stiffness $*10^6$ Pa	1st	2nd	3rd	4th	5th
1	1.4	1.7	1.8	2	6.5
1.8	1.55	1.8	1.9	2.05	6.5
3	1.65	2.05	2.2	2.25	6.55
4	1.7	2.2	2.4	2.5	6.55
5	1.7	2.35	2.55	2.65	6.6
6	1.7	2.5	2.7	2.85	6.6
7	1.75	2.7	2.85	2.95	6.6
8	1.75	2,8	3	3.15	6.6
9	1.75	2.9	3.1	3.25	6.65
10	1.75	3	3.25	3.4	6.65

Table 2.2. Effect of rubber pads' stiffness on transverse natural frequencies (Hz) (Dai et al. 2006)

Rubber pad stiffness $*10^6$ Pa	1st	2nd	3rd	4th	5th
1	0.45	1.7	4.3	5.2	7.6
1.8	0.55	1.75	4.3	5.25	7.6
3	0.7	1.8	4.25	5.35	7.65
4	0.75	1,8	4.3	5.45	7.65
5	0.85	1.85	4.35	5.5	7.7
6	0.9	1.85	4.3	5.65	7.7
7	0.95	1.9	4.3	5.7	7.73
8	1	1.9	4.3	5.8	7.75
9	1.05	1.95	4.35	5.85	7.75
10	1.05	1.95	4.3	5.9	7.8

2.3.2 Element Stiffness Degradation and Damage Algorithms

Inspection of structural components for damage is essential in decision making on the maintenance of structures. Dynamic testing has become an increasingly popular and important tool in structural health monitoring with the purpose of identifying damage. Damage inspection of structures is important in order to come up with a planned strategy for repair and maintenance works. Numerous research works have been published in the field of damage detection and a variety of methods has been developed and proposed.

Vibration test has been used for damage detection since 1970s and early 1980s by the offshore oil industry [Vandiver (1975); Begg et al. (1976); Coppolino and Rubin (1980)]. Cracks on main structural elements can be a major cause of concern since they can lead to structural failure. Thus, early crack detection is crucial in order to avoid sudden failure especially when there is the likelihood of overloading on the structure. Since the measuring of natural frequency is easier than that of change in structural damping, change can be detected from dynamic analysis using natural frequency and mode shapes.

Classification for damage identification is defined at four levels with increasing difficulty of determination namely detection of presence of damage, quantification of severity, locating damage position and prediction of the remaining service life of the structure (Rytter, 1993). To date, vibration-based damage identification methods applied to civil engineering structural elements provide for the first two levels of damage identification with sufficient degree of reliability.

A considerable number of researchers have used the change in the natural frequencies for damage detection (Salawu, 1997). From previous studies, it is observed that the effect on natural frequency when damage occurs in a structure is often of relatively low sensitivity. The alternative to using natural frequency as damage identification is by using mode shape, where Modal Assurance Criteria (MAC) is used to determine the level of correlation between modes from the undamaged and damaged cases (Doebling et al. 1998). MAC was first used by West (1984) to locate the structural damage without the use of prior finite element model. The concept of curvature mode shape was introduced by Pandey et al. (1991). It was demonstrated that the modal curvature was a much more sensitive damage indicator than the Modal Assurance Criteria (MAC) or CO-ordinate Modal Assurance Criteria (COMAC) values. This approach was extended by Ratcliffe (1997) using both analytical and experimental results of the curvature of a damaged beam without need of a priori knowledge of the undamaged state. It was found that the 1st frequency was more sensitive than the higher mode frequencies. Damage index method to locate the damage without the need to baseline data was developed by Stubbs and Kim (1996). Modal parameters of lower modes were found to have satisfactory precision in detecting the crack position and depth (Ruotolo and Surace, 1997). The change in curvature of mode shape to locate the damage shows higher sensitivity compared to the mode shape itself (Abdul Wahab and De Roeck, 1999).

Dynamic stiffness based on the experimental frequencies and mode shapes was used to detect the damage location and severity. It was found that at the ultimate damage state of the RC beam, the reduction in the stiffness was only 50%. On the other hand it was found that in order to get higher sensitivity in locating the damage, a dense measurement grid is required to calculate an accurate curvature for the higher modes (Maeck and De Roeck, 1999). Table 2.3 presents the adopted load steps for the tested beam and Figure 2.7 shows the corresponding crack pattern to each load step. When the dynamic bending stiffness based on modal parameters was used to detect the damage position and severity, it was found that the frequencies reduced by 27% when full damage occurred, which is equivalent to dynamic bending stiffness reducing to about 60%. The first frequency was the more sensitive one and the third mode was the less sensitive one. It was found that the mode shapes need to be obtained with a sufficient accuracy in order to be used for calculating the curvature. The stiffness showed increase in some cases after damage was induced, which justified the tension stiffening and it thus could not be neglected as stated by (Maeck et al., 2000). Figure 2.8 presents the stiffness degradation as detected using the mode shape curvature.

Table 2.3. Load steps (Maeck and De Roeck, 1999)

Load steps	Load (kN)
Step 0(reference)	0
Step 1	4
Step 2	6
Step 3	12
Step 4	18
Step 5	24
Step 6	25.4 (failure)

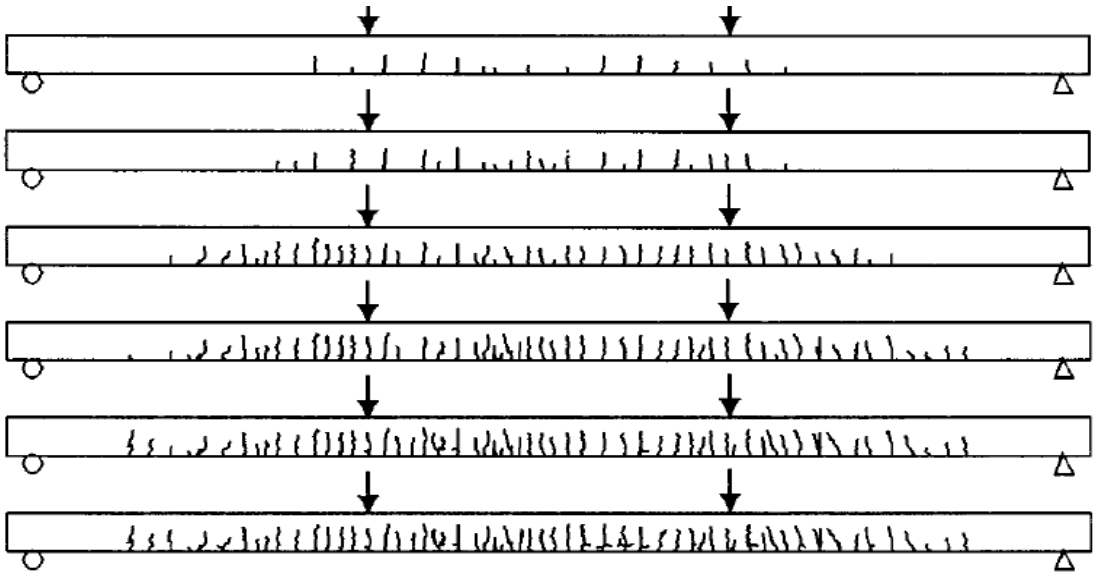

Figure 2.7. Crack pattern corresponding to six load steps (Maeck and De Roeck, 1999)

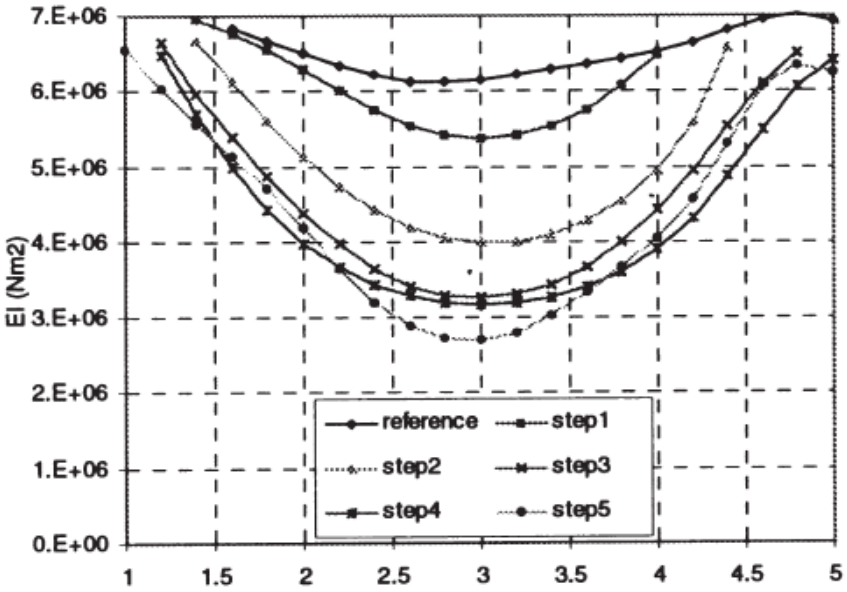

Figure 2.8. Dynamic stiffness degradation for first bending mode (Maeck et al., 2000)

The natural frequencies were used to detect the crack location and depth and were found to be able to predict the crack size with an error of 25% and the location with an error of 12%. (Lee and Chung, 2000). Natural frequencies and mode shapes were found to be useful in

detecting the existence of the damage, while MAC and COMAC were not useful for locating the damage (Alampalli, 2000). The trend in the natural frequencies was found to be sensitive to the corrosion deterioration state of RC beams (Abdul Razak and Choi, 2001), while damping changes were inconsistent (Kato and Shimida, 1986), (Salawu and Williams, 1995). Figure 2.9 presents the effect of the corrosion levels on the natural frequencies as found by (Abdul Razak and Choi, 2001).

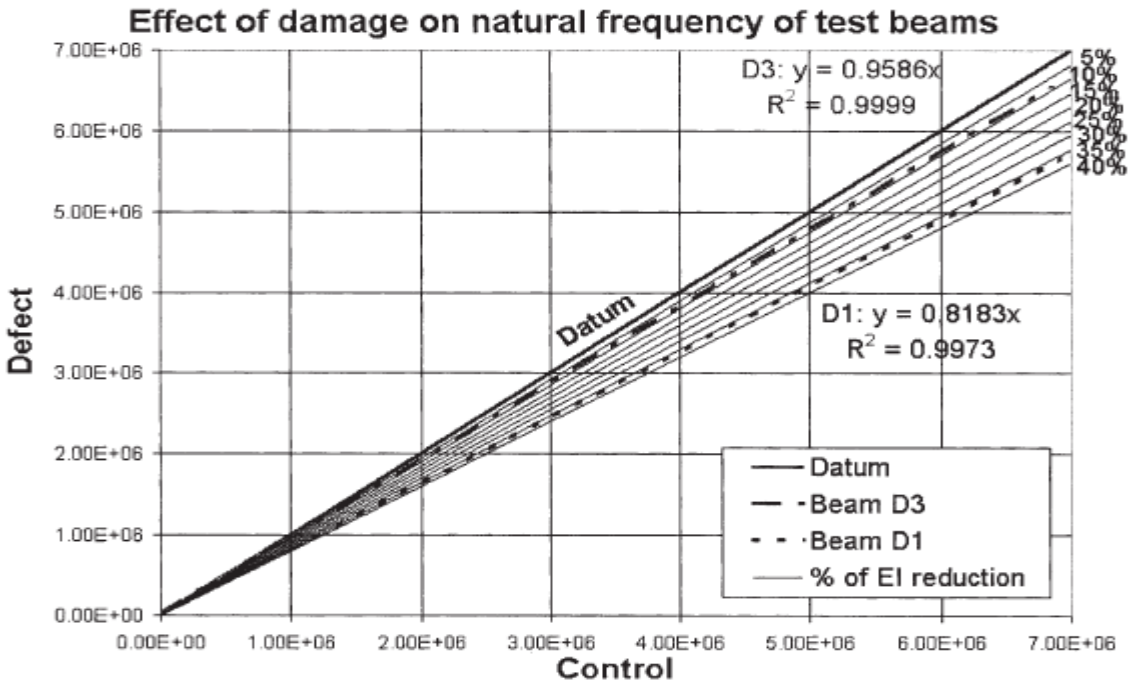

Figure 2.9. Effect of steel corrosion on natural frequency (Abdul Razak and Choi, 2001)

The increase in the number of cracks was found to reduce all natural frequencies (Khiem & Lien, 2001). Mode shapes were used to locate the damage in 3-D type structure and it was found that the use of several modes could result in better sensitivity. The proposed method was found to be significantly affected by noise especially for the small damage cases (Park and Kim, 2002).

Frequencies were found to be affected by the loading configuration, either symmetrical or asymmetrical, with odd modes more affected by the symmetrical configuration and the

even modes more affected by the asymmetrical configuration. The MAC factor was found to be less sensitive than frequencies, but it gave an indication of the symmetrical or asymmetrical nature of damage. It was also found that there was a difficulty in locating the damage in RC beams due to the fact that in RC beams the cracks are not only limited in the zone where the load is applied but spreads over a certain distance on both sides of the loaded zone (Ndambi et al. 2002)

Modal parameters were used to detect damage severity and location and it was found that they had low sensitivity to detection of damage location or they would detect the wrong location. They also underestimated the damage severity compared to the actual damage size (Kim and Stunns, 2002). Modal parameters turned out as good indicators using developed direct stiffness calculation to assess damage in RC structures from experimental natural frequencies, mode shapes and their derivatives (Johan, 2003). The case when few frequencies or mode shapes are available were investigated to detect the damage location and severity by use of either frequency or mode shape and both parameters were found to be able to detect the damage location with small error and were accurate in detecting the damage severity when it was located at mid-span but less accurate for damage at quarter-span (Kim et al. 2003). Figure 2.10 shows the results of the damage index for detecting of damage location found by (Kim et al. 2003).

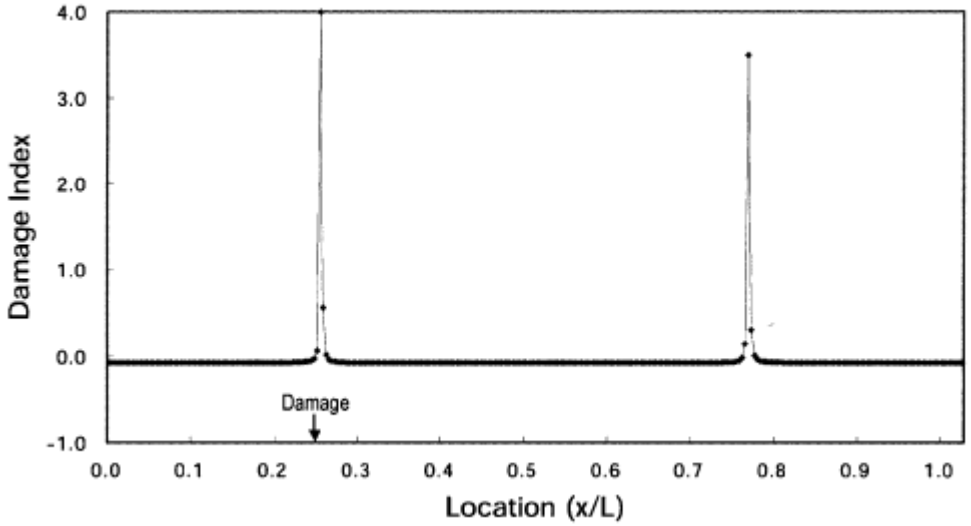

Figure 2.10. Damage localization results of FBDD method: damage case CL2 (Kim et al. 2003)

Natural frequencies have been used for detecting locations and sizes of multi cracks and they were found to be within an error of 15% compared to the actual locations and size (Patil and Maiti, 2003). Mode shapes curvature were found to be better in sensitivity to detect the damage location than the mode shape itself and lower modes had higher sensitivity than higher modes. On the other hand, an adequate number of mode shapes are required to detect multi cracks with higher accuracy (Dutta and Talukdar, 2004). The investigation by Douka et al. (2004) found a shift in the anti resonances of the cracked beam depending on the location and size of the cracks, which can be used as an additional information carrier for crack identification in a beam with cracks at two locations.

The intersection of the normalized frequency contours, in terms of normalized crack depth and location, with the constant natural frequencies planes was used to detect the crack location and depth. It was found that both location and depth of the cracks have a significant effect on the first and second natural frequencies, and the effect decrease as the cracks get closer to the support. Moreover, higher modes can give better accuracy for locating the damage (Nahvi and Jabbari, 2005). The number of required measured

frequencies was found to be equal to twice the number of cracks and was seen to be adequate in predicting the location of the multi-crack cases (Patil and Maiti, 2005). The instantaneous frequency was found to oscillate between frequencies corresponding to the open and close of the crack. The variation of the instantaneous frequency increases with increasing crack depth following a polynomial law and consequently can be used for estimation of crack size (Loutridis et al. 2005). Time domain method in which the parameters of a crack in a structural member were identified from strain or displacement measurement was proposed and the method was found to be effective for identifying the crack parameters with a certain degree of accuracy (Law and Lu, 2005). The natural frequencies were found to decrease to a larger extent as the crack size increased, and the change varied based on the location of the crack and the mode number (Choubey et al. 2006).

Local Stiffness Indicator (LSI) was proposed to detect damage location and was obtained by applying the fourth order centered finite difference formula to the regressed mode shape data, with no baseline data required. The algorithm was found to have higher intensity at the location of the actual crack, while higher intensity was also detected always at the supports which implied that the algorithm could not be used for detecting damage located near the support (Ismail et al. 2006). Figure 2.11 presents the results of the LSI algorithm (λ^4) found by (Ismail et al. 2006).

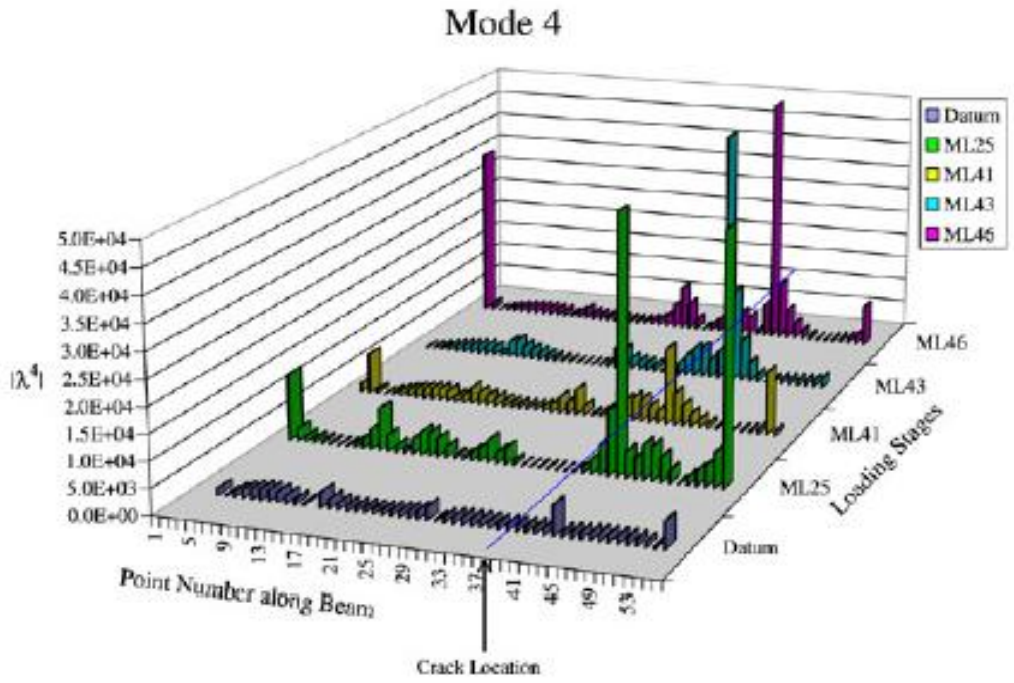

Figure 2.11 Location of damage for beam with load induced crack at 0.7L (Ismail et al. 2006)

The change in the natural frequencies is a function of the crack length and its location and also depends on the mode shapes (Choubey et al. 2006). The crack locations and sizes notably influence the natural frequencies and mode shapes of a cracked stepped beams especially when the cracks are located at the step parts of the beams (Kisaa and Gurelb, 2007). The structure becomes weaker than its previous condition when the crack size increases with time (Orhan, 2007). The effect of the temperature variation on the natural frequencies was evident (Kim et al. 2007).

COMAC and flexibility methods were found to be able to detect some damage locations but they also made some false identification (Xia et al. 2007). It was also found that the accelerometer could detect the damage if it was placed within less than 300mm from the actual damage location (Xia et al. 2007).

Lower modes were used to detect the damage location and severity, and it was found that the mode shapes are less sensitive for detecting damage while the modal damping is highly sensitive although inconsistent (Perera et al. 2008). The damping was found to be more sensitive to appearance of structural damage, while its statistical variations were more than that for natural frequencies (Guradelli et al. 2008). Modal flexibility for which the curvature is calculated from the deflected shapes instead of using modal vectors were investigated, and it was found that calculating the curvature needs very dense sensor resolution and the environmental effect on the data has to be eliminated (Catbas et al. 2008). Crack position and size was detected using the peak values on the irregularity profile of mode shapes, with the method being easily calculable and not requiring the datum data of the structure. The only disadvantage was that it required use of many sensors in order to get high accuracy mode shapes (Wang and Qiao, 2008). Investigation for some existing algorithm for location of damage based on mode shape curvature revealed that it was able to detect single crack while failed in detecting multiple cracks. Damage assessment of flexural members had been developed by Shih et al. (2009), where a multi criteria approach was applied. Results showed that the proposed multi-criteria method incorporating modal flexibility and modal strain energy method is effective in multiple damage assessment in beam and plate structures.

A modification was proposed and it was found that gave reasonable sensitivity but still needed to be improved (Choi et al. 2008). Measured natural frequencies were used in term of equal-eigen-value-change contours plotting between pairs of different frequencies for damage detection, and it was found that the first and third nodes are sufficient to get information regarding the damage extent and magnitude (Sathishkumar and Murthy, 2010). Modal identification errors influenced the sensitivity of the damage detection algorithms and it was found that when erroneous modals were used, it was better to use more than one algorithm for better sensitivity (Tomaszewska, 2010). Erroneous conclusion of damage detection algorithms can be a result of the effect of environmental conditions on the structural parameters (Limongelli, 2010). The dynamic behaviour of damaged structural

element was seen to change with the level of the excitation force, which could be used for damage detection. In the case of fine frequency and dense sensor resolutions, there is no need of the datum data (Kim and Lee, 2010). A new damage detection method based on the natural frequencies and the mode shape was proposed and proved as a good indicator that needed only the natural frequencies from the undamaged cas (Radzieński et al. 2011). The slope of the first mode shape was used for damage detection and it showed good results, the only concern being that the error in identifying the mode shape could cause an error in the damage detection results (Zhua et al. 2011). Fundamental mode shape and static deflection were used for damage detection and were found to have good sensitivity (Cao et al. 2011).

2.4 Flexural strengthening or repair system

Research on the use of FRP began in Europe in the 1960s (Bakis et al. 2002). The first investigation on the use of FRP plate bonding was at Swiss Fedral Laboratory for Materials Testing and Research (EMPA) in 1984 (Teng et al. 2002). FRP materials have the advantage of high tensile strength and excellent corrosion resistance, fatigue resistance, good performance at elevated temperatures, low density, and high specific stiffness and strength [Meier (1992); Almakt et al. (1998)].

Most research on using FRP plate bonding for flexural strengthening was carried out in the last decade [Ritchie et al. (1991); Saadatmanesh et al. (1991); Triantafillou et al. (1992)]. There has been tremendous growth in recent years as result of increasing global needs for structural performance improving and retrofitting works. Three schemes exist for the adhesion of FRP plates to the RC beams soffit namely adhesive bonding of prefabricated FRP plate, wet lay-up and resin infusion. The use of the bonded prefabricated FRP plate was found to ensure the highest degree of material uniformity and quality control

[Saadatmanesh et al. (1991); Quantrill et al. (1996); Ross et al. (1999)]. The wet lay-up method gives greatest flexibility for field use and is cheapest, while it is sensitive to unevenness of the beam soffit which can lead to debonding [Meier (1995); Karbhari and Zhao (1998)]. The resin infusion has similar characteristics to those of the wet lay-up but it is used less [Varastehpour and Hamelin (1997); Karbhari and Zhao (1998)]. The end anchorage prevents plate end debonding and can be bonded or bolted (Ritchie et al. 1991). The use of the end anchorage was found to at least delay the plate end debonding [Sharif et al. (1994);Garden and Hollaway (1998)]. Proper design of the anchorage system can increase the load capacity by up to 70% (Spadea et al. 1998). The CFRP strain reached 50% of its ultimate capacity without anchorage while it reached 86% of its ultimate capacity when the anchorage system was used (Spadea et al. 1998). More studies are required for better understanding of the effect in the anchorage regions of the FRP plates (Büyüköztürk and Hearing 1998).

CFRP plates were found to increase the flexural capacity within certain limits (Almakt et al. 1998). Externally bonded CFRP plates were found to perform well under the effect of impact loading (Erki and Meier 1999). Adding of anchoring system at the end of the plates can improve the impact performance of the strengthened beam (Erki and Meier 1999). Repair of a real bridge with externally bonded FRP plates was found to decrease the flexural stresses in the steel reinforcements and the mid-span deflection (Stallings et al. 2000). Strengthening of concrete beams with externally bonded FRP plates was found to increase the ultimate capacity by 70% and reduce the size and the density of the cracks along the beam length (Fanning and Kelly 2001). Significant increase in the ultimate capacity was observed after adding the externally bonded CFRP sheets (Nguyen et al. 2001). Ultimate capacity of strengthened beams increased by up to 230% and even for the

preloaded beam before strengthening, the ultimate capacity significantly increased which indicates good performance for repair situations (Rahimi and Hutchinson 2001). The magnitude of the increase in the ultimate capacity is related to the amount of the tensile and shear steel reinforcement and the properties of the concrete cover (Rahimi and Hutchinson 2001). Externally bonded CFRP sheets were found to enhance the performance and increase the capacity of the concrete beams under extreme loading and the magnitude of the increase in the ultimate capacity depends on the CFRP amount, steel reinforcement and failure mode (White et al. 2001).

Strengthening of corroded RC beams with externally bonded CFRP plates was found to increase the ultimate capacity by 37% to 87% (Masoud et al. 2001). Strengthening of the RC beam with one layer of the CFRP plate was found to increase the ultimate capacity by 200% and strengthening with two layers increased it by 250% (Capozucca and Cerri 2002). Figure 2.12 presents the comparison between experimental and theoretical results of the ultimate moment capacity of the strengthened and un-strengthened beams.

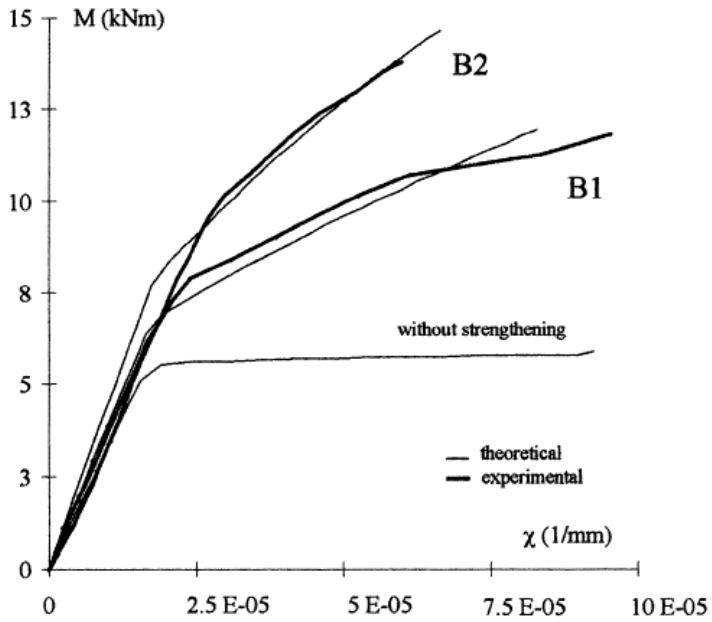

Figure 2.12. Comparison between theoretical and experimental moment against curvature diagrams (Capozucca and Cerri, 2002)

Strengthening of cracked bridge capping beams with externally bonded FRP sheets reduced the stresses of the steel reinforcement at the positive and negative moment regions and the location of the neutral axis at the positive moment region shifted downward (Hag-Elsafi et al. 2002). A state of the art review for the application of the FRP plates in construction was done by Bakis et al. (2002). Use of CFRP plates for repair of damaged prestress bridge girders restored a portion of the lost flexural stiffness and reduced the mid-span deflection (Klaiber et al. 2003). Repairing of corroded concrete beams with externally bonded CFRP sheets was found to increase the load capacity up to 30% (Kutarba, 2004).

Use of FRP sheets for repair of blast damaged RC beams showed significant improvement in its flexural stiffness over the unrepaired beams and even exceeded the undamaged beams (Hudson and Darwin, 2005). CFRP laminate for strengthening of RC beams showed the ability for doubling the load capacity with deflection close to that of the un-strengthened beams [Barros and Fortes (2005); Barros et al. (2006)]. The load capacity of the strengthened beams can increase if monolithic action exists between the beam and the FRP plates, and this can be achieved by using either chemical bonding material, epoxy resin, or mechanical shear connectors (Jumaat and Ashraful-Alam, 2006). The premature plate end debonding was found to be the major problem of using FRP plates for strengthening of RC beams and using proper end anchorage can prevent such failure (Jumaat and Ashraful-Alam, 2006). Repairing of impact damaged prestress concrete bridge girders with externally bonded CFRP sheets showed improvement in the capacity and even surpassed the capacity of the undamaged girders (Miller, 2006). CFRP sheets showed good ability to restore the ultimate capacity and even increase it, regardless of the pre-repair damage level and the concrete grade. Even when failure occurred as interfacial debonding it was possible to proceed with further CFRP replacement (Benjeddou et al. 2007). Figure 2.13 presents the

load against deflection curves corresponding to pre-repair damage levels as found by (Benjeddou et al. 2007).

Strengthening with wet lay-up based fabric strips showed strength enhancement of 73% and the strengthening with pultruded strips showed enhancement of 59% (Ghosh and Karbhari, 2007). Use of CFRP sheets for strengthening of RC beams could increase the strength up to 220% and significantly reduce the deflection (Decker, 2007). Retrofitting of bridge subjected to overload using CFRP sheets was conducted and significant increase in the bending stiffness was noticed at the ultimate limit state with relatively small increase at the service load levels. Moreover the cracks were monitored for any movement and there was none after almost three years later (Choo et al. 2007). Increasing the prestressing of the CFRP rod used for strengthening of RC beams resulted in increase in the flexural capacity but reduced the ductility (Badawi and Soudki, 2009). Use of CFRP sheets for repair of steel beams of steel-concrete composite girders increased the flexural strength by 51% (Fam et al. 2009).

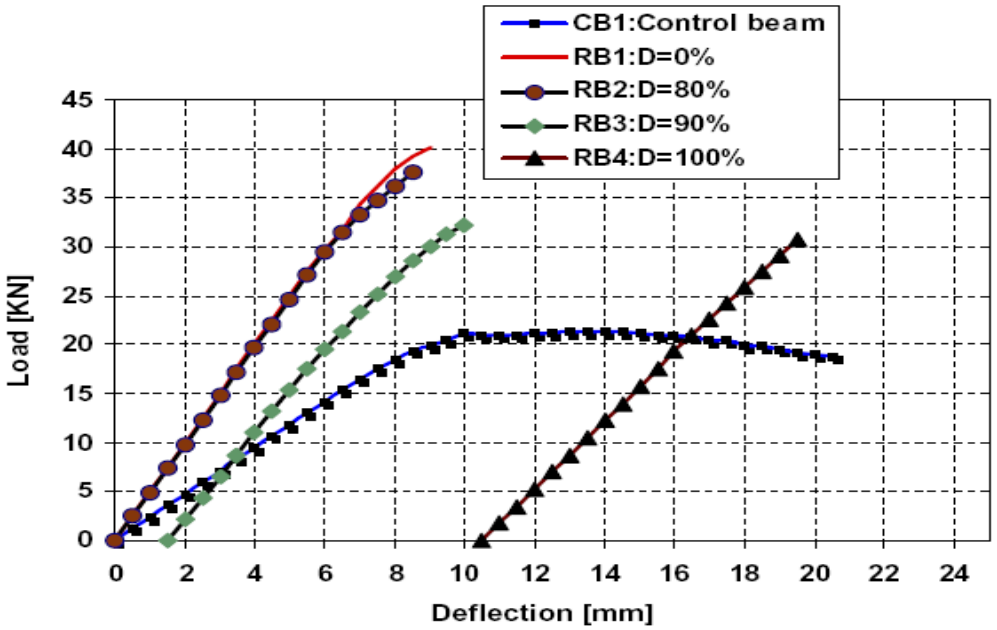

Figure 2.13. Load versus deflection curves for beams with different damage degree (Benjeddou et al. 2007)

Repair of corroded RC beams with bonded CFRP sheets restored the undamaged state stiffness and reduced the ultimate deflection compared to the un-strengthening beams (Al-Saidy et al. 2010). Use of CFRP sheets with U-shape anchorage can increase the capacity of the strengthened RC beam up to 10% to 24% depending on the number of the U-shape anchored along the beam length (El-Ghandour, 2011). Repair of damaged steel beams with CFRP sheets increased the ultimate capacity up to 22.5% and the pre-repair levels did not affect the strain development in the CFRP sheets while it did affect the debonding progression of the sheet (Kim and Brunell, 2011). CFRP plates were found to be unaffected by the change in the environmental conditions due to superior quality control during the manufacturing, while hand laid-up CFRP fabric was affected by the elevated temperature (Cromwell et al. 2011).

2.4.1 Failure modes

Based on early studies in the last decade on the use of the bonded FRP plates to beam soffit as flexural system, a number of failure modes have been observed. These modes can be generally classified as 1) flexural failure by FRP rapture, 2) flexural failure by crushing of concrete at compression, 3) shear failure, 4) concrete cover separation, 5) plate end interfacial debonding, 6) intermediate flexural crack induced interfacial debonding and 7) intermediate flexural shear crack induced interfacial debonding as shown in Figure 2.14 [Ritchie et al. (1991); Saadatmanesh and Ehsani (1991); Triantafillou and Plevris (1992); Sharif et al. (1994); Chajes et al. (1994); Heffernan and Erik (1996); Arduini and Nanni (1997); Ross et al. (1999); Bonacci and Maalej (2000)]. Proper design of the anchorage system can transfer the failure mode from brittle failure, explosive CFRP debonding, to ductile failure (Spadea et al. 1998). Shear and stress concentration at the cut-off point of the FRP plate and also the flexural cracks can lead to failure mode such as the plate peeling,

plate debonding, or local failure in the concrete layer between the FRP plate and longitudinal reinforcements (Almakt et al. 1998). Strengthened beams with CFRP plates fail by CFRP debonding under the effect of impact loading, and the use of the anchorage system prevents such failure (Erki and Meier, 1999). The maximum and minimum limits of the FRP plate for flexural strengthening have been established to ensure ductile behaviour of the strengthened concrete beam (El-Mihilmy and Tedesco, 2000). Strengthening of concrete beams with externally bonded FRP plates was found to fail by plate peel-off and the plate strain reached a strain rate of 5000 to 6000 μst (Fanning and Kelly, 2001). Three brittle failure modes were observed for beams strengthened with externally bonded CFRP sheets namely ripping of concrete, premature shear failure and hybrid mode as a combination of modes 1 and 2 (Nguyen et al. 2001).

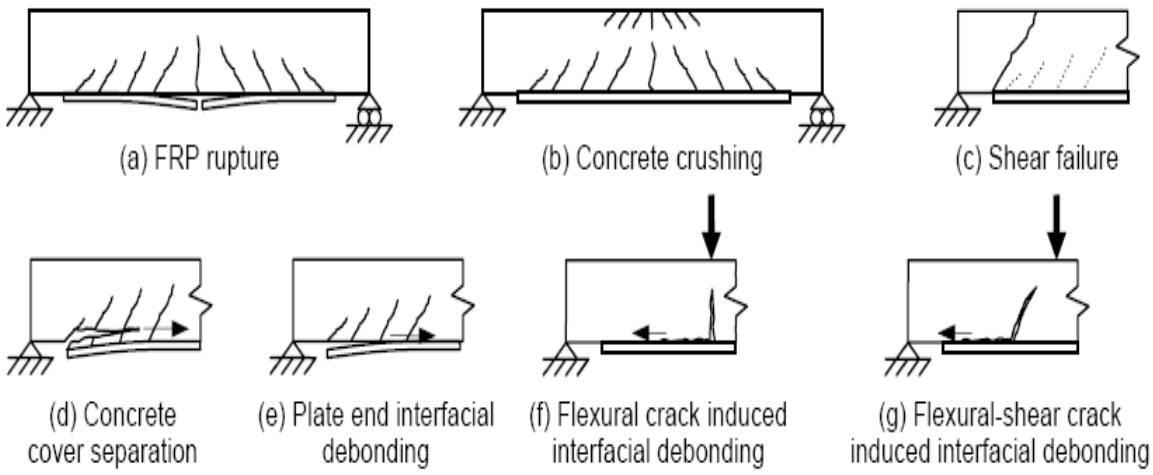

Figure 2.14. Failure modes of FRP flexural strengthening or repair

Externally bonded FRP plate for strengthening of concrete beam was found to fail as concrete cover failure with plate detachment at the point of the applied load within the shear span of the beam, and it moved towards the plate end with increase in the plate thickness (Rahimi and Hutchinson, 2001). The normal and shear stresses at the plate end

were found to increase with increase in the plate thickness (Rahimi and Hutchinson, 2001). The CFRP strain at the mid-span reached about 6000 to 7000 μst prior to failure, and the observed failure modes were bond splitting and plate peeling (White et al. 2001). More investigation is required for the local debonding around the flexural cracks and its effect on the efficiency of the resisting tensile stress (Malek and Patel, 2002). The observed mode of failure was detachment of concrete layer at the beam soffit, with maximum CFRP strain of 62% to 92% of its ultimate strain [Barros and Fortes, 2005; Barros et al. (2006)]. Repair of damaged RC beams with bonded CFRP sheets showed two main failure modes i.e. peeling off and interfacial debonding. It depended only on the sheet width, with a change from interfacial debonding to peeling off when the CFRP sheet width increased from 50mm to 100mm (Benjeddou et al. 2007). Flexural failure with FRP debonding was the main mode of failure observed by (Ghosh and Karbhari, 2007). Use of U-wraps allowed the FRP plates to reach fail capacity and fail in rupture (Decker, 2007). Prestressing of CFRP rods used for strengthening of RC beams can result in CFRP rupture failure (Badawi and Soudki, 2009). Use of CFRP sheets for repairing steel beams of steel-concrete composite girders results in CFRP debonding failure (Fam et al. 2009).

Use of U-shape CFRP anchored, for CFRP repair system of corroded RC structures, shifted the failure mode from CFRP debonding to CFRP rupture (Al-Saidy et al. 2010). Use of CFRP sheets with U-shape anchorage results in CFRP rupture failure mode, while increasing the number of the U-shape anchorage can shift the failure mode to combined flexural-shear mode (El-Ghandour, 2011). Stress concentration at the damage region prior to repair of steel beams with CFRP sheets results in local debonding failure (Kim and Brunell, 2011). Strengthened RC beam with externally bonded CFRP plate failed with

intermediate crack debonding while use of the GFRP fabric leading to failure with a GFRP rupture (Cromwell et al. 2011).

2.4.2 Concrete - FRP bond behaviour

A significant number of experimental and analytical works have been done in the last decade on the bond strength and behaviour of FRP plate to concrete interface. The experimental work was carried out using single shear test, double shear test or modified beam test [Van Gemer (1980); Swamy et al. (1986); Täljsten (1994); Ziraba et al. (1995); Chajes et al. (1996)]. The bond strength was found to be limited and could not always increase with increase in the bond length. This means the ultimate tensile strength of the FRP plate may never be reached regardless of the length on bond area. This lead to the concept of effective bond length beyond which there is no increase in bond strength [Täljsten (1994); Chajes et al. (1996); Yuan et al. (2001); Maeda et al. (1997); Yaun and Wu (1999)]. Most of the FRP/concrete joints were found to fail by crack propagation in the concrete adjacent to the adhesive-concrete interface, starting from the critically stressed position (Chen and Teng, 2001). The increase in the plate thickness was found to increase the bond stress along the interface between the externally bonded FRP plate and the concrete. The ratio of the plate width to the plate thickness was very significant in influencing the bond stresses at the plate end (Etman and Beeby, 2000). The treatment of the concrete surface with water jet showed better bond strength than ordinary sanding treatment as shown in Figure 2.15. (Toutanji and Ortiz, 2001).

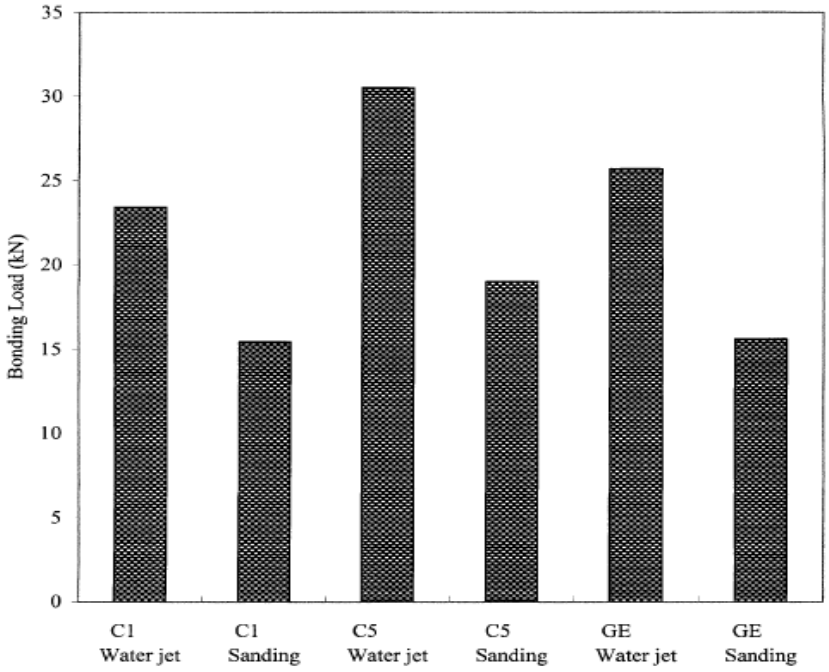

Figure 2.15. Comparison of bonding strength between using water jet and sanding treatment for the concrete surface (Toutanji and Ortiz, 2001)

Distribution of bond stress between FRP plate and concrete is non-uniform and the flexural bond development length is three times the effective bond length (Xiao et al. 2004). The bond between FRP plate and concrete is complex and involves a number of interacting parameters. It depends on the FRP geometrical and mechanical properties, concrete compressive strength and the ratio between FRP and concrete width (Pellegrino et al. 2005). The bond strength was controlled by the ultimate strain of the visco-elastic interface layer, and the anchoring mechanism of FRP sheets into concrete by FRP rod increased the capacity of the section and the anchoring strength depend on the concrete strength (Huang and Chen, 2005). The bond capacity has little correlation to the concrete compressive and tensile strength, while it is related to concrete surface tensile strength and aggregate content (Leung and Pan, 2005). The de-bonding in reinforced concrete prisms, retrofitted with bonded FRP plate was always caused due to the initiation of the cracks in the surrounding

area of the most stressed end (Sharma et al. 2006)**.** The tensile strength of the plate has an effect on both the ultimate bond strength and critical bond length as determined from the tests (Sharma et al. 2006). Wang (2006) established a bond-slip model to study the interface de-bonding induced by flexural cracks in FRP-Plated concrete beams and the cohesive zone model was established to analyze the intermediate crack debonding failure of FRP plated concrete beams. Ultimate load of bonded interface increases with the bond length before achieving the effective length and remains constant beyond that (Teng et al. 2006). The inclusion of the adhered shear deformations in RC beams reduces considerably the interfacial stresses concentrations (Benrahou et al. 2006). Existence of damage prior to strengthening with externally bonded CFRP sheets significantly affects the interfacial stresses especially when the damage region is equal or larger than the plate length (Benrahou et al. 2006). A review was done for understanding the debonding failures in FRP bonded to concrete systems and it was concluded that more research is needed for better understanding and quantification of the environmental effects on the debonding failures in FRP-adhesive-concrete systems (Büyüköztürk and Yu, 2006). Reverse tapered configuration was the most significant to reduce the bond stress concentration at the FRP plate end, while the mechanical anchorage was essential to ensure the effectiveness of the FRP-Concrete joint (Dawood et al. 2007). Ferracut et al. (2007) developed a procedure for deriving a non–linear mode interface law for FRP Concrete bonding, starting from experimental data. Tounsi and Benyoucef (2007) developed an analytical method to predict the distribution of the interfacial stress in concrete beams strengthening with FRP plates.

Temperature cycles of -10 to 10 ^{0}C and moisture cycles result in concrete substrate failure, while salt fog cycles create failure at the interface (Silva and Biscaia, 2008). The immersion

in salt water and the salt fog cycles caused considerable degradation of bond between FRP and concrete, but it did not affect the load capacity of the beams (Silva and Biscaia, 2008). Bond strength between CFRP plates and concrete was found to increase corresponding to the increase in the concrete strength or decrease in the CFRP plate width as shown in Figures 2.16 and 2.17, respectively. It can be improved using rational mechanical anchorages (Xue et al. 2008).

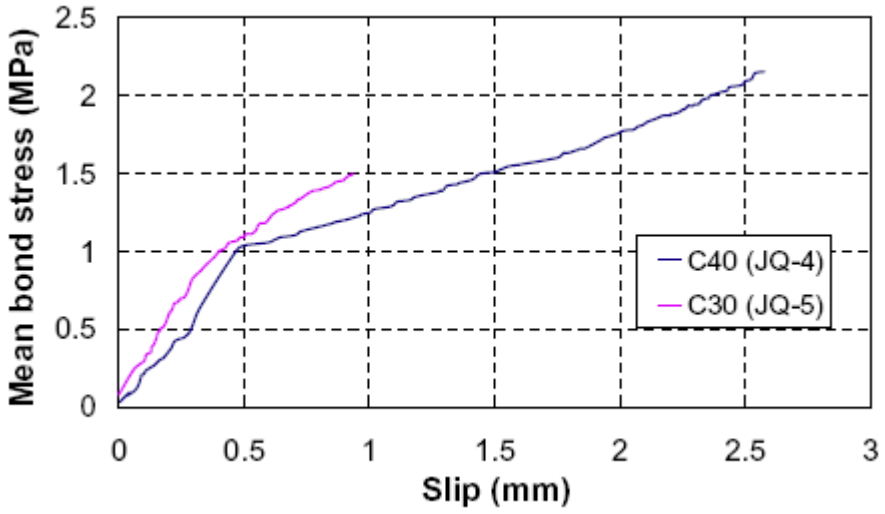

Figure 2.16 Comparison of specimens with 40 mm CFRP plates with two grades of concrete (Xue et al. 2008)

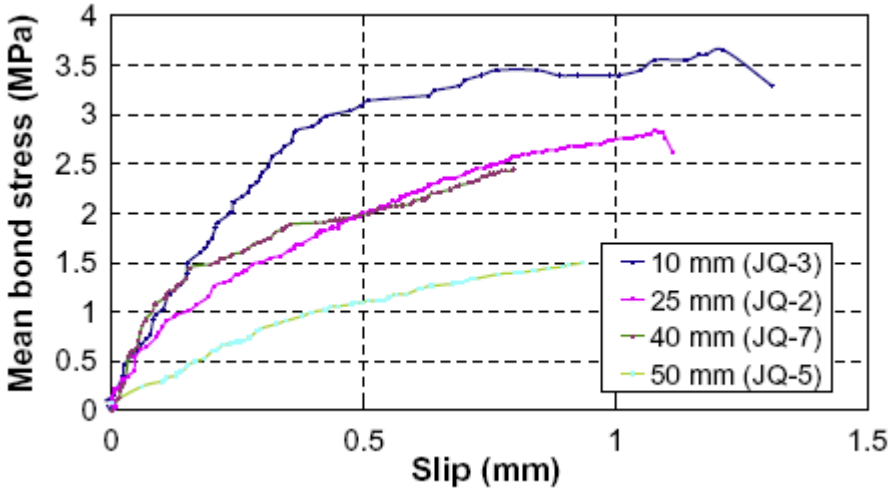

Figure 2.17. Comparison of specimens with different width of CFRP plates (Xue et al. 2008)

Changing the interface parameter can change the failure modes from interface debonding to concrete cohesive cracking (Qiao and Chen, 2008). Higher elasticity modulus of the FRP sheets results in lower interfacial stress concentration at the end of the plate. Adhesive material shear modulus has a significant effect on the interfacial stress at the end of the plate. Using flexible adhesive results in more uniform interfacial stress distribution and reduces the interfacial stress at the end of the plate and the FRP plate thickness and the fibre orientations have significant effect on the shear and normal stresses in the composite member (Benachour et al. 2008). Proposed cohesive model was able to represent the bond behaviour between the CFRP plate and concrete and showed that the increase in the ultimate capacity depends on the CFRP plate length (Obaidat et al. 2010).

2.5 Shear strengthening or repair

Studies on the use of the FRP plate bonding for shear strengthening started since 1990s [Al-Sulaimani et al. (1994); Arduini et al. (1994); Chajes et al. (1995); Alexander (1996); Araki et al. (1997); Fanning and Kelly (1999); Chaallal et al. (1998); Triantafillou (1998); Malek and Saadatmanesh (1998); Khalifa and Nanni (2000); Khalifa et al. (2000)], but they are still limited compared to the studies related to the use of FRP plates for flexural strengthening (Teng et al. 2002). Studies showed that the FRP plate fixed to the beam soffit for flexural strengthening dose not influence the shear capacity of the beam [Plevris (1995); Büyüköztürk and Hearing (1998)]. When both flexural and shear strengthening systems are suggested for an RC beam, it is advisable to do the shear strengthening first (Tan, 1999).

More studies are required for better understanding of the shear capacity of retrofitted beams with FRP plates (Büyüköztürk and Hearing, 1998). The strengthened beam stiffness was found to increase with the increase in the CFRP plate area on the beam sides which also

delayed the appearance of the first flexural crack (Li et al. 2001). Beams strengthened with bonded CFRP sheets showed improvement and an increase in the load capacity by 9% which is larger than that for the beam reinforced with steel stirrups of equivalent shear reinforcement ratio while the deflection was smaller by 16% (Barros et al. 2006). Use of GFRP externally bonded plates with proper application can significantly improve the ultimate capacity and the overall behaviour of the RC beams (Saafan, 2006). Shear strengthening of RC beams with FRP bonded plates showed improvement in the ultimate capacity, with 2-sides system increasing the capacity up to 7%, U-jacket system increasing it up to 38% to 68% and wrapping system increasing it up to 62% (Monti and Liotta, 2007). Bonding of CFRP sheets to the beam soffit shows no effect on the ultimate capacity or the failure mode, while application of the CFRP as externally anchored system with proper design can improve the performance and the ultimate capacity of the RC beams (Bencardino et al. 2007).

Use of anchorage system can enable the tensile steel reinforcement to yield before failure, the CFRP sheets to reach higher portion of their failure strain and the concrete at compression to reach higher strain values (Bencardino et al. 2007). Use of CFRP plates for strengthening of RC beams in shear results in smaller shear crack width which implies that the concrete contribution to the ultimate capacity is higher than for un-strengthened beams (Lee and Al-Mahaidi, 2008). Inclined CFRP sheets were found to be more effective for shear strengthening of RC beams than the vertical sheets as shown in Figure 2.18, and the contribution of the CFRP sheets to the ultimate shear capacity depends on the concrete tensile strength (Dias and Barros, 2010).

Use of U-shape anchored CFRP sheets for shear strengthening can increase the capacity up to 20% (El-Ghandour, 2011). Fibre direction of the CFRP sheets has significant affect on

the shear capacity of strengthened deep RC beams (Lee et al. 2011). Use of U-wrap CFRP strips increased the shear capacity of the RC beams up to 25%, while use of the U-wrap CFRP sheets increased it up to 50%. (Colalillo and Sheikh, 2011). Use of the close-wrap CFRP strips increased the shear capacity up to 75%, while use of the close-wrap CFRP sheets increased it up to 114% (Colalillo and Sheikh, 2011).

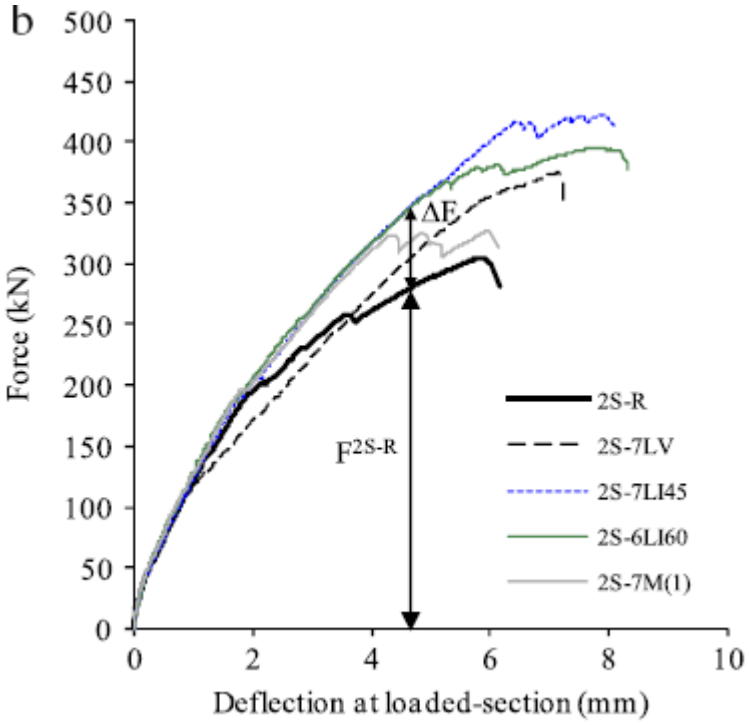

Figure 2.18. Force against deflection at the loaded-section for FRP strengthened beams (Dias and Barros, 2010)

2.5.1 Failure Modes

Studies carried out on the shear strengthening using FRP plate in the last decade observed a number of failure modes namely shear failure due to FRP rapture, shear failure due to FRP debonding, shear failure without FRP rapture and mechanical anchorage failure [Chajes et al. (1995); Araki et al. (1997); Chaallal et al. (1998); Funakawa et al. (1997); Sato et al. (1997) and Kage et al. (1997)]. Beams strengthened with bonded CFRP sheets fail with

shear failure due to the appearance of one major shear crack within the shear span of the beam as shown in Figure 2.19. (Barros et al. 2006).

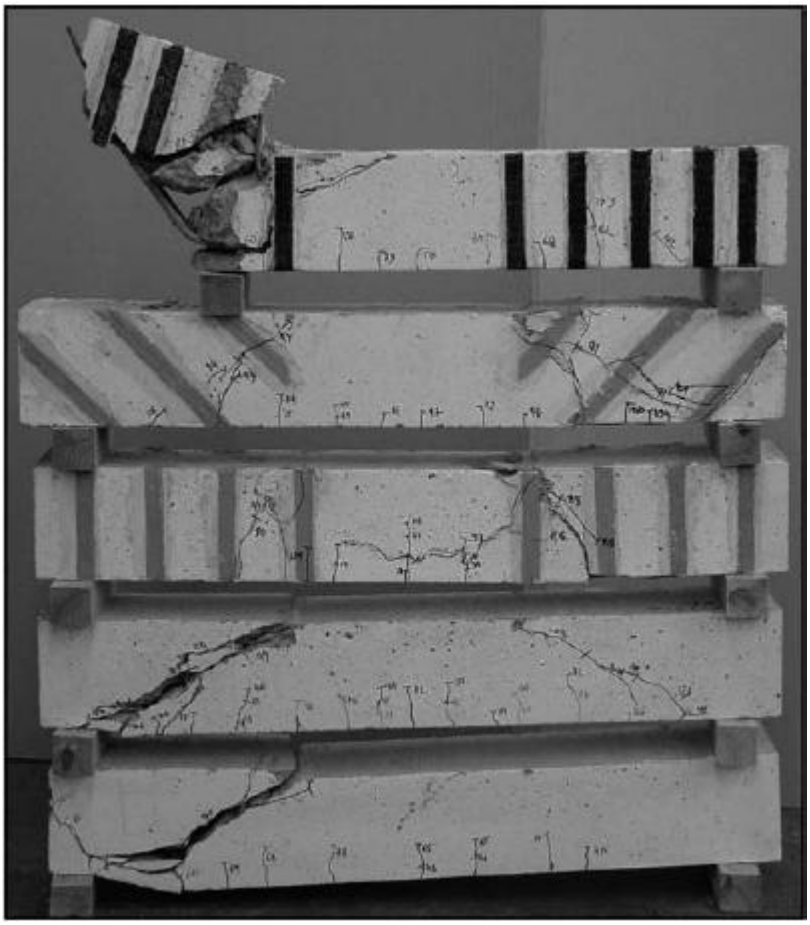

Figure 2.19. Failure modes found by (Barros et al. 2006)

Use of GFRP bonded plate can improve the mode of failure and change it from brittle shear failure to ductile flexural failure (Saafan, 2006). Load capacity and FRP debonding strain predicted using the model given by Niu and Wu (2001) showed better compatibility to the experimental results than that obtained using ACI-440 equations (Ghosh and Karbhari, 2007). Careful design of the anchorage system can transfer the predominantly brittle shear failure of strengthened beam with bonded CFRP sheets to ductile failure as shown in Figure 2.20 (Bencardino et al. 2007). Strengthening of RC beams with bonded FRP plates in shear, results in FRP debonding when the FRP ratio is the minimum, while with larger FRP ratio

the failure mode is due to separation of concrete cover (Dias and Barros, 2010). Strengthening of deep T-section RC beams with externally bonded CFRP sheet can lead to failure with CFRP rupture or partial delamination of CFRP sheets between the concrete surface and CFRP sheets (Lee et al. 2011). Use of the close wrap CFRP sheets or strips changed the failure mode of the U-wrap system from FRP debonding to FRP rupture (Colalillo and Sheikh, 2011).

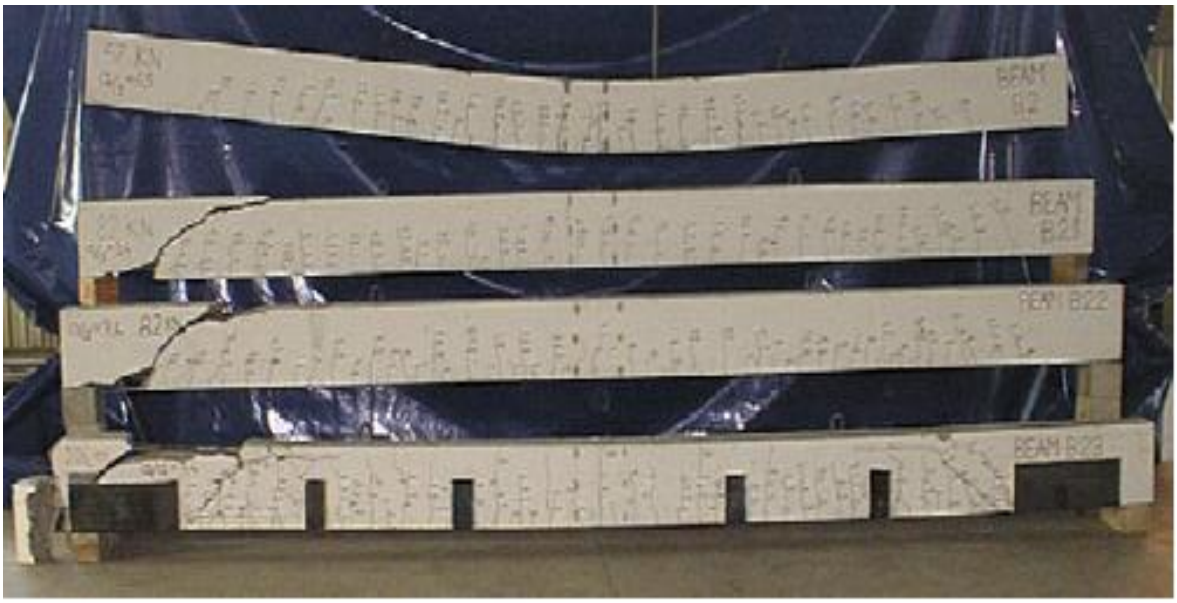

Figure 2.20. Failure modes of beams tested by Bencardino et al. (2007)

2.6 FRP repair assessment using modal parameters

The first dynamic assessment for the use of the FRP plate as externally bonded strengthening system by using the modal testing was conducted by Capozucca and Cerri (2002). Since then, only a small number of researchers used modal testing as dynamic assessment tool for the strengthening or repairing of RC beams with externally bonded FRP plate. Repair of damaged RC beam with FRP plate was found to result in decrease in the

natural frequencies for the first three bending modes, which seems to be an abnormal trend, as shown in Table 2.4 (Capozucca and Cerri, 2002).

Table 2.4. Expermintal result of natural freqiencies of the first three modes at diffenet phases (Capozucca and Cerri, 2002)

Specimen	Phase	Frequency (Hz)		
		Mode 1	Mode 2	Mode 3
Beam1	Undamaged	71.5	226	408.5
	After cracking	-	-	-
	After strengthening by CFRP sheets	55.5	147.5	291.5
	After bending test after strengthening	54	140.5	277

Dynamic parameters were used for the assessment of using FRP plate for repair of damaged RC beams and the bending frequencies of the repaired phase after exposure to load as the design load showed small increase compared to the pre-repair damage phase (Bonfiglioli and Pascale, 2006). Fundamental mode showed lower sensitivity while third and fourth modes showed higher sensitivity and the modal dampings were sensitive to both the damage and the repaired cases (Bonfiglioli and Pascale, 2006). Strengthening of RC shear walls with externally bonded CFRP sheets was found to increase the first three bending frequencies as shown in Table 2.5. (Meftah et al. 2006). Repair of damaged RC shear walls with externally bonded CFRP sheets resulted in increase in the first seven bending frequencies over the damaged walls, while the frequencies values were still less than the undamaged walls as illustrated in Table 2.6. (Meftah and Tounsi, 2007).

Table 2.5. Frequencies (Hz) after strengthening the shear wall with externally bonded GFRP and steel plates (Meftah et al. 2006)

Mode No.	Unstrengthened	Strengthened with GFRP plate	Strengthened with steel plate
1	0.63	0.648	0.684
2	3.306	3.335	3.437
3	5.1	5.178	5.358

Table 2.6. Frequencies (Hz) of damaged shear wall before and after repair with CFRP plates (Meftah and Tounsi, 2007)

Mode No.	Undamaged	Damaged	Repair
1	1.45	1,17	1.26
2	5.99	5.5	5.76
3	10.15	8.06	8.87
4	13.26	12.16	12.51
5	14.5	13.1	13.58
6	22.6	20.66	21.19
7	31.26	26.82	29.29

Modal testing was used for assessment of the repair of damaged RC beams with externally bonded CFRP sheets and there was decrease in the natural frequencies of the repaired phase with self weight compared to the damage phase for all the modes, as shown in Figure 2.21 (Baghiee et al. 2009). Exposure of the repaired beams to the pre-repair damage load resulted in increase in the natural frequencies for some cases depending on the flexural steel ratio and the number of the mode. Baghiee et al. (2009) justified the decrease in natural frequencies to be the effect of the environmental conditions such as the ambient temperature on the material properties. There was variance in the sensitivity of the bending modes to the repair of the damaged beams with bonded CFRP sheets depending on the flexural steel ratio and the pre-repair damage level. The use of MAC index shows smaller change as affected by the damage and repair compared to the natural frequencies, and the change was inconsistent which implies that it is an unreliable index.

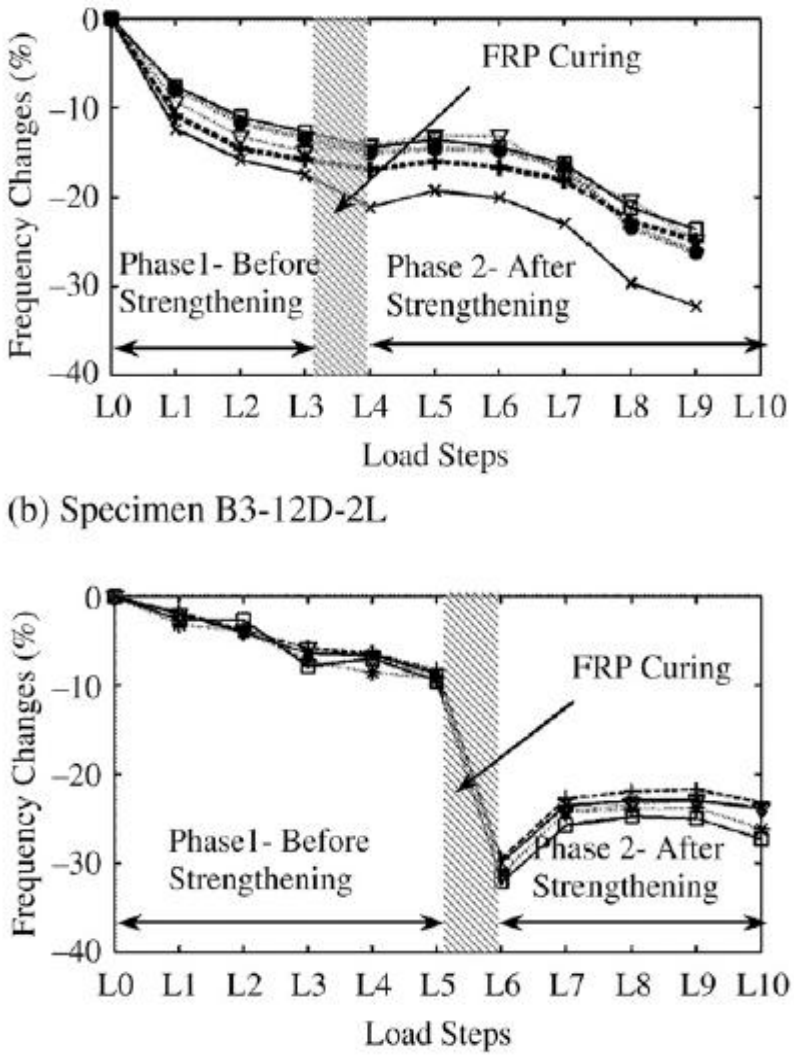

Figure 2.21. Frequency change before and after repair (Baghiee et al. 2009)

Dynamic assessment of damaged RC beams repaired with CFRP rods showed that there was decrease in the natural frequencies for all the modes after repair compared to the damage phase, followed by slight increase after exposing the repaired beams to the pre-repair damage load, as shown in Figure 2.22 (Capozucca, 2009). Capozucca (2009) justified the decrease in natural frequencies due to the extra mass of CFRP rods on the beam. Fundamental mode was more sensitive to the damage and repair (Capozucca, 2009). Modal testing carried out on real bridge repaired with externally bonded CFRP sheets

showed that both vertical and horizontal excitation modes are affected, with all the modes experiencing increase in the frequencies at the repair phase compared to the damage phase, as illustrated in Table 2.7 (Abdessemed et al. 2011).

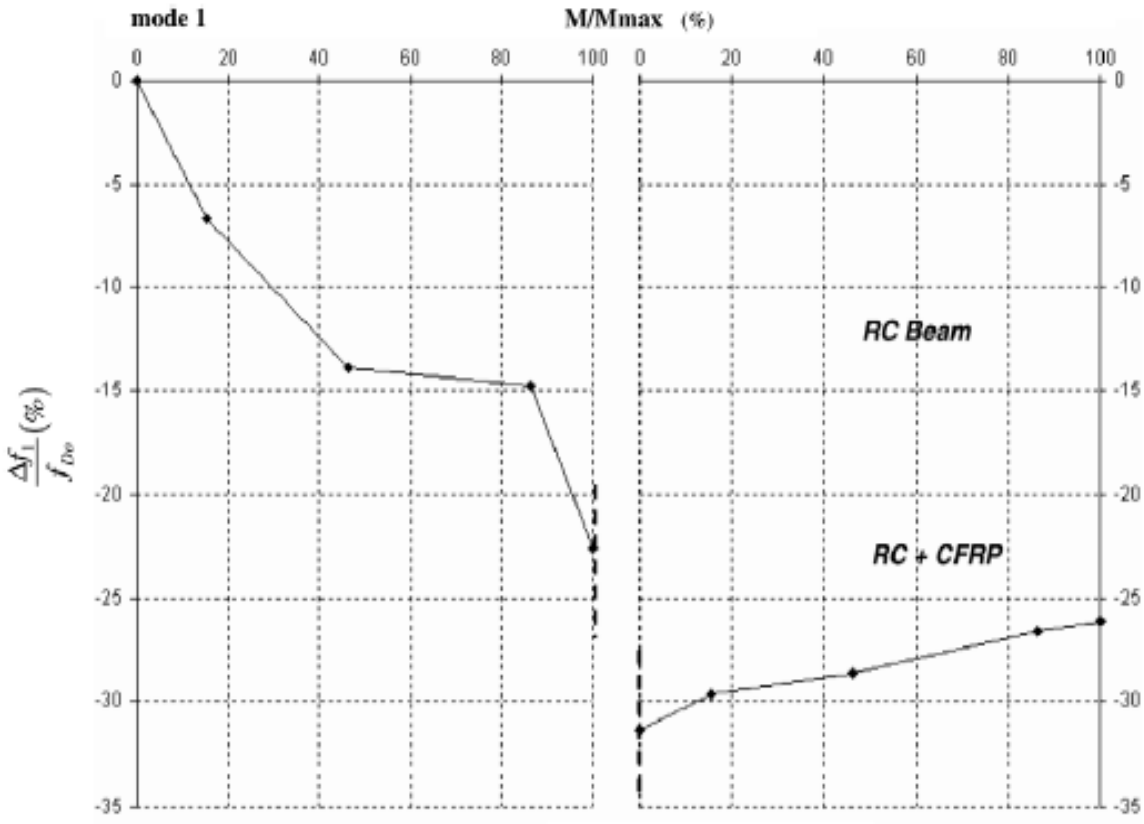

Figure 2.22. Frequency change against moment ratio (M/Mmax) for the first mode for beam B1 (Capozucca, 2009)

Table 2.7. Frequency (Hz) of first six modes at pre and post repair phases (Abdessemed et al. 2011)

Mode no.	Pre-repair phase	Post-repair phase	Mode of excitation
1	3.94	4.05	Vertical
2	4.55	4.67	Horizontal
3	4.89	5.00	Vertical
4	5.03	5.07	Horizontal
5	6.72	6.93	Vertical
6	7.23	7.36	Horizontal

2.7 Design guidelines

Many studies carried out in the last decade deal with the equations and principles used for the calculation of the FRP bonded plate contribution to the flexural capacity of the strengthening/repaired beams. Most of those researches suggest using the same design procedure for the un-strengthened beams while taking into consideration the brittle nature of the FRP plates [An et al. (1991); Chajes et al. (1994)]. Therefore, many design equations and guidelines were proposed for calculating the flexural capacity of the strengthened RC beams with bonded FRP plates based on the design approach of ACI-318 code [An et al. (1991); Chajes et al. (1994); Saadatmanesh and Malek (1998); Nanni et al. (1998); El-Mihilmy and Tedesco (2000), Chaallal et al. (1998); Lam and Teng (2001) and Teng et al. (2000)]. The effect of the pre-strengthening or existing strain in the beam soffit on the FRP bonded plates contribution to the flexural capacity has been studied by Lam and Teng(2001) and the effect was considered in the design equations as shown by Saadatmanesh and Malek (1998).

In the last decade, many studies have proposed mathematical models for the calculation of the FRP plate contribution to the shear capacity of the strengthened beams [Chen and Teng (2003a); Chen and Teng (2001); Chaallal et al. (1998); Chen and Teng (2003b); Funakawa et al. (1997); Khalifa et al. (1998); Triantafillou (1998); Gergely et al. (1998); Triantafillou and Antonopoulos (2000); Triantafillou and Fardis (1997).

The American Concrete Institute (ACI) started to consider the FRP bonded plate as construction material with the first work reported in a state of the art report on the use of the FRP for concrete structures in 1996 (ACI 440.R, 1996). The first design guideline for the use of the fibre composite materials was released by the ACI in 2000 (ACI 440.2R,

2000), followed by a guideline for the design of externally bonded FRP system in 2002 (ACI 440.2R, 2002). The work in the ACI was continually updated on the use of the externally bonded FRP plate or using of FRP bars as reinforcement, according to the finding of new researches and the needs arising [ACI 440.3R, 2004); (ACI 440.4R, 2004); (ACI 440.1R, 2006); (ACI 440R, 2007); (ACI 440.2R, 2008); (ACI 440.5, 2008); (ACI 440.6, 2008); (ACI 440.7R, 2010].

Normal and shear stresses near the cut-off point of the bonded FRP plate and the existence of the flexural cracks need to be considered while calculating the ultimate capacity of the strengthen beams (Almakt et al. 1998). The contribution of the shear stirrups to the ultimate shear capacity of strengthened beams with FRP plate was found to depend on the load sharing relationship with the FRP plates and the mode of failure (Hutchinson, 1999). A simple approach for the design of the concrete beams strengthen with externally bonded FRP plate was proposed where the maximum and minimum limits of the FRP plate were established (El-Mihilmy and Tedesco, 2000). A truss model was proposed for predicting the ultimate shear capacity and behaviour of strengthened beams with externally bonded FRP plates (Colotti and Spadea, 2001). Newhook et al.,(2002) proposed a design procedure to calculate the required FRP plate area for strengthening of concrete beams subject to flexural loading. A straightforward approach for the design of the concrete beam strengthen with externally bonded FRP plates was proposed by Malek and Patel (2002). The contribution of the FRP plate to the ultimate shear of strengthened beams depends on the quantity of the FRP and ratio between the steel stirrup and the FRP plates (Pellegrino and Modena, 2002). A theoretical method for predicting the ultimate capacity of cracked beams strengthen in flexural with FRP plates was proposed by Wu and Davies (2003). Comparison of guidelines for the design of externally bonded FRP plates for strengthening concrete structures according to ACI 440.2R (2002) and the technical report CEB-FIB.14

(2002) was done by Nezamian and Setunge (2004). The ACI 440.2R (2002) guideline was more conservative in prediction of flexural capacity while the CEB-FIB.14 (2002) guideline was a more accurate approach to check de-bonding of FRP from the concrete substrate . The FRP bonded plate contribution to the shear ultimate capacity was found to decrease as the effective depth of the beam increased and the FRP contribution was found to contain two parts i.e. the direct contribution and the indirect contribution (Qu et al. 2005). Shear capacity of strengthened beam with externally bonded FRP plate calculated using the ACI 440.R (1996) guideline was less than the experimental results by 20% (Anil, 2006). Partial interaction model for the quantification of the interaction between the shear steel stirrups and the external bonded FRP plates and its contribution to the ultimate shear capacity was developed, and it was found to be a complex problem since the steel stirrups can yield while the FRP is only ruptured. It was concluded that more research needs to be done for better understanding of the interaction between the internal stirrups and the external FRP plates (Mohamed-Ali et al. 2006). Numerical model for prediction of the FRP contribution to the shear capacity of strengthened RC beams was proposed by (Lu et al. 2009). Use of the equations of ACI 440.2R (2002) for predicting the CFRP plate contribution to the ultimate shear capacity resulted in larger values than the experiential results, while using the equations of Nanni et al (2004) resulted in 61% higher predicted values than the experimental results (Dias and Setunge, 2010). Use of the equations of ACI 440.2R (2002) for the calculation of the CFRP sheet contribution to the capacity of the strengthened deep RC beams showed an overestimate compared to the experimental results (Lee et al. 2011). Colotti and Swamy (2011) developed a mechanical model for predicting the failure load and failure mode of strengthened RC beams with FRP plates in flexural and shear.

2.8 Summary

There have been many studies using natural frequencies as indicators for damage detection or health monitoring in structural elements. These studies mainly highlight the trend in natural frequencies as element stiffness changes with different loading conditions and damage scenarios in the structural elements. Most of these studies were conducted on homogeneous and isotropic material such as steel or aluminium. There have been some experimental studies on the overall behaviour of the RC structural elements. Ismail (2005) found that the first natural frequency increased after damage was induced, the second frequency increase was only for the first loading cycle, while the subsequent frequency reductions were for all the applied loading cycles. The reason for the distinct increase in natural frequency when damage was induced was attributed to the bond action which was only initiated and activated once the steel was stressed i.e. after applying load, thus making the stiffness higher than an un-cracked condition. The stiffness showed increase in some cases after damage was induced which justified the action of the tension stiffening which could not be neglected (Maeck et al. 2000). These studies, however, did not consider the composite nature and action of having embedded steel bars in a concrete mass and subjecting it to loads which resemble the actual case of a reinforced concrete structural element. One of the objectives of this study is to investigate and relate the effect of composite action on the dynamic characteristics of the RC structural elements. The composite action arises from bond action between steel bars and surrounding concrete depending on the steel bar stress levels, concrete softening at the tension zones due to tension stiffening and cracking, and concrete softening at the compression zones due to concrete crushing. These are the factors which will influence the natural frequencies and these factors are dependent on the steel properties i.e. yield stress and concrete properties

namely the compressive strength and tensile stress. The phenomena of concrete softening in the tension and compression zones together with the bond action between the steel bars and the surrounding concrete occur in real RC structures while in-service, and are applicable to a majority of structures such as bridge girders, beams and slabs in framed buildings and other civil engineering structures.

To date there is no significant research undertaken to classify the damage source using the modal parameters. Structural elements can suffer deterioration due to either exposure to extreme loading conditions or due to the deterioration of the element materials over time. On the other hand, the supports may suffer loss in stiffness over time due to the effect of wear and tear in such cases where the elastic bearing is used as isolation in bridge girders and tall buildings. Therefore, to identify the source of deterioration in overall stiffness, which is due to either the structural element itself or the support stiffness, is one of the objectives of this study.

Studies have shown that the existing damage severity algorithms based on natural frequencies and/or mode shapes, experience low sensitivity, have different sensitivity for different modes, underestimate, require dense sensors grid, are erroneous, are affected by noise especially for small damage cases, affect loading configuration (either symmetrical or asymmetrical) and require an adequate number of modes. Based on aforementioned conclusions, this study aims to develop a new algorithm based on the combination between these two parameters i.e. frequency as global indicator and mode shape vectors as local indicator. This is anticipated to have higher sensitivity, considers the available number of modes, averages the considered set of modes by its own format, requires a number of sensors equal to the number of the carried modes and is sensitive to different damage configurations. The use of the modal parameter for damage detection is important in order to come up with a planned strategy for repair and maintenance works. This study develops

a more reliable weightage method to be used for the existing damage algorithms, which considers the different sensitivity of different modes and which is able to return with one stiffness deterioration value.

Previous studies showed that the mode shape vector and its second and fourth derivatives were used for detecting damage location and had some drawbacks regarding sensitivity and reliability such as mode shape curvature has higher sensitivity than the mode shape itself, dense sensor grids are required and a high accuracy is required for obtaining the mode shape to get reliable results. Besides, there are errors and failures of detection results, with the mode shape itself having low sensitivity and affected by the noise. Also, it is difficult for the mode shapes to locate damage in RC beams due to the fact that the cracks are not limited to the zone of applied load but spread over a certain distance on both zone sides. Mode shapes also underestimated, have different sensitivity to the actual damage location, with different modes having different sensitivity. Additionally, adequate mode numbers are required for higher sensitivity. The fourth derivative gave high values at the supports which makes it unreliable in detecting damage close to the supports while the second derivative was less sensitive for multi cracks. Errors in calculating the algorithms can influence the sensitivity.

Based on the aforementioned conclusions, this study modifies two of the exiting algorithms (one based on mode shape curvature and another based on the fourth derivatives) to improve its sensitivity, 2) develop a new algorithm based on the mode shape vector and its derivative which is believed to overcome the drawback of the exiting algorithms and increase the sensitivity to locate the damage regardless of location and level, and 3) develop an elimination procedure to cut-off the anomalies which can appear as a result to the mathematical calculation of the algorithms.

Previous studies showed a growth in recent years in the global need for structural performance improvement and retrofitting works using FRP sheets as externally bonded system. The use of the prefabricated FRP plate was found to ensure the highest degree of material uniformity and quality control. The pre-repair damage level and the flexural steel reinforcement ratio were found to influence the repair effectiveness using FRP bonded sheets. Although many researchers have examined the effectiveness and the failure modes of FRP bonded sheets as flexural strengthening system, a very limited number investigated the repair cases with only a few taking into consideration the effect of both the pre-repair damage level and the flexural steel ratio. This study aims to investigate the effectiveness and the failure modes of using CFRP bonded sheets for flexural repair of RC beams considering the effect of different pre-repair levels and the effect of the flexural steel code design limits.

Although many studies have been carried out on the use of FRP bonded sheets for flexural strengthening of RC structures, the use of the FRP sheets for the shear strengthening of the RC structures is still very limited. A number of researchers have pointed out that more studies are required for better understanding of the shear capacity and failure modes of repaired beams with FRP bonded plates. Moreover, the effect of the pre-repair damage level, shear stirrup ratio and the load location on the effectiveness and failure modes of the CFRP sheets as shear repair system needs to be investigated. This is one of the objectives of this present study.

Most of the existing studies are still based on the conventional static load test, which is time consuming, equipment and labour intensive and causes major disruptions to existing use. Moreover, previous researches showed that only very limited work has been carried out on the use of modal testing for the assessment of using FRP bonded sheets as flexural or shear repair systems. Even the few studies conducted show an abnormal trend of the natural

frequencies regarding the repair effectiveness. This study aims to use modal testing i.e. using the modal parameters as an assessment tool for the effectiveness of using CFRP as a flexural and shear system. The study will investigate the effect of different parameters i.e. different pre-repair damage levels, maximum and minimum flexural steel ratios, different shear stirrups ratios and damage at different locations from the supports, on the use of the modal testing as assessment tool. Moreover, the study attempts to overcome the shortcomings highlighted by the previous researchers regarding the use of the modal parameters for the effectiveness of the CFRP sheets as flexural and shear repair systems.

Although many studies have been carried out for the calculation of the FRP bonded plate contribution to the flexural and shear capacity of the strengthened or repaired beams, research is still ongoing in this area. Moreover, the work at the American Concrete Institute (ACI) is continually updated on the use of the externally bonded FRP plate according to the findings of new research. Based on previous studies, more research needs to be done for better understanding of the interaction between the internal stirrups-flexural steel and the external FRP plates. The contribution of the FRP plate to the ultimate shear of strengthened beams depends on the quantity of the ratio between the steel stirrup and the FRP plates. The ACI 440.2R2 (2002) guideline was more conservative in predicting flexural capacity. The ACI 440.R (1996) guideline predicted less shear load capacity values than the experimental results. Based on the aforementioned conclusions, and considering that the ACI Code is the standard code used for design in this study, this work aims to evaluate the equations of the ACI Code in predicting the ultimate flexural and shear capacities of repaired RC beams affected by different parameters i.e. different pre-repair damage levels, maximum and minimum flexural steel ratios, different shear stirrups ratios and damage at different locations from the supports.

Chapter 3: Damage Algorithms

3.1 Introduction

Many engineering structures, when exposed to various external loads such as earthquakes, traffic, explosion and vibration during their lifetime, suffer damage and deterioration over the years. This seriously affects their performance and may even lead to structural failure. Similar phenomena are observed in aerospace and mechanical engineering. In addition, inspection of structural components for damage is essential in making decisions on the maintenance of such structures. Dynamic testing has become an increasingly popular and important tool in structural health monitoring, with the purpose of identifying damage. According to Rytter (1993) classification for damage identification is defined at four levels with increasing difficulty of determination namely, detection of presence of damage, quantification of severity, locating damage positions and prediction of the remaining service life of the structure. To date, vibration-based damage identification methods applied to civil engineering structural elements provide for the first two levels of damage identification with sufficient degree of reliability.

The basic idea behind this approach is that modal parameters i.e. natural frequency, mode shape, and the modal damping, are functions of physical properties of structures, namely, mass, damping, and stiffness. Therefore, any change in the physical properties will cause detectable changes in the modal parameters.

As classified by Rytter (1993), damage detection can be aimed at quantifying the damage severity, or it can seek further to locate the damage locations. As presented in Chapter 2, a plethora of damage detection algorithms that aim to predict the damage severity and to

localize the damage locations were discussed. However, these algorithms have sensitivity problems, so this chapter will present firstly the modifications made on a few selected existing algorithms in order to increase their sensitivity, and followed by the development of new algorithms that are believed to have better sensitivity.

3.2 Damage severity algorithm

Previous researchers have used the change in the natural frequency and the change in the mode shape vector as indicators for the change in the structural stiffness due to damage. Based on the aforementioned conclusions drawn from the literature review at section 2.8, previous studies have shown that the existing damage severity algorithms based on natural frequencies and/or mode shapes had some drawbacks regarding sensitivity and reliability. This study aims to develop a new algorithm based on the combination between these two parameters i.e. frequency as global indicator and mode shape vectors as local indicator, which anticipated to have higher sensitivity and more reliability.

3.2.1 Natural frequency

The natural frequency, *f*, for transverse free vibration of a simply supported beam as suggested by Demeter (1973) and used by Abdul Razak and Choi (2001) is:

$$f = \frac{n^2\pi}{2}\sqrt{\frac{EI}{mL^4}} \tag{3.1}$$

where n is mode number, m is mass per unit length, and *L* is span length, is proportional to the square root of its flexural rigidity, *EI*,

$$f \propto \sqrt{EI} \tag{3.2}$$

Eq. (3.2) can be rewritten as:

$$f_n^2 \propto (EI) \tag{3.3}$$

The positive relation can be considered as:

$$f_n^2 = A(EI) \tag{3.4}$$

where

$$A = 2\, f_n \frac{\delta\, f_n}{\delta(EI)} \tag{3.5}$$

Eq. (3.5) can be rearranged as:

$$2\, f_n\, \delta f_n = A\, \delta(EI) \tag{3.6}$$

By substituting Eq.(3.4) into Eq.(3.6) , the following relationship is establish;

$$2\left(\frac{1}{f}\right)\partial f = \left(\frac{1}{EI}\right)\partial(EI) \tag{3.7}$$

which implies that a change in flexural rigidity (*EI*) will contribute to doubling of the change in natural frequency. This relates the change in the stiffness to the change in the frequency by a relationship assuming the nonlinear structural system behaves linearly as the excitation force used in the modal testing in the present study is considered small. Defining the index as:

$$\text{Frequency based stiffness index } = 2.\left(1 - \frac{f_{i,d}}{f_{i,c}}\right)\cdot 100\% \tag{3.8}$$

where $f_{i,c}$ and $f_{i,d}$ are the natural frequency at i^{th} mode for undamaged and damaged beam, respectively.

3.2.2 Mode shape

The method used to ascertain configuration errors between experimental mode shapes and eigenvectors predicted from the finite element model is called Modal Assurance Criterion (MAC) according to Ewins (2000). It is a correlation between experimental mode shapes and curve-fitted mode shapes and the correlation for the *i*th element is given by the following formula:

$$[\mathbf{MAC}_{\tilde{x}x}]_{ii} = \frac{\left(\{\tilde{\varphi}_i^{\mathrm{x}}\}^{\mathrm{T}}\{\varphi_{\mathrm{i}}^{\mathrm{x}}\}\right)^2}{\left(\{\tilde{\varphi}_{\mathrm{i}}^{\mathrm{x}}\}^{\mathrm{T}}\{\tilde{\varphi}_{\mathrm{i}}^{\mathrm{x}}\}\right)\left(\{\varphi_{\mathrm{i}}^{\mathrm{x}}\}^{\mathrm{T}}\{\varphi_{\mathrm{i}}^{\mathrm{x}}\}\right)} \tag{3.9}$$

where $[\tilde{\boldsymbol{\varphi}}^{x}] = [\boldsymbol{\varphi}^{A}] \cdot [\mathbf{C}] = [\boldsymbol{\varphi}^{A}][\boldsymbol{\varphi}^{A}]^{+}[\boldsymbol{\varphi}^{X}]$. Matrix $[\boldsymbol{\varphi}^{A}]$ is the analytical model mode shapes, $[\boldsymbol{\varphi}^{A}]^{+}$ is the pseudo-inverse of the matrix, and $[\mathbf{C}]$ is the curve-fitting matrix. The values of the diagonal elements of the MAC matrix give the curve-fit results. The modal assurance criteria (MAC) is used in this study as an indirect indicator for the stiffness change assuming that the nonlinear structural system behaves linear as the excitation force used in the modal testing in the present study is considered small. The use of MAC as an indicator for the stiffness change in this study is limited for the case where difference in the structural system is induced by stiffness deterioration.

Utilizing the concept in the previous paragraph, the stiffness deterioration indicator can be considered as the reduction in MAC values for the damage cases based on the datum case. Since MAC value is a fraction of 1.0, the reduction in MAC can be presented in form of (1-MAC) to indicate the percentage of the stiffness change.

$$\text{MAC based stiffness index} = 1 - \frac{\left|\sum_{i=1}^{n} \varphi_{i,c} \cdot \varphi_{i,d}\right|^{2}}{(\sum_{i=1}^{n} \varphi_{i,c} \cdot \varphi_{i,c})(\sum_{i=1}^{n} \varphi_{i,d} \cdot \varphi_{i,d})} \tag{3.10}$$

and $\varphi_{i,c}$ and $\varphi_{i,d}$ are the mode shapes at i^{th} mode for undamaged and damaged beam, respectively.

3.2.3 Combined modal parameter

This study will use a new proposed technique that utilizes both the eigenvalues and eigenvectors as indicators for the change in the structural stiffness due to damage. The indicator, called the combined modal parameters based stiffness index, is the stiffness percentages ratio of the damaged case to the control. The free vibration dynamic equilibrium equation can be expressed as:

$$\mathbf{M}\ddot{\mathbf{q}}(t) + \mathbf{K}\mathbf{q}(t) = 0 \tag{3.11}$$

where **K** is the stiffness matrix, **M** is the analytical mass matrix. The computation of Eigenvalue and Eigenvectors for Eq.(3.111) can be found in many references,[Ewins (2000) Heylen et al. (1999) and Maia et al. (1997)] .The solution to Eq.(3.11) will have the form:

$$\mathbf{q}(t) = \mathbf{\Phi}_m \, e^{\lambda t} \tag{3.12}$$

where $\lambda = \pm i\omega_m$, taking $\lambda = + i\omega_m$ and $i^2 = -1$ gives:

$$\ddot{\mathbf{q}}(t) = -{\omega_m}^2 \, \mathbf{\Phi}_m \, e^{i\omega_m t} \tag{3.13}$$

Substituting equations 3.12 and 3.13 into equation 3.11, and rearranged will lead to the Eigenvalue problem:

$$(\mathbf{K} - \, {\omega_m}^2 \mathbf{M}) \mathbf{\Phi}_m \, = 0 \tag{3.14}$$

Equation 3.14 can be re-written as:

$$\mathbf{K} \, \mathbf{\Phi}_m = {\omega_m}^2 \, \mathbf{M} \, \, \mathbf{\Phi}_m \tag{3.15}$$

Taking $\lambda = - i\omega_m$ gives the same solution as in Equations 3.14 and 3.15.

The Eigenvalue problem has m=1.....n solutions (${\omega_m}^2$ and $\mathbf{\Phi}_m$), and each solution satisfies Eq.(3.15). Taking into account *a* solutions corresponding to the first *a* natural modes (Eigenvectors), Eq.(3.15) can be re-written in compact form as:

$$\mathbf{K} \, \mathbf{\Phi} = \mathbf{M} \, \mathbf{\Phi} \, \mathbf{A} \tag{3.16}$$

$$\mathbf{Or} \qquad \mathbf{K} \, [\mathbf{\Phi}_1 \, , \ldots , \mathbf{\Phi}_a] = \mathbf{M} [\mathbf{\Phi}_1 \, , \ldots , \mathbf{\Phi}_a] \, diag \, (\omega_1^2, \ldots , \omega_a^2)$$

Where *a* is the mode number, $\mathbf{K} = [\blacksquare]_{a \times a}$ is the stiffness matrix, $\mathbf{M} = [\blacksquare]_{a \times a}$ is the mass matrix, $\mathbf{\Phi} = [\vdots\vdots\vdots]_{n \times a}$ is the Eigenvector matrix, and $\mathbf{A} = [\ddots]_{a \times a}$ is the Eigenvalue matrix. Note: For the purpose of this study, the number of solutions and thus of the Eigenvalues must be taken equal to the number of the degrees of freedom and thus of Eigenvectors; one Eigenvalue thus means one Eigenvector and *n* Eigenvalues implies *n* Eigenvectors.

The Eigenvector indicator matrix $\mathbf{\Phi}^* = [\vdots\vdots\vdots]_{\mathrm{a \times a}}$ is built by using the peak values of the measured modal displacement for the particular mode number *a*; for mode numbers less

than *a*, the values that correspond to the peak value location of mode number *a* are utilized. Figure 3.1 shows how to fill up the cells of the $\mathbf{\Phi}^*$ matrix if six modes are adopted, where it shows the selection of the degree of freedoms *D1* to *D6* as the peak values on the sixth mode shape (*M6*) and utilizing the same points *D1-D6* on Modes 1 to 5 (*M1*, *M2*, ...*M5*). The first column in the $\mathbf{\Phi}^*$ matrix will be filled up with the values of D1 at cell (1,1) to *D6* at cell (6,1) from first Mode (*M1*), and the same way for the rest of the columns until the fourth column, which would be filled up with values of *D1* to *D6* in cells (1,6) to cell (6,6) from the sixth mode (*M6*). The Eigenvalue indicator matrix $\mathbf{A}^* = [\ddots]_{a\times a}$ contains the measured Eigenvalues for each mode until mode number *a* in the diagonal.

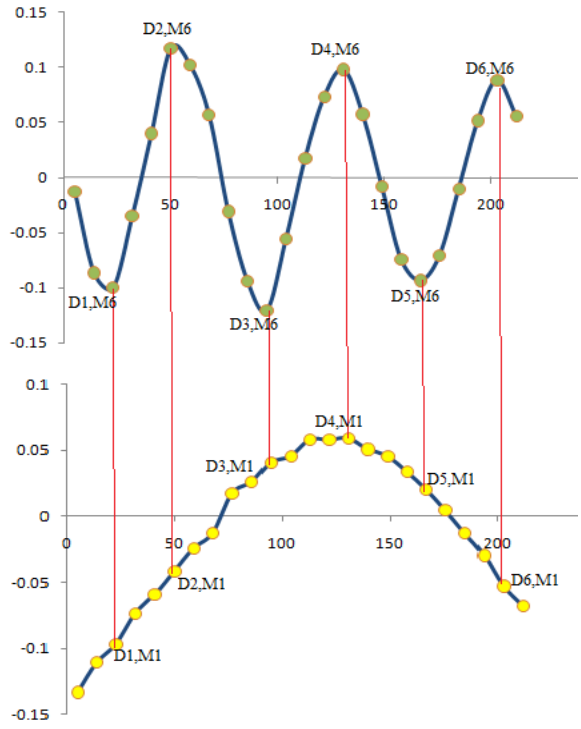

Figure 3.1.(a) Mode 1

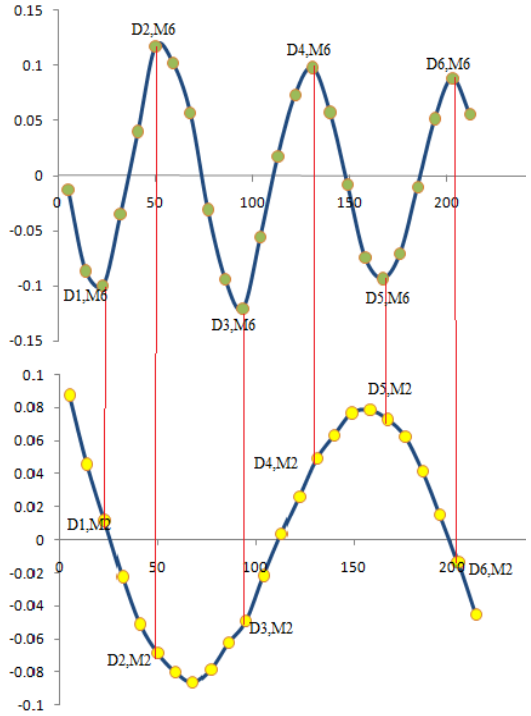

Figure 3.1. (b) Mode 2

Figure 3.1. Selection of peak points on the highest mode and utilization for the remaining modes, Mode 6 is the highest mode

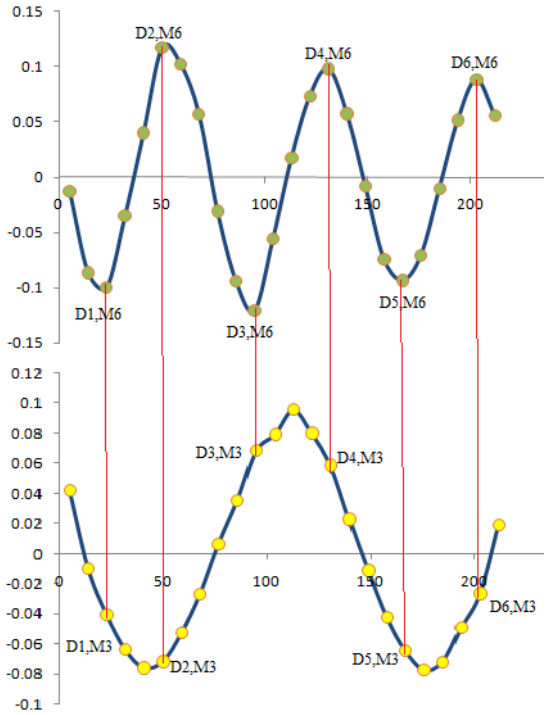

Figure 3.1.(c) Mode 3

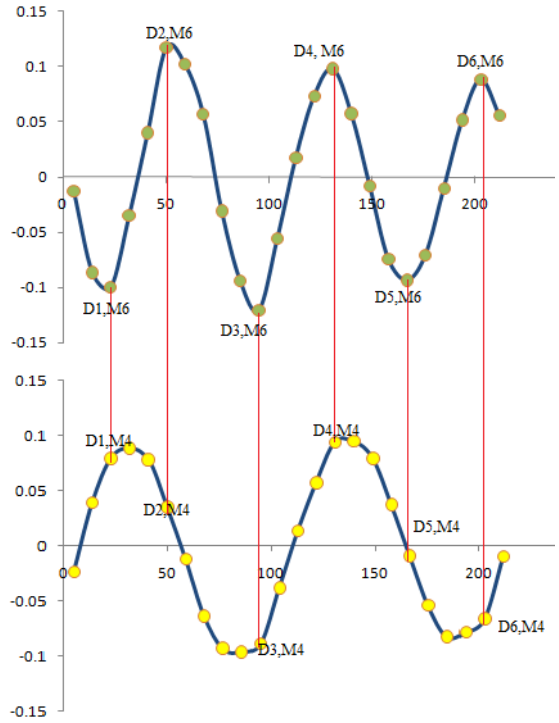

Figure 3.1. (d) Mode 4

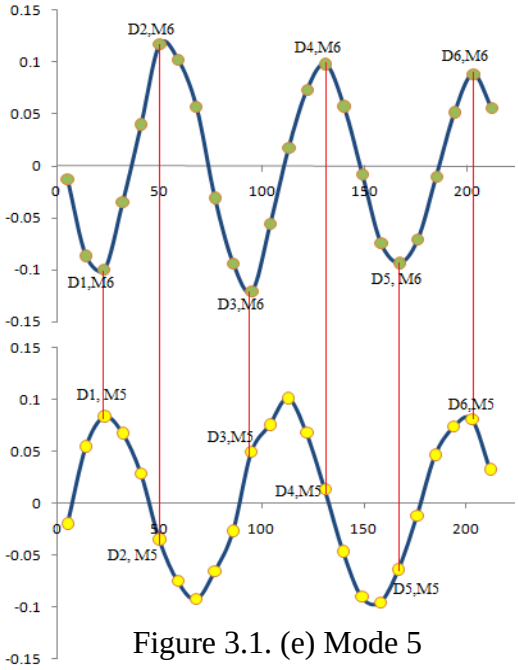

Figure 3.1. (e) Mode 5

Figure 3.1. Continue

For the case when six modes are considered as shown in Figure 3.1, the Eigenvector indicator matrix $\mathbf{\Phi}^*$ and Eigenvalue indicator matrix $\mathbf{A}^*$ for the sixth mode are as follows:

$$\mathbf{\Phi}^* = \begin{bmatrix} D1,M1 & D1,M2 & D1,M3 & D1.,M4 & D1,M5 & D1,M6 \\ D2,M1 & D2,M2 & D2,M3 & D2,M4 & D2.M5 & D2.M6 \\ D3,M1 & D3.M2 & D3.M3 & D3.M4 & D3.M5 & D3.M6 \\ D4,M1 & D4,M2 & D4,M3 & D4,M4 & D4,M5 & D4,M6 \\ D5,M1 & D5,M2 & D5,M3 & D5,M4 & D5,M5 & D5,M6 \\ D6,M1 & D6,M2 & D6,M3 & D6,M4 & D6,M5 & D6,M6 \end{bmatrix} \tag{3.17}$$

$$\mathbf{A}^* = \begin{bmatrix} \omega_1^2 & 0 & 0 & 0 & 0 & 0 \\ 0 & \omega_2^2 & 0 & 0 & 0 & 0 \\ 0 & 0 & \omega_3^2 & 0 & 0 & 0 \\ 0 & 0 & 0 & \omega_4^2 & 0 & 0 \\ 0 & 0 & 0 & 0 & \omega_5^2 & 0 \\ 0 & 0 & 0 & 0 & 0 & \omega_6^2 \end{bmatrix} \tag{3.18}$$

Based on Eigenvector indicator matrix $\mathbf{\Phi}^*$ and Eigenvalue indicator matrix $\mathbf{A}^*$, equation 3.16 can be re-written as

$$\mathbf{K}^* \mathbf{\Phi}^* = \mathbf{M}^* \mathbf{\Phi}^* \mathbf{A}^* \tag{3.19}$$

where K^* and M^* are stiffness and mass indicator matrices

Based on the assumption made for the purpose of this study by taking the number of the Eigenvalues equal to the number of the Eigenvectors, the indicator matrix $\mathbf{\Phi}^*$ is a square matrix and thus its inverse can exist. Eq.(3.19) can be further reduced into:

$$\mathbf{K}^* = \mathbf{M}^* \mathbf{\Phi}^* \mathbf{A}^* (\mathbf{\Phi}^*)^{-1} \tag{3.20}$$

For comparison of stiffness indicator matrices of both the undamaged (control) and damaged cases, considering that there is no reduction in mass for the damaged case, the matrix $\mathbf{M}^*$ remains constant for both control and damaged beams. Eq. (3.20) can be re-written as:

$$\mathbf{K}_c^* = \mathbf{\Phi}_c^* \mathbf{A}_c^* (\mathbf{\Phi}_c^*)^{-1} \tag{3.21}$$

and

$$\mathbf{K}_d^* = \mathbf{\Phi}_d^* \mathbf{A}_d^* (\mathbf{\Phi}_d^*)^{-1} \tag{3.22}$$

where indices *c* and *d* represent undamaged and damaged cases, respectively.

Subsequently, the Combined Modal Parameter (CMP) based stiffness index matrix, **CMP** $= [\blacksquare]_{a\times a}$, at each cell of the matrix is defined by

$$\mathbf{CMP(i,j)} = \left(1 - \frac{\mathbf{K}_d^*(i,j)}{\mathbf{K}_c^*(i,j)}\right) \cdot 100\% \tag{3.23}$$

The combined modal parameter based stiffness index will be calculated at each cell of the **CMP**(*i,j*) matrix, and then the average of the (*a*a*) cell values will be found to obtain one single value as shown in Eq. (3.24) below:

$$\text{Combined modal parameter based stiffness index} = \frac{\sum_{i=1,j=1}^{i=a,j=a} \mathbf{CMP}(i,j)}{a*a} \tag{3.24}$$

where combined modal parameter based stiffness index is the single value for the matrix **CMP**(*i.j*), '*i*' is the number of the Eigenvalue and '*j'* is

3.2.4 Proposed weighting method

Usually when researchers use the bending modes for purpose of damage detection, they will adopt a number of the available modes, and each one of these modes will return a value, indicating the severity of damage. Normally there will be a variance in the sensitivity of different modes, and the norm researchers have for deriving the global stiffness change is by taking the algebraic averaging, which is in the form of the mean, in terms of statistical analysis. This averaging method will always result in a constant weight for all the modes, which is equal to (1/n), where n is the total adopted modes.

This study is proposing a more reliable method for mode weighting than the normal averaging, where the method is based on the mode shapes of the bending modes for beam structures. The normal trend of the bending mode shapes for the first frequency will be like a sine wave with one peak, and for the second mode with two peaks, and will increase by 1 peak for each subsequent mode.

In order to make the beam move in accordance to the shape of any specific mode, it needs a force in the form of work which requires energy to be executed. The energy needed to move the beam in forming different modes will be varied, and this variance can be a function of the amount of wave peaks, where higher wave peaks need higher energy and *vice versa*. It's expected that the higher the energy needed for formation of the mode shape, the higher the sensitivity weight that mode shape would have.

The proposed weighting method (PWM) of multi-bending frequencies will be based on the calculation of the required energy for formation of the mode shape for these modes. This study suggests a simple approach for computing the required energy, whereby the area under the curves forming the mode shapes can be a good indicator for the required energy.

The area under the curves of the mode shapes will be calculated for each mode as (A_i) where "*i*" is the mode number, and the total area (A_t), as the summation of the areas of the adopted modes. The weighting of each specific mode is given in Equation 3.25. Figure 3.2 shows the area under the curve for the first six bending modes that will be adopted in this study.

$$W_i = \frac{A_i}{A_t} \tag{3.25}$$

And the weighted average based on the proposed weighting method (PWM) for all the adopted modes are;

$$\text{Weighted Average (PWM)}_{\text{DSA}} = \sum_{i=1}^{n} \text{DSA}_\text{i} * W_i \tag{3.26}$$

where *i* is the mode number, W_i is the weightage of mode *i*, and DSA_i is the damage severity algorithm at mode *i*.

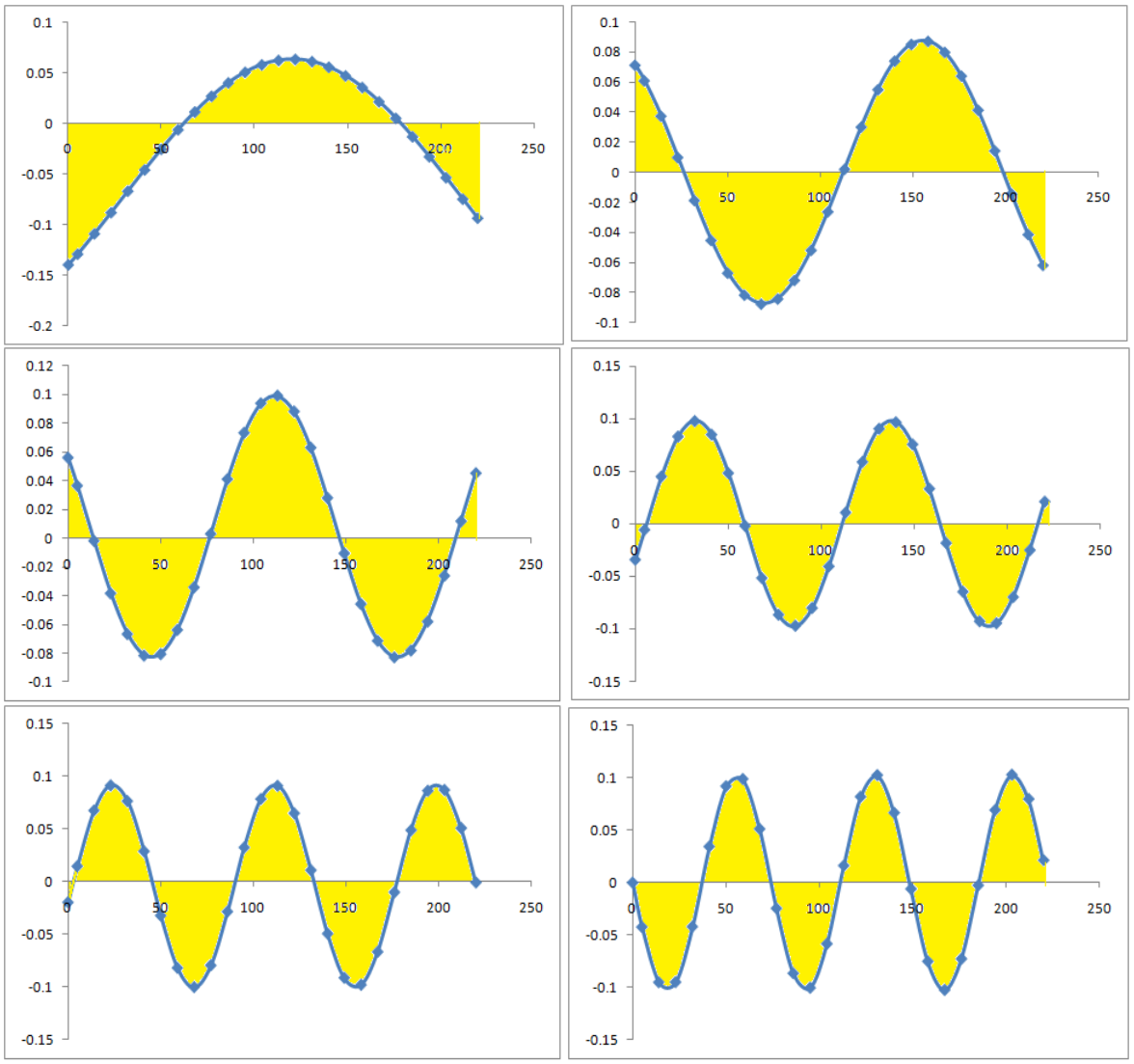

Figure 3.2. Area under the curve for each specific mode shape

3.3 Damage location algorithms

Based on the aforementioned conclusions drawn from the literature review at Section 2.8, previous studies showed that the mode shape vector and its second and fourth derivatives were used for detecting damage location and had some drawbacks regarding sensitivity and reliability. This study will propose modifications to two local damage indices in order to enhance their sensitivity to detect damage, one algorithm based on the change in curvature of mode shape and the other based on the fourth derivative of the mode shape. Moreover,

the study will propose a new damage location algorithm, which is anticipated to have a higher sensitivity in locating the damage.

3.3.1 Mode shape curvature

Proposed by Abdul Wahab and De Roeck (1999), the mode shape curvature at each point is computed from central difference approximation using mode displacement as given in Equation 3.27;

$$Ci = (y_{i+1} - 2y_i + y_{i-1}) / h^2 \tag{3.27}$$

where C is the curvature, i is node number, y is the eigen vector at i^{th} node, and h is the distance between each sequenced nodes.

Subsequently the change in curvature between two sets of mode vectors i.e. the control and damaged cases is as shown in Equation 3.28;

$$\text{CDF} = \frac{1}{N}\sum_{j=1}^{N}\left|C_{ci} - C_{di}\right| \tag{3.28}$$

where CDF is the Curvature Damage Factor, N is the total number of modes, c indicates control case when no load was applied and d indicates damage case when damage load was applied and released and C is the curvature at i^{th} node.

Previous studies show that CDF returned high values at the supports which is an anomaly and indicates a flaw in the algorithm. Thus CDF in its original form is rather unreliable when the damage location is near the support.

3.3.2 Mode shape fourth derivates

Proposed by Ismail et al. (2006), it is based on the equation for free vibration of the Euler beam as shown below:

$$\frac{d^4 y}{dx^2} - \lambda^4 \, y = 0 \tag{3.29}$$

Re-arranging the above equation in the following form;

$$\lambda^4 = \left| \frac{y^4}{y} \right| \tag{3.30}$$

In addition, applying the fourth order centered finite difference,

$$y^4 = (y_{i+2} - 4y_{i+1} + 6y_i - 4y_{i-1} + y_{i-2}) / h^4 \tag{3.31}$$

where y^4 is the fourth derivative.

Thus, the Local Stiffness Indicator is defined as,

$$LSI = \lambda^4 \tag{3.32}$$

Previous studies conclude that LSI is a less sensitive damage indicator for regions at the support, where the values appear as anomalies and this is the major drawback of LSI indicator in its original form.

3.3.3 Modified Curvature Damage Factor

The Curvature Damage Factor (CDF), proposed by Abdul Wahab and De Roeck (1999), accounts for all available mode shapes through the summation of the mode shape curvatures. The values of the mode shape curvature are dependent on the shape of each individual mode. Instead of reflecting the changes in the curvature due to damage, summation of the non-normalized mode shape curvature will distort the damage index in favour of higher modes, which would result in false damage identifications. To overcome this problem and in order to use the index for detecting damage location, which is a local phenomenon, it is proposed to calculate the change in curvature at each node for each respective mode considered and compare the values between the damage and control cases.

The mode shape curvature at each point is given in Equation 3.33.

$$Ci = (y_{i+1} - 2y_i + y_{i-1}) / h^2 \tag{3.33}$$

where C is the curvature, i is node number, y is the eigenvector at the i^{th} node, and h is the distance between each consecutive node. However, according to the proposed change above, the equation for the Modified Curvature Damage Factor MCDF is given as below.

$$\text{MCDF}_{ij} = \left| \frac{C_{di} - C_{ci}}{C_{ci}} \right| 100\% \tag{3.34}$$

where MCDF is the Modified Curvature Damage Factor, *i* is the node number and *j* is the mode shape number. *C* is the curvature at each node for both undamaged case *c* and damage case *d*.

3.3.4 Modified Local Stiffness Indicator

The Local Stiffness Indicator (LSI), developed by Ismail et al. (2006), was developed to have indicators for cases when data for the initial state of the structure before damage is unavailable. However, it was concluded that there exist anomalies due to boundary conditions, presumably due to the free vibration equation of the Euler beam used for simply supported case. Furthermore, the LSI is based on the fourth derivative of the mode shape, and any anomaly will be amplified depending on the degree of the derivative, and thus making it significant at the support. For cases when the data is available and to overcome the anomaly problem, the modified form is given by Equation 3.35, expressed as a ratio of the LSI for the damage and control cases. In this modified form, if there are anomalies due to boundary conditions at the supports, it will be eliminated by dividing the damage over control.

$$\text{MLSI}_{ij} = \frac{LSI_d}{LSI_C} = \left| \frac{y_d^4 * y_c}{y_c^4 * y_d} \right| \tag{3.35}$$

where MLSI is the modified indicator, *i* is the node number, *j* is the mode shape number, y^4 is the fourth derivative of the mode shape, and *y* is the mode vector. The subscripts *d* and *c* are the damage and undamaged cases, respectively.

3.3.5 Developed algorithm

This developed index is based on the free vibration equation, where the control equation of free vibration is shown below:

$$M.\frac{d^2y}{dx^2} + K\ y = 0 \tag{3.36}$$

where *y* f(x) is the mode shape vector, *x* is the distance along the beam length from one support and $\frac{d^2y}{dx^2}$ is the curvature of the mode shape at each point *x*. Let (- K/M) represent the Stiffness Index (SI); then;

$$SI = (\frac{d^2y}{dx^2})/\ y\ = \text{Curvature} / y = C/y \tag{3.37}$$

where *C* is the curvature, or the second derivative of the mode shape vector;

$$SI_c = \frac{C_c}{y_c}$$

$$SI_d = \frac{C_d}{y_d}$$

and where *c* is the indicator for the undamaged case, and *d* is the indicator for the damaged case.

Thus, the Stiffness Reduction Index (SRI) can be calculated as:

$$SRI = 1 - \frac{SI_d}{SI_c} = 1 - \frac{Cd * yc}{Cc * yd} \tag{3.38}$$

In the case of no reduction in stiffness, the SRI is equal to zero. At the point at which there is a reduction in stiffness, SI_d will be less than SI_c, and (SI_d/SI_c) will have a value less than 1. The difference between 1 and (SI_d/SI_c) will be the SRI.

3.3.6 Proposed anomaly eliminating procedures

Previous modifications made to the mathematical forms of the algorithms were done to improve their sensitivity for locating the damage. Moreover, the anomalies and the effect of noise on the Damage Location Algorithms (DLA) can be due to other reasons than the mathematical form of the specific damage location algorithm. In order to understand the reason for such anomalies, the mode shape patterns are highlighted, where different modes will have different patterns. Figure 3.3 presents the mode shape patterns of modes 1 to 4 for a simply supported beam as an example.

The mode shape patterns show there are some Degree of Freedoms (DOF) that will match the nodes along the beam length, which have mode vector values close to zero. Such behaviour may cause anomalies at the location of these nodes i.e. DOF, since multiplying or dividing by values close to zero may cause anomalies. In order to eliminate such anomalies it is suggested to eliminate the damage detection algorithm value at the DOF that matches the nodes and for each separate mode shape. From Figure 3.3, it can be concluded that for mode two, the DOF number 14, 1625 mm from the left support has to be eliminated, for mode three DOF number 10 & 18, which are located at 1125 & 2125mm, respectively, from the left support have to be eliminated, and for the fourth mode DOF number 20, which is located at 2375mm from the left support also has to be eliminated. Such effects of the node DOF can influence the ability of the damage location algorithms to localize the damage. This study will eliminate the effect of the node DOF for all the adopted mode shapes and for all the modified and the developed algorithms.

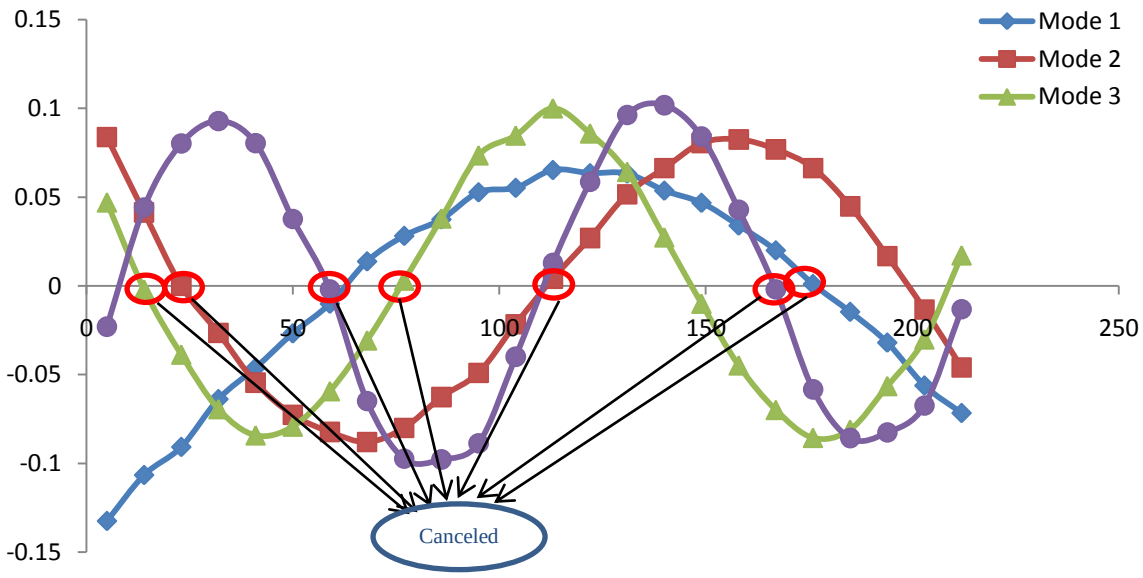

Figure 3.3. Mode shape patterns for the control case

3.3.6.1 Elimination of statistical anomalies

Since most of the damage location algorithms are based on the calculation of the second or the fourth derivatives of mode vectors, which will result in very small values i.e. 10^{-8}, such values during the multiplying or dividing will show as noise along the damage location algorithms. A procedure of statistical elimination is suggested in order to overcome this problem.

The procedure called the Statistical Anomalies Elimination (SAE) is based on statistical calculations, where the mean and the standard deviation for all damage location algorithm (DLA) values along the beam are as shown in the equations below.

$$\mu = \frac{\sum_{i=1}^{N} DLA}{N} \tag{3.39}$$

$$\sigma = \sqrt{\frac{1}{N}\sum_{i=1}^{N}(DLA - \mu)^2} \tag{3.40}$$

where μ is the mean, σ is the standard deviation, N is the total degree of freedom along the beam length and DLA is the damage location algorithm values.

The statistical anomalies elimination procedure will be as follows:

- Calculate the mean and the standard deviation values for the data set
- Find the upper band limit *L*

$$L = \mu + \sigma \tag{3.41}$$

- Find the main value σ_n again for the complete damage location algorithm data set, except the values that are more than the *L* value.
- Subtract the new main value σ_n from all the data set except the nodes that are higher than the *L* value.

$$DLA_i^f = DLA_i - \sigma_n \tag{3.42}$$

where DLA_i^f is the modified values for damage location algorithm, and *i* is the node number. The statistical anomalies elimination procedure will be applied to improve the sensitivity in the case of anomalies along the span length.

3.3.7 Proposed weighting method

For the modified and developed damage location algorithms (DLA), the form of the algorithms will be calculated for each mode separately in order to investigate the sensitivity of each individual mode. In order to monitor the overall behaviour of the damage location algorithms with respect to any damage level or scenario, the weighted average according to the proposed weighting method (PWM), can be used to come out with crack patterns from that specific damage location algorithm and based on the sensitivity of all the adopted modes, as shown in Equation (3.43).

$$\text{Weighted Average (PWM)}_{DLAj} = \sum_{i=1}^{i=n} DLAi, j * Wi \tag{3.43}$$

where DLAj is the damage location algorithms value at each degree of freedom, *i* is the mode number, *n* is the total mode numbers, and Wi is the weight for each specific mode.

The use of weighted average of different modes can result in the appearance of anomalies that can be cut-off by using the statistical anomalies elimination procedure.

3.4 Composite action phenomenon

The stiffness of RC elements under different loading conditions is a function of steel behaviour, concrete behaviour, and the interaction between them. Although many studies on the mechanical behaviour of RC elements have been conducted, research work in this area is ongoing due to the complexity arising from the composite nature of the materials (Marfia et al., 2004). Thus, an investigation on the relationship between the dynamic and static properties of RC elements should take into consideration the behaviour of each material under different conditions, the interaction between steel bar and concrete, and its influence on the overall element stiffness.

The relationship between the dynamic and static properties i.e. the natural frequency and the stiffness of the structural elements is expressed in the equation for transverse free vibration of a simply supported Bernoulli-Euler beam given by:

$$f = \frac{n^2\pi}{2}\sqrt{\frac{EI}{mL^4}} \tag{3.44}$$

where f is the natural frequency, n is the mode number, m is the mass per unit length, and L is the span length. Rewriting Equation 3.44, and representing the flexural rigidity, EI by the symbol K and assuming the mass and length are constant, the expression below is obtained,

$$f \propto \sqrt{K} \tag{3.45}$$

implying that a change in flexural rigidity causes changes in natural frequency.

For elements comprising either steel or plain concrete only, K is a function of their respective material properties, where the boundary conditions effect is ignored. For a

composite element, such as RC, the stiffness, *K*, is a function of both the individual material properties as well as the interaction between the materials. Thus, for RC, the following equation applies:

$$K_{RC} = K_{concrete} + K_{steel} + K_{bond} \quad (3.46)$$

Concrete stiffness is dependent on its behaviour under different loading conditions. For RC beams under flexural loading, the concrete stiffness is represented by its behaviour in compression as well as in tension as given below:

$$K_{concrete} = K_{tension} + K_{compression} \quad (3.47)$$

For RC beams under shear loading, the concrete stiffness will presented by its behaviour in compression, tension, and at the shear interface zone and as given below:

$$K_{concrete} = K_{tension} + K_{compression} + K_{shear} \quad (3.48)$$

The steel stiffness for an RC beam (i.e. K_{steel}) is the stiffness of steel under tension loading conditions only, since the steel is normally positioned in the tension zone. When a load is applied, the concrete stiffness will change according to the loading level and its behaviour under compression or tension. Cementitious materials are characterized by a softening response, which can vary depending on its strength in compression and tension.

Bond action at the interface between the steel bar and the surrounding concrete during loading and unloading can be explained by means of an interaction force. The interaction force is assumed to have no bonding action (BA) at the initial stages when no load is applied. As load is applied, bonding action will begin to grow as a compression-bond action (CBA) force at the interface between the steel and the surrounding concrete, and it will try to resist the tensile force in the steel bar. This compression-bond action force is affected by applied load, steel bar diameter, steel bar perimeter, steel bar shape, compressive strength, and steel bar properties.

When the applied load increases, the tensile force in the steel bar will also increase, resulting in an increase in the compression-bond action force at the interface to resist slipping. Under the same applied load, when the bar diameter increases, the tensile stress in the steel bar will decrease, which then leads to a decrease in resisting the compression-bond action force. In addition, when the bar diameter increases, the mean increase in bonding area will cause a decrease of compression-bond action force per unit area. For smooth bars with the absence of ribs, the compression-bond action force will decrease, and this can lead to slipping. When compressive strength increases, this will lead to more shear force action from the surrounding concrete, which leads to an increase in the compression-bond action force.

Problems on the steel surface, such as corrosion, will lead to a decrease in the compression-bond action force, and this can cause slipping. Figure 3.4 shows the longitudinal section in a simply supported RC beam, and Figure 3.5 shows the development of compression-bond action force on the steel bar perimeter under loading. When the applied load is released, tensile force in the concrete will be reduced. This will lead to growth in shear force resistance at the interface between the steel and the surrounding concrete. This shear force, which is in the form of tension-bond action (TBA) force, will lead to an increase in tension stiffness of the RC element. Figure 3.6 shows the development of tension-bond action resistant force on the steel bar perimeter.

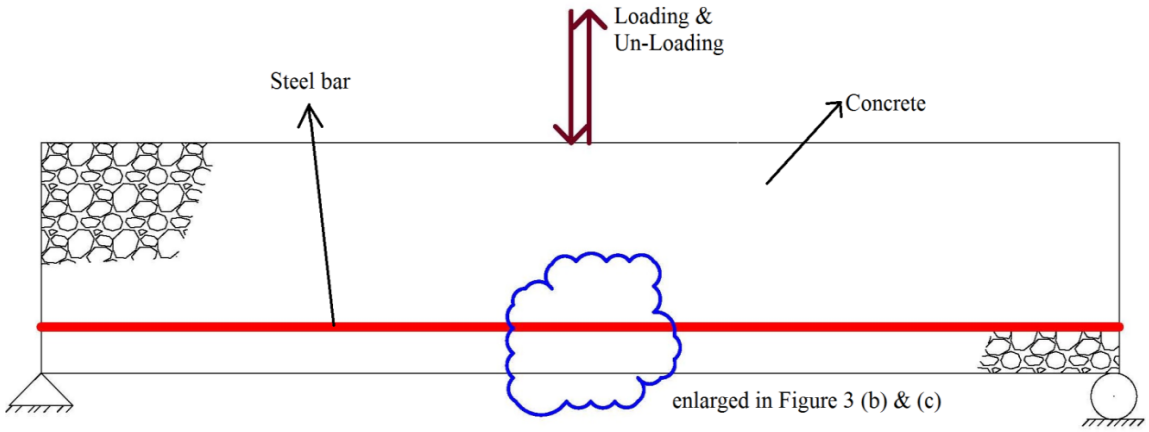

Figure 3.4. Longitudinal section in a simply supported RC beam under loading and un-loading

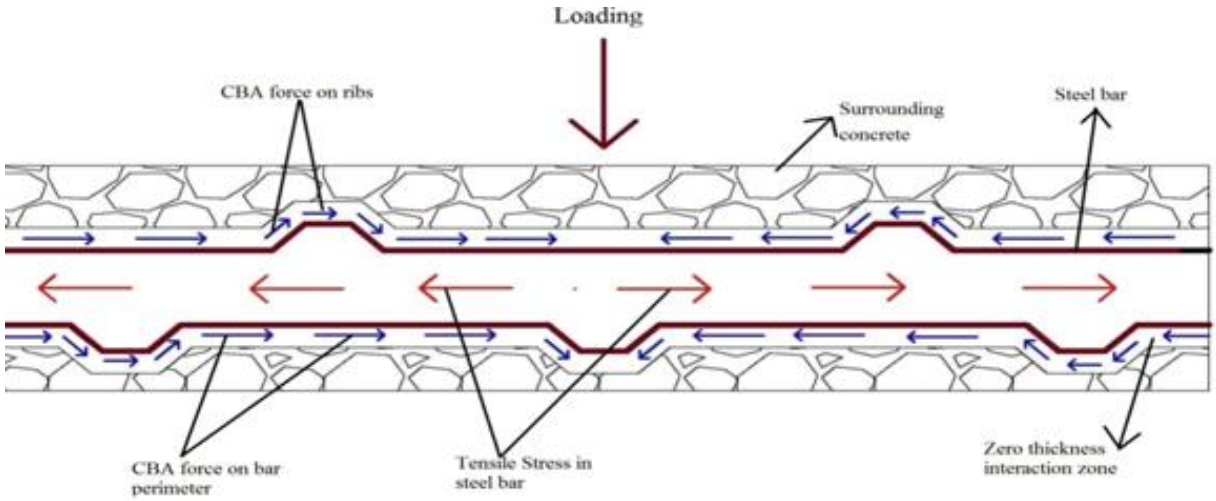

Figure 3.5. Development of compression-bond action (CBA) force in deformed bar

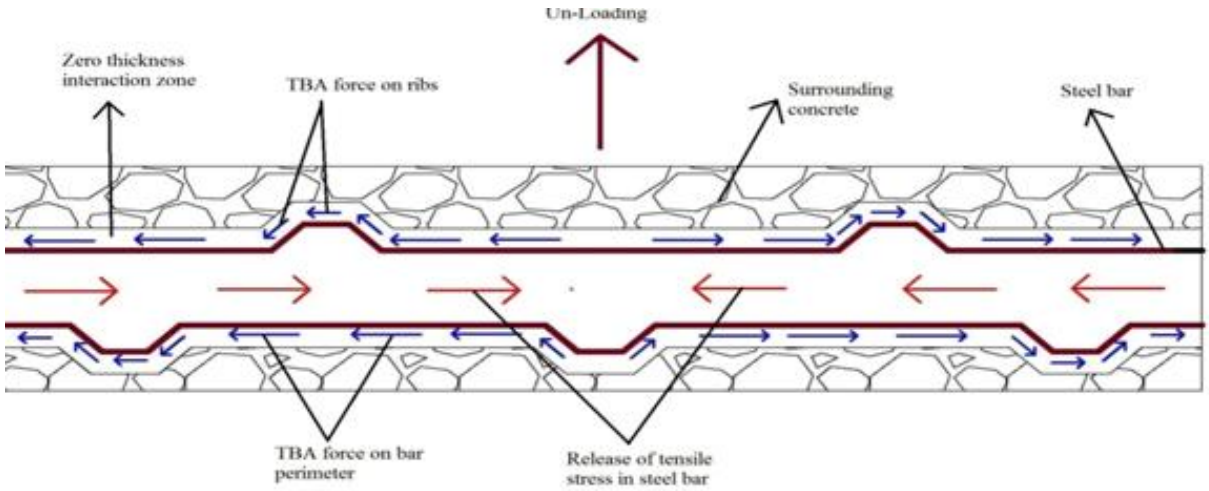

Figure 3.6. Development of tension-bond action (TBA) force in deformed bar

3.5 Summary

This chapter covered the analytical background of the damage detection algorithms, where it highlighted both damage severity and damage location algorithms. For each algorithm, it suggested the modification to the original form of the existing algorithms (which was described in Chapter 2), and subsequently developing new algorithms. The first section highlighted the damage severity algorithms, by presenting a new developed algorithm, which is perceive to be more sensitive in quantifying the damage severity compared to existing algorithms. Moreover, in this section a weighting method is proposed that is based on the area under the curve of the mode shape, which can assist in averaging the sensitivity of different modes. The second section covered the damage location algorithms, where the modifications to the original form of the existing algorithms were suggested. Developed algorithms have been proposed, which are believed to be more sensitive than the existing algorithms. Moreover, this section proposed an elimination procedure that is needed to cut-off the anomalies along the beam length. Finally, it is suggested to use the same proposed weighting method for the damage severity algorithm, for averaging of different modes to derive the overall crack patterns.

Chapter 4: Experimental Work

4.1 Introduction

This chapter presents the properties of the materials used in this study such as concrete, steel and CFRP sheets and the repair procedure. Reinforced concrete (RC) beams are used as the test specimen throughout this study. The test beam details comprise of the structural design and the testing procedures, including the static load test and modal testing.

4.2 Materials properties

The properties of the material used will be highlighted by presenting the design of the mix proportion and the tests carried out on concrete and steel such as the compressive strength, modulus of elasticity and tensile stress. The material properties of the CFRP sheets and their adhesive material will be adopted as given by the manufacturer's data sheets.

4.2.1 Mix proportion

Concrete is a material which is made by mixing cement, water, and aggregate in a certain mix proportion. This section will describe each component separately and elaborate on the mix proportion design. The concrete components are cement, water and fine and course aggregate. Ordinary Portland Cement (OPC) conforming to American Society for Testing and Materials ASTM C 150 type I (ASTM, 2000b) was used for this study and the cement was manufactured by Lafarge Cement, Malaysia. It was stored in air tight steel drums to keep moisture away. Water used for mixing and curing concrete was water from the pipe supply in the laboratory. The fine aggregate used was mining sand passing 4.75 mm sieve. The coarse aggregates were crushed granite with angular shape and rough surface and its

size ranging from 19-4.75 mm. The sieve analysis was according to the ASTM C136-1958, the specific gravity as well as absorption tests for both coarse and fine aggregate were done as specified in ASTM C 127-88 and ASTM C128-97 (ASTM, 1988, ASTM, 1997a), respectively.

The mix design of the concrete and selection of each component weight was done according to the Code ACI 211.1 (1991). Estimation of the required batch weights for the concrete involves a sequence of logical, straightforward steps which fit the characteristics of the available materials into a mixture suitable for the work. The mix design specifications may dictate maximum water-cement ratio, minimum cement content, slump, maximum size of aggregate, and the compressive strength. In the present study, the design aimed to achieve a compressive strength of 30 MPa in a period of 28 days with a design slump of 150 mm. The mix proportion used was based on a water-cement ratio of 0.59. The material weights are as shown in Table 4.1 below.

Table 4.1. Concrete mix proportion

Material	Wight Kg per M^3
Water	210
Cement	395
Coarse aggregate	895
Fine aggregate	780

4.2.2 Concrete properties

This section presents the tests carried out on the fresh and hardened concrete in order to study the properties of the concrete mixture. The slump test was conducted to evaluate workability and consistency of concrete. It was carried out in accordance to the American Standard (ASTM C172). The results of the slump test were monitored to be within the

range of 150mm ± 5%. The compressive strength test was done according to the American Standard (ASTM C39). After 24 hours of casting, the cylinders with diameter of 150mm and height of 300 mm were demoulded and left beside the cast beams to have the same curing and environmental conditions. An ELE testing machine with a 2000 kN capacity was used. The specimen was placed in the compression machine with the casting face in contact with the platens and a loading pace of 4.48 kN/sec. The compressive strength (N/mm^2) was determined using the following equation:

$$\sigma = \frac{\text{Failure load}}{\text{Area}} \tag{4.1}$$

The static modulus test was carried out in accordance with the relevant American Standard (ASTM C469). 150mm x 300mm cylinder samples were used. The compressometer i.e. strain measuring gauge, was attached axially to the specimen, which was then placed centrally in the ELE compression machine. A basic stress of 0.5 MPa was first applied and the strain recorded. The stress was increased steadily by 0.5 MPa/sec until the stress reached one third of the cylinder compressive strength of concrete. The stress was then maintained for 60 sec and the average strain from two loading cycles was recorded. The static modulus of elasticity E_c (N/mm^2) was determined as the average value taken from two specimens using the following equations;

$$\text{Strain coefficient} = \frac{0.002}{150} \times 0.5 \tag{4.2}$$

$$\varepsilon_{a \text{ or } b=} \text{Gauge division} \times \text{Strain coefficient} \tag{4.3}$$

$$E_c = \frac{\delta\sigma}{\delta\epsilon} = \frac{\sigma_a - \sigma_b}{\epsilon_a - \epsilon_b} \tag{4.4}$$

where σ_a = the upper loading stress = $f_c/3$ (N/mm^2), σ_b = the basic stress (0.5 N/mm^2), ε_a = the mean strain under the upper loading stress, ε_b = the mean strain under the basic stress.

4.2.3 Steel properties

The longitudinal reinforcing steel used was in the form of high tensile deformed bars of grade 460 with nominal diameters of 12mm and 16mm for tension and 8mm round steel bars for compression. For the shear stirrups, round steel bars with a nominal diameter of 6 mm were used. Five tension reinforcing steel bars from each diameter group were tested to acquire the yield stress and modulus of elasticity of the reinforcement. Each of the specimens was machined to remove the ribs and create a smooth surface at mid-length. The bars were tested in tension using a testing machine. The test was conducted in accordance with ASTM A 370.

4.2.4 Casting of beams

A laboratory concrete mixer with 0.2 m^3 capacity was used. All the solid materials were first fed into the mixer and the mixer was operated for one minute. Then three quarter parts of water were added followed by the SP which was followed by the remaining water. The freshly mixed concrete was then tested for slump. All moulds used in this study were made of steel. Prior to casting, the moulds were cleaned and oiled. The concrete was poured into the moulds in three consecutive layers. After each pour, a vibrator was set to run for three seconds to avoid excessive segregation and bleeding. After the final pour had been vibrated, the top surface was trowelled to give a smooth surface. Specimens were then covered with wet burlap and kept in the laboratory at a temperature of 30° and a relative humidity of 90%. After 24 hours the specimens were demoulded and transferred to their specific curing regime.

4.2.5 CFRP properties and application

In this study the products of SIKA, Sika-Carbo-Dur S1012 and Sika-Carbo-Dur S512, were used for both flexural and shear repair systems. The properties of the CFRP sheets are adopted as given by the SIKA data sheet. Since the CFRP sheets used were externally bonded, the Sikadur-30 which is also the product of SIKA was used as the adhesive layer between the CFRP sheets and the concrete beam surface.

For repair, flexural group RC beams were turned over while shear group beams were not. The tension face was roughened to get a suitable face to give as much friction as possible with the CFRP sheet. Figure 4.1 shows the roughened surface prepared using scaling hammer and fixing of the CFRP sheets for both flexural and shear cases. The surface was cleaned by using an air gun to avoid any dust on the surface, as the substrates must be sound, dry, clean and free from laitance, standing water, grease, oils, old surface treatments or coatings and all loosely adhering particles. The concrete was cleaned and prepared to achieve a laitance and contaminant free, open textured surface. When the concrete surface was prepared, the CFRP sheet was fixed by using Sikadur-30 adhesive material and then was left for one month for hardening.

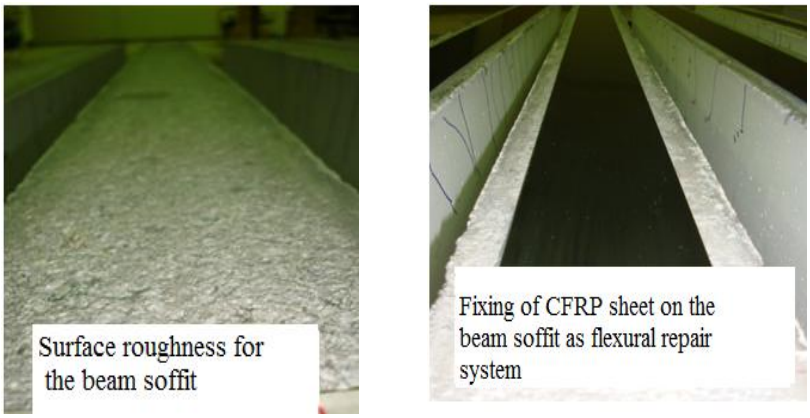

Figure 4.1. Surface roughness and fixing of CFRP sheets

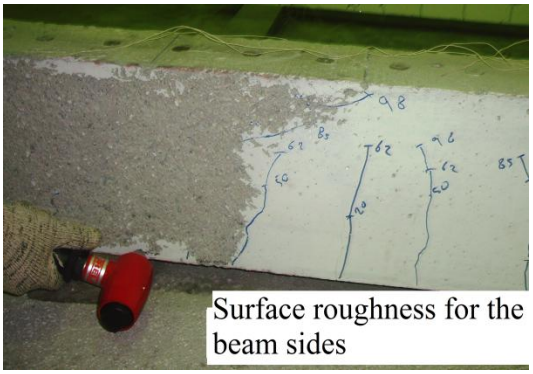

Figure 4.1. Continue

4.3 Test beams

A total of sixteen reinforced concrete (RC) beams have been used, eight of those for flexural damage scenario for both flexural steel design limits i.e. minimum ρ_{min} and maximum ρ_{max}. Four beams were used for the shear damage scenario at quarter-span with both design cases i.e. with and without steel shear stirrups. The last four beams were used for the shear damage scenario close to the support i.e. at 1.5 times the effective depth'd', for both design cases i.e. with and without steel shear stirrups. Table 4.2 shows the classification of the RC beams according to damage scenarios, design cases and damage levels. The notation used for the beam is explained in Figure 4.2, where the beams were in the form of B – X – Y – Z – K.

The properties of the concrete and steel bars for the RC beams in flexure and shear, which were determined according to the procedures mentioned in Sections 4.2.2. and 4.2.3, are shown in Table 4.3. The round steel bars of 8 mm and 6 mm diameters were tested and the results of all the samples were in close agreement with a yield stress of 260 N/mm^2 and elasticity module of 185,000 N/mm^2. The beams have a total length of 2.4m, clear span length of 2.2m and a cross section 150mm wide and 250mm deep.

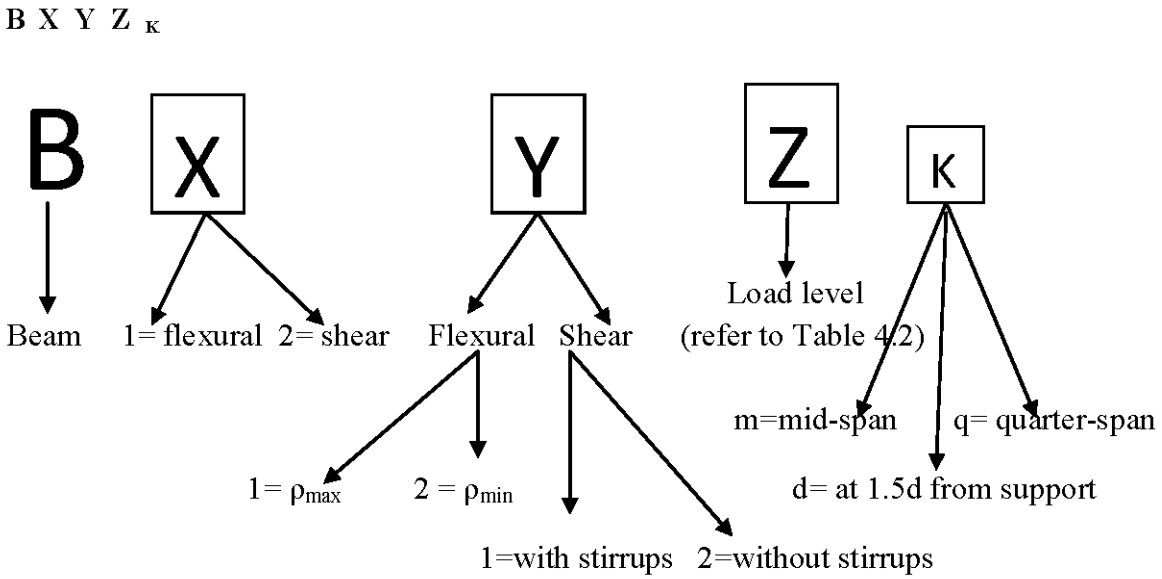

Figure 4.2. Beams notations

Table 4.2. Classification according to damage scenario, design case and damage level

Beam No.	Damage case	Design case	Load Level
B111m*	Flexural Group	ρ_{max}	Failure load
B112m			Design limit load
B113m			Steel yield limit load
B114m			Failure load
B121m*		ρ_{min}	Failure load
B122m			Design limit load
B123m			Steel yield limit load
B124m			Failure load
B211d	Shear at 1.5d from the support	With stirrups	Fully failure
B212d			Prior to failure
B221d		Without stirrups	Fully failure
B222d			Prior to failure
B211q	Shear at quarter-span	With stirrups	Design limit load
B212q			Failure load
B221q		Without stirrups	Design limit load
B222q			Failure load

** Beams B111m and B121m exposed to failure load at pre-repair phase and only used for the investigation at the pre-repair phase, where no repair procedure was involved.*

Table 4.3. Material properties

Beam No.	Concrete properties		Steel properties		
	Compressive strength (MPa)	Elasticity Modulus (GPa)	Yield Stress (MPa)	Rapture Stress (MPa)	Elasticity Modulus (GPa)
B111m	31.7	28	520	680	180
B112m	38	36	480	620	180
B113m	33	29	520	680	180
B114m	30	34	480	620	180
B121m	39.4	32	535	665	180
B122m	36	30	535	665	180
B123m	36	33	565	785	180
B124m	35	31	565	785	180
B211d	36	33	520	680	180
B212d	33	30	520	680	180
B221d	42	37	520	680	180
B222d	40	36	520	680	180
B211q	32.3	29	520	680	180
B212q	33	30	520	680	180
B221q	38	35	520	680	180
B222q	41	36	520	680	180

4.3.1 Flexural design

For the flexural structural design, both ACI 318 (2008) and ACI 420.2R (2002) were used. Based on the ACI Code, there is provision for two limits of the steel ratio in the tension layer as reinforcement requirements for structural elements are subjected to flexure. Minimum steel limit (ρ_{min}) is provided to prevent cracking due to thermal expansion while the maximum steel limit (ρ_{max}) is provided to prevent brittle failure due to crushing of concrete. Thus, in this study, taking into consideration the two steel ratio limits, one RC beam group was designed with ρ_{min} and the other designed with ρ_{max}, and both steel ratios were used to ensure that the failure is due to steel yielding and not brittle failure by concrete crushing.

4.3.1.1 Unrepaired beams

For the unrepaired beams, the RC beam strength is from a combination of the flexural steel bars, compression steel bars and the concrete. The RC beams were designed to resist a concentrated load located at the mid-span in addition to the beam self weight. The flexural beams were designed in shear to make sure that the beam will not fail in shear failure mode, by using shear stirrups with close spacing to ensure high shear resistance. The procedure of the design for the flexural using both ρ_{min} and ρ_{max} and the shear design to achieve the highest shear resistance was according to ACI 318 (2008) equations. For the purpose of calculating the ultimate capacity of the beam, no safety factors or environmental reduction factors were used. According to ACI 318 (2008), the balanced steel ratio is 0.0182 which is the limit between over and under reinforced. The maximum allowable steel ratio to prevent brittle failure of the concrete i.e. ρ_{max} is 0.0136 and the provided maximum steel ratio was 0.0131 by using two 16 mm diameter deformed steel bars as the main flexural reinforcement. The minimum allowable steel ratio to prevent shrinkage cracks i.e. ρ_{min} is 0.003 and the provided minimum steel ratio was 0.006 by using two 12 mm diameter deformed steel bars as the main flexural reinforcement. For both design cases two 8 mm diameter round steel bars were used as the compression reinforcement, and for the shear design 6mm diameter with spacing of 50mm where used along the beam length in order to achieve the highest shear resistance. Figure 4.3 shows the cross section detail for both groups ρ_{min} and ρ_{max}.

4.3.1.2 Repaired beams

The ACI 420.2R (2002) is used as the design guideline for externally bonded CFRP for repairing RC structures. The following assumptions are made in calculating the flexural

resistance of section strengthened with an externally bonded CFRP system i.e. design calculations are based on the actual dimensions, internal reinforcement arrangement, and material properties of the existing member. The strain in concrete and reinforcement is directly proportional to the distance from the natural axis, which means a plane section before loading remains plane after loading. There is no relative slip between external CFRP and the concrete. The shear deformation within adhesive layer is very thin with slight variations in its thickness. The maximum usable compression strain in the concrete is 0.003 and the CFRP has a linear elastic stress-strain relationship to failure.

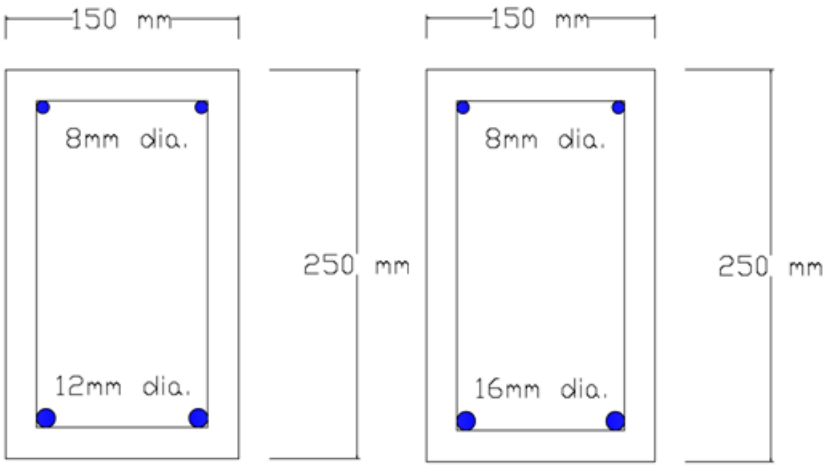

Figure 4.3. Cross section detail for flexural beams, with ρ_{min} (left) and with ρ_{max} (right)

The design of flexural repair with externally bonded CFRP sheets was based on achieving the maximum capacity without debonding failure of CFRP sheets in order to achieve the highest CFRP strength. CFRP flexural design aims to avoid the CFRP debonding failure mode. The pre-repair damage level was included in the calculation by considering the existing substrate strain value at the tension layer after applying the pre-repair damage load. The existing substrate strain was considered as the initial strain and excluded from the strain in the CFRP sheets. The design procedure was according to the ACI 420.2R (2002)

equations. For the ρ_{min} group, a CFRP sheet with 100mm width and 1.2 mm thickness was found to give the highest increase in the capacity before the CFRP debonding. While for ρ_{max} group a CFRP sheet with 50mm width and 1.2mm thickness gives the highest increase in the capacity before CFRP debonding. Using higher CFRP width is futile since the failure is controlled by CFRP debonding. The CFRP sheets were designed to be placed on the beam soffit and along the beam length between the supports.

4.3.2 Shear design

For the shear structural design, both ACI 318 (2008) and ACI 420.2R (2002) were used. There are two shear design cases i.e. one with internal shear stirrups in which the shear forces are resisted by the stirrups and concrete, while another without the internal shear stirrups in which all the shear forces are resisted solely by the concrete. This study will consider both design cases, with and without shear stirrups.

4.3.2.1 Unrepaired beams

For the unrepaired beams, the RC beam shear strength is from the contribution of the concrete and the shear stirrup in the case where it exists. The RC beams were designed to resist a concentrated load located at the quarter-span or at 1.5d from the support, where d is the effective beam depth and 1.5d is 32 cm, in addition to the self-weight of the beams. The shear group beams were designed in flexural to make sure that the beam would not fail in flexural, by using flexural steel bars with ρ_{max} to ensure high flexural capacity. The procedure of the shear design for both cases, with and without shear stirrups, as well as the flexural design to achieve the highest flexural capacity was according to ACI 318 (2008) equations. For the purpose of calculating the ultimate capacity of the beam, no safety factors or environmental reduction factors were used. For the group without shear stirrups,

two 16 mm diameter deformed steel bars were used as the main flexural reinforcement and no shear stirrups were used. For the group with stirrups, 6mm diameter steel bars with spacing of 100mm c/c were used as shear stirrups, two16 mm diameter deformed steel bars were used as the main flexural reinforcement and two 8 mm diameter not-deformed steel bars were used as the compression reinforcement. The same design was adopted for both shear damage scenarios, at quarter-span and at 1.5d from the supports. Figure 4.4 shows the cross section detail at the shear zone of the RC beams of both cases, with and without shear stirrups.

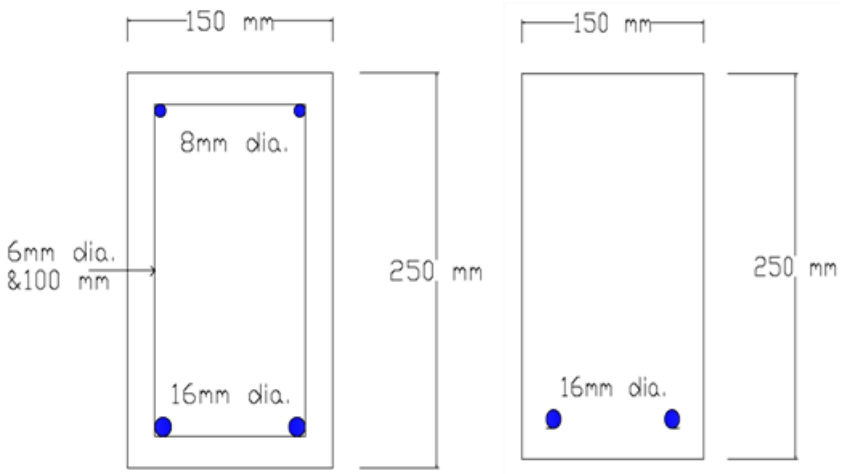

Figure 4.4. Cross section detail for shear beams, with stirrups (left) and without stirrups (right)

4.3.2.2 Repaired beams

The ACI 420.2R (2002) is used as the design guideline for repairing damaged beams in shear with externally bonded CFRP sheets. The ACI 420.2R (2002) considered three typical wrapping schemes for repairing or strengthening with external bonding namely 4 sided wrapping (complete wrapping) around the whole beam section, 3-sided wrapping (U–shaped wrapping) and 2-sided wrapping. Since the 4-sided wrapping cannot be used in

most existing structures while the 3-sided wrapping cannot be used in some structures, this study will use the two-sided wrapping to achieve the objective of this study. The objective of the repair with CFRP sheets design is to achieve the highest capacity by using the CFRP sheets within the limits of the ACI Codes. The limits set according to the criteria given in ACI 318 (2008) section 11.5.6.9 imply that the total shear resistance is taken as the sum of the contributions of the CFRP and steel stirrups. The design procedure was according to the ACI 420.2R (2002) equations. For the shear at quarter-span, three CFRP sheets with width of 100mm and thickness of 1.2mm are used on both sides of the beam between the quarter-span and the support within an inclined angle of 45^0 as shown in Figure 4.5. For shear damage at 1.5d from the support, two configurations were used. The first configuration consists of two CFRP sheets of 100m width and 1.2mm thickness with an inclined angle of 45^0 as shown in Figure 4.6. The second configuration uses two CFRP sheets of 100mm width and one of 50mm width placed vertically to cover the distance between 1.5d and the support as shown in Figure 4.7.

4.4 Testing Procedures

The aforementioned RC beams are tested using experimental approaches which include the static load test as well as modal testing. The static load test is carried out to obtain the static data such as load against deflection, load against steel strain and load against CFRP strain. The modal testing is carried out to obtain natural frequencies, mode shape and modal damping. The study includes two phases i.e. pre-repair phase for damage assessment and the post-repair phase for the CFRP repair assessment. The test procedures of each RC beam specimen are as shown in the flow chart in Figure 4.8, and the load cycles are shown in Tables 4.4 and 4.5.

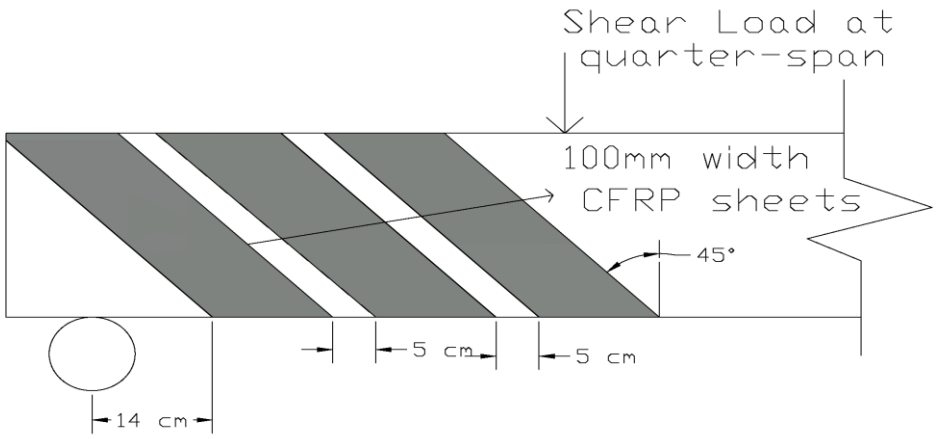

Figure 4.5. Repair configuration using CFRP sheets for shear damage at quarter-span

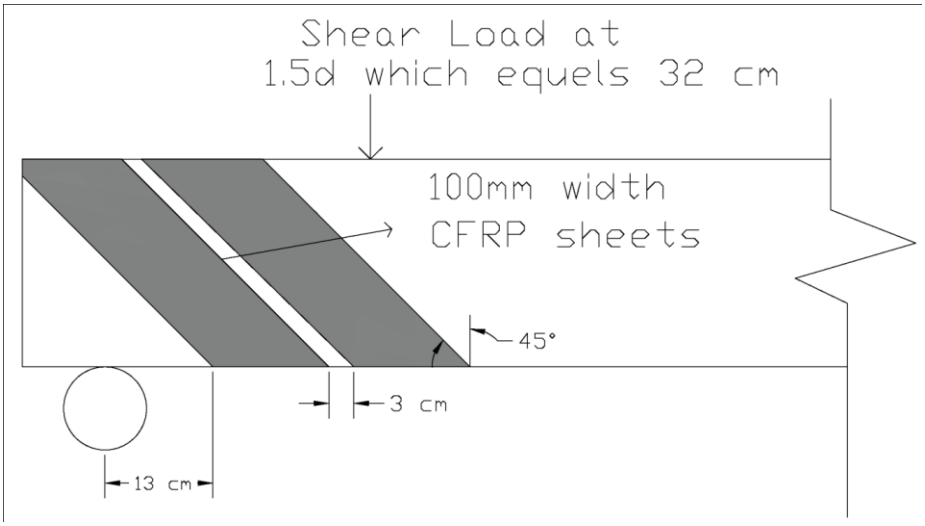

Figure 4.6. First repair configuration using CFRP sheets for shear damage at1.5d from the support

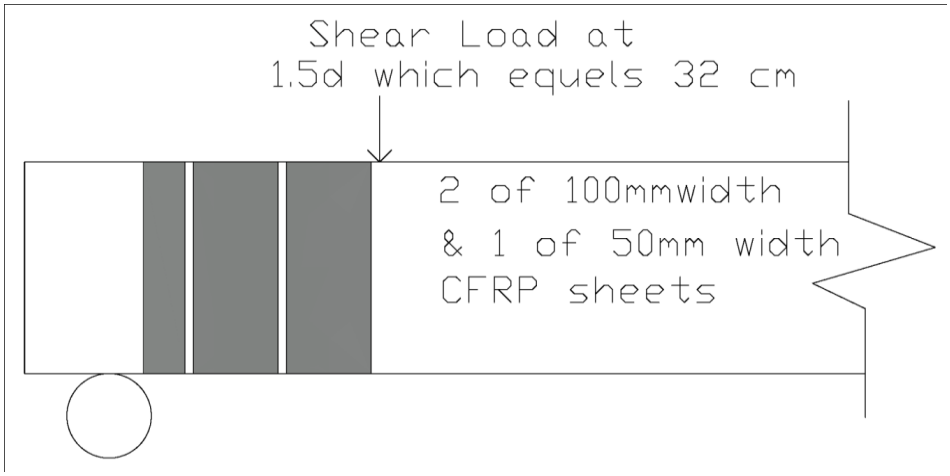

Figure 4.7. Second repair configuration using CFRP sheets for shear damage at1.5d from the support

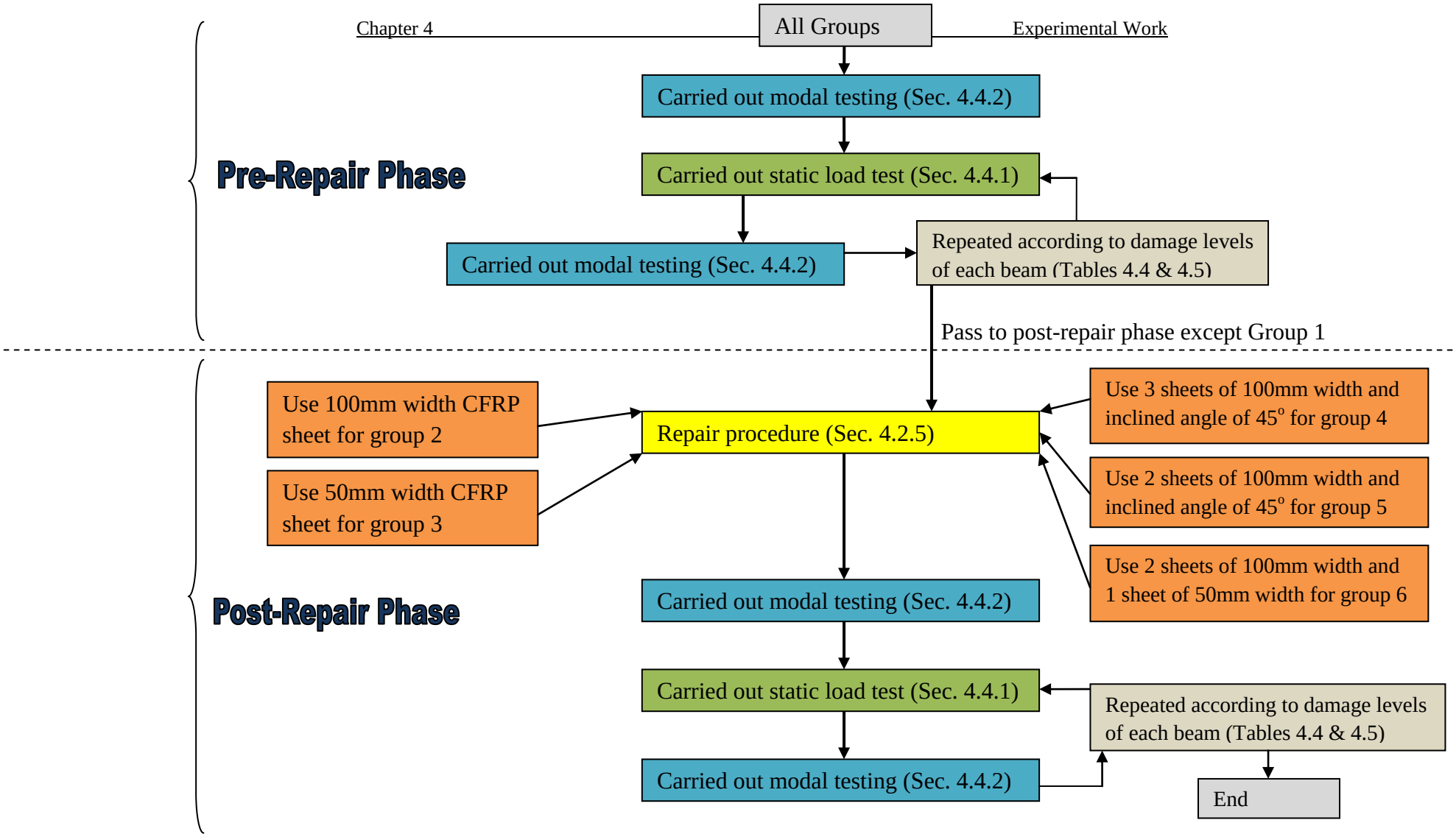

Group 1: Beams $B111_m$ and $B121_m$ Group 2: Beams $B122_m$, $B123_m$ and $B124_m$ Group 3: Beam $B112_m$, $B113_m$ and $B114_m$
Group 4: Beams $B211_q$, $B212_q$, $B221_q$, and $B222_q$ Group 5: Beams $B211_d$ and $B221_d$ Group 6: Beams $B212_d$ and $B222_d$

Figure 4.8. Flowchart for the test procedures of each RC beam

Table 4.4. Load cycles at pre and post repair phases for flexural group RC beams

Design	Flexural with ρ_{max}				Flexural with ρ_{min}			
Beam	$B111_m$	$B112_m$	$B113_m$	$B114_m$	$B121_m$	$B122_m$	$B123_m$	$B124_m$
Pre –Repair Phase	10 kN	40 kN	71 kN	82 kN	11 kN	25 kN	55 kN	85.8 kN (Failure)
	20 kN				20 kN			
	30 kN				30 kN			
	40 kN				40 kN			
	50 kN				50 kN			
	60 kN				60 kN			
	70 kN				70 kN			
	100 kN				72 kN (Failure)			
	107 kN (Failure)							
Post- Repair Phase	N/A	12 kN	12 kN	40 kN	N/A	25 kN	25 kN	25 kN
		40 kN	40 kN	70 kN		55 kN	55 kN	55 kN
		50 kN	71 kN	80 kN		70 kN	70 kN	85 kN
		60 kN	80 kN	90 kN		85 kN	85 kN	115 kN
		80 kN	100 kN	93 kN		100 kN	100 kN	127.5 kN
		100 kN	124.7 kN	94.5 kN (Failure)		115 kN	115 kN	128 kN (Failure)
		120 kN	101.5kN (Failure)			131 kN	130.7 kN	
		94 kN (Failure)				71 kN (Failure)	122 kN	
							84.8 kN (Failure)	

Table 4.5. Load cycles at pre and post repair phases for shear group RC beams

Location	Shear at quarter-span				Shear at 1.5d from the support			
Design	Without shear stirrups		With shear stirrups		Without shear stirrups		With shear stirrups	
Beam	$B221_q$	$B222_q$	$B211_q$	$B212_q$	$B221_d$	$B222_d$	$B211_d$	$B212_d$
Pre –Repair Phase	20 kN	25 kN (Design limit)	20 kN	48 kN (Design Limit)	155 kN	155 kN (Prior to Failure)	25 kN	126 kN (Prior to Failure)
	50 kN		50 kN		151 kN (Fully Failure)		41 kN	
	90 kN (Failure)		62 kN				56 kN	
			85 kN				67.5 kN	
			99 kN (Failure)				81 kN	
							96 kN	
							110 kN	
							135.5 kN	
							142.5 kN (Fully Failure)	
Post- Repair Phase	25 kN	25 kN	48 kN	48 kN	25 kN	25 kN	25 kN	25 kN
	84 kN	90 kN	100 kN	100 kN	150 kN	155 kN	135 kN	126 kN
	91 kN	120 kN	107 kN	117.5 kN	120 kN	165 kN (Failure)	143 kN	165 kN
	101 kN (Failure)	110 kN (Failure)	101 kN (Failure)	120 kN (Failure)	103 kN (Failure)		106 kN (Failure)	154 kN (Failure)

4.4.1 Static load test

Static test is used in this study to induce damage into the RC beams, and the obtained static data is used to find the flexural and shear stiffness. The static load test includes application of concentrated load to the RC beam at different locations depending on the required damage scenario i.e. flexural at mid-span, shear at quarter-span and shear at 1.5d from the support. A steel frame is used to apply the load using a load actuator controlled by a servo hydraulic pump, as shown in Figure 4.9.

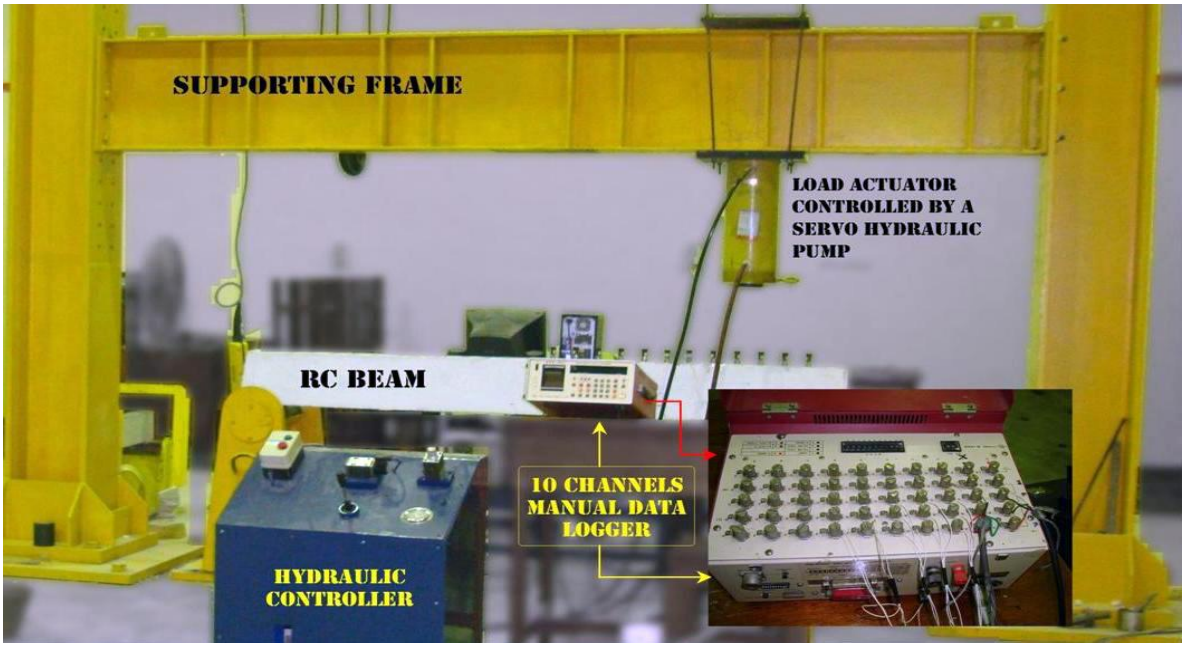

Figure 4.9. Static load tests machine and equipments

Load was applied gradually at a loading rate of 0.75 kN/min. and applied in cycles of loading and unloading. A 50mm displacement transducer was placed at the point of the maximum defection to measure the displacement. For the flexural loading, the maximum deflection was located at the mid-span. For the shear loading, the maximum deflection was located between the point of the applied load and the mid-span. For estimating the

maximum deflection location for shear loading, a finite element model was created as shown in Appendix A. The results show that the maximum deflection for the shear loading at quarter-span is at 82cm from the left support, while for shear damage at 1.5d is 70 cm from the left support.

The load cell of 250 kN capacity was placed directly below the hydraulic load actuator to measure the loads, as shown in Figure 4.10. The steel bar strain was measured using strain gauges fixed on the bars after cleaning and smoothing the surface at the applied load position.

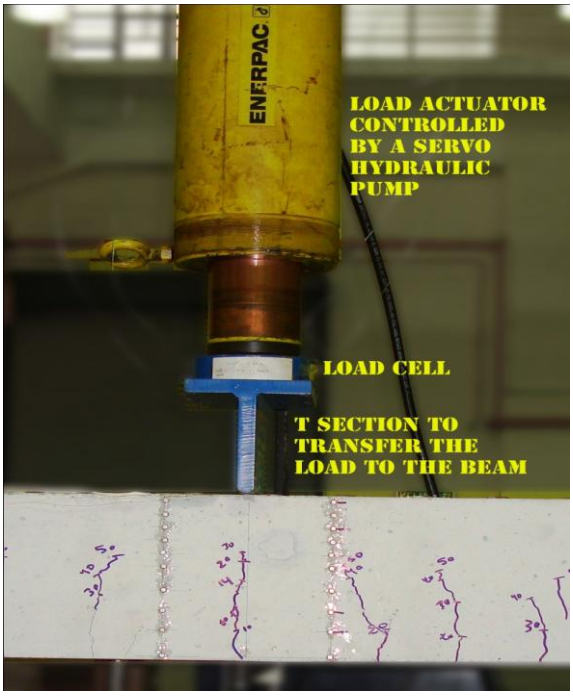

Figure 4.10. Load cell position in the static load test

The CFRP sheets strain was measured using strain gauges fixed on the CFRP sheets surface at the maximum expected strain position, which for flexural group is at the mid-span with the CFRP sheet placed on the beam soffit. The CFRP strain of shear group at quarter-span was monitored on each of the sheets (as mentioned in Section 4.3.2.2) on both sides of the

damaged beam corresponding to the load cycles, with the first strain gauge 'SG1' nearest to the quarter-span and the 'SG3' nearest to the supports, as shown in Figure 4.11). For shear damage at 1.5d (first and second configuration) the CFRP strain was monitored using strain gauges on each of the four sheets (of 100mm width as mentioned in Section 4.3.2.2) used on both sides of the damaged beam corresponding to the load cycles. The first strain gauge 'SG1' is nearest to the applied load point at 1.5d and the second strain gauge 'SG2' is the nearest to the supports, as shown in Figure 4.12. The load cell, displacement transducer, steel strain gauges and CFRP strain gauges were connected to the manual data logger, as shown in Figure 4.9, with data sets printed out for every loading cycle.

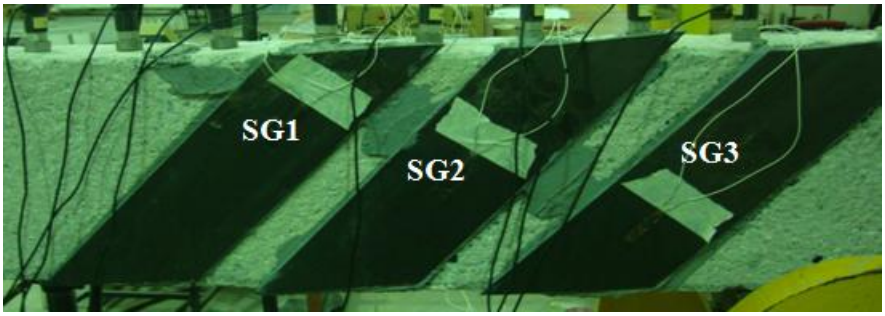

Figure 4.11. CFRP Strain gauge positions for repair of shear damage at quarter-span

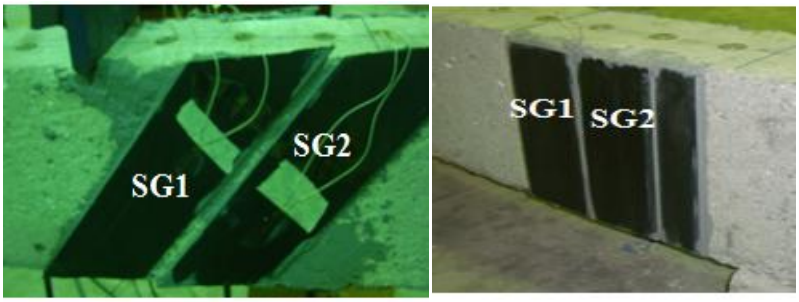

Figure 4.12. CFRP Strain gauge positions for repair of shear damage at 1.5d

4.4.2 Modal testing

Modal testing was carried out on the RC beams using transfer function technique. Accelerometers with a sensitivity of 100mV/g were used to pick up the response on the tested beam under forced excitation, as shown in Figure 4.13. The beam was randomly excited using an electromagnetic shaker, as shown in Figure 4.14, with a white noise signal source from an output channel of the digital signal analyser via a power amplifier, as shown in Figures 4.15 and 4.16, respectively. The vibration was transferred from the shaker to the beam via a plunger with a force transducer having a sensitivity 11.24mV/N attached to the top of the shaker to measure the input force, as shown in Figure 4.14. Both the input and output signals were fed to the signal analyser for real-time data acquisition and processing in the frequency domain. Figure 4.17 shows the positions of the accelerometers on the test beam and the modal test setup.

Initially, the frequency response function (FRF) spectrum within a bandwidth of 2.5kHz, to cover the first six natural frequencies, was obtained by executing Fast Fourier transform (FFT) on the time domain signals acquired. The number of lines used in the frequency bandwidth was 6401 (the maximum for the signal analyser) giving a resolution of 0.39Hz. The averaging of the repetitive FRF set of data was 100 times, and the overlap between each subsequent data set was 15%, in order to get higher accuracy. A total of 72 measurement points on the top surface of the beam were covered, by roving the accelerometers while keeping the excitation point permanently fixed. A total of twelve accelerometers were used and the accelerometers were roved from point to point until all the measurement points were covered. The measurement points were located on the top surface of the girder as shown in Figure 4.18, with points 1, 24, 25, 48, 49 and 72 located at the supports. The distance between each measurement point was 95mm and 60mm in the

longitudinal and transverse directions of the girder, respectively. The reference point was at the beam soffit and coincident to measurement point number 38 as shown in Figure 4.18.

The transfer functions for all the points are derived by dividing the Fourier transforms of the output (acceleration response) with the input (excitation force). Modal parameter extraction process is done by curve fitting the set of transfer function measurements in order to obtain the natural frequencies, mode shapes and damping ratios. In this study, the first six flexural modes were identified so as to be used.

The main assumption of using the modal testing is that the tested structure behaves as a linear system. Whilst in the real practices, the RC structures seldom behave in a completely linear fashion. In order to verify the validity of the assumption, the following were performed;

- Reciprocity check: natural frequencies have to be the same within the position of the measured points.
- Linearity check: natural frequencies have to be the same at different strengths of excitation.
- Repeatability check: modal parameters have to be stable within any number of repetitions.

For the reciprocity check, the RC beams were tested with two opposite locations on the RC beam chosen (one to the left of the mid-span and another to the right). First, the left point was used as the excitation point and the right point the acceleration measuring point. The second arrangement was vice versa. The results show that there was no significant change in the natural frequencies of the first six bending modes. For the linearity check, the RC beam was excited with different excitation forces within a range of the input voltage to the shaker of 100, 300, 600, 900 and 2000 mV, and the results show no significant change in

the natural frequencies of the first six bending modes. For the repeatability check, the RC beam was first tested at different times, i.e. morning, after-noon and evening, in order to examine the effect of environmental conditions i.e. temperature, humidity and the ambient noise level, on the natural frequencies. The results show no change in the natural frequencies. For the time invariance check, the RC beam was tested at different times after static load cycles, in order to check the effect of concrete creep. The results show that there was a significant drop in the natural frequencies after release of the applied static load either flexural or shear, when the modal testing carried out immediately. The natural frequencies recovered and became stable again within duration of 24 hours i.e. the maximum for different loading cycles and loading positions. Thus, for all beams, the modal test was carried out after 24 hours from the time of the static load release.

Figure 4.13. Accelerometers with a sensitivity of 100mV/g

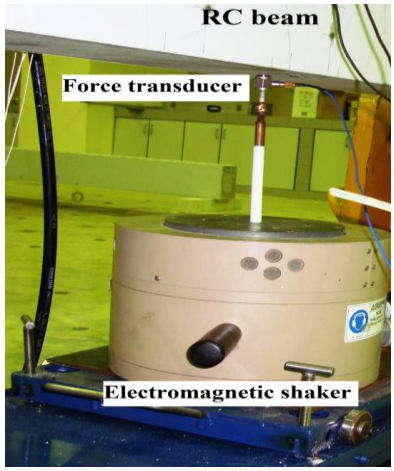

Figure 4.14. Electromagnetic shaker and force transducer connected at the top and attached the RC beam soffit

Figure 4.15. Digital signal analyser (OROS)

Figure 4.16. Power amplifier

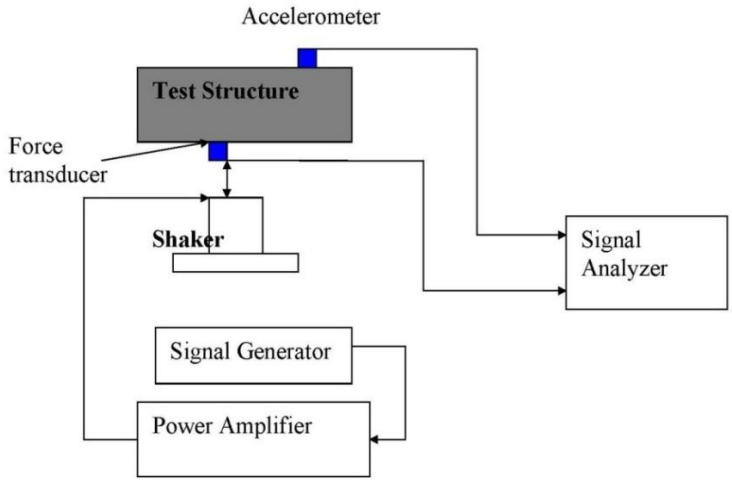

Figure 4.17. Modal test setup and RC beam at actual test

Figure 4.17. Continue

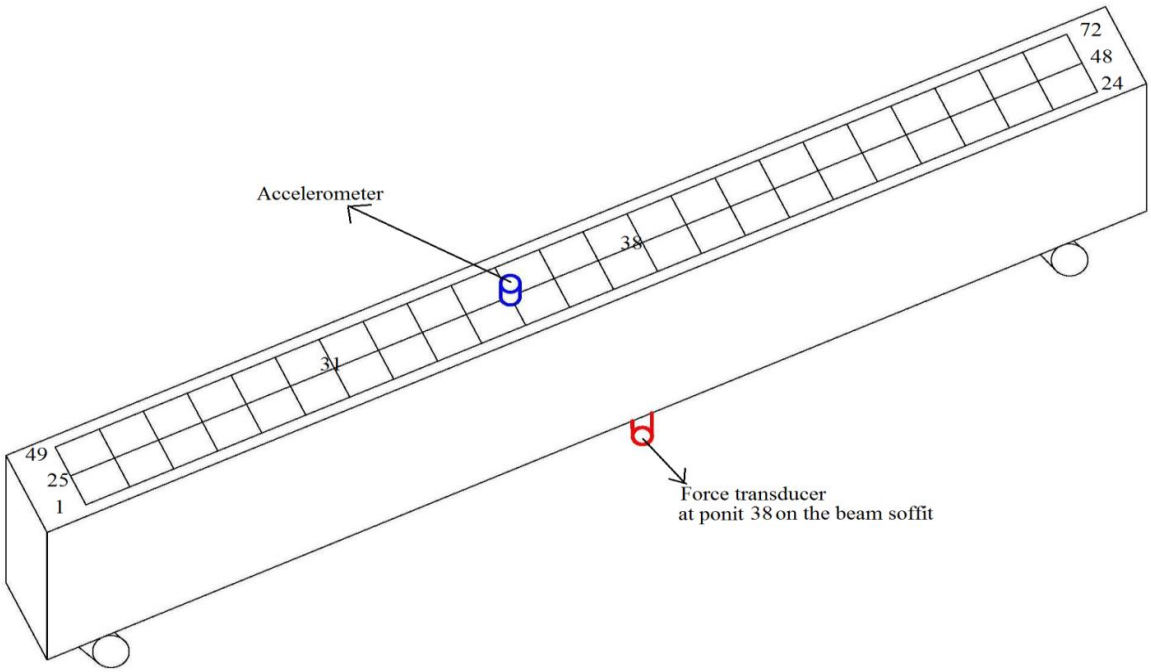

Figure 4.18. Measurements locations on the tested RC beam

Chapter 5: Damage Assessment

5.1 Introduction

This chapter presents the results obtained from the experimental approaches, for both dynamic and static testing in order to investigate the damage assessment procedures. Firstly, the results related to Composite Action Phenomenon (CAP) and its influence on the modal frequencies are presented. This is followed by the investigation on the identification of the damage type, that is, either due to damage loading effect on structural stiffness or change in the support stiffness. The chapter also presents the results related to damage severity by investigating the sensitivity of existing algorithms as well as a newly developed algorithm. Furthermore, the results of existing, modified, and newly developed damage location algorithms are presented and compared.

5.2 Composite action phenomenon

In order to investigate the composite action phenomenon in RC structures and its effect on the dynamic parameters discussed in Section 3.4, four RC beams are utilised, namely $B111_m$ (flexure with maximum steel ratio), $B121_m$ (flexure with minimum steel ratio), $B211_d$ (shear with a load of 1.5 the effective depth (d) from the left support), and $B211_q$ (shear with a load of 0.25L from the left support) (Note: refer to Section 4.3 for the beam details and properties).

Initially, the natural frequencies are obtained by conducting experimental modal analyses before the application of load, the results of which will serve as the data. Load is applied gradually at a loading rate of 4kN/min and is applied in cycles, that is, loading and

unloading. The first cycle is up to the first crack load, and subsequent cycles continue until prior to failure. After each cycle, the load is released and the natural frequencies for each respective load cycle are obtained from the modal testing. During the application of load for the static test, data for the load against deflection curves, steel strain curves, and residual strains in the steel bar after unloading is measured and recorded.

The natural frequencies of the first six bending modes are acquired, and in order to compare the damage cases with the control case, frequency change is used as shown in Equation 5.1.

$$\text{Frequency Change } (\%) = \frac{f_d - f_c}{f_c} .100\ \% \tag{5.1}$$

where *f* is the frequency, *d* indicates the damage case, and *c* indicates the undamaged case.

5.2.1 Flexure

Based on current guidelines and practices, such as the American Concrete Institute (ACI) design guidelines, there is provision for two limits of the steel ratio in the tension layer as reinforcement requirements for structural elements are subjected to flexure. Minimum steel limit (ρ_{min}) is provided to prevent cracking due to thermal expansion while the maximum steel limit (ρ_{max}) is provided to prevent brittle failure due to crushing of concrete. Thus, in this study, taking into consideration the two steel ratio limits, one RC beam is designed with ρ_{min} denoted as $B121_m$ and the other is designed with ρ_{max} denoted as $B111_m$, using 12 mm and 16 mm diameter bars respectively. In this study, both steel ratios (ρ_{min} and ρ_{max}) are used to ensure that failure occurs due to the steel yielding and not brittle failure as a result of concrete crushing. The RC beams are subjected to point loads located at the mid-span to induce flexural stresses much higher than shear stresses. The loads applied and number of cracks at each damage level for beams $B111_m$ and $B121_m$ are illustrated in Table 5.1.

Table 5.1. Applied load and cracks for beams $B111_m$ and $B121_m$

Damage Level (DL)	Applied Load		Number of Cracks	
	$B111_m$	$B121_m$	$B111_m$	$B121_m$
Control	0 KN	0 KN	N/A	N/A
DL 1	10 KN	11 KN	1 (First crack)	1 (First crack)
DL 2	20 KN	20 KN	6	3
DL 3	30 KN	30 KN	9	7
DL 4	40 KN	40 KN	11	9
DL 5	50 KN	50 KN	12	13
DL 6	60KN	60 KN	15	16
DL 7	70KN	70 KN(prior to failure load of 72 kN)	15	16
DL 8	100 KN(prior to failure load of 107 kN)	N/A	16	N/A

5.2.1.1 Maximum steel ratio

The results of the maximum steel ratio (ρ_{max}) for beam $B111_m$ in Figure 5.1 shows a comparison between the natural frequencies of the damage cases and the control. It is evident that different modes have different levels of sensitivity for each damage level. In particular, mode 1 shows a contrasting trend when compared to the other modes as the damage level increases. Figure 5.2 shows the load against mid-span deflection plots at different damage levels up to failure. The failure occurs at 107 kN as flexural failure, where the flexural steel first ruptures, followed by the concrete crushing. The steel yields at 70 kN as shown in Figure 5.3, which presents the increase in steel strain under applied loading at each step of the damage level. The crack patterns corresponding to each load cycle and up to failure are illustrated in Appendix B.

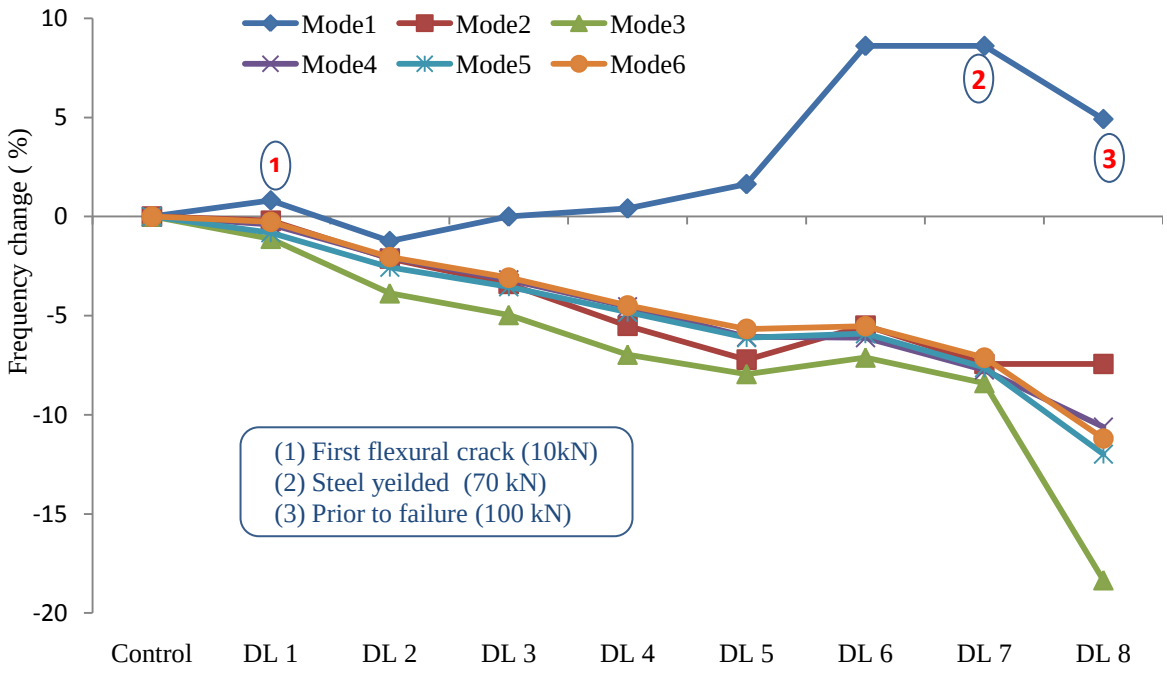

Figure 5.1. Frequency changes at different damage levels for beam $B111_m$

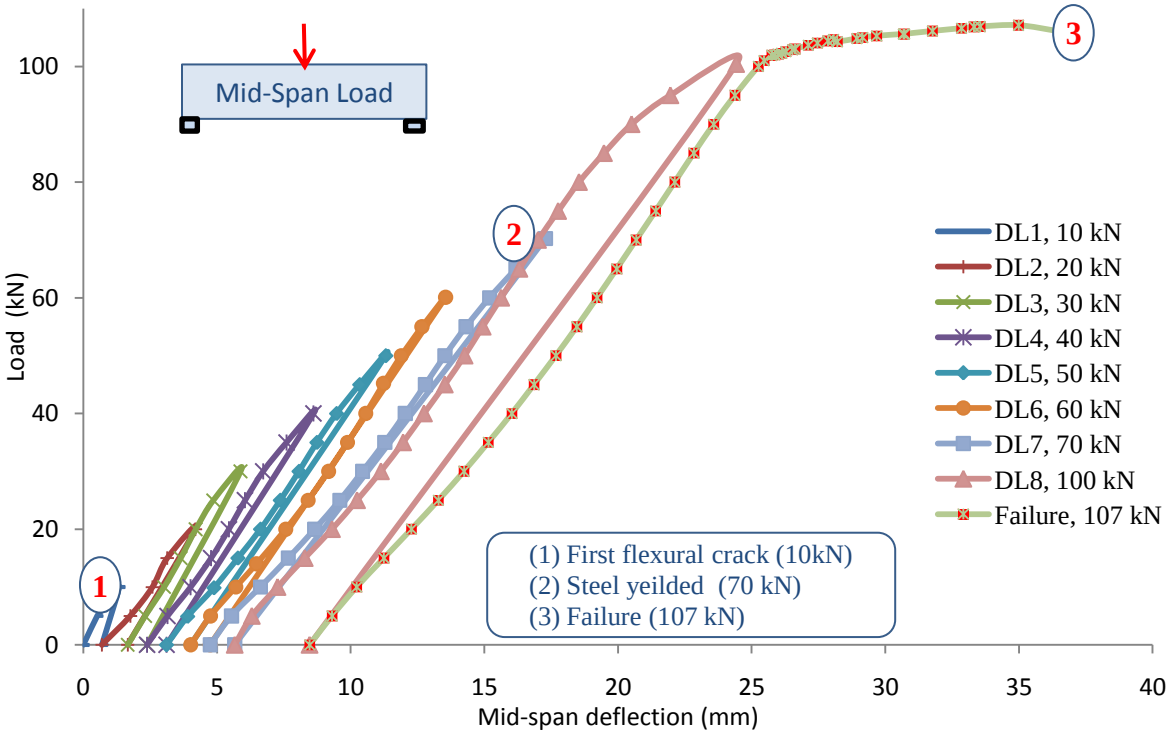

Figure 5.2. Load against mid-span deflection for damage levels of beam $B111_m$

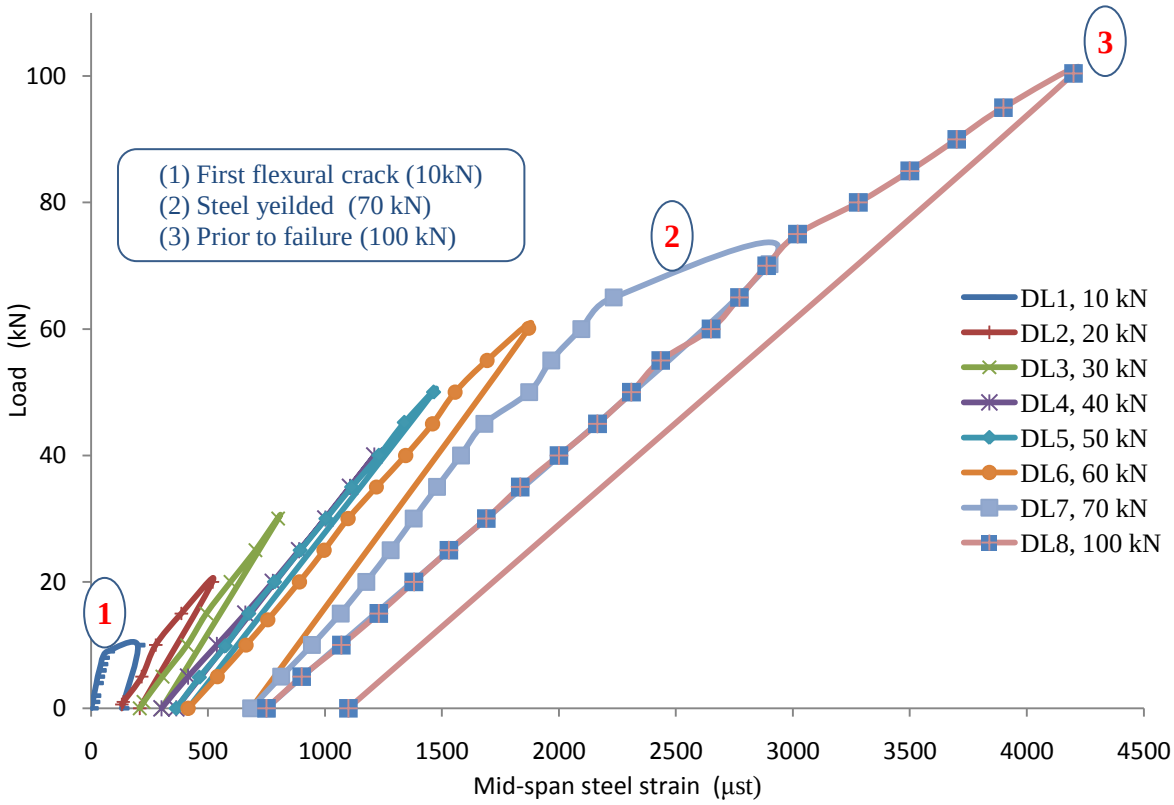

Figure 5.3. Load against steel strain for damage levels of $B111_m$

For level 1 damage, when the applied load is 10kN, the first crack appears on the tension face. Consequently, the concrete behaves nonlinearly due to the crack, leading to a decrease in concrete stiffness in tension; that is, $K_{tension}$ [Marfia et al.(2004), Hughes and Chapman (1966), Kupfer et al. (1969)]. As a result there is an overall reduction of the global RC stiffness, K_{RC}. Concrete in compression still behaves as a linear material, since the compressive stress is lower than 30% of the compressive strength. Thus, the concrete stiffness in compression to $K_{compression}$ is unaffected [Marfia et al. (2004), Karsan and Jirsa (1969), Kupfer et al. (1969)]. The steel behaves linearly since it has not yielded, and thus the steel stiffness K_{steel} is also unaffected and does not have any effect on the global RC stiffness, K_{RC}. Bond action is initiated when the steel strain reaches approximately 200µst, and this causes increased resistance and compression-bond action, as illustrated in Figure 3.5 in Chapter 3.

When the load is released, the steel tends to return to its original state prior to loading, but the tension-bond action resists this phenomenon, as illustrated in Figure 3.6 in Chapter 3. The residual strain in the steel is 132μst, as indicated in Figure 5.4 which presents the residual strain for each damage level at the unloading stage. The tensile residual strain arising from the tension-bond action increases the RC element stiffness because of the pretension bonding action, which in turn increases the bond stiffness, K_{bond}, and consequently an increase in overall RC stiffness, K_{RC} occurs.

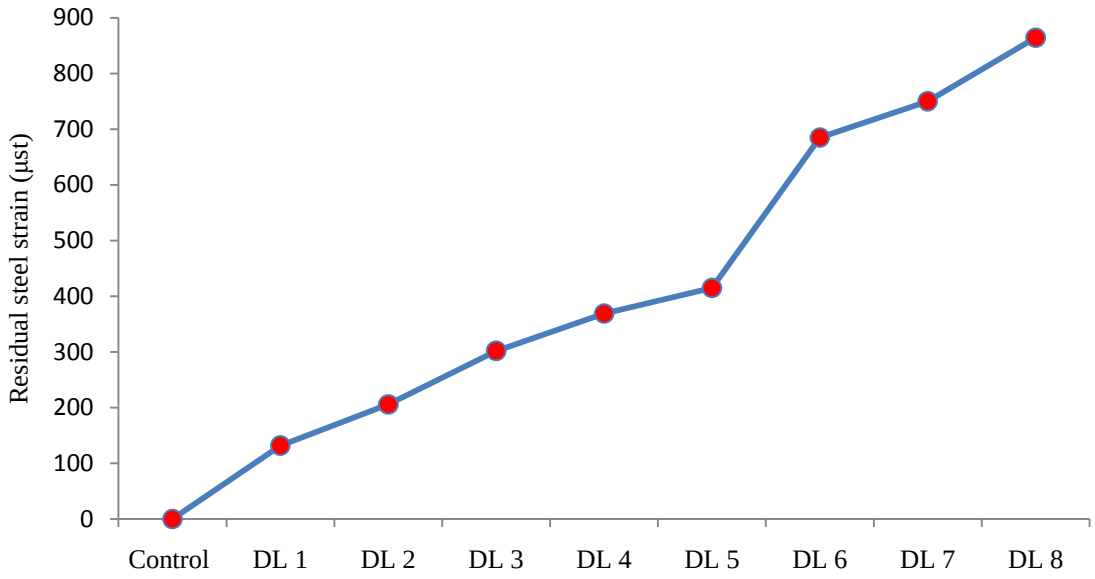

Figure 5.4. Residual steel strains upon unloading at each damage level for $B111_m$

At this stage, that is, upon unloading after inducing level 1 damage, the overall stiffness of the RC beam is governed by two effects. Firstly, a decrease due to the softening of the concrete in the tension zone is influenced by the appearance of the first crack. Secondly there is an increase due to the tension-bond action at the interface between the steel and the concrete. As a consequence of the composite action phenomenon in the RC beam, each individual effect has its own influence on the natural frequencies and is observed to be different. Thus, as observed from Figure 5.1, the increase in the first natural frequency

namely Mode 1, is related to the increase in bond stiffness, K_{bond}. The second natural frequency namely Mode 2, shows no change where the increase in the bond stiffness cancels out the softening of the concrete in tension. The decrease in the other natural frequencies is related to the softening of concrete in tension $K_{tension}$. The same trend is observed by Ismail (2005)**,** where an increase in the first natural frequency occurs just after applying the flexural loading to the RC beam.

When the load is increased to 20 kN, the number of cracks in the tension zone increases to six, as shown in Table 5.1. This leads to a further decrease of concrete stiffness in tension, $K_{tension}$. The residual strain in the steel after unloading for this stage is 208μst, as indicated in Figure 5.4. This residual strain, which reflects the tension-bond action, implies that there is a further increase in the interaction stiffness, $K_{bond,}$ when compared to the previous load stage. The decrease in concrete stiffness as the number of cracks increases is much higher when compared to the decrease in the bond stiffness, K_{bond}. This is manifested in the decrease in frequencies for all the modes which is shown in Figure 5.1 and arises from the effect of concrete softening.

At an applied load of 30 kN, the number of cracks in the tension zone increases to nine, as demonstrated in Table 5.1, and this leads to a further increase in concrete softening and a decrease of concrete stiffness in tension, $K_{tension}$. The residual strain in the steel is 302μst, as given in Figure 5.4, which is an increase of 50% compared to the previous load stage. Correspondingly, the natural frequency for Mode 1, which is sensitive to changes in the bond stiffness, K_{bond}, experiences an increase, while the natural frequencies for all the other modes are reduced due to the decrease in concrete stiffness in tension, $K_{tension}$, which is a result of concrete softening.

Subsequently, when the damage load is increased progressively to 40 kN, 50 kN, and 60 kN, it is apparent from Figure 5.1 that the trend remains the same. The first natural

frequency increases gradually with an increase in the interaction stiffness, while the other natural frequencies experience a reduction with the softening of the concrete in tension and compression. Under increasing loads, more cracks appear on the tension side, leading to a decrease of concrete stiffness in tension, $K_{tension}$. The concrete in the compression zone begins to behave nonlinearly when the compression strength exceeds 30% of f_c, resulting in a decrease of concrete stiffness in compression, $K_{compression}$ [Marfia et al. (2004); Karsan and Jirsa (1969); Kupfer et al. (1969)]. However, since the steel strain is still less than the yield strain, as indicated in Figure 5.3, the steel stiffness, K_{steel}, remains constant. The tension-bond action increases gradually as the residual strains increase, as in Figure 5.4. This leads to an increase in bond stiffness, K_{bond}.

When the applied load reaches 70 kN, the strain in the steel is 2850μ, and the steel reaches its plastic limit, which leads to a decrease in K_{steel}. The concrete continues to soften while the residual strain in the steel increases to 750μst. At this stage, the overall element stiffness, K_{RC}, is affected by both the nonlinearity of the concrete and steel as well as the increase in tension-bond action. The effect of this composite behaviour on the global stiffness, and subsequently on the natural frequencies of the modes, is reflected in Figure 5.1. The yielding of the steel is indicated by Mode 1, whereby there is no change in the natural frequency, although there is an increase in tension-bond interaction. The other modes consistently decrease in line with the decrease in the concrete stiffness ($K_{tension}$ and $K_{compression}$) and steel stiffness (K_{steel}).

Finally, at a load of 100 kN, which is prior to failure, the steel strain recorded is 5370μst. Major stiffness loss and a decrease in K_{steel} is seen. Consequently, this affects the bond between the concrete and the reinforcement, leading to slipping. Prior to failure, the natural frequencies of all the modes are governed by the loss in stiffness of the two constituent

materials in the RC beam, and the effect of the bond stiffness, K_{bond}, is non-existent. This is apparent from Figure 5.1, whereby all the natural frequencies exhibit a decreasing trend.

5.2.1.2 Minimum steel ratio

The results of the minimum steel ratio (ρ_{min}) beam $B121_m$, are given in Figure 5.5 and show a comparison of natural frequencies for Modes 1 to 6 for different levels of damage with the control. It is observed that Mode 1 has an opposite trend compared to the other modes which consistently decrease with increasing levels of damage. Following the same line of argument in the previous section, the sensitivity of each of the modes to the changes in the various components of stiffness of the composite RC beam are presented.

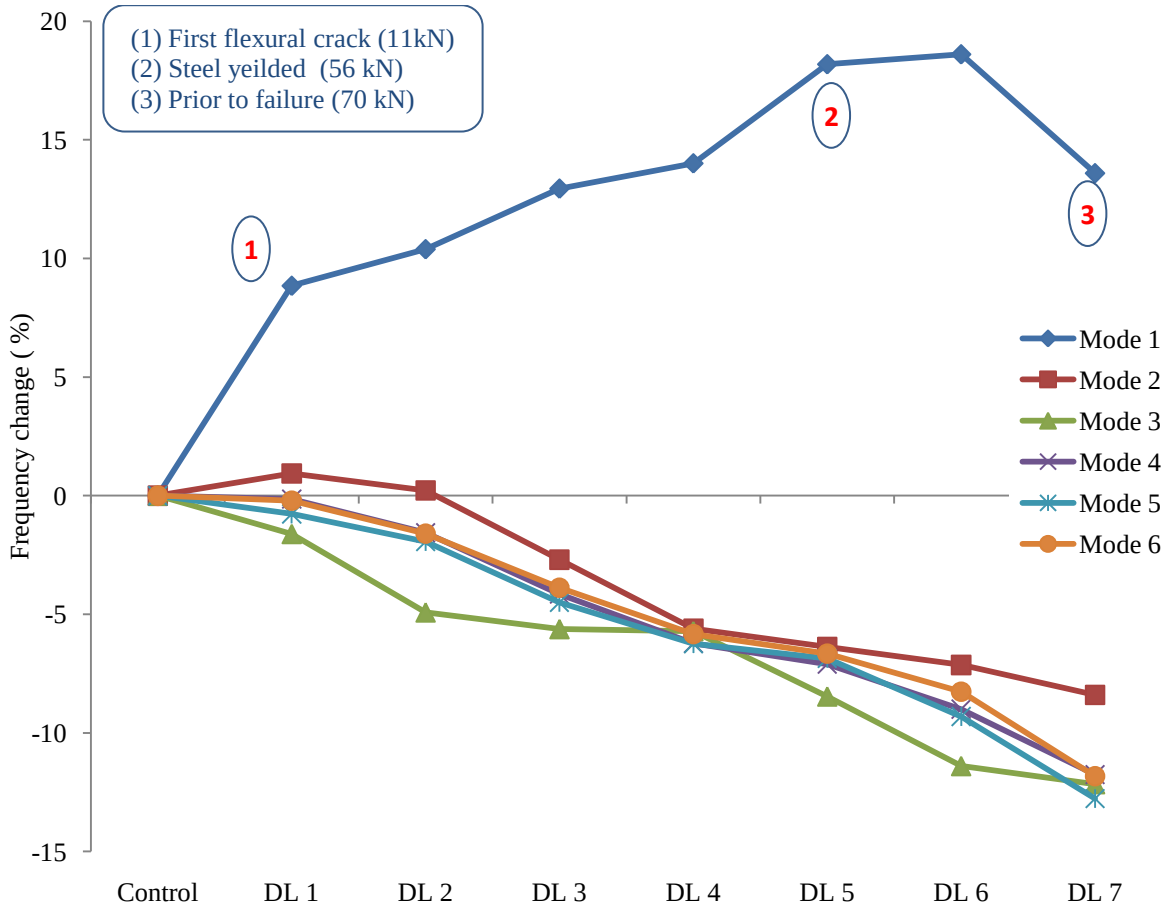

Figure 5.5. Frequency changes at different damage levels for beam $B121_m$

The damage level loads and number of cracks are shown in Table 5.1. Figure 5.6 shows the load against mid-span deflection plots corresponding to each load cycle until failure. The failure occurs at 71 kN as flexural failure, where the steel ruptures followed by the concrete crushing. The steel yields at a load of 56 kN as shown in Figure 5.7 which presents the strain under loading at each damage level. The crack patterns corresponding to the load cycles and up to failure are illustrated in Appendix B.

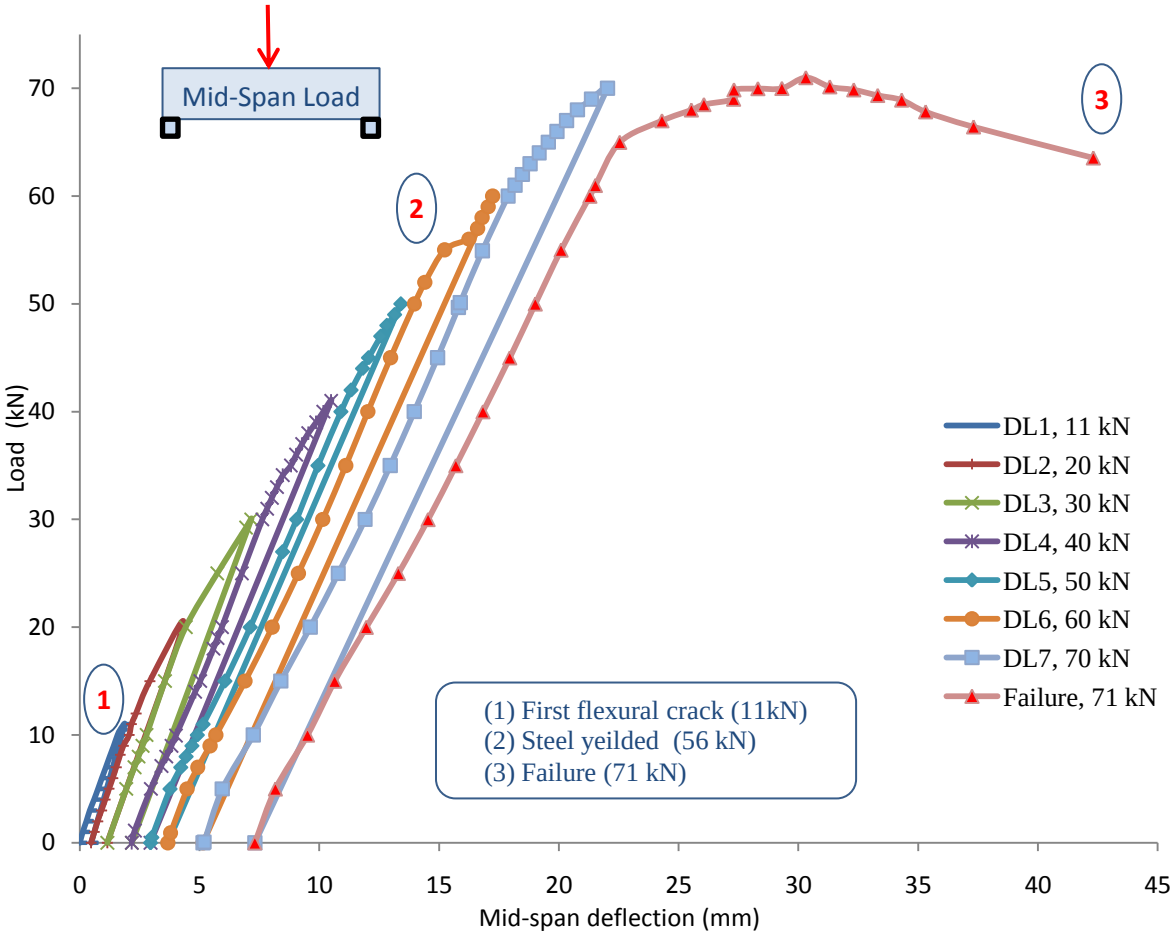

Figure 5.6. Load against mid-span defection for damage levels of $B121_m$

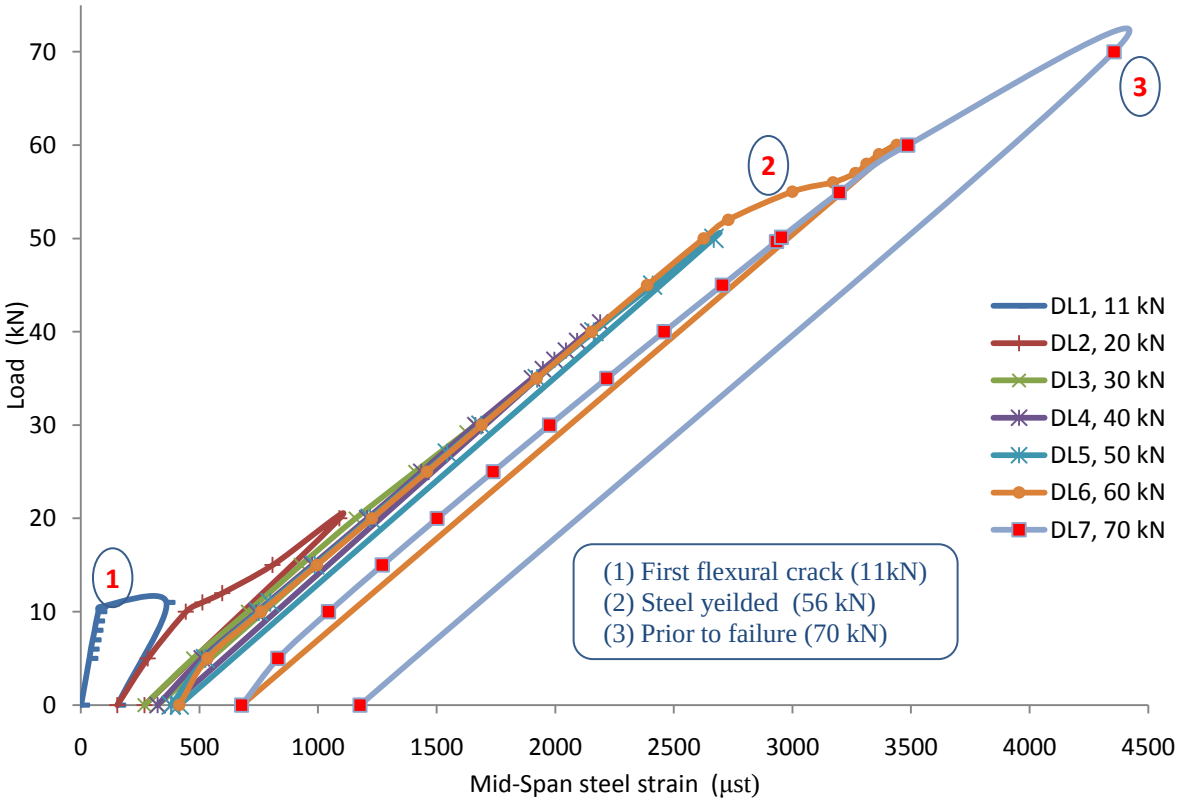

Figure 5.7. Load against mid-span steel strain for damage levels of beam $B121_m$

For beam $B121_m$ the first crack load is 11 kN, and from Figure 5.7, the corresponding steel strain is 360µst when bond action is initiated. The residual strain in the steel after unloading at this stage is 160µst, as indicated in Figure 5.8 which presents the residual strain for each damage level at the unloading stage. As discussed previously, based on composite action, this residual strain leads to pre-tension bonding action, which increases the interaction stiffness. As is evident from Figure 5.5, the natural frequencies for Modes 1 and 2 are influenced by this increase in K_{bond}. The natural frequencies for the other modes are influenced by the decrease in concrete stiffness, $K_{tension}$, due to softening arising from the emergence of the first crack.

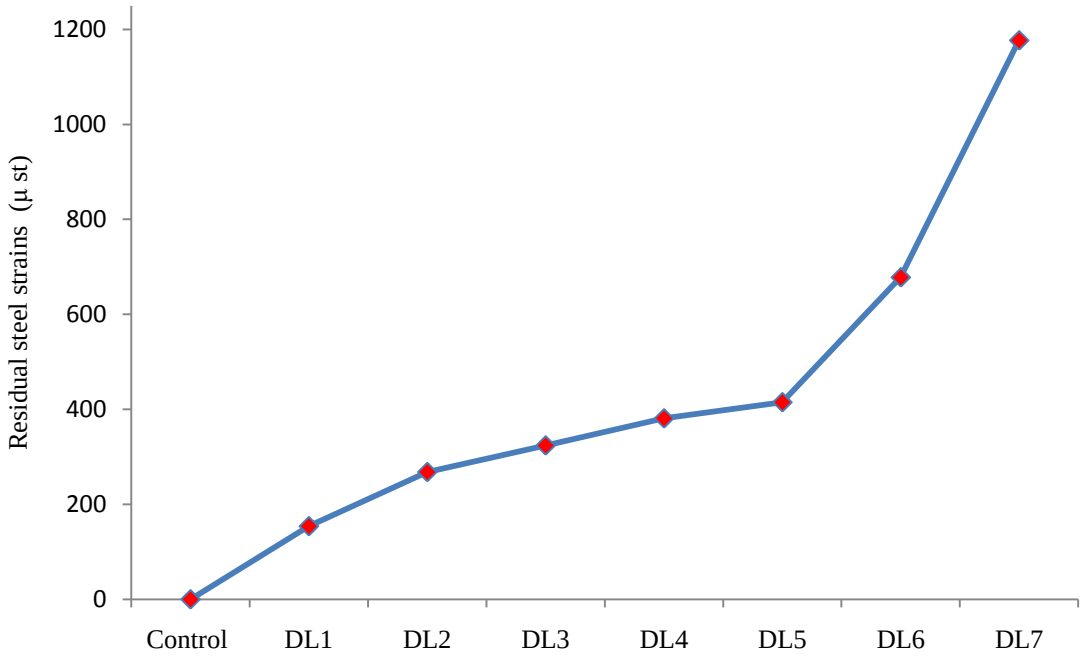

Figure 5.8. Residual steel strains upon unloading at each damage level for beam $B121_m$

It is observed that the effects of the composite action phenomenon (CAP) on the natural frequencies are different for beams $B111_m$ and $B121_m$ due to the different amount of steel reinforcement provided and the different compressive strengths of the concrete. The relationship between steel bar diameter and bonding action is inversely proportional. For larger steel bar diameters, the steel area is higher, but the tension force in the steel bar (i.e. $T = A_s \bullet F_s$) is lower, giving less tension-bond action. In addition, with the larger steel bar diameter, the bar perimeter is larger, leading to a larger interface between the steel and the concrete and hence a lower bond force per unit area. Higher compressive strength will lead to more shear force from the surrounding concrete resulting in an increase in bond action. Beam $B121_m$ is reinforced with less steel compared to beam $B111_m$ and the concrete for beam $B121_m$ has a higher compressive strength than $B111_m$. Thus, beam $B121_m$ possesses a higher tension-bond force leading to a much higher increase in the bond stiffness, K_{bond}. The larger bond stiffness, K_{bond} for $B121_m$ leads to a higher increase in the first natural

frequency. This is apparent from the increase in frequency for $B121_m$ and $B111_m$, which is 9% and 1.5%, respectively. The effect carries over to the second natural frequency for $B121_m$ where the increase in frequency is 1.5%, while for $B111_m$ there is no increase. This is similar to the experimental results obtained by Ismail (2005), where an increase in the first and second natural frequency occurs early during the loading cycles using RC beams reinforced with the minimum steel ratio (ρ_{min}).

At damage level 2, with an applied load of 20 kN, there are only three cracks in the tension zone as shown in Table 5.1 compared to six cracks for beam $B111_m$. The residual steel strain after unloading at this stage is also higher with a value of 270μst compared to 200μst for beam $B111_m$. Hence, the increase in bond stiffness, K_{bond}, at this stage is higher compared to the decrease in the tension stiffness of concrete, $K_{tension}$, due to cracking and softening. The overall effect is manifested in the trend shown in the first natural frequency, which continuously increases while the second natural frequency shows a much shallower drop. The other natural frequencies consistently exhibit a drop, which is related to the softening of concrete, $K_{tension}$.

At higher increments of the loading and just prior to failure, the trend in the changes of the natural frequencies is similar to beam $B111_m$. For the first natural frequency, the changes are governed by the increase in the bond stiffness, K_{bond}, until just prior to the yielding of the steel and failure of the beam. The highest increase in the first natural frequency for beam $B121_m$ (ρ_{min}) is 18.6% while for beam $B111_m$ (ρ_{max}) it is only 8.6%, just prior to the yielding of the steel. This is due to lower bar diameter and higher concrete compressive strength of beam $B121_m$ compared to beam $B111_m$. For the natural frequencies of all the other modes, the influence of the decrease in concrete stiffness ($K_{tension}$ and $K_{compression}$) and steel stiffness (K_{steel}) has a dominant effect when the steel yields. The lowest change for Modes 2 to 5 is 12.7 % for beam $B121_m$ (see Figure 5.1), while it is 18.4% for beam

$B111_m$ (see Figure 5.5). This is due to the higher compressive strength for beam $B121_m$ compared to $B111_m$, where higher concrete compressive strength will reduce the concrete softening at tension and compression zones at the same damage level.

5.2.2 Shear

For the shear case, two RC beams denoted by $B211_d$ and $B211_q$ are subjected to a point load at a distance of 1.5d from the support and at quarter-span respectively. The applied loads and the number of cracks corresponding to each load cycle for beams $B211_d$ and $B211_q$ are shown in Table 5.2.

Table 5.2. Damage levels and corresponding number of cracks for $B211_d$ and $B211_q$

Damage Level (DL)	Applied Load		Number of Cracks	
	$B211_d$	$B211_q$	$B211_d$	$B211_q$
Control	0 kN	0 kN	N/A	N/A
DL 1	25 kN	20 kN	1 (first flexural crack)	1(first flexural crack)
DL 2	41 kN	50 kN	3	9(first shear crack)
DL 3	56 kN	62kN	7	10(diagonal shear crack)
DL 4	67.5 kN	85kN	8	13
DL 5	81 kN	99 kN	10(first shear crack)	16
DL 6	96 kN	N/A	12(diagonal shear crack)	N/A
DL 7	110 kN	N/A	13	N/A
DL 8	135.5 kN	N/A	14	N/A
DL9	142.5 kN	N.A	14	N.A

5.2.2.1 Shear at 1.5d

The results for the shear case at 1.5d from the support, where much higher shear stress than the flexural stress is induced, may highlight the influence of the shear stresses on the composite action in the RC beams and its influence on the modal frequencies. Figure 5.9 shows the frequency change corresponding to the damage levels. The beam fails at 142.5 kN as shown in Figure 5.10 which presents the load against the maximum deflection (between 1.5d from the support and the mid-span) corresponding to the load cycles and up to failure.

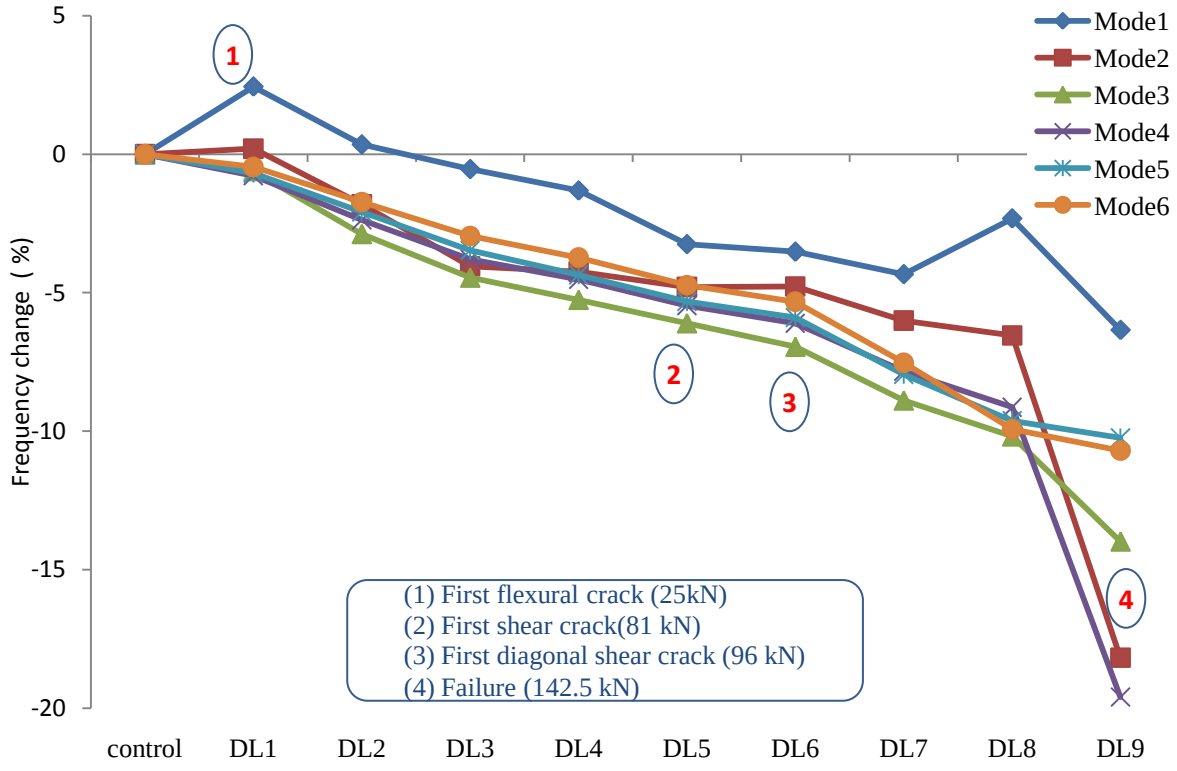

Figure 5.9. Frequency changes corresponding to the damage levels for beam $B211_d$

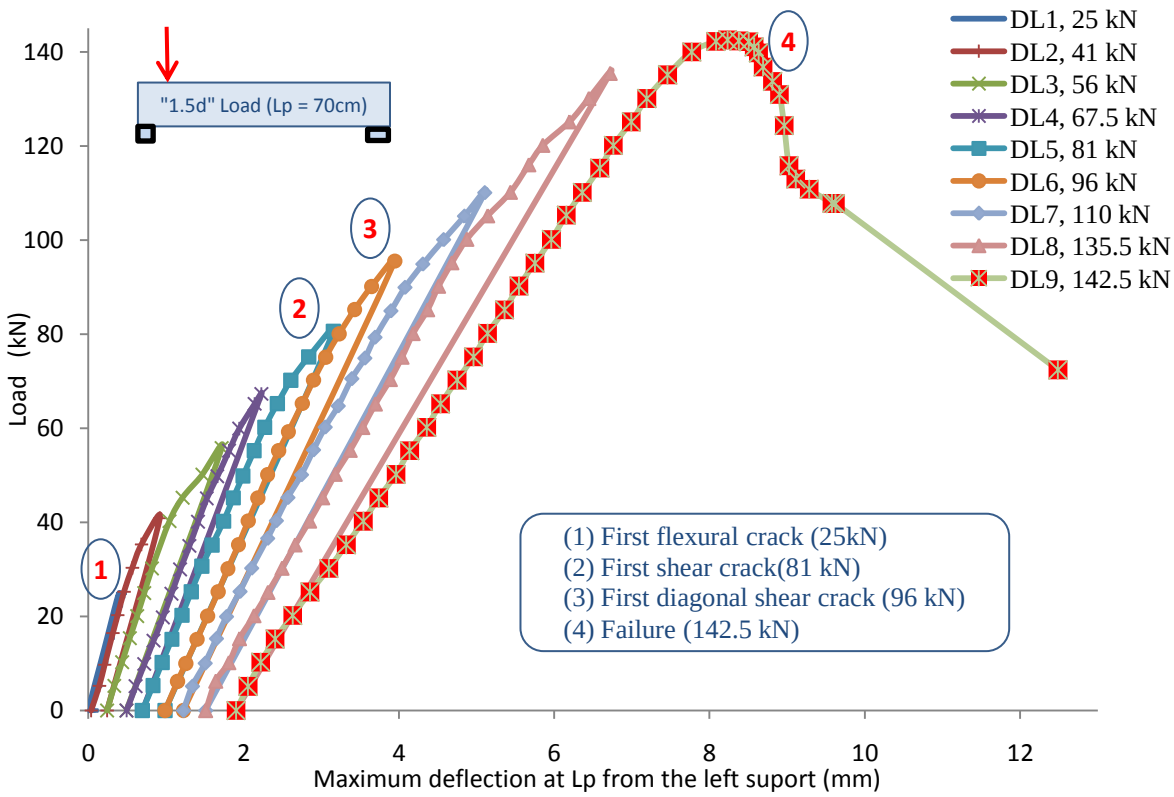

Figure 5.10. Load against maximum deflection for damage levels of beam $B211_d$

The failure of the beam is a result of diagonal shear cracking. The crack pattern of the beam corresponding to each load cycle and the failure mode are illustrated in Appendix B. The steel does not yield even at failure where the steel reaches 2280 μst as shown in Figure 5.11. The results show that for the first damage level, when the load is 25 kN, the first flexural cracks appear with a corresponding steel strain of 225μst when bond action is initiated. The residual strain in the steel after unloading at this stage is 100μst, as indicated in Figure 5.12. This residual strain leads to pre-tension bonding action, which increases the interaction stiffness. As is evident from Figure 5.9, the natural frequencies for Mode 1 increase by approximately 2.5% as a result of the increase in K_{bond}, while for Mode 2 there is no noticeable change where the increase in K_{bond} cancels out the concrete softening due to the appearance of the first crack. The natural frequencies for the other modes are

influenced by the decrease in concrete stiffness, $K_{tension}$, due to concrete softening arising from the emergence of the first crack.

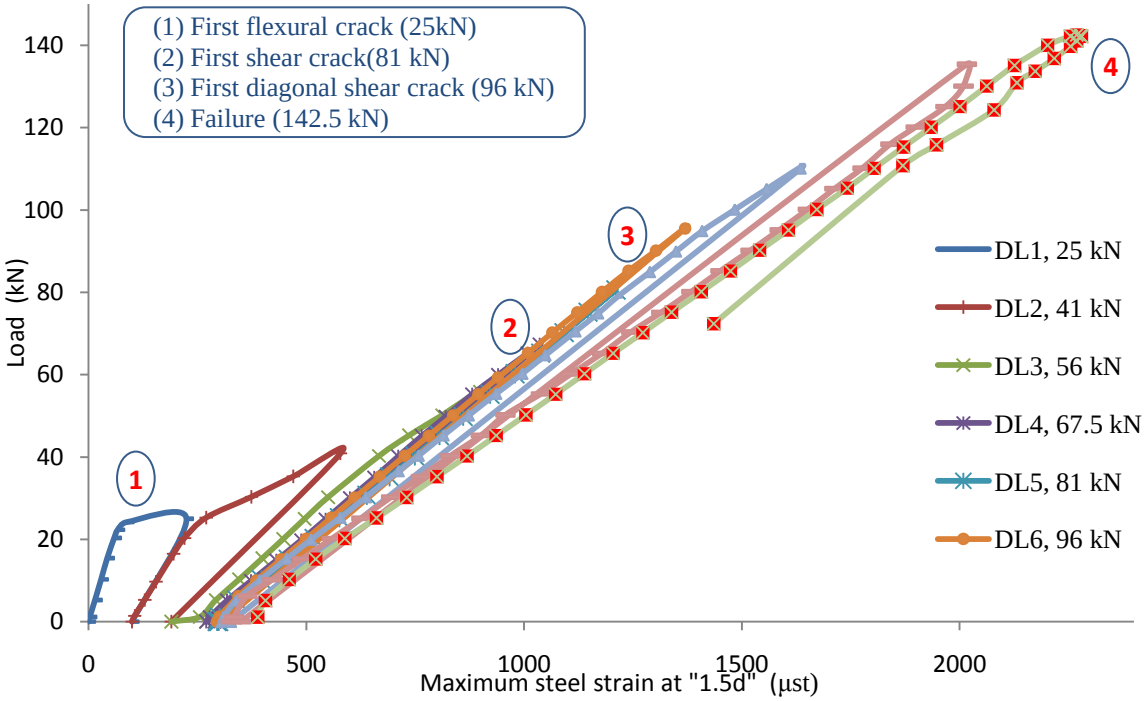

Figure 5.11. Load against maximum steel strain for damage levels of beam $B211_d$

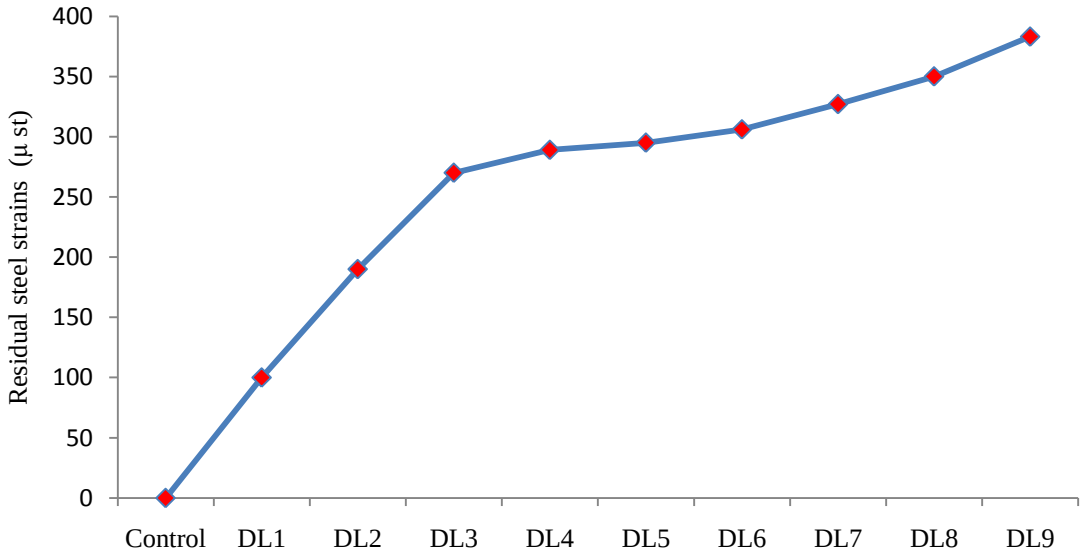

Figure 5.12. Residual steel strains upon unloading at each damage level for $B211_d$

At the second damage level, when the load is 40 kN, more flexural cracks appear and three cracks are visible. The increase in the steel strain and its residual steel strain creates an insufficient bonding action which makes the influence of the increase in the interaction stiffness higher than the influence of the concrete softening due to the appearance of cracks. This causes the first frequency to decrease in a similar trend to the other bending frequencies.

At a load of 55 kN, which is the third damage level, the number of flexural cracks increases to seven, and the steel strain reaches 900μst with a corresponding residual strain of 270 μst. The increase in the residual steel strain increases the interaction stiffness K_{bond} and the increase in number of flexural cracks decreases the concrete stiffness $K_{concrete}$. However, the effect of the bond action is smaller than the effect of the concrete softening on the first natural frequency. As a result, the first frequency displays a smaller decrease than the other modes compared to the control. At damage level 5, the increase in the residual steel strain is small where it reaches 289 μst only, and the number of flexural cracks increases to eight. As a result, the bending frequencies are more affected by the reduction in the concrete stiffness, as opposed to the influence of increase in the interaction stiffness. As evidence for this, the first frequency shows a reduction to 1.3% where the effect of the bond action is less than the effect of the concrete softening, while the other frequencies show a higher decrease.

The first shear crack occurs at the fifth damage level with a load of 81 kN as shown in Figure 5.10. This leads to a reduction in the concrete stiffness by reducing the shear component of the stiffness, and also influences the residual steel strain, where a limited increase is noticed. The number of cracks increases to ten which leads to a reduction in the concrete stiffness and causes a reduction in all the bending frequencies. The first frequency

shows a decrease of 3.3 % which is less than the decrease of the other modes due to the reasons mentioned above. For the sixth and the seventh damage levels, the same phenomenon is influencing the bending frequencies. The sharp decrease in the concrete stiffness in tension, compression and shear affects the pattern whereby all the bending frequencies show a drop.

At a load of 135 kN (the eighth damage level), which is the level prior to failure, the residual steel strain reaches 350μst. There is only one additional crack observed which leads to an increase in the interaction stiffness K_{bond}. This influences the first frequency, where it is noticed that there is an increase when compared to the previous damage level. Finally, when the failure occurs at 142.5 kN (the ninth damage level), the reduction in the concrete stiffness, either in the tension or the shear part of it, is too high and this governs the pattern, where all frequencies show a decrease.

Based on the above mentioned observation it can be deduced that for RC beams subjected to shear loads close to the supports, bending frequency pattern will be different compared to the flexural case. The increase in the interaction stiffness caused by the tension bond action will have less influence on the first bending frequency than the decrease of the concrete stiffness due to more concrete cracks forming. The appearance of the shear cracks will influence the first bending frequencies more than the other modes. This may be due to the fact that the shear crack near the end of the steel bar on the supports will have negative influence on the residual steel strain. As illustrated in Figure 5.13, for shear load at 1.5d from the support there is less tension bond action force due to shear cracks at the end of the steel bar and shorter bar length to the end support. For flexural load at mid-span there is higher tension bond action force due to longer bar length at the end support and less effect from the cracks. This will lead to a reduction in the tension bond action force. In addition, the decrease in the concrete stiffness in tension, compression and shear will have a stronger

effect on the first bending frequency. The effect on steel stiffness is unnoticeable whereby even at failure of the beam the steel strain reaches 2073 μst, which is less than its yield strain.

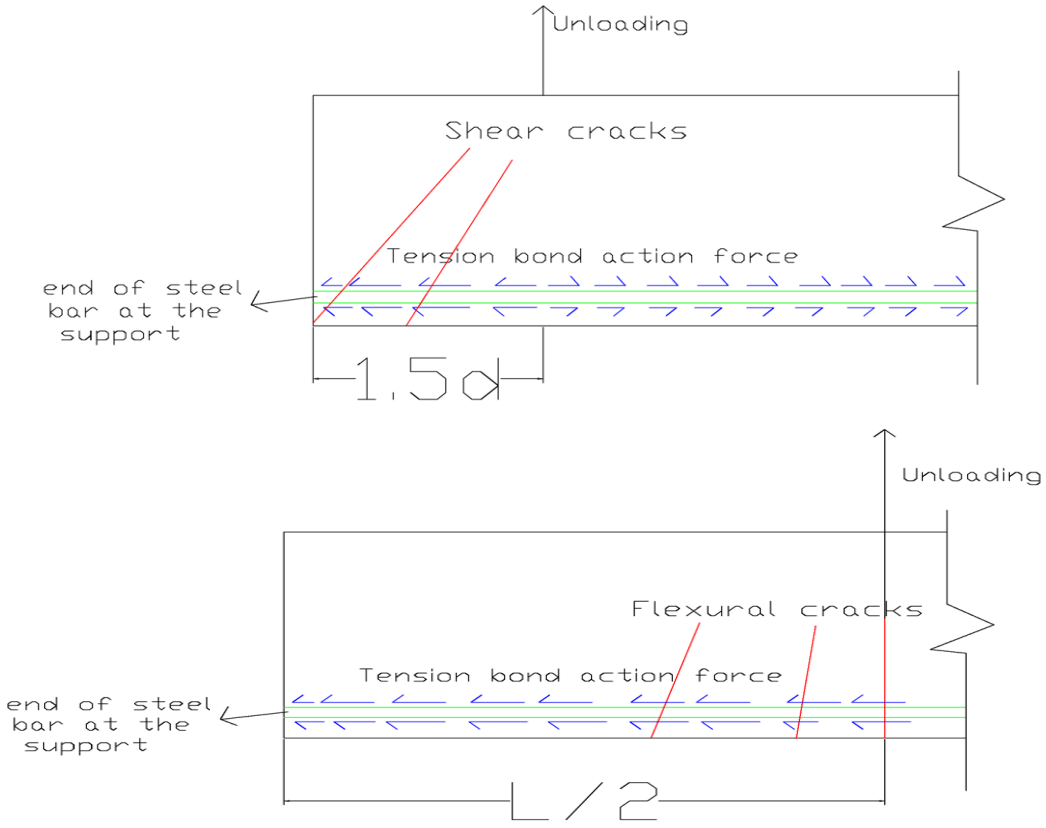

Figure 5.13. Effect of load position on the tension bond action force

5.2.2.2 Shear at quarter-span

The results for the case when the applied load is located at the quarter-span, where both the flexural and the shear stresses are active, are given in Figure 5.14. The beam fails in shear due to a diagonal shear crack when the applied load is 99 kN as in Figure 5.15 which shows the load against the maximum deflection corresponding to each load cycle up to failure.

The steel yields at 90 kN as shown in Figure 5.16. The crack patterns corresponding to each load cycle up to failure are shown in Appendix B.

Compared to the previous cases, when the flexural or the shear stresses alone are governing the RC beam behaviour, the present case shows that since both flexural and shear stresses are active, the frequency pattern wavers between the range of the previous cases. For the first damage level, when the load is 20 kN, the residual steel strain reaches 103 μst as shown in Figure 5.17 and this influences the interaction stiffness, which leads to an increase of the first bending frequency up to 4.4%. The occurrence of the first flexural crack influences the concrete tension stiffness, which leads to a decrease in the other bending modes.

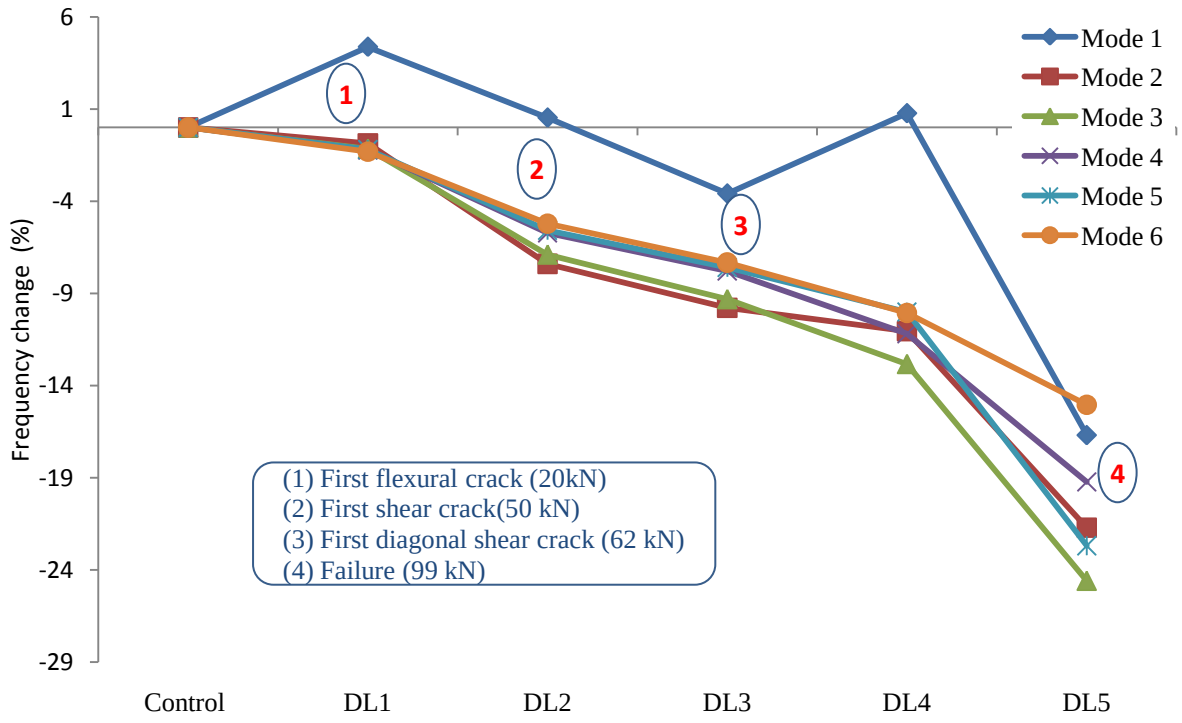

Figure 5.14. Frequency changes at different damage levels for beam $B211_q$

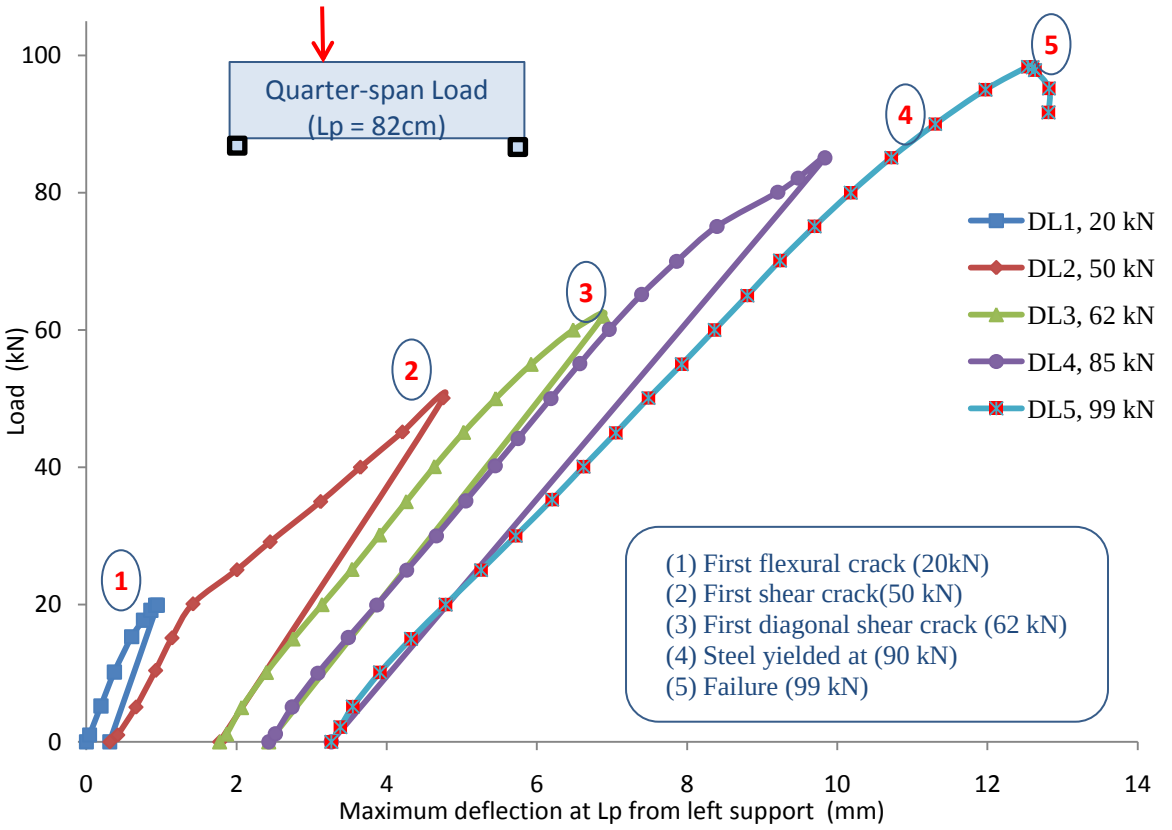

Figure 5.15. Load against maximum deflection for damage levels of beam $B211_q$

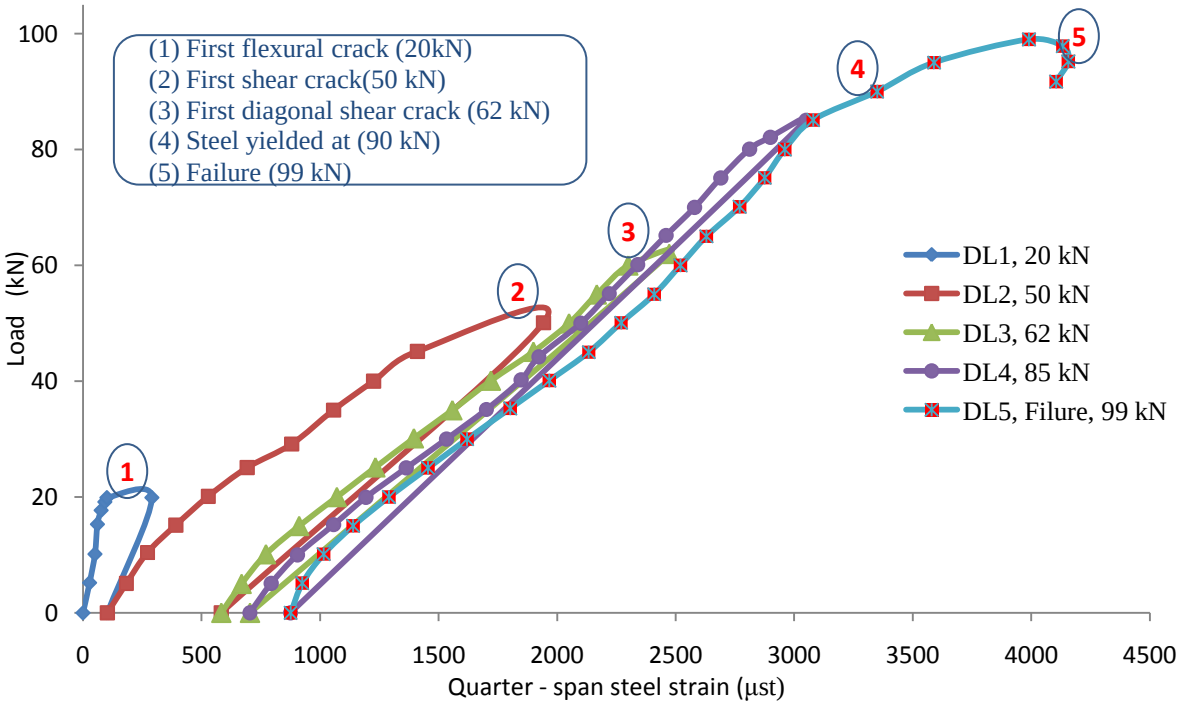

Figure 5.16. Load against quarter-span steel strain for damage levels of beam $B211_q$

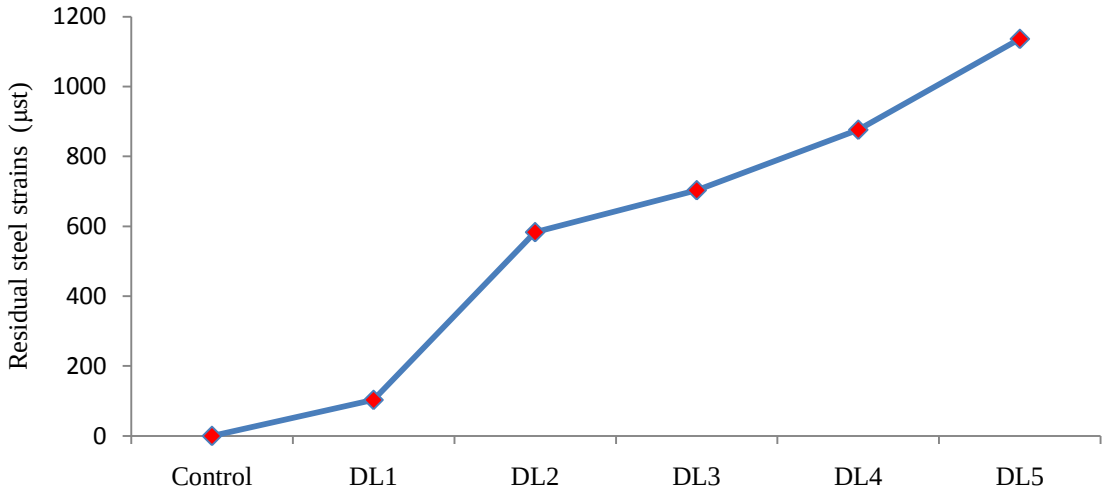

Figure 5.17. Residual steel strains upon unloading at each damage level for $B211_q$

At a load of 50 kN the first shear crack, at the zone between the applied load and the support, appears as shown in Figure 5.14. The total number of cracks increases to nine, which leads to a decrease in the concrete stiffness in tension and shear. The residual steel strain reaches 583 µst, which increases the interaction stiffness. A balancing effect of both shear crack and residual steel strain influences the first bending frequency to reduce its value and thus it is only 0.5% higher than the control. The reduction of the concrete stiffness also influences the other bending frequencies to drop.

When the first diagonal crack appears at a load of 62.5 kN as shown in Figure 5.14, the concrete stiffness decreases significantly, which is caused by the reduction in the shear component of the stiffness. The residual steel strain increases by only 120 µst compared to the previous level, which leads to a limited increase in the interaction stiffness. This results in reducing the first frequency up to 3.5% less than the control, while the other modes decrease even more.

At the fourth damage level, at a load of 85 kN which is prior to failure, the residual steel strain increases to 880 µst which in turn increases the interaction stiffness. The number of

cracks increases to thirteen which also decreases the concrete stiffness. This leads to an increase of the first bending frequency higher than the control by 0.7%, and reduces the other frequencies by a higher percentage.

Finally, when the failure occurs in pure shear mode, there are sixteen cracks in total , which reduces the concrete tension stiffness, thus the diagonal crack becomes wider and decreases the concrete shear stiffness. The steel reaches its plastic limit when the steel strain is 4160 μst, which decreases the steel stiffness. The overall stiffness is governed by the plasticity of the steel as well as the reduction in the concrete stiffness, which leads to a decrease in all the bending frequencies, whereby the first bending frequency falls to 17% of the control value.

Based on this investigation, it can be summarised that when both the shear and the flexural stresses are active, the first bending frequency will be governed by both shear cracks and the residual steel strain. When the failure mode is a diagonal shear failure, the reduction in the first bending frequency will depend on the state of the steel strain, whereby if the steel yields as in beam $B211_q$, the reduction will be higher where it reaches 17%. However if the steel has not yielded as in beam $B211_d$, the reduction will be limited to only 6.4%.

5.3 Damage identification

This section presents the identification of damage as a result of the support condition or the RC element stiffness. In order to identify the damage type, beam $B211_d$ is used, and is initially tested when there is no damage induced and the modal data is acquired for different elastic bearing deterioration levels. Subsequently the damage is induced into the RC beam by applying a concentrated point load located at 1.5d from the left support which

increases gradually up to 50 kN (beam failure load is 142.5 kN). The modal data is again acquired for different support conditions.

For the purpose of evaluating the effect of the elastic bearing deterioration levels, three different bearing stiffness measurements are adopted to simulate the levels of deterioration. For the cases of no deterioration (ND) and partial deterioration (PD), rubber pads with a stiffness of 10MN/mm and 3MN/mm are used respectively. In addition, for the case of full deterioration (FD), the elastic bearings are removed and the beam is supported directly on the underlying structural elements to simulate the condition for elastic bearing with zero stiffness. Table 5.3 shows the elastic bearing support conditions adopted in this study where six cases are considered. Figure 5.18 shows the test beam supported either on rubber pads, that is, no deterioration or partial deterioration cases, or on the underlying structural element, that is, on steel rollers for the full deterioration case. The first six bending modes obtained from modal analysis are utilised in establishing the effect of the elastic stiffness of the support on modal parameters. This analysis is used when the deterioration is identical at both supports and when there is a difference in deterioration between left and right end supports.

Table 5.3. Elastic bearing support condition and stiffness

Support Conditions	Left support condition	Right support condition	Left elastic bearing stiffness	Right elastic bearing stiffness
ND -ND	No Deterioration	No Deterioration	10 MN/m	10 MN /m
ND - PD	No Deterioration	Partial Deterioration	10 MN/m	3 MN/m
ND - FD	No Deterioration	Full deterioration	10 MN/m	0 MPa
PD - PD	Partial Deterioration	Partial Deterioration	3 MN/m	3 MN/m
PD - FD	Partial Deterioration	Full deterioration	3 MN/m	0 MPa
FD - FD	Full deterioration	Full deterioration	0 MPa	0 MPa

The results highlight the effects of the elastic bearing support conditions on the Frequency Response Function (FRF) patterns, as well as MAC and frequency based stiffness indices as given in Sections 3.2.1 and 3.2.1.

. 

ND & PD elastic bearing supports FD elastic bearing supports

Figure 5.18. RC beam supported on different support conditions

During modal testing, the Frequency Response Function (FRF) is acquired. Mathematically, the FRF is defined as the Fourier transform of the output, that is, acceleration divided by the Fourier transform of the input, namely force. In general, the parameter estimation routines are curve fits in the Laplace domain. The next stage of modal testing involves the analysis of the measured FRF data to find the theoretical model which most closely resembles the behaviour of the actual test specimen. The FRF is drawn based on the chosen frequency bandwidth, in relation to modulus and frequency. The frequency bandwidth used in this study is 4.5kHz. The modulus is the relationship between the input excitation force and the output response acceleration. The FRF comprises the raw data for modal parameters. Any change in the modal parameters will be first detected in the FRF patterns for all the measured points. Figure 5.19 shows the FRF patterns for the 24

measured points on the undamaged beam for three different elastic bearing deterioration levels, which are the same for both supports.

The results show that the FRF of the 24 measured points are smooth for both no deterioration and partial deterioration cases. For the full deterioration case, the FRF is not smooth and exhibits irregularities. For the first 400Hz of bandwidth, where Mode 1 is located, it can be observed that the FRFs have multiple peaks, which relate to the rigid body modes, mixed modes and the first bending mode. Furthermore it is evident that for the bandwidths (600 to 1300 Hz), wherein Modes 3 and 4 are located, the irregularities of the FRF are in the form of close or twin peaks.

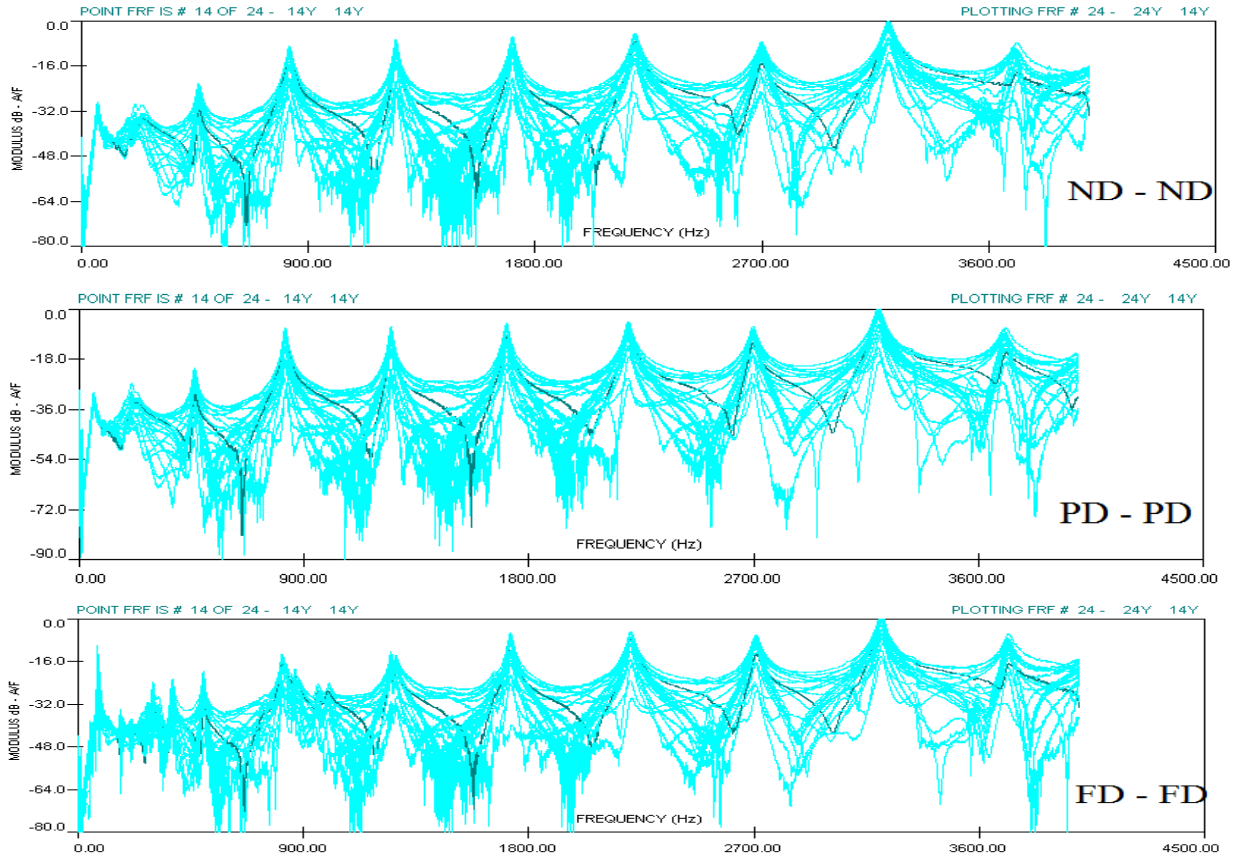

Figure 5.19. FRF for the same deterioration levels on both supports

The FRF for the three different support conditions are shown in Figure 5.20, which indicates that the FRF is still smooth for the first case when there is partial deterioration on

the right support only. This can be a result of the small difference in elastic bearing support stiffness at both supports. However, when full deterioration occurs on the right support, irregularities can be observed in the form of multiple and also close or twin peaks. This could be due to the large difference in elastic-bearing support stiffness between both the supports. This phenomenon is similar to the cases of the same level of deterioration at both the supports as discussed above. The effect of support deterioration on the FRF patterns for the damaged beam is similar to that of the undamaged beam.

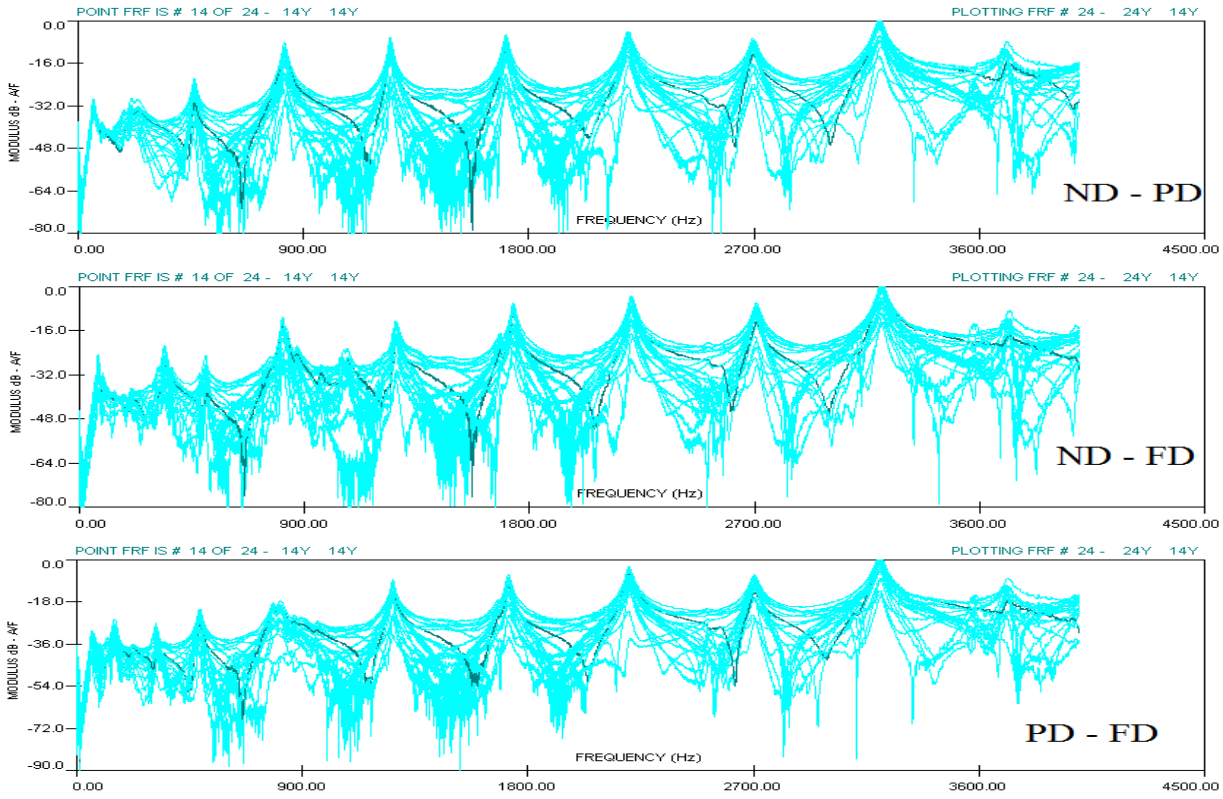

Figure 5.20. FRF for different deterioration levels on both supports

The first six bending mode shapes for the undamaged beam are considered for comparison of the effects of elastic bearing support stiffness using the Modal Assurance Criteria (MAC). Table 5.4 shows MAC values for the first six bending modes for similar elastic bearing deterioration levels at both supports. For partial deterioration at the supports, the

deviation in the mode shapes when compared to no deterioration is insignificant. However when full deterioration occurs, the lower modes, especially Modes 1, 2 and 3 are affected, whereby the degree of correlation of the mode shapes is lower. Nevertheless, the MAC values do not fall below 90%. The effect of different deterioration at the supports is shown in Table 5.5. The MAC values of the lower modes are again affected to a much greater extent when full deterioration occurs at the right support. The MAC values of Mode 1 and Mode 2 are below or close to 90%, indicating that the modes are uncorrelated. The effect of support deterioration on the MAC values for the damaged beam is similar to that of the undamaged beam.

Table 5.4. MAC values for different elastic bearing support stiffness for modes 1 to 6

Elastic bearing stiffness cases	Mode 1	Mode 2	Mode 3	Mode 4	Mode 5	Mode 6
ND – ND	1	1	1	1	1	1
PD - PD	0.978	0.999	1.000	1.000	0.998	0.996
FD - FD	0.921	0.964	0.965	0.995	0.995	0.995

Table 5.5. MAC values for the first six modes for differential deterioration at both supports

Elastic bearing stiffness cases	Mode 1	Mode 2	Mode 3	Mode 4	Mode 5	Mode 6
ND - ND	1	1	1	1	1	1
ND - PD	0.982	0.999	0.999	1.000	1.000	0.999
ND - FD	0.670	0.906	0.992	0.989	0.981	0.997
PD -FD	0.500	0.947	0.951	0.998	0.996	0.996

Next, the results of the frequency based stiffness index (as given in Section 3.2.1) for two cases, namely the deterioration in the elastic-bearing support stiffness for the undamaged and damaged beam, are presented and discussed. Figure 5.21 shows the stiffness change based on frequency for the first six bending frequencies for different support deterioration levels of the undamaged beam.

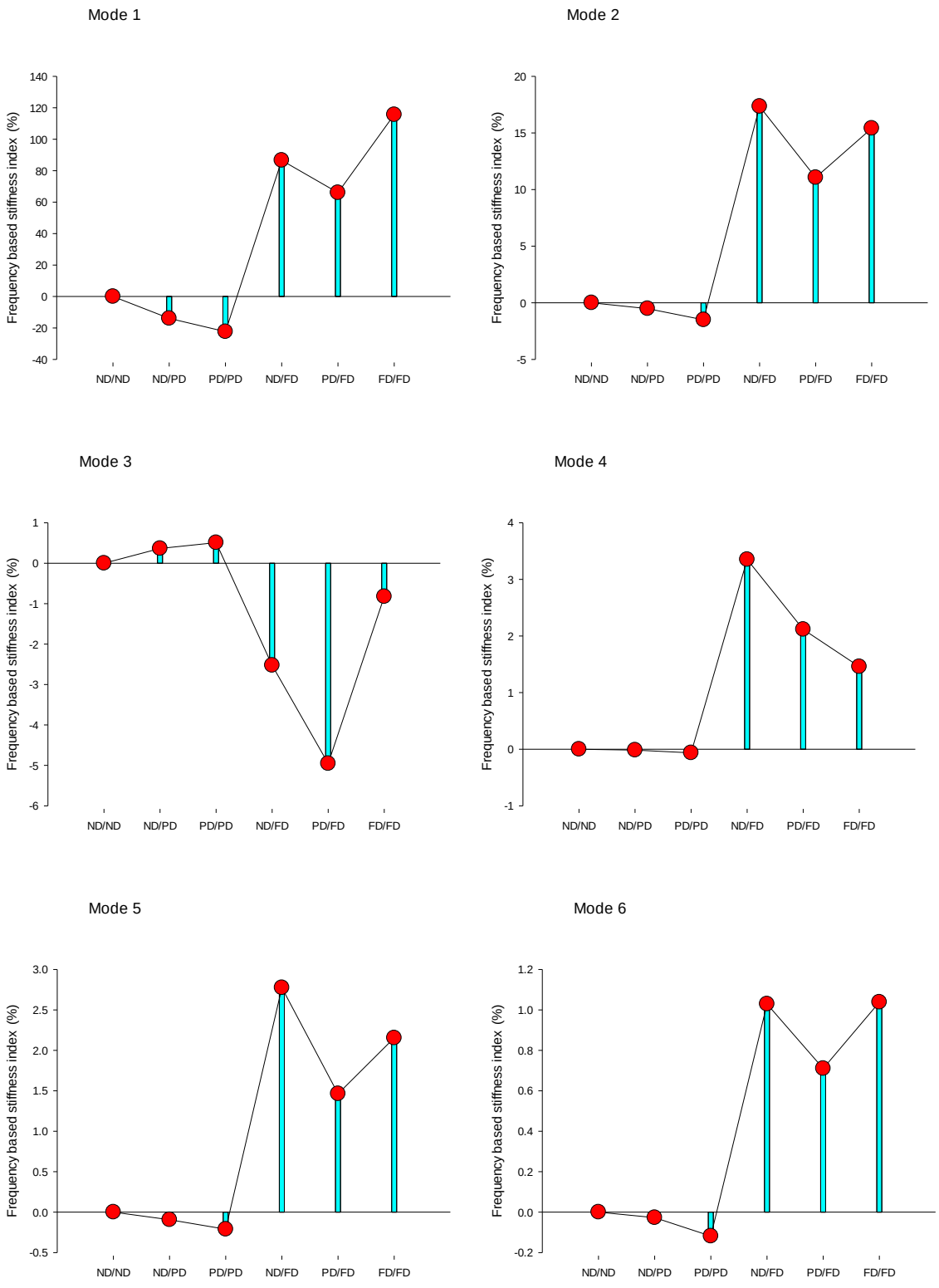

Figure 5.21. Frequency based stiffness index results for the first six bending frequencies of the undamaged beam

A direct relationship is evident between the elastic bearing support and the stiffness change based on frequency. All the bending frequencies, with the exception of bending frequency for Mode 3, show a decrease in the stiffness when there is partial deterioration in the elastic bearing supports (PD-PD). They subsequently increase when full deterioration occurs (FD-FD) on either one or both supports. This is probably due to the fact that when full deterioration of the elastic bearing occurs, the RC beam is supported directly on the structural element underneath which possesses higher stiffness and thus influences the bending frequencies.

However, the third bending frequency shows a contrasting trend, whereby it shows an increase in the stiffness due to partial deterioration on either both supports (PD-PD) or one support (ND-PD), and decreases when full deterioration occurs on either both supports (FD-FD) or one support (ND-FD). Under normal circumstances the trend in bending frequencies when there is deterioration in the elastic bearing supports or deterioration in the structural element stiffness is a decrease, and vice versa. However, in this particular case, the only deterioration that is induced in the structural system is the elastic bearing stiffness. Indeed, the atypical trend exhibited by the bending frequency of Mode 3, singles it out as an indicator for the occurrence of this type of deterioration. Mode 1 is the most sensitive to changes in support stiffness wherein it detects a stiffness decrease of 22% when partial deterioration occurs and an increase of 115% when there is full deterioration. The sensitivity of Mode 2 is lower when compared to Mode 1 but much higher when compared to all of the other modes, which show similar sensitivities to changes in elastic bearing support stiffness.

However for Modes 4, 5 and 6, the stiffness decrease is rather small or insignificant, which indicates their insensitivity to change in support conditions from no deterioration at both ends, that is, ND-ND, to no deterioration at the left support and partial deterioration at the

right support, that is, ND-PD. The trend is reversed, namely, the frequencies show a stiffness increase when the condition at the supports changes from no deterioration at both ends to no deterioration at the left support and full deterioration at the right support, that is, ND-FD. All the modes with the exception of Mode 3 sense this change as reflected in the values of the frequency based stiffness index. However the increase in frequency based stiffness index is lower for the case when the support conditions change from ND-ND to PD-FD. The same reason applies as discussed above for the significant change in trend when there is full deterioration at one of the supports. As indicated earlier, Mode 3 shows a consistent opposite trend when compared to the other modes. It shows a small stiffness increase when there is partial deterioration on the right support (ND-PD). However when full deterioration occurs on the right support (ND-FD), the frequency shows stiffness decrease and is highest when the supports suffer partial and full deterioration on the left and right support (PD-FD), respectively. This consistent trend is shown either when the deterioration at both the supports is identical or different. It is also a useful indicator in terms of identifying the change in the bending frequencies due to the deterioration in the elastic bearing stiffness.

After inducing damage in the RC beam by applying a load, modal testing is carried when there is no deterioration in the elastic bearing support. Table 5.6 shows the values of the first six bending frequencies for the case of no deterioration in elastic bearing supports for the undamaged and damaged beam. The results show that there is a reduction in all of the bending frequencies with the exception of Mode 1, and this reduction is due to concrete softening influenced by cracks in the flexural and shear zone. For Mode 1, the result shows that there is an increase after the damage is induced, and possibly due to the bond action in the interface zone between the flexural steel bars and the surrounding concrete. Under

loading the bond stress will be initiated, which leads to an increase in stiffness and as a result influences the first bending frequency.

Table 5.6. First six bending frequencies for the undamaged and damaged RC beam

RC Beam stiffness	Elastic bearing stiffness	Mode 1 Hz	Mode 2 Hz	Mode 3 Hz	Mode 4 Hz	Mode 5 Hz	Mode 6 Hz
No damage	ND – ND	237.3	464.7	823.7	1247.4	1708.8	2196.3
Damage under 50 kN	ND – ND	247.8	450.3	788.6	1200.2	1650.8	2130.2
Frequency based stiffness index (%)		8.8	-6.2	-8.5	-7.6	-6.8	-6.0

Table 5.7 presents the MAC values of the first six bending modes for the case of no deterioration in the elastic bearing supports for the undamaged and damaged beam. The results show that the first mode is the less sensitive mode while higher modes have higher sensitivity to the load induced damage in the beam. Upon comparing the MAC values when the damage is induced in the beam itself (Table 5.7) to the case when the deterioration is in the supports (Tables 5.4 and 5.5) it is evident that this is a good damage identification indicator. When there is elastic bearing stiffness deterioration, Mode 1 will be the most sensitive to the stiffness change followed by Mode 2, while for the rest of the modes the sensitivity is low. However when there is a structural element stiffness defect, the higher modes will be more sensitive to the stiffness change while the first mode will be less sensitive.

Table 5.7. MAC values based on comparison of damaged and undamaged beam

Mode 1	Mode 2	Mode 3	Mode 4	Mode 5	Mode 6
0.997	0.997	0.992	0.990	0.988	0.985

When the damage is inflicted on the RC beam, the elastic bearing supports are changed to investigate the effect of the support deterioration on the frequency based stiffness index. Figure 5.22 illustrates the frequency based stiffness index values for the first six bending frequencies for different support stiffness deterioration levels. The results show that for all the bending modes except for Mode 3, there is a reduction in the stiffness when there is partial deterioration in the elastic support either on both supports (PD-PD) or on one support (ND-PD). Moreover, an increase in the stiffness is apparent when there is full deterioration in the elastic supports, either on both supports (FD-FD) or on one support (ND-FD), which means that the beam is affected by the stiffness of the underlying. For Mode 3, the pattern shows little or no change in the stiffness when there is partial deterioration on one support (ND-PD) or on both supports (PD-PD), followed by a decrease when there is full deterioration, either on one support (ND-FD) or both supports (FD-FD). Mode 1 is the most sensitive mode followed by Mode 2 and then the rest.

Thus, the third bending frequency is identified as an indicator for the occurrence of different types of damage considered. If there is deterioration in the structural element stiffness, Mode 3 will show a decrease in the stiffness as well as the other modes. When there is partial deterioration in the elastic bearing without deterioration in the structural element stiffness, Mode 3 will show an increase in the stiffness, while the rest will show a decrease. When there is full deterioration in the elastic bearing without deterioration in the structural element, Mode 3 will show a decrease in the stiffness, while the rest will show an increase. When both forms of deterioration occur, namely the elastic bearing stiffness deterioration and structural element stiffness deterioration, Mode 3, together with the rest of the modes, will monitor the elastic support condition. If Mode 3 increases and the other modes show a decrease, this indicates a partial deterioration in the elastic supports. If Mode 3 decreases and the other modes show an increase, this indicates full deterioration in the

elastic supports. Finally, if Mode 3 and the other modes decrease, this indicates deterioration in the structural element stiffness.

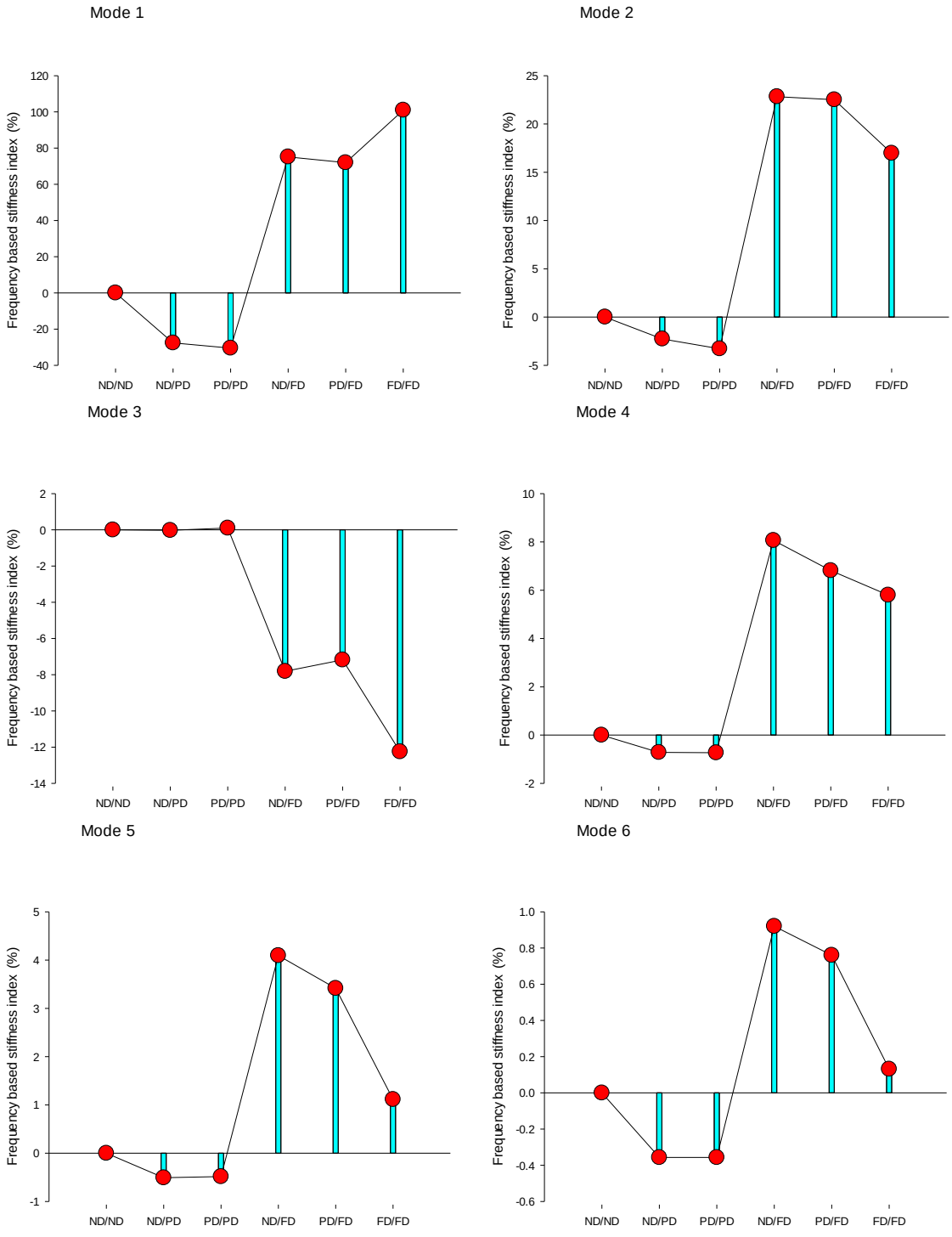

Figure 5.22. Frequency based stiffness index results for the first six bending frequencies for the damaged beam

5.4 Damage severity algorithms

This section deals with the results of the damage severity algorithms by firstly presenting the sensitivity of the existing algorithms, followed by the results of the developed algorithm, as discussed in Section 3.2.3. A proposed weighting method is applied on the existing algorithms which are used to monitor frequency based stiffness index and MAC based stiffness index, for averaging values of the considered set of modes. The developed algorithm is in the form of combined modal parameter based stiffness index. In addition, the results of the stiffness change based on the static tests are presented and compared with the dynamic damage severity algorithms to assess its sensitivity.

In order to ascertain the sensitivity of both existing and developed damage severity algorithms for assessing the actual stiffness change due to damage, different damage scenarios in the RC beams are considered. The damage scenarios are introduced to beams $B121_m$, $B211_q$ and $B211_d$ by applying a concentrated load at mid-span to induce maximum flexural stresses, a concentrated load at quarter-span in order to induce both the flexural and shear stresses, and a concentrated load at 1.5d distance from one support to induce higher shear stresses, respectively.

5.4.1 Existing algorithms

The existing damage severity algorithms described in Sections 3.2.1 and 3.2.2, will be applied to the modal parameters in order to determine their sensitivity when it comes to monitoring the change in the global stiffness for different damage scenarios. Since different modes show different sensitivity for the stiffness deterioration and different influence on the stiffness component, the proposed weighting method discussed in Section 3.2.4, will be used to find the sensitivity weightage of each mode.

5.4.1.1 Proposed weighting method

The mode weightage calculated from the proposed weighting method is used to compute the average value for the stiffness change based on set of modes. The area under the curve for each specific mode is calculated from the mode shape of the control case as well as from different damage levels. The weightage results of different damage levels are similar to the control case, thus the weightage values of the control case are adopted. Table 5.8 illustrates the area under the curve and the weightage for each mode. The results show the difference in each mode weighting between proposed weighting method and the normal average, that is, the mean. The results show that Modes 1 to 3 show less weighting in the weighted average than the normal average by 18.4%, 11.2% and 5.8%, respectively. Modes 4 to 6 show higher weighting in the weighted average than the normal average by 9.2%, 8.6% and 17.6%, respectively. The results show that higher modes will have higher weighting in the proposed method which is based on the energy needed to form the mode shape. It requires higher energy to form higher mode shapes. The weighting of the proposed method for the first six modes are adopted in the next section of this study. Appendix C presents a sample of the average value calculations based on the proposed weighting method for both existing algorithms, namely frequency based stiffness index and MAC based stiffness index.

Table 5.8. Mode weighting based on weighted average and normal average for the adopted modes

Mode Number	Area under the curve for control case (unit ^{2})	Weighting		Different %
		weighted average	average/mean	
M1	9.69	0.136	0.1667	81.6
M2	10.56	0.148	0.1667	88.8
M3	11.23	0.157	0.1667	94.2
M4	13.01	0.182	0.1667	109.2
M5	12.89	0.181	0.1667	108.6
M6	13.96	0.196	0.1667	117.6
Total Area	71.36	1	1	

5.4.1.2 Frequency based stiffness index

The algorithm discussed in Section 3.2.1 relates the change in the stiffness to the change in the frequency by a relationship assuming that the nonlinear structural system behaves linearly. The results of the algorithm are averaged for all of the six considered bending modes using the proposed weighting method as described in the previous section and as illustrated in Appendix C. The results of the frequency based stiffness index for three different damage scenarios, namely beams $B121_m$, $B211_q$ and $B211_d$ as previously mentioned, correspond to each damage level and are shown in Figure 5.23. The damage level is defined as the damage load (see Tables 5.1 and 5.2) divided by the failure load of the beam, that is, for beam $B121_m$ with a load of 11 kN, the damage level is 15.5 %. The results show that the frequency based stiffness index shows least deterioration when there is flexural damage on beam $B121_m$, and it indicates a stiffness increase when the damage

level is 0.15 due to the influence of the composite action phenomenon on the first bending mode.

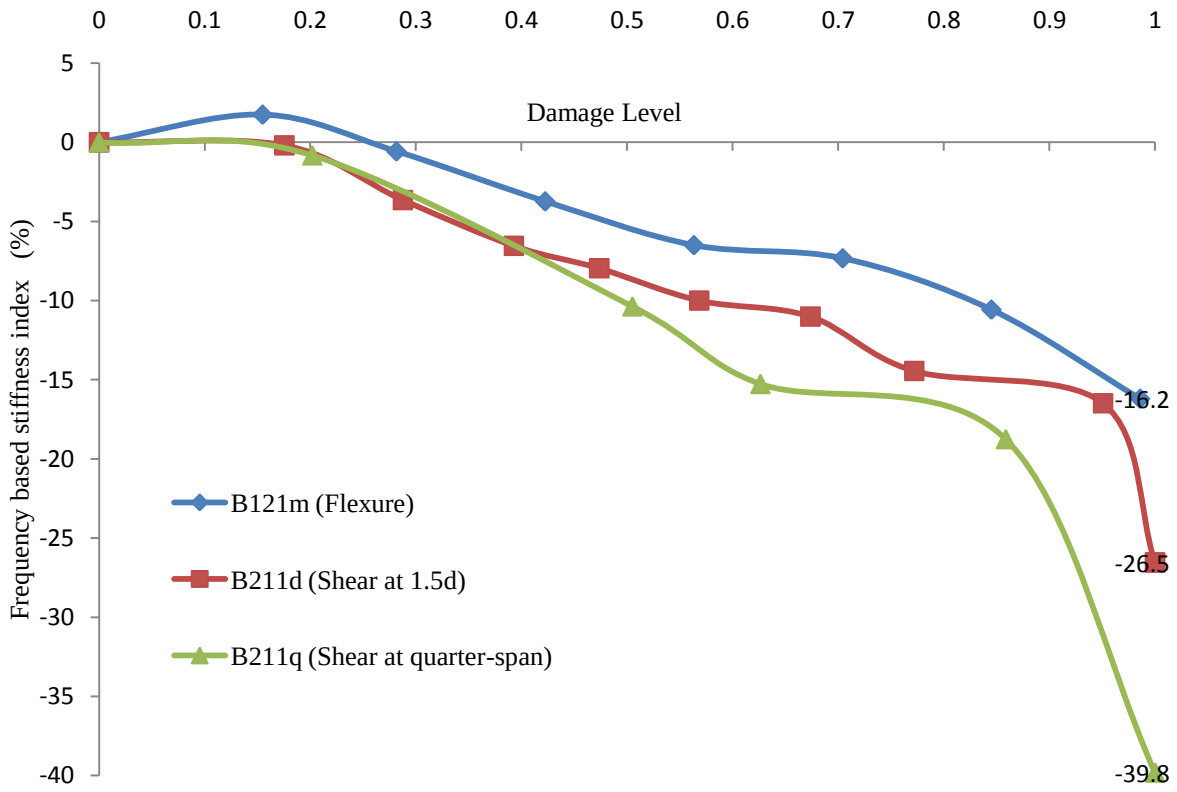

Figure 5.23. Weighted average values of frequency based stiffness index for different damage scenarios

The maximum flexural deterioration is recorded at failure with an index value of 16.2%. For the shear damage scenario, when the load is applied close to the support at a distance of 1.5d, it gives higher stiffness deterioration than the flexural case. This is due to the fact that for the shear damage the concrete stiffness suffers deterioration in its tension, compression and shear component. This is in contrast to the flexural damage where there is no deterioration in the shear component of the concrete stiffness $K_{concrete}$. However, the stiffness deterioration is still less than the shear damage scenario when the load is applied at quarter-span, and where the index values are 26.5 % and 39.8% for shear damage close to

support and at quarter-span, respectively. This is due to the fact that when the load is applied at quarter-span, both flexural and shear stiffness suffer more deterioration when compared to the case when only the shear or the flexural stiffness is affected. The trend in stiffness change for the flexural beam up to the damage level of 0.56, can be considered as linear. However, beyond the damage level of 0.56, the stiffness change starts to behave in a nonlinear manner. For the shear damage, when the load is close to the support, the same damage level of approximately 0.57 can be considered as the limit for the linear trend of the stiffness change. For shear damage, when the load is applied at the quarter-span, a damage ratio of 0.62 can be considered as the limit for linearity, whereas beyond that ratio the stiffness deterioration can be considered as nonlinear.

5.4.1.3 MAC based stiffness index

The modal assurance criteria (MAC) is a test for the compatibility of two different sets of mode shape vectors and is used in this study as an indirect indicator for the stiffness change assuming that the nonlinear structural system behaves linearly as described in Section 3.2.2. The use of MAC as an indicator for the stiffness change in this study is limited for the case where difference in the structural system is induced by stiffness deterioration. The results of the algorithm are averaged for all of the six adopted bending modes using the proposed weighting method as described in the previous section and as illustrated in Appendix C. The results of the MAC based stiffness index for three different damage scenarios namely beams $B121_m$, $B211_q$ and $B211_d$ as previously mentioned, correspond to each damage level and are shown in Figure 5.24. The results show that the MAC based stiffness index generally indicates small differences even prior to failure, where it detects a difference of less than 7.5%. The MAC based stiffness index is more affected by full damage in the beams, especially for the shear damage scenarios, where it detects stiffness

deterioration of more than 47%. The flexural damage induces less stiffness deterioration at failure, where the stiffness deterioration is only 5.3%.

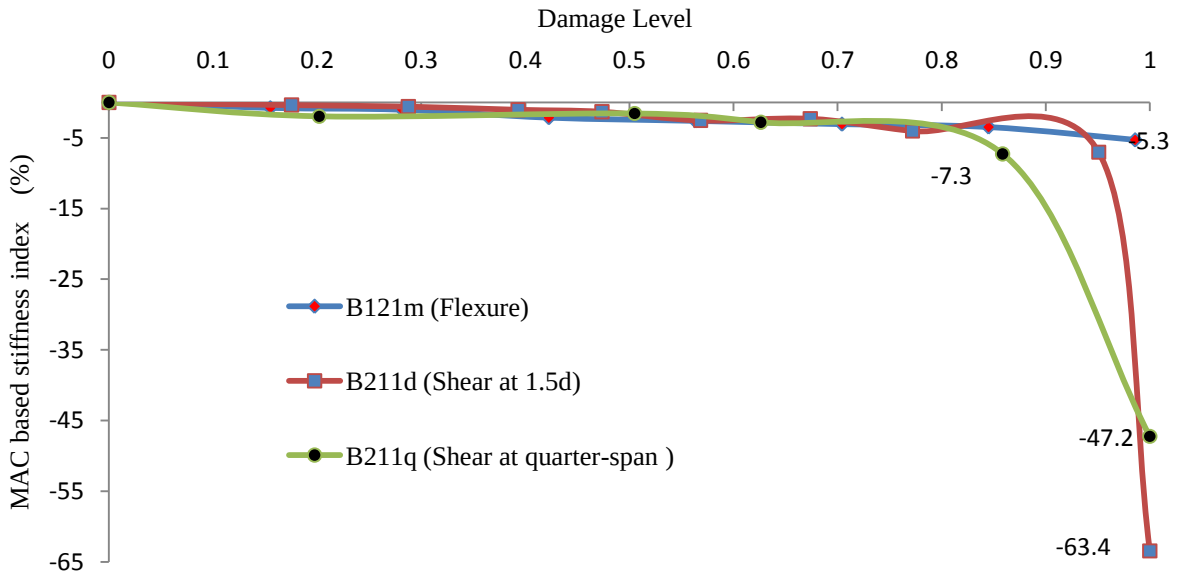

Figure 5.24. Weighted average values for MAC based stiffness index for different damage scenarios

5.4.2 Developed algorithm

This section presents the results of the developed damage severity algorithm, referred to as combined modal parameters based stiffness index as mentioned in Section 3.2.3 The developed algorithm will obtain only one value for the stiffness change for any set of bending modes which are considered as corresponding to each damage level. This avoids the need to use the proposed weighting method for averaging. The objective is to increase the damage detection sensitivity compared to the existing algorithms, since stiffness change based on frequency detects damage deterioration of only 39.8% at failure and the stiffness change based on MAC detects only 7.3% prior to failure. The main difference between developed and existing algorithms is that the developed algorithm detect global stiffness

change through frequency while the local stiffness change is detected through the mode shape vector, corresponding to each damage level.

The same three damage scenarios which are used to illustrate the existing algorithms are used to verify the sensitivity of the developed algorithm. Figure 5.25 illustrates the values of the combined modal parameter based stiffness index values corresponding to the damage levels for different damage scenarios. The results show that flexural damage gives the least stiffness deterioration, for all of the damage levels. Shear damage when the load is applied close to the support shows the highest stiffness deterioration for all the damage levels. At a damage level of less than 0.2, the stiffness deterioration indicated is less than 2.5%, whatever the damage scenario. At 0.5 damage level however, a stiffness deterioration of about 18% is observed. Prior to failure, where the damage level is 0.99, the flexural damage induces a stiffness deterioration of 30.5%. At failure, the shear damage scenarios induce a stiffness deterioration of 83% and 62% for beam $B211_d$ and $B211_q$ respectively.

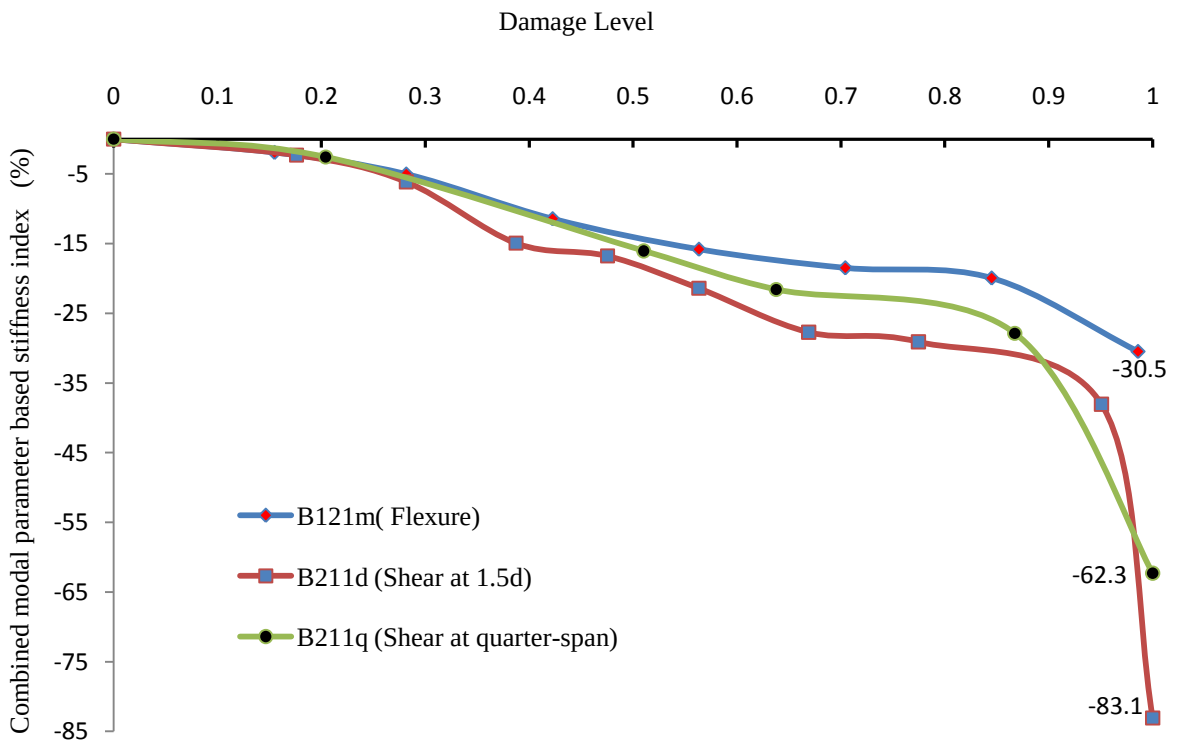

Figure 5.25. Combined modal parameter based stiffness index values for the three damage scenarios

5.4.3 Direct stiffness indicator

This section presents the use of an indicator based on the results of static load test of the structures, for stiffness change. By performing the static test on the beams prior to the modal testing, the load-deflection characteristics at certain locations on the RC beam span are obtained, and this data is used to calculate the direct stiffness indicator.

The relationship for stiffness from load-deflection plots for flexural and shear damage scenarios is discussed in Appendix D and the stiffness change based on the static load test data is established. Figure 5.26 illustrates the values of direct stiffness indicator for the same adopted damage scenarios in the previous sections using beams $B121_m$, $B211_d$ and $B211_q$.

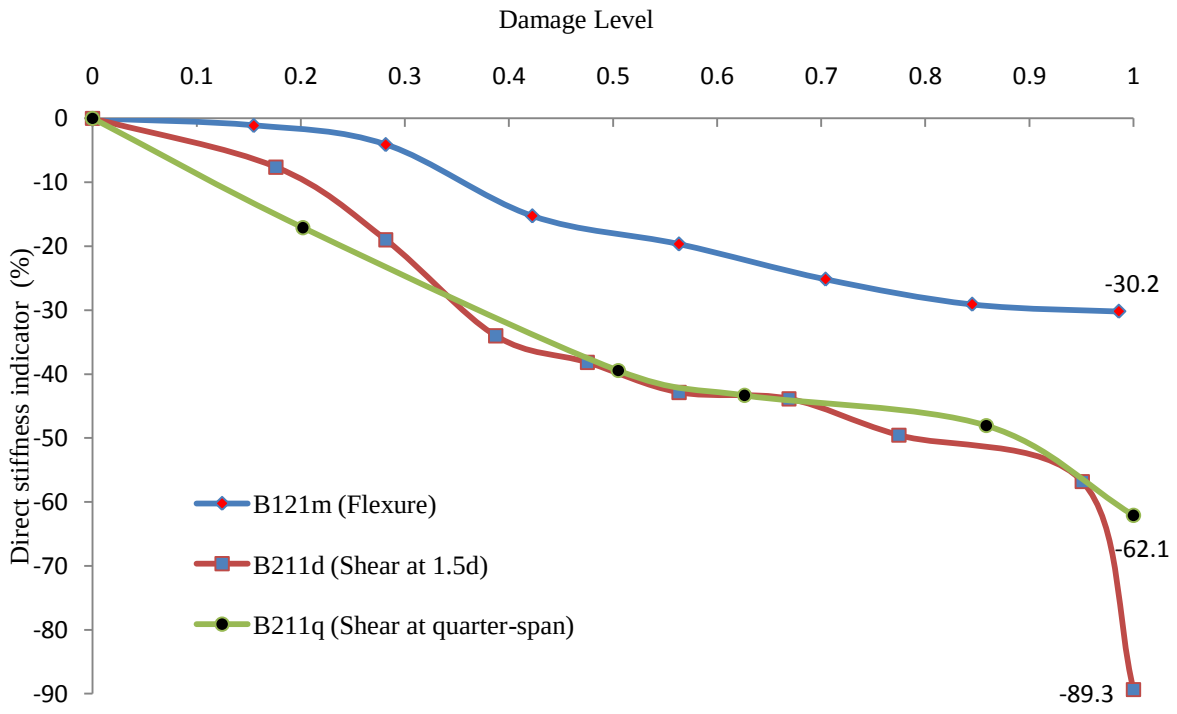

Figure 5.26. Stiffness change based on direct stiffness indicator for three damage scenarios

The results show that the flexural damage scenario has the smallest stiffness deterioration for all damage levels. At early damage levels up to 0.5, the shear damage at 1.5d from the support has the highest stiffness deterioration, while beyond 0.5 damage level the shear damage at the quarter-span has the highest stiffness deterioration. For the flexural damage, the results show that at early damage levels beyond the first crack, the stiffness deterioration is approximately 1%, and at the damage level prior to the design limit, that is, at 25kN, the stiffness deterioration reaches 4%. Beyond the design limit there is a rapid decrease in the stiffness to give a deterioration of 15 % at a damage level of 0.42. The stiffness deterioration continues to increase before reaching 30.2 % prior to failure at a damage level of 0.99.

For the shear damage at 1.5d, the occurrence of the first flexural crack the stiffness deterioration reaches around 7%, and the stiffness deterioration continues to increase before reaching 43% when the first shear crack appears at a damage level of 0.56. Prior to failure, when the damage level is 0.95, the stiffness deterioration reaches approximately 57%, while when failure occurs, there is a rapid decrease in the stiffness and it reaches 89.3%. For the quarter-span shear damage the results show that when the first flexural crack appears at a damage level of 0.2, the stiffness deterioration reaches 17%, however, when the first shear crack appears at a damage level of 0.51 the stiffness deterioration reaches 39%. Prior to failure, when the damage level is 0.86, the stiffness deterioration is around 48%, while at failure the deterioration increases to 62.1%.

5.4.4 Comparison of algorithm

A comparison between the developed and existing modal parameter based algorithms as well as the direct stiffness indicator based on the static load test, is carried out in order to evaluate the sensitivity in quantifying global stiffness changes for flexural and shear damage scenarios. For the flexural damage, Figure 5.27 presents the results of stiffness change for the developed, existing (frequency and MAC) and static load test algorithms corresponding to different damage levels.

The general trend of the algorithms corresponding to the damage level shows that the MAC based stiffness index gives the lowest sensitivity for stiffness change for all damage levels. The combined modal parameter based stiffness index gives the highest sensitivity, as modal parameter based algorithm, to detect the stiffness deterioration for all damage levels. At 0.15 damage level the frequency based stiffness index is influenced by the increase in the bond stiffness K_{bond} due to the composite action phenomenon. However, both MAC and combined modal parameter based stiffness indices show a decrease in stiffness at 0.15 damage level. These are based on the mode shape vectors and are unable to classify the change in stiffness as either an increase or decrease. Beyond the design limit, and at a damage level of 0.42, the stiffness deterioration indicated is 3.7%, 2.2%, 11.4% and 15.25% based on frequency, MAC, combined modal parameter and static load test data respectively. At a damage level of 0.85, the stiffness deterioration reaches 10.6%, 3.5%, 20% and 29% based on frequency, MAC, combined modal parameter and static load test data respectively. At prior to failure when the damage level is 0.99, the stiffness deterioration is 16.2%, 5.3, 30.2% and 30.2% based on frequency, MAC, combined modal parameter and static load test data respectively.

The results show that the combined modal parameter based stiffness index has a higher sensitivity than any of the existing damage algorithms, where the values are much closer to the direct stiffness indicator. The developed algorithm gives slightly higher deterioration values until the design limit, after which the values are lower and give similar values of approximately 30.5% at failure, compared with the direct stiffness indicator.

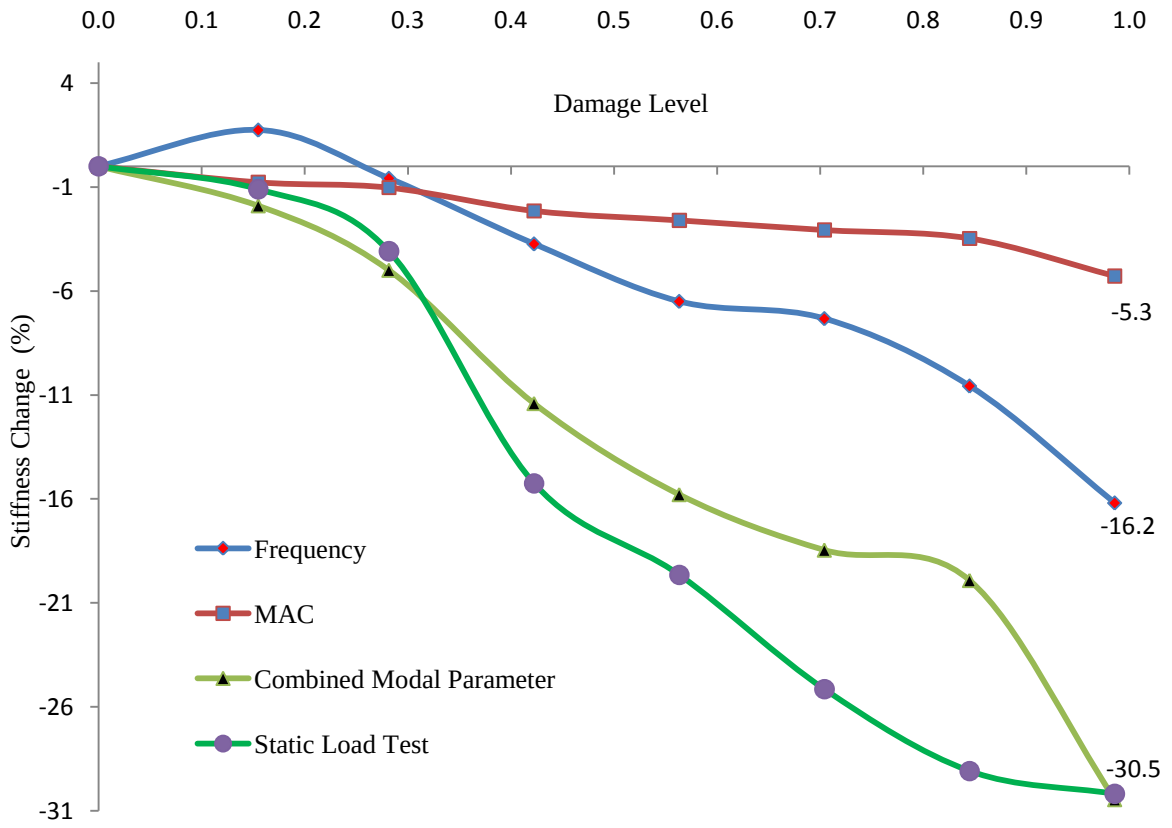

Figure 5.27. Comparison of algorithms for the flexural damage scenario

Figure 5.28 shows the comparison of modal parameter based algorithms by taking the static load test data as the datum, for the flexural damage scenario. The figure shows the static load test data as a horizontal line with a constant value of 1.0, while modal parameter based algorithms are presented as the difference between its values and the static load test values for each damage level. The results show that the developed algorithm has a higher value than the static algorithm by 70%, before displaying lower values than the static algorithm

beyond the second damage level. Following this, it reaches the same value as the static algorithm prior to failure. The frequency based algorithm shows negative values at the first damage level indicating an increase in the stiffness affect by the composite action phenomenon. It begins to display positive values, indicating stiffness deterioration, while it is still less than the static algorithm even up to prior to failure where it detects less 50% less deterioration. The MAC based algorithm shows much less value than the static algorithm for all damage levels and even up to prior to failure where it detects 80% less deterioration.

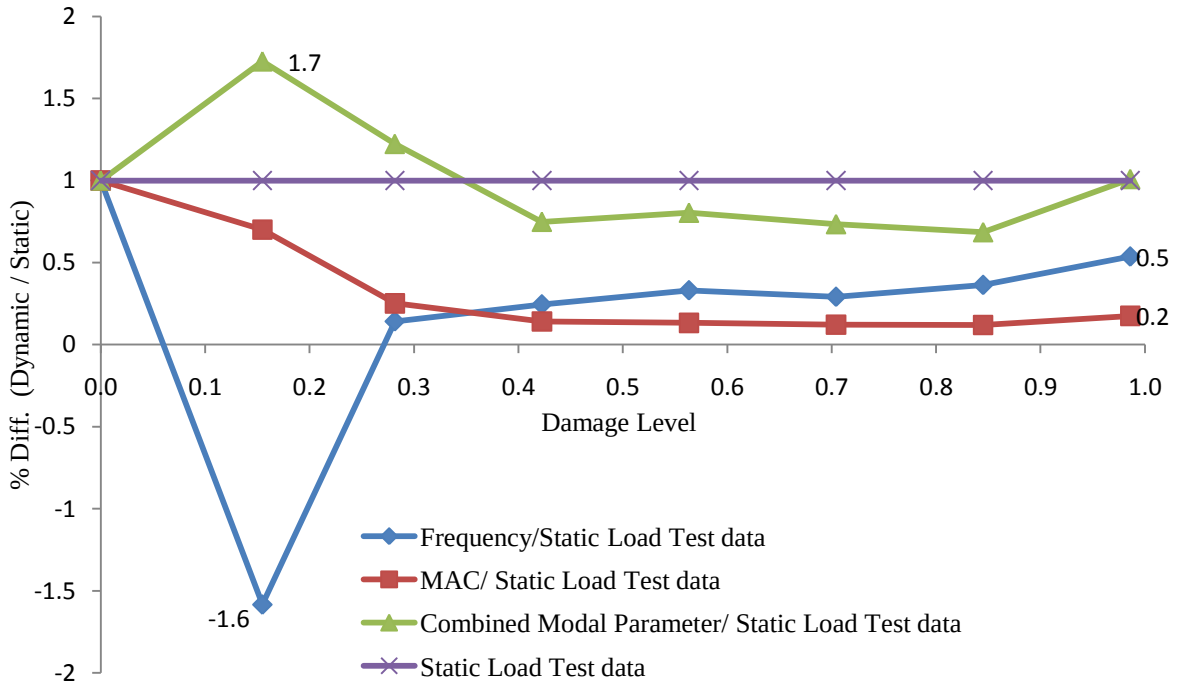

Figure 5.28. Comparison of modal parameter based algorithms to the static load test algorithm for flexural damage scenario

For the shear damage at 1.5 d, the developed and existing algorithms based on the modal parameters are compared with the static load test data as shown in Figure 5.29. The results show that up to failure the MAC based stiffness index has the smallest sensitivity, and the developed algorithm the highest. The static load test base algorithm shows much more sensitivity for the stiffness deterioration when compared to the other algorithms for all damage levels.

Prior to failure, the stiffness deterioration indicated is 7% based on MAC, 16.5% based on frequency and 38% based on combined modal parameters, while based on static load test data it is 57%. When failure occurs, the stiffness change based on MAC indicates higher deterioration than the stiffness change based on frequency, where it indicates stiffness deterioration of 63.4%. However the stiffness change based on MAC still indicates less deterioration than the stiffness change based on combined modal parameters, which indicates deterioration of 83.1%. The static load test based algorithm gives the highest sensitivity by indicating stiffness deterioration of 89.3%. The developed algorithm shows a much improved sensitivity when compared to the existing algorithms. However, it still has less sensitivity than the static load test based algorithm.

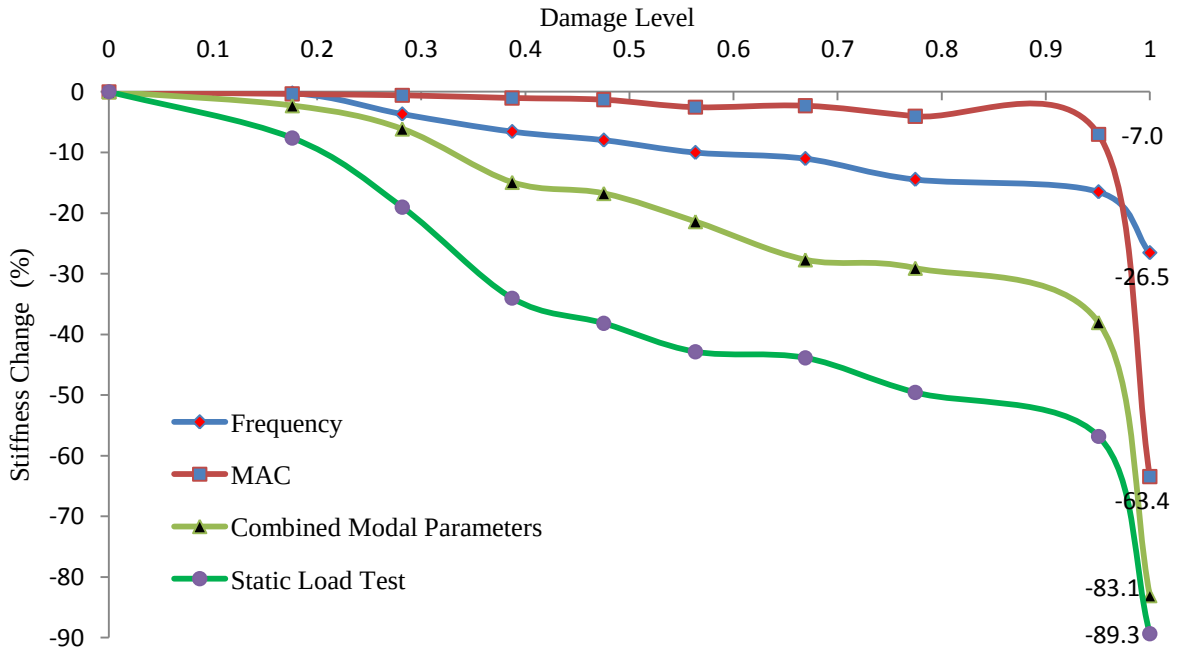

Figure 5.29. Comparison of algorithms for the shear damage scenario at 1.5d

The comparison of modal parameter based algorithms is carried out by taking the static load test data as the datum for the shear damage at 1.5d. This comparison is summarised in Figure 5.30. The results show that the developed algorithm has smaller values than the static algorithm for all damage levels, and the difference between developed and static

algorithms is reduced for higher damage levels and reaches 7% at failure. The frequency based algorithm shows much smaller values than the static algorithm where at first damage level the difference is 98%. Following this, the difference becomes smaller for higher damage levels and reaches 70% at failure. For the MAC based algorithm the results are much smaller than the static algorithm and are even smaller than the frequency based algorithm. The difference then becomes smaller for higher damage levels and reaches 29% based on the static algorithm.

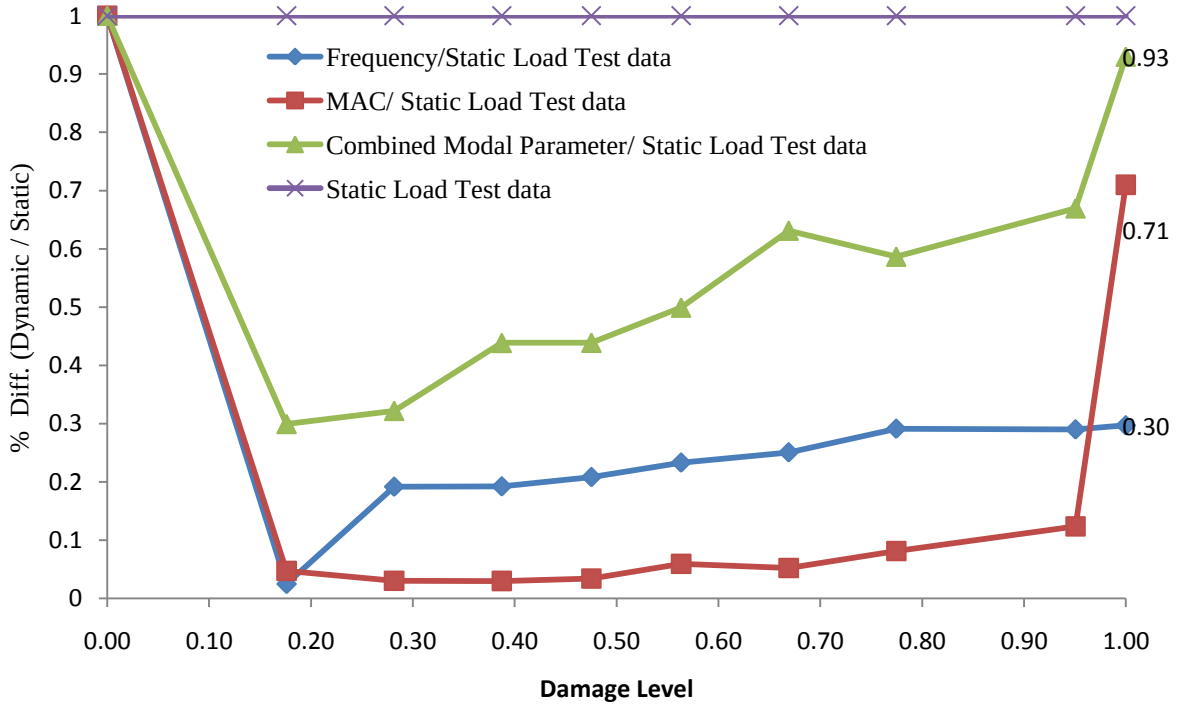

Figure 5.30. Comparison of modal parameter based algorithms to the static load test algorithm for shear damage scenario at 1.5d

Beam $B211_q$ is used to investigate the shear damage at quarter-span and the results of the stiffness change based on frequency, MAC, combined modal parameters and static load test data are shown in Figure 5.31.

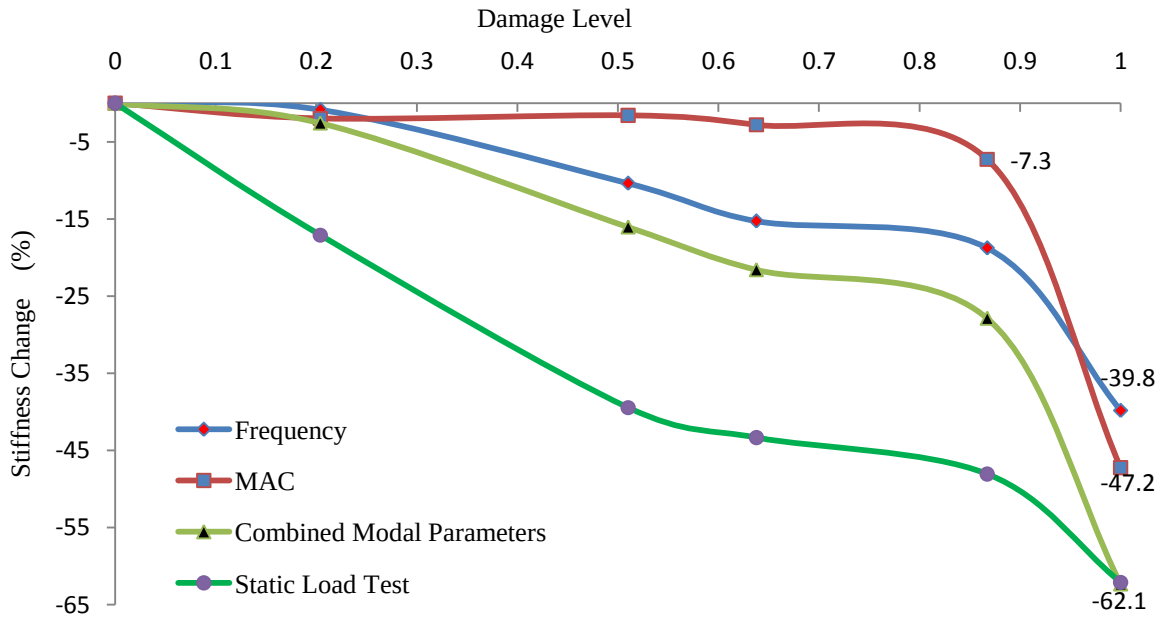

Figure 5.31. Comparison of algorithms for the shear damage at quarter-span

The results show that at 0.2 damage level, frequency based stiffness index has the smallest sensitivity where it detects a deterioration of less than 1%, while the developed algorithm gives the highest among the modal parameter algorithms by indicating a deterioration of 2.6%. For higher damage levels until just prior to failure, the MAC based stiffness index indicates the least stiffness deterioration, while the developed algorithm still has the highest sensitivity. When failure occurs, the MAC based stiffness index has a higher sensitivity than the frequency based stiffness index, although it is still less sensitive when compared to the developed algorithm. The static load test based algorithm is more affected by damage, where it detects the highest stiffness deterioration compared to modal parameter algorithms for all damage levels. The developed algorithm has improved sensitivity and is much closer to the results from the static load test based algorithm. Moreover, at failure it matches the static load test based algorithm where both indicate deterioration damage of 62.1%.

The comparison of modal parameters based algorithms is carried out by taking the static load test data as the datum for shear damage at quarter-span. The results are shown in

Figure 5.32. The developed algorithm shows much smaller values than the static algorithm at first damage level, before the difference becomes smaller for higher damage levels to reach same value at failure. The frequency based algorithm shows values which are 95% smaller than the static algorithm at first damage level. The difference then becomes smaller for higher damage levels and reaches 36% at failure. The MAC based algorithm shows the smallest values when compared to the static algorithm for all damage levels except at failure where the difference is reduced and reaches 24%.

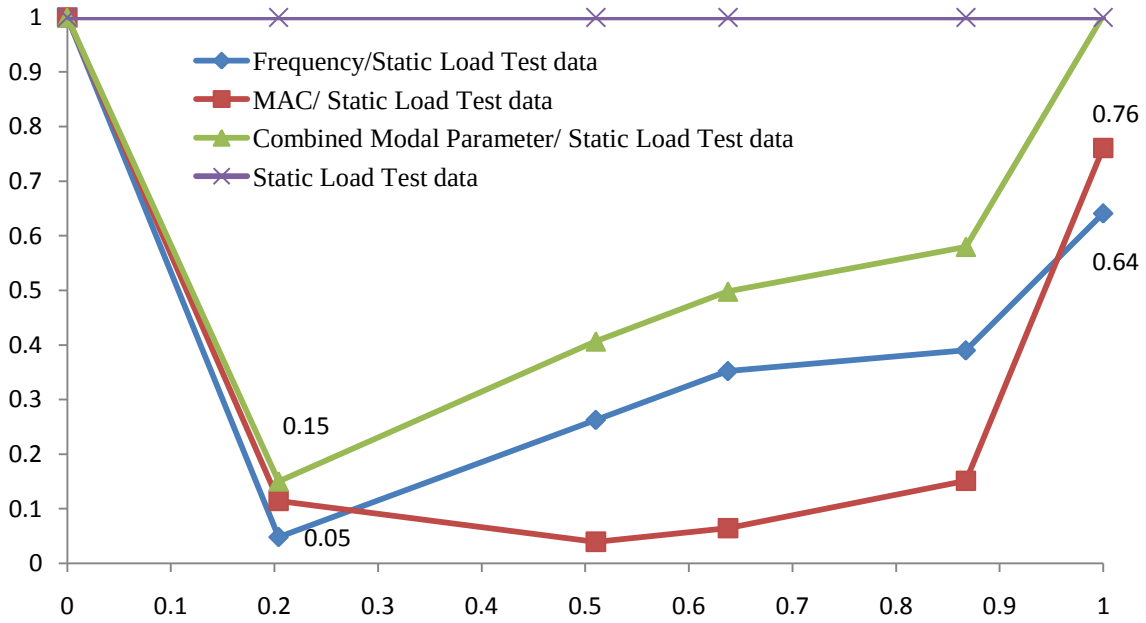

Figure 5.32. Comparison of modal parameter based algorithms to the static load test algorithm for shear damage scenario at quarter-span

The results of the developed and existing damage severity modal parameter algorithms as well as the static load test algorithm for different damage levels and scenarios shows that the developed algorithm based on the combined modal parameters increases the sensitivity of the existing algorithms. The static load test based algorithm always gives the highest sensitivity when compared to the other algorithms, except at failure where the developed algorithm matches the same sensitivity.

5.5 Damage location algorithms

This section presents and compares the results of the existing, modified and developed damage location algorithms by incorporating the anomalies of the elimination procedure. In order to justify the sensitivity and reliability of the existing, modified and developed damage location algorithms, three damage scenarios are considered, namely flexural damage, shear damage at 1.5d and shear damage at quarter-span as for beams $B121_m$, $B211_d$ and $B212_q$ respectively. The discussion covers the existing algorithms in the form of the CDF and LSI, the modified algorithms in the form of the MCDF and MLSI and the developed algorithm in the form of the SRI. The first six bending modes are considered for the calculation of the existing, modified, and developed algorithms.

5.5.1 Existing algorithms

As discussed previously in Section 3.3.1 and 3.3.2, CDF is related to the second derivative of the mode vectors, that is, curvature, while LSI is related to the fourth derivative of the mode vectors. The result of these algorithms will be shown without considering any anomaly elimination procedure in order to highlight their sensitivity in its original form.

5.5.1.1 Flexural damage at mid-span

The sensitivity of the existing algorithms will be verified for the flexural damage, for beam $B121_m$. The ensuing discussion only covers three damage levels rather than all of the damage levels induced on beam $B121_m$ as mentioned previously. The considered damage levels will be the first damage level when the first flexural crack appears at 11 kN, the second damage level, which is prior to the serviceability limit, and the third damage level which is beyond the serviceability limit. The higher damage levels will not be covered

where the crack pattern can easily be seen using visual inspection. Figure 5.33 shows the actual crack pattern at the first damage level, and Figures 5.34 and 5.35 show the CDF and LSI results for the first damage level.

The actual crack pattern shows a single crack located 112cm from the left support. The CDF results show that there are anomalies along the beam length as well as at the supports, and detected cracks between 60 and 110 cm. The CDF shows weakness in the ability to detect a single crack at the mid-span. For LSI all the modes give anomalies at the supports, and detected cracks between 60 and 110 cm. Thus LSI has a reduced ability to detect a single crack located at the mid-span.

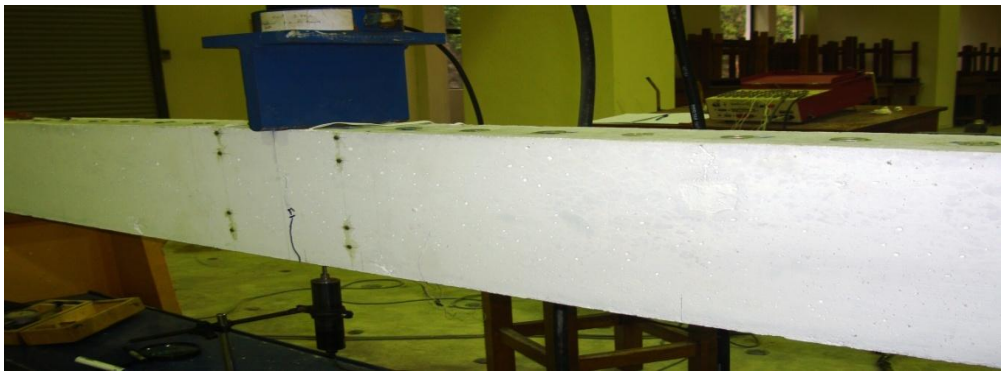

Figure 5.33. Actual crack pattern at first damage level for beam $B121_m$

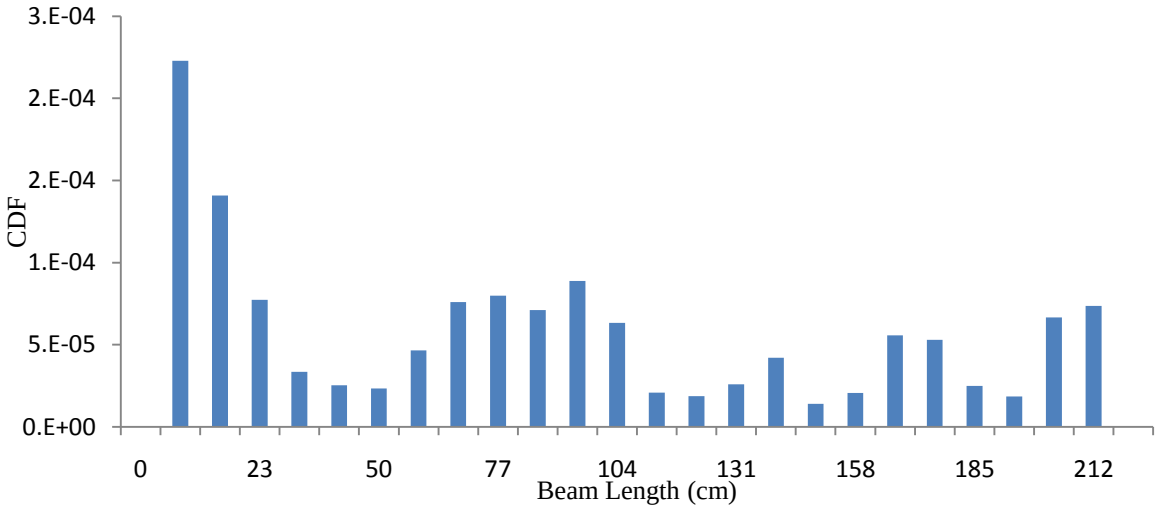

Figure 5.34. CDF at first damage level for beam $B121_m$

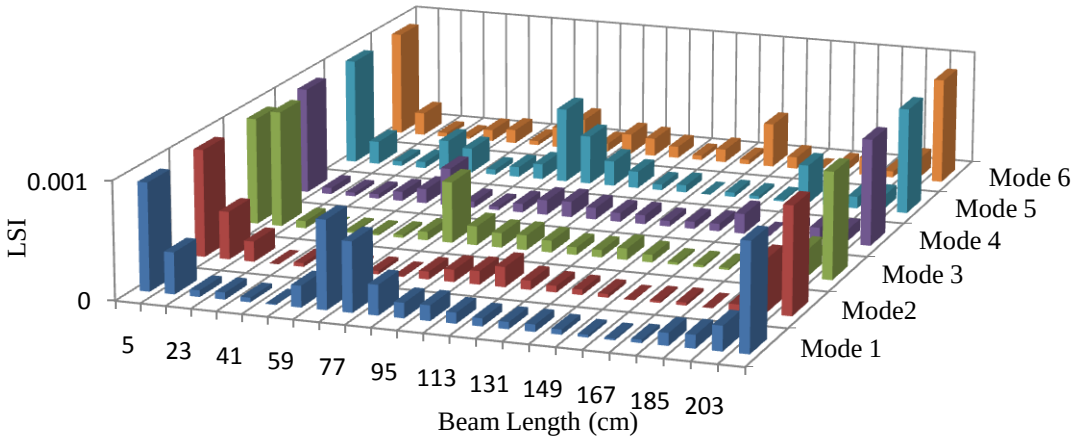

Figure 5.35. LSI at first damage level for beam $B121_m$

The actual crack pattern at the second damage level is as shown in Figure 5.36, and the results of CDF and LSI are shown in Figures 5.37 and 5.38. The actual crack pattern shows three cracks located at the zone between 95 and 135 cm from the left support. The CDF indicates anomalies along the beam length as well as at the supports. CDF indicates cracks located between 50 and 104 cm from the left support as well as at 160 to 185 cm from the left support. Thus CDF results for the single crack at the first damage level and the multiple cracks at the second damage level, indicate the inability to detect the actual location of the cracks and anomalies at the supports. The LSI results appear better than CDF where it detects cracks at the mid-span zone, but there are still anomalies at the supports and a weakness in detecting the actual crack location for multiple cracks.

The results of the existing algorithms show low ability for detecting single and multiple cracks. Therefore it is not implemented further for the third damage level with the appearance of more cracks. The existing algorithms must be modified or revised to overcome the support anomalies, anomalies along the beam length and the lower sensitivity.

Figure 5.36. Actual crack pattern at second damage level for beam $B121_m$

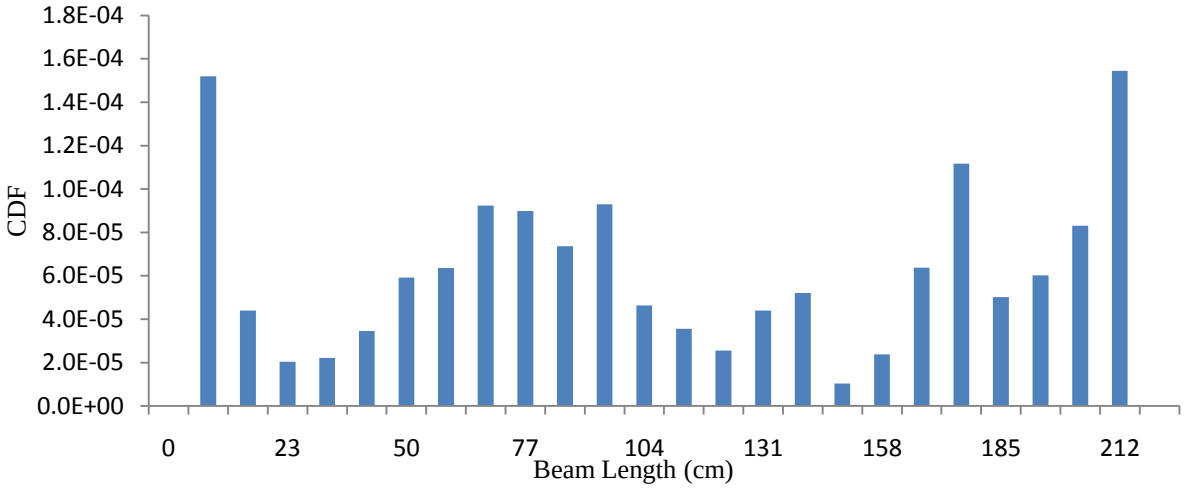

Figure 5.37. CDF at second damage level for beam $B121_m$

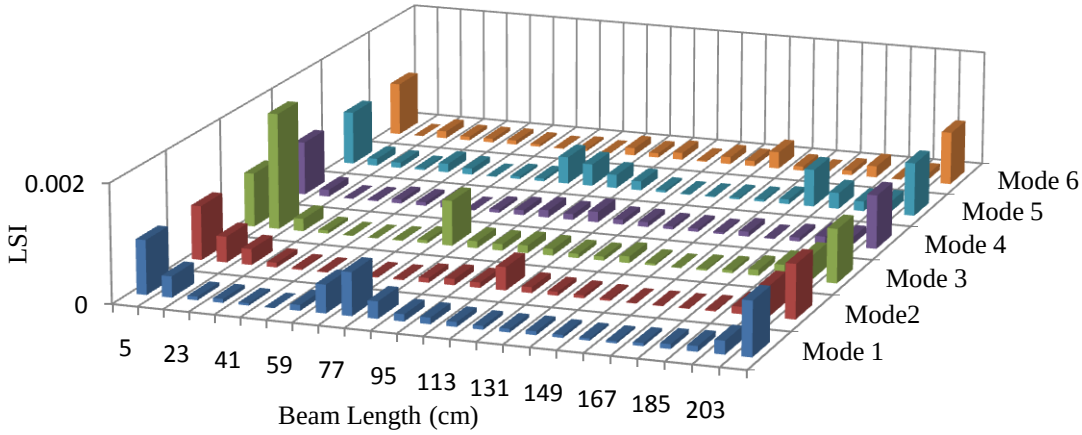

Figure 5.38. LSI at second damage level for beam $B121_m$

5.5.1.2 Shear damage at 1.5d

For the shear damage scenario close to the support, the damage load is applied as a concentrated load at a distance of 1.5d (effective depth) from the left support. The damage is induced in stages, and the first damage level is when the first flexural crack appears at 25 kN. Subsequently the second chosen level is when the applied load is 56 kN, which is close to the design limit. The third chosen level is when the applied load is 81 kN, where the first shear crack appears at the zone between the supports and the applied load point. Finally, the last chosen level is when the applied load is 96 kN, where the first diagonal shear crack appears at the supports.

Figure 5.39 presents the actual crack pattern of beam $B211_d$ at the first chosen level, and the results of CDF and LSI are illustrated in Figures 5.40 and 5.41. The actual crack pattern at the first damage level shows a single flexural crack at a distance of approximately 30 cm from the left support. The CDF results show the presence of anomalies along the beam length as well as near the supports. It detects cracks between 23 cm and 85 cm from the left support, indicating low ability of the CDF to detect single cracks. The LSI results show anomalies at both supports for all of the considered six modes. The LSI is not able to detect the single crack located at 30 cm from the left support.

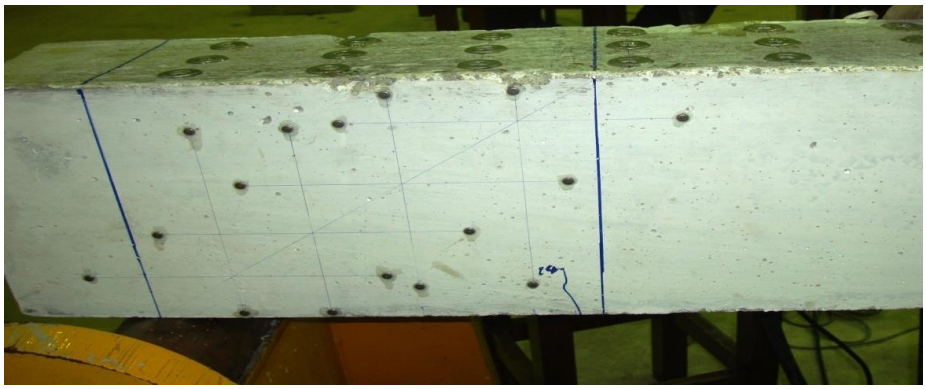

Figure 5.39. Actual crack pattern at first chosen level for beam $B211_d$

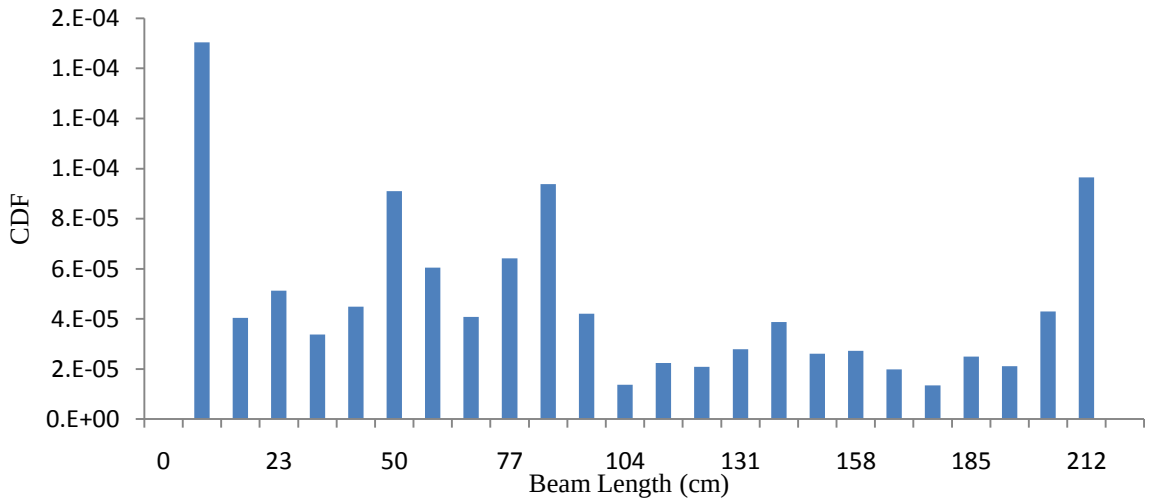

Figure 5.40. CDF at first chosen level for beam $B211_d$

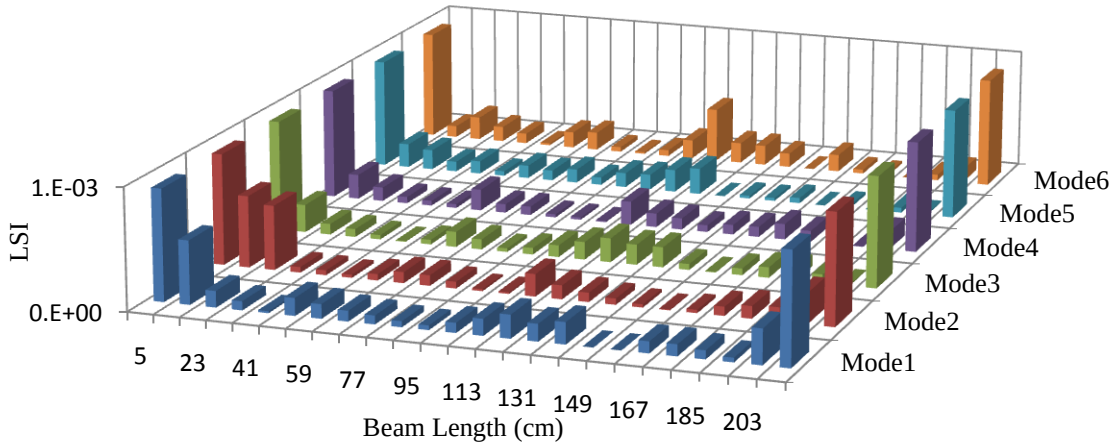

Figure 5.41. LSI at first chosen level for beam $B211_d$

Figure 5.42 shows the actual crack pattern of the second chosen level when the applied load is 56 kN. The results of CDF and LSI are illustrated in Figures 5.43 and 5.44. The actual crack pattern shows multiple cracks located at the distance between 30cm and 120 cm from the left support. The CDF algorithm results show anomalies at the supports and along the beam length. Moreover, it is unable to locate the actual crack. The LSI results show anomalies at the supports, and the detected crack positions do not match the actual crack locations. The results show that the existing algorithms are not able to locate the cracks for

either single crack or multiple cracks located between 1.5d from the support until the mid-span. This raises the need to modify the algorithms or to formulate new algorithms which can overcome the sensitivity problem of the existing algorithms. Since the existing algorithms are not able to detect the crack locations for the damage cases considered so far, it is unnecessary to proceed to the higher damage levels.

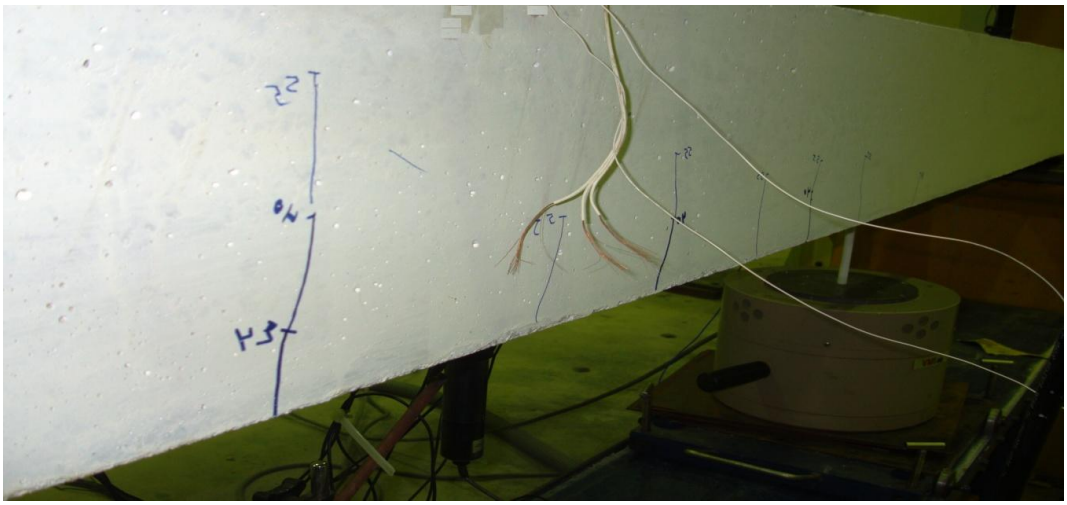

Figure 5.42. Actual crack pattern at second chosen level for beam $B211_d$

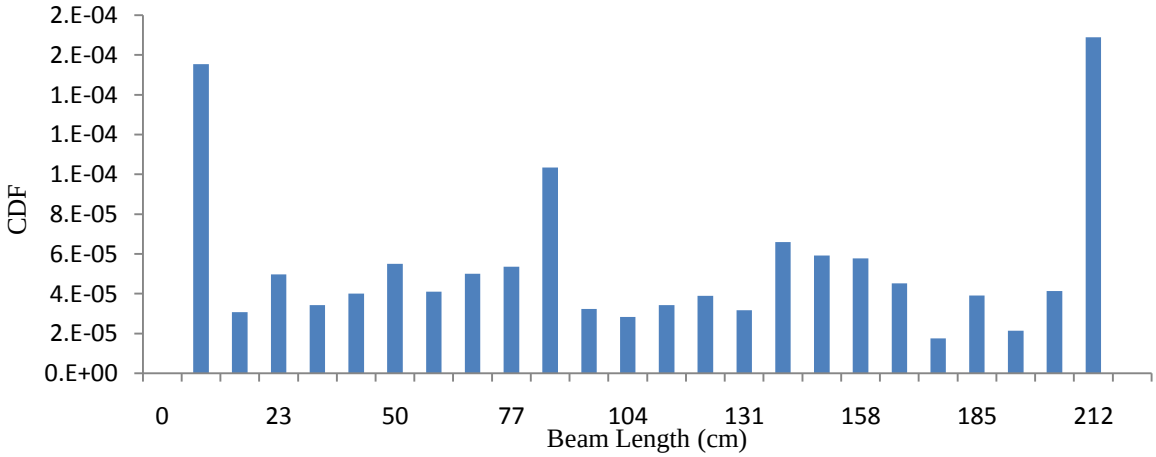

Figure 5.43. CDF at second chosen level for beam $B211_d$

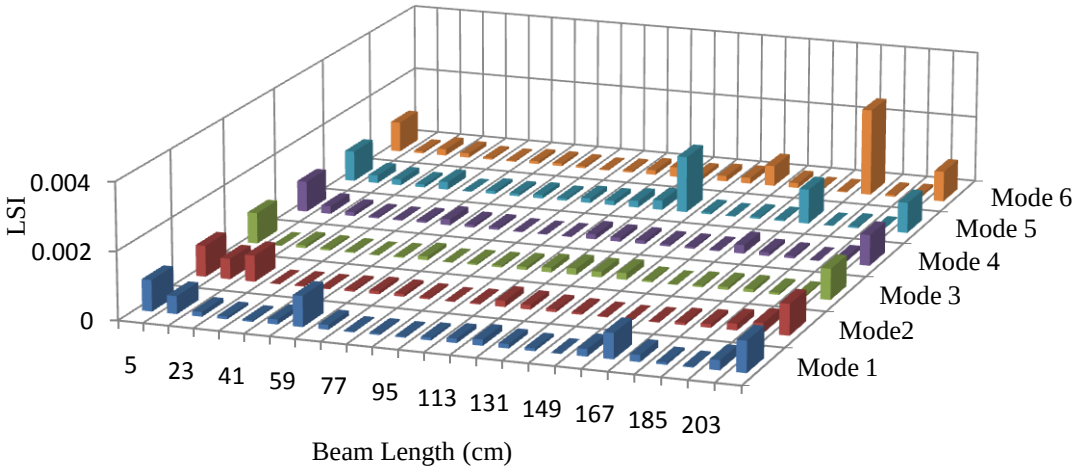

Figure 5.44. LSI at second chosen level for beam $B211_d$

5.5.1.3. Shear damage at quarter-span

For the shear damage at quarter-span, the load is applied at the quarter-span in order to induce shear and flexural stresses into the RC beam. The load is applied at different damage levels, where the first level is up to 20 kN with the first flexural crack occurrence, the second level is up to 50 kN when the first shear crack appears between the support and the quarter-span. The third chosen level is up to 62 kN when the first diagonal shear crack appears at the supports. Figure 5.45 shows the actual crack pattern at the first damage level of beam B211q, while Figures 5.46 and 5.47 show the results of the CDF and LSI algorithms. The actual crack pattern shows a single crack located at a distance of approximately 55cm from the left support. The CDF results detect cracks at the zone between 40cm and 60 cm, which is close to the actual single crack location. Anomalies remain along the beam length and at the supports. For the LSI results for Mode 1, cracking is detected at the zone of the actual crack location, while there are still anomalies at the supports. The rest of the modes show inaccuracies in detecting the actual crack location.

Figure 5.45. Actual crack pattern at first damage level for beam $B211_q$

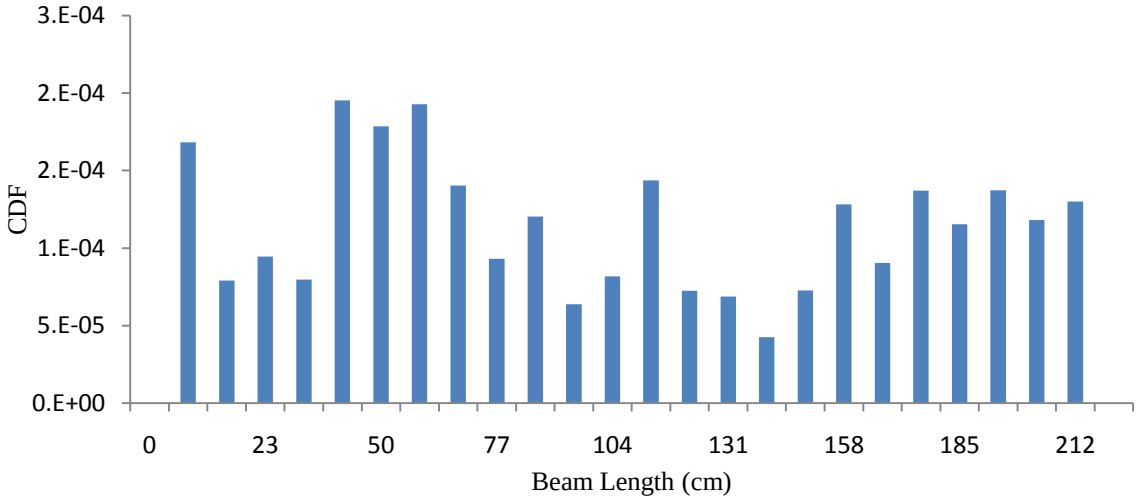

Figure 5.46. CDF at first damage level for beam $B211_q$

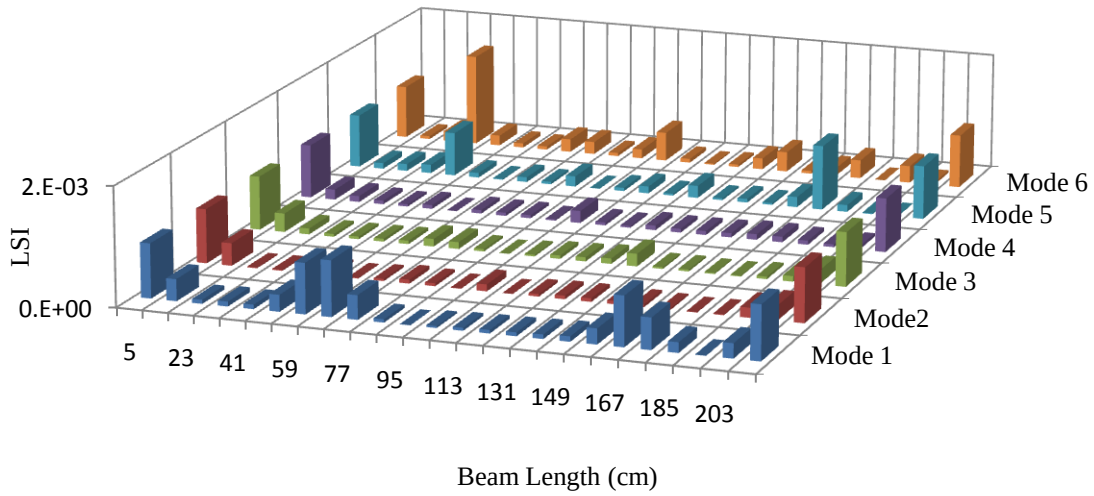

Figure 5.47. LSI at first damage level for beam $B211_q$

For the second damage level, when the first crack appears at the shear zone, Figure 5.48 shows the actual crack pattern and Figures 5.49 and 5.50 show the results of the CDF and LSI algorithms. The actual crack pattern shows multiple cracks located between 30cm and 160cm from the left support. The CDF algorithm detects cracks between 70cm and 85cm and anomalies along the beam length. For the LSI, results of Modes 1, 4, 5, and 6, indicate some cracks within the zone of the actual crack locations, while anomalies still appear at the support as well as at the zones when there is no actual cracking.

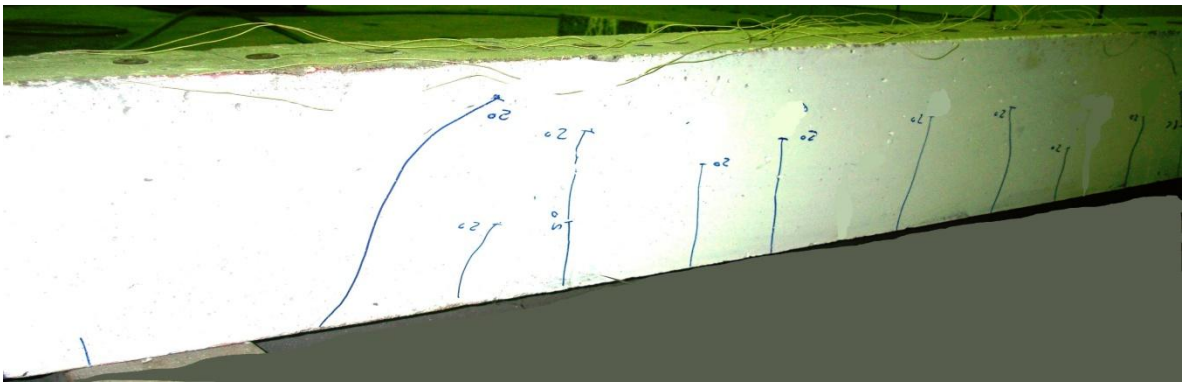

Figure 5.48. Actual crack pattern at second damage level for beam $B211_q$

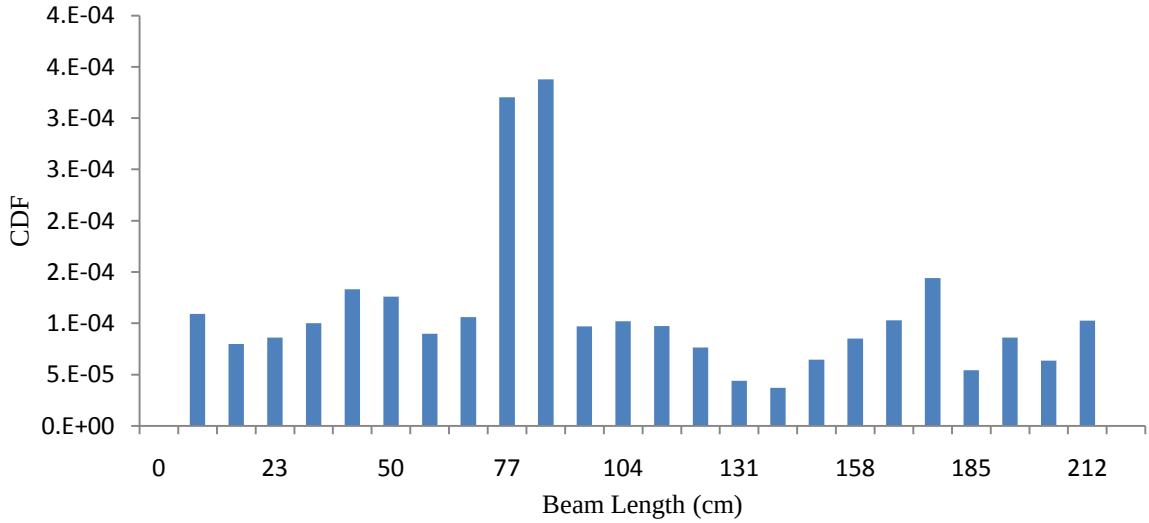

Figure 5.49. CDF at second damage level for beam $B211_q$

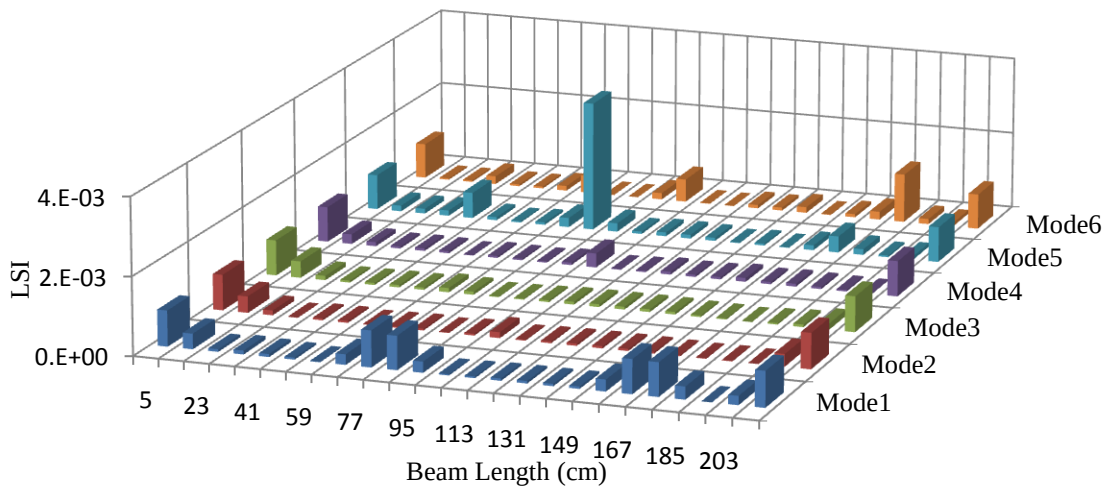

Figure 5.50. LSI at second damage level for beam $B211_q$

The results for the damage at the quarter-span show a better ability for the existing algorithms to detect single cracks, while less sensitivity in detecting the multiple cracks is noticed. Thus, no further damage levels are considered for applying the existing DLA.

The results show that the existing algorithms show a better ability to detect the single crack location when the damage load is applied at the quarter-span compared to the mid-span and 1.5d cases. For the multiple crack cases, inaccuracies and poor sensitivity is apparent. Thus, the existing algorithms must be modified, or new algorithms must be established in order to overcome the problem of poor sensitivity to detect cracks at different locations, multiple cracks, anomalies at the supports, and anomalies along the beam length. The next part of this study aims to modify and develop damage algorithms to be more sensitive for locating cracks wherever they are located and whatever their number. Moreover, through the elimination of the anomalies along the beam length as well as at the supports, it is expected that there will be significant improvement.

5.5.2 Modified CDF algorithm

The existing algorithms are modified as discussed in Sections 3.3.3, 3.3.4 and 3.3.5, involving the equations in the form of the MCDF, MLSI, SRI and anomaly elimination procedures proposed as mentioned in Section 3.3.6. In the following discussion the results of the modified CDF algorithm, the use of the normalised procedure and the application of the proposed anomaly elimination procedures are presented for the same flexural damage scenario as previously considered.

The actual crack pattern at the first damage level is shown in Figure 5.33, and the MCDF algorithms results are shown in Figure 5.51. The results show that each mode has different peak values at a particular distance along the beam length, that is, Mode 5 shows the highest value while Mode 1 gives the lowest, which makes it difficult to compare the sensitivity of the modes for locating the actual crack location. It must not be forgotten that MCDF is an algorithm for locating the actual crack position and not for quantifying the crack depth. This means that the value is not a decisive factor to consider but more important is the consistency of the MCDF pattern along the beam length in order to be able to locate the actual cracks.

The normalising procedure is a simple way to present different modes with different peak values or intensities in one 3-D graph without affecting the sensitivity of each individual mode. The normalising procedure calculation is very simple, where it can be done by dividing the algorithm values along the beam length for each specific mode by the highest intensity in that mode. This results is making the height value equal to unity and the other algorithm values along the beam length equal to a fraction. Such simple calculations would not affect the sensitivity of the individual mode, where it is akin to zooming in or zooming

out in order to show the whole set of considered modes on one scale and to make it easier for comparison.

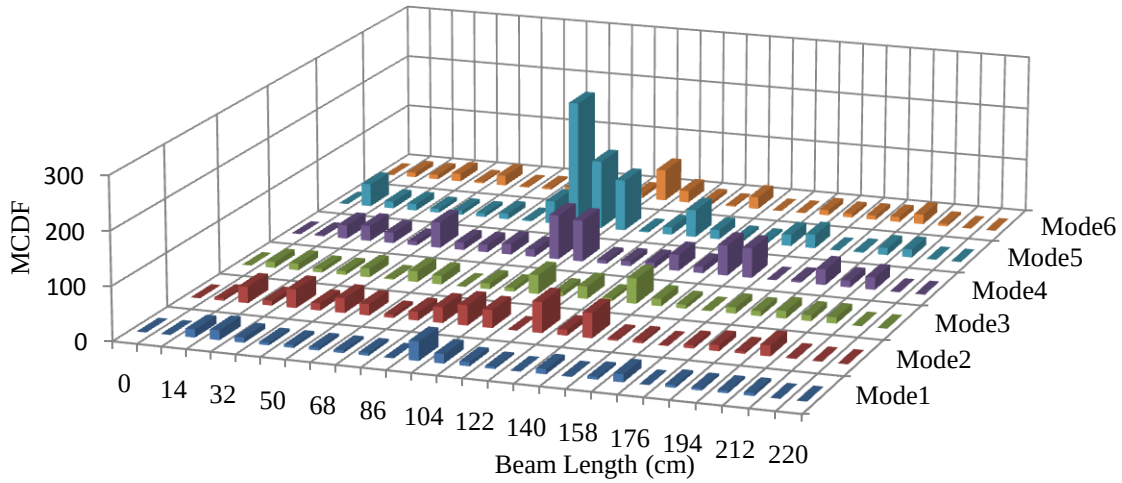

Figure 5.51. MCDF at first damage level for beam $B121_m$

Figure 5.52 presents the normalised MCDF values at the first damage level for the considered modes. The results give a better comparison without affecting the sensitivity for each individual mode. The normalising procedure will be applied to the rest of the results whenever several modes need to be compared in one 3-D graph.

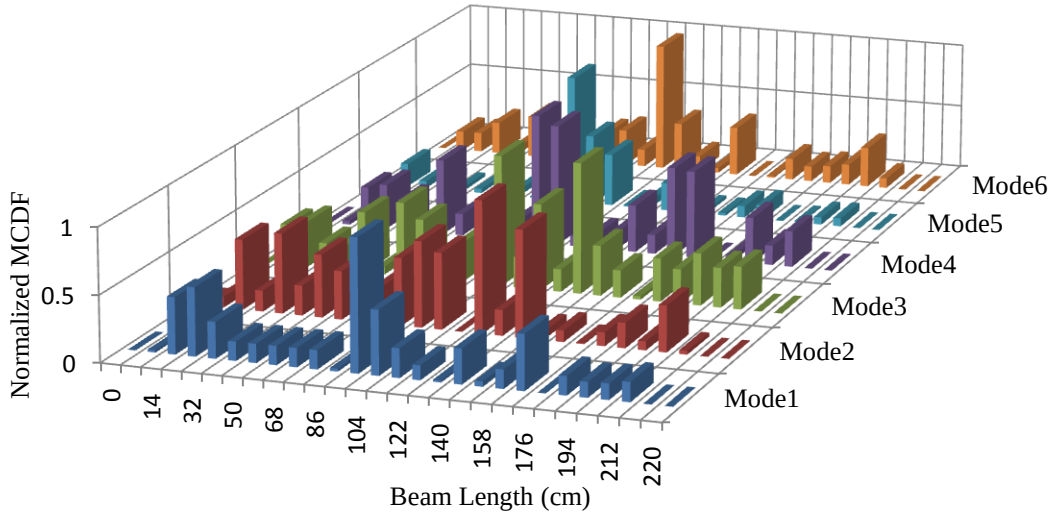

Figure 5.52. Normalized MCDF at first damage level for beam $B121_m$

The results of the normalised MCDF show a better sensitivity than the original CDF algorithm in detecting the crack location. The actual crack pattern shows a single crack located at 112cm from the left support. The MCDF results show that the first mode detects a major peak located at 95cm and minor peaks located at 23cm, 105cm, and 160cm from the left support. The second mode detects multiple peaks along the beam length and a major peak located at 120cm from the left support. The third mode shows multiple minor peaks, while major peaks are at 105cm and 140 cm from the left support. The fourth mode detects a major peak at 110 cm, and minor peaks at 50 and 160 cm. The fifth mode detects major peaks between 80 and 105cm from the left support. The sixth mode detects a major peak at 105 cm from the left support and some minor peaks along the beam length. All the modes show anomalies along the beam length.

The overall performance of MCDF shows a better ability to detect single cracks located at mid-span than the original CDF. Since most of the algorithms are based on the calculation of the second or the fourth derivatives of mode vectors, this results in very small values of the order of 10^{-8}. Such values during multiplication or division, give the anomalies along the beam length. In order to overcome such anomalies, the Statistical Anomalies Elimination (SAE) procedure, as described in Section 3.3.6.1, is performed on the normalised MCDF results at the first damage level of beam $B121_m$, and the results are shown in Figure 5.53. The results show that the SAE procedure cut-off the anomalies along the beam length, while retaining the peak values. The major peaks can be considered as the actual cracks, while the minor peaks could either be micro-cracks in the RC beam not detectable through visual inspection, or are stress concentration points.

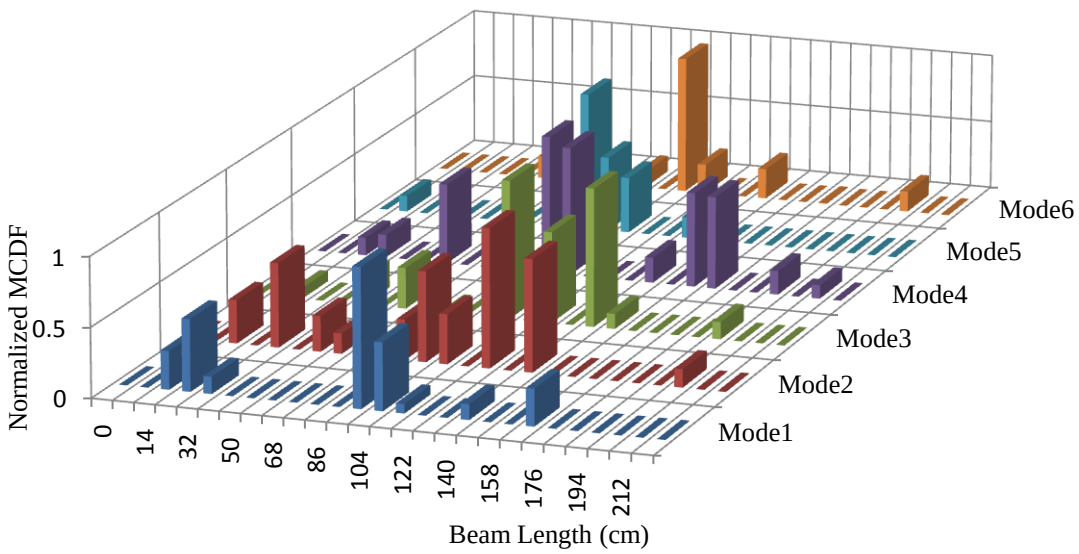

Figure 5.53. Normalized MCDF after SAE at first damage level, $B121_m$

The SAE procedure shows a good ability to cut-off the anomalies along the beam length resulting from mathematical calculations of the algorithms, without affecting the actual sensitivity. All of the modes indicate major peaks close to the actual location of the crack, but they are either to the left or to the right of the exact location. These can either be micro-cracks in the RC beam or stress concentration points at the mid-span where the flexural stresses are high.

At the second damage level there are three cracks located at 95cm, 112cm, and 135 cm from the left support, and the actual crack pattern is shown in Figure 5.36. The MCDF is calculated from the second level data and the results of the normalised MCDF are as shown in Figure 5.54. The results show better sensitivity for MCDF than the original CDF algorithm in detecting the three crack locations, and the normalised modified algorithm cut-off the anomalies at the support significantly. The results show a good ability for detecting the location of the actual cracks. Generally, modes 1, 2, 4 and 5 show good sensitivity in detecting the three cracks located at the mid-span. Mode 3 indicates peaks within the zone of the actual crack as well as close to the actual crack locations. However mode 6 returns

lower peaks within the zone of the actual cracks as opposed to the zone to the left and right of the actual crack location.

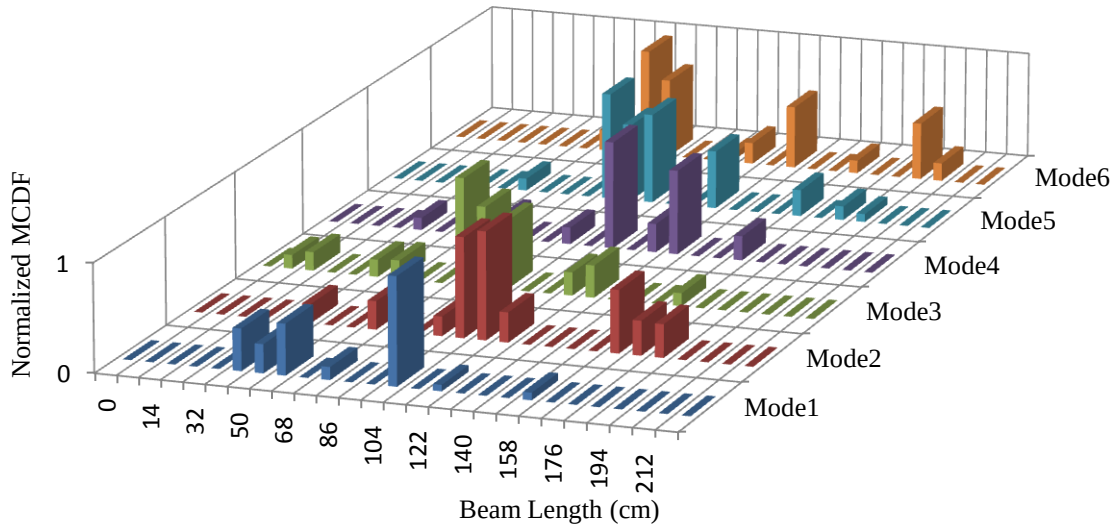

Figure 5.54. Normalized MCDF after SAE at second damage level, $B121_m$

Since the MCDF shows good agreement with the actual crack pattern, it will be implemented for the case of multiple cracks arising due to the damage level beyond the design limits. The actual crack pattern of beam $B121_m$ at the third damage level is shown in Figure 5.55, and the normalised MCDF results, after performing the SAE procedure for the considered modes are shown in Figure 5.56.

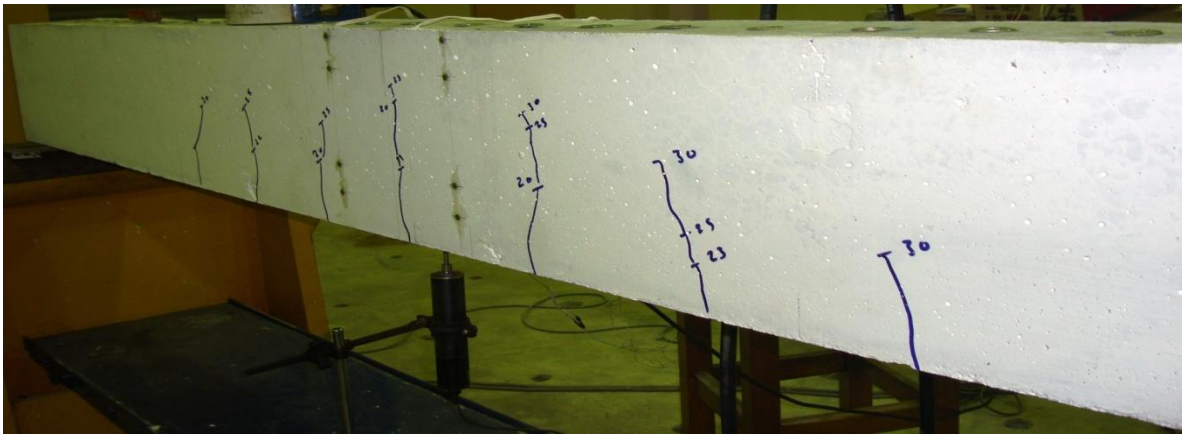

Figure 5.55. Actual crack pattern at third damage level for beam $B121_m$

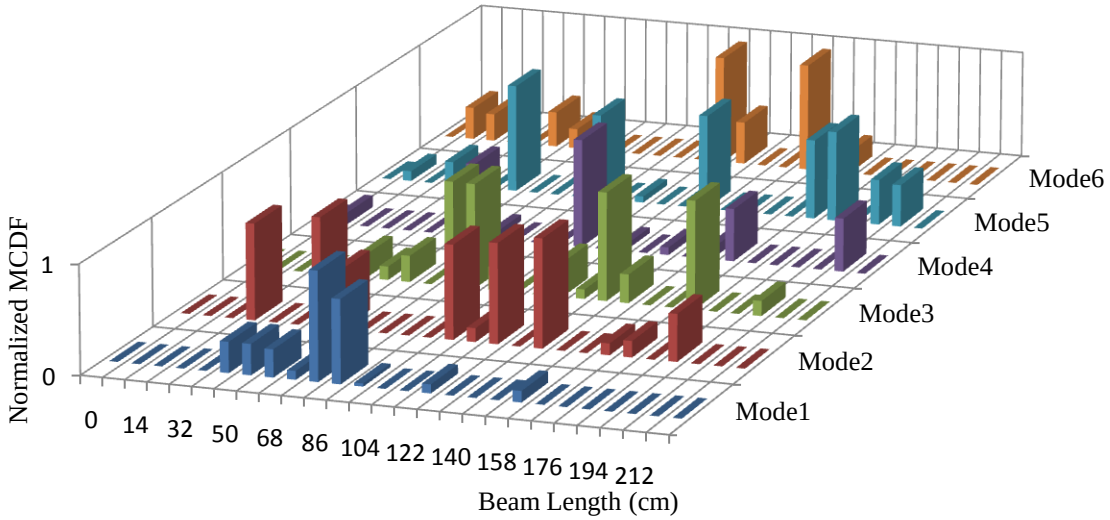

Figure 5.56. Normalized MCDF after SAE at third damage level, $B121_m$

The normalised MCDF results show that all the modes give high peaks located within the zone of the actual crack pattern. Modes 1 and 4 detect major peaks at the zone of the actual cracks and some minor peaks to the left of the zone. Modes 2 and 3 detect major peaks at the zone of the actual cracks and some minor peaks to the left and right of the actual crack zone. Mode 5 detects major peaks at the zone of the actual crack and some major peaks to the left and right of the zone, while Mode 6 detects major and minor peaks at the zone of the actual cracks. The major peaks can be considered as the actual cracks, while the minor peaks could either be micro-cracks in the RC beam and not detectable or stress concentration points.

5.5.3 Modified LSI algorithm

This section presents the results of the modified LSI algorithm with the same adopted flexural damage levels for beam $B121_m$. The aforementioned normalised procedure is used for the purpose of comparing the set of considered modes in one 3-D graph. The SAE procedure shows good results for cutting-off the anomalies, which appear due to the

mathematical calculation of the MCDF values for all of the considered modes and at all of the adopted damage levels. Thus, the SAE procedure will be performed directly on the results of the normalised MLSI for all the modes and for all of the adopted damage levels. The actual crack pattern at the first damage level of beam $B121_m$ is shown in Figure 5.33, and the results of the normalised MLSI after performing SAE procedure for the considered modes are shown in Figure 5.57.

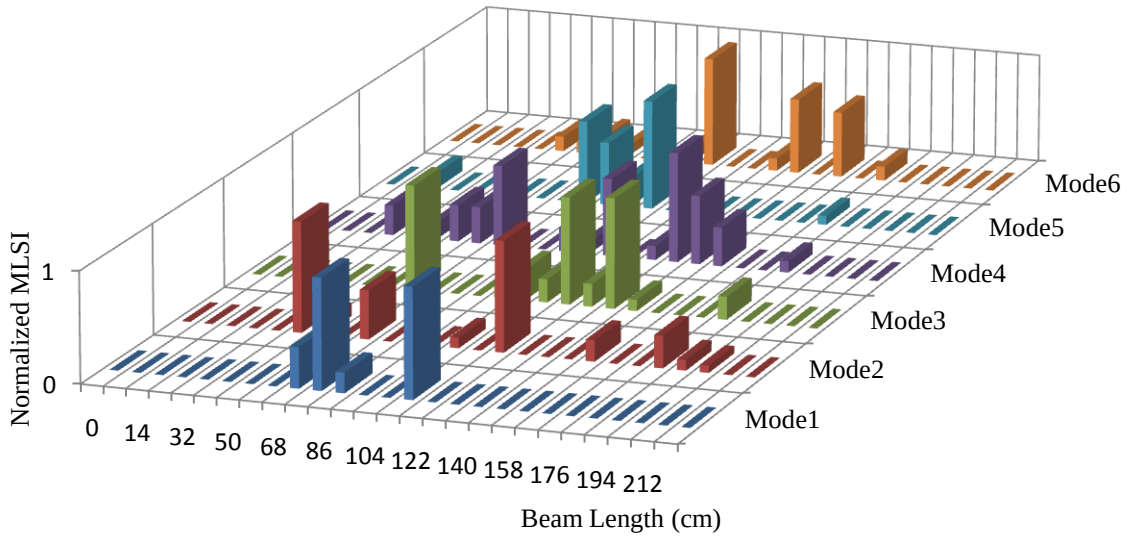

Figure 5.57. Normalized MLSI after SAE at first damage level, $B121_m$

The results show better sensitivity for the MLSI than the original LSI algorithm in detecting single cracks. The modified form of LSI (MLSI) cut-off the anomalies at the supports, while implementing the SAE procedure cut-off the anomalies along the beam length. Modes 1, 2, and 5 detect major peaks at the zone of the actual crack and some minor peaks to the left of the zone. Mode 3 detects a major peak at the zone of the actual crack and minor peaks to the right of the zone. Mode 4 detects minor peaks at the zone of the actual crack and some major peaks to the left and right of the zone, whilst Mode 6 detects major peaks at the zone of the actual crack and some minor peaks to the right of the zone.

The minor peaks detected by all of the considered modes can be micro-cracks or stress concentration points in the RC beam.

The actual crack pattern of beam $B121_m$ at the second damage level is shown in Figure 5.36, and the normalised MLSI results after performing the SAE procedure at the second damage level are shown in Figure 5.58.

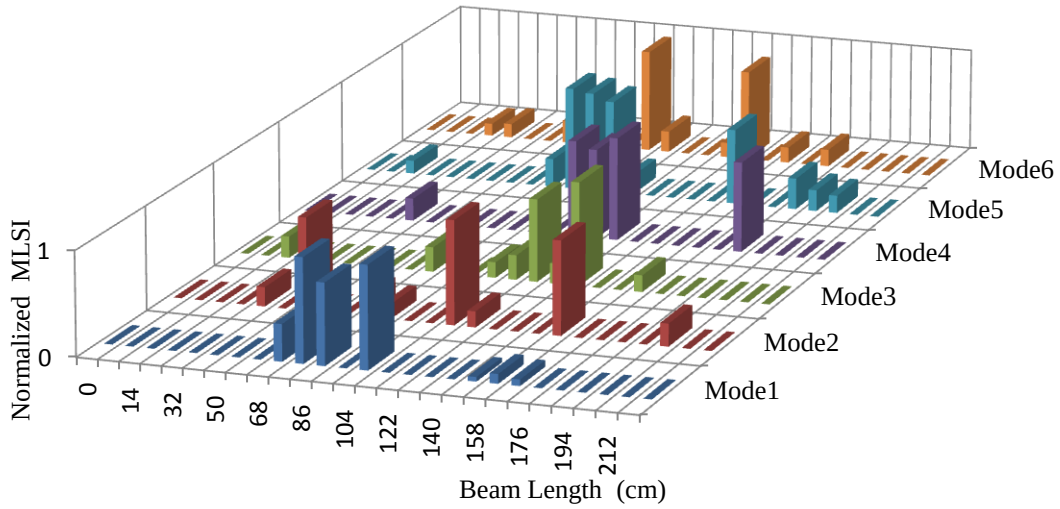

Figure 5.58. Normalized MLSI after SAE at second damage level, $B121_m$

The results show that the modified MLSI improves the sensitivity of the original LSI, where it becomes more sensitive in detecting the crack locations. The first mode detects major peaks within the zone of the actual cracks and some major and minor peaks to the left of the zone. Modes 2 and 5 detect major peaks at the zone of the actual cracks and some major peaks to the left and right of the zone, while Modes 3, 4, and 6 detect major peaks within the actual crack zone and some major and minor peaks to the right of the zone. All of the modes detect minor peaks along the beam length and close to the actual crack zone, which could be micro-cracks or stress concentration points in the RC.

Since MLSI shows a good ability to detect multiple crack case, it will be implemented to detect further multiple crack cases. The actual crack patterns of the beam $B121_m$ at the third

damage level is as shown in Figure 5.55, and the normalised MLSI results at the same damage level are shown in Figure 5.59 where the SAE procedure is performed.

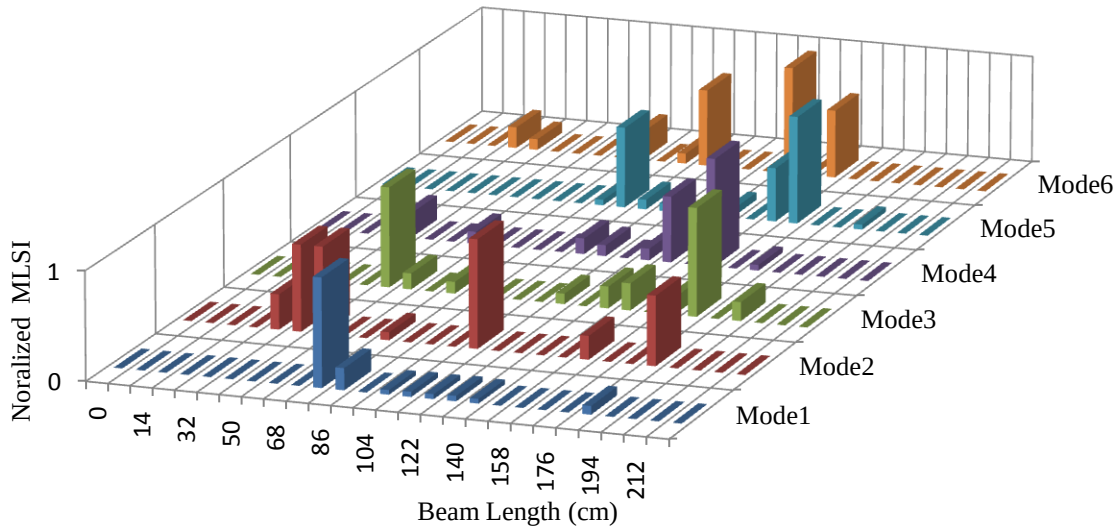

Figure 5.59. Normalized MLSI after SAE at third damage level, $B121_m$

The results show good sensitivity for the MLSI to detect multiple crack cases. Modes 1, 4, 5 and 6 detect major and minor peaks at the zone of the actual cracks. Mode 2 detects major and minor peaks in the actual cracks zone as well as close to the left and right of the zone. Mode 3 detects minor peaks in the zone of the actual cracks and major peaks close to the left and right of the zone. The major and minor peaks to the left and right of the actual crack zone can be undetectable micro-cracks or stress concentration points in the RC beam at the mid-span. The MLSI shows good sensitivity to detect the crack patterns at different damage levels and the SAE procedure is validated as a good anomalies elimination procedure to cut-off the anomalies which appear due to mathematical calculation.

5.5.4 Developed SRI algorithm

This section will present the results of the developed damage location algorithm SRI, which is established in this study to highlight the main contribution of this study to the detection

of the damage location, in addition to the modification of the existing algorithms and the proposed statistical anomalies elimination procedure. The aforementioned normalised procedure is used for the purpose of comparing the set of the considered modes in one 3-D graph. This is due to the fact that the SAE procedure shows good results for cutting-off the anomalies in both MCDF and MLSI values for all the considered modes as well as all of the adopted damage levels. Thus, the SAE procedure will be performed directly on the results of the normalised MLSI for all the modes and for all of the adopted damage levels. The SRI algorithm will be examined for the same flexural damage scenario and at the same damage levels as adopted previously. The actual crack patterns at the first damage level for beam $B121_m$ are as shown in Figure 5.33, and Figure 5.60 presents the normalised SRI values at the first damage level where the SAE procedure is performed.

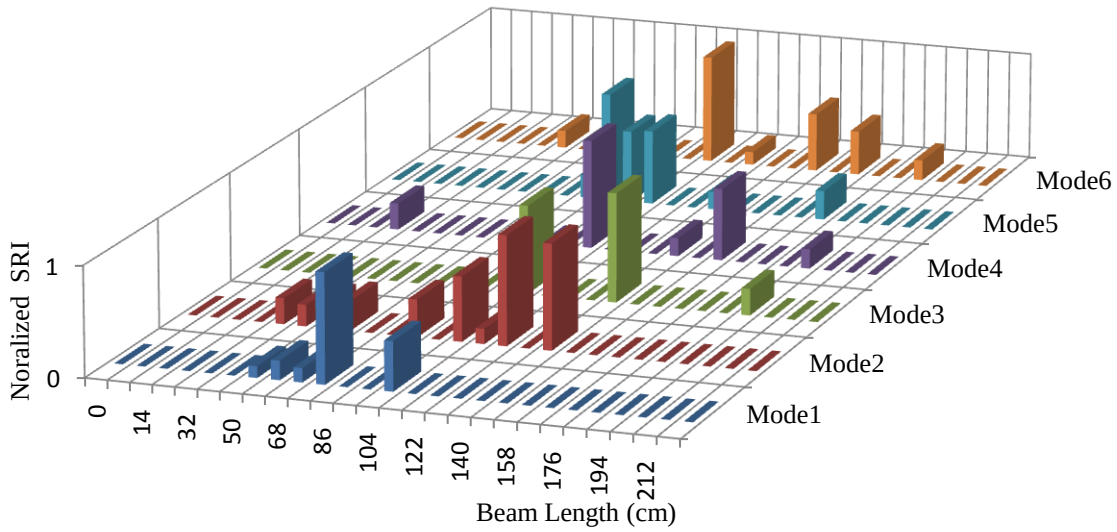

Figure 5.60. Normalized SRI after SAE at first damage level, $B121_m$

The results show a good ability from the developed algorithm to detect single cracks at mid-span. The first mode detects minor peaks at the zone of the actual crack and major peaks to the left of the zone. Mode 2 detects minor peaks at the zone of the actual crack as

well as major peaks to the right and minor peaks to the left of the zone. Mode 3 detects major peaks at the zone of the actual crack and major peaks to the right of the zone. Modes 4 and 6 detect major peaks at the actual crack zone and minor peaks to the right of the zone, whilst Mode 5 detects major peaks at the zone of the actual crack zone and major peaks to the left of the zone.

The developed algorithm will be examined for multiple crack cases to validate its sensitivity at different damage levels. The actual crack patterns at the second damage level for beam $B121_m$ are shown in Figure 5.36 and the normalised SRI results at the second damage level after performing the SAE procedure are shown in Figure 5.61.

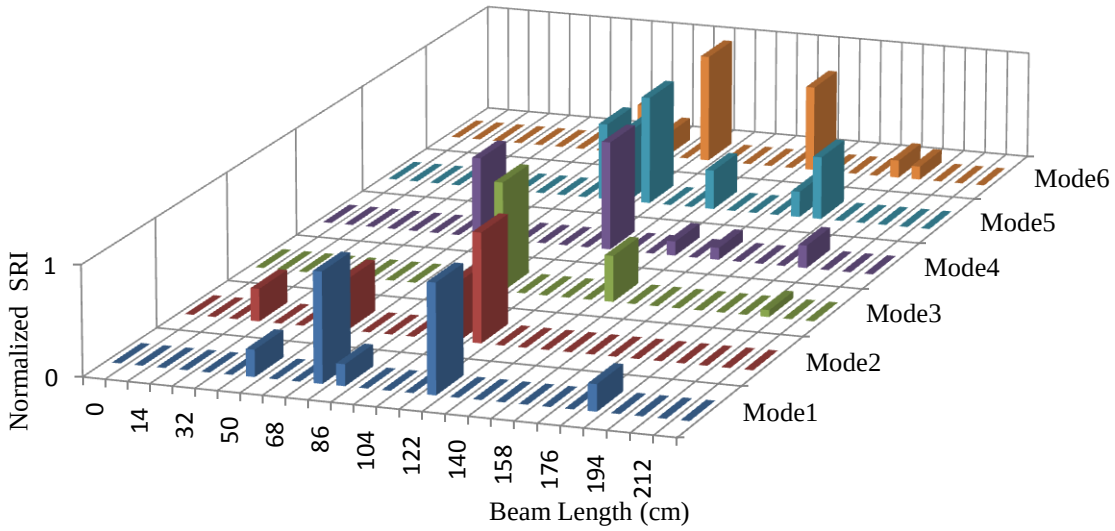

Figure 5.61. Normalized SRI after SAE at second damage level, $B121_m$

The results show good ability from the SRI algorithm to detect multiple cracks located at the mid-span. Mode 1 detects a major peak at the zone of the actual cracks and a major peak to the left of the zone. Modes 2 and 4 detect major peaks within the zone of the actual cracks and minor peaks to the left of the zone. Mode 3 detects a major peak at the actual cracks zone and a minor peak to the right of the zone. Modes 5 and 6 detect major peaks in the zone of the actual cracks and minor peaks to the left and right of the zone.

Since the SRI shows good ability to detect three cracks located at the mid-span, its sensitivity will be examined further at the third damage level. The actual cracks at the third damage level for beam $B121_m$ are as shown in Figure 5.55, and the SRI values at the third damage level when the SAE procedure is used are shown in Figure 5.62.

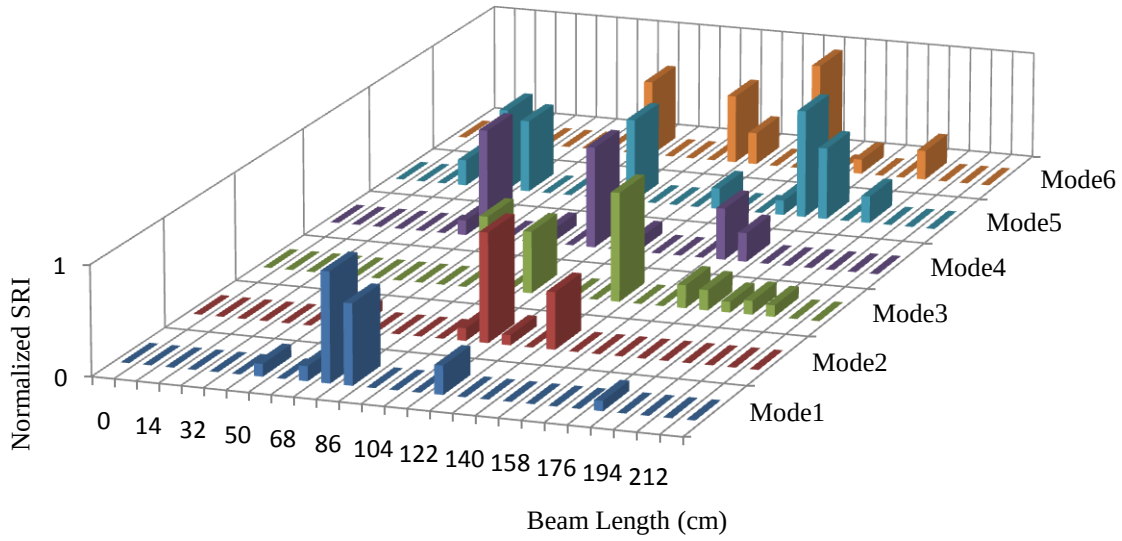

Figure 5.62. Normalized SRI after SAE at third damage level, $B121_m$

The results show good ability from the SRI algorithm to locate the crack positions in the case of multiple cracks, and the SAE procedure helps to cut-off most of the anomalies along the beam length. Modes 1, 2, 3, and 6 detect major peaks in the zone of the actual cracks. Mode 4 detects major peaks in the zone of the actual cracks and major peaks to the left of zone, whilst Mode 5 detects major peaks in the zone of the actual cracks and some major peaks to the left and right of the zone.

5.5.5 Comparison of algorithms

In order to detect the crack locations using the modified and developed dynamic algorithms by taking into account all the considered modes, the weighted average according to proposed weighting method (PWM), as described in Section 3.3.7, will be applied for the

averaging of the algorithms. Anomalies can appear along the beam length. These are a result of the mathematical calculation of the algorithms or are due to performing of PWM averaging of different mode shapes. Thus the SAE procedure will be applied in order to cut-off such anomalies. The damage location algorithms are used for locating the actual crack position and not for quantifying the crack depth. This means that the value is not a decisive factor to consider but more importantly the consistency of the algorithm pattern along the beam length. The results of developed and modified algorithms are plotted together after normalising its values using the aforementioned normalised procedure in order to facilitate a comparison. Figure 5.63 shows a flow chart illustrating the procedures applied to the algorithms before the comparison. The sensitivity of the modified and developed algorithms will be examined at three damage scenarios namely flexural damage at mid-span as for beam $B121_m$, shear damage at 1.5d as for beam $B211_d$ and shear damage at quarter-span as for beam $B211_q$.

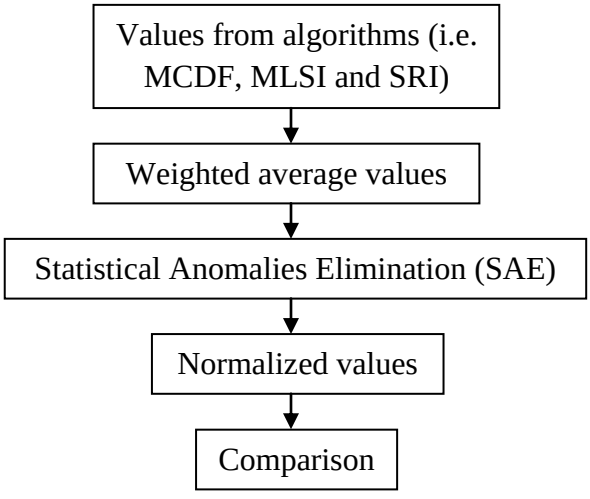

Figure 5.63. Flow chart for the procedures applied to the algorithms prior to comparison

5.5.5.1 Flexural damage at mid-span

The normalised weighted average values after performing the SAE procedure for each algorithm are recorded. These values are taken at the first, second, and third damage levels respectively, and are illustrated in Figures 5.64 to 5.66. The results of the first damage level show good sensitivity for modified and developed algorithms. All the algorithms detect major peaks at the zone of the actual cracks. MCDF and SRI detect one major peak located in the zone of the actual crack, while MLSI detects two major peaks in the zone. MLSI detect five peaks to the left and right of the actual crack zone, and MCDF detects three peaks to the left and right of the zone, while SRI detects only two peaks to the left and right of the zone. All of the algorithms show a good sensitivity for locating the three cracks located at the mid-span for the second damage level. MCDF detects three peaks in the zone of the actual cracks and two peaks to the left of the zone. MLSI detects four peaks in the zone of the actual cracks and four peaks to the left and right of the zone. SRI detects three peaks at the zone of the actual cracks and two peaks to the left and right of the zone. The MLSI detects more peaks around the actual crack zone than MCDF and SRI.

At the third damage level, where there are six cracks located at a distance of between 62 cm to 166 cm from the left support, all the algorithms show very good sensitivity to detect the multiple cracks. MCDF detects six peaks at the zone of the actual cracks and two peaks to the left of the zone. MLSI detects five peaks at the zone of the actual cracks and two peaks to the left and right of the zone. SRI detects seven peaks at the zone of the actual cracks and one peak to the left of the zone. The cracks detected by SRI are the closest to the actual cracks in terms of the number of cracks inside and outside the actual crack zone.

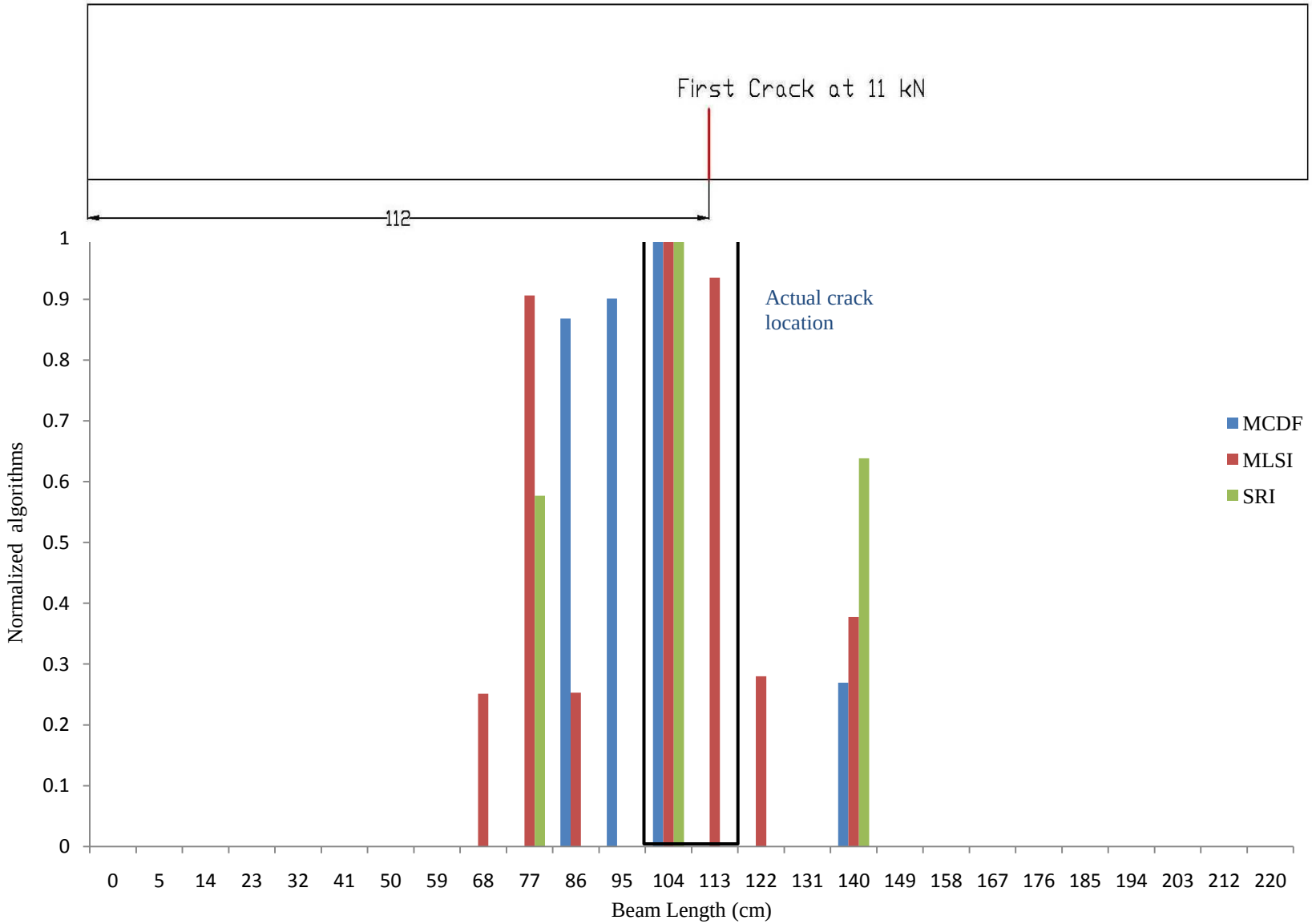

Figure 5.64. Normalised MCDF, MLSI and SRI at first damage level, $B121_m$

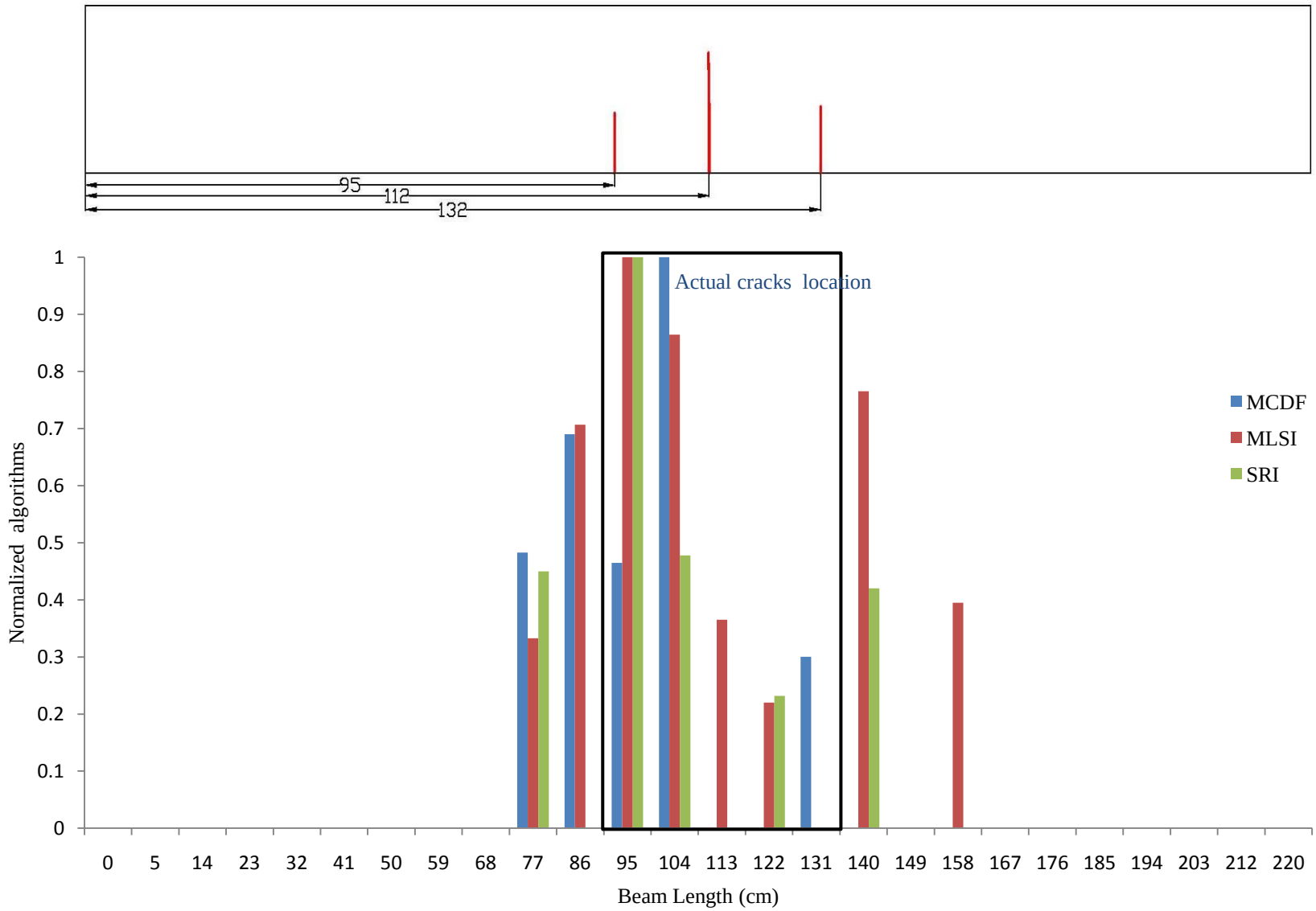

Figure 5.65. Normalised MCDF, MLSI and SRI at second damage level, $B121_m$

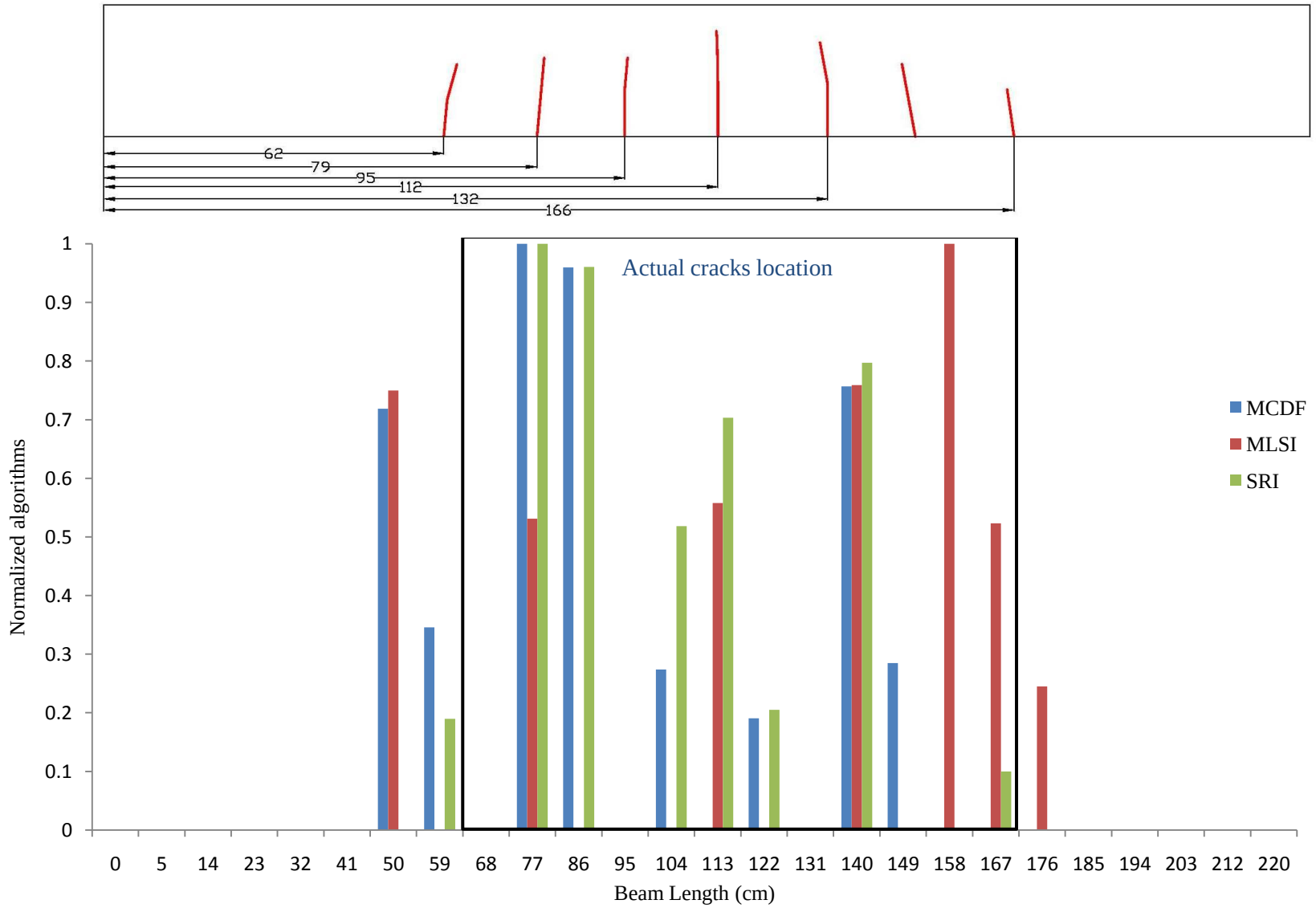

Figure 5.66. Normalised MCDF, MLSI and SRI at third damage level, $B121_m$

5.5.5.2 Shear damage at 1.5d

The ability of the modified and developed algorithms to detect single and multiple cracks for the shear damage scenario when the applied load is located at 1.5d from the left support will be assessed for $B211_d$. The actual crack pattern of beam $B211_d$ at the first and second damage levels is shown in Figures 5.39 and 5.42, respectively. The crack pattern at the third chosen damage level, when the first shear crack appears at the shear zone, is shown in Figure 5.67. For the fourth chosen damage level, when the first diagonal shear crack appears at the left support, the crack pattern is shown in Figure 5.68. Figures 5.69 to 5.72 present the normalised weighted average values after performing the SAE procedure for each algorithm for the first, second, third, and fourth chosen damage levels, where SAE procedure is used after performing the PWM averaging.

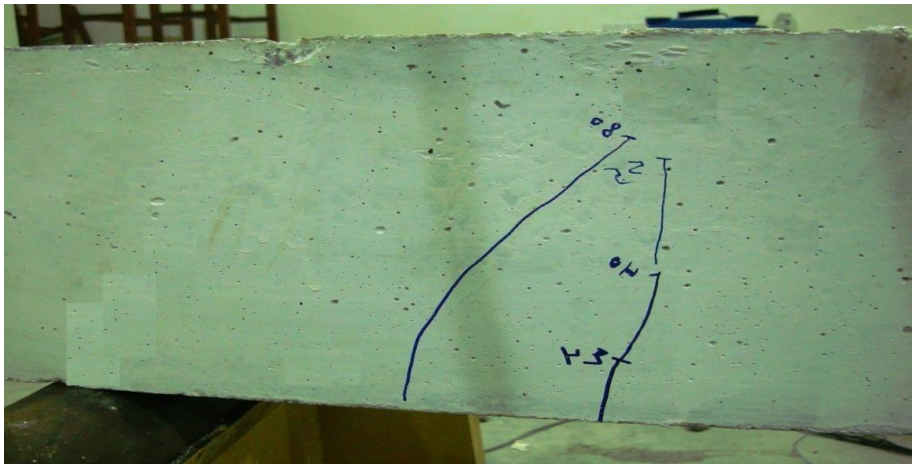

Figure 5.67. Actual cracks pattern at third chosen damage level for beam $B211_d$

The results show better sensitivity for the modified compared to the original algorithms for locating single cracks at 1.5d from the left support. MCDF detects a single peak at the zone of the actual crack and two peaks to the left and right of the zone. MLSI detects a peak in the zone of the actual crack and another peak to the right of the zone. The results show good sensitivity for the developed algorithm to detect the single crack in the shear zone,

while it detects another two peaks to the right of the actual crack zone. At the second damage level, the results show good sensitivity for the modified and developed algorithms in locating the actual crack positions. MCDF and MLSI detect seven peaks at the zone of the actual cracks and other peaks to the right of the zone. The developed SRI algorithm detects eight peaks in the zone of the actual cracks and one peak to the right of the zone. The results show good sensitivity for the modified and developed algorithms to detect the multiple cracks and the shear crack located between the support and 1.5d.

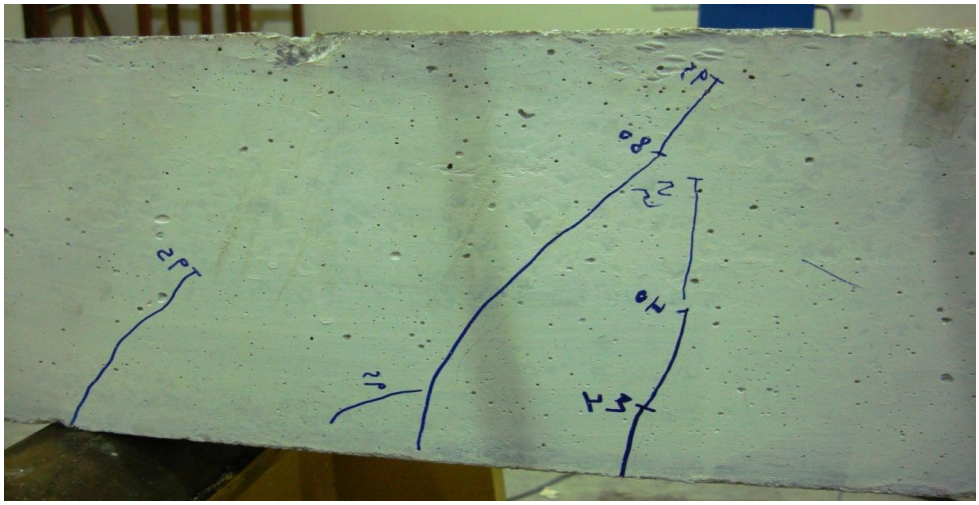

Figure 5.68. Actual cracks pattern at fourth chosen damage level for beam $B211_d$

MCDF detects nine peaks in the zone of the actual cracks including the first shear crack, and one more peak to the right of the zone. MLSI is not able to detect the first shear crack and detects eight peaks located in the zone of the actual cracks and one peak to the right of the zone. The developed SRI algorithm shows good agreement with the actual cracks pattern. The detected peaks to the left and right of the actual crack zone may be due to the presence of micro-cracks or stress concentration points in the RC beam.

The results show that modified algorithms are not able to detect the diagonal shear crack at the supports, while good agreement with the actual crack pattern for the rest of the multiple cracks is noticed. MCDF detects ten peaks including the first shear crack at the zone of the actual cracks and two peaks to the right of the zone. MLSI detects nine peaks at the zone of the actual cracks and two peaks to the left of the zone. The results show that the developed SRI algorithm detects a crack close to the left support in addition to the shear crack located between the support and 1.5d. The developed algorithm shows good sensitivity for locating multiple cracks in the shear zone. The developed algorithm detects ten peaks including first shear crack and diagonal crack in the zone of the actual cracks and one peak to the right of the zone.

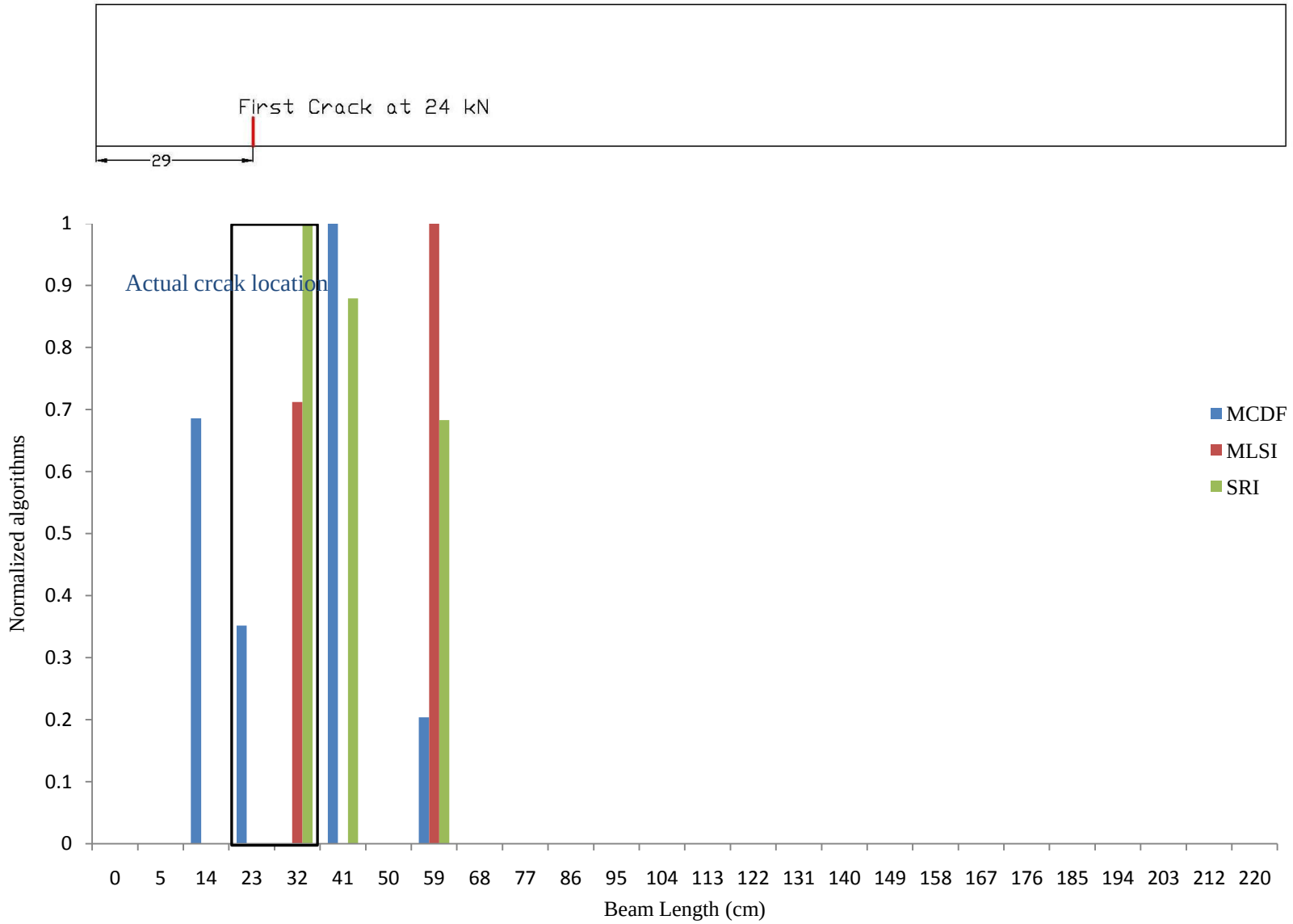

Figure 5.69. Normalised MCDF, MLSI and SRI at first damage level, $B211_d$

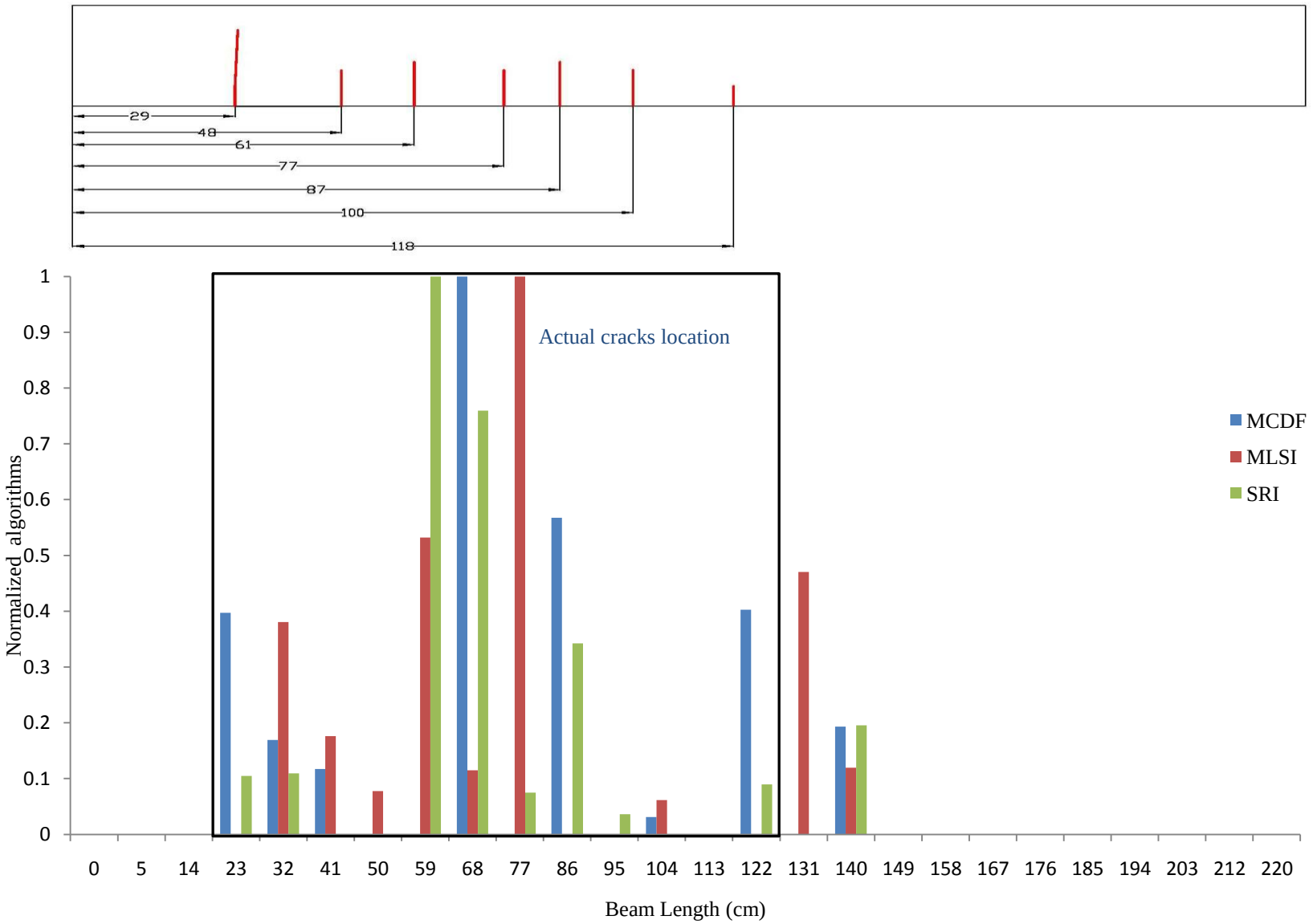

Figure 5.70. Normalised MCDF, MLSI and SRI at second damage level, $B211_d$

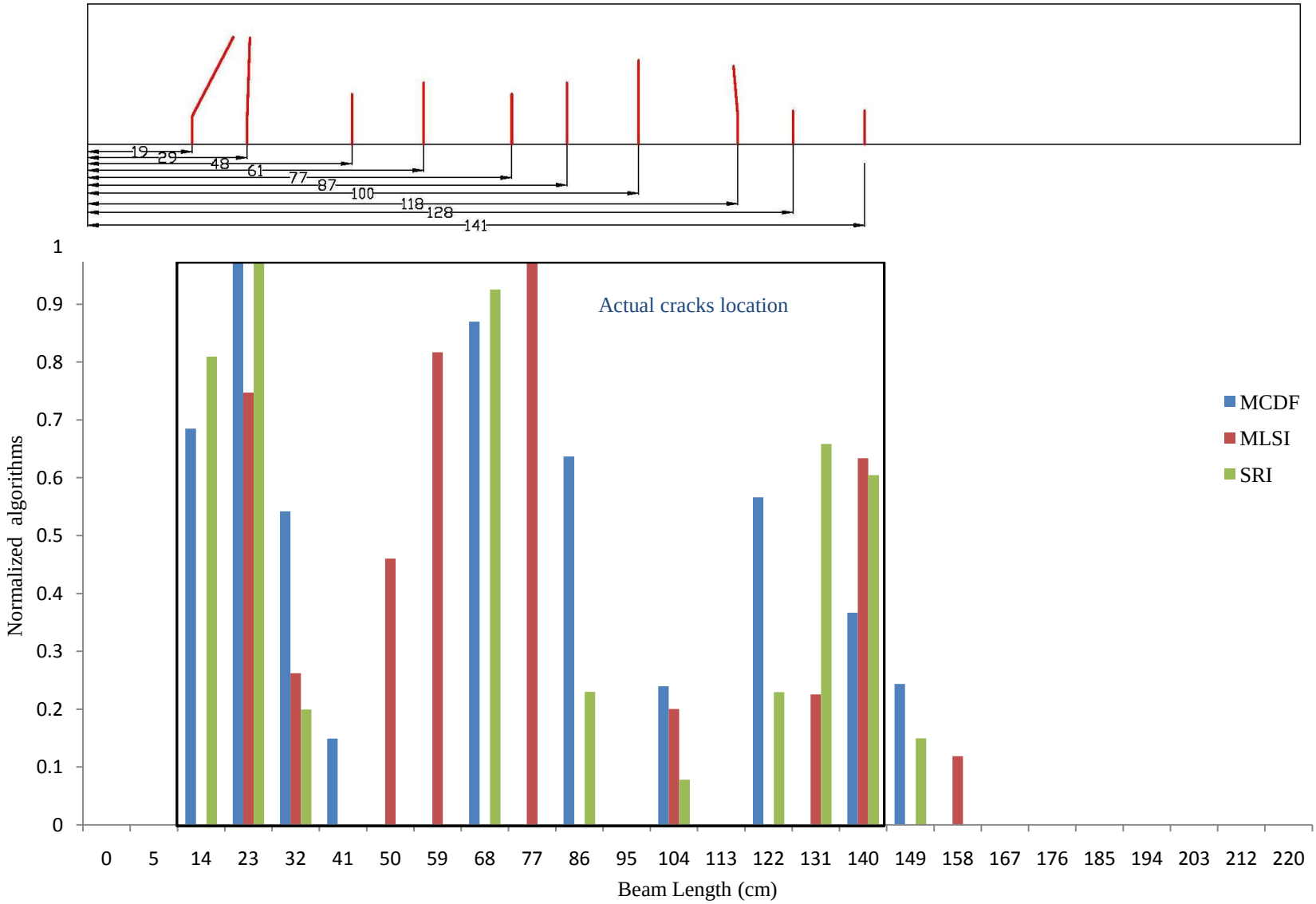

Figure 5.71. Normalised MCDF, MLSI and SRI at third chosen damage level, $B211_d$

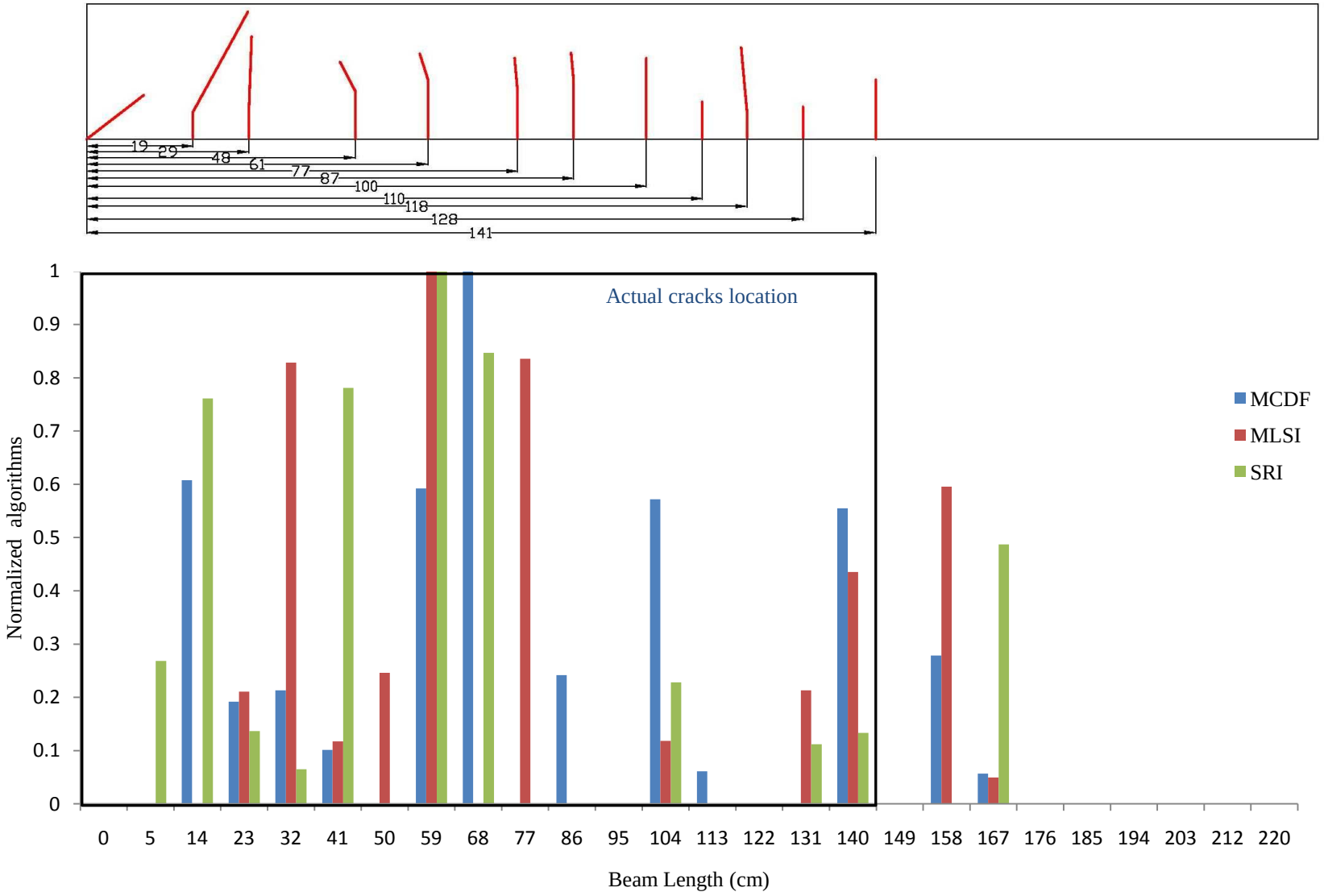

Figure 5.72. Normalised MCDF, MLSI and SRI at fourth chosen damage level, $B211_d$

5.5.5.3 Shear damage at the quarter-span

This section discusses the sensitivity of the modified and developed algorithms for locating cracks due to shear damage at the quarter-span as for beam $B211_q$. The first damage levels are when the first flexural crack appears. The second damage level is when first shear crack appears in the zone between the left support and the quarter-span and the third damage level is when the first diagonal shear crack appears at the left support. The actual crack pattern of beam $B211_q$ at the first and second damage levels is shown in Figures 5.45 and 6.48, respectively. The first diagonal shear crack appears near the left support at the third damage level as shown in Figure 5.73. Figures 5.74 to 5.76 present the normalised weighted average values after performing SAE procedure for the modified and developed algorithm at the first, second and third damage levels. The exact location of the actual cracks is also shown for the purpose of comparison.

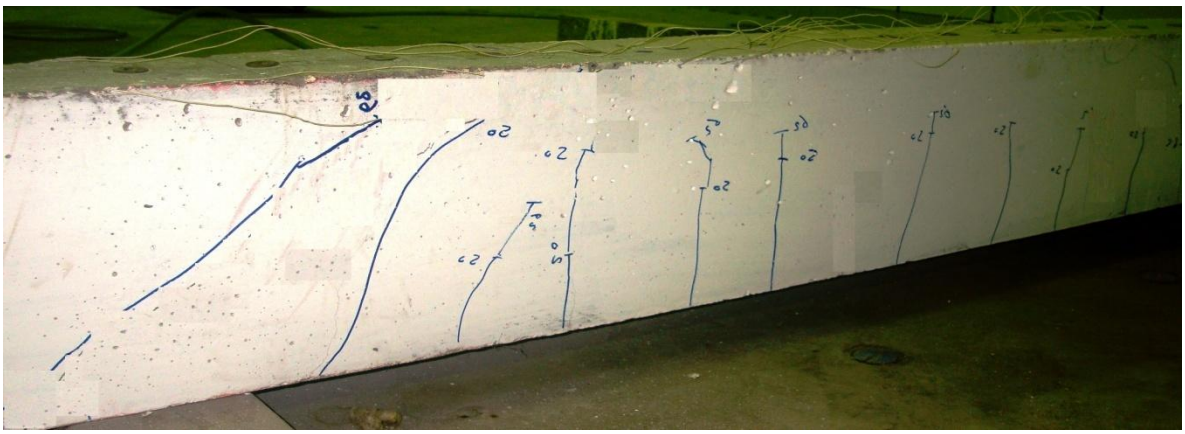

Figure 5.73. Actual crack patterns at third damage level for beam $B211_q$

The actual crack pattern at the first damage level shows a single crack 52cm from the left support. MCDF detects one major peak close to the actual crack zone and three minor peaks to the right and left of the zone. MLSI detects one minor peak in the zone of the actual crack, one major peak to the right of the zone and two minor peaks to the left of the zone. The developed SRI algorithm detects one major peak in the zone of the actual crack and two minor peaks to the left and right of the zone. MCDF and SRI are both more sensitive with regards to detecting a single crack when compared to the MLSI.

At the second damage level, there are eleven cracks in the zone which are 31cm and 161 cm from the left support. MCDF, MLSI and SRI detect seven, five and eight peaks respectively. This illustrates that the developed SRI algorithm more closely resembles the actual number of cracks. MLSI is not able to detect the first shear crack between the left support and the quarter-span, while MCDF and SRI are able to do so. All of the algorithms show poor sensitivity to detect the cracks at the mid-span and further to the right support, that is, not detecting the crack zone until 122cm from the left support while the actual crack zone is until 161 cm.

There are twelve cracks according to the actual crack pattern at the third damage level. MCDF, MLSI and SRI detect thirteen, nine, and ten cracks, respectively. This shows the MCDF as being closer to the actual number of cracks. All of the algorithms are able to detect the first diagonal shear crack, while MLSI remains unable to detect the first shear crack between the left support and the quarter-span.

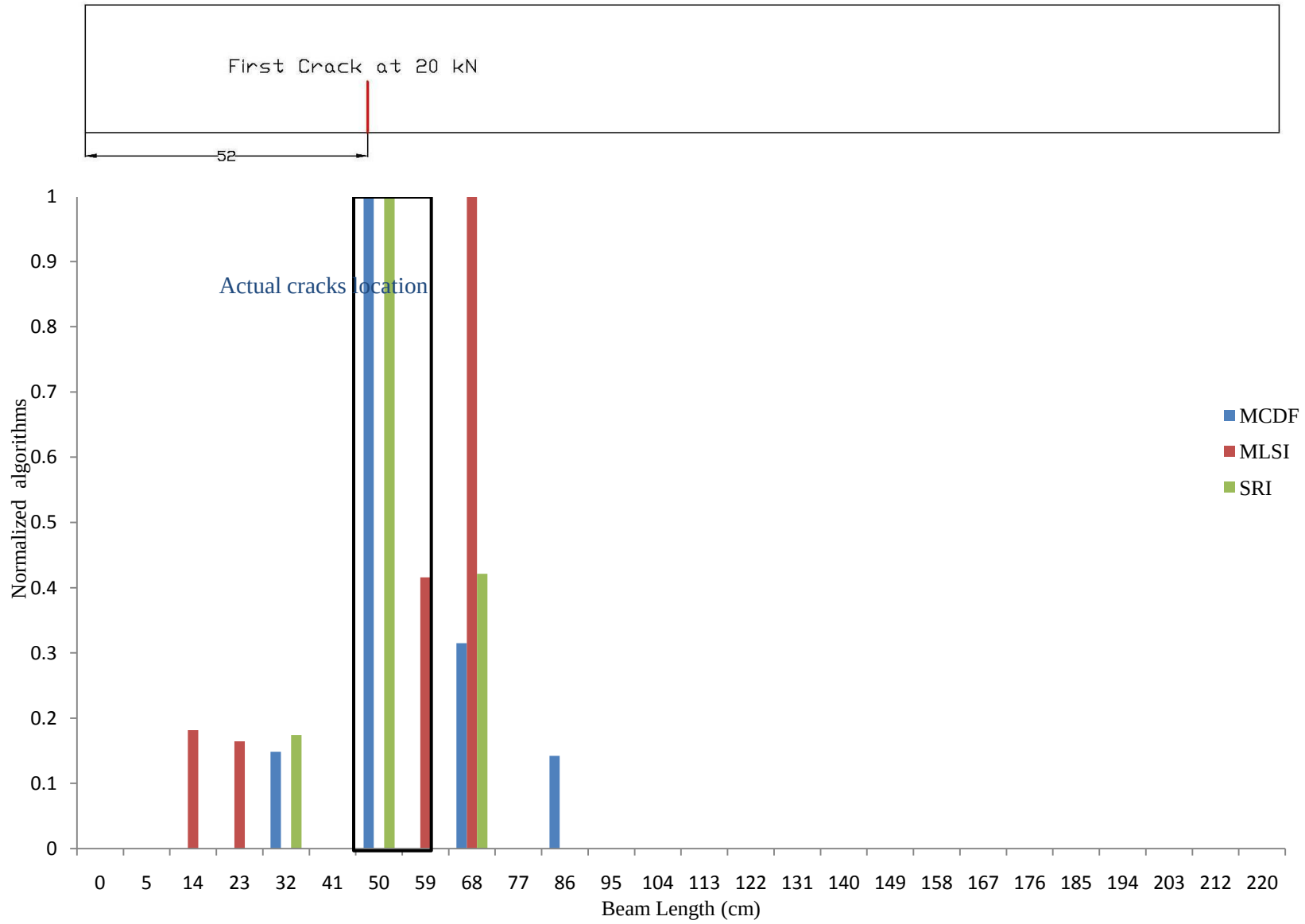

Figure 5.74. Normalised MCDF, MLSI and SRI at first damage level, $B211_q$

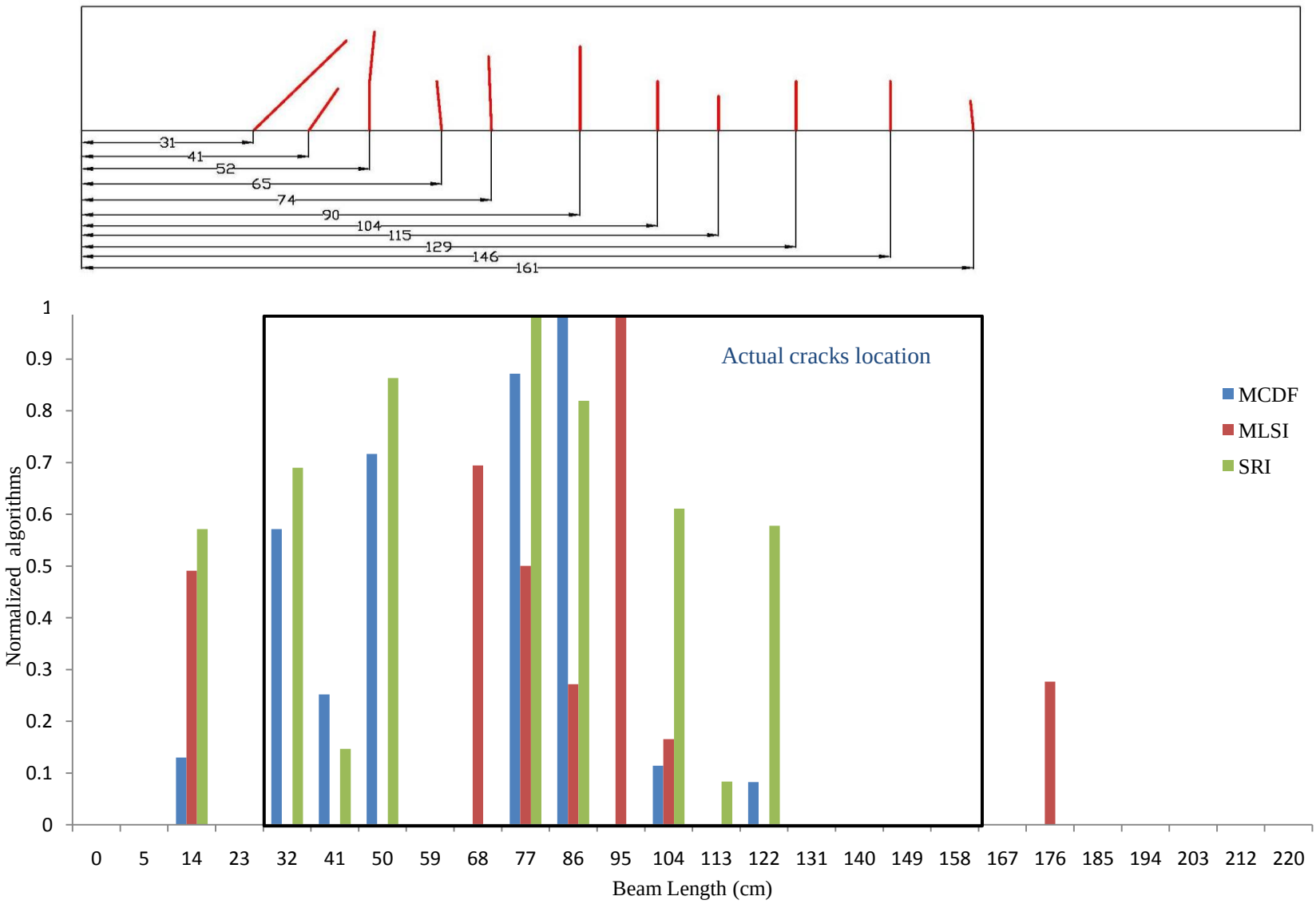

Figure 5.75. Normalised MCDF, MLSI and SRI at second damage level, $B211_q$

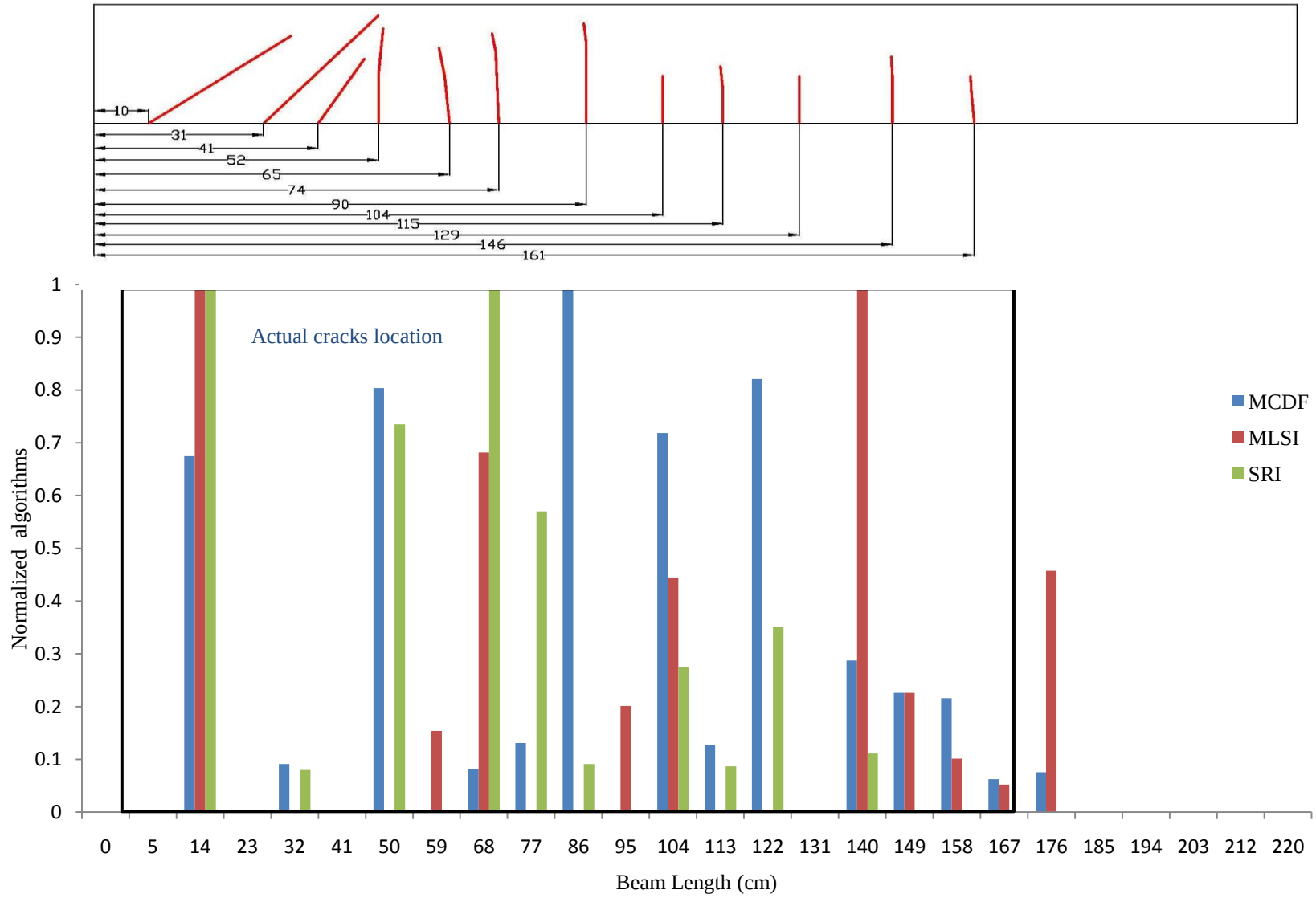

Figure 5.76. Normalised MCDF, MLSI and SRI at third damage level, $B211_q$

5.6 Summary

This chapter covers the results relating to the first three objectives of this study. In the first section, the study investigates the influence of the composite action phenomenon (CAP) in RC beams on the modal frequencies under different damage scenarios namely: flexural damage scenario includes the effect of the reinforced steel ration and shear damage scenarios at 1.5d from the support and at the quarter-span. In the second section, the study highlights the ability of damage type classification, where two beam stiffness cases are investigated; first, when there is no defect in the beam and then when there are defects in the beam. The study shows the influence of the support stiffness levels on the modal frequencies and attempts to explain the effect of the support stiffness and the RC beam stiffness deterioration on the frequency response function, the mode shapes, and the modal frequencies where the trend of each adopted mode is highlighted.

In the third section the study investigates the sensitivity of the existing and developed combined modal parameters damage severity algorithms under three damage scenarios; flexural damage; shear damage at 1.5d, and shear damage at quarter-span. Finally, the study compares the sensitivity of the developed and existing damage severity algorithms, which are based on the modal testing, to the stiffness change indicators based on the static data. The fourth section highlights the sensitivity of the existing, modified and developed damage location algorithms under different damage scenarios (flexural damage, shear damage at 1.5 d, and shear damage at quarter-span). The study highlights the sensitivity of each algorithm at each damage scenario at different levels, where it is first examined in order to validate its ability to detect single cracks and then multiple cracks; moreover, the algorithms are examined to highlight their ability to detect shear cracks.

Chapter 6: CFRP Repair Assessment

6.1 Introduction

This chapter presents the data related to the use of modal testing with a view to assessing the effectiveness of the Carbon Fibre Reinforced Polymer CFRP sheet used in flexural and shear repair systems. The results are compared and verified using data obtained from static load test. In addition, the evaluation of the ACI Code for the flexural and shear design of the RC beam with CFRP repair system is also presented in this chapter.

6.2 Flexural repair system

This section focuses on the use of the CFRP sheets as a flexural repair system. For any RC beam designed in flexure, the reinforcement must be within specific limits (ACI 318, 2008), where the minimum reinforcement limit (ρ_{min}) is provided to avoid cracking due to thermal expansion and shrinkage. The maximum steel limit (ρ_{max}) is provided to prevent brittle failure due to concrete crushing. This study takes into consideration the two steel ratio limits in order to understand the effectiveness of the CFRP sheets repair system within the range of the two limits where the structures in reality, are designed within these limits.

6.2.1 Minimum steel limit (ρ_{min})

This section presents the results related to the use of the CFRP sheet as a flexural repair system when the reinforced beams are designed with the minimum steel limit (ρ_{min}). The effectiveness of the CFRP sheets as flexure repair system are investigated under the effect of pre-repair damage level, where three damage levels are considered namely

design load, steel yield load and failure load. This section covers the static evaluation, dynamic evaluation, and the monitoring of the repaired beam to investigate its behaviour during its subsequent service life. The beams with minimum steel are designated as B122m, B123m and B124m.

6.2.1.1 Static evaluation

The static data obtained from the static load test of the RC beams at the pre-repair stages and the post-repair stages are presented. The static data includes load against deflection curves, load against steel strain curves and load against CFRP strain curves. The crack patterns corresponding to each loading cycle are plotted and appended. This section presents the results for beams B122m, B123m and B124m, which are designed using ρ_{min}, where two 12mm diameter steel bars are used in the flexural zone. The beams are then repaired using CFRP sheets according to the repair procedure mentioned in Section 4.2.5. The repair is in accordance with Code ACI 420.2R (2002) and as mentioned in Section 4.3.1.2, a 100mm width CFRP sheet is used for all the three beams.

6.2.1.1.1 Beam B121m

Beam B121m is damaged under 25 kN concentrated load at mid-span which is considered the design limit. After the repair, load is applied in cycles, where the load cycles and the corresponding number of cracks are shown in Table 6.1. The load against deflection curves at pre and post repair stages are shown in Figure 6.1. The flexural steel strain is monitored by fixing a strain gauge on the steel bars at mid-span, and the data obtained at pre and post repair stages are shown in Figure 6.2. For post-repair stages, the CFRP strain is monitored by fixing a strain gauge on the CFRP surface at mid-span and the data obtained corresponding to each load cycle are shown in Figure 6.3. The crack patterns are plotted out for each load cycle and are shown in Appendix B.

Table 6.1. Load cycles and corresponding number of cracks for beam B122m

Load Cycles (kN)	Number of Cracks	Remark
25	7	Pre-repair stage
25	7	Post-repair stage
55	12	
70	20	
85	21	
100	26	
115	28	Steel Yielded
131	28	CFRP debonded
71	28	Failure

The results in Figures 6.1 to 6.3 show that the repaired beam reaches a load capacity of 131 kN and the corresponding CFRP debonding strain reaches 6150 μst. Beyond the CFRP debonding point, steel strain shows a rapid decrease corresponding to the rapid decrease in applied load and the rapid increase in deflection. The beam records a steel strain of 4300 μst, which is less than the rupture strain of steel, that is, beyond 6000 μst. This indicates that the steel did not rupture and was the reason behind the ability of the beam to withstand a load of up to 71 kN after the CFRP debonding. This is considered the capacity of the unrepaired section, wherein most of the tension stresses are taken up by the CFRP sheets at the stage before the CFRP debonding. After CFRP debonds the failure mode is flexural failure which means that the concrete did not fail and all the stresses are taken up by the un-ruptured steel. The increase in capacity due to adding of the CFRP sheet is evaluated based on the repaired capacity (131 kN) divided by the unrepaired capacity (71 kN) which gives an increase of 184.5%.

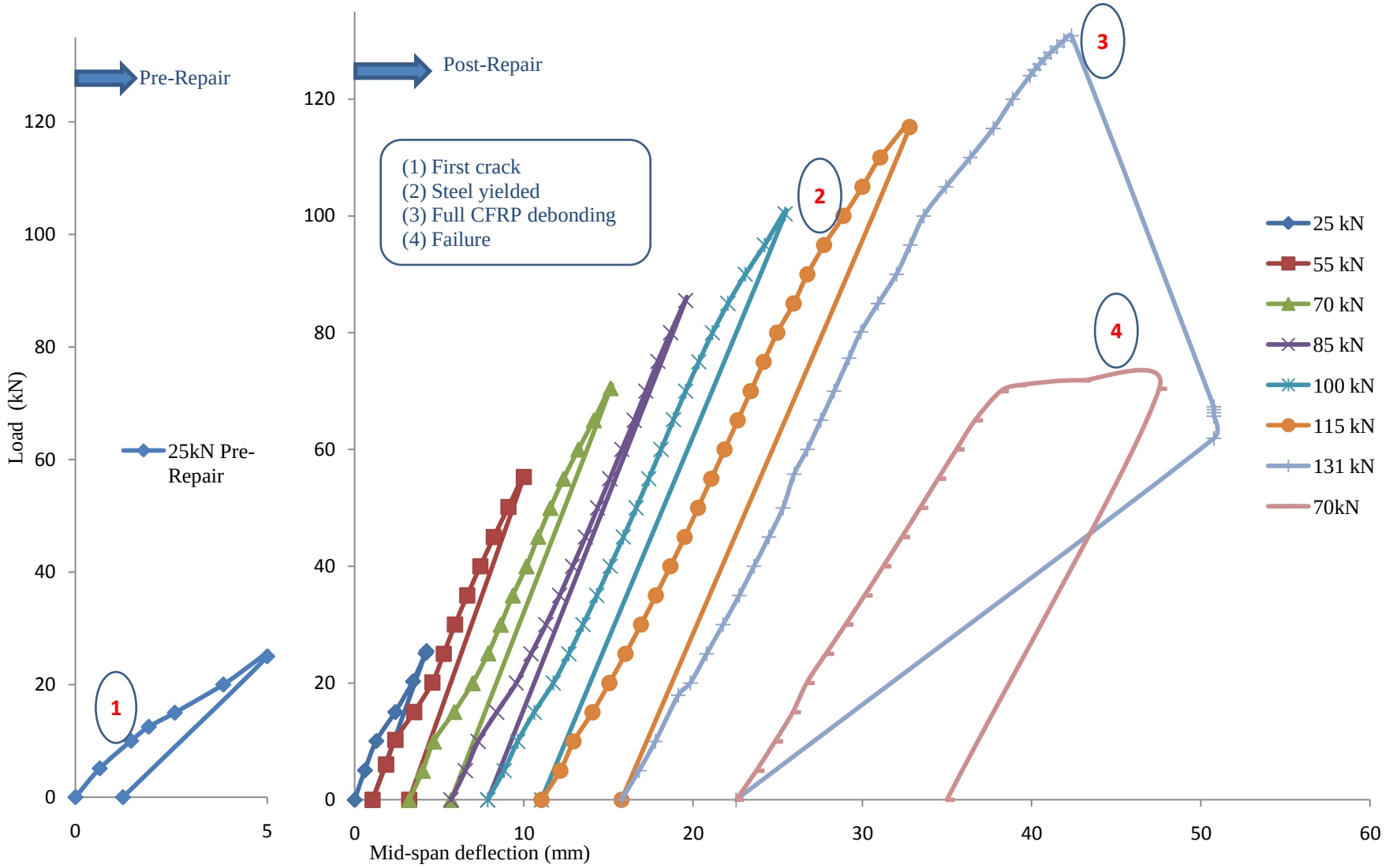

Figure 6.1. Load against mid-span deflection at pre and post repair stages for beam B122m

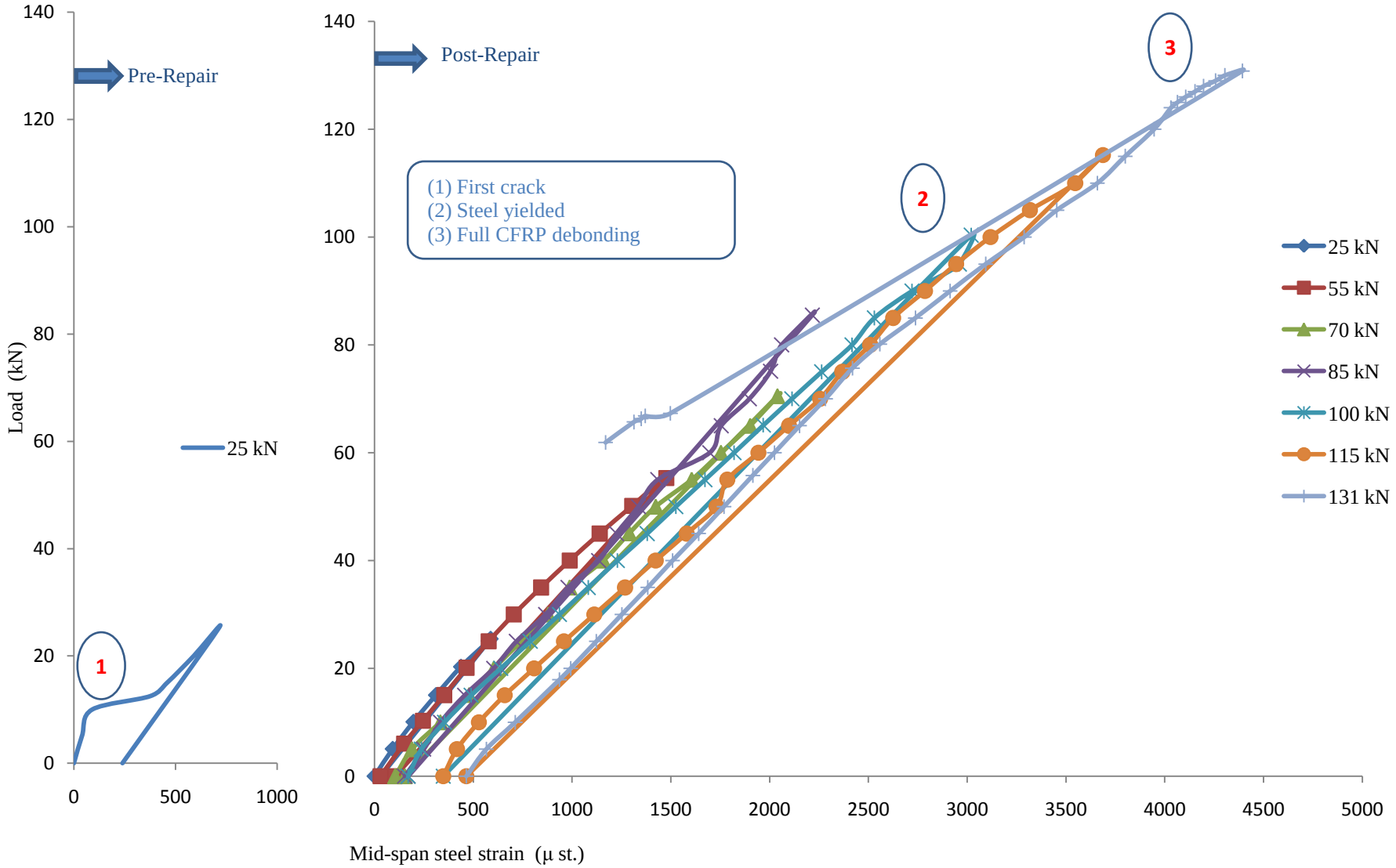

Figure 6.2. Load against mid-span steel strain at pre and post repair stages for beam B122m

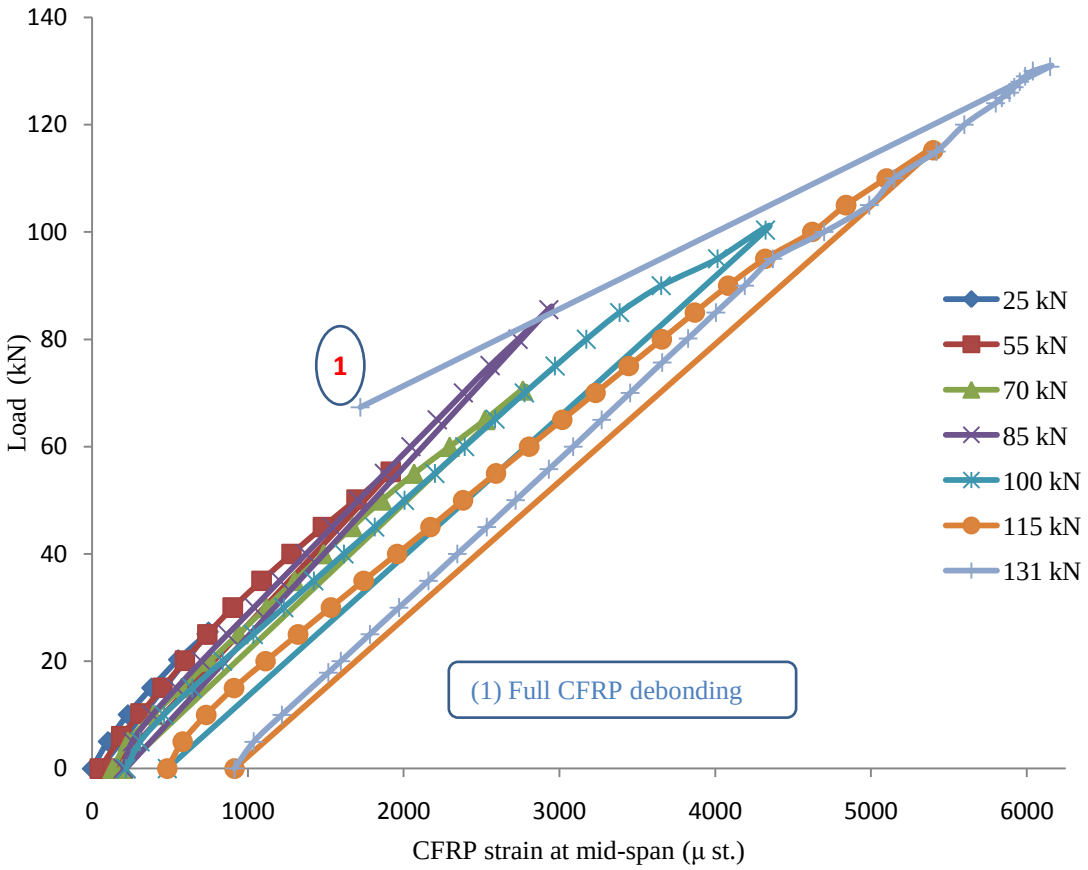

Figure 6.3. Load against mid-span CFRP strain at post-repair stages for beam B122m

6.2.1.1.2 Beam B123m

The reinforced beam B123m is damaged under 55 kN concentrated loading at mid-span which is considered close to the yield limit of the steel reinforcement. After inducing damage, the beam is repaired and the load is applied in cycles, where the load cycles and the corresponding number of cracks are shown in Table 6.2. The load against deflection curves at pre and post repair stages are shown in Figure 6.4. The load against steel strain curves at pre and post repair stages are shown in Figure 6.5. For post-repair stage, the curves of load vs. CFRP strain are shown in Figure 6.6. The crack patterns are plotted out for each load cycle and are illustrated in Appendix B.

Table 6.2. Load cycles and corresponding number of cracks for beam B123m

Load Cycles (kN)	Number of cracks	Remark
55	11	Pre-repair stage
25	11	Post-repair stage
55	16	
70	19	
85	20	
100	24	
115	25	
130	26	Maximum capacity/CFRP start debonding
122	27	CFRP fully debond
80	27	Failure

The results show that the maximum load capacity reached is 130.7 kN after which the initial debonding begins to occur. For the following load cycle, full debonding occurs at 122 kN corresponding to a CFRP strain of 5300 μst. Beyond the CFRP full debonding, there is a rapid increase in the deflection corresponding to a rapid decrease in the applied load. Similarly the steel strain shows a rapid decrease beyond the full debonding of CFRP corresponding to a rapid decrease in the applied load. The steel reaches a strain of 4700 μst. which is still below the rupture strain. This is the reason behind the ability of the beam to withstand loads of up to 84.8 kN beyond the full debonding of the CFRP sheets, where the failure mode is flexural failure without concrete crushing. This ability is due to the action of the unruptured steel where it carries all the tension stresses up to rupture beyond 7000 μst, and this load is the capacity of the unrepaired section. The increase in the load capacity by fixing the CFRP sheets as computed before is 154.1%.

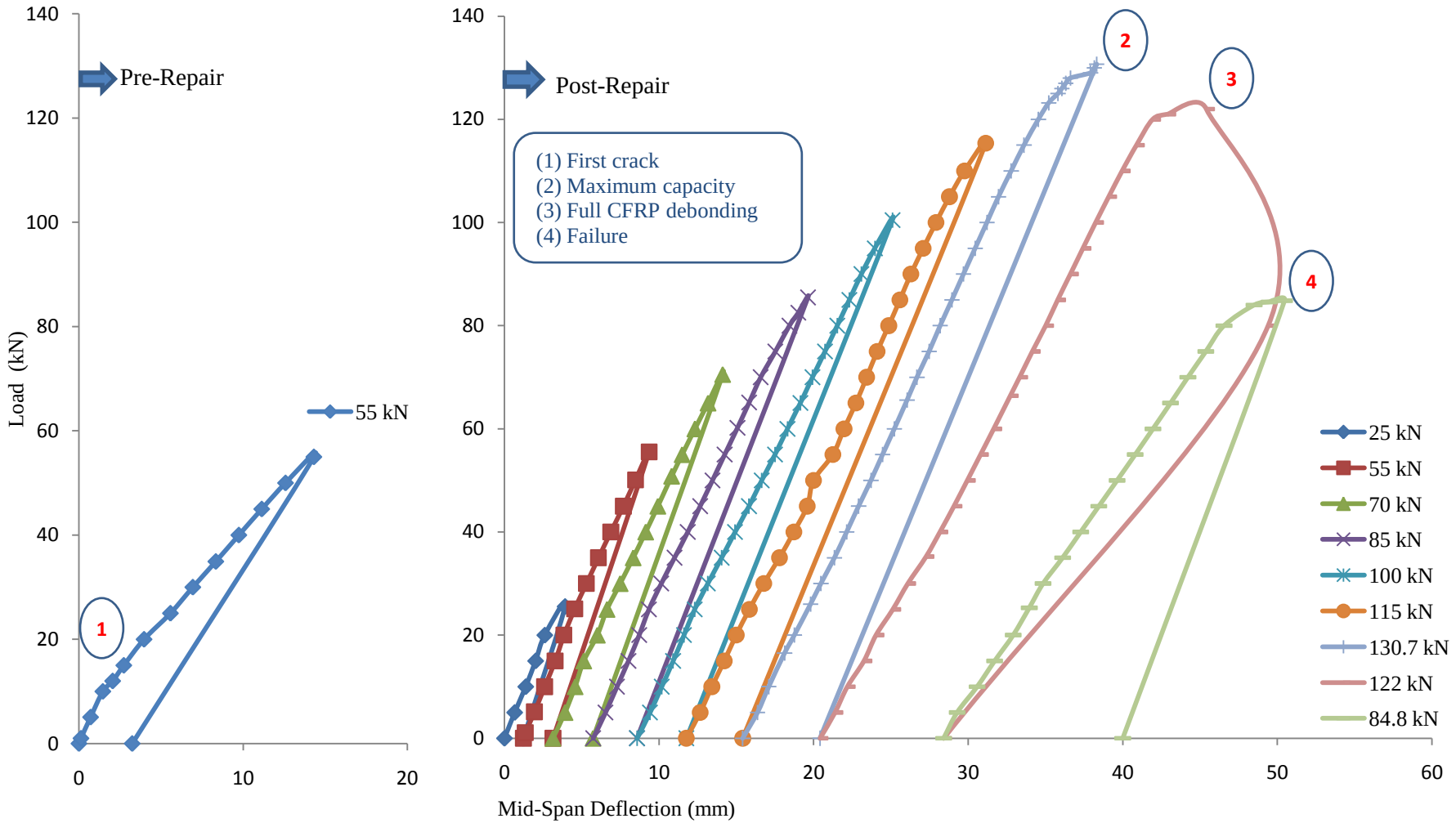

Figure 6.4. Load against mid-span deflection at pre and post repair stages for beam B123m

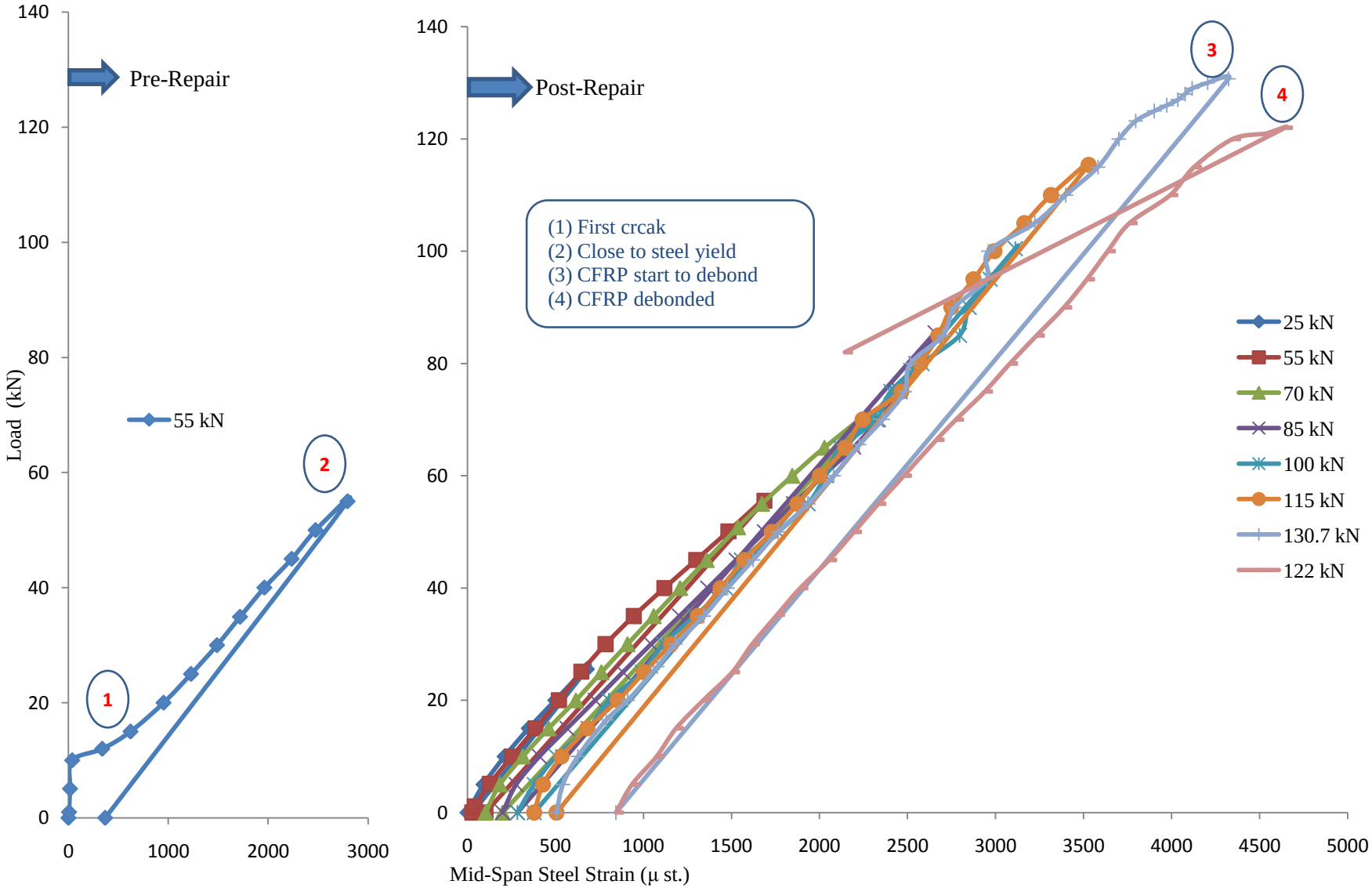

Figure 6.5. Load against mid-span steel strain at pre and post repair stages for beam B123m

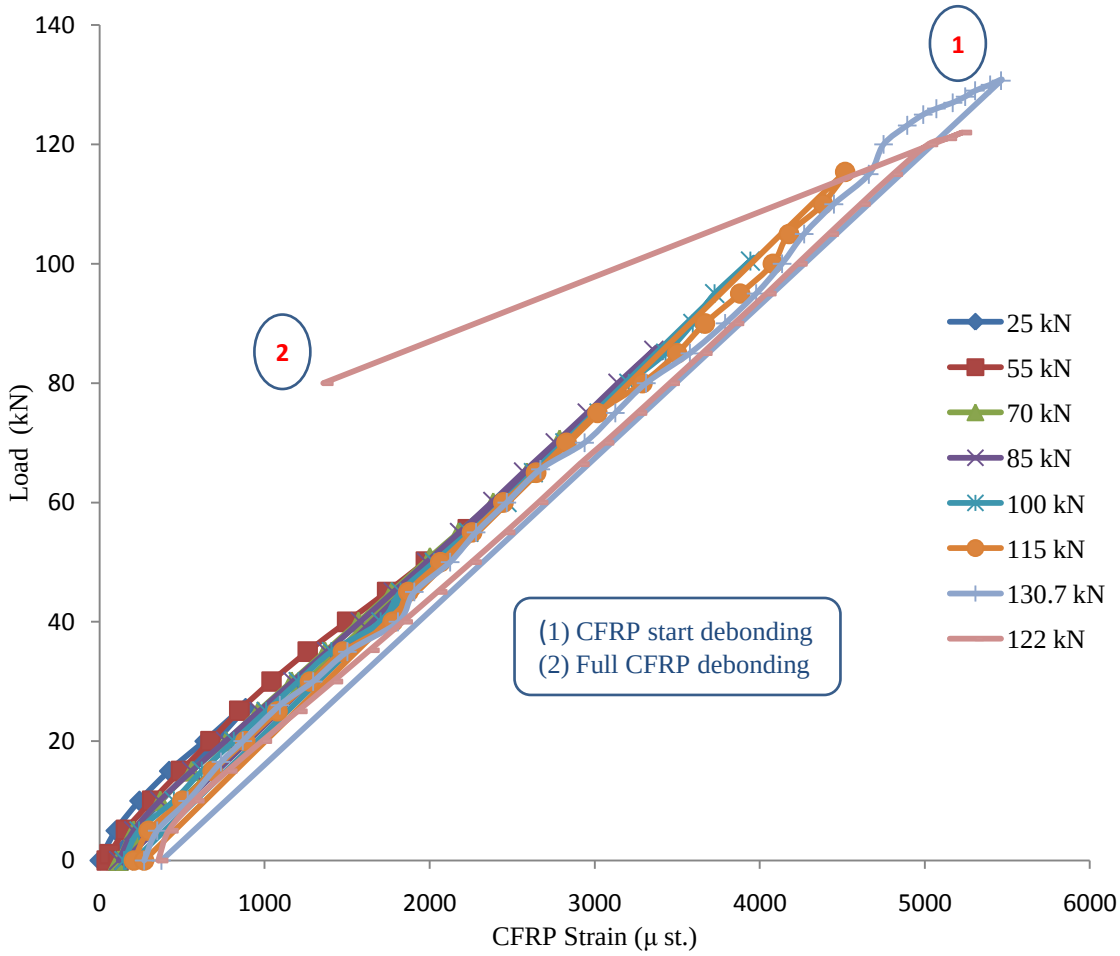

Figure 6.6. Load against mid-span CFRP strain at post-repair stage for beam B123m

6.2.1.1.3 Beam B124m

The reinforced beam B124m is damaged under failure load which reaches 85.8 kN where the steel properties are shown in Table 4.3. The applied load is stopped when the failure is initiated which is indicated by the load against the deflection curve becoming horizontal. After the induced damage, the beam is repaired and the load is applied in cycles. The load cycles and corresponding number of cracks are shown in Table 6.3. The load against deflection curves for load cycles at pre and post repair stages are shown in Figure 6.7. The curves of load against steel strain at pre-repair stage are shown in Figure 6.8. No data for the steel strain at post-repair stage is recorded since the strain gauges were broken when failure occurred at the pre-repair stage. For post-repair stages,

the load against CFRP strain is shown in Figure 6.9. The crack patterns are monitored for each load cycle and are illustrated in Appendix B.

Table 6.3. Load cycles and corresponding number of cracks for beam B124m

Load Cycles (kN)	Number of cracks	Remark
85.8	15	Pre-repair stage
25	15	Post-repair stage
55	15	
85	16	
115	17	
127.5	19	Maximum capacity/CFRP debonding begins
128	21	CFRP fully debonded

The results show that at the pre-repair stage the failure begins at 85 kN and the load against deflection curve starts to become horizontal. The steel begins to rupture when it reaches a strain of 6000 μst at 85.6 kN. Following this, at a load of 85.8 kN, the load is released and the strain gauge breaks. The CFRP begins to debond at 127 kN load, and full CFRP debonding occurs at 128 kN where the CFRP strain records 5900 μst. When full debonding occurs, there is a rapid increase in the deflection corresponding to the rapid decrease in the applied load. The increase in the load capacity due to application of the CFRP sheets is 149.2%.

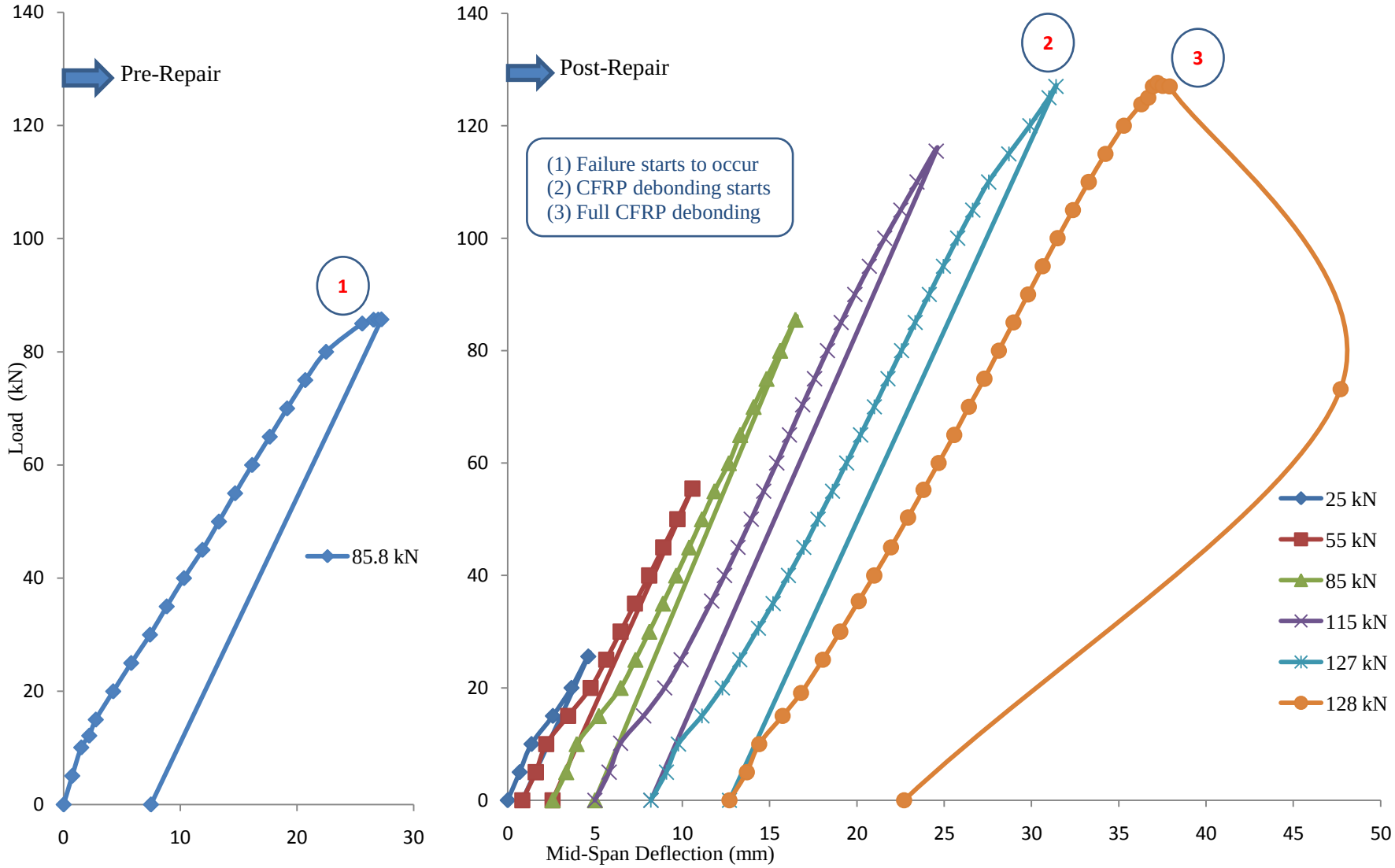

Figure 6.7. Load against mid-span deflection at pre and post repair stages for beam B124m

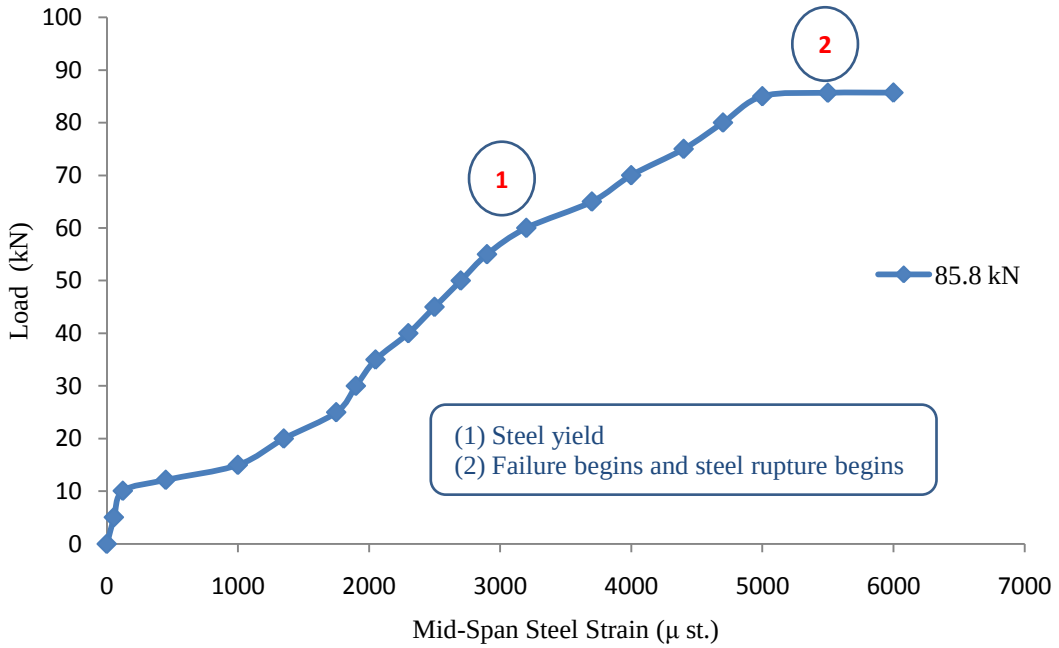

Figure 6.8. Load against mid-span steel strain at pre-repair stage for beam B124m

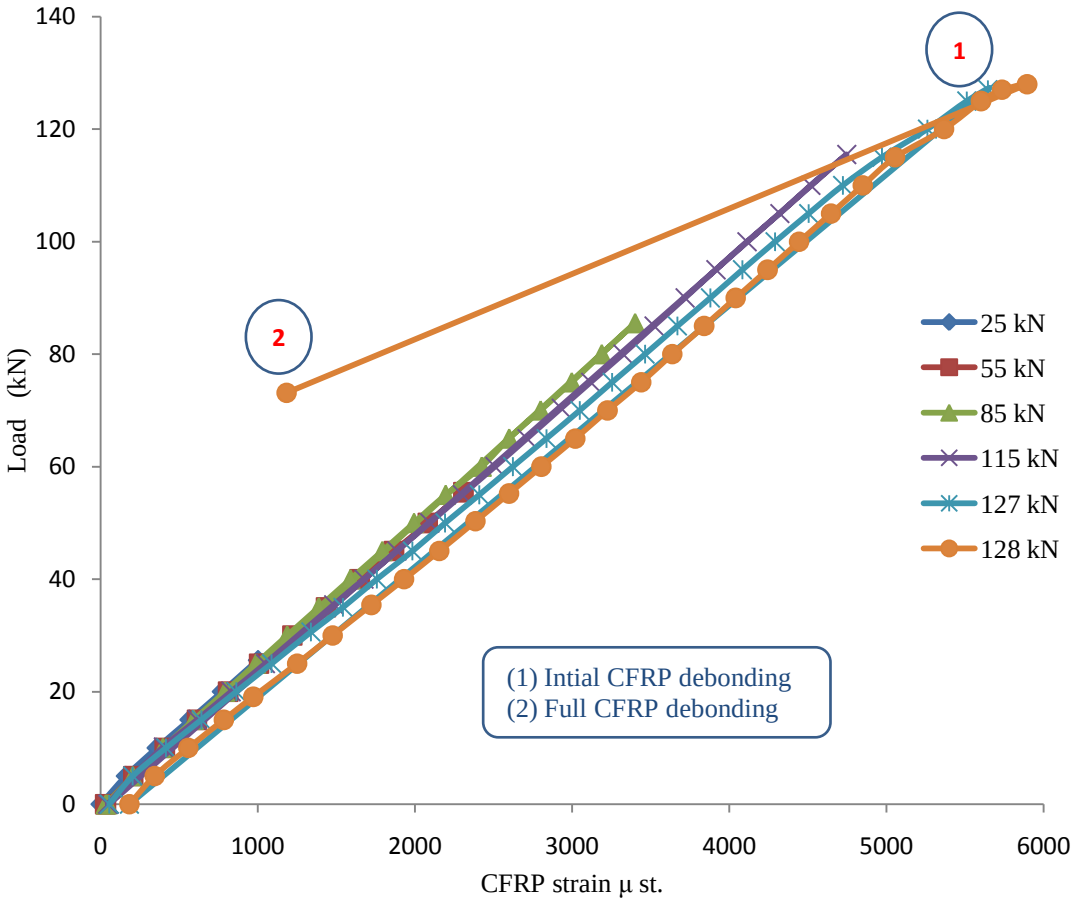

Figure 6.9. Load against mid-span CFRP strain at post-repair stage for beam B124m

6.2.1.2 Dynamic evaluation

The use of modal parameters to highlight the effectiveness of the CFRP sheet repair system is discussed herein. The change in modal parameters is influenced by the damage induced at pre-repair stage, and the recovery of the modal parameters by fixing the externally bonded CFRP sheets is monitored. In order to highlight the recovery in the modal characteristic, the frequency based stiffness index, as illustrated in Section 3.2.1, is adopted as it is able to detect the increase or decrease in the frequency. The Modal Assurance Criteria (MAC) based stiffness index is not used because it shows no indication of whether there is an increase or decrease in the mode vectors and only computes a change value. Since the combined modal parameter based stiffness index depends on the mode vectors, it is not used either. The modal damping is monitored at pre and post repair stages due to its expected high sensitivity to the fixing of high modulus CFRP sheets, where it is monitored using the percentage in damping changing as given in Equation 6.1:

$$\text{Damping Change} = \frac{Dr \text{ or } Dd - Du}{Du} .100\ \% \tag{6.1}$$

where *Dr* or *Dd* is the damping ratio at repaired or damaged state and *Du* is the damping ratio at undamaged state. The relationship between the modal damping and the stiffness is inversely proportional where decreasing the stiffness increases the damping and vice-versa. For the repair procedure, the beam is turned upside down to enable easy access to the soffit and it is turned over after repair. The turning of the beam causes a change in the deflection of the beam. Therefore the direct stiffness indicator based on the static load test data is not used as it is no longer credible.

6.2.1.2.1 Beam B122m

The frequency based stiffness index results are presented and discussed for each individual mode as well as the average values for all the modes using the Proposed Weightage Method (PWM). The dynamic evaluation results for beam B122m are presented at the stages illustrated in Table 6.4 and as shown in Figure 6.10.

Table 6.4. Stages considered for the dynamic evaluation of beam B122m

Notation	Remark
C	Undamaged stage
D	Pre-repair damaged stage
R0H	Immediately after turning the beam over after repair
R24H	24 hours after turning the beam over after repair
RD	Subjected to pre-repair damage load

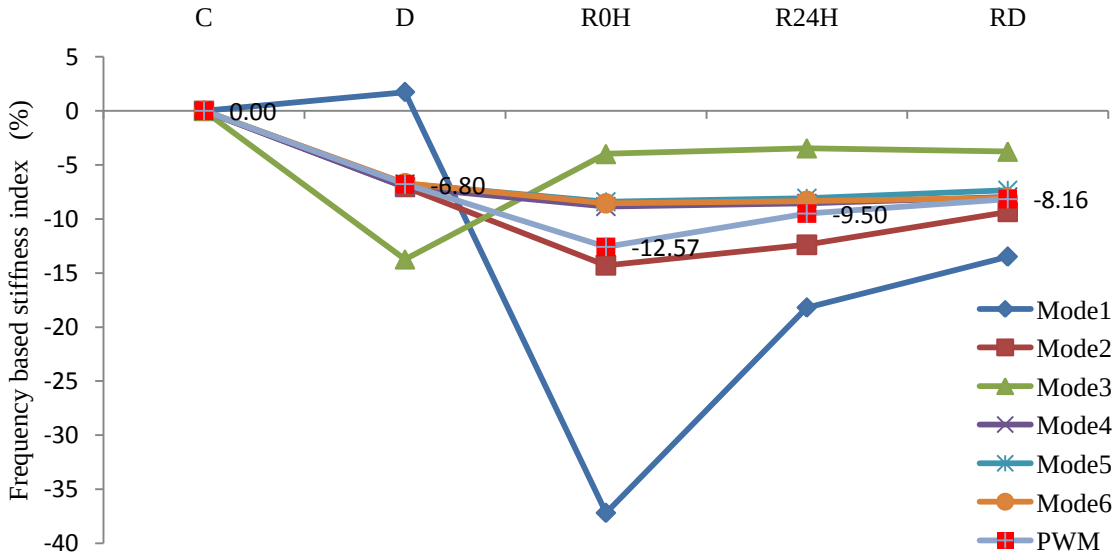

Figure 6.10. Frequency based stiffness index and weighted average results for beam B122m

The results show that different modes exhibit different trends corresponding to the aforementioned stages starting from undamaged to post-repair stages. Mode 1 shows an increase in the index value at pre-repair damaged stage, due to the composite action

phenomenon (CAP) as described in Section 3.4. The R0H stage shows a big decrease in frequency which is an abnormal trend since the addition of the CFRP sheets increases the beam stiffness and correspondingly the frequency should increase. The repaired beam is monitored after turning it over and it is noted that when the beam's self weight acts on the CFRP sheet and the effect is an increase in the index values when compared to R0H stage. Following this the repaired beam is loaded to the same pre-repair damage load and the index trend shows further increase which is abnormal and must be investigated further. Mode 2 shows a decrease at pre-repair stage which is due to the deterioration of the concrete stiffness $K_{concrete}$. At R0H stage, the second mode shows a decrease which is again an abnormal trend as it is supposed to register an increase due to the additional stiffness from the CFRP sheets. At R24H stage, the second mode shows a slight increase, when compared to R0H stage, due to the influence of the self weight of the beam. After applying a load at the RD stage, the second mode shows further increase which again is abnormal. Thus, the trend for frequency change of the second mode must be further discussed. The fourth, fifth and sixth modes shows similar trends to the second mode with a slight difference in the index values.

The third mode is the only mode which shows the expected trend, where at pre-repair stage a decrease in the index is apparent due to the deterioration of the concrete stiffness $K_{concrete}$. After the repair and at R0H stage, this mode shows an increase in the index value due to the increase in the overall stiffness from the added CFRP sheets which is to be expected. At R24H stage, a small increase in index value is noted due to the influence of the beam self weight. After applying load at the RD stage, the index value remains the same as at R24H stage.

The decrease in the index values at R0H stage, for modes 1 to 6 with the exception of Mode3 show an abnormal trend. Furthermore the increase in index values after the R0H stage and subsequently up to the stage when the pre-repair damage load is applied must

be investigated. In order to highlight the overall change in stiffness using the frequency based stiffness index and based on all considered bending modes, the weighted average using PWM procedure, as illustrated in Section 3.2.4, is performed and its results are also shown in Figure 6.10. The weighted average index trend shows a decrease at stage R0H, with an increase being noted at stage R24H when compared to stage R0H. A further increase in the weighted average index value is noted after applying a load at stage RD. The weighted average index values show that even within the increase after applying a load at stage RD, the value is still slightly less than the pre-repair damage stage which is abnormal. The phenomenon of decrease in frequency based stiffness index after fixing the CFRP sheets needs to be investigated in detail. However, considering stage R0H as the datum, the stiffness recovery indicated using the frequency based stiffness index beyond that stage (stage RD as compared to stage R0H) is equal to 4.41%.

Since the frequency based stiffness index which is based on the bending frequencies shows abnormal trends with respect to assessing the repair effectiveness, the modal damping is expected to be more influenced by the increase in the stiffness after the fixing of the CFRP sheets. The results of the damping change are shown in Figure 6.11. The results show that there is an increase in the modal damping for all the modes at pre-repair damage stage with the exception of Mode 3 which shows a decrease. This trend is observed for all the modes except for Mode 3 which is expected since modal damping is inversely proportional to the stiffness. All the modes except Mode 3 show a decrease in the modal damping at stage R0H due to the increase in the stiffness of the beam. At the R24H stage, the damping change results for all the modes show a slight increase with the exception of Mode 6 which shows a small decrease. At RD stage, the damping change values show a slight increase for all the modes except for Mode 4 which shows a decrease and for Mode 6 there is no noticeable change.

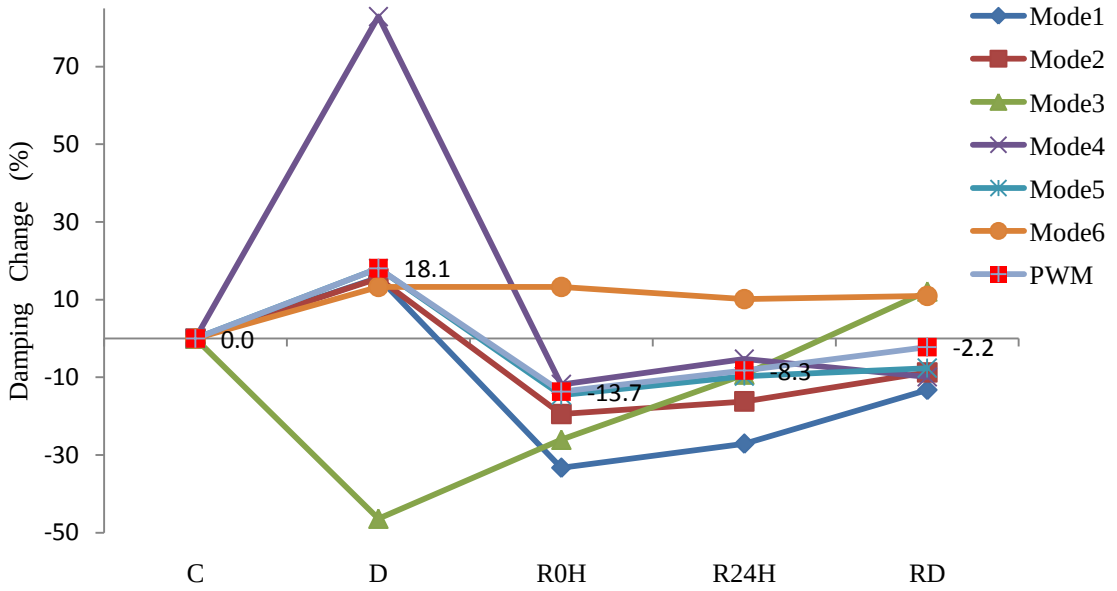

Figure 6.11. Damping change and weighted average results for beam B122m

In order to highlight the overall trend of the stiffness change using the damping change as an indirect indicator and based on all the considered modes, the weighted average using PWM procedure is performed on the damping change values and the results are also shown in Figure 6.11. The trend of the weighted average values of the damping change shows the expected increase in the modal damping, indicating stiffness deterioration due to the beam being subjected to damage load. The damping change indicates an increase of 31.7% at stage R0H when compared to stage D. This can be considered as an indicator for the amount of the stiffness recovery. At R24H stage, the damping change shows an increase of 26.3% when compared to stage D. When the beam is loaded at stage RD the damping change indicates a decrease of 11.45% when compared to stage R0H.

The modal damping exhibits the expected trend for stiffness change, as indicated by the damping change as indirect indicator, at the pre and post repair stages. This is an indicator for the effectiveness of repair with externally bonded CFRP sheets. However the unexpected trend of the bending frequencies must be explained and validated.

Previous researchers carrying out similar work have obtained results for the cases of undamaged, pre-repair damage, post-repair under self weight, and post-repair under same pre-repair damage load. All the results confirm that there is a decrease in the frequency values after the fixing of the CFRP sheets to the RC beam and show a slight increase when the same pre-repair damage load is applied [Capozucca and Cerri (2002); Bonfiglioli and Pascale (2006); Baghiee et al. (2009) and Capozucca (2009)].

Baghiee et al. (2009) explained the decrease in natural frequencies due to the effect of the environmental conditions such as the ambient temperature on the material properties. In this present study all these environmental conditions are eliminated by testing the samples after one year of their casting date, which avoids the aging effect on the material properties and subsequently on the modal parameters. Moreover, the modal testing is carried out at different temperature and humidity conditions and turns out the same, which invalidates the abnormal modal parameter trend explanation put forward by Baghiee et al. (2009). Capozucca (2009) attributed the decrease in natural frequencies to the extra mass of CFRP in the beam. The effect of the extra mass of the CFRP on the modal parameters is investigated in the present study by adding equivalent mass of the CFRP sheet and an adhesive layer to the beam. Table 6.5 shows the frequency values before and after adding extra mass equivalent to the CFRP sheet and an adhesive layer on the RC beam. The results show that there is no noticeable effect of the CFRP sheets and the adhesive layer weight on the dynamic properties due to its small weight when compared to the weight of the RC beam. The RC beam weighs 202 kg while CFRP, its adhesive, weighs 4 kg.

Meftah and Tounsi (2007) performed dynamic assessment of a shear wall repaired with externally bonded CFRP sheets in the laboratory and observed that the repair with the CFRP sheets increased the stiffness at the post-repair stage while it wa still less than the undamaged stage. The difference between the work carried out by Meftah and

Tounsi (2007) and the present study is that the earlier uses CFRP sheets for shear repair, fixed on the sides of the walls. The abnormal trend in frequency is related to the flexure behaviour of the beams.

Table 6.5. Frequency values with different mass for beam B122m

Beam Mass	Natural Frequency Hz					
	Mode 1	Mode 2	Mode 3	Mode 4	Mode 5	Mode 6
Without extra mass	220	430	777	1181	1630	2096
With extra mass	219.5	430.5	777	1179	1629	2096
Difference %	-0.22	0.11	0	-0.16	-0.07	0

Recently, in 2011, Abdessemed et al., performed dynamic assessment of the flexural repair of an actual bridge with externally bonded CFRP sheets and found that adding the CFRP sheets increased the frequencies of the bridge for all the considered bending modes. This highlights that under normal procedure for flexure repair and the fixing of the CFRP sheets, the natural frequencies of the bridge increases. The repair procedure adopted by Abdessemed et al. (2011) was different compared to the present study in that the bridge girders were not turned over while the CFRP sheets were fixed to the soffit. However as in previous studies [Capozucca and Cerri (2002), Bonfiglioli and Pascale (2006), Baghiee et al. (2009) and Capozucca (2009)], the RC beams in this study are turned over in order to facilitate and make it easier to fix the CFRP sheets and consequently the soffit is in compression under the beam's self weight.

6.2.1.2.1 A Composite action phenomenon of repaired RC beams

The composite action phenomenon of repaired RC beams with externally bonded CFRP sheets can explain the abnormal trend of bending frequencies at the post-repaired stages. The cracked surface, that is the beam soffit, is under initial compression force when the beam is turned over as shown in Figure 6.12. After fixing the CFRP sheets to the RC

surface, the adhesive layer set and hardened after which the initial compression force influences the adhesive layer, leading to growth of compression interaction force in the layer. This has a negative effect on the stiffness which in turn affects dynamic parameters. Compression interaction force is retained inside the adhesive layer during the hardening process as shown in Figure 6.13. The negative effect of compression interaction force reduces slightly when the repaired RC beam is turned over again to its original position, that is, beam soffit at the tension face. This phenomenon starts when the applied self weight influences the tension face and a tension interaction force develop at the adhesive layer between the concrete surface and CFRP sheets. Tension interaction force will try to balance or overcome the compression interaction force and this depends on the applied load and the time lapse needed for deflection recovery and creep settlement after the effect of the self weight after turning the beam over as shown in Figure 6.14. The phenomenon of compression and tension interaction forces control the behaviour of the bending frequencies, even after application of a load to the repaired beam where the load applied works to increase the tension interaction force and make it higher than the compression interaction force. This leads to increasing the bending frequencies at certain applied load, while with further application of load the overall stiffness is influenced by the deterioration in the concrete stiffness.

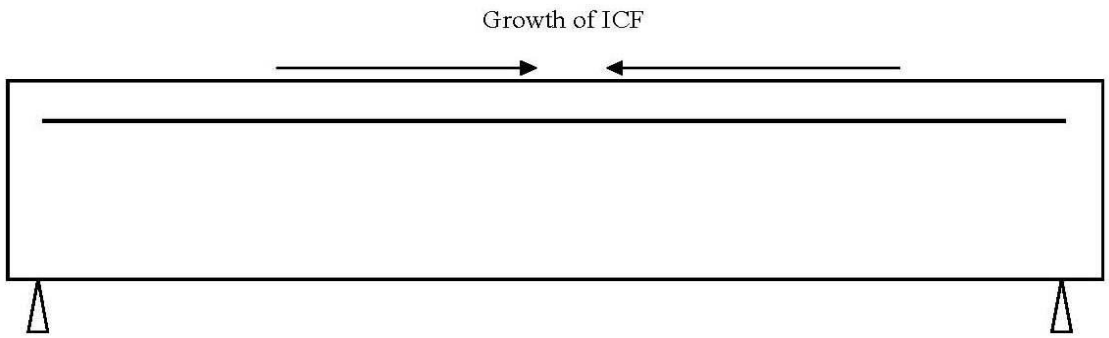

Figure 6.12. Growth of initial compression force (ICF) on the tension face of the RC beam

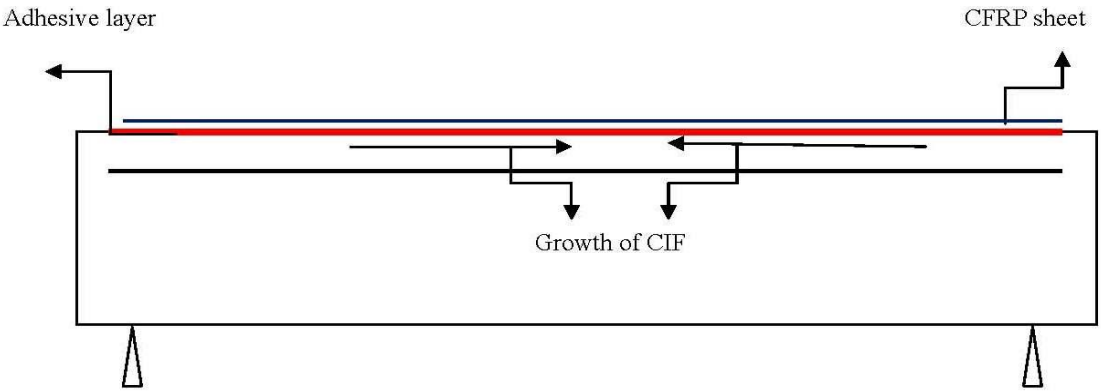

Figure 6.13. Creating of compression interaction force (CIF) inside the adhesive layer during the repair procedure

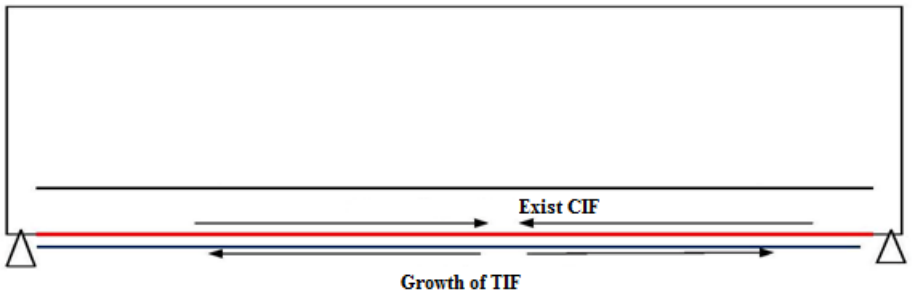

Figure 6.14. Growth of tension interaction force (TIF) influenced by beam self weight

Based on composite action phenomenon for RC beams (as mentioned in Section 3.4) and repaired RC beams, it is important to remember that if the tension zone (beam soffit) is subjected to further tension stresses under the effect of tension bond action at the interface between the steel bar and the surrounding concrete, would lead to an increase in the bond stiffness K_{bond} which in turn influences the overall stiffness even if there is deterioration of the concrete component. When the tension zone (beam soffit) is subjected to compression stresses affected by the compression interaction force which develops between the CFRP and concrete surface, it leads to a decrease in the adhesive bond stiffness which influences the overall stiffness even if there is an increase in stiffness by adding the CFRP sheets.

Composite action for the repaired RC beams influences all the bending frequencies and is used to justify the abnormal frequency trend. For the first mode, the immediate post-repair stage is influenced by the composite action of repaired RC beams as the compression interaction force builds up inside the adhesive layer. When the beam is turned over to its original position the tension interaction force is not able to balance the compression interaction force which results in a decrease in the first frequency. When the beam is left for 24 hours to give enough time for deflection recovery and creep settlement, the tension interaction force increases which leads to an increase in the adhesive bond stiffness, which then increases the first frequency. Applying load to the beam equal to the pre-repair damage load leads to a further increase in the tension interaction force which influences the adhesive bond stiffness and as a result increases the first frequency. The same explanation can be drawn for the second mode with difference in the absolute value of the stiffness recovery at R24H and RD stages. The same explanation applies to Modes 4 to 6, however these are less affected by the compression interaction force and are even less affected by the tension interaction force. The composite action of repaired RC beams can be avoided by repairing damaged beams without turning them over which prevents the growth of initial compression force and also avoids the growth of the compression interaction force. This is the case in the application of the CFRP repair system in real structures, with normal repair procedure.

6.2.1.2.1 B Validation of composite action phenomenon

In order to validate the influence of composite action phenomenon for repaired beams on the modal frequencies in CFRP repair beams, the normal repair procedure is conducted on a laboratory sample. According to Abdessemed et al. (2011), the normal repair procedure gave good assessment for the CFRP repair system. Beam (VB) is used to monitor the modal frequencies influenced by the repair with CFRP sheets, where it

has the same dimensions and properties as beam B122m and is subjected to the first crack load (10 kN) at the pre-repair stage. The beam is repaired with 100mm width CFRP sheet and is fixed accordingly without turning the beam over as shown in Figure 6.15. The modal frequencies are acquired and the frequency based stiffness index values are as shown in Figure 6.16, for the stages namely undamaged (C), pre-repair damaged (D), post-repair under self weight (R) and post repair- after being subjected to pre-repair damage load(RD).

Figure 6.15. Repair with CFRP sheet according to RRP for beam VB

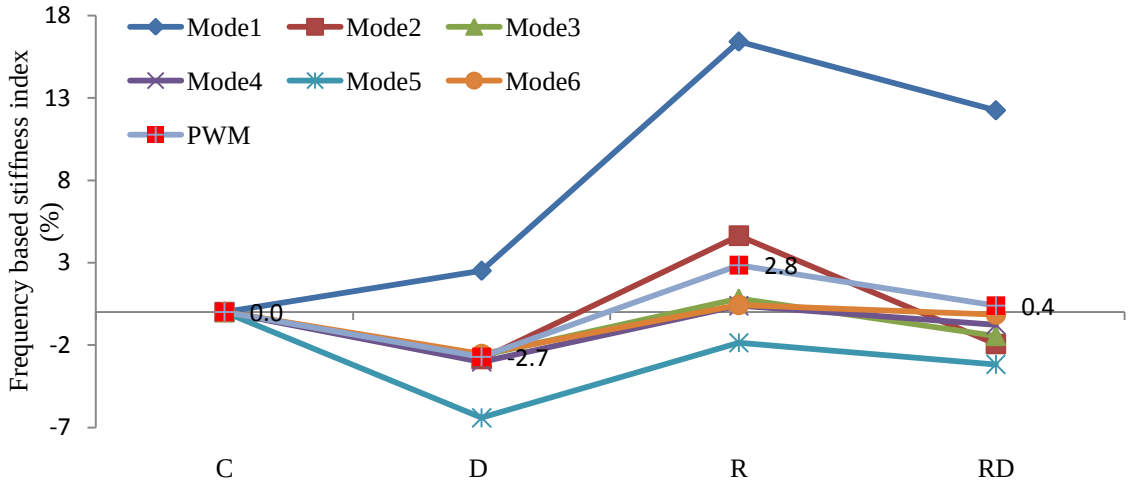

Figure 6.16. Frequency based stiffness index and weighted average (PWM) results for beam VB

The results prove that the influence of the composite action of repaired RC beams on the modal frequencies can be avoided by repairing the beams without turning them over. At the pre-repair stage, Mode 1 shows an increase affected by the composite action of RC beams (CAP) while Modes 2 to 6 show a decrease affected by the concrete softening. When the beam is repaired and after 18 days, all considered modes show an increase in the index values indicating an increase in the overall stiffness by adding the CFRP sheet. This validates the effectiveness of the repair with the CFRP sheets by indicating an increase in stiffness. However, when the repaired beam is subjected to a load at stage RD, all the modes show a decrease in the index values indicating a deterioration in the overall stiffness. Thus repair procedure without turning the beam over creates full activation of the adhesive bond under the beam's self weight. Since different modes show different stiffness change values, and in order to highlight the overall stiffness deterioration and recovery at pre and post repair stages, the weighted averaging according to PWM is calculated and the results are also shown in Figure 6.16. The results show that the overall stiffness suffered a deterioration of approximately 2.7% at pre-repair damage stage. Following this, the stiffness shows a recovery of 5.6% at stage R when compared to stage D. When the repaired beam is subjected to a load at RD stage, the index decreases due the overall stiffness deterioration.

The results show that fixing the CFRP sheets to damaged RC beams according to laboratory repairing procedure, means that it is influenced by the composite action phenomenon of repaired RC beams. On the other hand, fixing the CFRP according to the normal repair procedure avoids the effect of the composite action phenomenon of repaired RC beams on the modal frequencies. The assessment of repair effectiveness for the normal repair procedure is notable from the trend of all the modes by comparing post-repair stage (R) to pre-repair damaged stage (D), where the adhesive bond is fully effective under the beam self weight highlighting a stiffness recovery of around 5.6%.

The assessment of repair effectiveness for the laboratory repair procedure is not indicated from the modes trend by comparing post-repair stage to pre-repair stage. In order to assess the effectiveness it needs to compare post-repair damage stage when the beam is subjected to a load equal to the same as pre-repair damage load which equal to the design load limit, immediately after turning the beam over to its original position. This highlighted a stiffness recovery of about 4.4 %. Calculated stiffness recovery of laboratory repair procedure is an indicator of the actual stiffness recovered as it depends on the induced tension interaction force and existing compression interaction force. This is dependent on the adhesive properties, CFRP width, and loading rates at pre and post-repair stages.

At this point it is important to highlight that in the present study all of the flexural beams are tested and repaired in accordance with the laboratory repair procedure, as this is expected to give the normal trend for the modal frequencies. In addition, when there is an abnormal trend for the bending frequencies, beam VB is cast and repaired in accordance with normal repair procedure in order to validate the influence of the composite action phenomenon of repaired RC beams. Thus, all of the assessed flexural beams are used in the same way to gage the effectiveness of CFRP sheets for beam B122m, since it is not possible to revise the repair procedure.

6.2.1.2.1 C Adhesive setting time

The repair of the beam VB according to the normal repair procedure presents the opportunity to monitor the setting time of the adhesive material and to compare it with the suggested time given by the manufacture. In general, the strength and the load carrying capacity of repaired RC structures with CFRP sheets depends on the properties of the adhesive interface layer. Moreover, the modal parameters which are used for the

assessment of the CFRP repair system are affected by the properties and behaviour of the adhesive interface between CFRP sheets and the RC structure. Adhesive material requires time to set in order to achieve the maximum design capacity. Most producers of the adhesive material provide technical data on the increase of the capacity with time up to the maximum capacity. The proposed setting time given by the adhesive material producers is based on the static tests performed on the adhesive material and its properties such as adhesive compressive strength, tensile and shear stresses against the setting time. Since the modal parameters are more sensitive than the static properties, this study highlights the effect of the setting time on the modal frequencies and compares the setting time given by the manufacture. Figure 6.17 shows the compressive strength against, shear stress and tensile stress versus setting time provided by the producer of the adhesive material. The results show that all the strength properties reach their maximum values after 7 days, hence the proposed 7 days maturation age of the adhesive material.

Figure 6.18 presents the frequency based stiffness index values of the beam VB for different times, that is, from 12 hours to 18 days, for the considered bending modes and indicates the maximum time for the adhesive strength to be fully developed. The results show that all the modes are influenced by the setting of the adhesive material, and Mode 1 is the most affected while Mode 6 is the least affected.

The first mode shows a gradual increase in the index values until they reach a value of approximately 6% after 15 days and remain constant for 18 days. Modes 3, 5 and 6 indicate that 15 days is the maximum setting time, while Modes 2 and 4 indicate 11 days instead. The weighted average results according to PWM are also highlighted in Figure 6.18, and are based on the overall stiffness change. Using weighted average, 15 days is considered as the maturation age of the adhesive material based on the dynamic parameters.

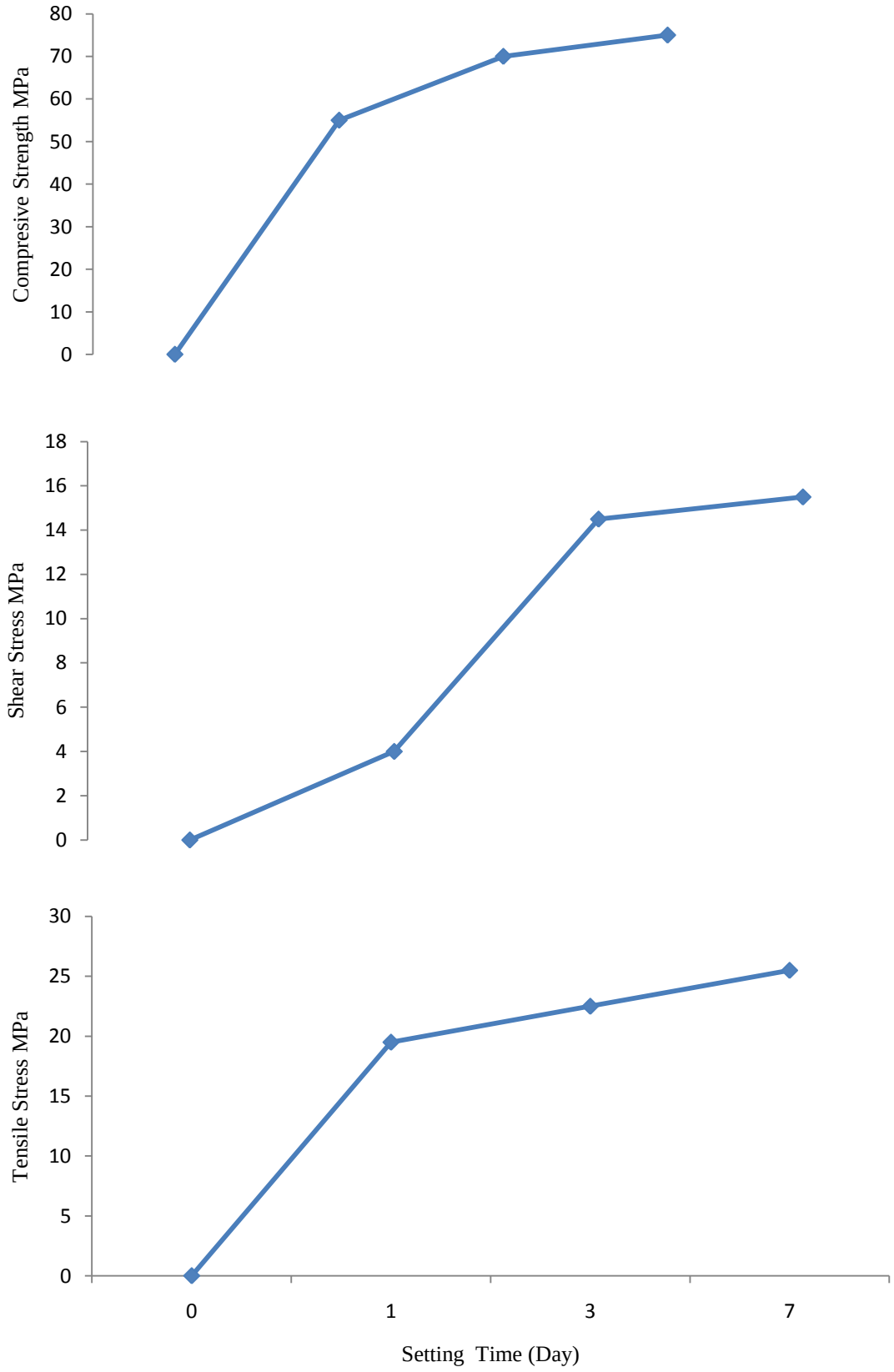

Figure 6.17. Adhesive material properties against setting time

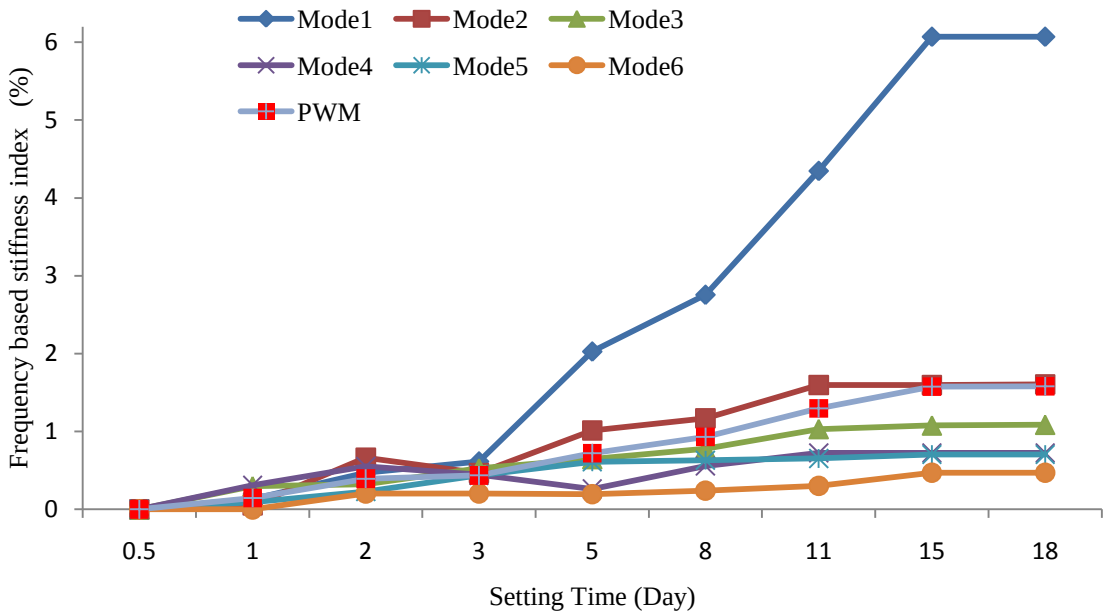

Figure 6.18. Frequency based stiffness index and weighted average (PWM) results corresponding to the adhesive setting time

6.2.1.2.2 Beam B123m

Beam B123m is subjected to a damage load of 55 kN which is close to the steel yield load as shown in Figures 6.4 and 6.5, and the beam is repaired according to the laboratory repair procedure. In order to highlight the effectiveness of the CFRP repair system, the frequency based stiffness index changes are highlighted in Figure 6.19, which present the index values as well as the weighted average values in accordance with PWM procedure. The results are shown at stages illustrated in Table 6.6.

Table 6.6. Stages considered for the dynamic evaluation of beam B123m

Notation	Remark
C	Undamaged stage
D	Pre-repair damaged stage
R0H	Immediately after turning the beam over after repair
R24H	24 hours after turning the beam over after repair
RDL	Subjected to design load
RD	Subjected to pre-repair damage load

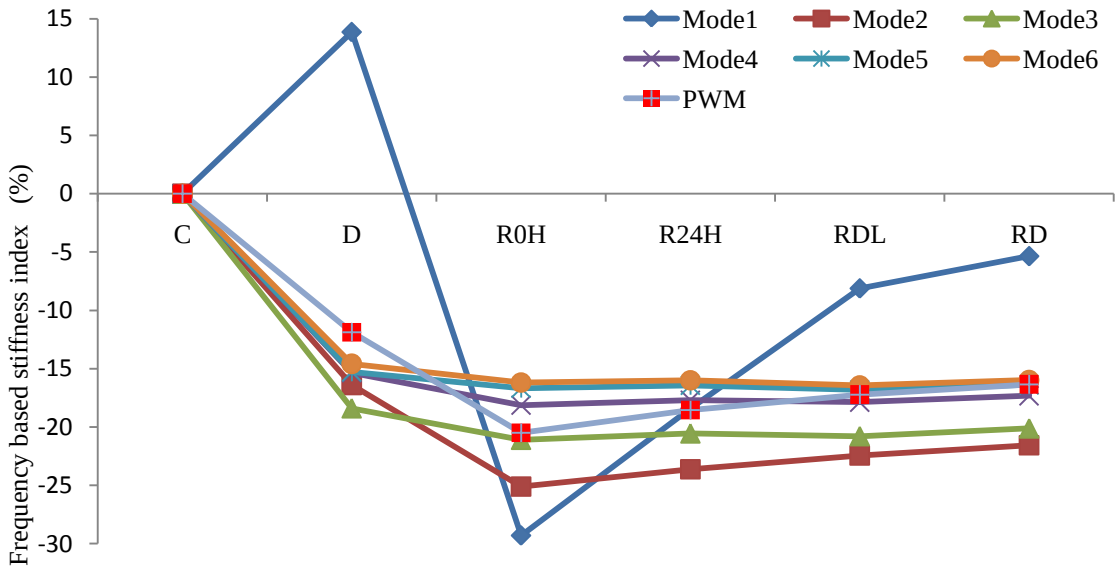

Figure 6.19. Frequency based stiffness index and weighted average (PWM) results for beam B123m

The results show that at pre-repair damage level, all the considered modes show a decrease in the index values which are affected by the concrete softening. Mode 1 shows an increase in the index value due to the increase in the bond stiffness. When the beam is repaired according to the laboratory repair procedure and when it is turned over to its original position at stage R0H, all the modes show a decrease in the index values which is probably due to the influence of the composite action phenomenon of repaired RC beams on the modal frequencies. Mode 1 shows an increase at stage R24H as compared to stage R0H while the remaining modes show a slight increase. When the beam is subjected to a load at stage RDL all the modes show an increase in the index values which are affected by the increase in the tension interaction force. A high increase in the index value for Mode 1 and a slight increase for the other modes is noted at stage RD. The results show that all the modes are affected by the composite action phenomenon of repaired RC beams. The stiffness recovery starts to appear when the beam self weight begins to influence the adhesive bond interface and when the repaired beam is subjected to load. The results show that different modes have different stiffness

recovery for all the adopted stages. In order to extrapolate a trend of the stiffness change based on all the considered modes, the weighted average of the index values according to PWM is calculated and the results are shown in Figure 6.19. The results show a decrease in the overall stiffness after repair with the CFRP sheets based on the laboratory repair procedure. It starts to recover after the influence of the self weight and after subjecting the beam to load cycles. The stiffness recovery based on the difference between stage R24H and stage R0H, RDL and R0H and RD and R0H is 1.94%, 3.3% and 4.15%, respectively.

The damping change as an indirect indicator for the stiffness change is calculated and is shown in Figure 6.20. The results show that at pre-repair damage stage all the modes show an increase in the damping values indicating a decrease in the stiffness. When the beam is repaired and at stage R0H, all the modes show a decrease in the damping change values indicating an increase in the stiffness. At stage R24H, Modes 1 and 4 show a further decrease in the damping change values when compared to stage R0H, while the remaining modes show an increase. For remaining stages, when the repaired beam is subjected to load cycles, different modes show different trends.

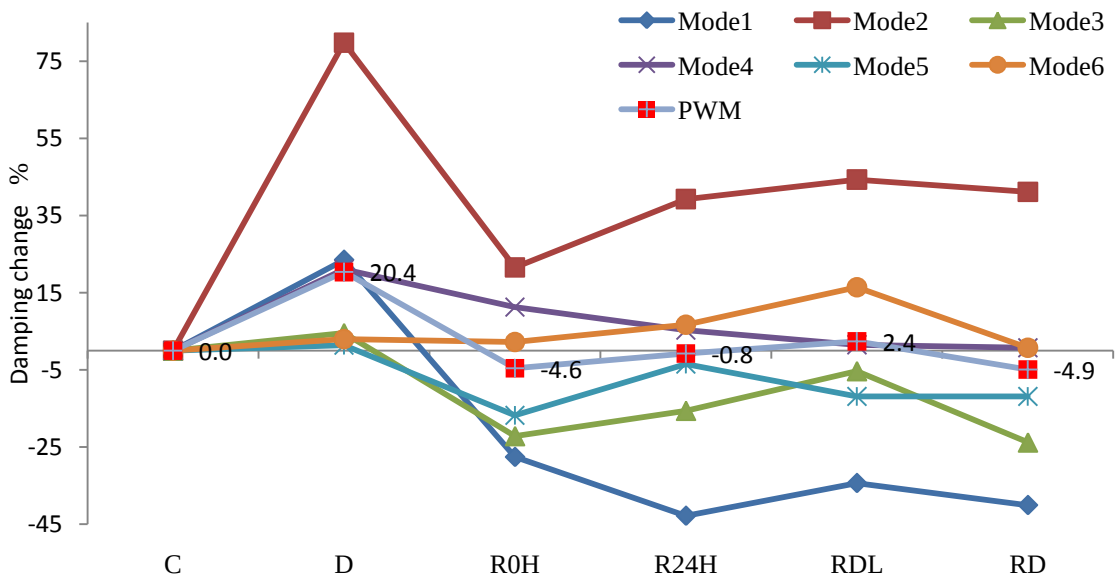

Figure 6.20. Damping change and weighted average (PWM) results for beam B123m

In order to highlight the overall stiffness change based on all the considered modes, the weighted average (PWM) is calculated and the values are shown in Figure 6.20. The overall stiffness based on the considered modes and as indicated by the damping change show a decrease at the pre-repair damage stage by increasing the damping values. It shows a recovery of 24.9% at stage R0H when compared to stage D. At stage R24H, the damping change shows a slight increase indicating a stiffness decrease when compared to R0H stage. Subjecting the repaired beam to load at stage RDL shows an increase in the damping change indicating stiffness decrease when compared to R0H stage. However, subjecting the repaired beam to the same as the pre-repair damage load at stage RD, shows a decrease in the damping change indicating a stiffness increase when compared to stage RDL.

6.2.1.2.3 Beam B124m

Beam B124m is subjected to load until the failure begins to occur at 85.8 kN at the pre-repair stage as shown in Figure 6.7. The beam is repaired according to laboratory repair procedure, and is then subjected to load cycles up to failure. The frequency based stiffness index is calculated at different stages as shown in Table 6.7. Figure 6.21 presents the frequency based stiffness index values and the weighted average (PWM) results for the considered modes at the adopted stages.

Table 6.7. Stages considered for the dynamic evaluation of beam B124m

Notation	Remark
C	Undamaged stage
D	Pre-repair damaged stage
R0H	Immediately after turning the beam over after repair
R24H	24 hours after turning the beam over after repair
RDL	Subjected to design load
RD	Subjected to pre-repair damage load

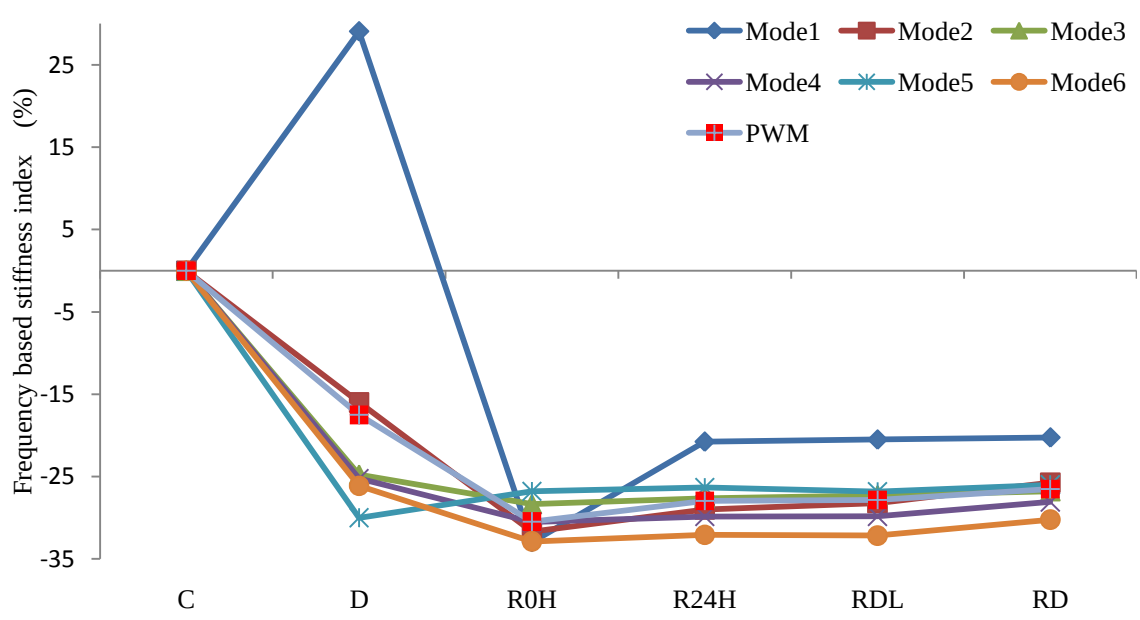

Figure 6.21. Frequency based stiffness index and weighted average (PWM) results for beam B124m

The results show that at pre-repair stage all the modes demonstrate a decrease in the index values which are influenced by the concrete softening, with the exception of Mode 1 which shows an increase due to the bond stiffness according to composite action phenomenon of RC beams. After repairing the beam at stage R0H, all the modes show a decrease due to the composite action phenomenon of repaired RC beams, with the exception of Mode 5 which shows an increase in the index value. When the beam is left to allow for the self weight to influence the adhesive bond interface at stage R24H, all the modes show an increase due to the tension interaction force. Subjecting the beam to loads equal to those of the design load at stage RDL results in a slight increase in the index values for all of the modes except for Mode 5 which shows a slight decrease. Finally, when the beam is subjected to a load equal to the pre-repair damage load at stage RD, all the modes show a slight increase due to the effect of the increase in the tension interaction force. Since different modes show different stiffness recovery or change and in order to highlight the overall stiffness change based on the all considered modes, weighted average according to PWM procedure is calculated for the frequency

based stiffness index values and the results are shown in Figure 6.21. The results show that the overall stiffness suffered deterioration at the stage R0H as influenced by the composite action phenomenon of repaired RC beams. Following this it recovers under the effect of the self weight at stage R24H where the recovered stiffness is 2.5% in comparison with stage R0H. Subjecting the beam to load at stage RDL increases the stiffness where its recovery is 2.62% as based on stage R0H. Subjecting the beam to further loading at stage RD increases the stiffness where its recovery is 3.94% as based on stage R0H.

The damping change values are calculated and are shown in Figure 6.22. These values present the values at the same stage adopted for the frequency based stiffness index. The weighted average according to the PWM procedure is performed and its results are shown in Figure 6.22. The results show an increase in the damping for all the considered modes at pre-repair damage stage which are influenced by the stiffness deterioration. After repairing the beam and at stage R0H, all the modes show a decrease in the damping values which are influenced by the increase in the stiffness caused by fixing the CFRP sheets except for Mode 6 which showed increase in the damping value. For stage R24H and RDL, some modes show a decrease and some show an increase in damping values when compared to stage R0H. When the beam is subjected to a load equal to that at pre-repair damage stage, all the modes show a decrease in damping values when compared to stage R24H and RDL, indicating an increase in the stiffness.

The weighted average according to PWM procedure is calculated for the damping change values to highlight the overall stiffness deterioration and recovery based on all the considered modes as shown in Figure 6.22. The overall stiffness shows a deterioration of 19.6% at the pre-repair damage stage, before demonstrating a recovery of 19.17% at stage R0H when compared to stage D. There is no change in the stiffness recovery at stage R24H. A slight increase in the stiffness recovery is observed under the

influence of the design load at stage RDL where it is 19.8%. A further increase of 24.5% in stiffness recovery is observed at stage RD under the influence of the pre-repair damage load.

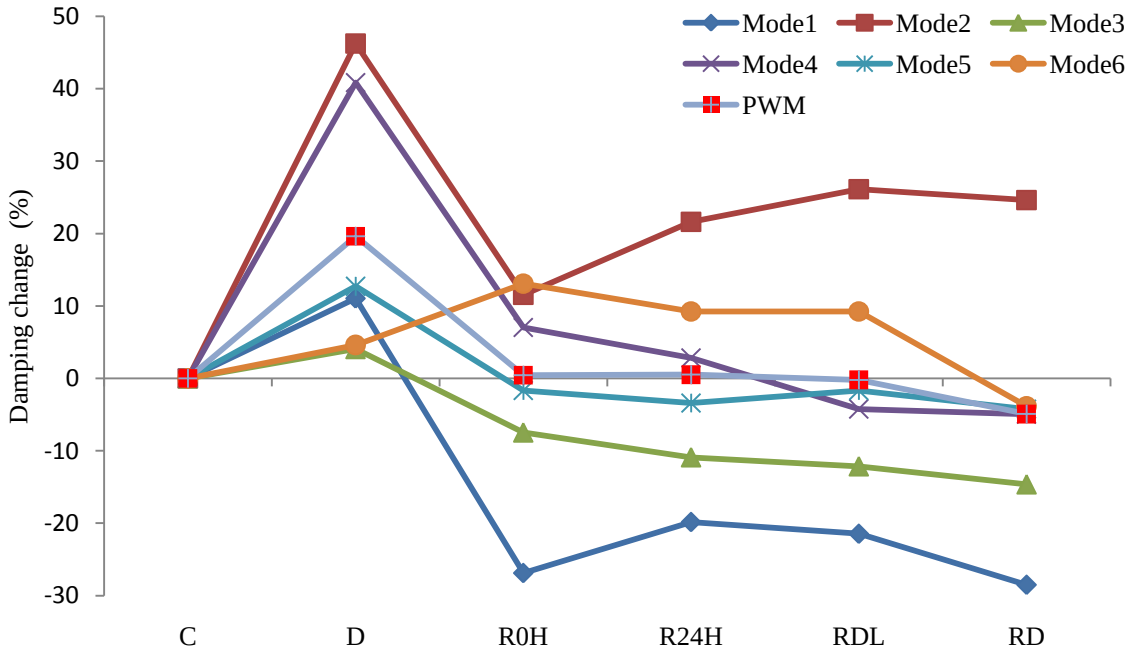

Figure 6.22. Damping change and weighted average (PWM) results for beam B124m

6.2.1.3 CFRP repair effectiveness

The previous section highlights the increase in the ultimate load capacity based on the static data and the stiffness recovery based on the dynamic data. This section highlights the relationship between the static and the dynamic data which emerges with the effectiveness of the CFRP repair system at different pre-repair damage levels. The damage level is calculated based on the percentage of the applied load at pre-repair stage to the ultimate capacity of the unrepaired sections. The stiffness recovery, as indicated by the ratio of increase in the ultimate load capacity, is calculated based on the increase in the ultimate capacity of the repaired sections to the ultimate capacity of the unrepaired sections. The stiffness effectiveness based on the dynamic data is highlighted based on both frequency based stiffness index and damping change. For

frequency based stiffness index, the repair effectiveness is calculated as the difference between the weighted average index value at the stage of being subjected to design limit load of 25 kN compared to the weighted average index value at the repair stage immediately after turning the beam over to its original position. This is it to give the ability for tension interaction force to be activated and to balance compression interaction force according to the composite action phenomenon of repaired RC beams. The repair effectiveness based on the damping change is calculated as the difference between the weighted average value of damping change at the repaired stage after 24 hours from turning the beam over compared to the weighted average value of damping change at pre-repair damage stage. Figure 6.23 shows the repair effectiveness based on the static and dynamic data of beams B122m, B123m, and B124m, corresponding to 0.35, 0.65 and 1 damage levels, respectively.

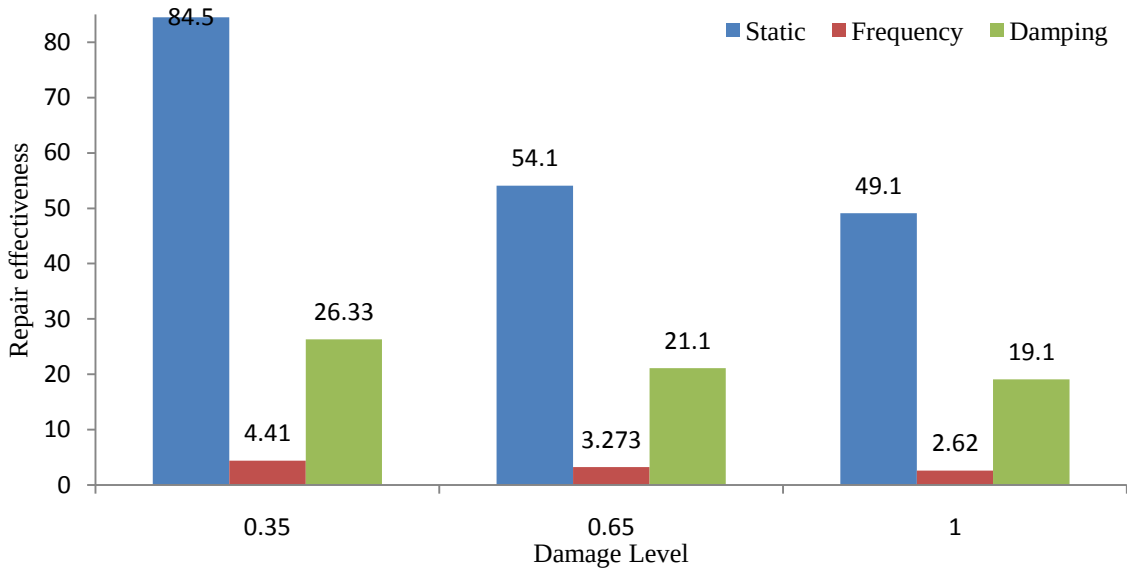

Figure 6.23. CFRP repair effectiveness based on static and dynamic data for ρ_{min} group

The results show that the effectiveness of the repair using CFRP sheets decreases as the pre-repair damage level increases. Regardless, even with the pre-repair damage level at 100%, the repair with CFRP sheets helps to recover the stiffness and increase the load capacity of the repaired beams. At a damage level of 35% which is the design load limit,

repair with CFRP sheets increases the ultimate capacity by 85% and the corresponding stiffness recovery based on the dynamic data is 4.41% and 26.3% according to frequency based stiffness index and damping change respectively. At the damage level of 65% which is close to the steel yield load limit, the increase in the load capacity and the stiffness recovery is reduced, and at a damage level of 100% the increase in the load capacity is only 49% with the stiffness recovery totalling 2.62% and 19% judging from frequency based stiffness index and damping change, respectively. The increase in the load capacity of 49 to 85 % corresponding to 100 to 35% pre-repair damage levels for beams design according to the minimum steel requirement (ρ_{min}) is in good agreement with the literature where an increase of 89 to 136% was noticed for the strengthening cases of 0% pre-repair damage level [Nguyen et al. (2001) and Rahimi and Hutchinson (2001)].

6.2.1.4 Monitoring of repaired beams

This section reports the results obtained during monitoring of the repaired beam under loading up to failure in order to highlight its behaviour during the service life of the structures. Moreover, failure modes of the repaired beams with externally bonded CFRP sheets are reported. The monitoring focuses on the trend of the bending frequencies at different load cycles to highlight the behaviour at higher loading levels, and to predict the early steps of the CFRP debonding and the full debonding using the bending frequencies. The frequency based stiffness index is used to monitor the stiffness change corresponding to the applied load, and the datum stiffness based on the stiffness after turning the beam over, that is, stage R0H. Table 6.8 presents the applied load and notations used to plot the frequency based stiffness index values as shown in Figure 6.24 for beam B122m.

The results show that for Modes 2 to 6, the frequency based stiffness index increases up to stage RD, affected by the activation of the adhesive bond. All the modes start to

decrease as loading is further applied due to the concrete stiffness deterioration as evident from the appearance of new cracks as shown in Table 6.1. The stiffness deterioration indicated by Modes 2 to 6 is still small until stage R115 but shows a rapid decrease beyond stage R115 due to full debonding of the CFRP sheets.

Table 6.8. Load cycles for post-repair stage of beam B122m

Load (kN)	Notations	Remark
0	R0H	Immediately after turning the beam over after repair
0	R24H	24 hours after turning the beam over after repair
25	RD	Subjected to pre-repair damage load
55	R55	
70	R70	
85	R85	
100	R100	
115	R115	
131	R131D	Full CFRP debonding

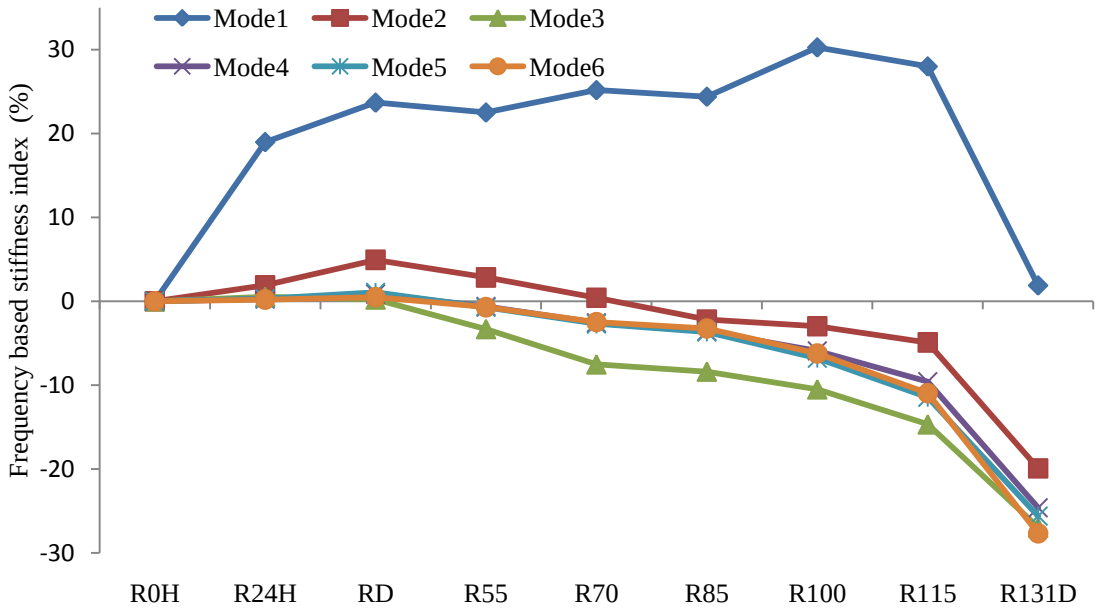

Figure 6.24. Frequency based stiffness index results for the monitoring of beam B122m

Mode 1 shows a rapid increase after the influence of the self weight at stage R24H due to activation of the tension interaction forces. A slight increase is noted for further load cycles to reach the maximum increase at stage R100 as a result of the increase in the

tension interaction force which activates the adhesive bond without being affected by the concrete stiffness deterioration. When flexural cracks at mid-span induce an intermediate crack at the adhesive layer prior to stage R115, the first mode shows slight decrease, while beyond stage R115 it shows a rapid decrease in the frequency based stiffness index value indicating the full debonding on the CFRP sheets. This highlights the first mode as indicator for the CFRP sheet debonding, where the rest of the modes start to show a decrease in frequency based stiffness index values when new cracks start to appear beyond stage RD. The first mode only shows a decrease when the CFRP starts to debond (beyond stage R100), or is fully debonded (beyond stage R115).

The failure occurs when the flexural cracks at the mid-span extend to the adhesive interface between the CFRP sheets and the concrete surface, to induce intermediate cracks which cause full debonding upon further loading. Figure 6.25 shows the appearance of intermediate cracks (IC) in the adhesive layer at stage R115, and the full CFRP debonding at stage R131D.

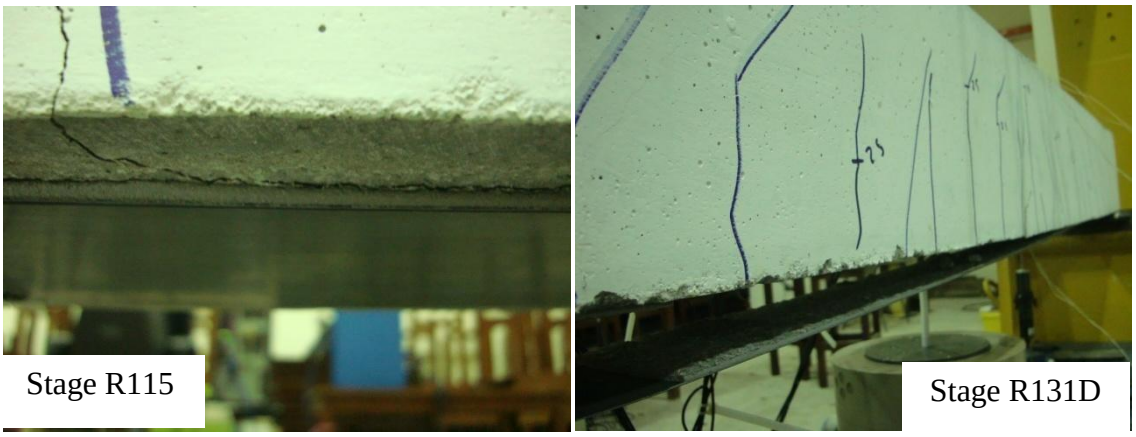

Figure 6.25. Induced intermediate cracks debonding and failure mode for beam B122m

Table 6.9 presents the applied load and notation used to plot the frequency based stiffness index values for beam B123m as shown in Figure 6.26. The datum index value is based on the value after turning the beam over, that is, stage R0H. The results show that Modes 1 and 2 demonstrate a slight increase in the frequency based stiffness index

values beyond stage RD as a result of the activation of the adhesive bond due to increasing of tension interaction force. The increase continues until stage R115 and beyond that the frequency based stiffness index for Modes 1 and 2 shows a slight decrease where the flexural cracks induce intermediate cracks at the adhesive layer. Rapid decrease in the index value for Modes 1 and 2 is noted beyond stage R130 until stage R122d which indicates the full debonding of the CFRP sheet. Modes 3 to 5 show a slight increase in index values beyond stage RD until stage R70 which is due to the limited concrete deterioration and indicates that the modes are affected by the activation of the adhesive bond. Between stages R70 and R85 there is no change. Modes 3 to 5 are affected by both the adhesive bond activation as well as the concrete stiffness deterioration. Beyond stage R85, Modes 3 to 5 show a gradual decrease until stage R130 as result of the concrete stiffness deterioration. Rapid decrease is observed beyond stage R130 which indicates the full CFRP debonding. For Mode 6, the influence of the concrete stiffness deterioration starts beyond stage RD with a slight decrease being noted until stage R130 after which rapid decrease occurs when the CFRP is fully debonded at stage R122D. Modes 1 and 2 can be seen as indicators for predicting the creation of the intermediate cracks debonding at early stages before full debonding occurs, where both show an increase in the index value until stage R115, and beyond that the intermediate crack appears at the adhesive layer. The failure occurs when the flexural cracks at the mid-span extend to the adhesive layer, to induce intermediate cracks which cause full debonding upon further loading. Figure 6.27 shows the creation of the intermediate cracks debonding at stage R130 and the full CFRP intermediate cracks debonding at stag R122D.

Table 6.9. Load cycles for the post-repair stages of beam B123m

Load (kN)	Notation	Remark
0	R0H	Immediately after turning the beam over after repair
0	R24H	24 hours after turning the beam over after repair
25	RDL	Subjected to design load limit
55	RD	Subjected to pre-repair damage load
70	R70	
85	R85	
100	R100	
115	R115	
130.7	R130	CFRP starts debonding
122	R122D	Full CFRP debonding

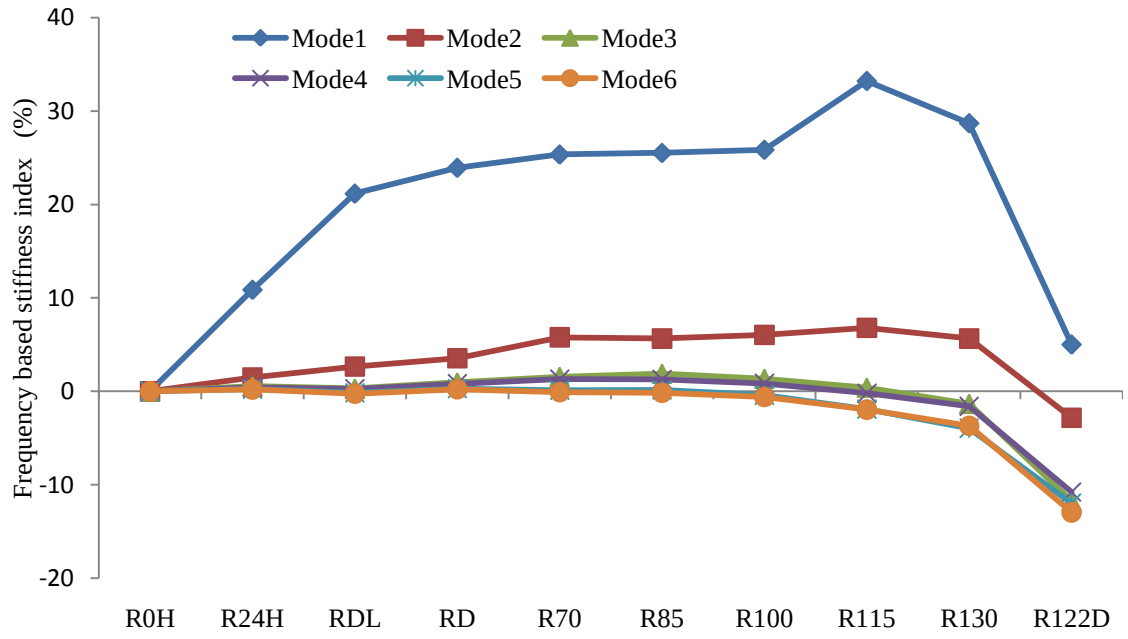

Figure 6.26. Frequency based stiffness index values for the monitoring of beam B123m

Figure 6.27. Induced intermediate cracks debonding and failure mode for beam B123m

Table 6.10 presents the applied load and notation used to plot the frequency based stiffness index values at the monitoring stages of beam B124m as shown in Figure 6.28. The datum index value is used as the value at stage R0H. The results show that all the modes indicate an increase in the index values until stage R115 with the exception of Mode 5 which shows a decrease beyond stage RD. Beyond stage R115 all the modes show a decrease as a result of which flexural cracks induce intermediate cracks at the adhesive layer. A rapid decrease is observed beyond stage R127 when full debonding of CFRP occurs at stage R128D.

Table 6.10. Load cycles for the post-repair stages of beam B124m

Load (kN)	Notation	Remark
0	R0H	Immediately after turning the beam over after repair
0	R24H	24 hours after turning the beam over after repair
25	RDL	Subjected to design load limit
85	RD	Subjected to pre-repair damage load
115	R115	
127	R127	CFRP starts debonding
128	R128D	Full CFRP debonding

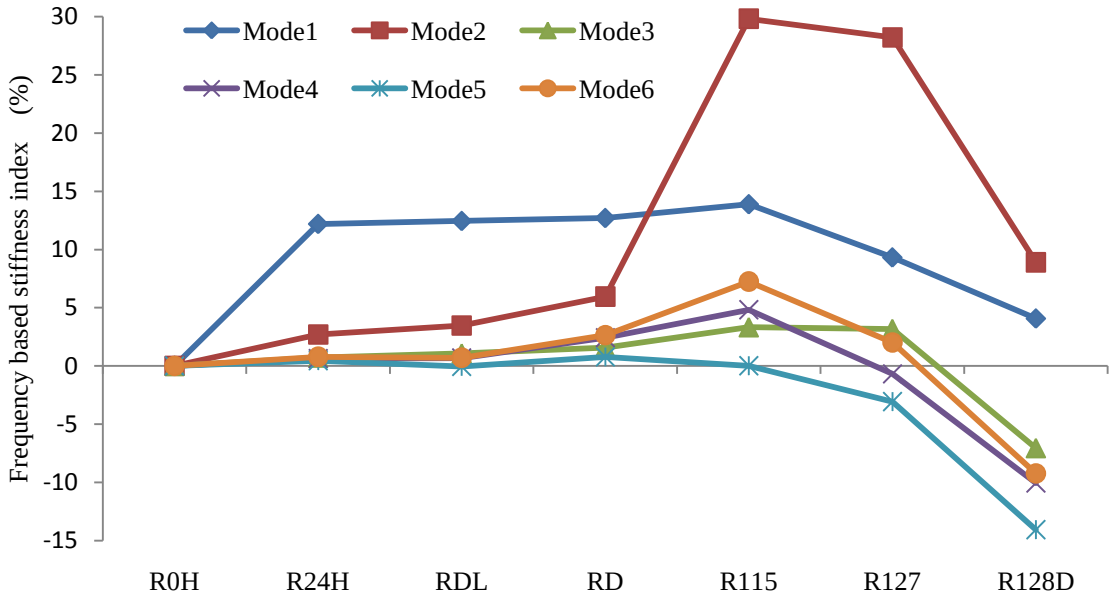

Figure 6.28. Frequency based stiffness index values for the monitoring of beam B124m

The failure occurs when the flexural cracks at the mid-span extend to the adhesive layer, which induces intermediate cracks in the adhesive layer beyond stage R115. These intermediate cracks develop to cause the full CFRP debonding upon further loading. Figure 6.29 presents the creation of the intermediate cracks beyond stage R115, and the full CFRP debonding at stage R128D.

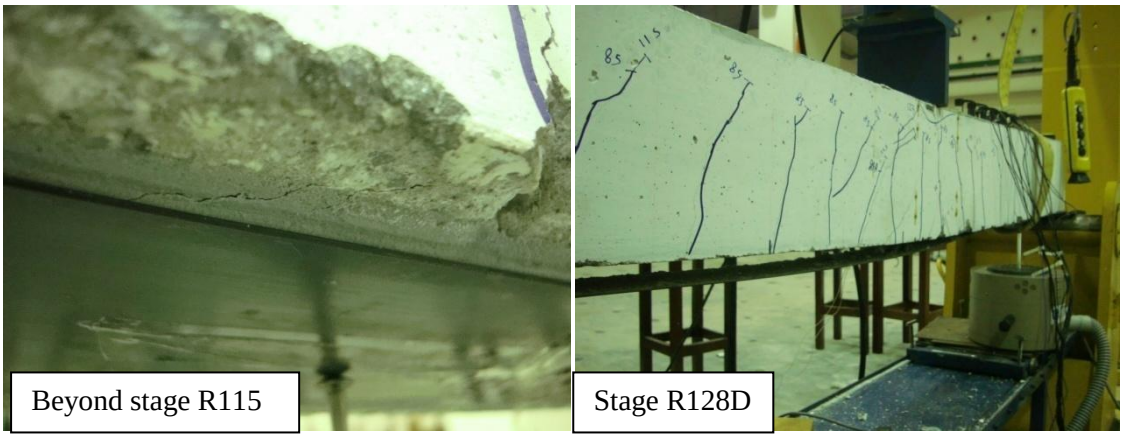

Figure 6.29. Induced intermediate cracks debonding and failure mode for beam B124m

The results during monitoring of the CFRP repaired beams show that the trend of frequency based stiffness index of the different modes depends on the pre-repair damage levels. These results are in agreement with the findings of Benjeddou et al. (2007). For low pre-repair damage levels, the concrete stiffness deterioration at the pre-repair stage has limited influence due to a small number of cracks as in beam B122, that is, only seven cracks. Thus, at post-repair stage, the concrete stiffness deterioration starts at low loading levels and has a bigger influence than the activation of the adhesive bond stiffness on most of the bending modes except for Mode 1 which is influenced by the adhesive bond stiffness activation. For intermediate pre-repair damage levels, the concrete stiffness deterioration is greater at pre-repair stage, which makes the concrete stiffness deterioration at the post-repair stage less influential on the bending modes, with the exception of Modes 1 and 2 which are influenced by the activation of the adhesive bond stiffness. For extreme pre-repair damage level, the concrete stiffness

deterioration reaches high levels at pre-repair stage, which limits the concrete stiffness deterioration at post-repair stage. Thus, the effect on the bending modes is smaller compared to the adhesive bond stiffness activation which influences Modes 1, 2, 4 and 6 at to higher loading levels. The failure is governed by the intermediate crack debonding with the CFRP strains between 5400 and 6200 μst whph is in good agreement with the results obtained by Choi et al. (2004). However, the findings by Choi et al. (2004) were with regards to strengthening, while Benjeddou et al. (2007) showed that the failure mode for repair work was peeling off CFRP sheets at the ends.

6.2.2 Maximum steel limit (ρ_{max})

This section covers the results related to use of CFRP sheet as flexural repair system when the reinforced steel is designed to be close to ρ_{max}. The effectiveness of the CFRP sheets as flexural repair system is investigated under the effect of different pre-repair damage levels, where three levels are considered i.e. design load, close to the steel yield load and failure load. The results present static evaluation, dynamic evaluation, and the monitoring of the repaired beams to investigate its behaviour during subsequent service life. The beams with ρ_{max} are designated as B112m, B113m and B114m.

6.2.2.1 Static evaluation

The static data obtained from the static load test of the RC beams at pre and post repair stages are presented. The static data includes load against deflection curves, load against steel strain curves and load against CFRP strain curves. This section presents the results for beams B112m, B113m and B114m, which are designed using ρ_{max}, where two 16mm diameter steel bars are used in the flexural zone. The beams are then repaired using CFRP sheets according to the repair procedure mentioned in Section 4.2.5. The repair is in accordance with ACI 440.2R (2002) Code as mentioned in Section 4.3.1.2, where 50mm width CFRP sheet is used for all the three beams.

6.2.2.1.1 Beam B112m

Beam B112m is subjected to a damage load of 40 kN, which is close to the design load, at pre-repair stage. After repair, the beam is subjected to load cycles up to failure, as shown in Table 6.11 which presents the load cycles and the corresponding number of cracks. The load against CFRP strain at post-repair stages are shown in Figure 6.30 .The load against deflection curves at pre and post repair stages are shown in Figure 6.31. The load against steel strain curves at pre and post repair stages are shown in Figure 6.32. The crack patterns corresponding to each load cycle are appended in Appendix B.

Table 6.11. Load cycles and corresponding number of cracks for beam B112m

Load Cycles (kN)	Number of cracks	Remark
40	9	Pre-repair stage
12	9	Post-repair stage
40	9	
50	14	
60	15	
80	16	
100	18	
120	18	CFRP starts debonding
115	18	Full CFRP debonding
93.5	18	Failure

The results show that the repaired beam is able to withstand up to 120 kN as maximum load capacity. The CFRP debonding starts beyond a load of 100 kN and more cracks in the adhesive layer appear at load of 120 kN which leads to full CFRP debonding at a load of 115 kN. The CFRP strain reaches 5700 μst prior to fully debonding. When the CFRP is debonded the load drops from 115 kN to 86 kN. Following this the beam is loaded again to ascertain the beam capacity with the CFRP sheets fully debonded, which can be considered as the unrepaired beam capacity, where it fails at load 93.5 kN.

The steel reaches a strain of 4250 µst when full CFRP debonding occurs, which is less than the rupture strain at 6500 µst, which can be the reason behind the ability of the beam to withstand loads up to 93.5 kN after full CFRP debonding. The increase in the load capacity due to adding the CFRP sheets is evaluated based on the maximum capacity of repaired section (120 kN) divided by the maximum capacity of the unrepaired section (93.5 kN) which gives an increase of 128.4%.

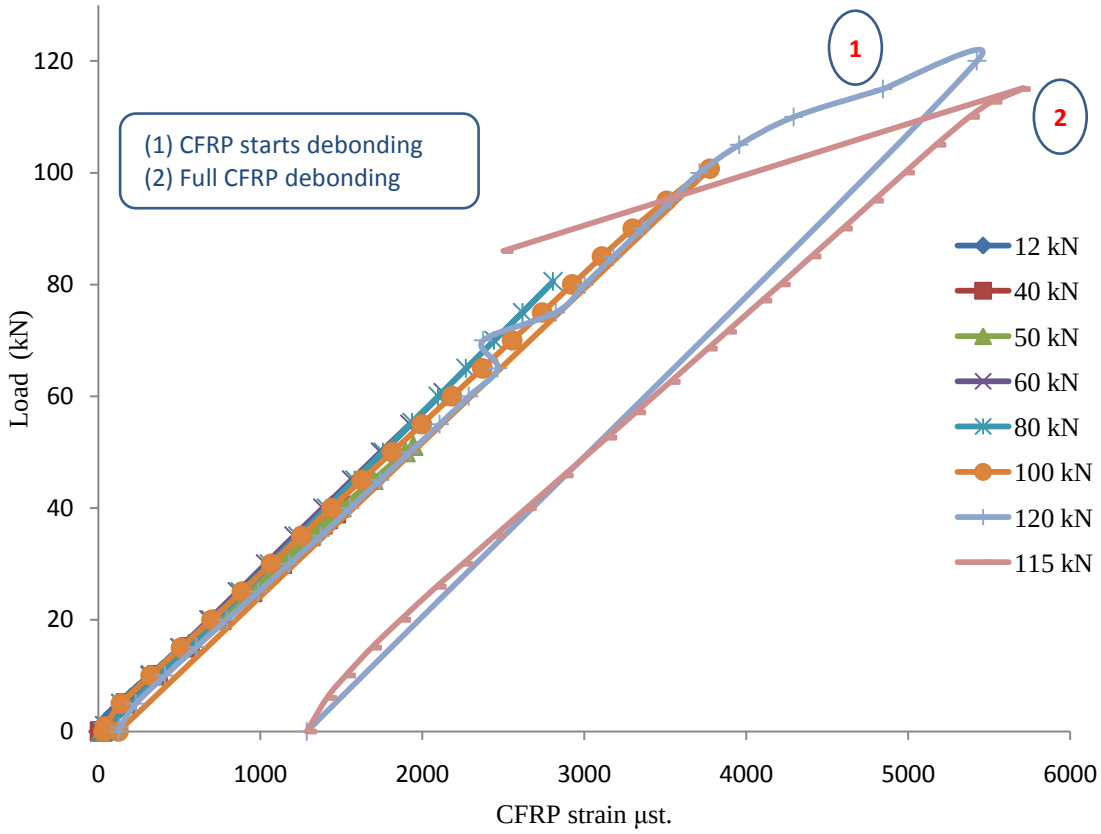

Figure 6.30. Load against mid-span CFRP strain curves at post-repair stage for beam B112m

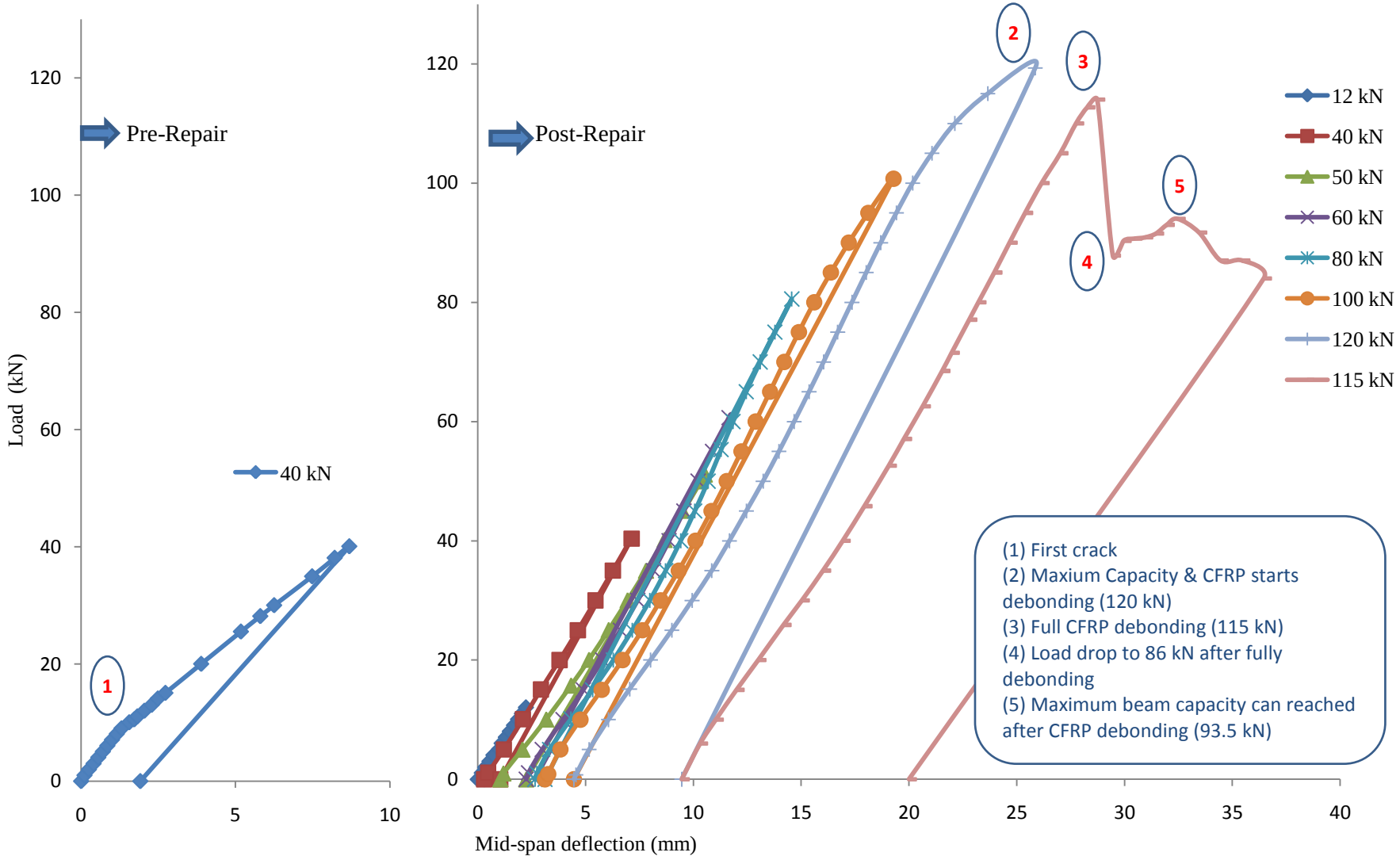

Figure 6.31. Load against mid-span deflection curves at pre and post repair stages for beam B112m

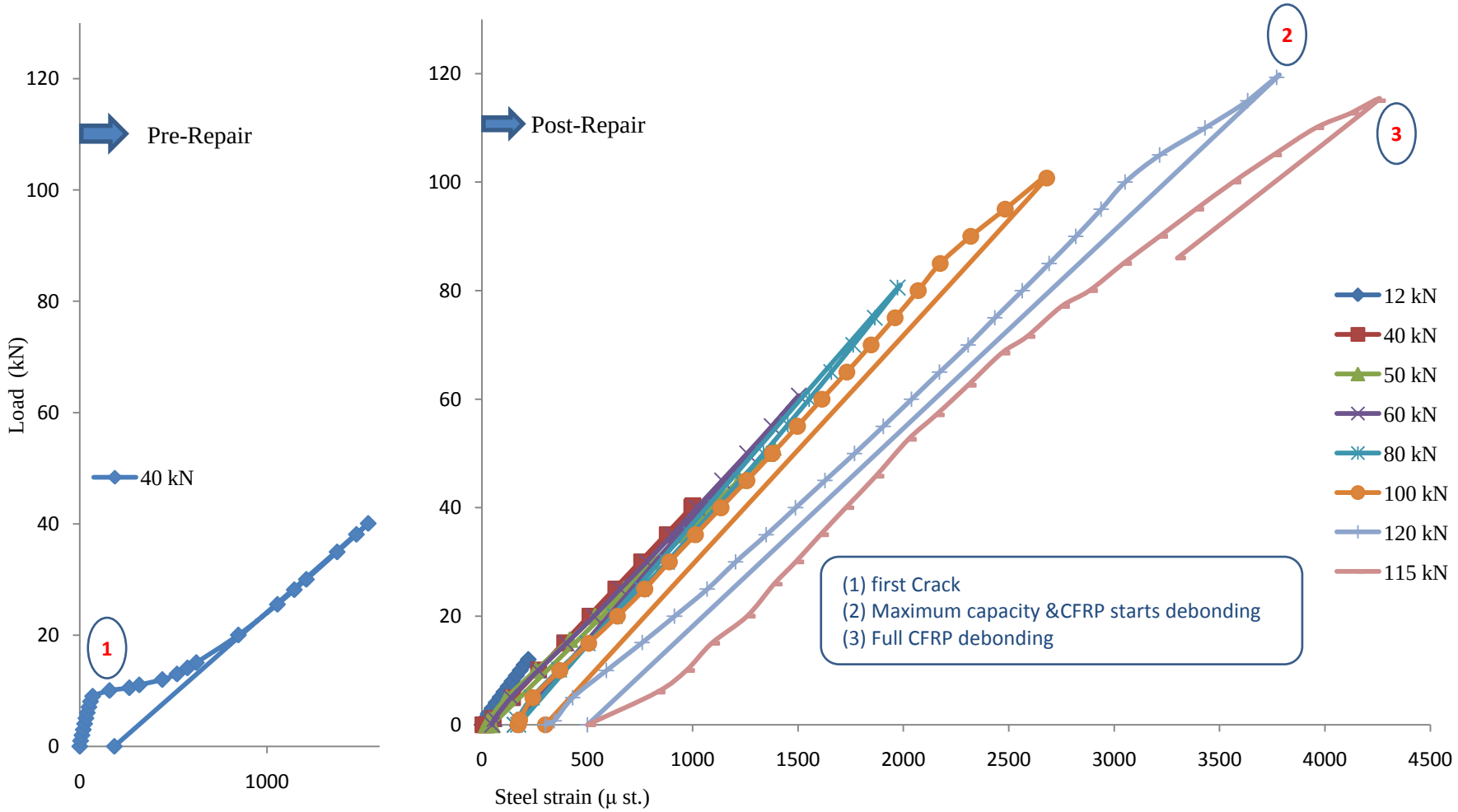

Figure 6.32. Load against mid-span steel strain curves at pre and post repair stages for beam B112m

6.2.2.1.2 Beam B113m

Beam B113m is subjected to damage load of 71 kN which is close to the steel yield load at the pre-repair stage. After repair, the beam is subjected to load cycles up to failure, where the load cycles and corresponding number of cracks are shown in Table 6.12. The load against deflection curves at pre and post repair stages are shown in Figure 6.33. The load against steel strain curves at pre and post repair stages are shown in Figure 6.34. The load against CFRP strain at post-repair stages are shown in Figure 6.35. The crack patterns corresponding to each load cycle are appended in Appendix B.

Table 6.12. Load cycles and corresponding number of cracks for beam B113m

Load Cycles (kN)	Number of cracks	Remark
71	15	Pre-repair stage
12	15	Post-repair stage
40	15	
71	16	
80	16	
100	17	
124.7	20	CFRP deboned
101.5	20	Failure

The results show that the beam is damaged under load of 71 kN which is close to the steel yield limit where the steel reaches a strain of approximately 3000 μst at pre-repair stage. After repair, the beam is able to withstand a load of 124.7 kN where full CFRP debonding occurs with corresponding CFRP strain of 5430 μst. The steel strain reaches 4770 μst , when full CFRP debonding occurs, which is less than the rupture limit and this is the reason behind the ability of the beam to withstand load of 101.5 kN after full CFRP debonded. The increase in the load capacity by adding the CFRP sheets is evaluated based on the maximum capacity of the repaired section (124.7 kN) divided by the maximum capacity of the unrepaired section (101.5 kN) which gives an increase of 122.8%.

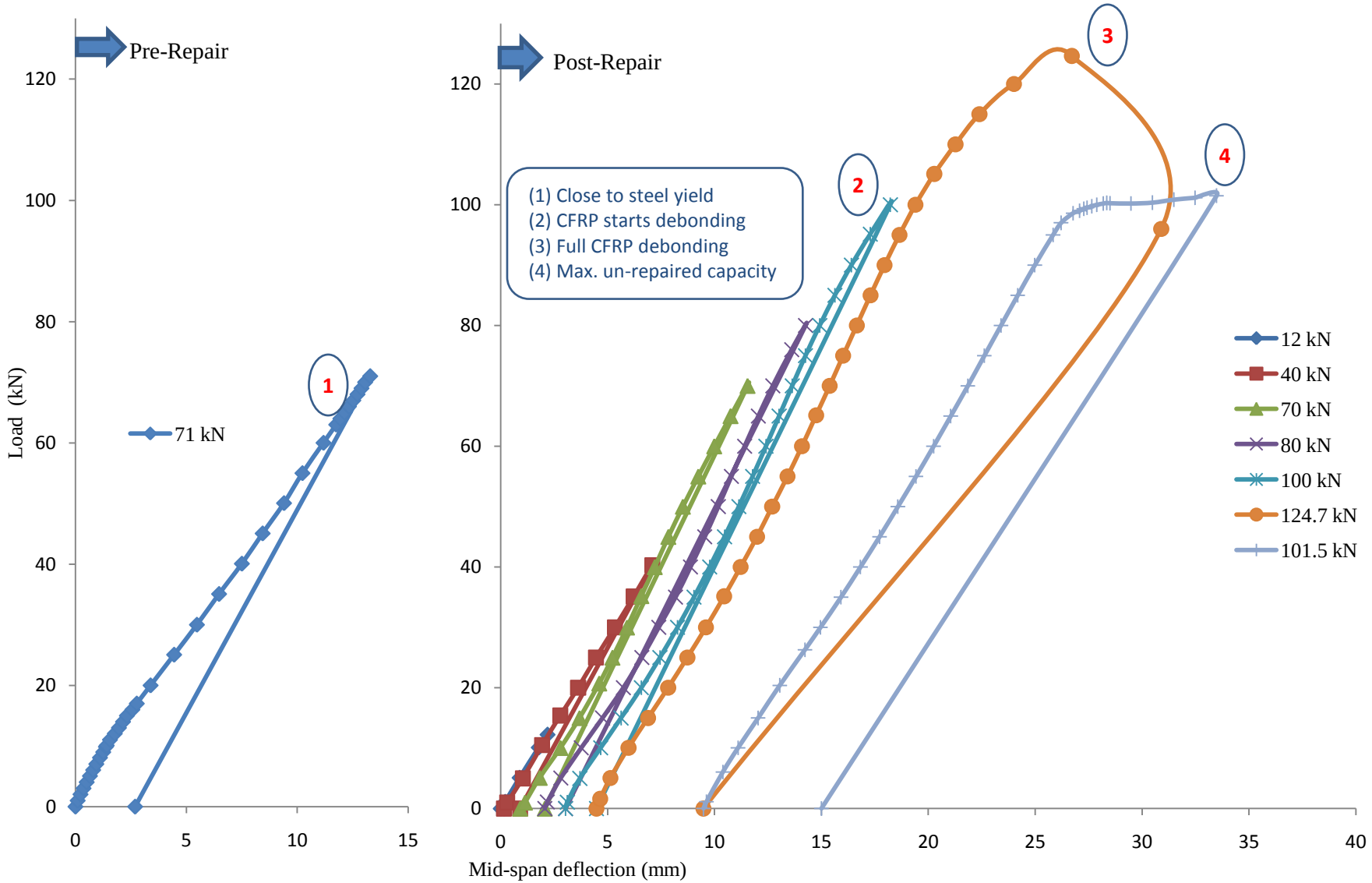

Figure 6.33. Load against mid-span deflection curves at pre and post repair stages for beam B113m

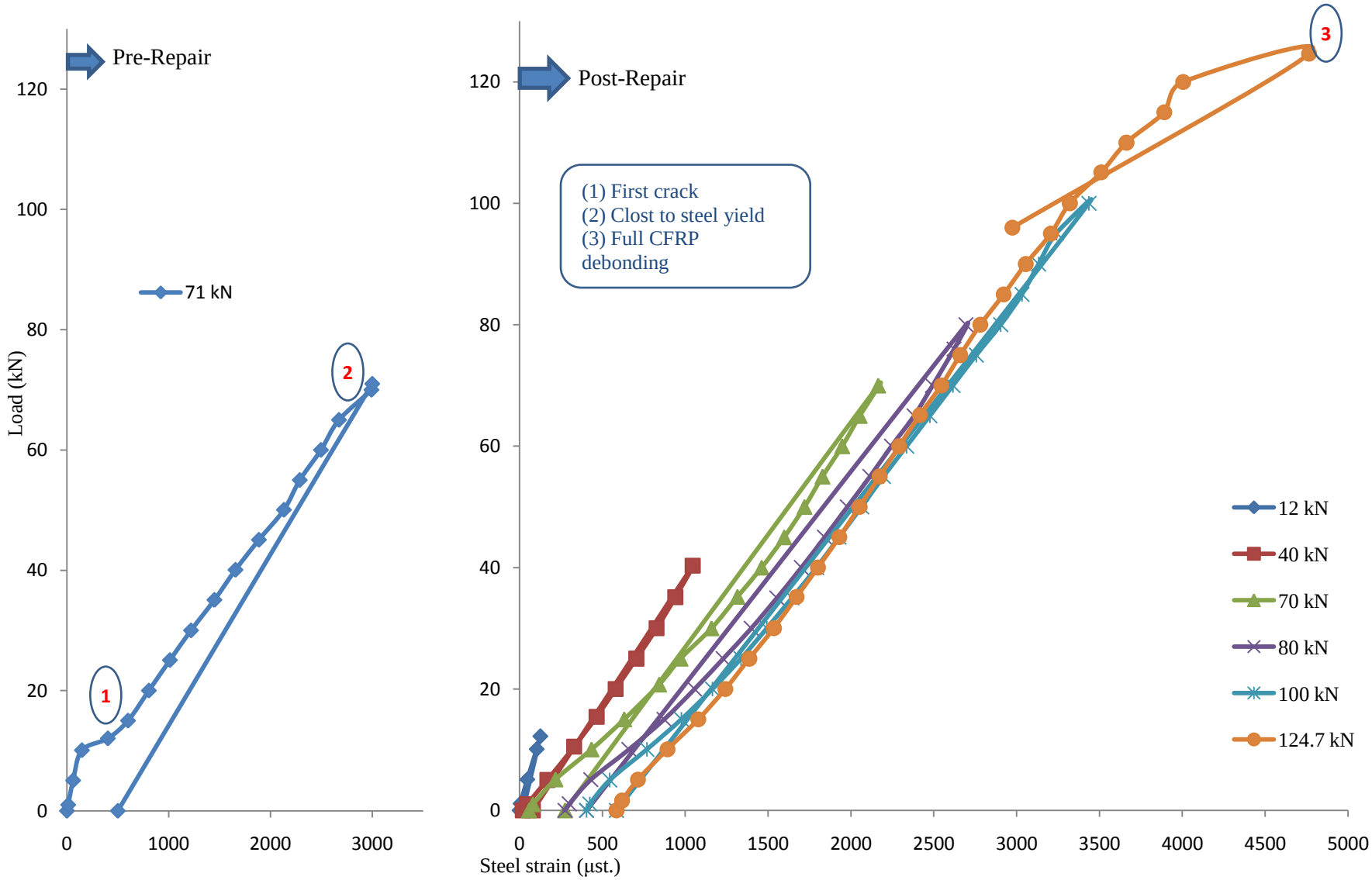

Figure 6.34 Load against mid-span steel strain curves at pre and post repair stages for beam B113m

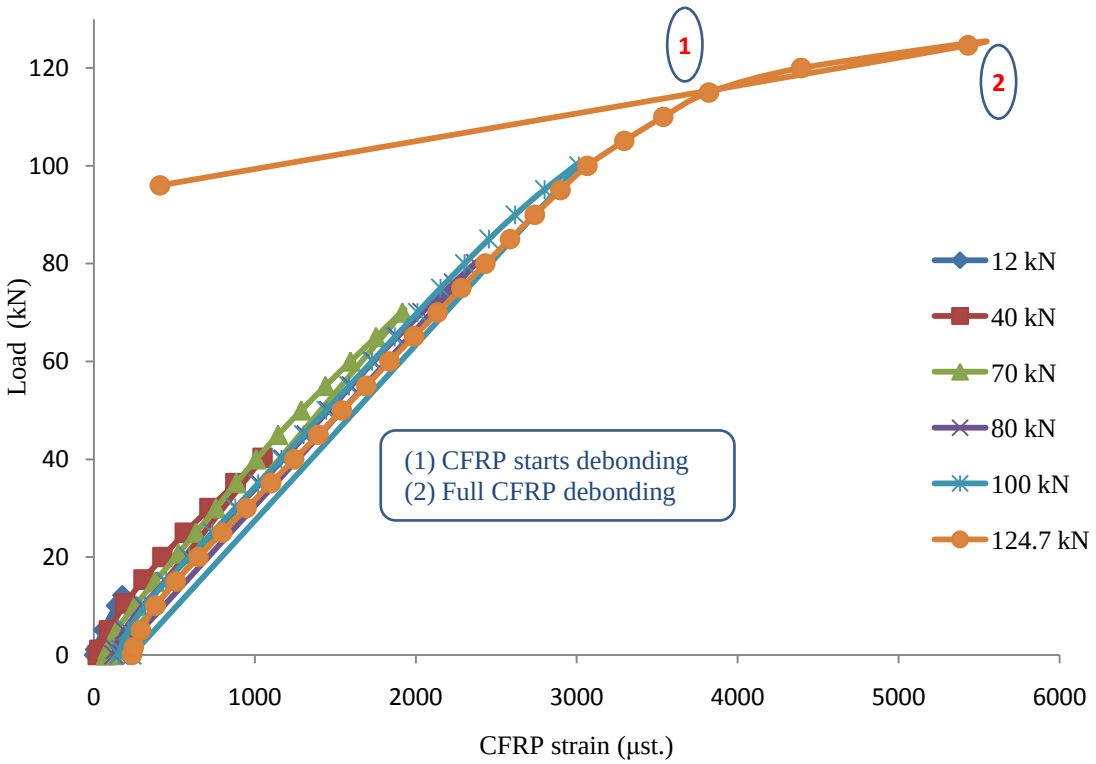

Figure 6.35. Load against mid-span CFRP strain curves at post-repair stage for beam B113m

6.2.2.1.3 Beam B114m

Beam B114m is damaged under the failure load of 82 kN at pre-repair stage, where the load is applied until the load against deflection curve becomes horizontal indicating the start of failure. The steel strain reaches the rupture limit where there is a rapid increase in the steel strain beyond the steel yield limit. After repair, the beam is subjected to load cycles up to failure, where the load cycles and the corresponding number of cracks are shown in Table 6.13. The load against CFRP strain at post-repair stages are as shown in Figure 6.36. The load against deflection curves at pre and post repair stages are shown in Figure 6.37. The load against steel strain curves at pre-repair stage are shown in Figure 6.38, where no data is carried out at the post-repair stages since the train gauge is broken when failure occurs at pre-repair stage. The crack patterns corresponding to each load cycle are appended in Appendix B.

Table 6.13. Load cycles and corresponding number of cracks for beam B114m

Load Cycles (kN)	Number of cracks	Remark
11.5	1	First crack at Pre-repair stage
82	13	Pre-repair stage
40	13	Post-repair stage
70	13	
80	14	
90	14	CFRP starts debonding
93	16	
94.5	16	Full CFRP debonding

The results show that the beam is able to withstand loading of up to 94.5 kN after repair with externally bonded CFRP sheets. The CFRP starts to debond at 90 kN and is fully debonded at 94.5 kN with corresponding CFRP strain of 4800 µst. The increase in the load capacity for beam B114m due to fixing the CFRP sheet is evaluated based on the maximum capacity of the repaired section (94.5 kN) divided by the maximum capacity of the unrepaired section (82 kN) which gives an increase of 115.3%.

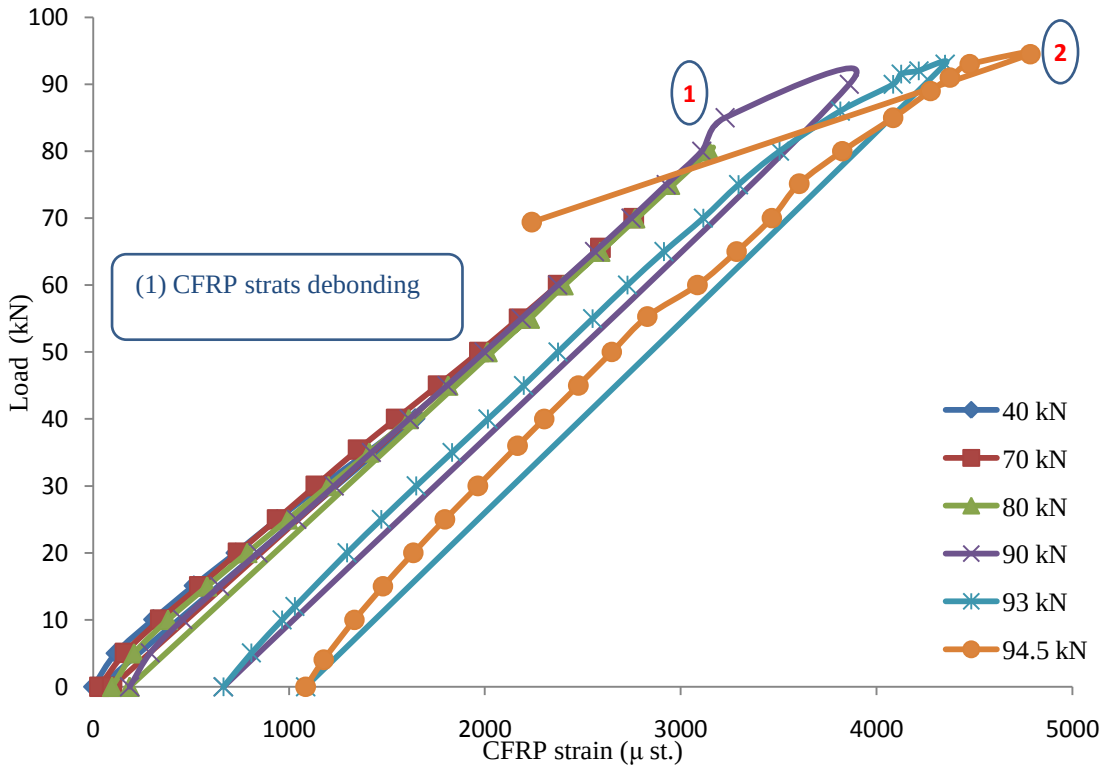

Figure 6.36. Load against CFRP strain at post-repair stage for beam B114m

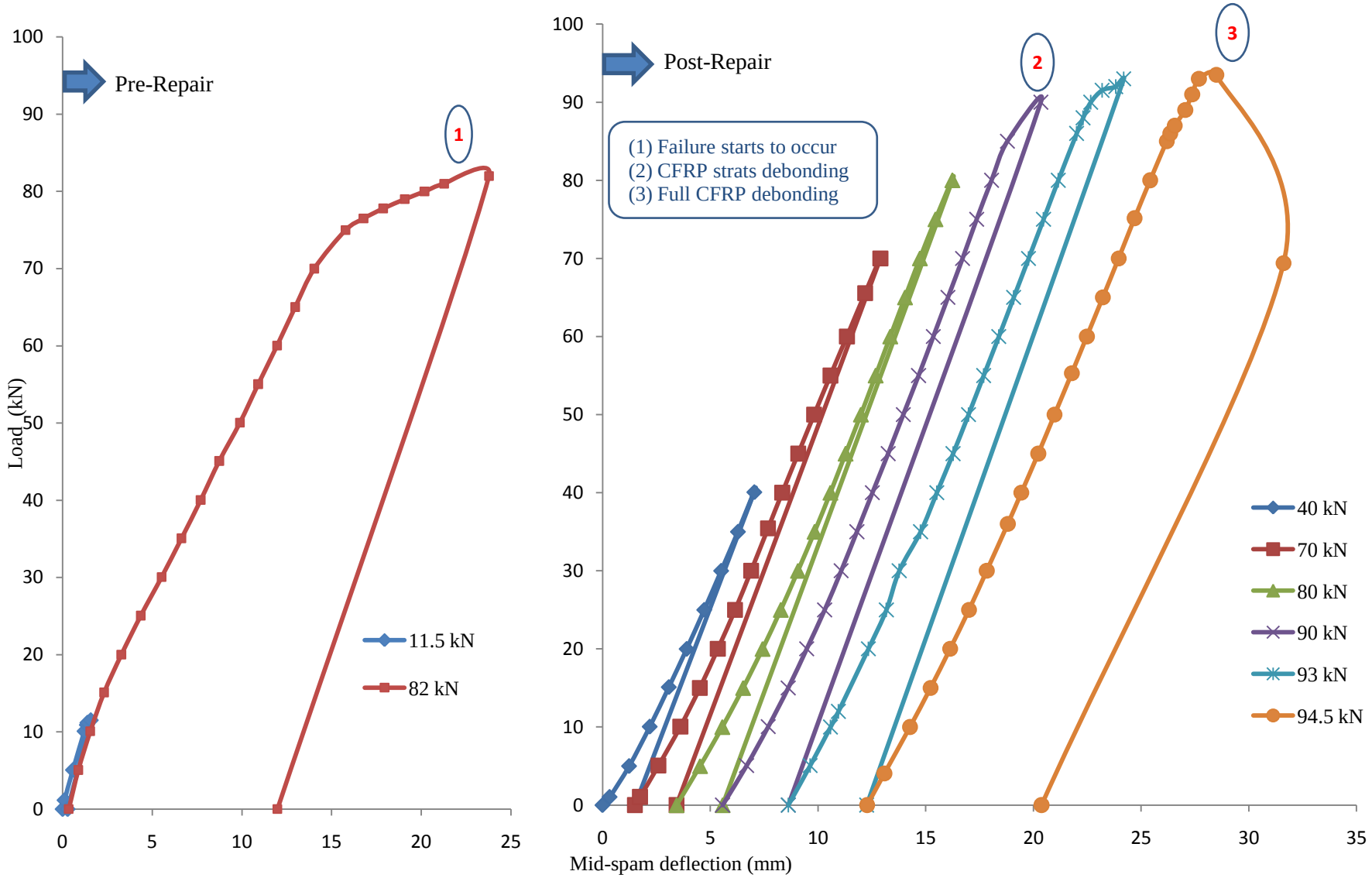

Figure 6.37. Load against mid-span deflection at pre and post repair stages for beam B114m

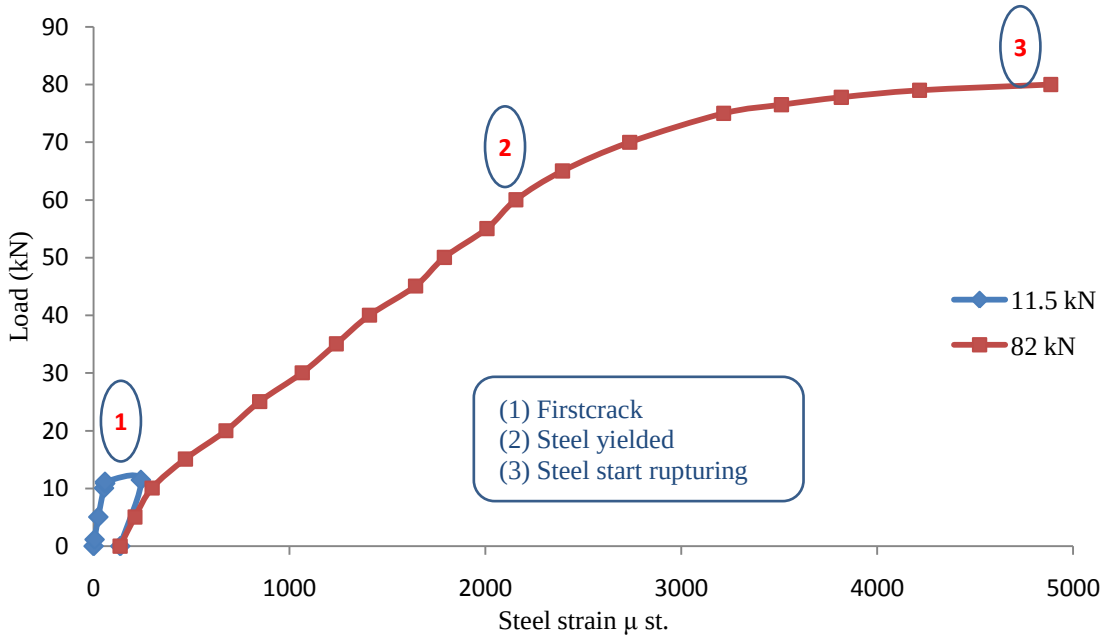

Figure 6.38. Load against mid-span steel strain at pre-repair stage for beam B114m

6.2.2.2 Dynamic evaluation

This section discusses the use of the modal parameters to highlight the effectiveness of the CFRP repair system. The change in the modal parameters by the damage induced at the pre-repair stage and the recovery of the modal parameter by fixing the externally bonded CFRP sheets at the post-repair stage is monitored. In order to highlight the change in the modal parameters, the frequency based stiffness index and the damping change as indirect stiffness indicator are adopted.

6.2.2.2.1 Beam B112m

Frequency based stiffness index and damping change data for beam B112m is highlighted at the stages illustrated in Table 6.14. The frequency based stiffness index values for all the considered modes and weighted average values according to PWM are shown in Figure 6.39.

Table 6.14. Stages considered for the dynamic evaluation of beam B112m

Notation	Remark
C	Undamaged stage
D	Pre-repair damaged stage
R0H	Immediately after turning the beam over after repair
R24H	24 hours after turning the beam over after repair
RD	Subjected to pre-repair damage load

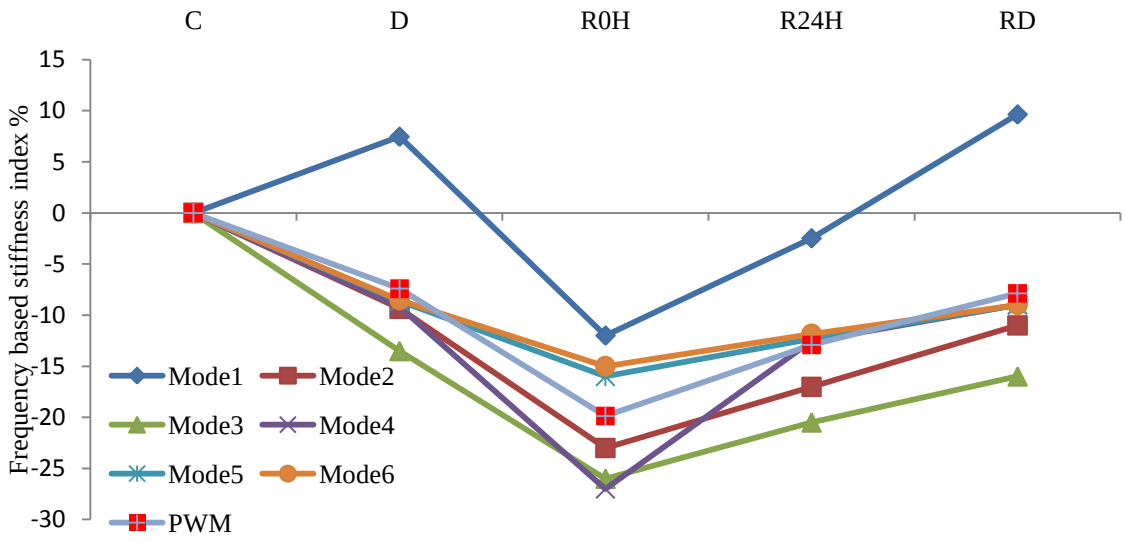

Figure 6.39. Frequency based stiffness index and weighted average (PWM) results for beam B112m

The results show that all the modes indicate a decrease in frequency based stiffness index value when the beam is subjected to damage at the pre-repair damage stage with the exception of Mode 1 which indicates an increase as a result of the composite action phenomenon of RC beams. All of the modes indicate a decrease in the frequency based stiffness index values at stage R0H, which are influenced by the composite action phenomenon of repaired RC beams due to repairing the beam and according to the laboratory repair procedure. When the beam self weight influences the adhesive layer, all the modes indicate an increase in the index values when compared to stage R0H. All the modes show an increase in the index values, after subjecting the repaired beam to load at stage RD, which indicates an increase in the overall stiffness by activation of the adhesive bond stiffness.

Since the results show a different stiffness change trend at different modes and in order to highlight the overall stiffness change, the weighted average (PWM) is calculated based on the considered modes and the results are shown in Figure 6.39. The overall stiffness shows a decrease at the pre-repair damage stage which is influenced by the concrete stiffness deterioration. The overall stiffness indicates a further decrease at stage R0H which is influenced by the effect of the composite action phenomenon of repaired RC beams. The beam self weight influences the adhesive layer and activates the adhesive bond at stage R24H. Thus, the stiffness increases whilst a stiffness recovery of 6.95% compared to stage R0H is observed. Subjecting the repaired beam to design load at stage RD helps to increase the tension interaction force which increases the adhesive bond stiffness. Subsequently the overall stiffness increases further with a stiffness recovery of 12% compared to stage R0H.

The damping change is calculated for the same stages illustrated in Table 6.14, and the results are shown in Figure 6.40. The results show that damping change has a different trend at different modes, where all the modes show an increase in the damping values at pre-repair damage stage indicating deterioration in the stiffness except for Modes 3 and 4 which show decreases in the damping values. After repair the beam at stage R0H, all the modes show a decrease in the damping values indicating an increase in the overall stiffness. The beam self weight influences the adhesive layer at stage R24H and all the modes show an increase in the damping values as compared to stage R0H. Subjecting the repaired beam to a load at stage RD shows that all the modes indicate a further increase in the damping values as compared to stage R0H except for Mode 5 which shows a decrease. The weighted average (PWM) is calculated in order to formulate the trend of the stiffness changing based on all the considered modes and the results are shown in Figure 6.40. The results show that the damping increases at the pre-repair

damage stage which indicates stiffness deterioration. Then damping decreases after fixing the CFRP sheets at stage R0H which indicates stiffness increase, where the stiffness recovery is 18% compared to stage D. When the beam self weight influences the adhesive layer, after turned the beam over again to its original position, that is, beam soffit at the tension face, a slight increase in the damping is observed which indicates a stiffness decrease, where the stiffness recovery is only 14.1% compared to stage D. Subjecting the repaired beam to load at stage RD results in a further increase in the damping, which indicates a stiffness decrease as compared to stages R0H and D.

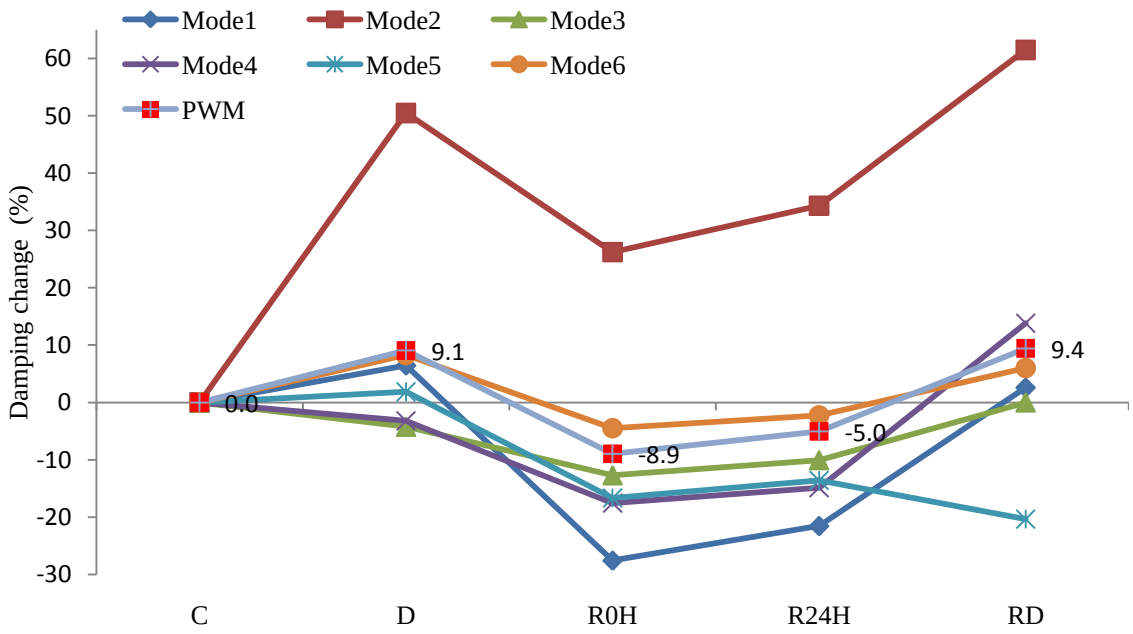

Figure 6.40. Damping change and weighted average (PWM) results for beam B112m

6.2.2.2.2 Beam B113m

The frequency based stiffness index and damping change data for beam B113m are highlighted at the stages shown in Table 6.15. The frequency based stiffness index and weighted average (PWM) results for each stage are shown in Figure 6.41. The results show that all the modes indicate a decrease in frequency based stiffness index values

when the beam is subjected to damage load at the pre-repair damage stage. This is true for all except for Mode 1 which indicates an increase as results of the composite action phenomenon of RC beams. At stage R0H, all the modes indicate a decrease in the frequency based stiffness index values which are influenced by the composite action phenomenon of repaired RC beams. Following this, when the beam self weight influences the adhesive layer at stage R24H, all the modes indicate an increase in the index values compared to stage R0H.

Table 6.15. Stages considered for the dynamic evaluation of beam B113m

Notation	Remark
C	Undamaged stage
D	Pre-repair damaged stage
R0H	Immediately after turning the beam over after repair
R24H	24 hours after turning the beam over after repair
RDL	Subjected to the design load
RD	Subjected to pre-repair damage load

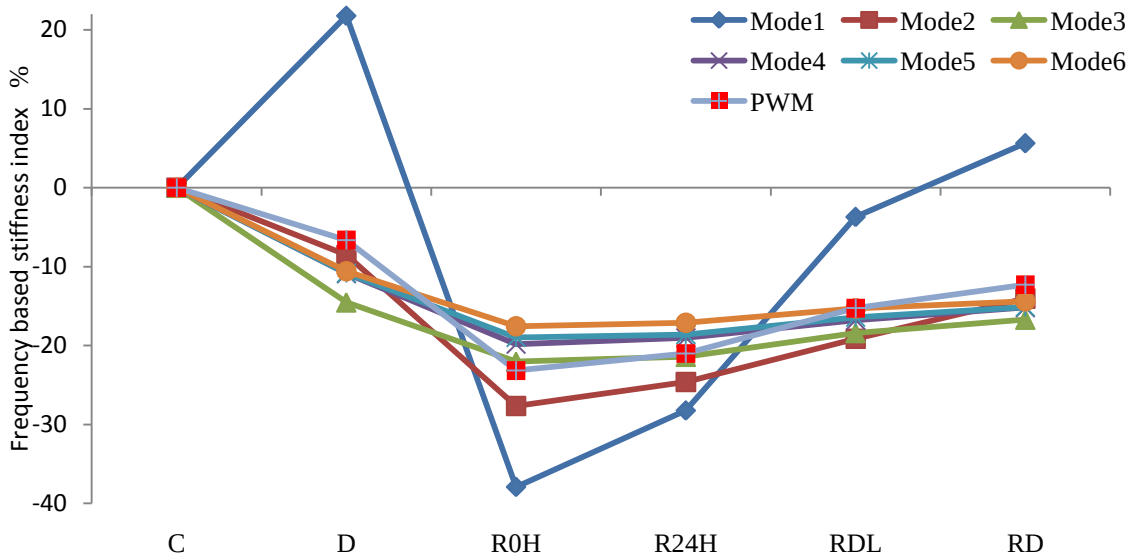

Figure 6.41. Frequency based stiffness index and weighted average (PWM) results for beam B113m

After subjecting the repaired beam to load at stage RDL, all the modes show a further increase in the index values which indicates an increase in the stiffness as a result of the

activation of the adhesive bond stiffness. Subjecting the repaired beam to further load at stage RD results in a further increase in the index values; a direct result of the increase in the adhesive bond stiffness. Mode 1 is the most affected by the activation of the adhesive bond stiffness. The results show that different modes exhibit different stiffness change and in order to highlight the overall stiffness change, the weighted average (PWM) of the frequency based stiffness index is calculated and the results are shown in Figure 6.41. The index shows a decrease at the pre-repair damage stage (D) which indicates a stiffness decrease as a result of the concrete stiffness deterioration. When the beam is repaired at stage R0H, the index shows a decrease as compared to stage D, which indicates a stiffness decrease due to the composite action phenomenon of repaired RC beams. At stage R24H the beam self weight influences the adhesive layer and activates the adhesive bond which results in increasing the index value and thus a stiffness recovery of 2.2% as compared to stage R0H is observed. Subjecting the repaired beam to load at stage RDL assists in increasing the activation of the adhesive bond stiffness, and subsequently increases the overall stiffness where a stiffness recovery of 7.9% as compared to stage R0H is observed. At stage RD when the beam is subjected to further loading, the tension interaction forces increase which further activates the adhesive bond stiffness. Thus, the overall stiffness indicates a further increase of 10.9% as compared to stage R0H.

The damping change is calculated for the same selected stages for the frequency based stiffness index, and the results are shown in Figure 6.42. The results show that damping change has different trends at different modes. At the pre-repair damage stage all the modes show an increase in the damping values which indicates stiffness deterioration. After repair of the beam with CFRP sheets, all the modes show a decrease in the damping values which indicates an increase in overall stiffness. When the beam self

weight influences the adhesive layer at stage R24H, a slight increase in the damping values, as compared to stage R0H, is observed. Subjecting the repaired beam to a load at stage RDL results in a further increase in the damping values, as compared to R0H, for all the modes except for Mode5. When the beam is subjected to a further load at stage RD, all the modes indicate a further decrease in the damping values, as compared to stage R0H, except for Mode 6.

The weighted average (PWM) is calculated in order to formulate the trend of the overall stiffness change based on all the considered modes and the results are shown in Figure 6.42. The results show that the at the pre-repair damage stage, the damping is increased which indicates stiffness decrease. Following the fixing of the CFRP sheets at stage R0H, the damping is decreased which indicates stiffness increase where the stiffness recovery is 16% as compared to stage D. When the beam self weight influences the adhesive layer at stage R24H, a slight increase in the damping is observed which indicates a stiffness decrease where the stiffness recovery becomes 10.4% compared to stage D. Subjecting the repaired beam to load at stages RDL and RD results in a further increase in the damping which indicates a stiffness decrease.

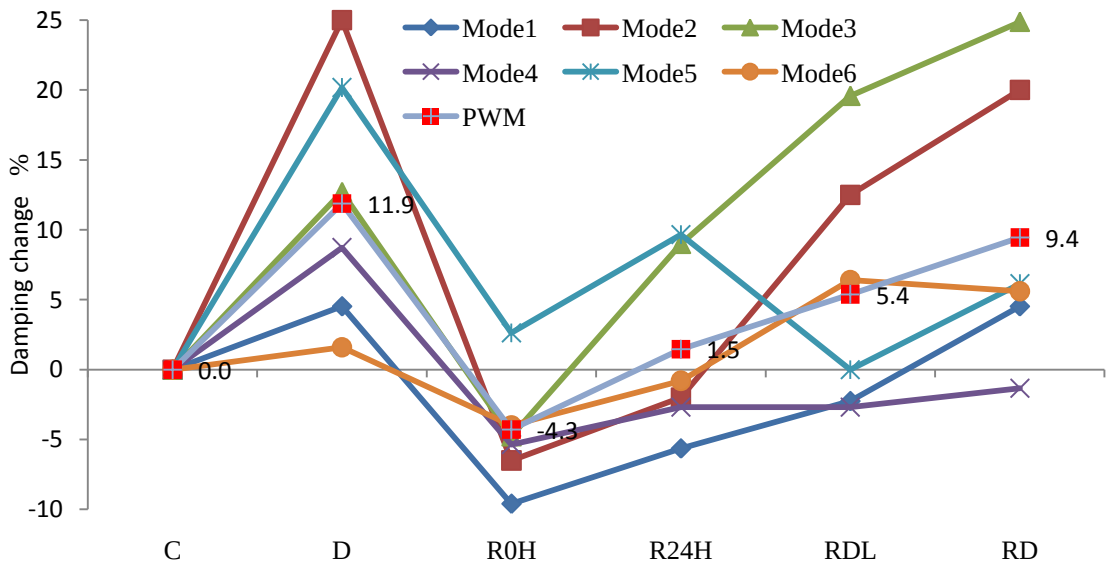

Figure 6.42. Damping change and weighted average (PWM) results for beam B113m

6.2.2.2.3 Beam B114m

The dynamic data for both frequency based stiffness index and damping change for beam B114m are highlighted at the stages illustrated in Table 6.16. The frequency based stiffness index values at each stage are shown in Figure 6.43. The results show that all the modes indicate a decrease in frequency based stiffness index when the beam is subjected to damage load at the pre-repair damage stage except for Mode 1 which indicates an increase due to the effect of the composite action phenomenon of repaired RC beams. All the modes indicate a decrease in the index value at stage R0H, which is influenced by the composite action phenomenon of repaired RC beams except for Mode 5 which indicates an increase. When the beam self weight influences the adhesive layer at stage R24H, all the modes indicate an increase in the index values as compared to stage R0H. After subjecting the repaired beam to load at stage RDL, all the modes show a further increase in the index values which indicates an increase in the stiffness due to activation of the adhesive bond stiffness. Subjecting the repaired beam to further loading at stage RD results in a further increase in the index values which is due to the increase of the adhesive bond stiffness. Mode 1 is most affected by the activation of the adhesive bond stiffness.

The results show that different modes exhibit different stiffness changes and in order to highlight the overall stiffness change, the weighted average (PWM) is calculated and the results are shown in Figure 6.43. The overall stiffness, as indicated by the frequency based stiffness index, shows a decrease at the pre-repair damage stage which is influenced by the concrete stiffness deterioration. At stage R0H, the overall stiffness indicates a further decrease which is due to the effect of the composite action phenomenon of repaired RC beams. When the beam self weight influences the adhesive layer at stage R24H, the adhesive bond is activated, thus after increasing the stiffness, a stiffness recovery of 1.6% as compared to stage R0H is observed. Subjecting the

repaired beam to load at stage RDL helps to increase the activation of the adhesive bond stiffness, and subsequently increases the overall stiffness where the stiffness recovery becomes 3.64% compared to stage R0H. At stage RD, the tension interaction force increases which in turn increases the activated adhesive bond stiffness, and subsequently increases the overall stiffness.

Table 6.16. Stages considered for the dynamic evaluation of beam B114m

Notation	Remark
C	Undamaged stage
D	Pre-repair damaged stage
R0H	Immediately after turning the beam over after repair
R24H	24 hours after turning the beam over after repair
RDL	Subjected to the design load
RD	Subjected to pre-repair damage load

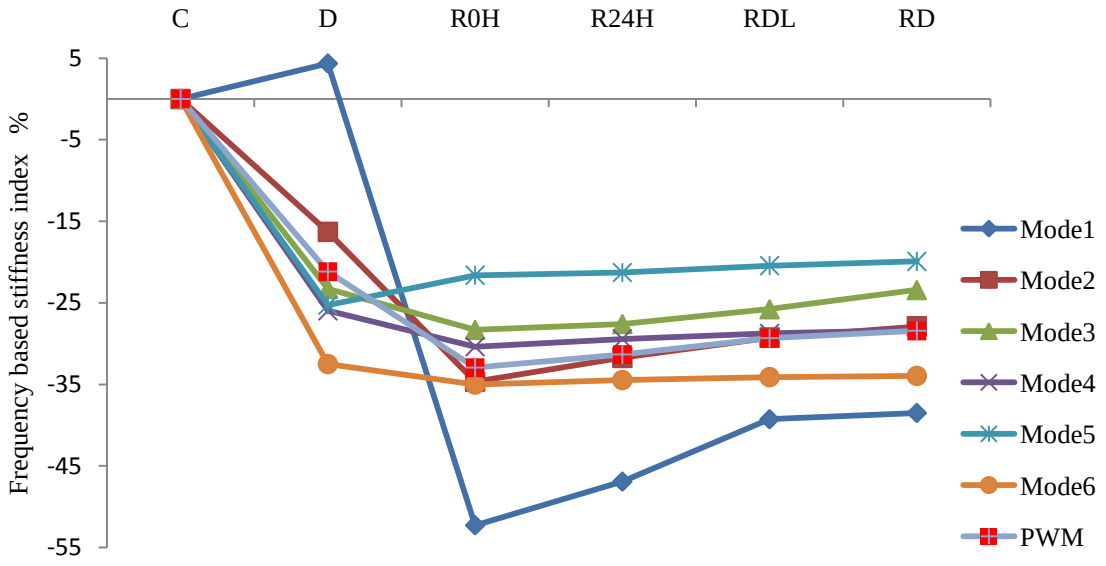

Figure 6.43. Frequency based stiffness index and weighted average (PWM) results for beam B114m

The damping change is calculated at the same selected stages for the frequency based stiffness index, and the results are shown in Figure 6.44. The results show that damping change has different trends at different modes. All the modes show an increase in the damping values at pre-repair damage stage which indicates stiffness deterioration. After

repairing the beam with CFRP sheets at stage R0H, all the modes show a decrease in the damping values which indicates an increase in overall stiffness. When the beam self weight influences the adhesive layer at stage R24H, this results in an an increase of the damping values compared to stage R0H. Modes 1 and 6 indicate a further increase in the damping values at stage RDL compared to stage R0H, whilst Modes 2, 3, and 4 indicate no change. Mode 5 on the other hand, indicates a decrease in the damping value. At stage RD, all the modes indicate a further decrease in the damping values after compared to stage R0H, with the exception of Mode 6 which indicates a slight increase. The weighted average (PWM) is calculated in order to obtain the overall stiffness change trend based on all the considered modes and the results are shown in Figure 6.44. The results show that the overall stiffness, as indicated by the weighted average of the damping change, shows a decrease at the pre-repair damage stage. After fixing the CFRP sheets at stage R0H, the result shows an increase in the stiffness where the stiffness recovery is 8.3 % as compared to stage D. When the beam self weight influences the adhesive layer, a slight decrease in the stiffness is observed where the stiffness recovery becomes 5.75 % as compared to stage D. Subjecting the repaired beam to load at stages RDL and RD results in a further decrease in the stiffness.

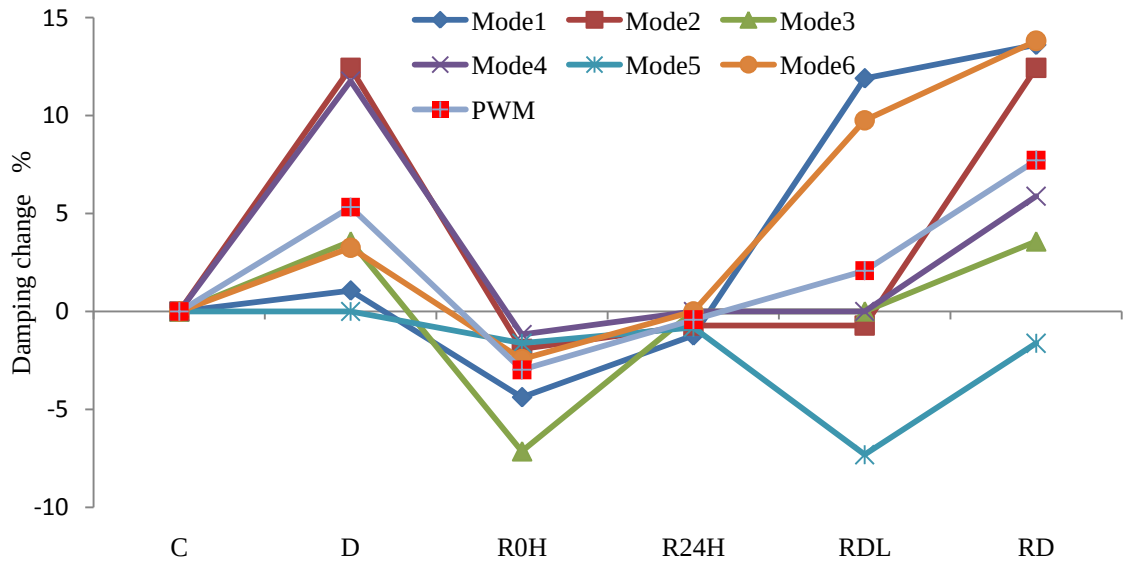

Figure 6.44. Damping change and weighted average (PWM) results for beam B114m

6.2.2.3 CFRP repair effectiveness

This section highlights the relationship between static and dynamic data for the effectiveness of the CFRP repair system for different pre-repair damage levels and for flexural beams designed according to ρ_{max}. The stiffness recovery based on the static data is calculated based on the ratio of the increase in the ultimate capacity of the repaired sections to the ultimate capacity of the unrepaired sections. The stiffness effectiveness based on the dynamic data is calculated based on both frequency based stiffness index and damping change. For frequency based stiffness index, the repair effectiveness is calculated as the stiffness recovery of the repaired beam after being subjected to a load equal to the design load compared to the stiffness at the stage immediately after turning the beam over to its original position. For the damping change, the repair effectiveness is calculated as the stiffness recovery of the repaired beam at 24 hours after turning the beam over to the stiffness at pre-repair damage stage. Figure 6.45 shows the repair effectiveness based on the static and dynamic data and corresponding to the damage levels of beams B112m, B113m, and B114m.

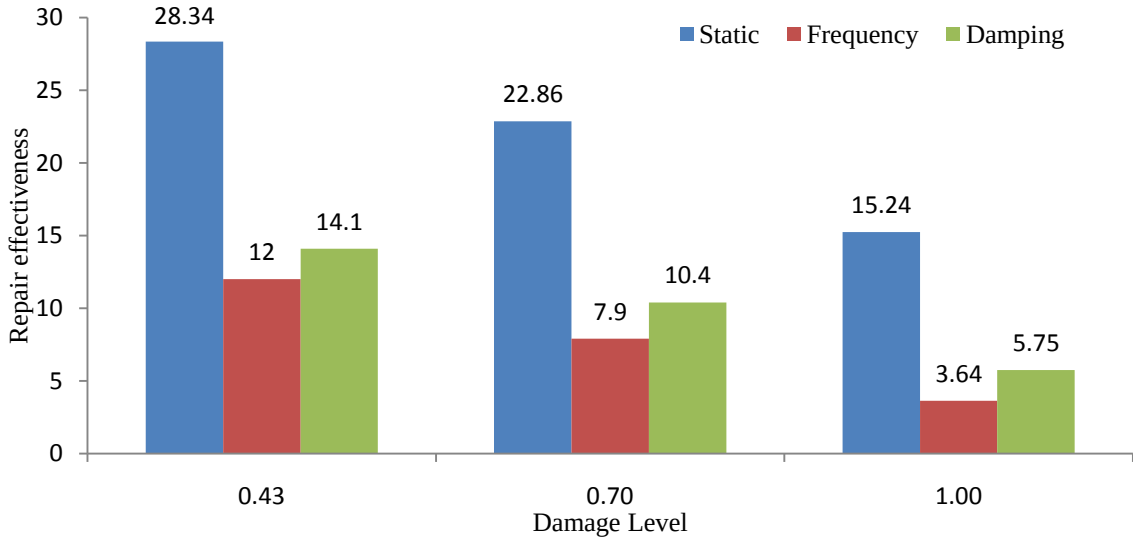

Figure 6.45. CFRP repair effectiveness based on static and dynamic data for ρ_{max} group

The results show that fixing of the CFRP sheets as flexural repair system for flexural beams with ρ_{max}, is effective regardless of the pre-repair damage level. The increase in

the load capacity depends on the pre-repair damage level which is compatible with the findings of Benjeddou et al. (2007) and Hudson and Darwin (2005). For damage level of 43% which is close to the design load limit, the repair with CFRP sheets increases the ultimate capacity by 29% and the corresponding stiffness recovery is 12% and 14.1% based on frequency based stiffness index and damping change, respectively. For pre-repair damage level of 100%, the increase in the load capacity is limited to 15.3% with corresponding stiffness recovery of 3.64% and 5.75% based on frequency based stiffness index and damping change, respectively. The increase in the ultimate load capacity for repaired flexural beams design according to ρ_{max} of 15.3% to 28.4% is in good agreement with the literature where an increase of 10% to 28% was obtained by El-Ghandour (2011) and Rahimi and Hutchinson (2001) for strengthening case with 0% pre-repair damage level, and an increase of 23% was obtained by Büyüköztürk and Hearing (1998) for repair case.

6.2.2.4 Monitoring of repaired beams

This section reports the results obtained during monitoring of the repaired beam under loading up to failure in order to highlight its behaviour during the service life of the structures. The failure modes of the repaired beams with externally bonded CFRP sheets are also reported. The monitoring focuses on the trend of the bending frequencies at different load cycles in order to highlight the behaviour at higher loading levels, and to predict the early steps of the CFRP debonding and the full debonding using the bending frequencies. The frequency based stiffness index is used to monitor the stiffness change corresponding to the applied load, and the datum stiffness based on the stiffness after turning the beam over, that is, stage R0H. Table 6.17 presents the applied load and notations used to plot the frequency based stiffness index values as shown in Figure 6.46 for beam B112m.

Table 6.17. Load cycles for post-repair stage for beam B112m

Load (kN)	Notations	Remark
0	R0H	Immediately after turning the beam over after repair
0	R24H	24 hours from turning the beam over after repair
40	RD	Subjected to pre-repair damage load
50	R50	
60	R60	
80	R80	
100	R100	
120	R120	
115	R115D	Full CFRP debonding and failure

The results show that Modes 2 to 6 indicate an increase in the frequency based stiffness index and up to stage RD which are affected by the activation of the adhesive bond, and then begin to indicate a decrease at further stages due to the effect of the concrete stiffness deterioration which is in turn due to the appearance of new cracks as shown in Table 6.9. The stiffness deterioration indicated by Modes 2 to 6 is small until stage R100 after which it shows a more significant decrease, which indicates the beginning of the CFRP debonding. Beyond stage R120 there is a rapid decrease in the frequency based stiffness index values, which indicates the full debonding of the CFRP sheets.

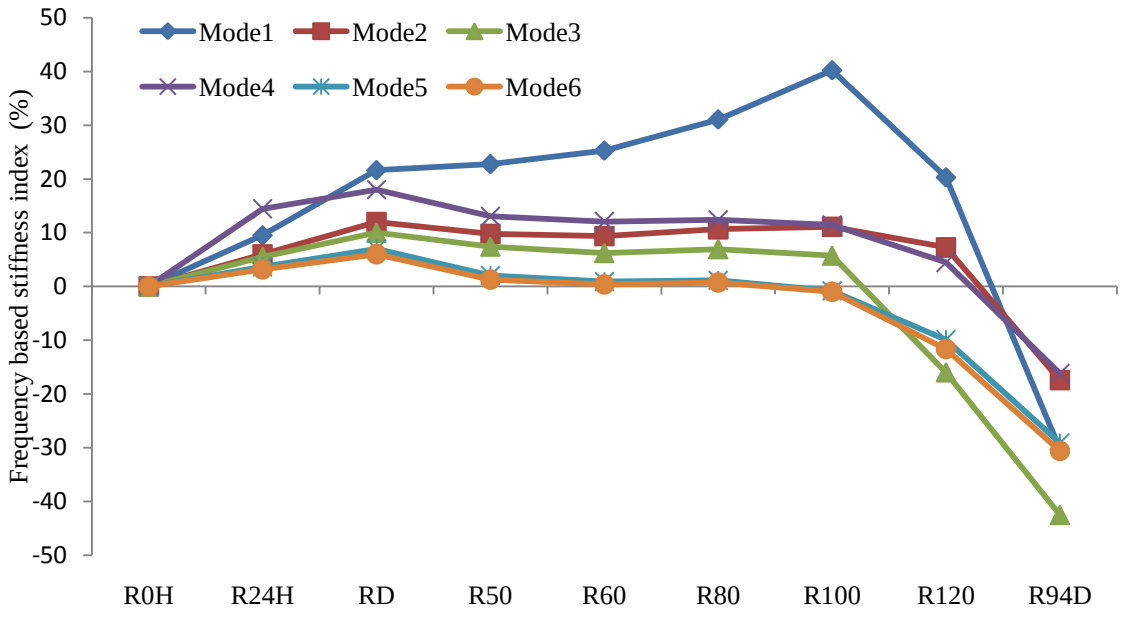

Figure 6.46. Frequency based stiffness index values for the monitoring of beam B112m

Mode 1 shows a rapid increase in the index value at stage R24H and at stage RD by activation of the tension interaction forces. A further increase is noted for further stages to reach the maximum increase at stage R100 which is affected by the increase in the tension interaction forces which activate the adhesive bond stiffness. When flexural cracks at mid-span induce intermediate cracks at the adhesive layer at the stage beyond R100, the first mode shows a decrease in the index value. Beyond stage R120, Mode 1 shows a rapid decrease in frequency based stiffness index value which indicates the full CFRP debonding. This highlights the first mode as an indicator for the CFRP sheet debonding, whereas for all the remaining modes the index starts to decrease when new cracks appear, with the exception of Mode 1 which only indicates a decrease when CFRP sheets begin to debond or are fully debonded.

The failure mode is an intermediate induced crack debonding, where the flexural cracks at the mid-span extend to the adhesive interface between the CFRP sheets and the concrete surface, thus inducing intermediate cracks which cause the full CFRP debonding at higher loading. Figure 6.47 shows the actual cracks in the beam at stage R120, where intermediate induced cracks appear in the adhesive layer, and at stage R115D when the full CFRP debonding occurs.

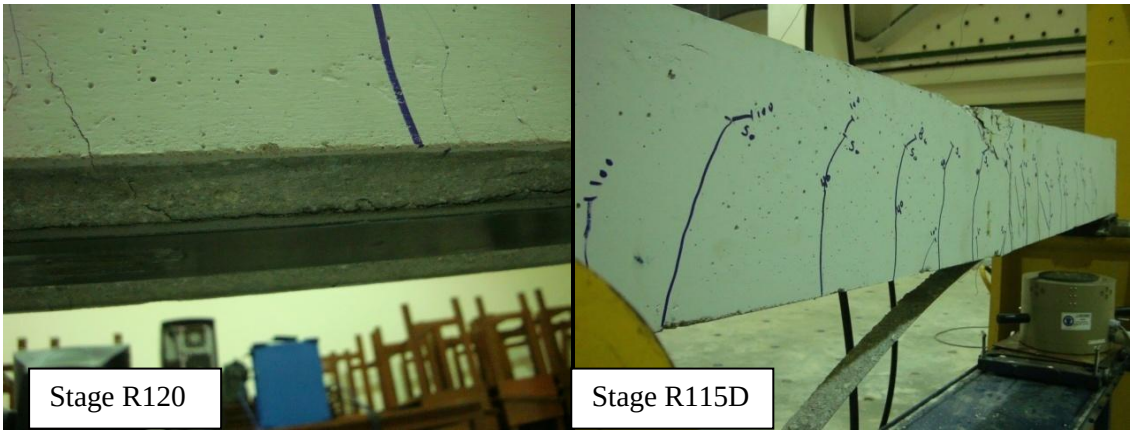

Figure 6.47. Induced IC debonding and failure mode for beam B112m

Table 6.18 presents the applied load and notation used to plot the frequency based stiffness index as shown in Figure 6.48 for beam B113m. The results show that Modes 1 and 2 indicate a slight increase in the frequency based stiffness index values beyond stage RD which are affected by the activation of the adhesive bond. The increase continues until stage R100, after which the frequency based stiffness index shows a slight decrease, where the flexural cracks induce intermediate cracks at the adhesive layer. Following this a rapid decrease is noted at stage R124D indicating the full CFRP debonding. Modes 3 to 6 show a slight increase in the frequency based stiffness index values beyond stage RD until stage R80, which are affected by the activation of the bond stiffness and limitation of concrete deterioration. Modes 3 to 6 show a gradual decrease beyond stage R80 and until stage R100, where rapid decrease is noted indicating the full CFRP debonding. Modes 1 and 2 can be indicators for predicting the onset of the intermediate crack debonding prior to full debonding, where both modes only indicate a decrease in the index values beyond stage R100 when intermediate cracks are induced into the adhesive layer.

Table 6.18. Load cycles for post-repair stage of beam B113m

Load (kN)	Notation	Remark
0	R0H	Immediately after turning the beam over after repair
0	R24H	24 hours from turning the beam over after repair
40	RDL	Subjected to design load
70	RD	Subjected to pre-repair damage load
80	R80	
100	R100	CFRP starts debonding
124.7	R124D	Full CFRP debonding

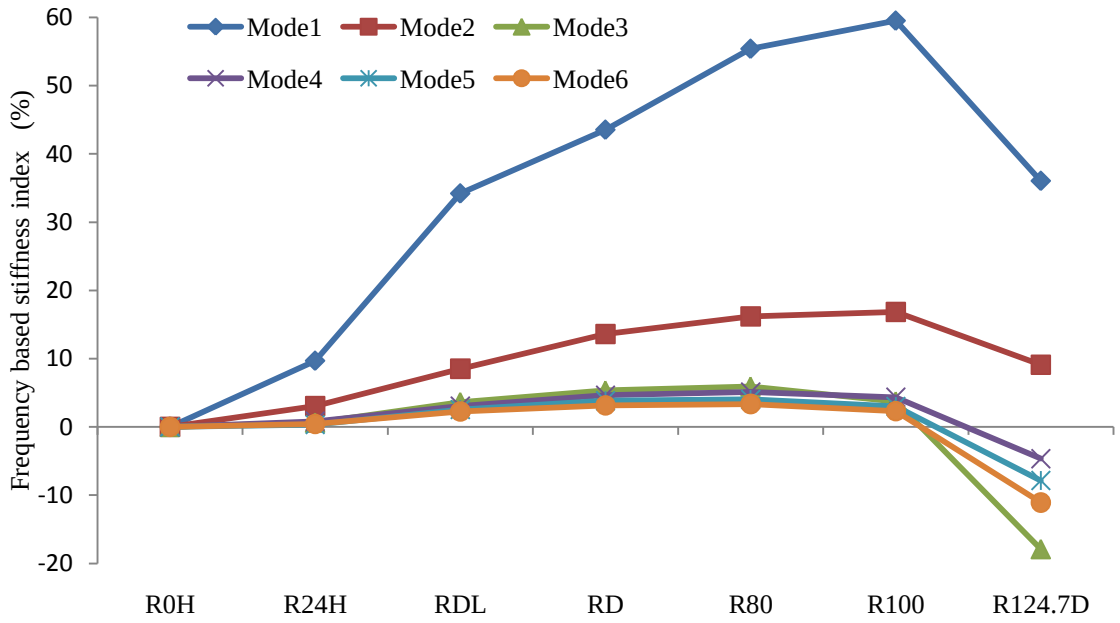

Figure 6.48. Frequency based stiffness index values for the monitoring of beam B113m

The failure mode is an intermediate induced crack debonding, where the flexural cracks at the mid-span extend to the adhesive interface between the CFRP sheets and the concrete surface, to induce intermediate cracks which cause the full CFRP debonding at higher loading. Figure 6.49 shows the intermediate induced cracks which appear in the adhesive layer at stage R100, and the full CFRP debonding at stage R124D.

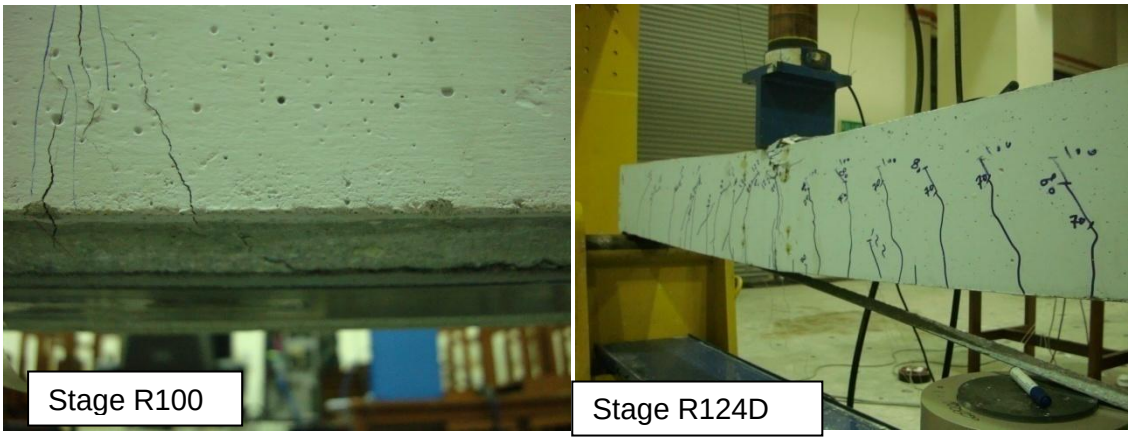

Figure 6.49. Induced IC debonding and failure mode for beam B113m

Table 6.19 presents the applied load and notations used to plot the frequency based stiffness index change for beam B114m as shown in Figure 6.50. The results show that for all the modes the frequency based stiffness index starts to decrease at stage R90

which is due to the influence of the appearance of the induced intermediate crack at the adhesive layer. Following this, a further decrease is noted at stage R93 when more cracks appear at the adhesive layer. A rapid decrease in the frequency based stiffness index values is noted when CFRP full debonding occurs at stage R94D. The concrete stiffness deterioration beyond stage RD is limited where only 2 cracks appear, thus all the modes are governed by the activation of the adhesive bond stiffness until stage R90, after which the intermediate cracks are induced into the adhesive layer.

Table 6.19. Load cycles for post-repair stage of beam B114m

Load (kN)	Notation	Remark
0	R0H	Immediately after turning the beam over after repair
0	R24H	24 hours from turning the beam over after repair
40	RDL	Subjected to design load
82	RD	Subjected to pre-repair damage load
90	R90	
93	R93	CFRP starts debonding
94.5	R94D	Full CFRP debonding

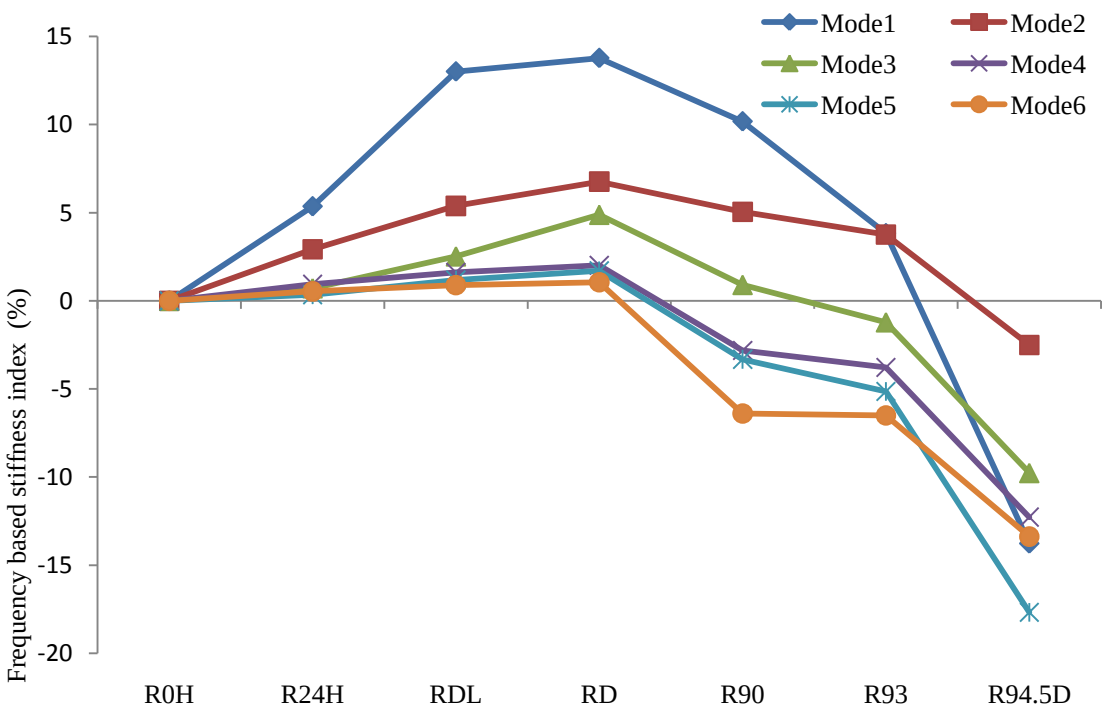

Figure 6.50. Frequency based stiffness index for the monitor of beam B114m

The failure mode is an intermediate induced crack debonding, where the flexural cracks at the mid-span extend to the adhesive interface between the CFRP sheets and the concrete surface, to induce intermediate cracks which cause the full CFRP debonding at higher loading. Figure 6.51 shows the intermediate induced cracks which appear in the adhesive layer at stage R90, and the full CFRP debonding at stage R94D.

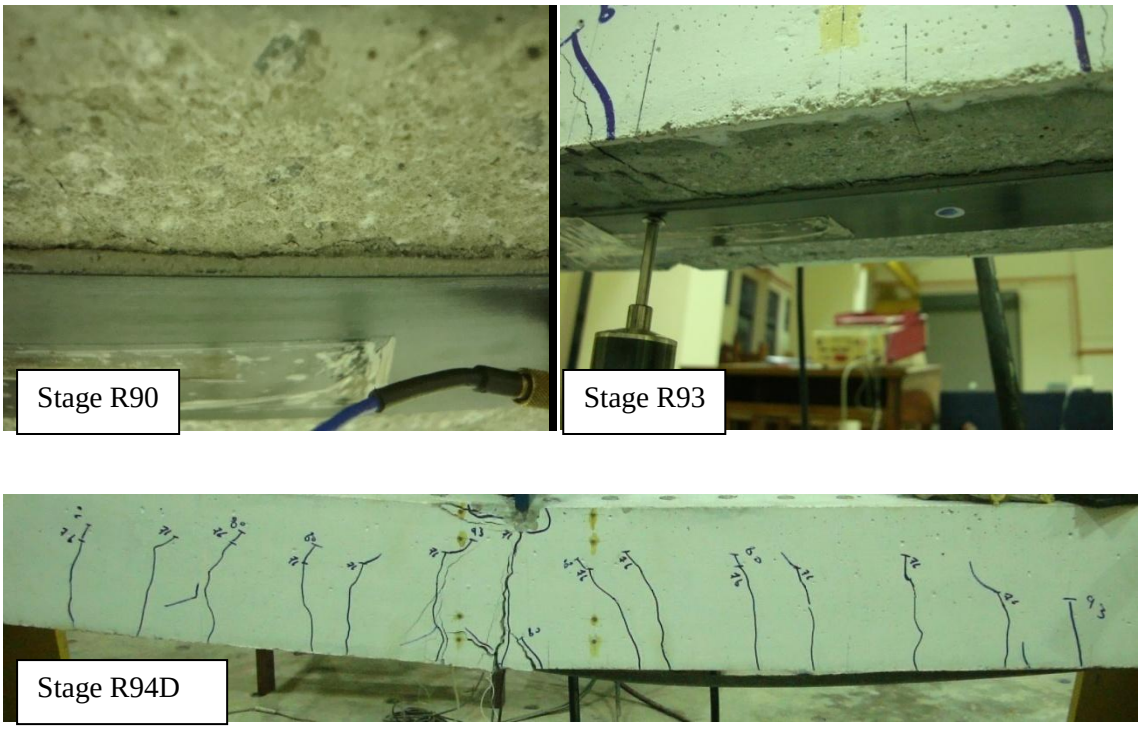

Figure 6.51. Induced IC and failure mode for beam B114m

The results during monitoring stages of the CFRP repaired RC beams show that the trend of the modes depend on the pre-repair damage levels. For low pre-repair damage levels the concrete stiffness deterioration has limited influence at the pre-repair stage due to the small number of cracks as in beam B112m. Thus, at the post-repair stage the concrete stiffness deterioration starts at low loading levels and has a bigger influence than the activation of the adhesive bond stiffness on most of the bending modes accept for Mode 1 which is influenced by the activation of the adhesive bond stiffness.

For intermediate pre-repair damage levels, the concrete stiffness deterioration is greater at the pre-repair stage, which means that the concrete stiffness deterioration at the post-repair stage has less of an influence on the bending modes while the adhesive bond stiffness activation is influenced by both Modes 1 and 2. For extreme pre-repair damage level, the concrete stiffness deterioration reaches high levels at the pre-repair stage, which results in limited concrete stiffness deterioration at the post-repair stage. Thus the effect on the bending frequencies is smaller when compared to adhesive bond stiffness activation. The failure of the CFRP repaired flexural beams designed with ρ_{max} is governed by the intermediate crack debonding which is in good agreement with the findings of Büyüköztürk and Hearing (1998), and different from the failure observed by Benjeddou et al. (2007) which was peeling of CFRP sheets at the ends.

6.2.3 Effect of steel ratio

This section summaries the influence of the design criteria with respect to the design steel ratio, on the effectiveness of the CFRP repair system. It highlights the effect of the steel ratio on the increase of the load capacity, the repair effectiveness based on the frequency based stiffness index recovery, the repair effectiveness based on the damping change recovery, and the failure mode.

The privided ρ_{min} is 0.006 and ρ_{max} is 0.0131, where ρ_{min} and ρ_{max} according to the ACI 318 (2008) design code is 0.003 and 0.0136, respectively. According to the ACI 440.2R (2002) design code, the beams with the minimum steel ratio are repaired using 100mm width of the CFRP sheets, while the beams with the maximum steel ratio are repaired using 50 mm width CFRP sheets. The minimum steel group beams increase the capacity of the repair with CFRP sheets to withstand higher load capacity compared to the maximum steel group. When the pre-repair damage load equals the design load, the increase in load capacity for minimum and maximum steel group beams is 84.5% and

28.3%, respectively. The big difference between used ρ_{min}, that is, 0.006, and the balanced steel ratio of 0.0182 according to the ACI 318 (2008) design code, gives the repaired beams the ability to increase the load capacity by 49 to 84.5%. On the other hand, the small difference between used ρ_{max}, that is, 0.0131, and the balanced steel ratio, 0.0182, is that the repaired beams have less ability to increase in the load capacity where a limited increase of 15.3 to 28.4% is observed. The load capacity increases for both ρ_{min} and ρ_{max} group beams. This is in good agreement with previous work, as reported by Benjeddou et al. (2007) who found that the increase in the load capacity after repairing with externally bonded CFRP sheets was between 40 to 87% for beams designed with a steel ratio between the ρ_{min} and ρ_{max}.

The effect of the pre-repair damage levels on the increase of the load capacity is affected by the design requirements of the steel ratio. The effect of the pre-repair damage level which equals the steel yield load, on the increase in the load capacity for ρ_{min} beams, is higher when compared to the ρ_{max} beams. The effects of pre-repair damage level which equals the failure load, on the increase in the load capacity, is higher for the maximum steel beams. Thus, the repair effectiveness of the RC beams depends on the ratio of the steel provided to the balanced steel and this is in good agreement with the work of Rahimi and Hutchinson (2001).

Frequency based stiffness index values show that the ρ_{max} group has higher recovery stiffness than ρ_{min}, which is due to the width effect of the CFRP sheet on the composite action phenomenon of repaired RC beams. For ρ_{min} the 100mm CFRP sheets width increases the area affected by the compression interaction force compared to ρ_{max} where only 50mm CFRP width is used. After turning the beam over to its original position, tension interaction force starts to develop under the effect of the beam self weight or subsequent applied loads and is the same for both ρ_{min} and ρ_{max}. Thus higher

compression interaction force due to CFRP width for ρ_{min} group, results in lower recovery compared to ρ_{max} group.

Existence of the flexural cracks at pre-repair damage stage for both steel ratios governs the failure mode and is due to intermediate induced crack debonding, where the flexural cracks influence the adhesive layer and induce intermediate cracks. The cracks propagate to cause debonding at higher load levels.

6.3. Shear damage at quarter-span

This section presents the results related to the repair effectiveness of the CFRP sheets for shear damage located at quarter-span from left support. Two groups are used according to the design criteria, one is designed with internal shear stirrups where the shear forces are resisted by the stirrups and concrete. Another is designed without the internal shear stirrups where all the shear forces are resisted solely by the concrete. Each group is investigated at two pre-repair damage levels where the first level is the design limit load and the other is the maximum load at which failure occurs. The results presented are for the increase in ultimate load capacity, the stiffness recovery based on the frequency based stiffness index and the stiffness recovery based on the damping change. Moreover, the section presents the monitoring of the repaired beams to investigate its behaviour during its subsequent service life. The failure modes are discussed in detail.

6.3.1 Beams with stirrups

Beams B211q and B212q are used to investigate the repair effectiveness of CFRP sheet as shear repair system. The results cover the static evaluation where load against deflection, load against steel strain, and load against CFRP strain are highlighted. The dynamic evaluation highlights the stiffness recovery based on frequency based stiffness

index and damping change. The monitoring of the frequency based stiffness index results corresponding to load cycles at the post-repair stages is presented.

6.3.1.1 Static evaluation

For beam B211q which is designed with shear stirrups, Table 6.20 shows the load cycles and the corresponding number of cracks at pre and post repair stages. The load against deflection curves at pre-repair stage are presented in Figure 5.15 and at post-repair in Figure 6.52. The loads against steel strain curves at pre-repair stage are shown in Figure 5.16, and at the post-repair stage are shown in Figure 6.53. The deflection as shown in Figures 5.15 and 6.52 is the maximum measured deflection which is located at the zone between quarter-span and mid-span as discussed in Section 4.4.1. The steel strain presented in Figures 5.16 and 6.53 is the strain of the flexure steel bars located at quarter-span. The initial strain at post-repair stage is the remainder strain from the pre-repair damage stage where the beam is not turned over during the repair procedure, thus the remainder strain in the steel bars from the pre-repair damage stage is the datum for the steel strain at the post-repair. The crack patterns at pre and post repair stages are illustrated in Appendix B.

Table 6.20. Load cycles and corresponding number of cracks for beam B211q

Load Cycles (kN)	Number of cracks	Remark
20	1	First flexural crack
50	9	First shear crack
62	10	Diagonal shear crack
85	13	
99	16	Pre-repair stage
48	16	Post-repair stage
100	16	Steel yield stage
107	18	CFRP starts debonding
101	19	Failure

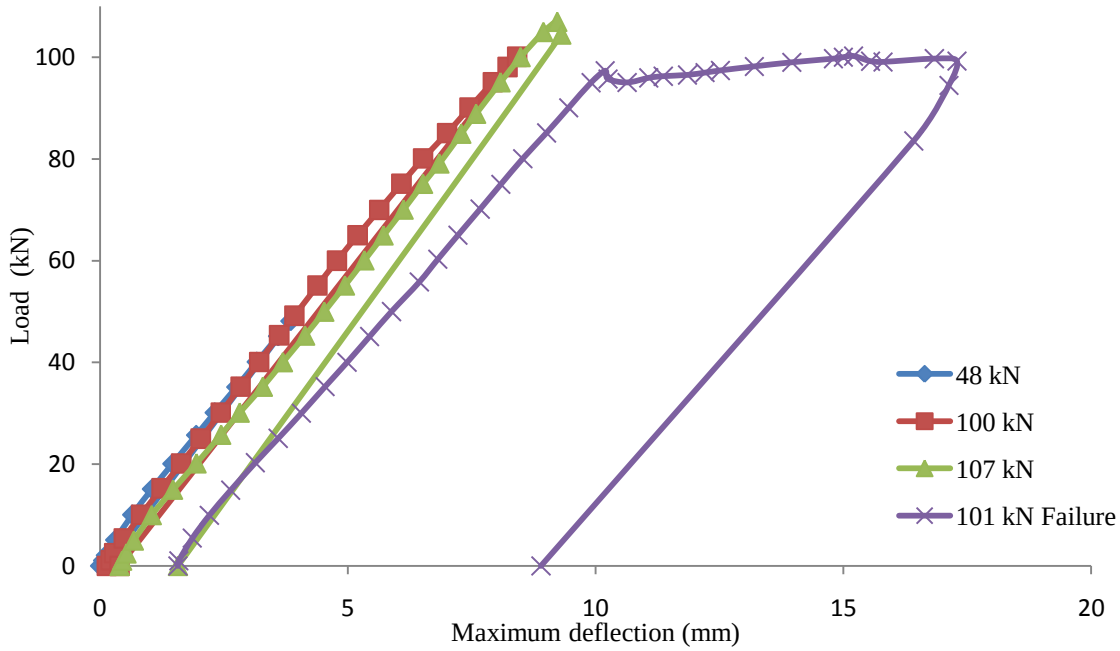

Figure 6.52. Load against maximum deflection at post-repair stage for beam B211q

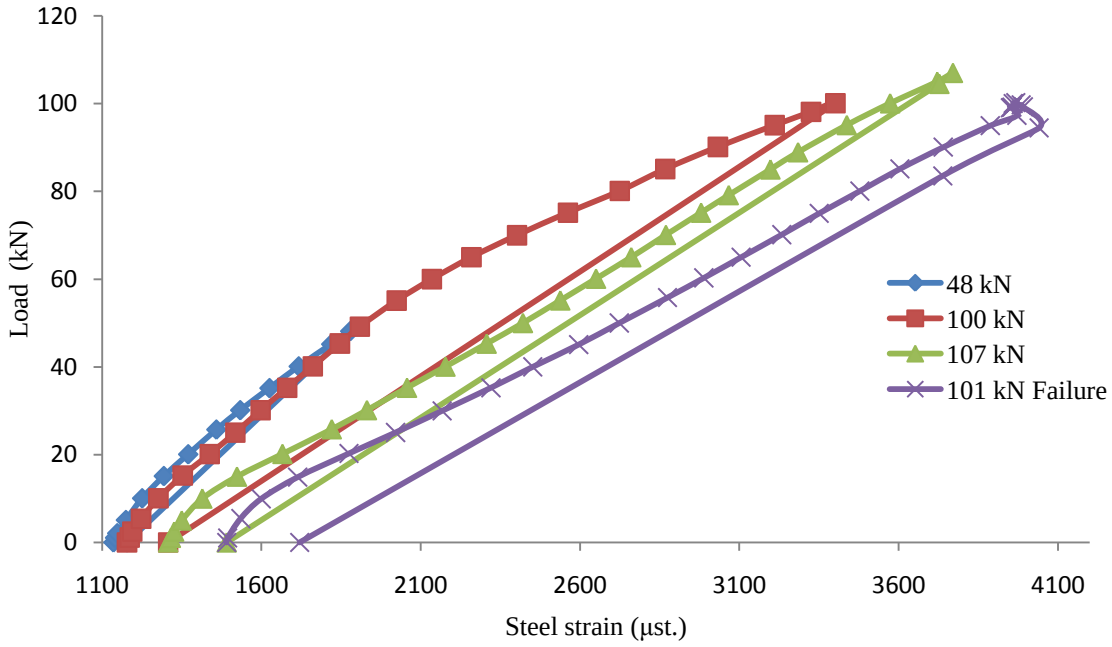

Figure 6.53. Load against quarter-span steel strain at post-repair stage for beam B211q

The results show that the beam is damaged under the failure load of 99 kN at pre-repair stage where the steel yields at 90 kN. The CFRP repair system for the shear damage at quarter-span is designed according to the ACI code and as mentioned in Section 4.3.2.2. After repair with externally bonded CFRP sheets, the beam is able to withstand a maximum load of 107 kN and failure begins to occur at the next load cycle at 101kN. The steel strain at post-repair stage reaches values smaller than the pre-repair damage

stage, where the presence of CFRP on both beam sides at the shear zone helps to absorb the stress together with the flexural steel. The increase in the load capacity equals the maximum capacity of the repaired beam (107kN) divided by the maximum capacity of the unrepaired beam (99kN) which is equal to 108.1%.

The CFRP strain is monitored on each one of the six used sheets on both sides of the damaged beam corresponding to the load cycles, where first strain gauge 'SG1' is the nearest to the quarter-span and the SG3 is the nearest to the supports. Figure 6.54 shows the results of the CFRP strain corresponding to each load cycle for strain gauges SG1, SG2 and SG3. The results show that the highest strain is recorded at the second strain gauge which is located between the support and the quarter-span, with maximum strains of 700μst which is still considered low compared to the ultimate CFRP strain. The first strain gauge records negative values which indicates a compression force due to the location of the strain gauge near the applied point load at low load levels. At higher load levels, first strain gauge starts to record positive strain values indicating tension forces along the CFRP sheet. The first strain gauge indicates that the CFRP sheet still resists the load without any release in the strain values up to failure, while second and third strain gauges indicate a release in the strain values beyond 100 kN which is due to the appearance of some cracks at the adhesive layer between the CFRP sheets and the concrete surface. The failure is a combination of flexural and CFRP delamination, where the flexural crack under the applied load progresses into the CFRP adhesive layer located at the quarter-span. The presence of the CFRP sheets prevents the progression of pre-repair flexural cracks on the beam sides. Fresh cracks begin to appear towards the point of stress concentration at the tip of the CFRP sheet and progress further into the beam soffit where there is no CFRP sheet, as shown in Figure 6.55. The flexural crack progresses into the adhesive layer of the first CFRP sheet at quarter-span triggering CFRP delamination.

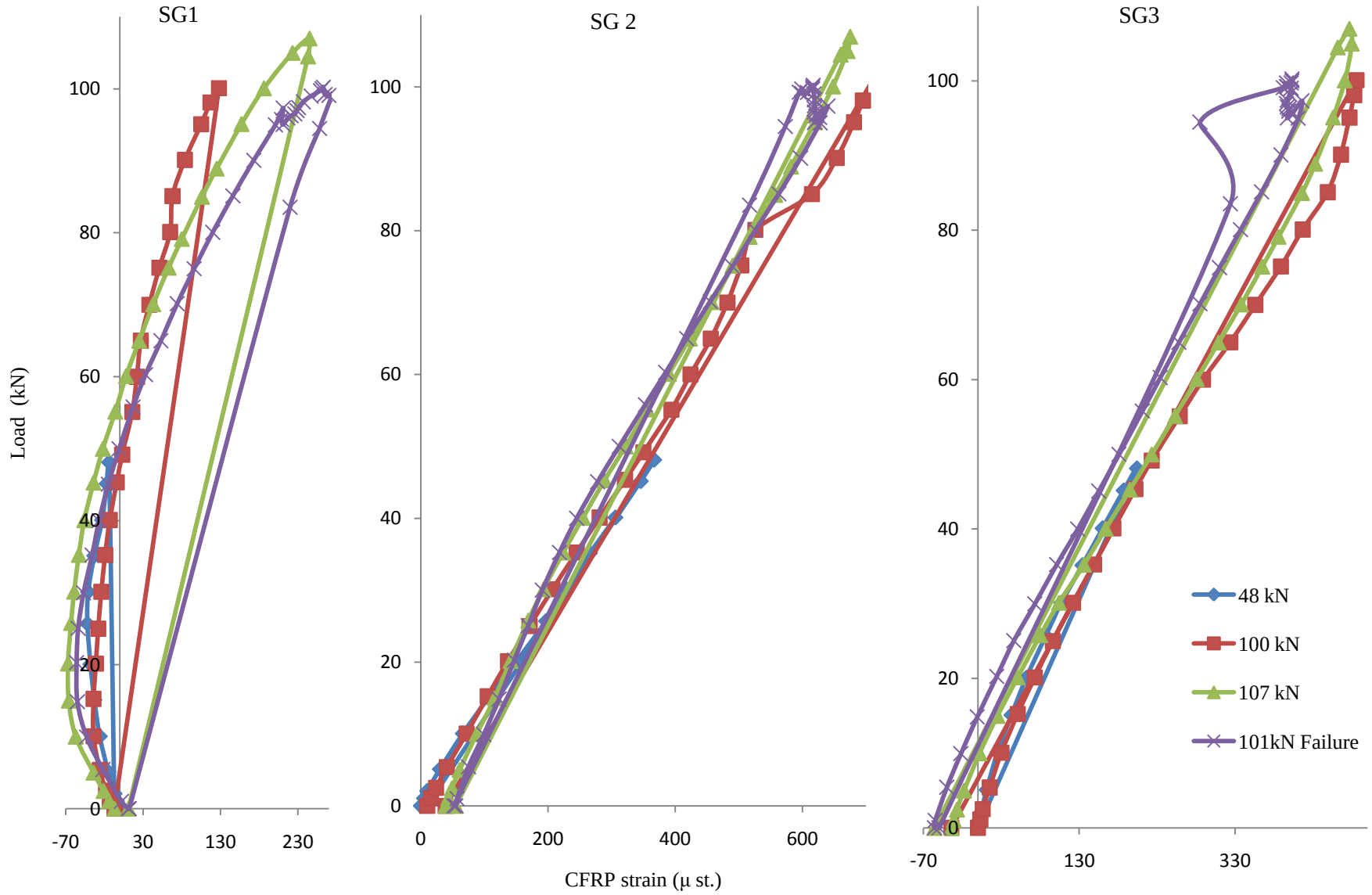

Figure 6.54. Load against CFRP strain curves at post-repair damage stage for beam B211q

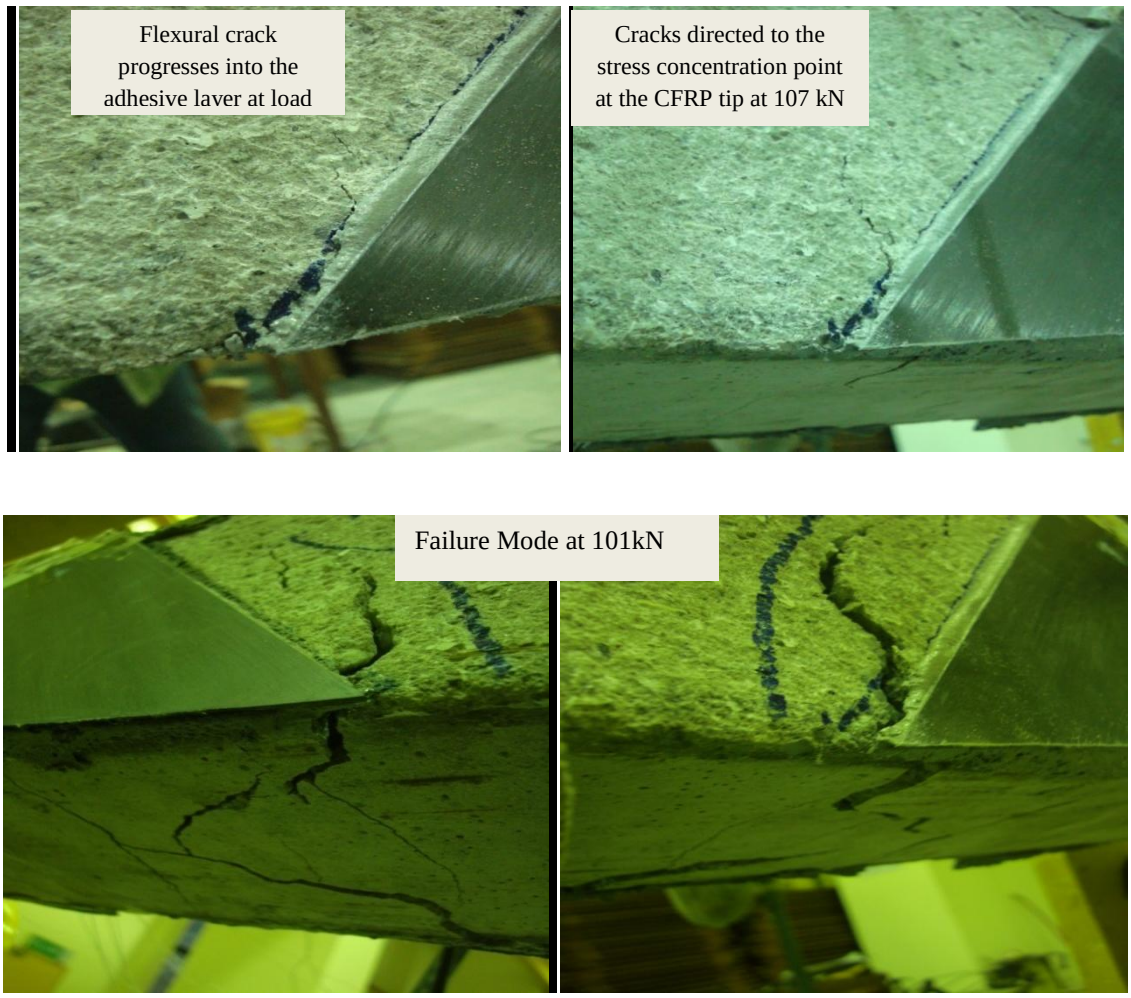

Figure 6.55. Failure mode for beam B211q

Table 6.21 shows the load cycles and the corresponding number of cracks for beam B212q. The load against deflection curves at pre and post repair stages are shown in Figure 6.56, whilst Figure 6.57 shows the load against steel strain curves at pre and post repair stages. The strain values at strain gauges SG1, SG2, and SG3 are shown Figure 6.58. The crack patterns at pre and post repair stages are illustrated in Appendix B.

The results show that beam B212q is damaged under a load of 48 kN at pre-repair damage stage which is close to the design load. After repair with externally bonded CFRP sheets, the repaired beam is able to withstand a load of 120 kN. The shear capacity for the unrepaired section depends on the concrete compressive strength with same shear stirrups properties. For beam B212q the compressive strength is the same as for beam B211q, therefore the expected unrepaired capacity for beam B212q is

estimated as that for beam B211q which is 99kN. The increase in the load capacity is the ultimate capacity of the repaired beam (120 kN) divided by the ultimate capacity of the unrepaired beam (99 kN) which is equal to 121.2%.

The steel is yielded prior to failure, at post repair stage, and starts to rupture when the failure occurs as shown in Figure 6.57. The record CFRP strain is higher at the strain gauge which is nearest to the quarter-span, while the second and third strain gauges show smaller values. The first and third strain gauges show no release in the CFRP strain values until a load of 120kN. The second strain gauge shows a release after a load of 100kN and a further release at load of 120kN which is due to the progression of pre-repair flexural cracks in the adhesive layer between the CFRP sheets and the concrete surface. The failure is similar to the aforementioned failure for beam B211q due to the progression of flexural cracks in the adhesive layer. Figure 6.59 shows the onset of the failure cracks and the failure mode for beam B212q.

Table 6.21. Load cycles and corresponding number of cracks for beam B212q

Load Cycles (kN)	Number of cracks	Remark
26.5	5	First shear crack
48	9	Pre-repair stage
48	10	Post-repair stage
100	12	
117.5	16	CFRP starts debonding
120	16	Full CFRP debonding and failure

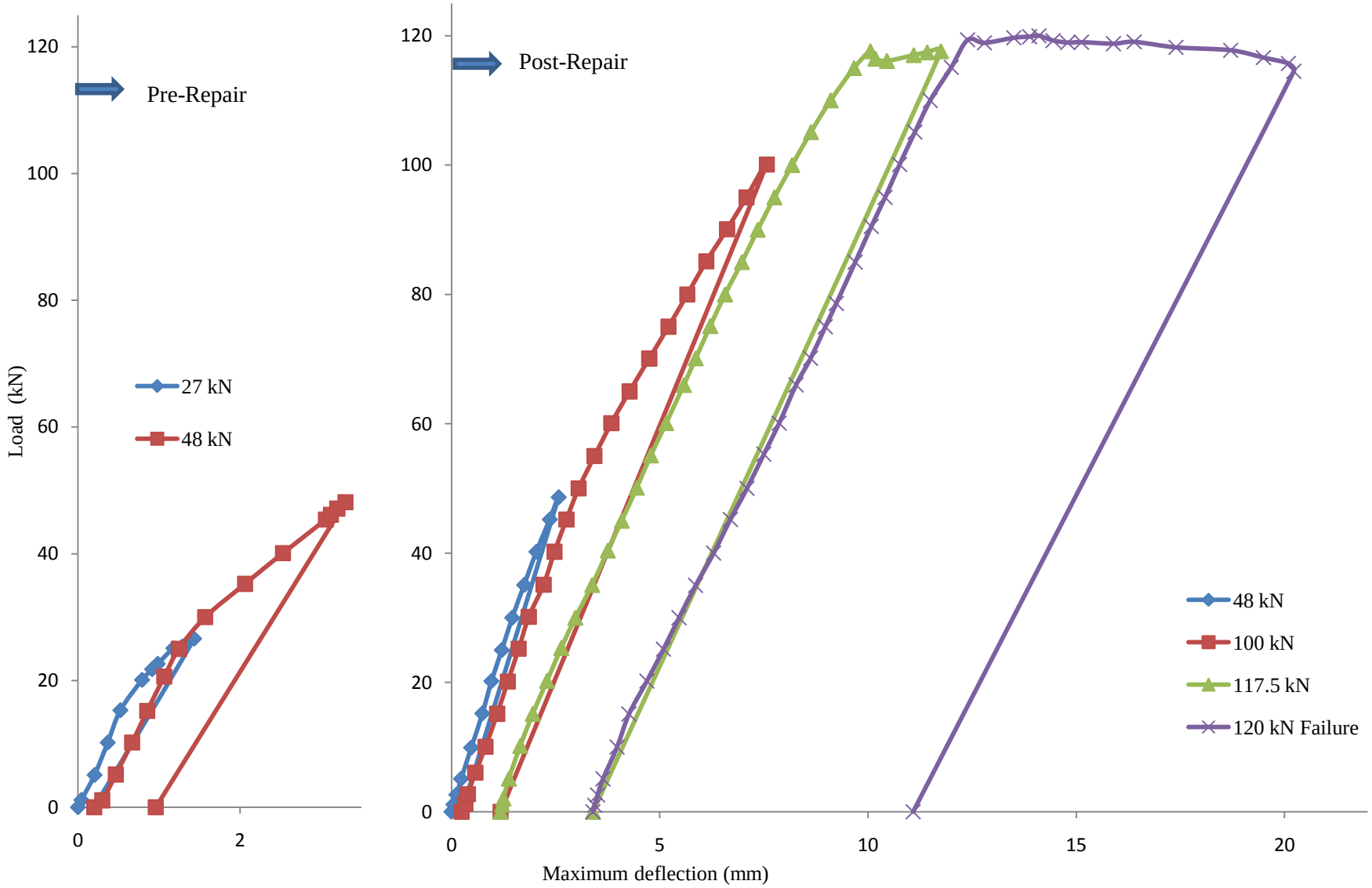

Figure 6.56. Load against maximum deflection at pre and post repair stages for beam B212q

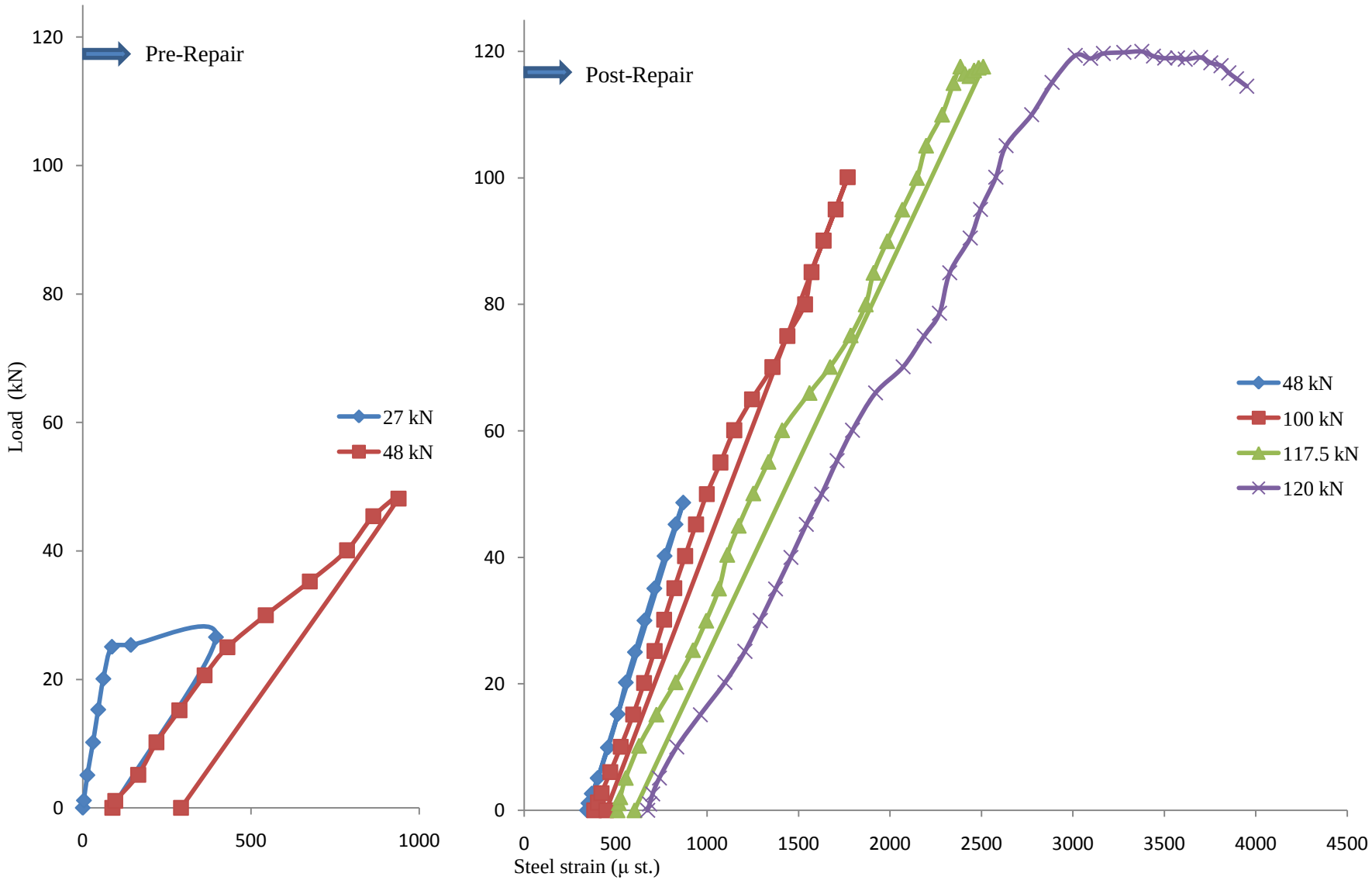

Figure 6.57. Load against quarter-span steel strain at pre and post repair stages for beam B212q

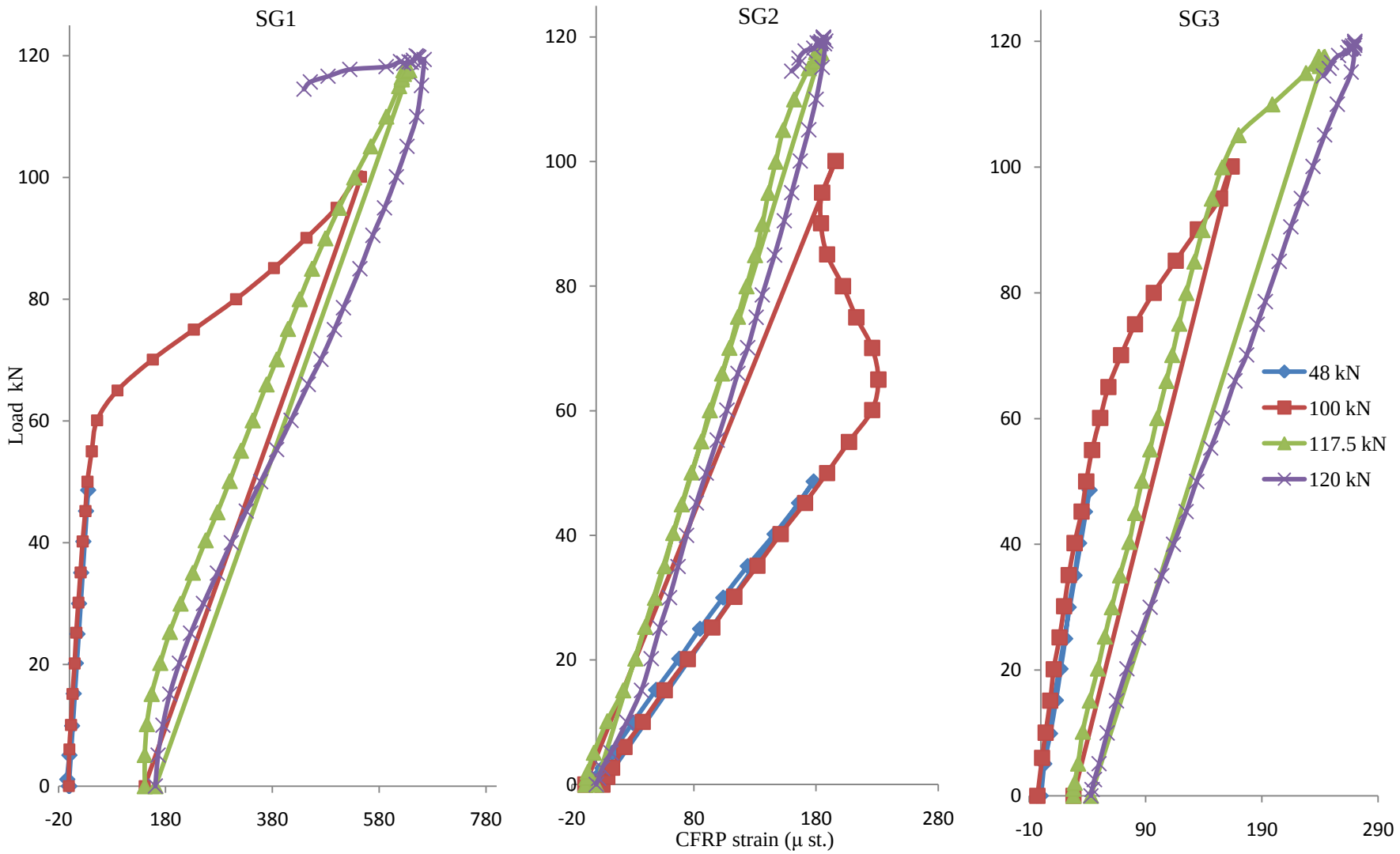

Figure 6.58. Load against CFRP strain curves at post-repair stages for beam B212q

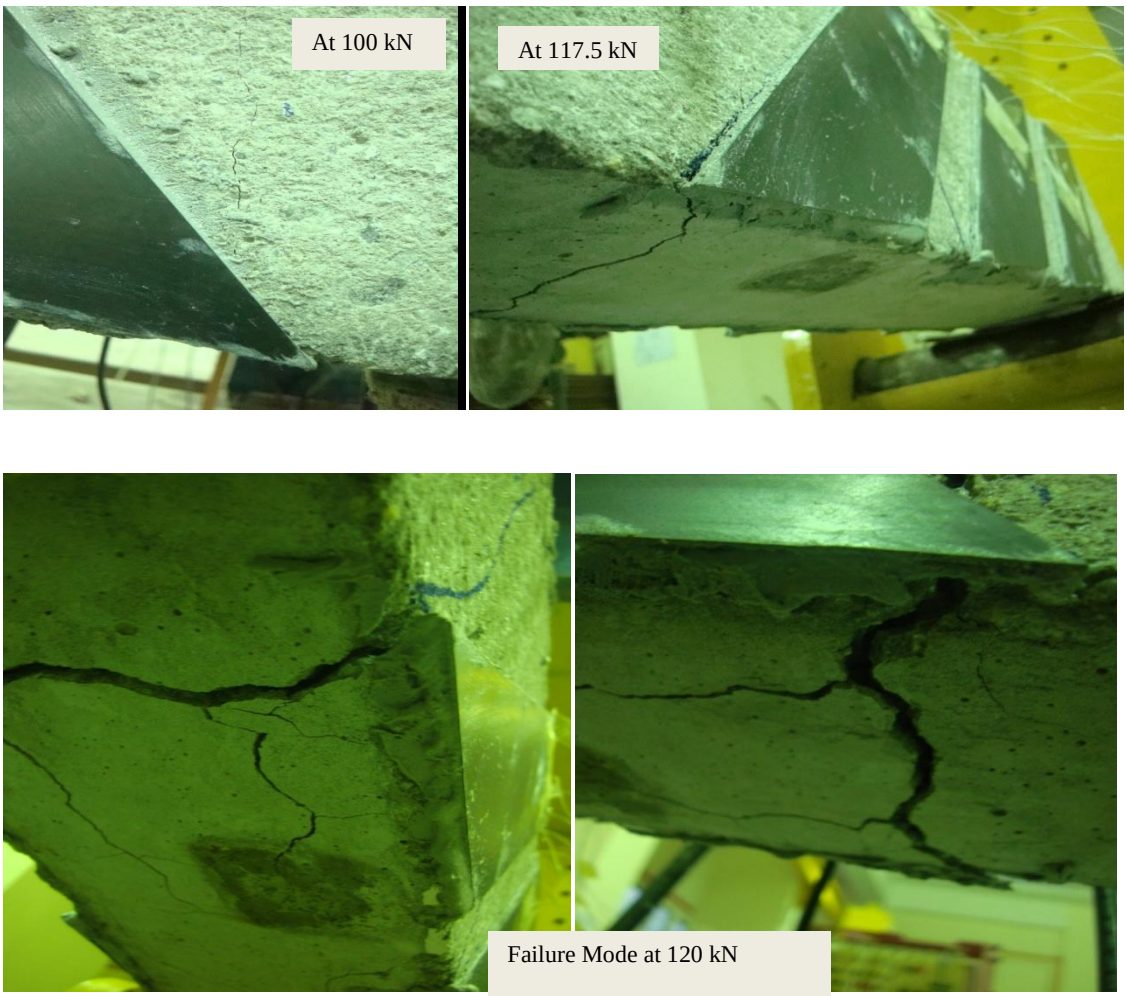

Figure 6.59. Failure mode for beam B212q

The CFRP strain values are higher at the CFRP sheet which is nearer to the quarter-span for the low pre-repair damage level, while the CFRP sheet which is located between the quarter-span and the support shows a higher value in the case of higher pre-repair damage level. The maximum CFRP strain is 700μst which is considered low value compared to the ultimate CFRP strain. The steel reaches its yielded limit for both beams, that is, B211q and B212q. For low pre-repair damage level, that is, B212q, higher load capacity at post-repair stage is recorded with higher steel strain values prior to failure. The failure of both beams is due to the progression of the pre-repair flexural cracks in the CFRP sheets which is located at the quarter-span and is directed to the tip of stress concentration of the CFRP sheets. This causes the CFRP sheet to delaminate.

6.3.1.2 Dynamic evaluation

This section presents the dynamic evaluation of CFRP shear repair effectiveness based on frequency based stiffness index and damping change. The adopted stages are as illustrated in Table 6.22 and Figure 6.60 shows the frequency based stiffness index and the weighted average (PWM) results for beam B211q.

Table 6.22. Stages considered for the dynamic evaluation of the shear beams

Notation	Remark
C	Undamaged stage
D	Pre-repair damaged stage
R	Post-repair stage under the self weight

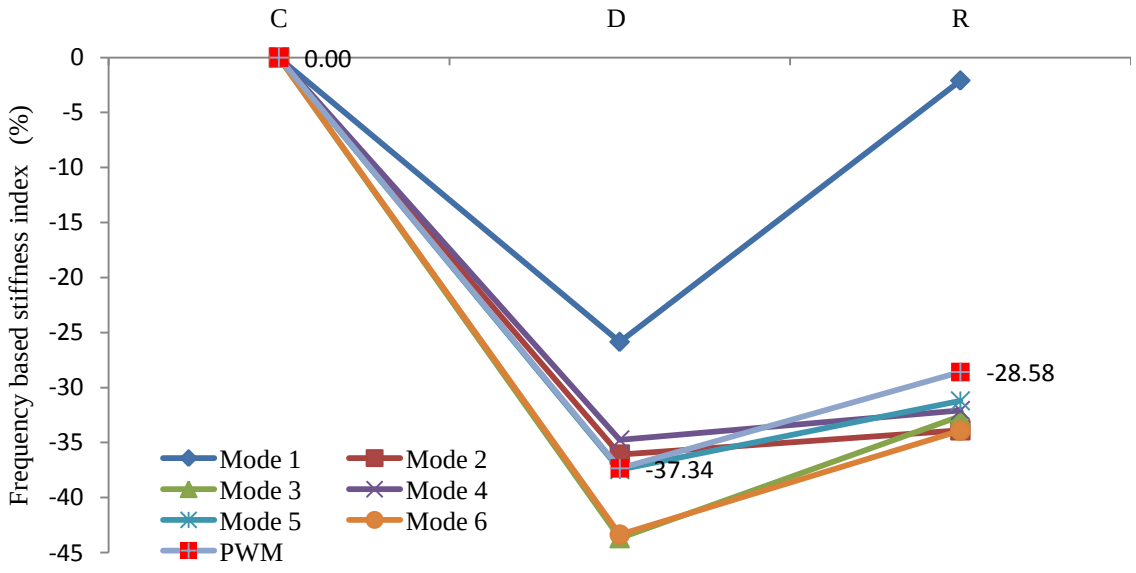

Figure 6.60. Frequency based stiffness index and weighted average (PWM) results for beam B211q

The results show that all the modes show stiffness deterioration, as indicated by the frequency based stiffness index. This is shown at the pre-repair damage stage and is due to the occurring of failure at load 99kN. The application of CFRP sheets to the beam sides helps to recover the stiffness where all the modes show an increase in the index

values at stage R which indicates stiffness recovery though still less than the undamaged stage. The results support the justification of the flexural group affected by the composite action phenomenon of repaired RC beams, where there is no effect of such phenomenon on the modal parameters since the CFRP sheets are added to the beam sides without turning the beam over. The modal frequencies prove to be a good indicator for the repair effectiveness where all the modes indicate an increase in the stiffness by fixing the CFRP sheets. The weighted average highlights the pattern of the overall stiffness change based on all the considered modes. The weighted average shows stiffness deterioration of 38% at pre-repair damage stage. Following this a stiffness deterioration of 28.6% compared to undamaged stiffness is observed at post-repair stage, which indicates a stiffness recovery of 8.7% compared to pre-repair damage stage.

Figure 6.61 shows stiffness change at pre and post repair stages based on the damping change for beam B211q. The adopted stages are the same as that for the frequency based stiffness index and the weighted average (PWM) is performed and the results are also shown in Figure 6.61. The results show that all the modes indicate an increase in the damping values at pre-repair damage stage which indicates stiffness deterioration except for Mode 1 which indicates a damping decrease. Repair with externally bonded CFRP sheets influences all the modes, where all the modes show a decrease in the damping values compared to pre-repair damage stage which indicates stiffness recovery. The weighted average shows the overall stiffness change where a stiffness deterioration of 39.2% at pre-repair damage stage is observed. At post-repair stage, the stiffness deterioration decreases to only 25.4%, which indicates stiffness recovery of 13.8% compared to pre-repair damage stage.

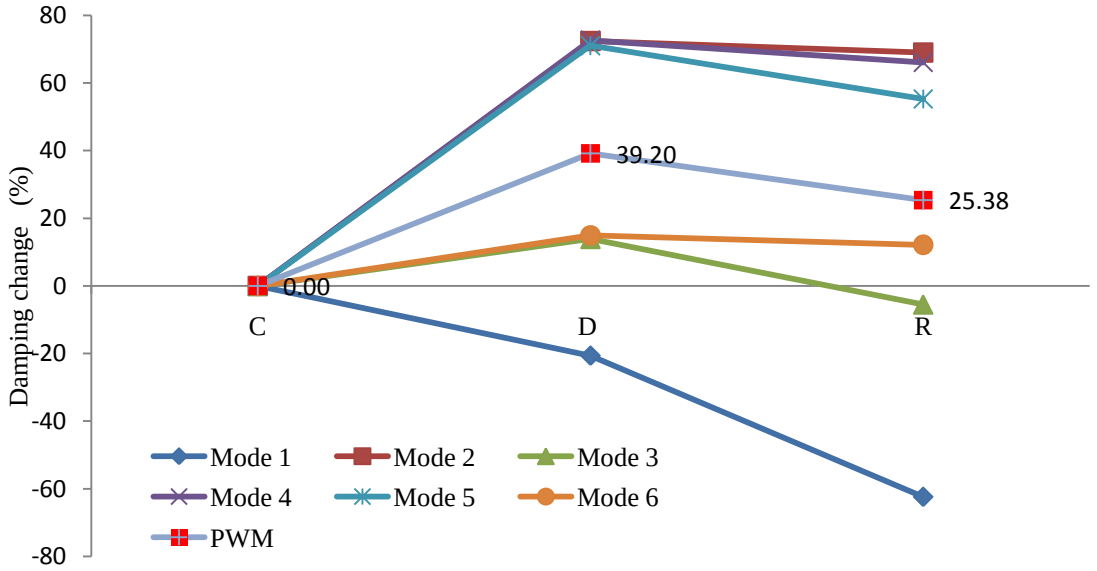

Figure 6.61. Damping change and weighted average (PWM) results for beam B211q

The frequency based stiffness index results to indicate the repair effectiveness for beam B212q are shown in Figure 6.62, where the weighted averaging (PWM) is calculated and presented. The same stages illustrated in Table 6.22 are considered to plot the frequency based stiffness index results. The results show that all the modes demonstrate a decrease in the frequency based stiffness index values at pre-repair damage stage except for Mode 1 which is influenced by the composite action phenomenon of RC beams. At post-repair stage, the frequency based stiffness index values show an increase for all the modes compared to stage D. All the modes show less value than the undamaged stage except for Mode 1 which shows higher value. The weighted average (PWM) results show an increase in the index values which indicates stiffness deterioration of 13.1% at pre-repair damage stage. At post repair stage, the weighted average results show an increase in the index value compared to stage D, which indicates a stiffness recovery of 10.6%.

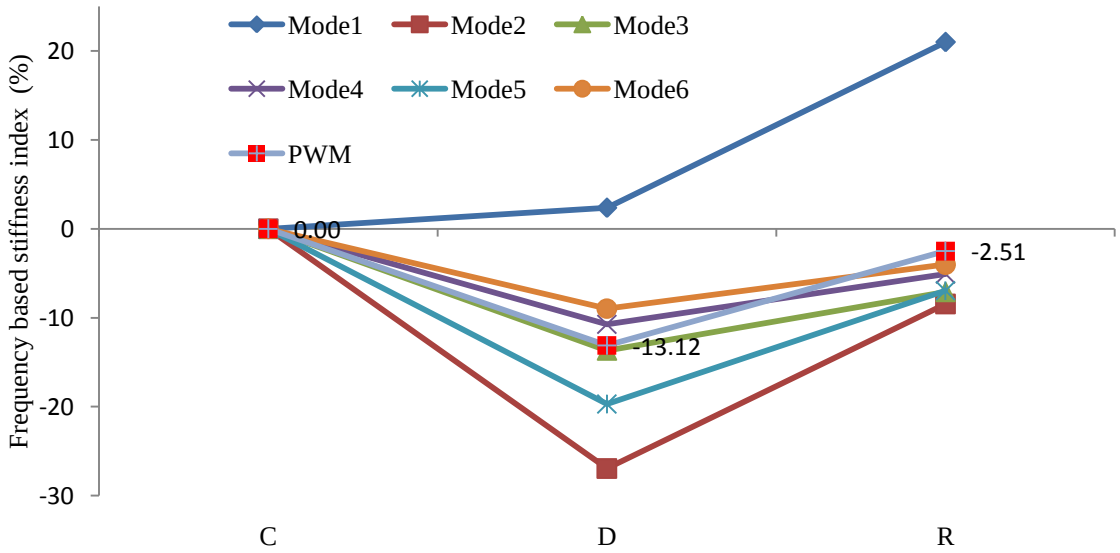

Figure 6.62. Frequency based stiffness index and weighted average (PWM) results for beam B212q

The damping change for beam B212q is calculated for all the considered modes at the same stages as illustrated in Table 6.22, and the results are shown in Figure 6.63. This figure also presents the weighted average (PWM) values. The results for all the modes show an increase in the damping values at the pre-repair damage stage which indicates stiffness deterioration. At post-repair stage, all the modes show a decrease in the damping values compared to stage D which indicates an increase in stiffness. Since different modes show different stiffness change, the weighted average is calculated and its results show stiffness deterioration of 21.3% at the pre-repair damage stage and 5.1% at the post-repair stage. Thus a stiffness recovery of 16.1% at the post-repair stage compared to the pre-repair damage stage is observed.

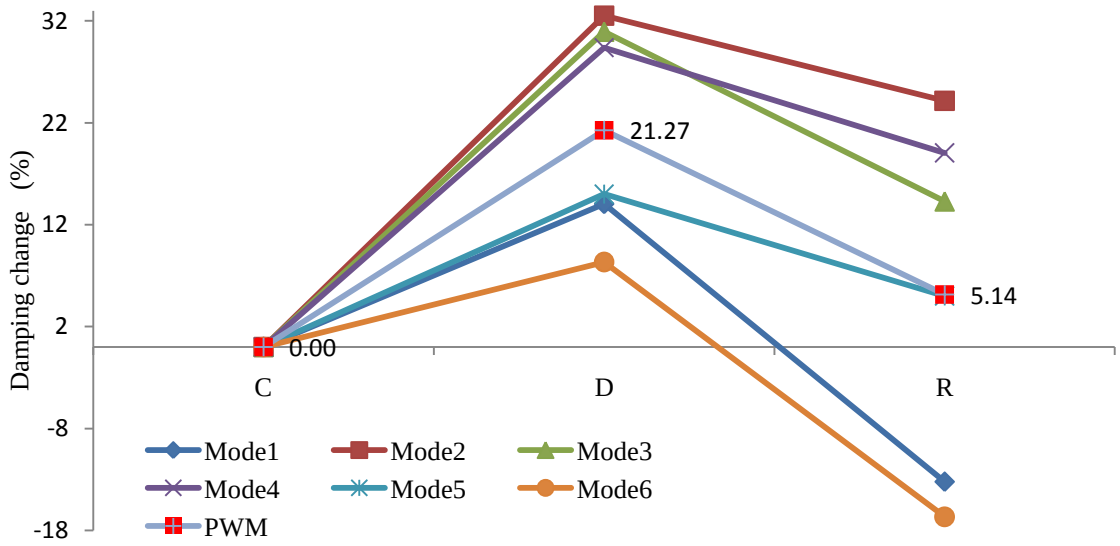

Figure 6.63. Damping change and weighted average (PWM) results for beam B212q

6.3.1.3 CFRP repair effectiveness

This section presents the relationship between the static and dynamic data in order to ascertain the effectiveness of the CFRP repair system at different pre-repair damage levels. The damage level is calculated based on the percentage of the applied load at pre-repair stage to the ultimate capacity of the unrepaired sections. The stiffness recovery as indicated by the ratio of increase in the ultimate load capacity is calculated based on the increase in the ultimate capacity of the repaired sections to the ultimate capacity of the unrepaired sections. The stiffness effectiveness based on the dynamic data is highlighted based on both frequency based stiffness index and damping change. For frequency based stiffness index and damping change, the repair effectiveness is calculated as the different between the weighted average index value at post-repair stage compared to the weighted average index value at the pre-repair damage stage. Figure 6.64 shows the repair effectiveness based on the static and dynamic data and also corresponds to the damage ratios of beams B211q and B212q.

The results show that repair with externally bonded CFRP sheets recovers the stiffness and increases the load capacity by at least 8% regardless of the pre-repair damage level. The damping change shows higher stiffness recovery than the frequency based stiffness index. For low pre-repair damage level, repair with CFRP sheets increases the load capacity by 21.2%, with corresponding stiffness recovery of 10.6% and 16.1 % based on frequency based stiffness index and damping change, respectively. The load capacity of repaired beams at post-repair stage depends on the pre-repair damage level, where higher load capacity is observed for lower pre-repair damage level. The increase in the ultimate load capacity is between 8.1% to 21.2% which is in good agreement with findings of El-Ghandour (2011) and Pellegrino and Modena (2002) who noted an increase of 19 to 50% for cases of zero pre-repair damage level.

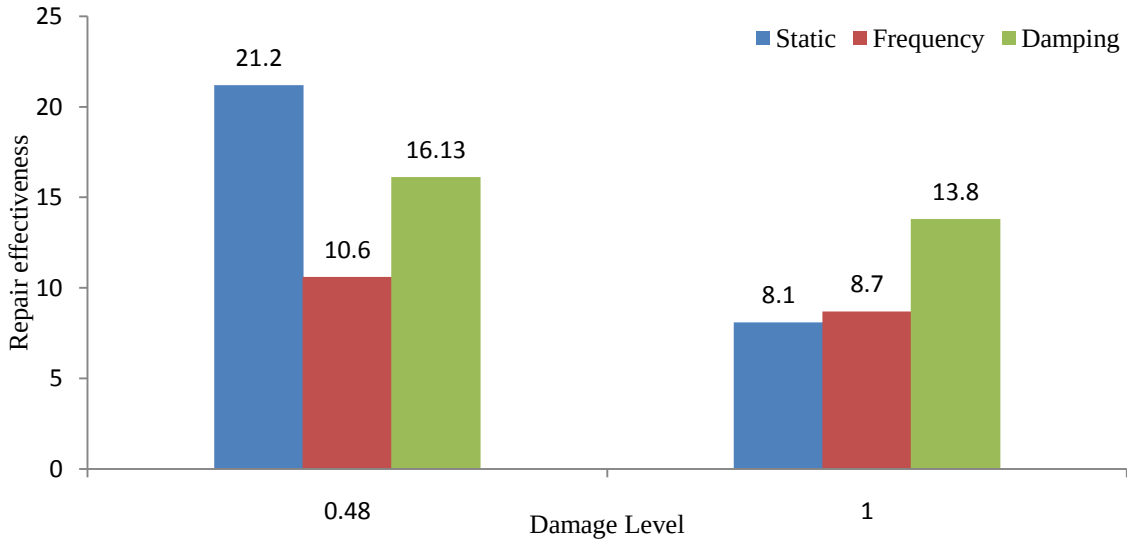

Figure 6.64. CFRP repair effectiveness based on static and dynamic data for shear at quarter-span and beams with shear stirrups

6.3.1.4 Monitoring of repaired beams

Beams B211q and B212q are tested under load cycles at post-repair stages until failure as mentioned in the static evaluation. The dynamic test is carried out to monitor the behaviour of the repaired beam during its service life. The frequency based stiffness index is calculated after each load cycle at post-repair stages for both repaired beams. Table 6.23 shows the load cycles and notation at the post-repair stages used to plot the

frequency based stiffness index during the monitoring of the repaired beams. Figure 6.65 shows the frequency based stiffness index for post-repair stage of beam B211q, where stage 'R' is used as the datum for the index values at higher loading stages.

Table 6.23. Load cycles for the post-repair stages of beam B211q

Load (kN)	Notation	Remark
0	R	Post-repair under self weight
48	R48	
99	RD	Subjected to pre-repair load
107	R107	Cracks progression into the adhesive layer
101	R101	Failure

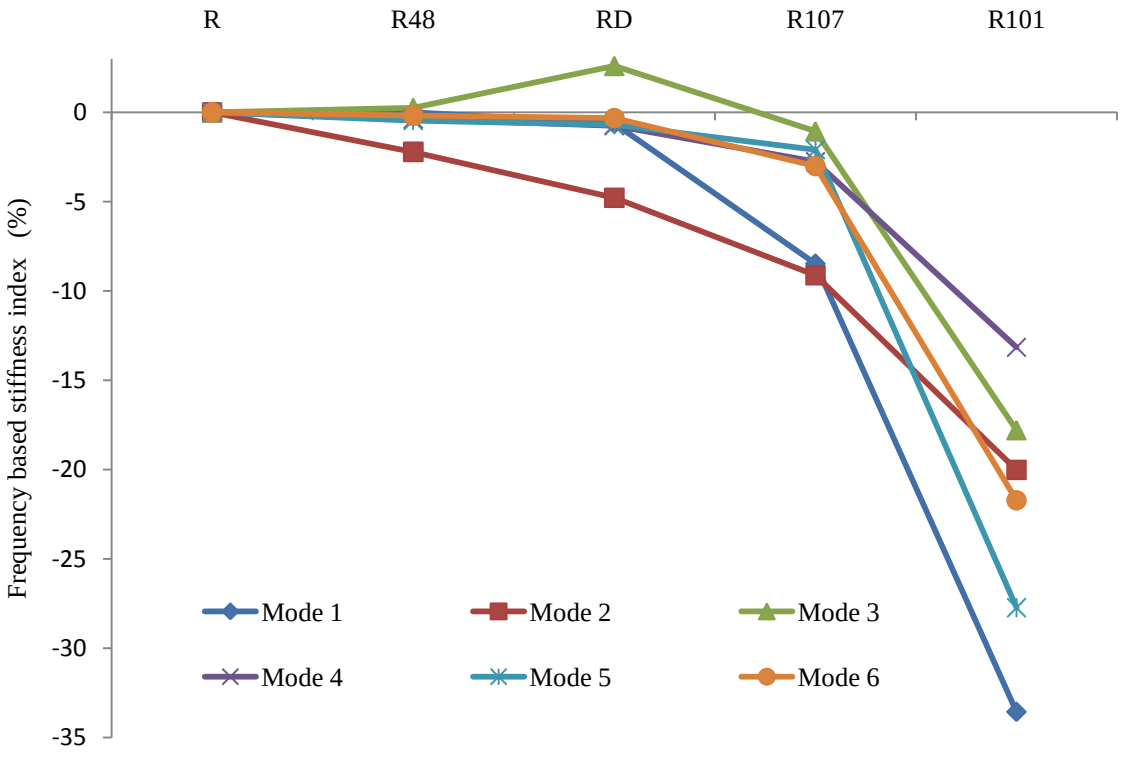

Figure 6.65. Frequency based stiffness index values for the monitoring of beam B211q

The results show that all the modes demonstrate indistinguishable change in the frequency based stiffness index values at stage R48 except for Mode 2 which shows a decrease. At stage RD, all the modes show a decrease in the index values except for

Mode 3 which shows an increase. Beyond stage RD, all bending modes show a decrease in the frequency based stiffness index values which are affected by the progression of the flexure and shear cracks in the adhesive layer between the CFRP sheets and the concrete surface as shown in Figure 6.55. When failure occurs at stage R101, a rapid decrease in the frequency based stiffness index values can be seen for all of the considered modes.

Table 6.24 presents the load cycles and notation used to plot the frequency based stiffness index results at the monitoring stages for beam B212q. Figure 6.66 presents the frequency based stiffness index values at the post-repair stages and corresponding to each load cycle up to failure for beam B212q. Stage 'R' is the datum for the index values at higher loading stages.

The results at stage RD show that Modes 4 to 6 indicate a slight increase in the frequency based stiffness index values while Modes 1 to 3 indicate a slight decrease which is due to the appearance of new cracks in the beam indicating concrete stiffness deterioration. A further decrease in frequency based stiffness index values for all the modes is observed at stages R100 and R117 which is due to the influence of the concrete stiffness deterioration and the progression of the cracks in the adhesive layer. At stage R120, the failure occurred and the frequency based stiffness index shows a rapid decrease.

Table 6.24. Load cycles for the post-repair stages of beam B212q

Load (kN)	Notation	Remark
0	R	Post-repair under self weight
48	RD	Subjected to pre-repair load
100	R100	
117	R117	Cracks progression into the adhesive layer
120	R120	Failure

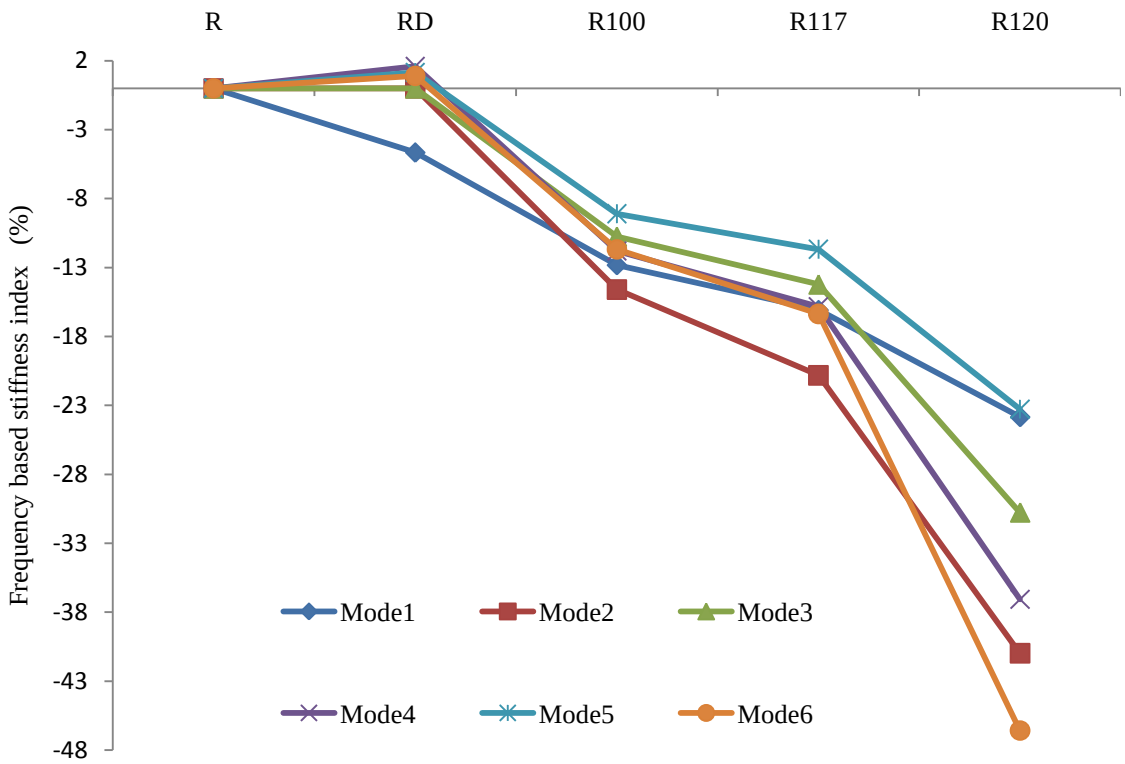

Figure 6.66. Frequency based stiffness index values for the monitoring of beam B212q

6.3.2 Beams without stirrups

Beams B221q and B222q are used to investigate the repair effectiveness of the CFRP sheet as shear repair system for the design case when no shear stirrups are used. The results cover the static and dynamitic evaluations and the monitoring of the repaired beams. For the static evaluation the load against deflection, load against steel strain, load against CFRP strain and failure modes are highlighted. For the dynamic evaluation the stiffness recovery based on frequency based stiffness index and damping change are highlighted. For the monitoring of the repaired beams, the frequency based stiffness index results corresponding to load cycles at the post-repair stages are present.

6.3.2.1 Static evaluation

Table 6.25 shows the load cycles and the corresponding number of cracks for beam B221q at pre and post repair stages. The loads against deflection curves at pre and post repair stages are shown in Figure 6.67. The loads against steel strain curves at pre and post repair stages are shown in Figure 6.68. The deflection shown in Figure 6.67 is the maximum measured deflection which is located at the zone between quarter-span and mid-span as discussed in Section 4.4.1. The steel strain presented in Figure 6.68 is the strain of flexural steel bars located at quarter-span. The initial strain at the post-repair stage is the remainder strain from the pre-repair stage where the beam is not turned over during the repair procedure. Figure 6.69 shows the load against CFRP strain at strain gauges SG1, SG2 and SG3. The crack patterns at pre and post repair stages are illustrated in Appendix B.

Table 6.25 Load cycles and corresponding number of cracks for beam B221q

Load Cycles (kN)	Number of cracks	Remark
20	1	First flexural crack
50	7	
90	14	Pre-repair stage
25	14	Post-repair stage
84	14	
91	16	CFRP starts debonding
101	17	Full CFRP debonding and failure

The results show that the beam is damaged under failure load at 90 kN at pre-repair damage stage where the steel yields at 85 kN. The damaged beams are repaired with CFRP sheets where repair design is in accordance with ACI 440.2R (2002) Code as discussed in Section 4.3.2.2. After repair, the beam is able to withstand a load of 101 kN, where the failure occurs. The steel starts to rupture at high load levels, and the

strain gauge wire brakes prior to failure. The increase in load capacity is equal to the maximum capacity of the repaired section (101 kN) divided by the maximum capacity of the unrepaired section (90 kN) which equals 112.2%. The CFRP strain corresponding to the load cycles is monitored on each of the six sheets on both sides of the damaged beam, where the first strain gauge (SG1) is the closest to quarter-span and third stain gauge (SG3) is the closest to the supports. The results show that higher strain is recorded at second strain gauge (SG2) which is located between the support and quarter-span. Maximum record strain value is 700μst which is considered a small value when compared to the ultimate strain of the CFRP sheets. The first strain gauge indicates that the CFRP sheet which is located at quarter-span is able to support the load without any release in strain up to failure. Third strain gauge indicates a release in the CFRP strain beyond a load of 84 kN where new cracks start to appear at the adhesive layer between the CFRP sheets and the concrete surface.

The failure is a combination of flexure and CFRP delamination, where the flexure crack under applied load progresses into the adhesive layer of the CFRP sheets which are located at quarter-span. The presence of the CFRP sheets prevent the extension of flexure crack on the beam sides and fresh cracks are generated towards the point of stress concentration at the tip of the CFRP sheet as shown in Figure 6.70. Finally, the induced crack in the adhesive layer of the CFRP sheet at quarter-span triggers CFRP delamination, and the steel starts to rupture as shown in Figure 6.68 where a steel strain of 5000μst is observed prior to failure.

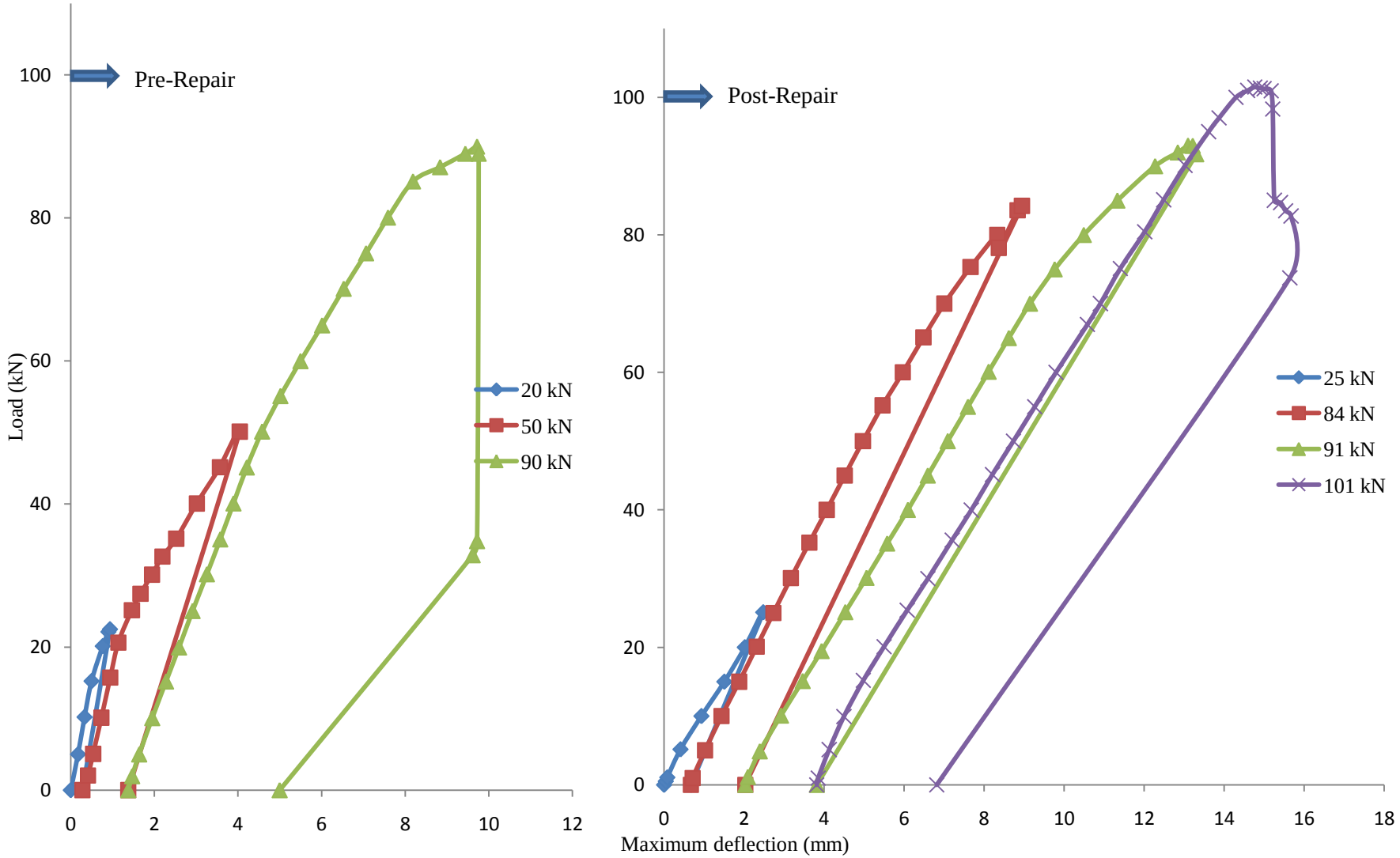

Figure 6.67. Load against maximum deflection at pre and post repair stages for beam B221q

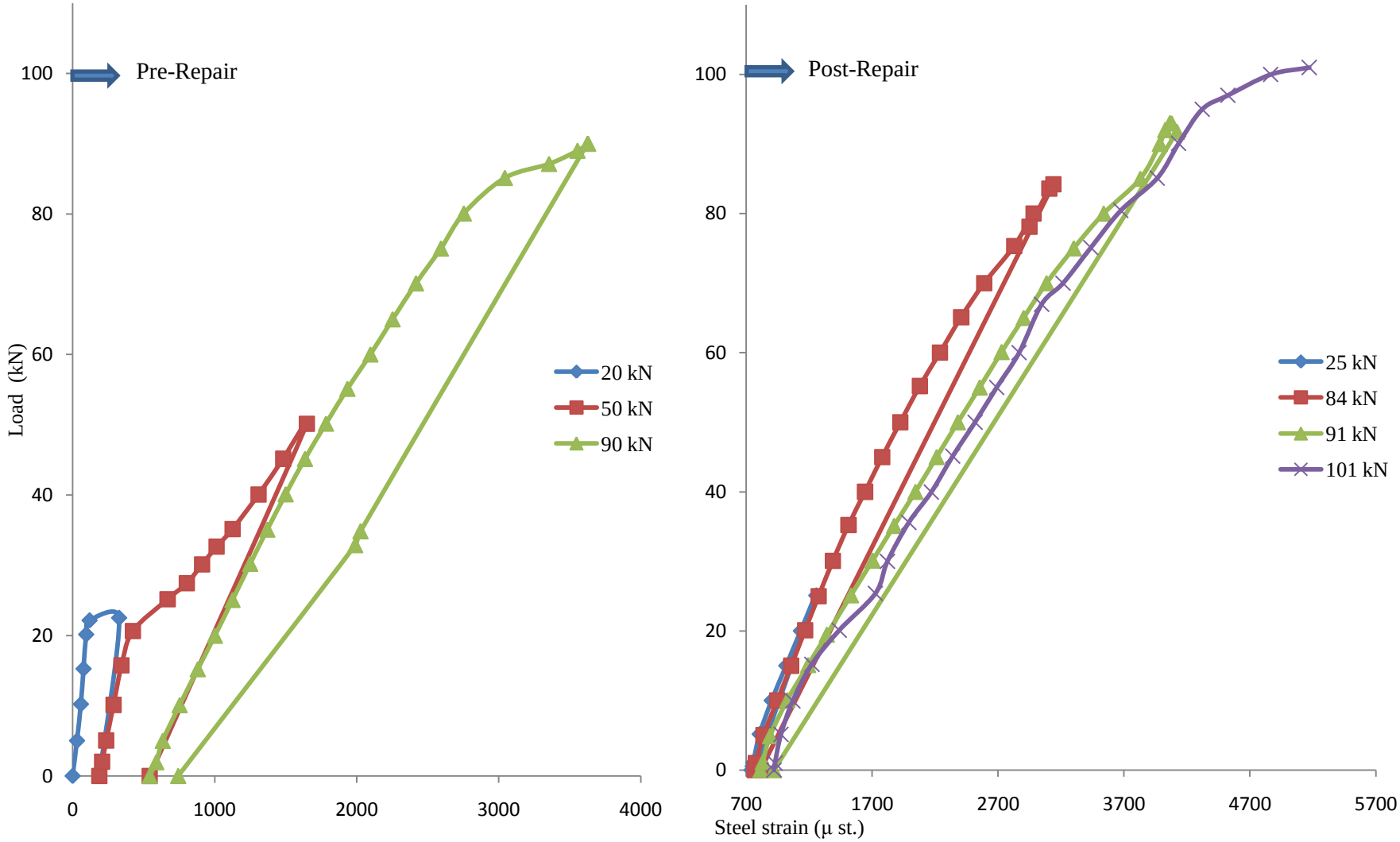

Figure 6.68. Load against quarter-span steel strain at pre and post repair stages for beam B221q

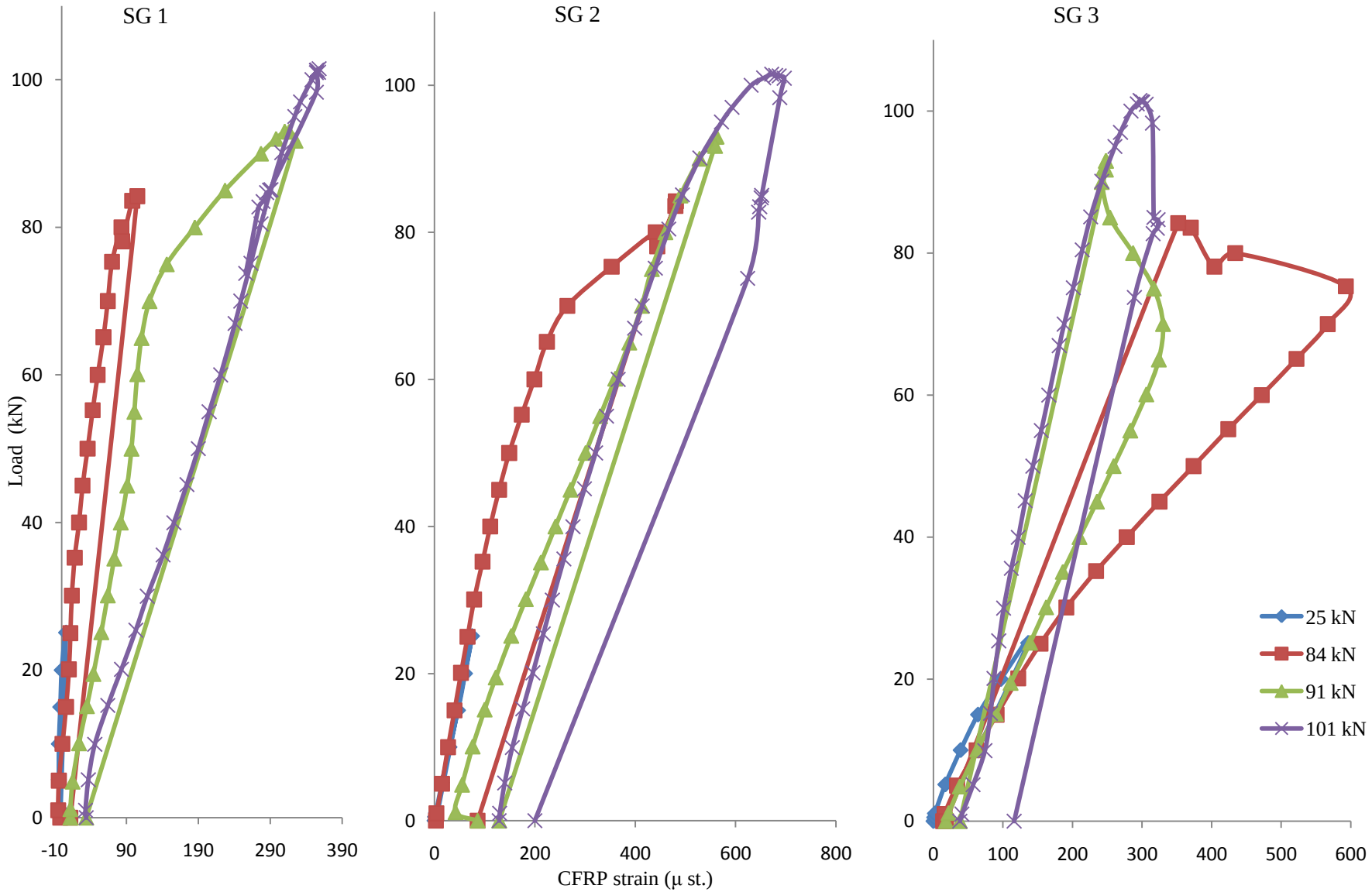

Figure 6.69. Load against CFRP strain for SG1, SG2 and SG3 for beam B221q

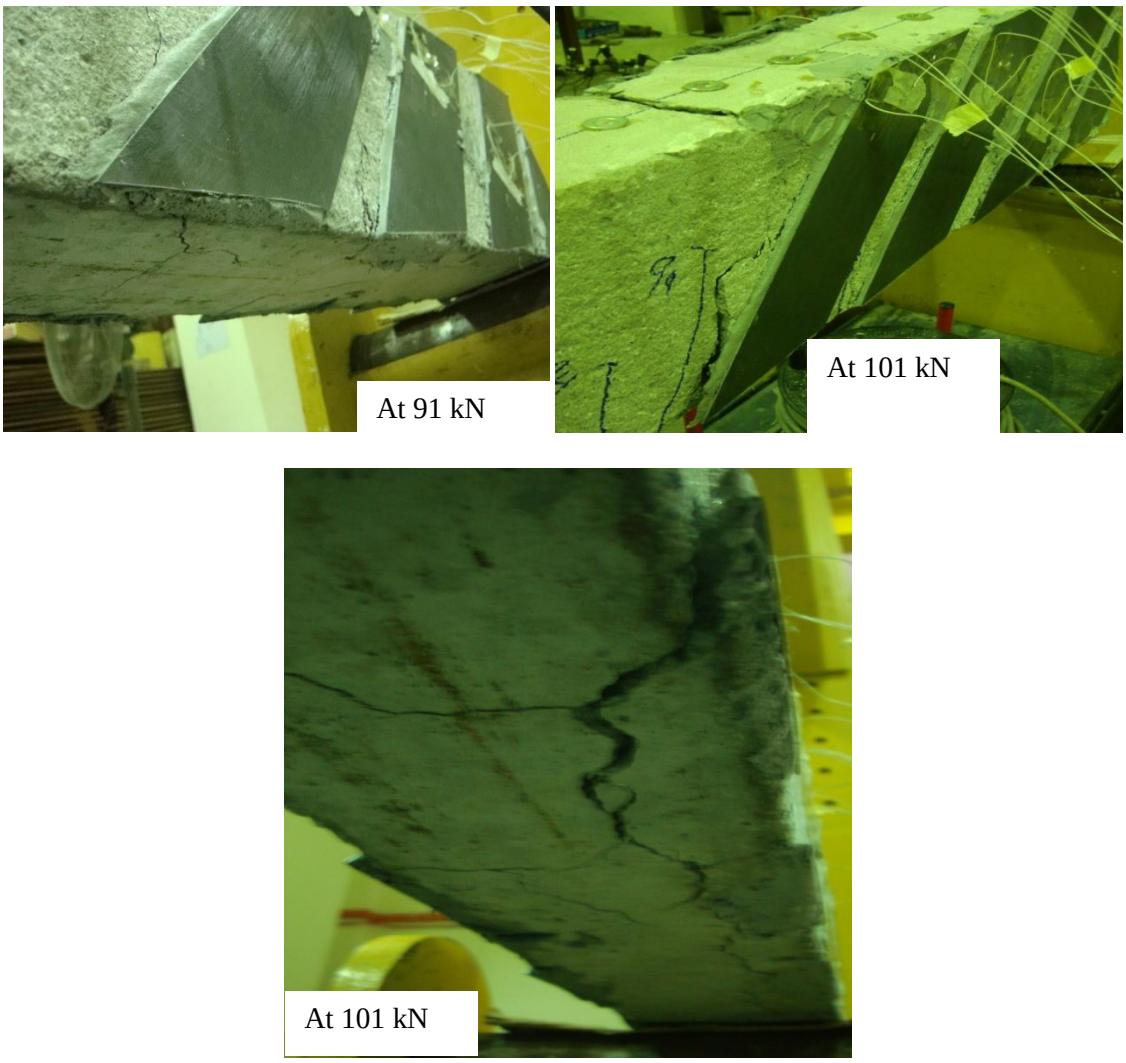

Figure 6.70. Failure mode for beam B221q

For beam B222q, Table 6.26 shows the load cycles and the corresponding number of cracks for beam B222q at pre and post repair stages. Figure 6.71 shows the load against deflection curves and Figure 6.72 shows the load against steel strain curves at pre and post repair stages. Figure 6.73 shows the load against CFRP strain curves at post-repair stage. The crack patterns at pre and post repair stages are appended as Appendix B.

The results show that the beam is damaged under a load of 25 kN at pre-repair damage stage and is able to withstand a load of 120 kN after repair with externally bonded CFRP sheets in accordance with the repair design as discussed in Section 4.3.2.2. The ultimate capacity of the unrepaired section depends on the concrete compressive

strength. Therefore, the unrepaired capacity for beam B222q is the same as for beam B221q which is 90 kN, since beam B222q has the same compressive strength as beam B221q. The increase in load capacity is calculated as the ultimate capacity of the repaired section (120 kN) divided by the ultimate capacity of the unrepaired section (90 kN) which is equal to 133.3%.

Table 6.26 Load cycles and corresponding number of cracks for beam B222q

Load Cycles (kN)	Number of cracks	Remark
25	4	Pre-repair stage
25	4	Post-repair stage
90	10	
120	13	CFRP starts debonding
110	14	Full CFRP debonding and failure

The steel yielded prior to failure and starts to rupture when failure begins. The CFRP strain is higher at the first strain gauge, the nearest to quarter-span, while the second strain gauge shows the lowest value. All strain gauges show that the CFRP strain releases beyond loads of 90kN. The failure is a combination of flexure and CFRP delamination, where the flexural crack under applied load progresses into the adhesive layer at the CFRP sheets located at quarter-span. Fresh cracks appear towards the point of stress concentration at the tip of the CFRP sheet as shown in Figure 6.74. Finally, the flexural crack progresses further into the adhesive layer of the first CFRP sheet at quarter-span triggering CFRP delamination, where steel starts to rupture as shown in Figure 6.72 upon reaching a strain of over 5000μst prior to failure.

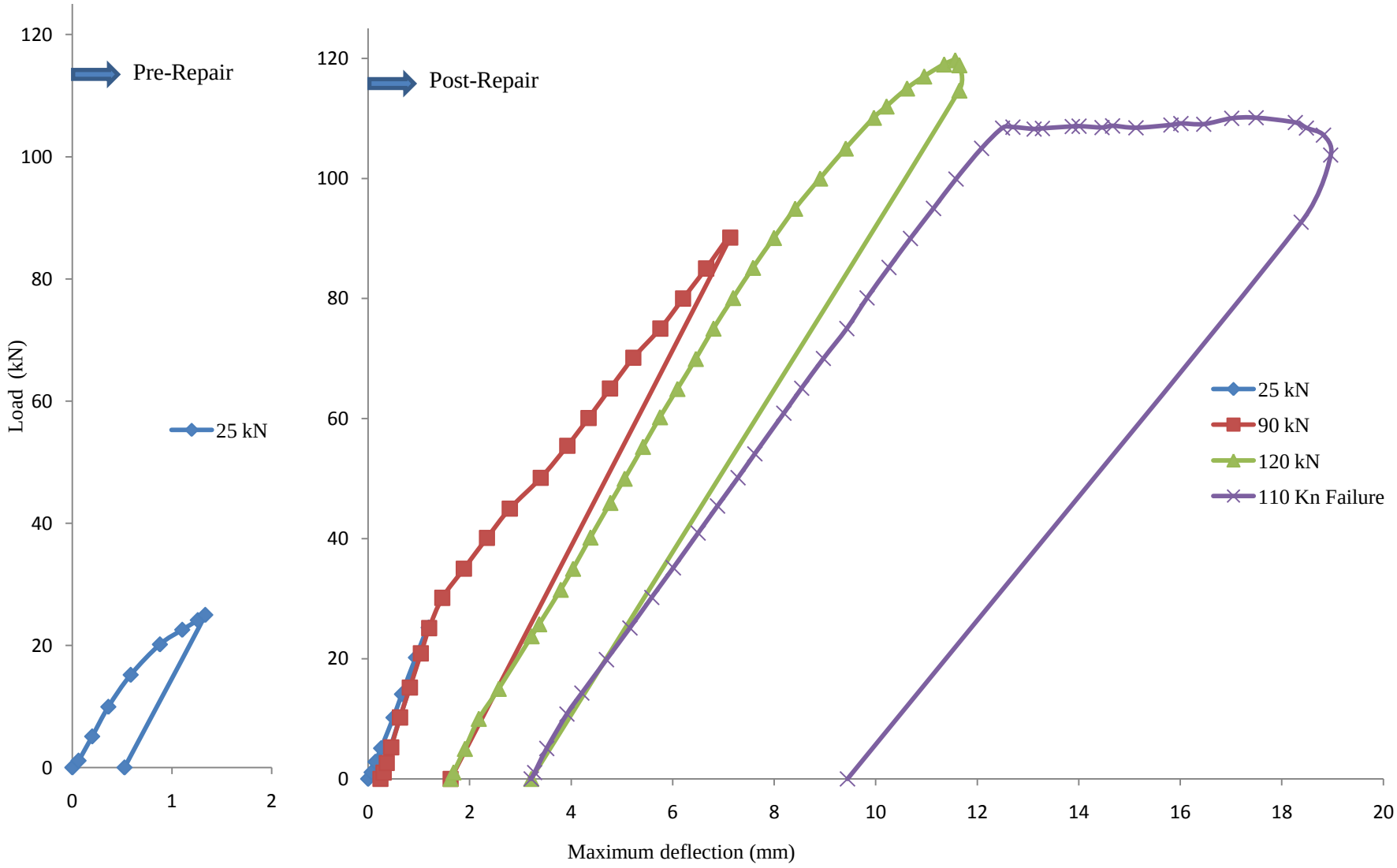

Figure 6.71. Load against maximum deflection at pre and post repair stages for beam B222q

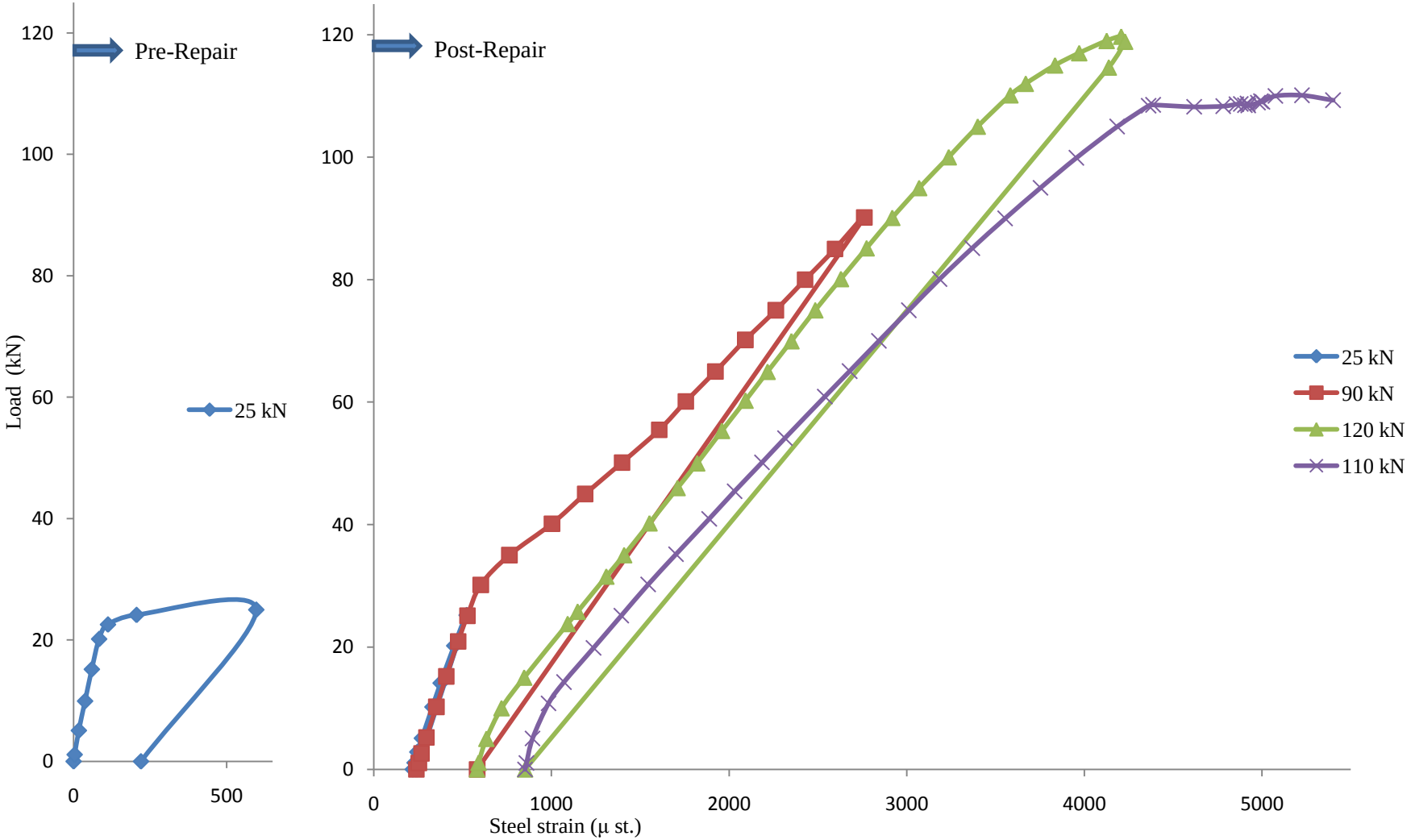

Figure 6.72. Load against quarter-span steel strain at pre and post repair stages for beam B222q

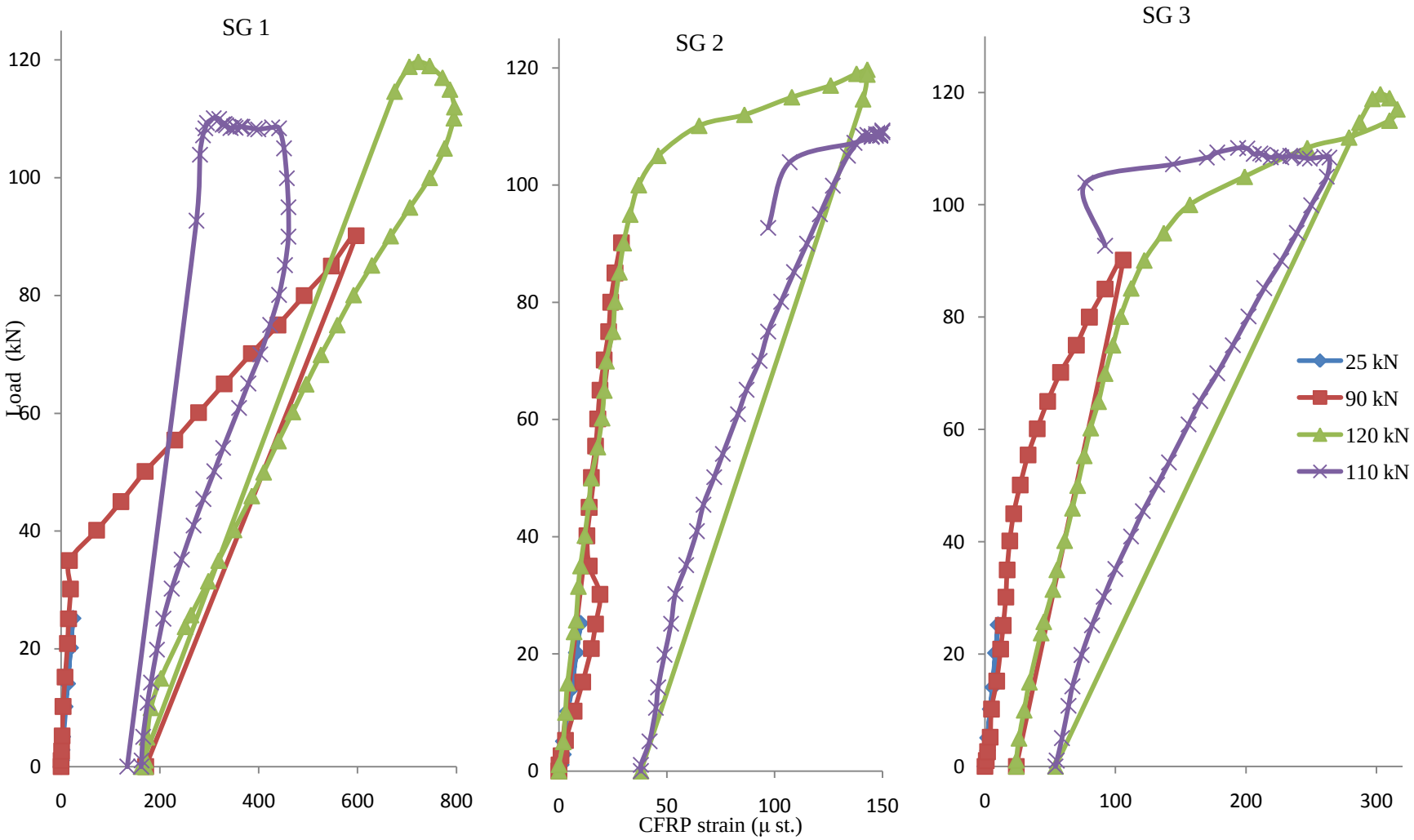

Figure 6.73. Load against CFRP strain at post-repair stages for beam B222q

Figure 6.74. Failure mode of beam B222q

6.3.2.2 Dynamic evaluation

This section presents the dynamic evaluation of CFRP shear repair effectiveness based on frequency based stiffness index and damping change. The adopted stages are as illustrated in Table 6.22 whilst Figure 6.75 shows the frequency based stiffness index and the weighted average (PWM) results for beam B221q.

The results show that all the modes demonstrate a decrease in the frequency based stiffness index at pre-repair damage stage which indicates a stiffness deterioration due to the occurrence of failure under a load of 90kN. Fixing the CFRP sheets to the beam sides helps to recover the stiffness where all the modes indicate stiffness recovery, as indicated by the frequency based stiffness index, compared to the pre-repair damage

stage. However, the index values at post-repair stage are still less than those at the undamaged stage. The results support the composite action phenomenon of repaired RC beams in flexural group, where there is no effect from such phenomenon on the modal parameters of the shear group repaired beams since the CFRP sheets are added to the beam sides without turning the beam over. The modal frequencies prove to be a good indicator for the CFRP repair effectiveness where all the adopted modes indicate an increase in the stiffness after the application of CFRP sheets. The weighted averages (PWM) are shown in Figure 6.75 and highlight the pattern of the overall change in stiffness based on all the considered modes. The weighted average results show a stiffness deterioration of 39.1% at pre-repair damage stage as indicated by the frequency based stiffness index. Following this the stiffness is recovered after being repaired with CFRP sheets where the stiffness deterioration is reduced to 28.5% compared to the undamaged stage. Thus, the stiffness recovery is 10.6% compared to the pre-repair damage stage, after fixing the CFRP sheets.

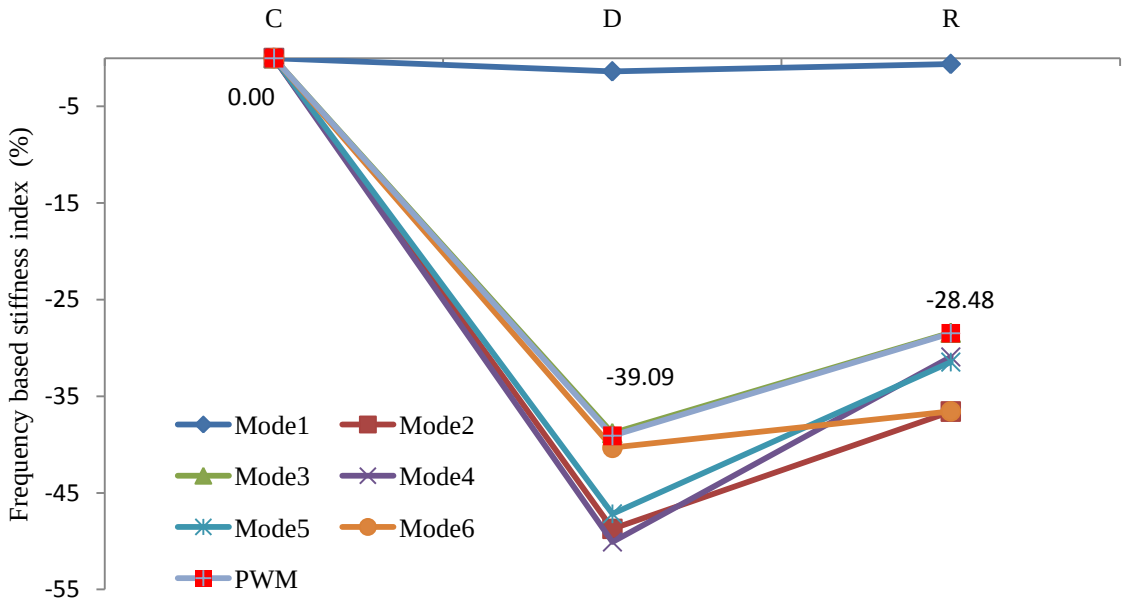

Figure 6.75. Frequency based stiffness index and weighted average (PWM) results for beam B221q

Figure 6.76 shows the trend of the damping change at pre and post repair stages for beam B221q. The adopted stages are the same as those for the frequency based stiffness index. The weighted average (PWM) is calculated and the results are also shown in Figure 6.76. The results show that Modes 2, 4, 5 and 6 indicate an increase in the damping values which indicate deterioration in stiffness at the pre-repair damage stage, while Modes 1 and 3 show a decrease in the damping values. Repairing the beam with externally bonded CFRP sheets influences all the modes, where it shows a decrease in the damping values which indicate recovery in the stiffness. The weighted average (PWM) shows the overall change in stiffness as indicated by the damping change where it indicates stiffness deterioration of 26.6% at the pre-repair damage stage and at post-repair the stiffness deterioration decreases to only 11.3%. Thus a stiffness recovery of 15.58% at stage R compared to stage D is observed.

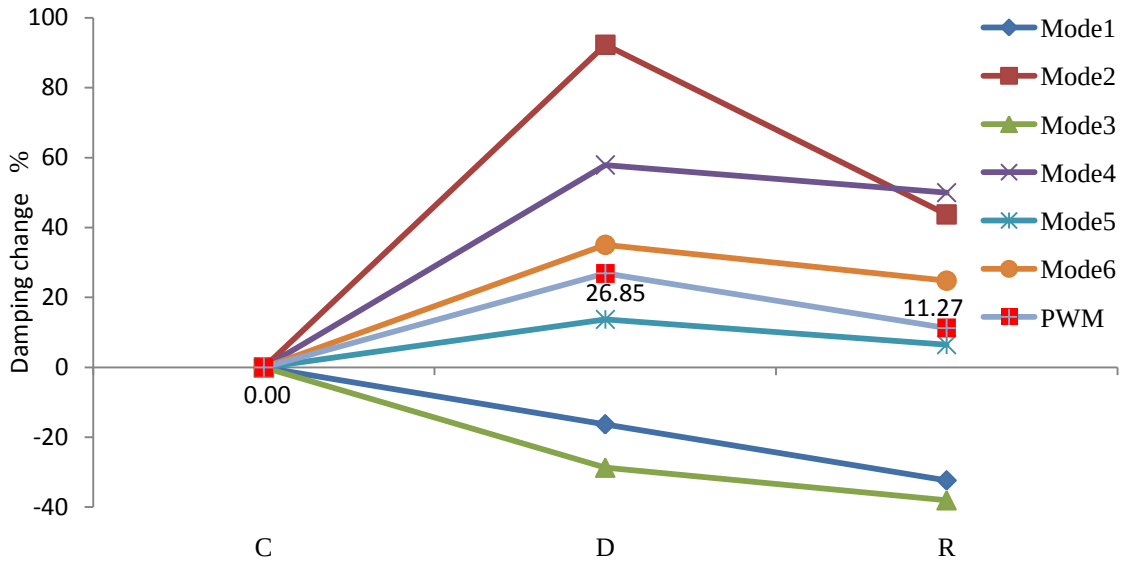

Figure 6.76. Damping change and weighted average (PWM) results for beam B221q

The frequency based stiffness index results for beam B222q are shown in Figure 6.77, where the adopted stages are the same as those illustrated in Table 6.22. The weighted average (PWM) is calculated and presented in Figure 6.77. The results show that all of the bending modes indicate a decrease in the frequency based stiffness index values at

pre-repair damage stage except for Mode 1 which shows an increase as a result of the composite action phenomenon of RC beams. At stage R, all the modes show an increase in the frequency based stiffness index values compared to stage D. All the modes show index values at the post-repair stage close to those at the undamaged stage, except for Mode 1 which shows a higher value. The weighted average shows a stiffness deterioration of 10% at the pre-repair damage stage. The stiffness recovery at post-repair stage is 11.92% compared to the pre-repair damage stage.

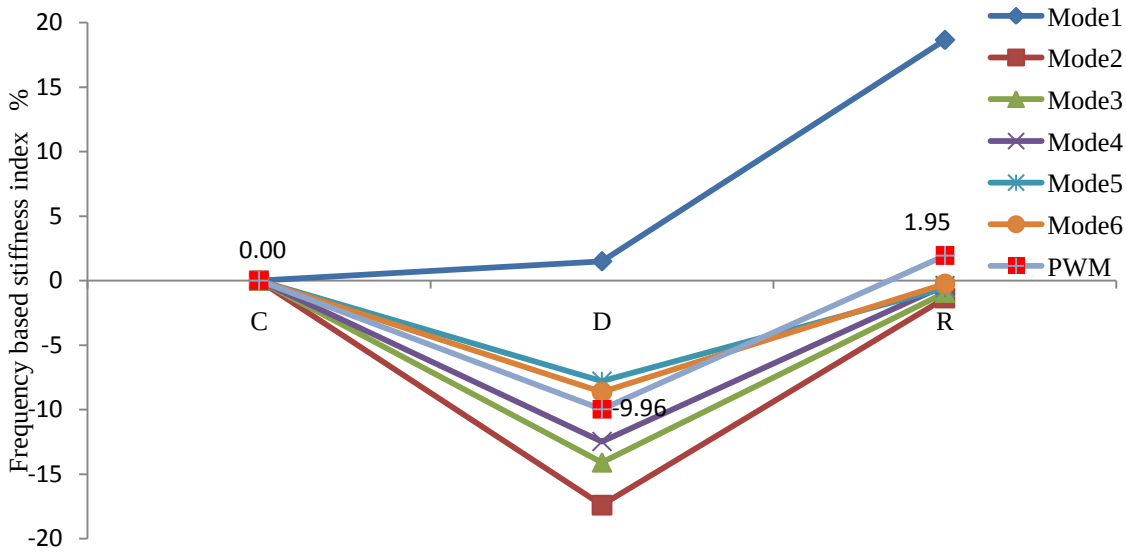

Figure 6.77. Frequency based stiffness index and weighted average (PWM) results for beam B222q

The damping change for beam B222q is calculated for all the modes at the same stages illustrated in Table 6.22, and the results are shown in Figure 6.78. The weighted average (PWM) of the damping change value based on the considered modes is calculated and the results are presented in Figure 6.78. The results show that all the modes indicate an increase in the damping values at the pre-repair damage stage with the exception of Mode 5 which indicates a decrease. After repair with CFRP sheets, all the modes show a decrease in the damping change values compared to stage D, which indicates an increase in the stiffness. Since different modes show different changes, the weighted

average (PWM) is calculated and the results show a stiffness deterioration of 17.4% at the pre-repair damage stage. Following this, a stiffness recovery of 18.8% at the post-repair stage compared to the pre-repair stage is observed.

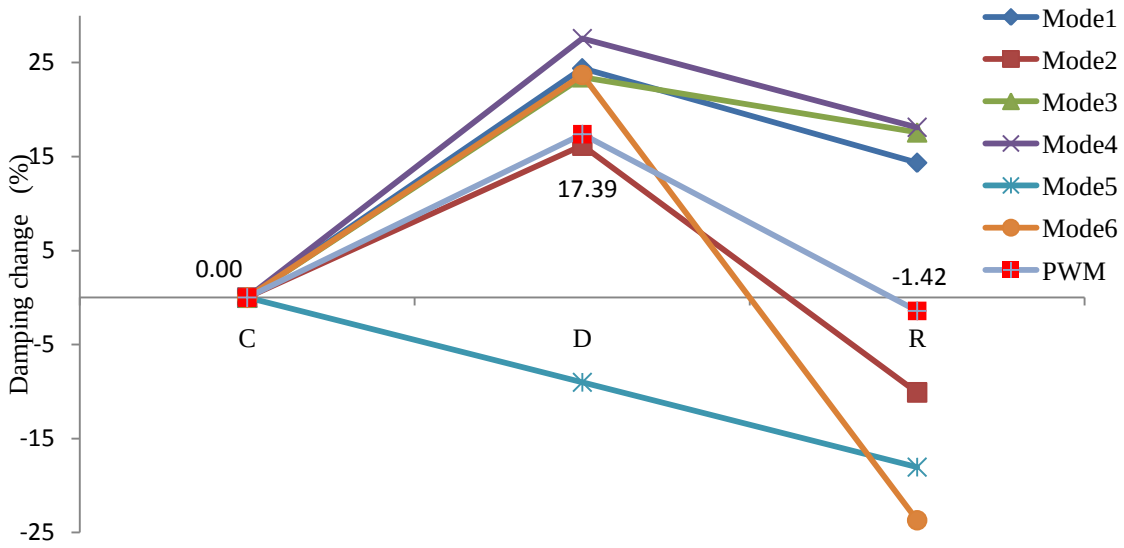

Figure 6.78. Damping change and weighted average (PWM) results for beam B222q

6.3.2.3 CFRP repair effectiveness

This section presents the relationship between the static and dynamic data in order to ascertain the effectiveness of the CFRP repair system at different pre-repair damage levels. The damage level is calculated based on the percentage of the applied load at pre-repair stage to the ultimate capacity of the unrepaired sections. The stiffness recovery as indicated by the ratio of increase in the ultimate load capacity is calculated based on the increase in the ultimate capacity of the repaired sections to the ultimate capacity of the unrepaired sections. The stiffness effectiveness based on the dynamic data is highlighted based on both frequency based stiffness index and damping change. For frequency based stiffness index and damping change, the repair effectiveness are calculated as the difference between the weighted average index value at the post-repair

stage compared to the weighted average index value at the pre-repair damage stage. Figure 6.79 shows the repair effectiveness based on the static and dynamic data and corresponding to the damage ratios of beams B221q and B222q.

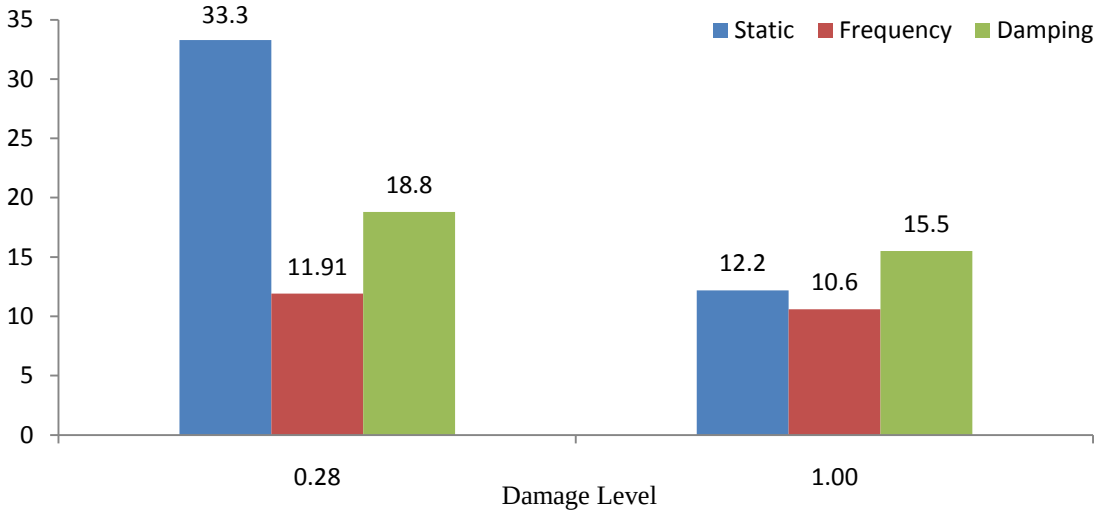

Figure 6.79. CFRP repair effectiveness based on static and dynamic data for shear at quarter span and beams without shear stirrups

The results show that repairing the beam with CFRP sheets recovers the stiffness and increases the load capacity by at least 12.2%, regardless of the pre-repair damage level. For dynamic indicators, damping change shows a higher stiffness recovery than the frequency based stiffness index. For pre-repair damage level close to the design load, the repair with CFRP sheets increases the load capacity by 33.3% with a corresponding stiffness recovery of 11.92% and 18.8% based on frequency based stiffness index and damping change, respectively. The increase in load capacity of 12.2 to 33.3% corresponding to the pre-repair damage levels for shear beams without stirrups is in good agreement with the findings of Pellegrino and Modena (2002).

6.3.2.4 Monitoring of repaired beams

Beams B221q and B222q are tested under load cycles at post-repair stages until failure as mentioned in the static evaluation, and the dynamic test is carried out to monitor the behaviour of the repaired beam during its service life. The frequency based stiffness

index is calculated after each load cycle at the post-repair stages for both repaired beams. Table 6.27 shows the load cycles and notation at the post-repair stages used to plot the frequency based stiffness index during the monitoring of the repaired beams. Figure 6.80 shows the frequency based stiffness index for the post-repair stage of beam B221q, whereas stage 'R' is used as the datum for the index values at higher loading stages.

Table 6.27. Load cycles for the post-repair stages of beam B221q

Load (kN)	Notation	Remark
0	R	Post-repair under self weight
25	R25	
84	R84	
91	RD	Subjected to pre-repair load
101	R101	Failure

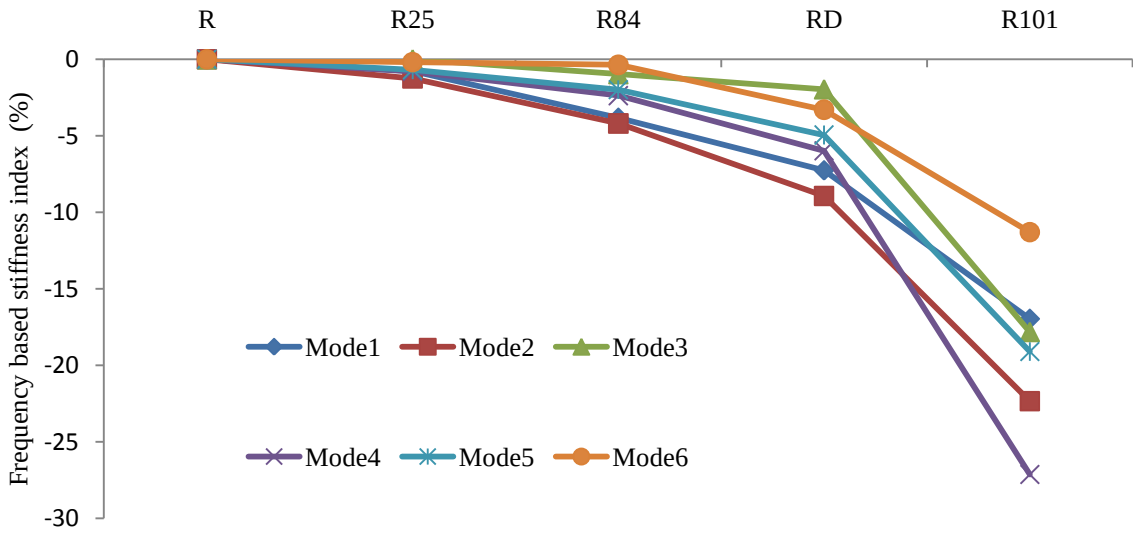

Figure 6.80. Frequency based stiffness index values for the monitoring of beam B221q

The results show that all the modes indicate a small decrease in the frequency based stiffness index values at stage R25 except for Modes 3 and 6 which show no change. At stage R84 all modes show a further decrease in the index values which is due to the progression of the flexural crack in the adhesive layer between the CFRP sheet and the

concrete surface. At stage RD where the applied load is the pre-repair damage load, all modes show a further decrease in the frequency based stiffness index values due to the progression of the flexural cracks in the adhesive layer and the appearance of the new cracks in the beam as shown in Table 6.25. Beyond stage RD, all the modes show a rapid decrease in the frequency based stiffness index values due to the induced flexural and shear cracks in the adhesive layer between the CFRP sheets and the beam surface as shown in Figure 6.70, where the failure occurs as a combination of flexural failure and CFRP delamination.

Figure 6.81 presents the frequency based stiffness index values at the post-repair stage corresponding to each load cycle up to failure for beam B222q, and Table 6.28 shows the load cycles and nota tion at the post-repair stages used to plot the frequency based stiffness index during the monitoring of the repaired beams. Stage 'R' is the datum for the frequency based stiffness index values at the following stages.

The results show that all modes indicate a small decrease in the frequency based stiffness index values at stage RD. A rapid decrease at stage R90 is observed which is due to the appearance of six new cracks in the beam, as illustrated in Table 6.26. These in turn indicate a decrease in the concrete stiffness and the progression of flexural cracks into the adhesive layer. At stage R120, a further decrease in the frequency based stiffness index values is noted for all modes. However the decrease is less than at stage R90, where only three new cracks appear in the beam as illustrated in Table 6.26. When failure occurs at stage R110, a rapid decrease is noted for all the modes due to the combination of the flexural failure and CFRP delamination, as shown in Figure 6.74.

Table 6.28. Load cycles for the post-repair stages of beam B222q

Load (kN)	Notation	Remark
0	R	Post-repair under self weight
25	RD	Subjected to pre-repair load
90	R90	
120	R120	
110	R110	Failure

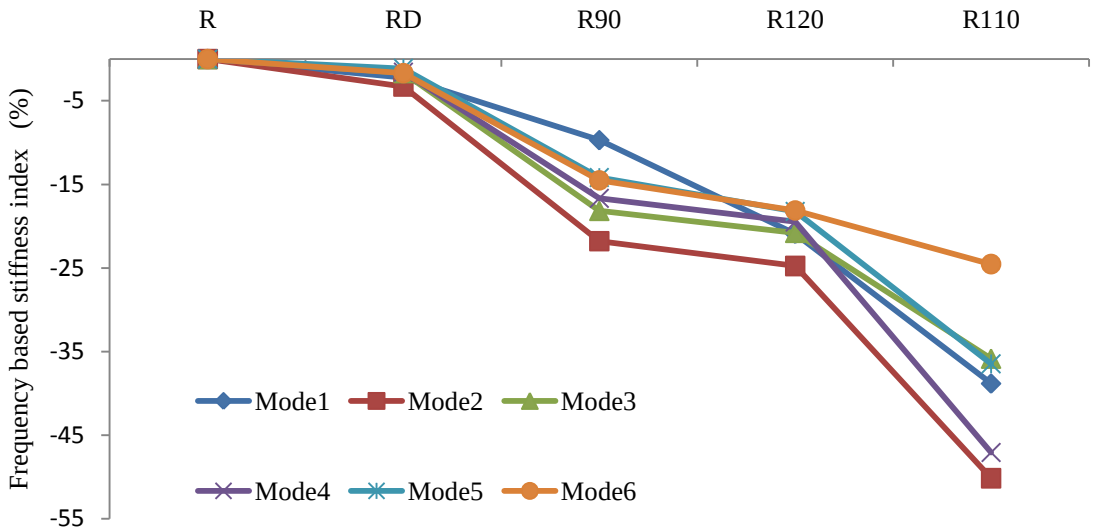

Figure 6.81. Frequency based stiffness index values for the monitoring of beam B222q

6.3.3 Effect of shear stirrups

The previous sections have presented the results of the CFRP repair system for shear damage at quarter-span where both design cases with and without shear stirrups are investigated. This section has summarised the effect of the design criteria, with and without shear stirrups, on the repair effectiveness using CFRP sheets. The results show that the presence of shear stirrups results in a lower contribution from the CFRP sheets to the ultimate capacity. Beams designed without shear stirrups indicate an increase in the ultimate capacity of 12.2 to 33.3% after repair with CFRP sheets, while beams designed with stirrups show an increase of 8.1 to 21.2%. The higher contribution from

the CFRP sheets to the ultimate capacity in the design case without shear stirrups is in good agreement with the findings of Pellegrino and Modena (2002). Steel reaches its yield strain prior to failure for both design cases.

The recorded CFRP strains are smaller than 800 μst for both design cases, which is considered a small value when compared to the ultimate strain of the CFRP sheets, and the presence of stirrups results in less strain by only 100μst. Such a low strain value was observed by Triantafillou (1998) and Li et al. (2001), where Triantafillou (1998) concluded that the two-sided strengthening procedure using externally bonded FRP sheets delaminated before the loss of aggregate interlock in the beam which resulted in unusable strain, hence the need to find the effective strain for the FRP sheets. For both design cases, higher CFRP strain is recorded on the first sheet at quarter-span for low pre-repair damage level, and on the second CFRP sheet, between quarter-span and the support, for high pre-repair damage level.

The failure mode of both design cases is due to the progression of the pre-repair flexural crack into the CFRP sheets located at quarter-span which is directed to the concentrated stress tip of the CFRP sheets, which in turn causes the CFRP sheet to delaminate. Such failure mode varies from the findings in the literature where the observed modes were a combination of shear and CFRP debonding failure (El-Ghandour, 2011), shear failure and concrete cover delamination (Pellegrino and Modena, 2002) and shear failure with FRP rupture [Chajes et al. (1995), Araki et al. (1997), Funakawa (1997), Kage et al. (1997), Sato et al. (1997), Chaallal et al. (1998a)]. The dynamic indices for the stiffness recovery, frequency based stiffness index and damping change, show higher values for the design case without shear stirrups than the design case with shear stirrups and for both pre-repair damage levels.

6.4 Shear damage at 1.5d

This section presents the results related to the repair effectiveness of the CFRP sheets for shear damage located at 1.5 the effective depth (d), from either one of the supports. Two design criteria are used, the first is designed with internal shear stirrups where shear forces are resisted by stirrups and concrete whilst the second is designed without internal shear stirrups where all shear forces are resisted solely by the concrete. Each design case is investigated at two pre-repair damage levels where the first damage level is at the maximum load at which failure starts to occur. This can be noticed when the load against deflection curve just begins to be horizontal. The second damage level is at the failure load where the beam is fully damaged. The repair design and procedure is as mentioned in Sections 4.2.5 and 4.3.2.2.

6.4.1 Beams with stirrups

Beams B211d and B212d are designed with internal shear stirrups and are used to investigate the repair effectiveness of CFRP sheets as a shear repair system. The results cover the static and dynamic evaluations and the monitoring of the repaired beams. For the static evaluation, the load against deflection, load against steel strain, load against CFRP strain and failure modes are highlighted. For the dynamic evaluation, the stiffness recovery based on frequency based stiffness index and damping change are highlighted. For the monitoring of the repaired beams, the frequency based stiffness index results corresponding to load cycles at the post-repair stages are also presented.

6.4.1.1 Static evaluation

The load cycles at the pre-repair damage stage for beam B211d are shown in Table 5.2, and the load cycles with the corresponding number of cracks at post-repair stages are shown in Table 6.29. The loads against deflection curves at the pre-repair stage are presented in Figure 5.10, and the loads against deflection curves at the post-repair stage are shown in Figure 6.82. The loads against steel strain curves at pre-repair stage are shown in Figure 5.11, and the loads against steel strain curves at post-repair stage are shown in Figure 6.83. The deflections shown in Figures 5.10 and 6.82 are the maximum measured deflections located at the zone between 1.5d from the support and the mid-span as discussed in Section 4.4.1. The steel strain presented in Figures 5.11 and 6.83 is the strain of flexural steel bars at 1.5d from the support. The remaining steel strain from pre-repair stage is the datum for the post-repair stages, where the beam is not turned over during the repair procedure and the steel strain remains unchanged. The crack patterns at pre and post repair stages are illustrated in Appendix B.

Table 6.29. Load cycles and corresponding number of cracks for beam B211d

Load Cycles (kN)	Number of cracks	Remark
142.5	14	Pre-repair stage
25	14	Post-repair stage
135	14	
143	14	CFRP starts debonding
106	14	Full CFRP debonding and failure

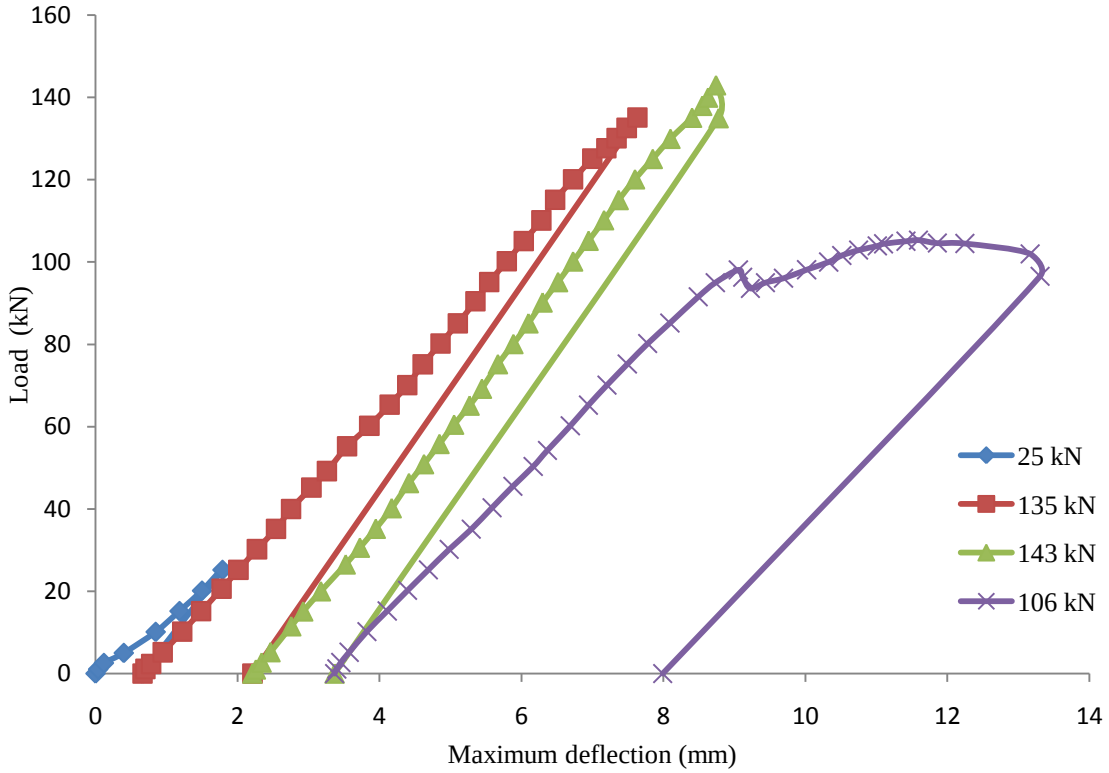

Figure 6.82. Load against maximum deflection at post-repair stage for beam B211d

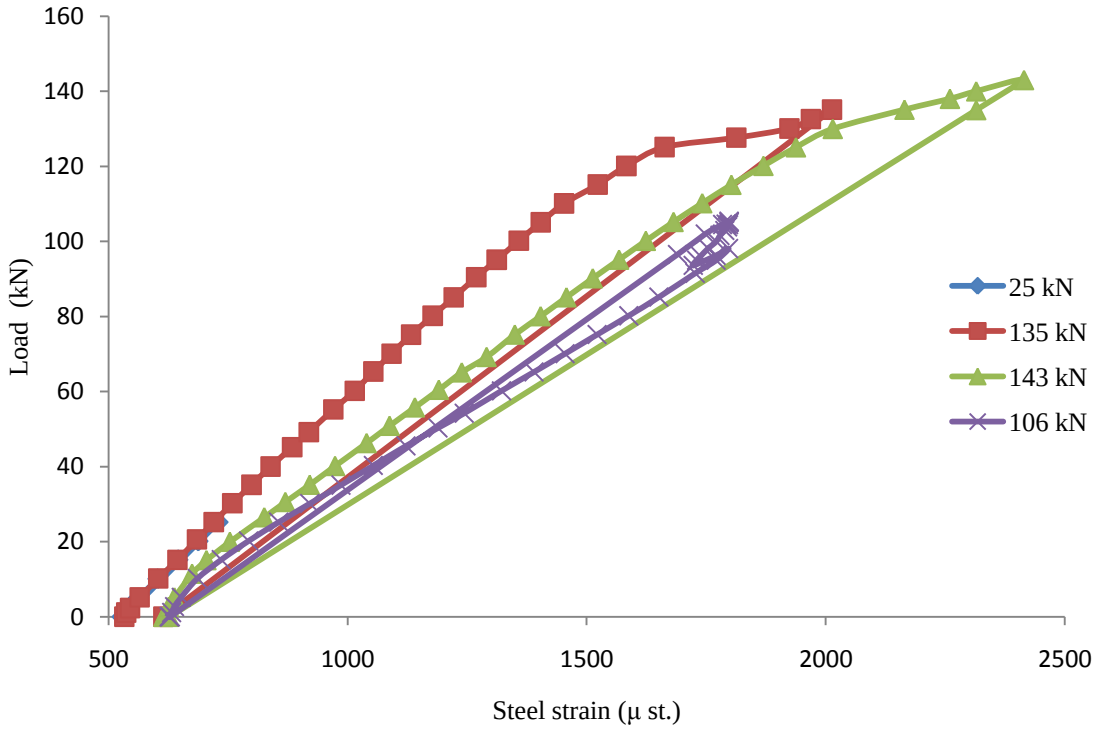

Figure 6.83. Load against steel strain at post-repair stage for beam B211d

The results show that the beam is fully damaged under a failure load of 142.5 kN at pre-repair damaged stage despite no yielding of steel. After repair with externally bonded inclined CFRP sheets, the beam is able to withstand a maximum load of 143 kN before failure occurs at the subsequent load cycle of 106 kN. Steel has not reached its yield limit prior to failure at post-repair stage either. The increase in load capacity equals the maximum capacity of the repaired section (143 kN) divided by the maximum capacity of the unrepaired section (142.5 kN) which is 100.4%. Thus, the fully damaged beam due to shear failure at 1.5d can recover its original capacity after repair with externally inclined CFRP sheets.

The result illustrated in Figure 6.84 shows that a higher CFRP strain is recorded at second strain gauge (SG2), however its value is less than 1000μst. The results indicate that the CFRP sheet still supports the loading without any strain release until a load of 135 kN, after which the strain is released due to the appearance of cracks in the adhesive layer between the CFRP sheets and the concrete surface.

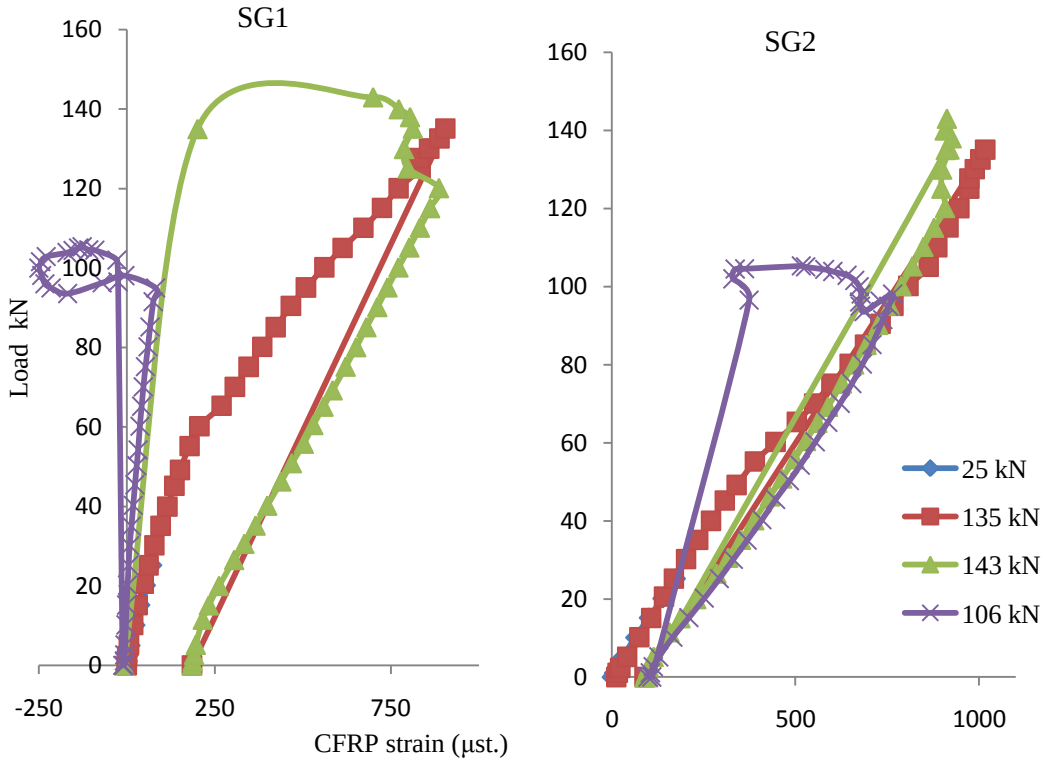

Figure 6.84. Load against CFRP strain at SG1 and SG2 for beam B211d

The failure mode is a combination of shear failure and CFRP debonding, where the shear cracks progress into the adhesive layer. Ideally, shear failure would have been in the form of an inclined line on the surface of the beam starting from the point of applied load to the support. However, the presence of the CFRP sheets prevent such a failure. Consequently, the combination of shear cracks which progress into the adhesive layer of the first CFRP sheet, close to 1.5d from the support at the upper tip, and into the second CFRP sheet close to the support at the bottom tip, resulted in CFRP debonding as shown in Figure 6.85.

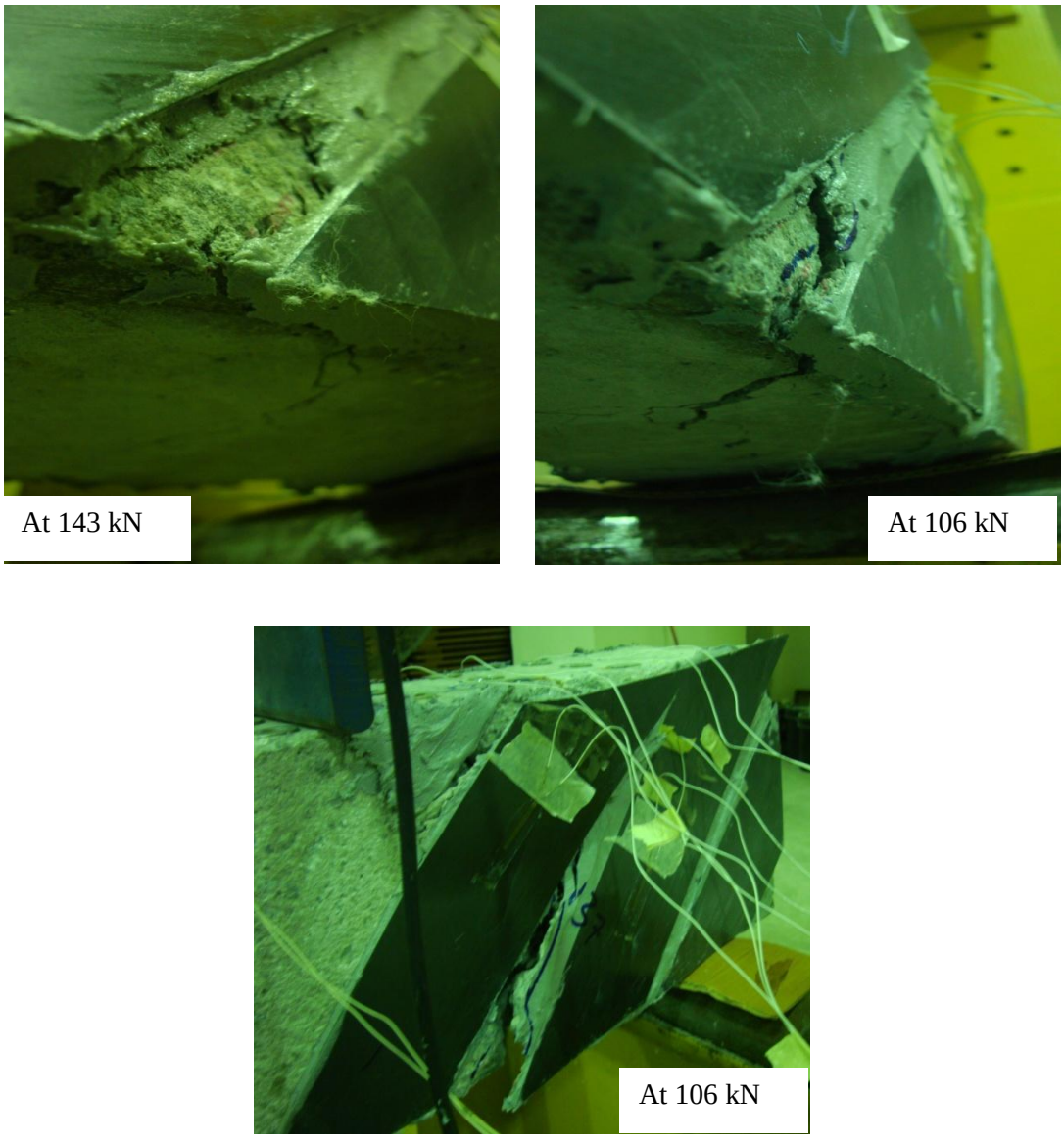

Figure 6.85. Failure mode for beam B211d

For beam B212d, the load cycles and corresponding number of cracks are shown in Table 6.30. The load against deflection curves and load against steel strain curves at pre and post repair stages are shown in Figures 6.86 and 6.87 respectively. The CFRP strain values at first and second strain gauges (SG1and SG2), which are positioned on vertical CFRP sheets, are shown in Figure 6.88. The crack patterns at pre and post repair stages are illustrated in Appendix B.

The results show that the beam is damaged under a maximum load of 126 kN at the pre-repair stage and the repaired beam is able to withstand a load of 165 kN. The increase in the load capacity is the repaired section capacity (165 kN) divided by the unrepaired section capacity (126 kN) which is equal to 130.9%. The steel strain values show that steel has not yielded prior to maximum load capacity at pre-repair stage. The strain gauge wire breaks before the maximum capacity of 126kN is reached at the pre-repair stage, therefore no steel strain data is recorded for post-repair stage. The CFRP strain is higher at the second strain gauge (SG2) which is close to the support. The first strain gauge shows a release in strain beyond a load of 126 kN, while the second strain gauge shows a release after loads of 165 kN.

Table 6.30. Load cycles and corresponding number of cracks for beam B212d

Load Cycles (kN)	Number of cracks	Remark
126	17	Pre-repair stage
25	17	Post-repair stage
126	17	
165	18	CFRP starts debonding
154	19	Full CFRP debonding and failure

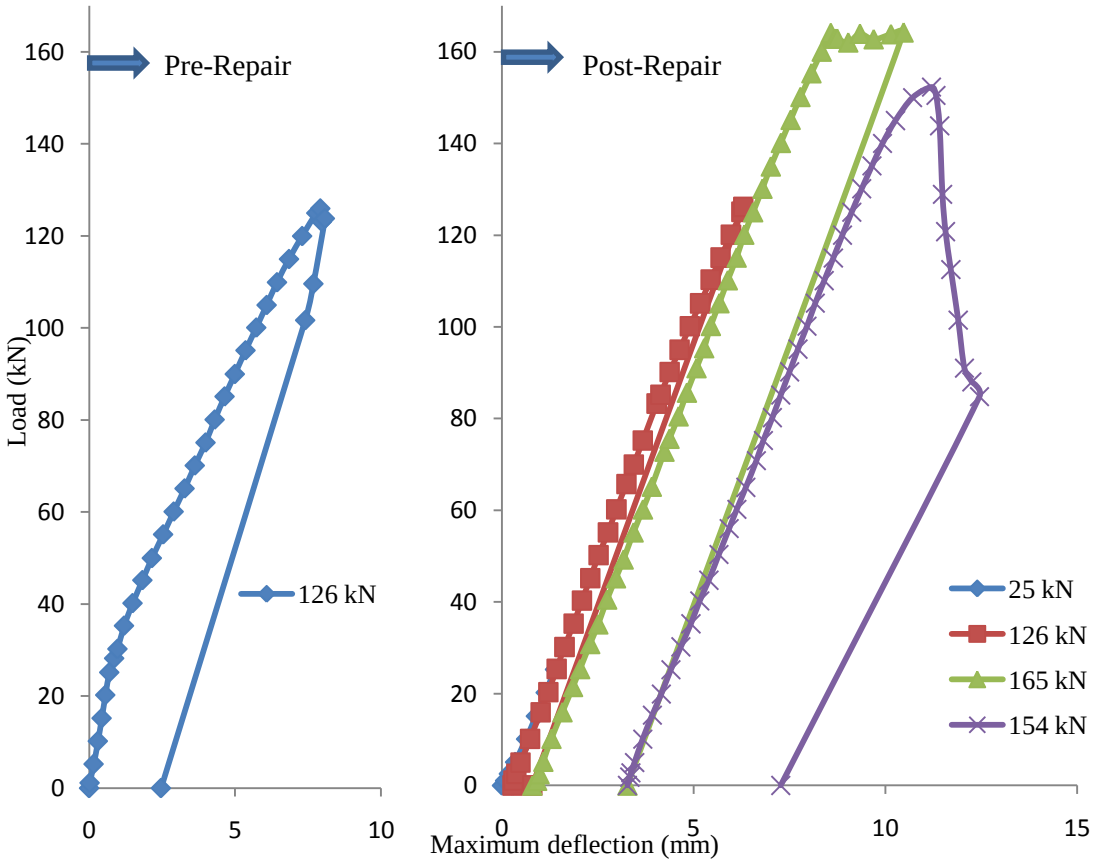

Figure 6.86. Load against maximum deflection at pre and post repair stages for beam B212d

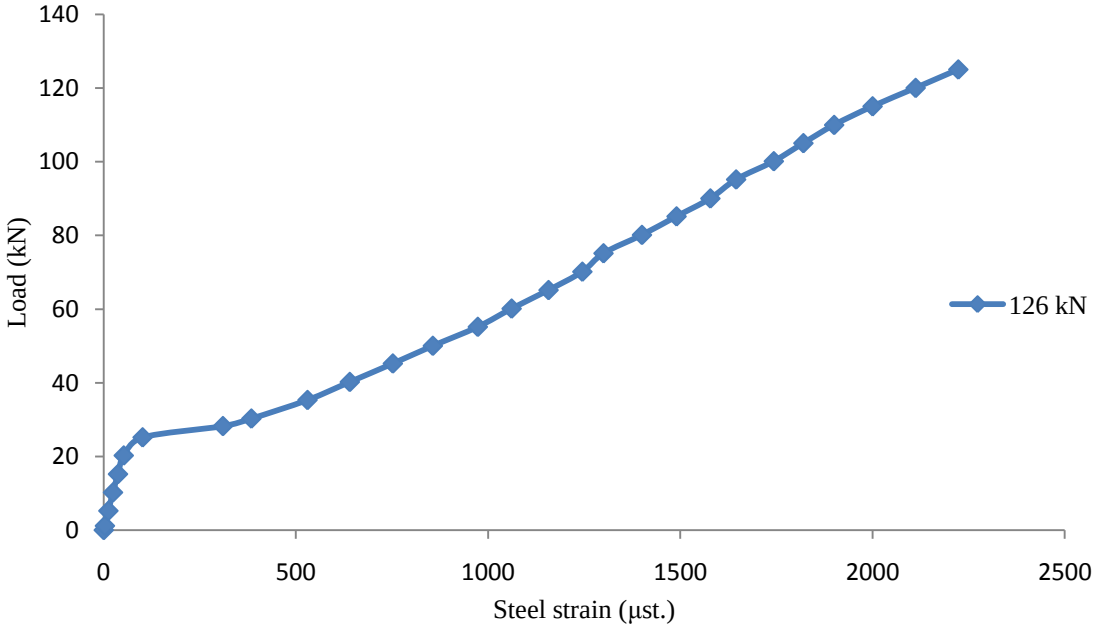

Figure 6.87. Load against steel strain for beam B212d at pre-repair stage

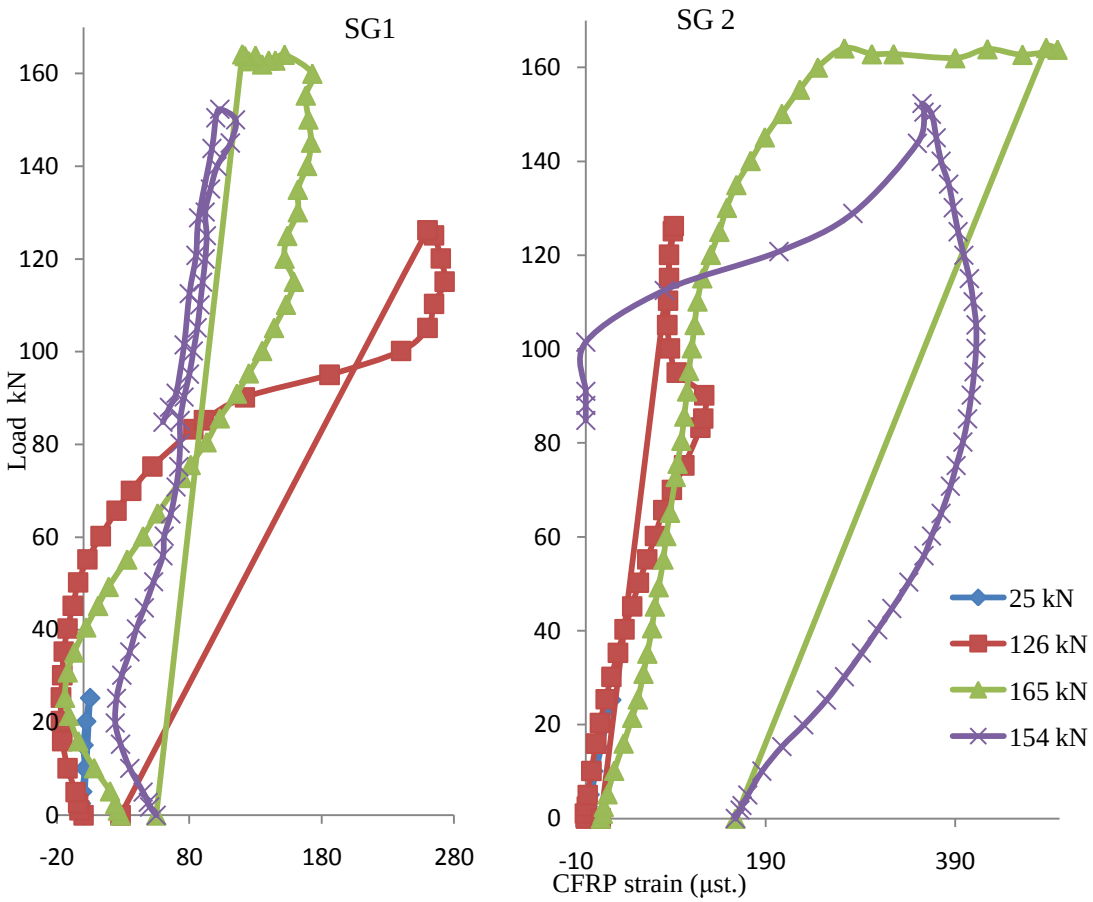

Figure 6.88. Load against CFRP strain at SG1 and SG2 for beam B212d

The failure mode is a combination of shear failure and CFRP debonding, where shear cracks progress into the adhesive layer. The presence of the CFRP sheets prevents shear failure which would have occurred on the surface of the beam starting from the point of the applied load to the support. The combination of shear cracks which progress into the adhesive layer through the upper tip of the first CFRP sheet close to 1.5d, and the bottom tip of the second CFRP sheet close to support, result in CFRP debonding as shown in Figure 6.89. When subjected to stress perpendicular to the fibre direction, a crack is observed on the vertical CFRP sheet at a load cycle of 126 kN. This is due to the weakness of CFRP in that vertical direction.

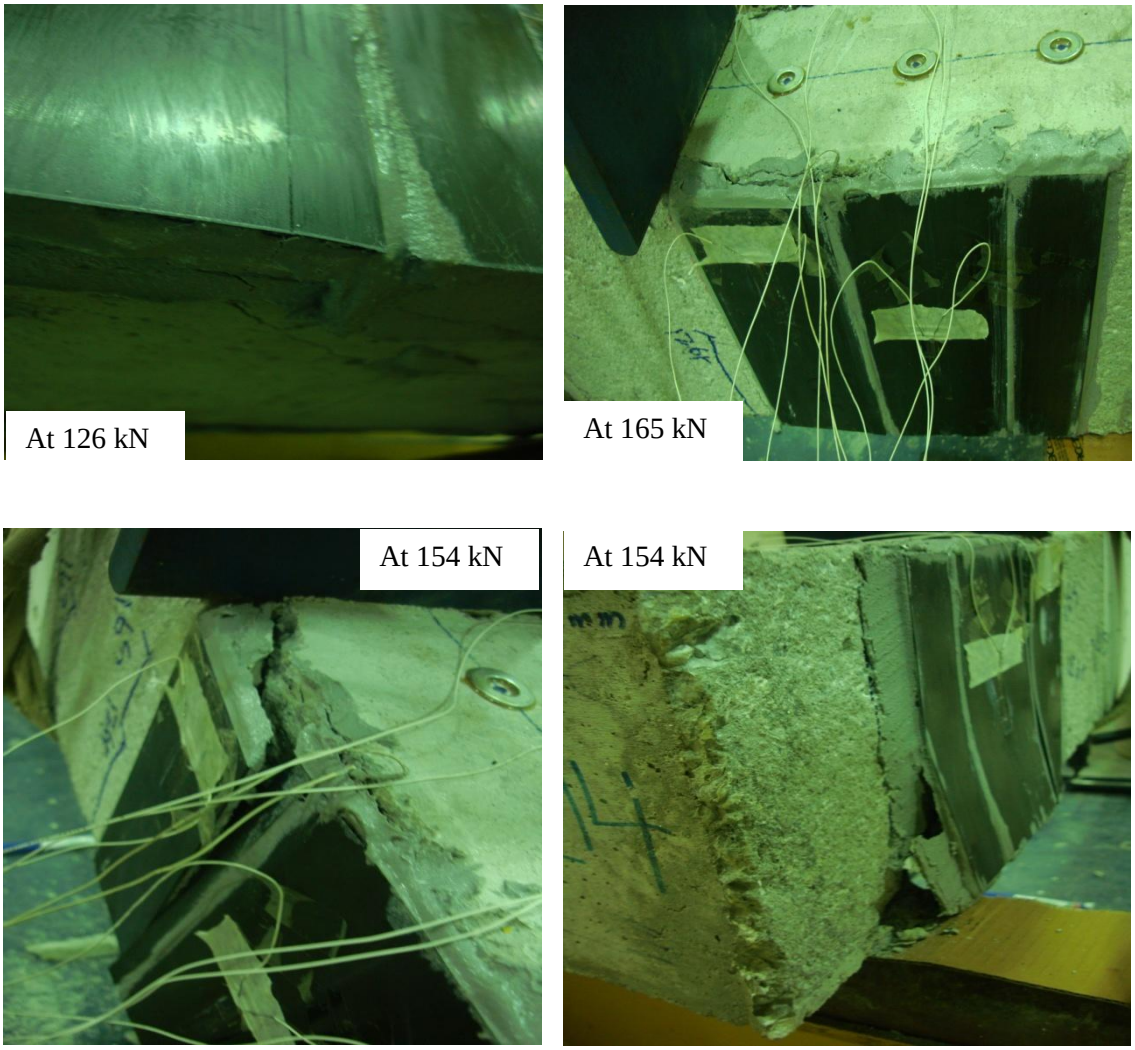

Figure 6.89. Failure mode of beam B212d

6.4.1.2 Dynamic evaluation

This section presents the dynamic evaluation of CFRP shear repair effectiveness based on frequency based stiffness index and damping change. The adopted stages are as illustrated in Table 6.22 and Figure 6.90 shows the frequency based stiffness index and the weighted average (PWM) results for beam B211d.

The results show that all the modes indicate a decrease in the frequency based stiffness index at pre-repair stage where the failure occurs at a load of 142.5 kN, while repair with CFRP sheets helps to increase the index value at the post repair stage. The modal frequencies are highlighted as good indicators for repair effectiveness where all the

modes indicate an increase in the frequency based stiffness index values by fixing the CFRP sheets. Thus, repairing the shear damage beams without turning them over avoids the influence of the composite action phenomenon of repaired RC beams on the modal frequencies. The weighted average (PWM) is calculated, as shown in Figure 6.90, and these results highlight the pattern of the overall stiffness change based on all the considered modes. The weighted average shows a stiffness deterioration of 39.3%, as indicated by the frequency based stiffness index, at pre-repair stage. Following this the stiffness is recovered after repair where the stiffness deterioration decreases to 35.7 % compared to undamaged stage. This indicates a stiffness recovery of 3.5% compared to the pre-repair damage stage.

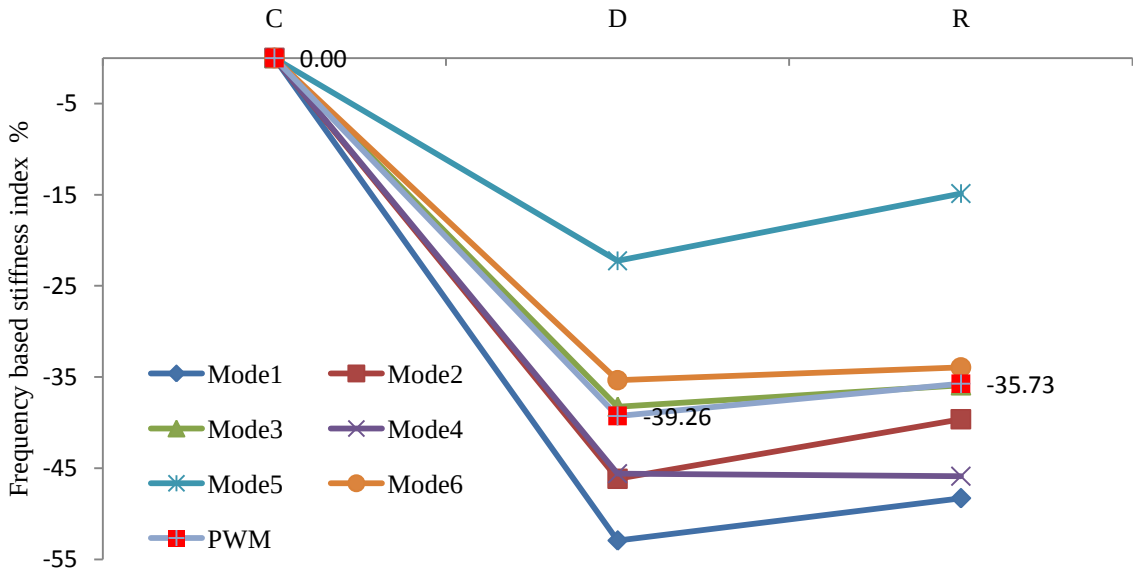

Figure 6.90. Frequency based stiffness index and weighted average (PWM) results for beam B211d

Figure 6.91 shows the damping change for beam B211d at pre and post repair stages. The adopted stages are the same as those for the frequency based stiffness index. The weighted average (PWM) is calculated and the results are also shown in Figure 6.91. The results show that all modes highlighted increase in the damping values at pre-repair stage which indicates stiffness deterioration. Repairing the beam with CFRP sheets influences all the modes, where a decrease in the damping values is observed which

indicates stiffness recovery. The weighted average shows the overall stiffness change based on the averaging of all the considered modes. The stiffness deterioration of 25.5%, as indicated by the damping change, is indicated at pre-repair damage stage. The stiffness deterioration decreases to 19.4% at post-repair stage compared to the undamaged stage. Thus, the stiffness recovery at post-repair stage, indicated using the damping change, is 6% compared to the pre-repair damage stage.

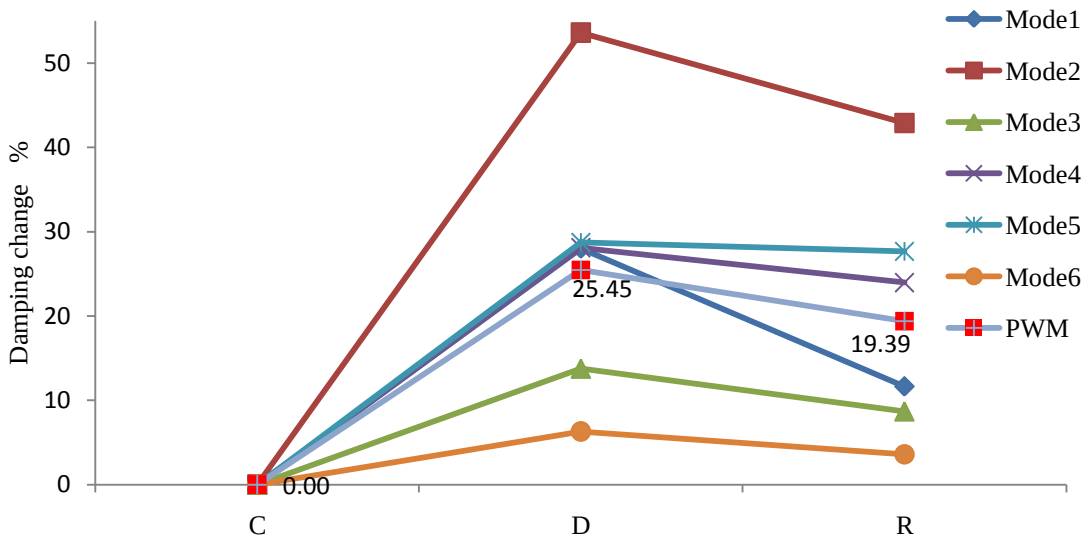

Figure 6.91. Damping change and weighted average (PWM) results for beam B211d

The frequency based stiffness index results for beam B212d are shown in Figure 6.92 at the same stages illustrated in Table 6.22, where the weighted averaging (PWM) is calculated and its results are also shown. The results show that all the modes indicate a decrease in the frequency based stiffness index values at pre-repair stage which are due to the stiffness deterioration. All the modes show an increase in the frequency based stiffness index values at the post-repair-stage compared to the pre-repair damage stage. At the post-repair stage, all the modes show lower index values when compared to the undamaged stage. The weighted average shows a stiffness deterioration of 39.5%, as indicated using frequency based stiffness index, at pre-repair stage. The stiffness deterioration decreases to 27.9% at the post-repair stage compared to the undamaged

stage. Thus, the stiffness recovery at the post-repair stage is 11.56% compared to the pre-repair stage.

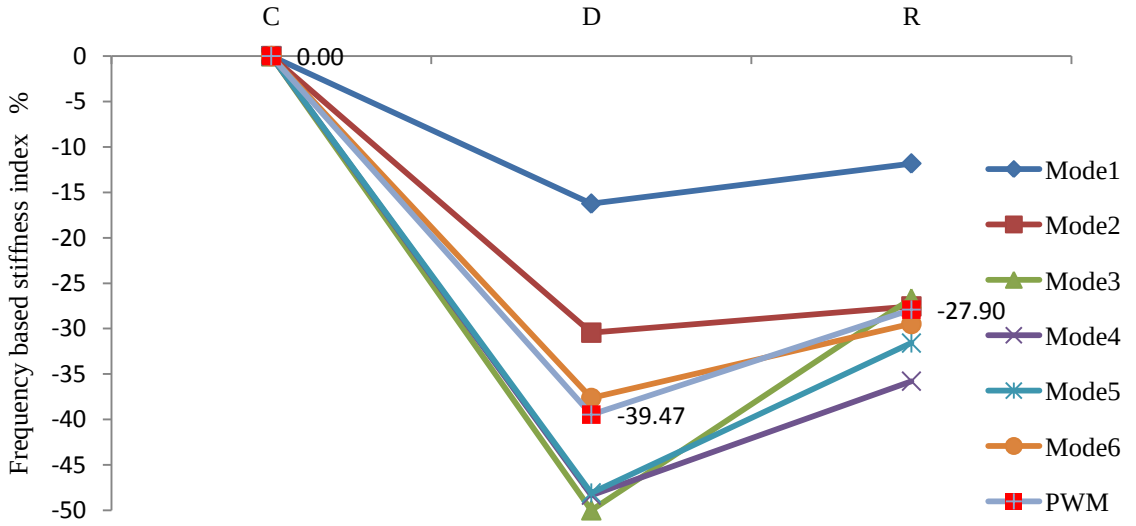

Figure 6.92. Frequency based stiffness index and weighted average (PWM) results for beam B212d

The damping change for beam B2112d is calculated for all the considered modes and the results are shown in Figure 6.93, which also presents the weighted average (PWM) results. The results show that all modes indicate an increase in the damping values at pre-repair damage stage except for Mode 3 which shows a decrease. After fixing the CFRP sheets, all the modes show a decrease in the damping values compared to stage D. The weighted average (PWM) results show a stiffness deterioration of 36.3% at the pre-repair damage stage before stiffness deterioration decreases to 12.5% at the post-repair stage which indicates a stiffness recovery of 23.8% compared to the pre-repair damage stage.

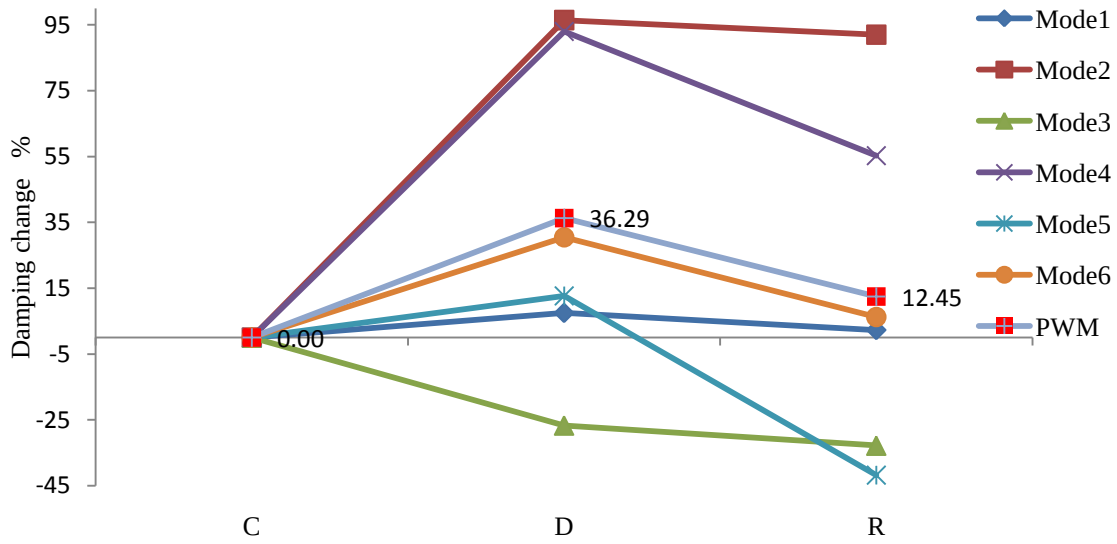

Figure 6.93. Damping change and weighted average (PWM) results for beam B2112d

6.4.1.3 CFRP repair effectiveness

This section presents the relationship between the static and dynamic data in order to obtain the effectiveness of the CFRP repair system at different pre-repair damage levels. The damage level is calculated based on the percentage of the applied load at pre-repair stage to the ultimate capacity of the unrepaired sections. Since both beams B211d and B212d are damaged under maximum capacity and the only difference is that beam B211d is fully failed while beam B212d is not, despite the maximum load, the damage ratio of beam B211d is 100% and the damage ratio of beam B212d is 99%. The stiffness recovery as indicated by the ratio of increase in the ultimate load capacity, is calculated based on the increase in the ultimate capacity of the repaired sections to the ultimate capacity of the unrepaired sections. The stiffness effectiveness based on the dynamic data is highlighted based on both frequency based stiffness index and damping change. For frequency based stiffness index and damping change, the repair effectiveness is calculated as the difference between the weighted average index value at post-repair stage compared to the weighted average index value at the pre-repair

damage stage. Figure 6.94 presents the CFRP repair effectiveness based on static and dynamic data.

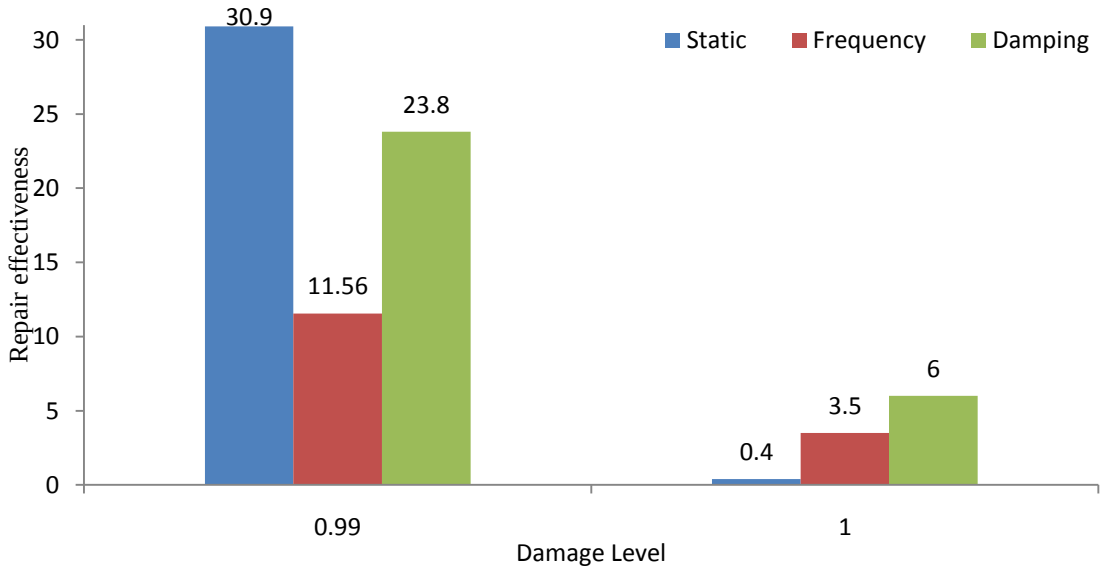

Figure 6.94. CFRP repair effectiveness based on static and dynamic data for shear at 1.5d and beams with stirrups

The results show that repair with externally bonded CFRP sheets recovers the stiffness whatever the pre-repair damage level. The dynamic data shows better sensitivity to the stiffness recovery than the increase in load capacity for the case of full failure at pre-repair damage stage. However, the damping change and frequency based stiffness index indicate a stiffness recovery of 6% and 3%, respectively, while load capacity shows no increase. For the pre-repair damage stage when failure just begins to occur, load capacity increases by 30.9% which is considered a very good indicator of the effectiveness of the CFRP sheets as shear repair system even when it is fixed vertically. The damping change and frequency based stiffness index indicate a stiffness recovery of 23.9% and 11.6% respectively.

6.4.1.4 Monitoring of repaired beams

The repaired beams B211d and B212d are tested under load cycles at post-repair stages until failure as mentioned in the static evaluation, and the dynamic test is carried out to monitor the behaviour of the repaired beam during its service life. The frequency based

stiffness index is calculated after each load cycle at post-repair stages for both repaired beams. Table 6.31 shows the load cycles and notation at the post-repair stages used to plot the frequency based stiffness index during the monitoring of the repaired beam B211d. Figure 6.95 shows the frequency based stiffness index for post-repair stage of beam B211d, where stage 'R' is used as the datum for the index values at higher loading stages.

Table 6.31. Load cycles for the post-repair stages of beam B211d

Load (kN)	Notation	Remark
0	R	Post-repair under self weight
25	R25	
135	R135	
143	RD	Subjected to pre-repair load
106	R106	Failure

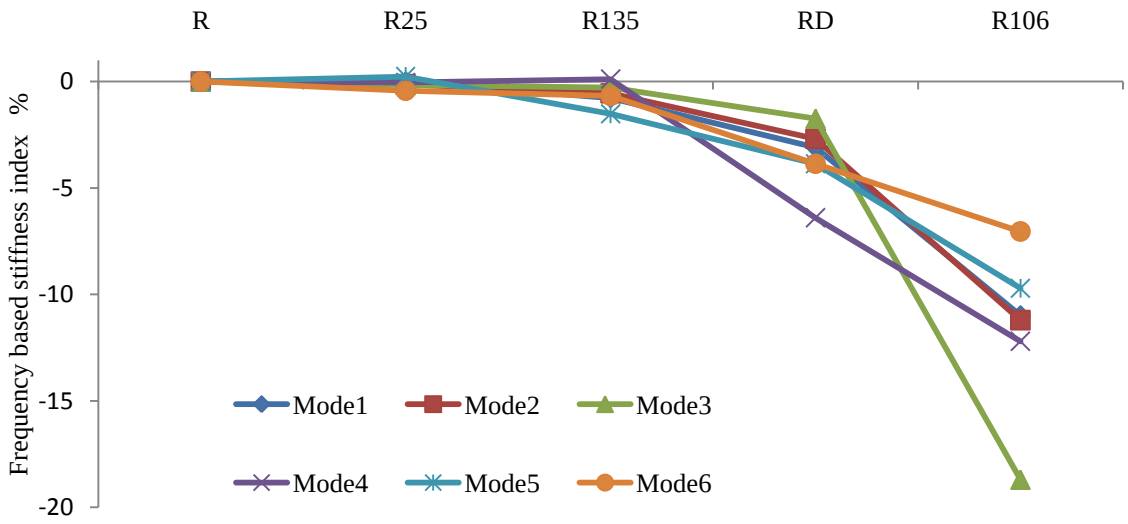

Figure 6.95. Frequency based stiffness index values for the monitoring of beam B211d

The results show that there is no distinct change in the frequency based stiffness index values at stage R25. A slight decrease is observed for some of the modes at stage R135 where higher load is applied, which is due to the progression of the shear crack into the adhesive layer. At stage RD when a load of 143 kN is applied, all modes show a further

decrease in the frequency based stiffness index values which indicates a stiffness deterioration as influenced by the progression of shear cracks into the adhesive layer as shown in Figure 6.85. When failure occurs at stage R106, all the modes show a rapid decrease in the frequency based stiffness index values indicating full debonding of CFRP sheets.

Table 6.32 shows the load cycles and notation at the post-repair stages used to plot the frequency based stiffness index during the monitoring of the repaired beam B212d. Figure 6.96 shows the frequency based stiffness index for post-repair stage of beam B212d, where stage 'R' is used as the datum for the index values at higher loading stages.

Table 6.32. Load cycles for the post-repair stages of beam B212d

Load (kN)	Notation	Remark
0	R	Post-repair under self weight
25	R25	
126	RD	Subjected to pre-repair load
165	R165	
154	R154	Failure

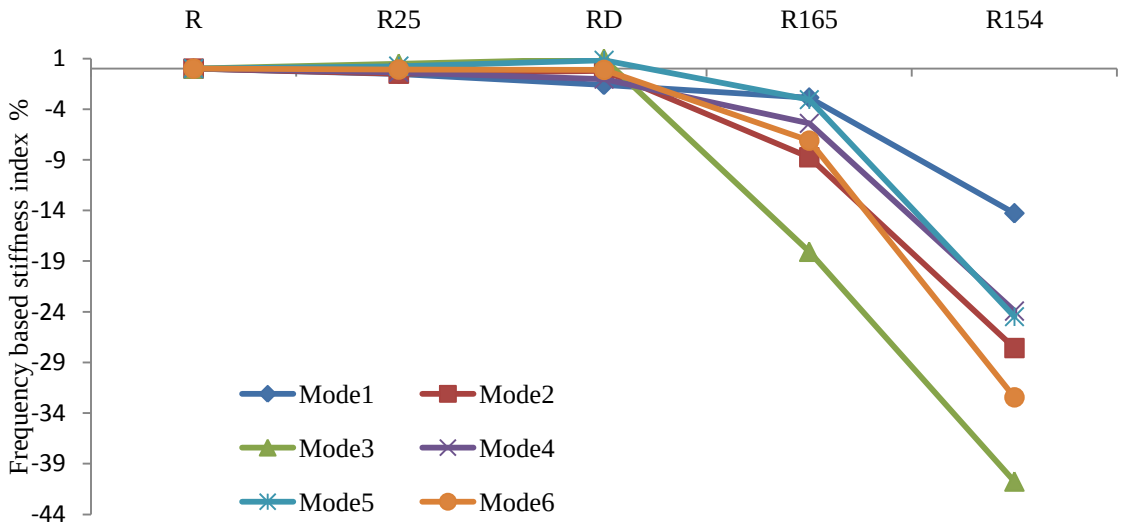

Figure 6.96. Frequency based stiffness index values for the monitoring of beam B212d

The results show that all the modes indicate no distinct change in the frequency based stiffness index values at stage R25. A slight decrease is noted for some of the modes at stage RD where the load is 126 kN, which is due to the progression of the shear crack in the adhesive layer. A further decrease is noted for all modes at stage R165 which indicates a stiffness deterioration influenced by the progression of shear cracks into the adhesive layer as shown in Figure 6.89. When the failure occurs at stage R154, all the modes show a rapid decrease in the frequency based stiffness index values indicating the full debonding of the CFRP sheet.

6.4.2 Beams without stirrups

Beams B221d and B222d are designed without internal shear stirrups and are used to investigate the repair effectiveness of CFRP sheets as shear repair system. The results include static evaluation, dynamic evaluation and monitoring of repaired beams. Moreover, the failure modes for both beams are discussed. Beam B221d is fully damaged at the pre-repair damage stage while beam B222d is subjected to the maximum load capacity without being fully damaged at the pre-repair damage stage.

6.4.2.1 Static evaluation

The static data includes load against deflection curves, load against steel strain curves, and load against CFRP strain curves for both beams at pre and post repair stages. Table 6.33 shows the load cycles and the corresponding number of cracks at pre and post repair stages for beam B221d. The load against steel strain curves at pre-repair stage are shown in Figure 6.97, and load against deflection curves at pre and post repair stages are shown in Figure 6.98, and. The steel strain presented in Figure 6.97 is the strain of flexural steel bars at 1.5d from the support. The deflection shown in Figure 6.98 is the

maximum measured deflection located at the zone between 1.5d from the support and mid-span, as discussed in Section 4.4.1.

Table 6.33. Load cycles and corresponding number of cracks for beam B221d

Load Cycles (kN)	Number of cracks	Remark
155	15	Maximum load at Pre-repair stage
151	15	Pre-repair stage
25	15	Post-repair stage
150	15	
120	15	CFRP starts debonding
103	15	Full CFRP debonding and failure

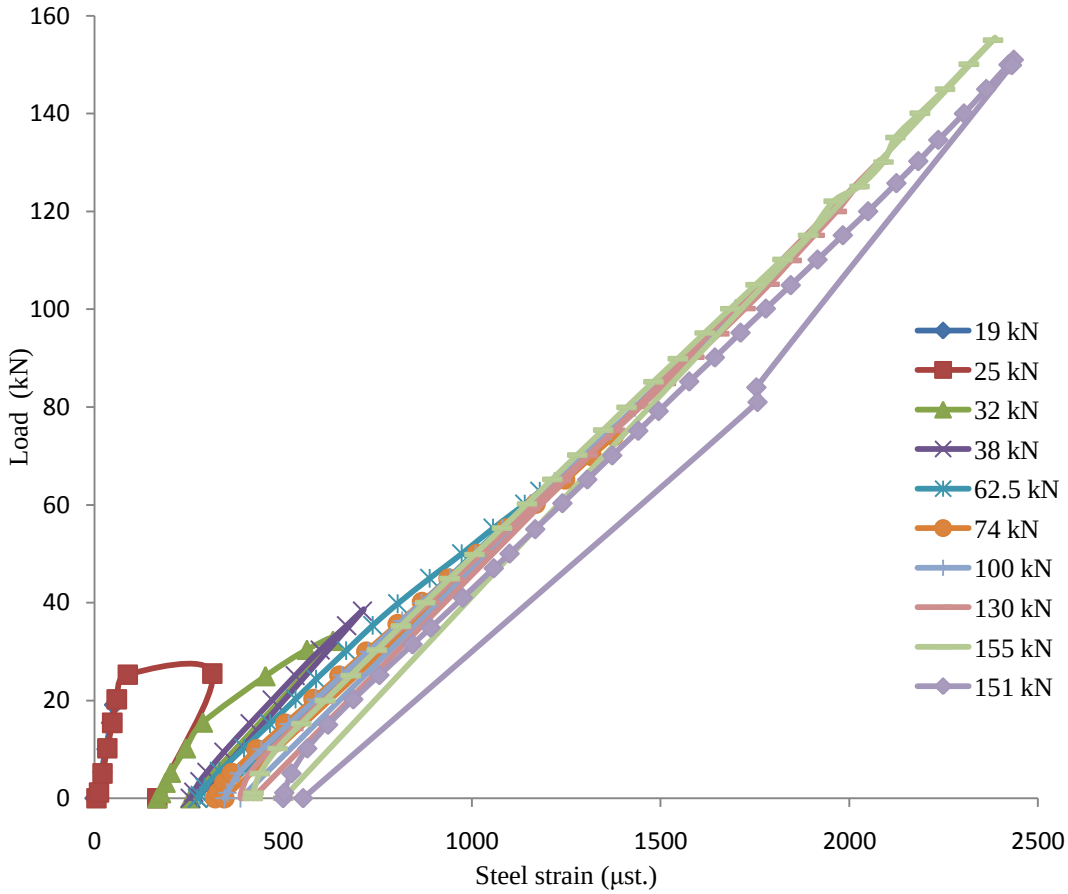

Figure 6.97. Load against steel strain at pre-repair stages for beam B221d

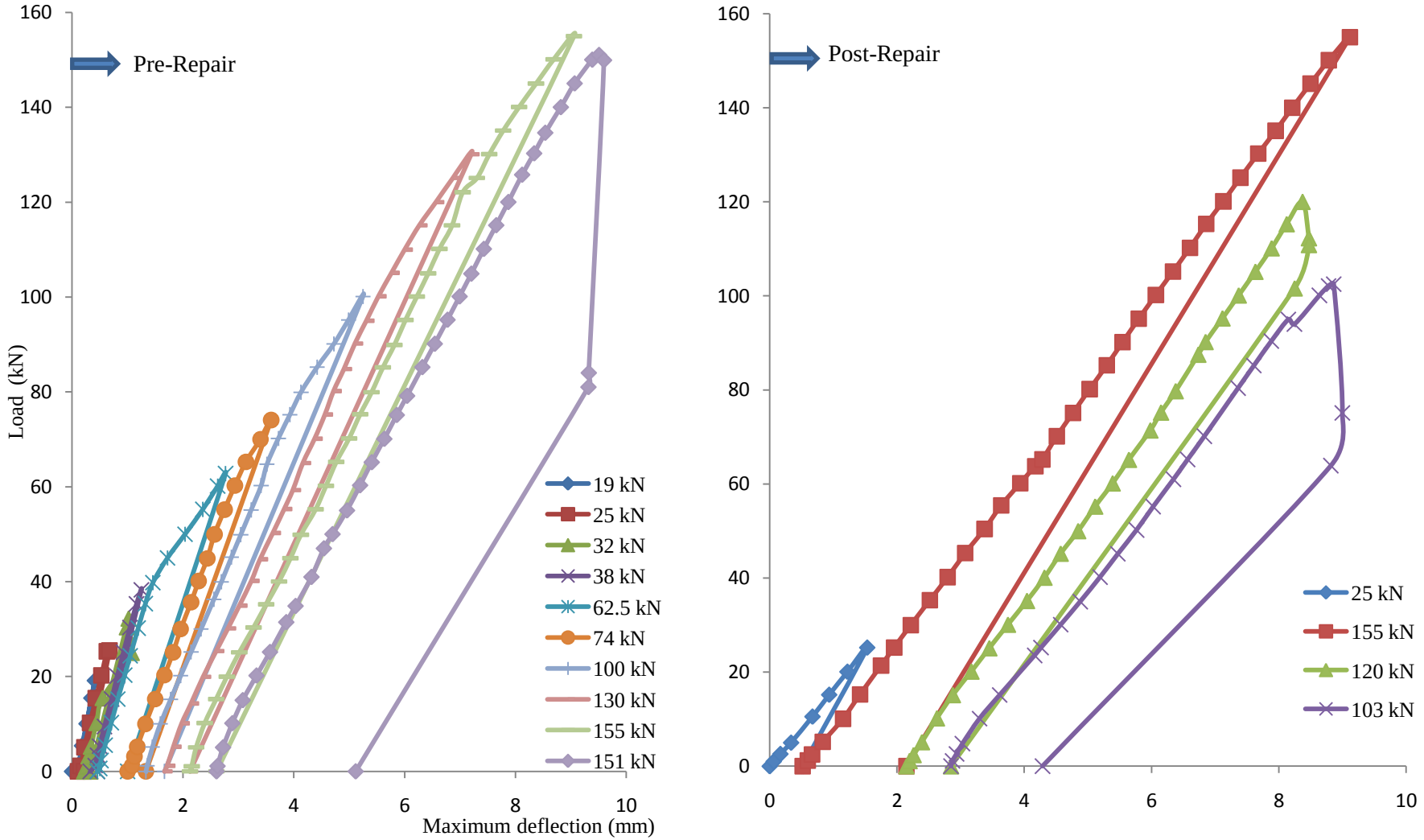

Figure 6.98. Load against maximum deflection at pre and post repair stages for beam B221d

The results show that the beam is damaged under failure load of 155 kN at the pre-repair damage stage. After repair, the beam with CFRP sheets is able to withstand a load of 155 kN. The CFRP debonding starts to occur at the next load cycle of 120 kN and the failure occurs at 103 kN. The increase in load capacity is the maximum capacity of the repaired section (155 kN) divided by the maximum capacity of the unrepaired section (155 kN) which is equal to 100.0%. Thus, the repaired beam is able to recover the same load capacity as the unrepaired section where serious failure occurs at the pre-repair damage stage. Steel strain values show that steel does not yield prior to maximum load capacity at the pre-repair damage stage, and then the strain gauge wire breaks during the repair procedure, so no steel strain data is recorded at the post-repair stage. The CFRP repair design and procedure is as discussed in Sections 4.2.5 and 4.3.2.2. The CFRP strain is monitored on the four CFRP sheets on both sides of the damaged beam corresponding to the load cycles, where first strain gauge (SG1) is nearest to 1.5d from the support and second strain gauge (SG2) is closest to the support. Figure 6.99 shows the results of the CFRP strain corresponding to each of the load cycles for both strain gauges.

The result shows that higher strain is recorded at the first strain gauge where it reaches a strain of about 1600μst, while the second strain gauge records a strain of less than 200 μst. The first strain gauge indicates that the CFRP sheet is still able to carry the load without any release in strain up to a load of 120 kN after which a release in the CFRP strain is noted. This release is due to the influence of the shear crack in the adhesive layer, meanwhile the second strain gauge indicates the release start at a load of 155 kN where some cracks start to appear at the adhesive layer.

The failure mode of beam B221d is a combination of shear failure and CFRP debonding mode. The presence of the CFRP sheets prevents a typical shear failure which would result in an inclined crack on the surface of the beam starting from the point of the applied load to the support. The result is a combination of shear crack which progresses into the adhesive layer at the upper tip of the first CFRP sheet close to 1.5d and the bottom tip of the second CFRP sheet close to support, causing CFRP debonding as shown in Figure 6.100.

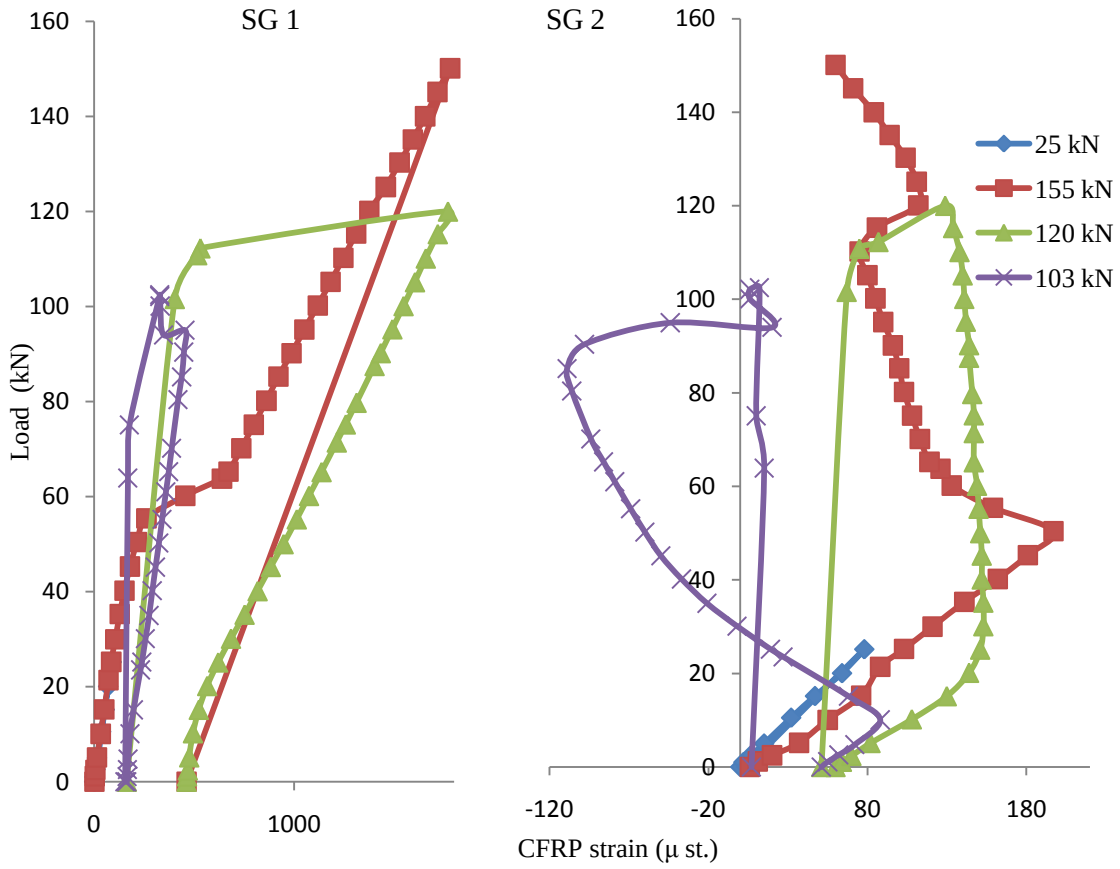

Figure 6.99. Load against CFRP strain for beam B221d at post-repair stages

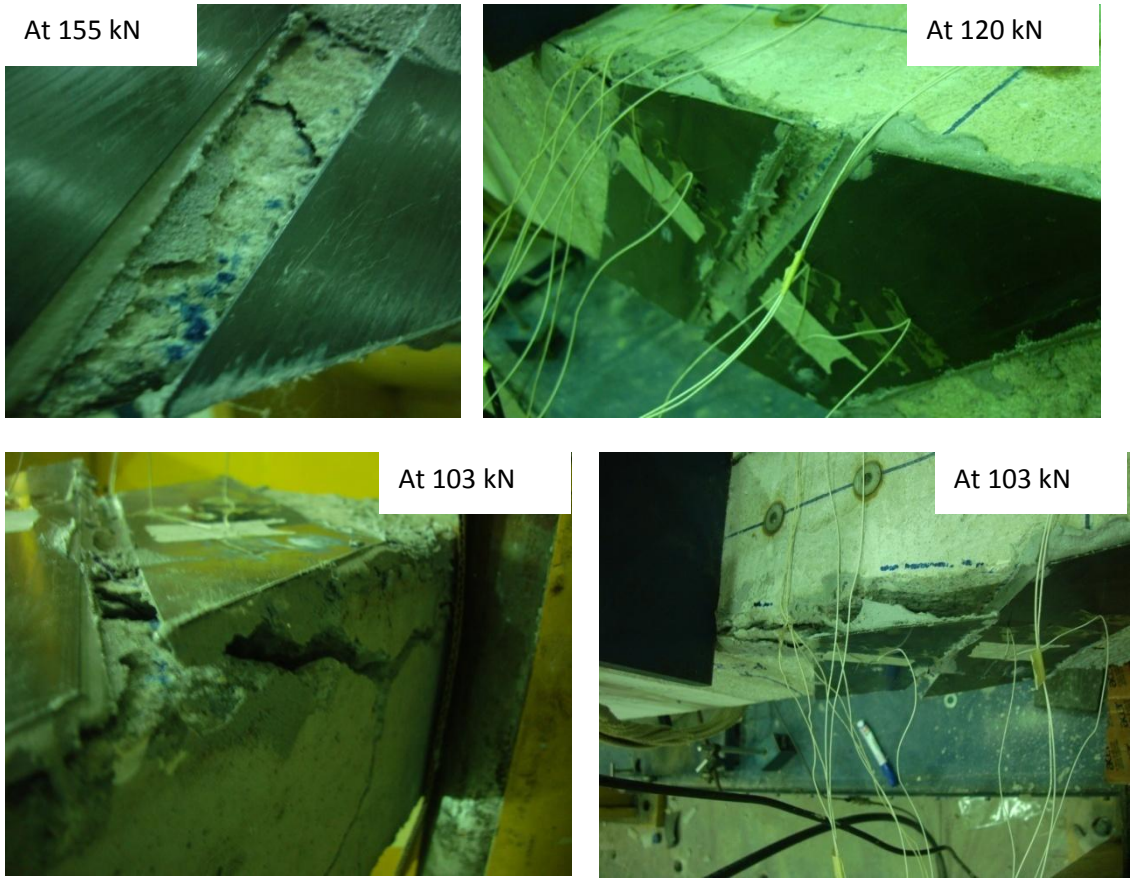

Figure 6.100. Failure mode for beam B221d

Table 6.34 illustrates the load cycles and corresponding number of cracks for beam B222d at pre and post repair stages. Figure 6.101 shows load against deflection curves and Figure 6.102 shows load against steel strain curves at pre and post repair stages for beam B222d. The CFRP sheet design is as discussed in Section 4.3.2.2. Figure 6.103 shows load against CFRP strain for beam B222d at first and second strain gauges (SG1 and SG2), where first strain gauge is the nearest to 1.5d from the support.

Table 6.34. Load cycles and corresponding number of cracks for beam B222d

Load Cycles (kN)	Number of cracks	Remark
155	13	Pre-repair stage
25	13	Post-repair stage
155	14	CFRP starts debonding
165	14	Full CFRP debonding and failure

The results show that the beam is damaged under a load of 155 kN at the pre-repair damage stage which is the maximum capacity of the unrepaired section despite allowing full failure. The beam is able to withstand a load of 165 kN after repair with CFRP sheets. The increase in the load capacity is the repaired section capacity (165 kN) divided by the unrepaired section capacity (155 kN) which is equal to 106.5 %. Steel does not reach its yield strain at either the pre-repair stage or the post-repair stage. The CFRP strain is higher at the first strain gauge however it is less than 500 μst. The first strain gauge shows no release in the strain until failure at 165 kN. The second strain gage shows release after a load of 155kN which is due to the progression of the shear crack into the adhesive layer at the second CFRP sheet and the appearance of the crack in the second CFRP sheet as shown in Figure 6.104.

The failure mode is a combination of shear failure and CFRP debonding, where shear cracks progress into the adhesive layer. The presence of the CFRP sheets prevents typical shear failure where an inclined crack would have appeared on the surface of the beam starting from the point of the applied load to the support. Finally a combination of shear crack at the upper tip of the first CFRP sheet close to 1.5d, and the bottom tip of the second CFRP sheet close to support, results in CFRP debonding as shown in Figure 6.104. Since the CFRP sheets are fixed vertically and are subjected to stress perpendicular to their fibre direction, a crack is noted on the CFRP sheet at a load of 155 kN due to the weakness of CFRP in that orientation.

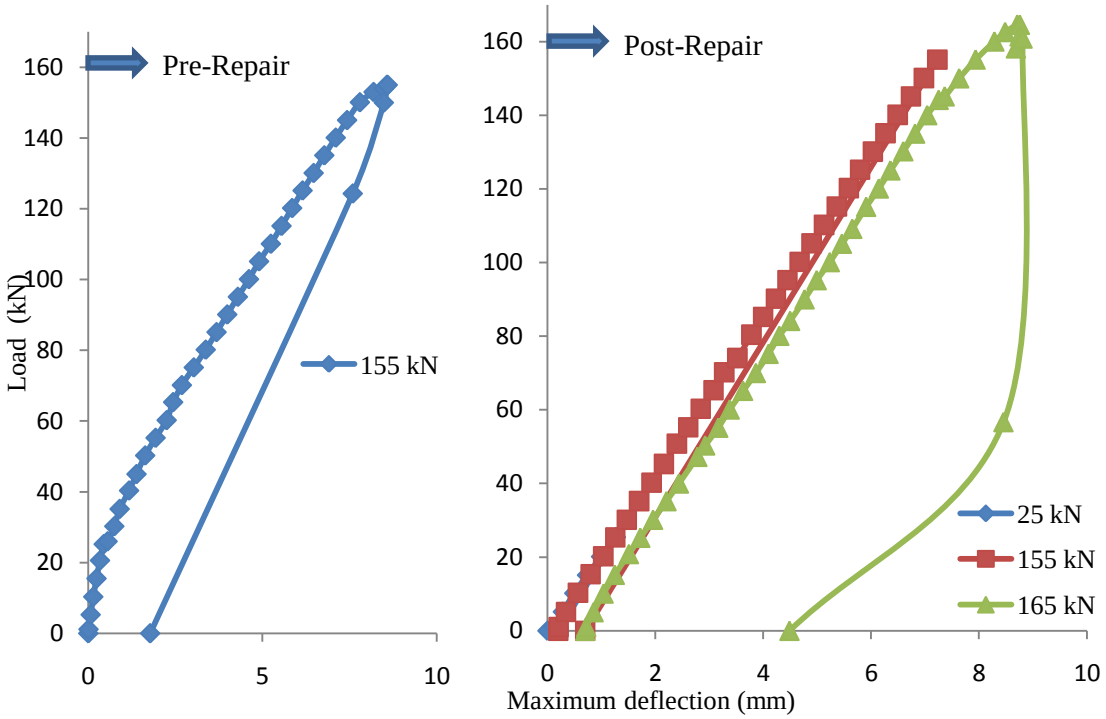

Figure 6.101. Load against deflection curves at pre and post repair stages for beam B222d

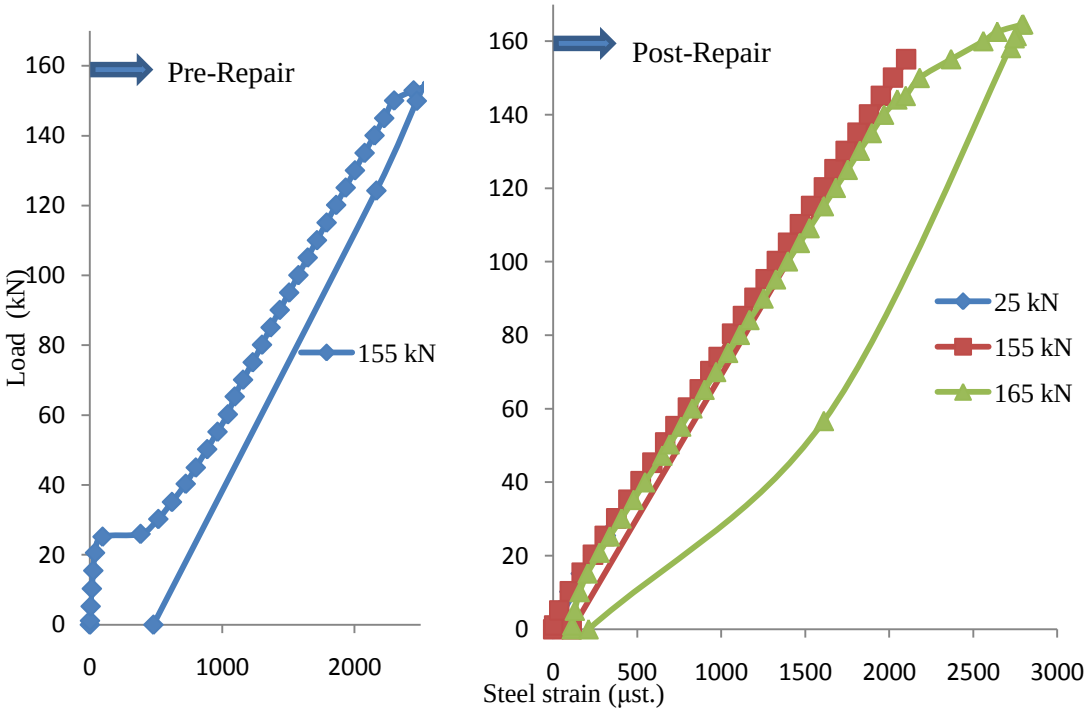

Figure 6.102. Load against steel strain at pre and post repair stages for beam B222d

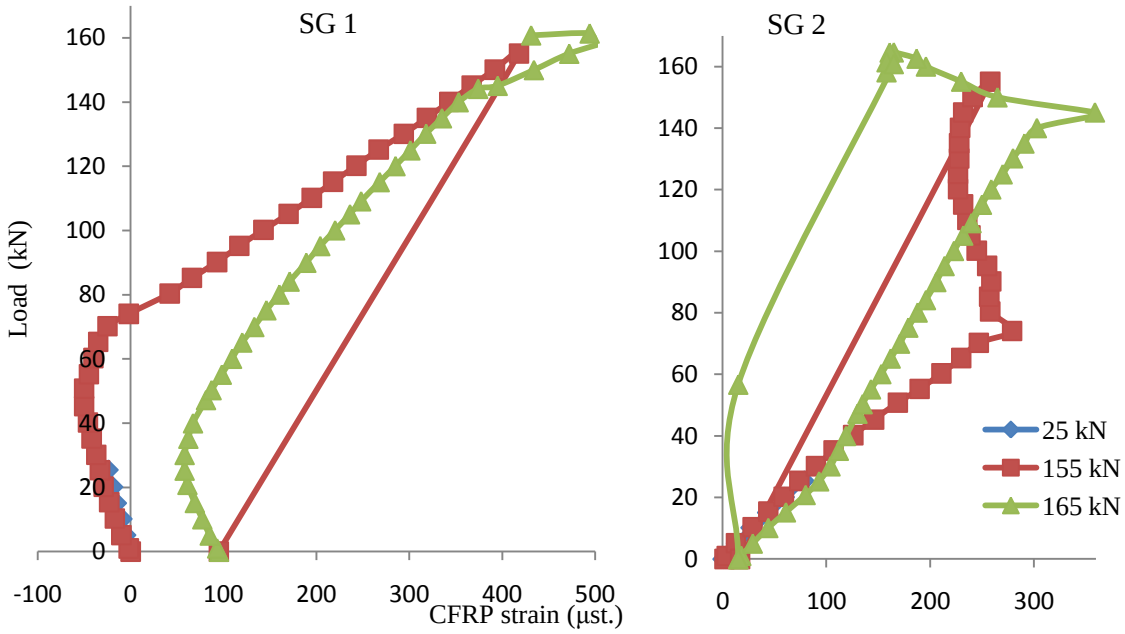

Figure 6.103. Load against CFRP strain at SG1 and SG2 for beam B222d

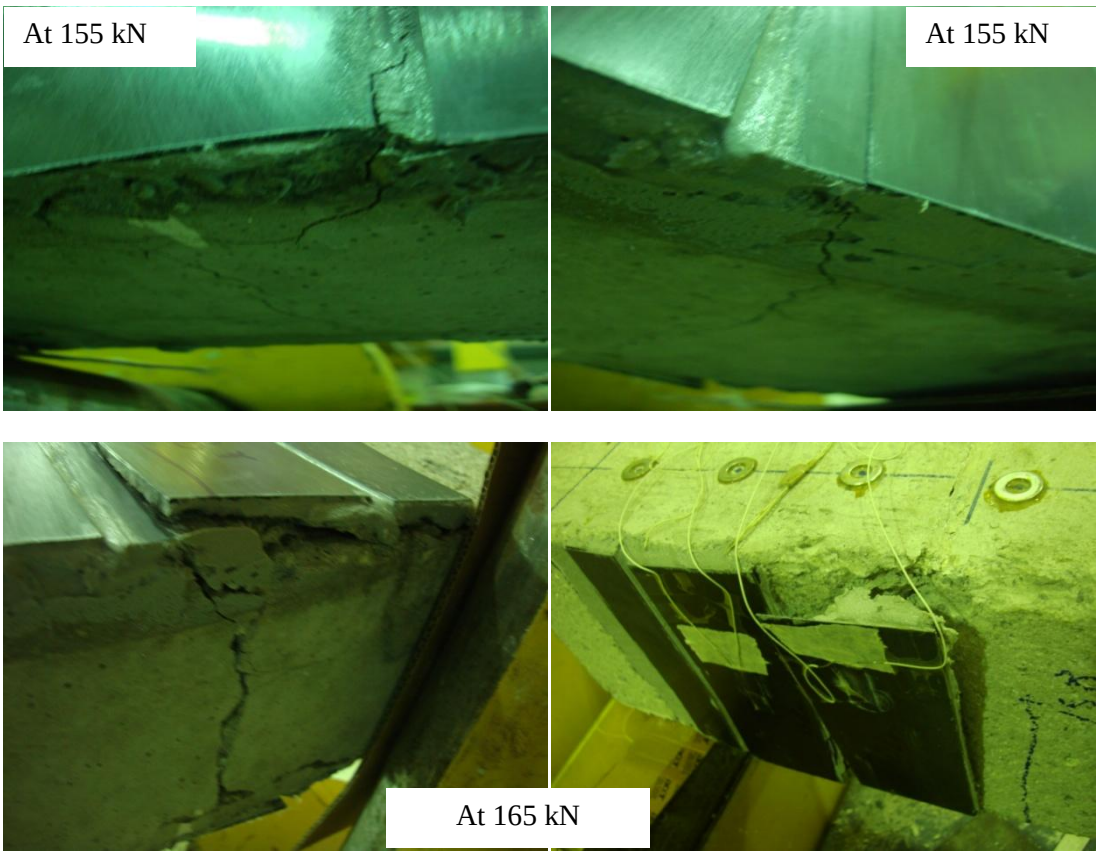

Figure 6.104. Failure mode of beam B222d

6.4.2.2 Dynamic evaluation

This section presents the dynamic evaluation of CFRP shear repair effectiveness based on frequency based stiffness index and damping change. The adopted stages are as illustrated in Table 6.22 and Figure 6.105 shows the frequency based stiffness index and the weighted average (PWM) results for beam B221d.

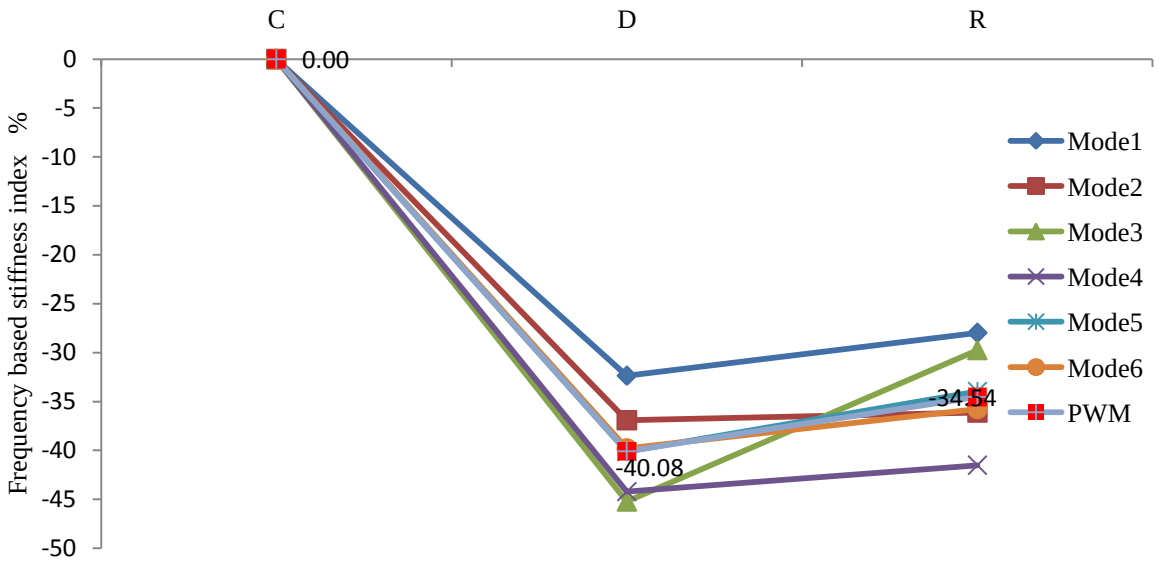

Figure 6.105. Frequency based stiffness index and weighted average (PWM) results for beam B221d

The results show that all modes indicate a decrease in the frequency based stiffness index at pre-repair stage where failure occurs at load 155kN, while fixing the CFRP sheets to the beam sides results in an increase of the frequency based stiffness index values compared to pre-repair damage stage. The weighted average (PWM) highlights the pattern of the overall stiffness change, as indicated using frequency based stiffness index, based on all the considered modes. The weighted average shows a stiffness deterioration of 40% at pre-repair damage stage, and then stiffness is recovered at post repair stage where the stiffness deterioration decreases to 34.5% compared to the undamaged stage. Thus, the stiffness

recovery is 5.5% compared to the pre-repair damage stage. The modal frequencies are highlighted as a good indicator for the repair effectiveness where all the modes indicate an increase in the stiffness after fixing of the CFRP sheets.

Figure 6.106 shows the damping change at pre and post repair stages for beam B221d. The adopted stages are the same as for the frequency based stiffness index, and the weighted average (PWM) is calculated and the results are also shown in Figure 6.106. The results show that all modes highlight an increase in the damping values at the pre-repair stage except for Mode 3 where a decrease in the damping value is noted. Repairing the beam with CFRP sheets influences all the considered modes, where it shows a decrease in the damping change values. The weighted average (PWM) shows the overall stiffness change, as indicated using damping change, based on all considered modes. Weighted average indicates a stiffness deterioration of 18.4% at the pre-repair stage. Following this, the stiffness deterioration decreases to 9.2% at the post-repair stage compared to the undamaged stage. Thus, the stiffness recovery is 9.2% compared to the pre-repair damage stage.

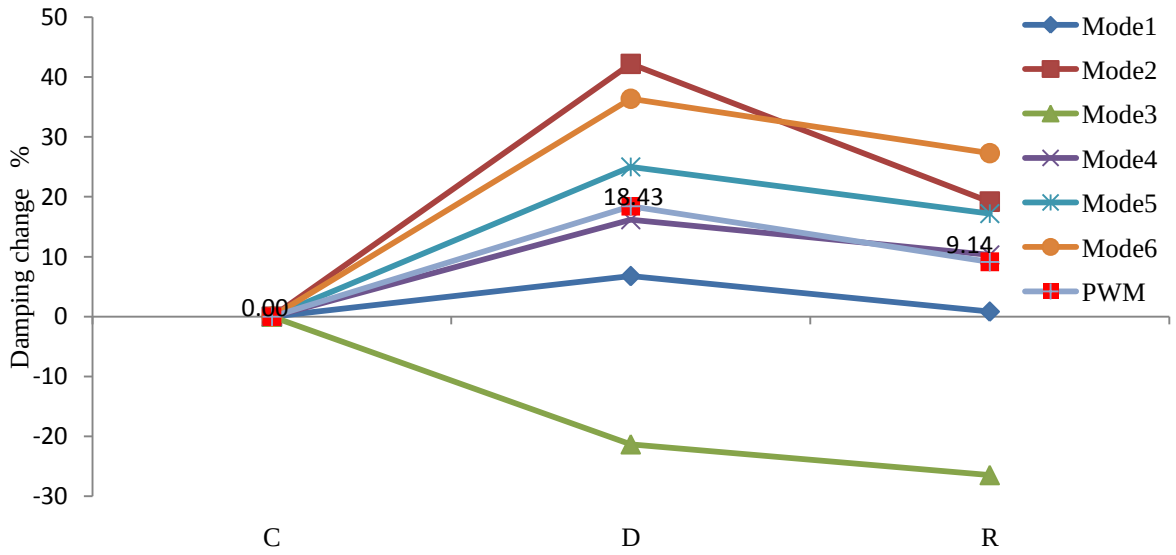

Figure 6.106. Damping change and weighted average (PWM) results for beam B221d

The frequency based stiffness index results for repair effectiveness index of beam B222d are shown in Figure 6.107, where the average averaging (PWM) is calculated and its results are also shown. The results show that all modes indicate a decrease in the frequency based stiffness index values at the pre-repair damage stage. At post-repair damage stage, all the modes show an increase in the index values. However, the index values for all the modes are less than those of the unrepaired stage. The weighted average shows a stiffness deterioration of 38.2% at pre-repair stage. Following this, stiffness deterioration reduces to 29.8% after fixing the CFRP sheets. Thus, the stiffness recovery at post-repair stage is 8.4% compared to pre-repair damage stage.

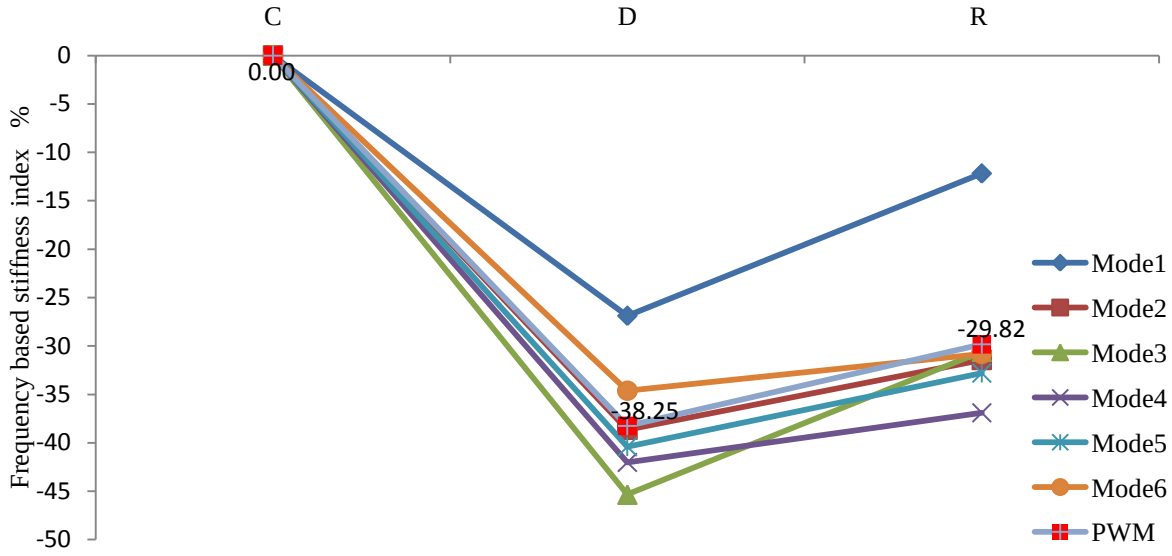

Figure 6.107. Frequency based stiffness index and weighted average (PWM) results for beam B222d

The damping change for beam B222d is calculated for all considered modes at the same stages illustrated in Table 6.22, and the results are shown in Figure 6.108 where the weighted average (PWM) is calculated and its results are also presented. The results show that all the modes indicate an increase in the damping values at pre-repair except for Mode

3 which indicates a decrease. Fixing the CFRP sheets influences all modes, where all the modes show a decrease in the damping values compared to the undamaged stage D. The weighted average results show a stiffness deterioration of 28% at the pre-repair stage before the stiffness deterioration decreases to 14.4% compared to the unrepaired stage, which indicates a stiffness recovery of 13.6%, compared to the pre-repair damage stage.

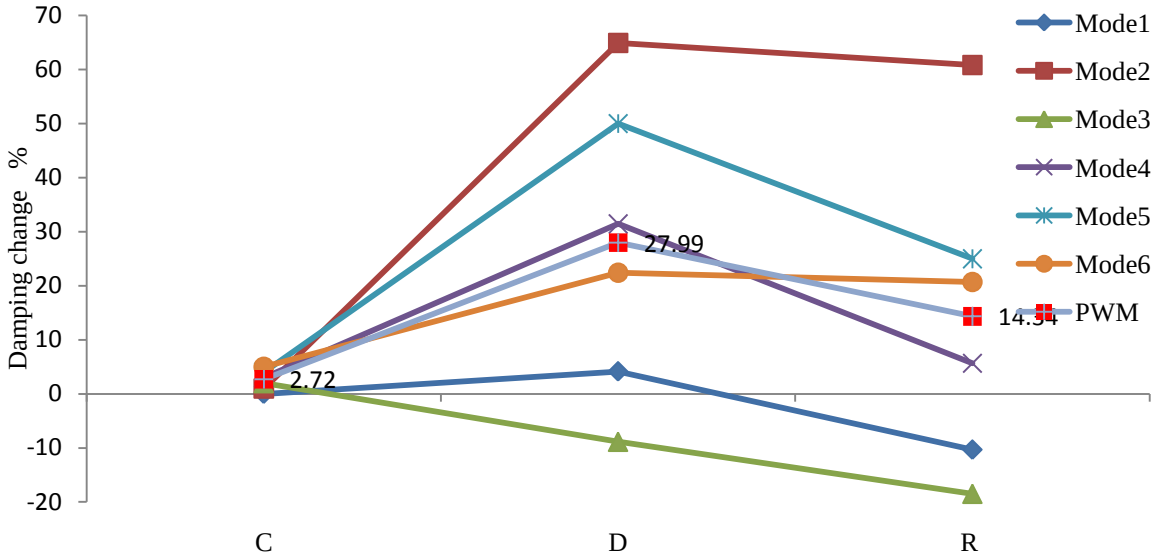

Figure 6.108. Damping change and weighted average (PWM) results for beam B222d

6.4.2.3 CFRP repair effectiveness

This section presents the relationship between the static and dynamic data in order to obtain the effectiveness of the CFRP repair system at different pre-repair damage levels. The damage level is calculated based on the percentage of the applied load at pre-repair stage to the ultimate capacity of the unrepaired sections. Since both beams B221d and B222d are damaged under maximum capacity and the only difference is that beam B221d is fully failed while beam B222d is not despite the maximum load, the damage ratio of beam B221d is 100% and the damage ratio of beam B222d is 99%.

The stiffness recovery as indicated by the ratio of increase in the ultimate load capacity is calculated based on the increase in the ultimate capacity of the repaired sections to the ultimate capacity of the unrepaired sections. The stiffness effectiveness based on the dynamic data is highlighted based on both frequency based stiffness index and damping change. For frequency based stiffness index and damping change, the repair effectiveness is calculated as the difference between the weighted average index value at the post-repair stage compared to the weighted average index value at the pre-repair damage stage. Figure 6.109 presents the repair effectiveness based on the static and dynamic data.

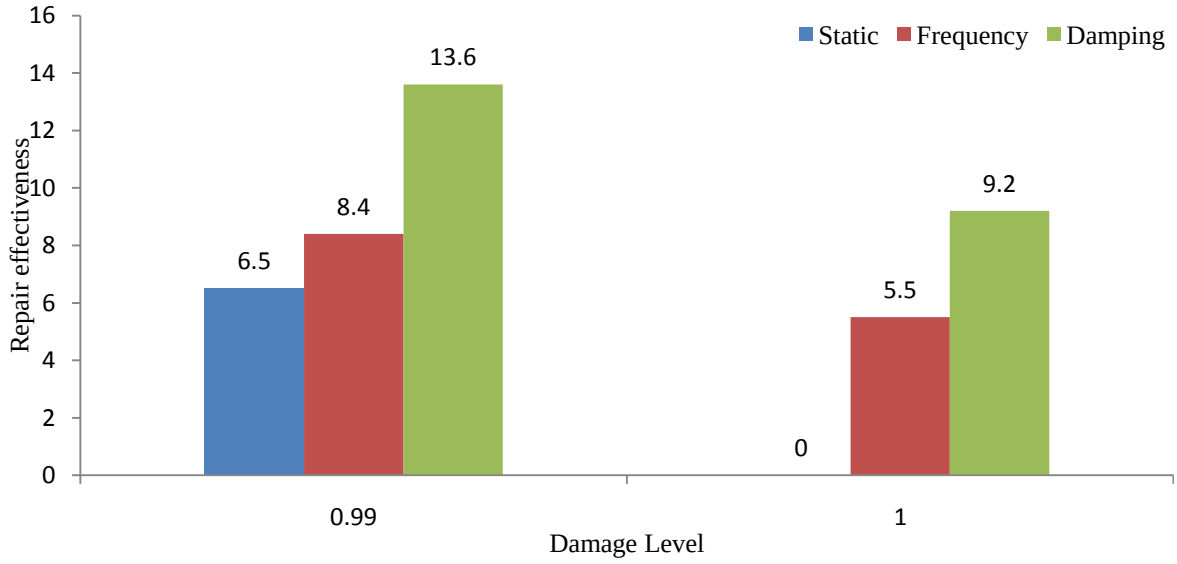

Figure 6.109. CFRP repair effectiveness based on static and dynamic data for shear at 1.5d and beams without shear stirrups

The results show that repairing the beam with externally bonded CFRP sheets recovers the stiffness whatever the pre-repair damage level. Dynamic data show better stiffness recovery than the increase in load capacity for the case of full failure at the pre-repair damage stage, where the damping change and frequency based stiffness index indicate a stiffness recovery of 9.2% and 5.5%, respectively, while load capacity shows no increase. For the pre-repair damage stage when the failure just begins to occur, load capacity increases by 6.5% which

is considered a good indicator for the effectiveness of CFRP sheets as shear repair system even when it is fixed vertically on the beam side. The dynamic data, that is, damping change and frequency based stiffness index, indicate a stiffness recovery of 13.6% and 8.4% respectively.

6.4.2.4 Monitoring of repaired beams

The repaired beams B221d and B222d are tested under load cycles at post-repair stages until failure as mentioned in the static evaluation, and the dynamic test is carried out to monitor the behaviour of the repaired beam during its service life. The frequency based stiffness index is calculated after each load cycle at post-repair stages for both repaired beams. Table 6.35 shows the load cycles and notation at the post-repair stages used to plot the frequency based stiffness index during the monitoring of the repaired beam B221d. Figure 6.110 shows the frequency based stiffness index for post-repair stage of beam B221d, where stage 'R' is used as the datum for the index values at higher loading stages.

Table 6.35. Load cycles for the post-repair stages of beam B221d

Load (kN)	Notation	Remark
0	R	Post-repair under self weight
25	R25	
155	RD	Subjected to pre-repair load
122	R122	
103	R103	Failure

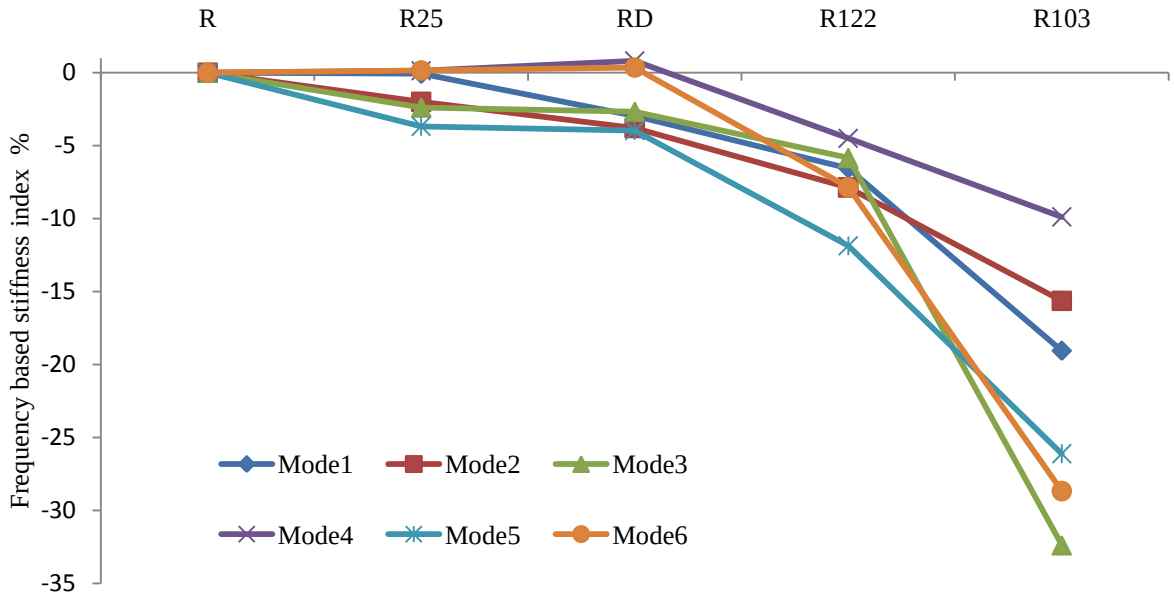

Figure 6.110. Frequency based stiffness index values for the monitoring of beam B221d

The results show that Modes 2, 3 and 5 indicate a slight decrease in the frequency based stiffness index values at stage R25. At stage RD, Modes 1, 2, 3 and 5 show further decreases in the frequency based stiffness index values which is due to the progression of the shear cracks into the CFRP adhesive layer. Beyond stage RD where further cracks appear in the adhesive layer, all the modes show a decrease in the frequency based stiffness index values. A rapid decrease in the frequency based stiffness index values is noted for all modes at stage R103 when the failure occurs.

Table 6.36 shows the load cycles and notation of the post-repair stages used to plot the frequency based stiffness index during the monitoring of the repaired beam B222d. Figure 6.111 presents the frequency based stiffness index values for beam B222d, where stage ‘R’ is used as the datum for the index values at higher loading stages.

Table 6.36. Load cycles for the post-repair stages of beam B222d

Load (kN)	Notation	Remark
0	R	Post-repair under self weight
25	R25	
155	RD	Subjected to pre-repair load
103	R165	Failure

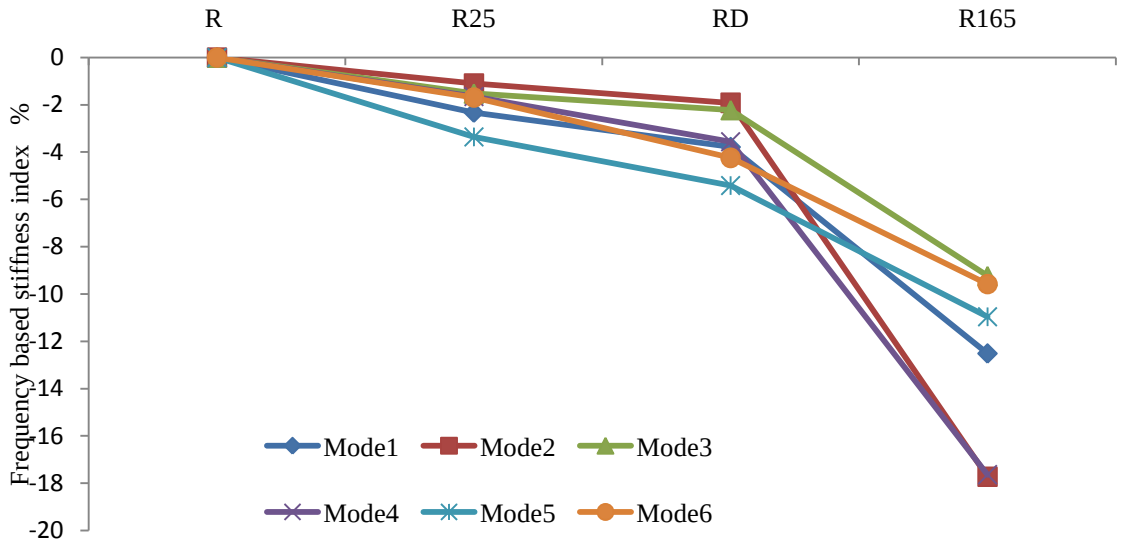

Figure 6.111. Frequency based stiffness index values for the monitoring of beam B222d

The results show that all modes indicate a slight decrease in the frequency based stiffness index values at stage R25, followed by a further decrease at stage RD where the shear crack progresses into the CFRP sheets' adhesive layer. At stage R165, more cracks appear in the adhesive layer which results in a rapid decrease in the frequency based stiffness index values beyond stage RD indicating full CFRP debonding.

6.4.3 Effect of the shear stirrups

This section summarised the effect of the shear stirrups on the contribution from CFRP sheets on the ultimate load capacity of the repaired beams. The results show that there is no contribution from shear stirrups to load capacity of the beam at pre-repair stage. Thus, the shear stirrups contribution is neglected at post-repair stage. The increase in load capacity for beam B212d is higher compared to beam B222d and this difference is not due to the presence of the shear stirrups but due to the difference in the concrete compressive strength. The compressive strength is 33MPa and 40 MPa for beams B212d and B222d, respectively, thus at the pre-repair stage beam B212d withstands a load of 126 kN while beam B222d withstands a load of 155 kN. At the post-repair stage there is a similar contribution from the CFRP sheets to the ultimate capacity for both beams, and both beams withstand a load of 165 kN. The increase in load capacity for beam B212d is 130.9%, while for beam B222d is 6.5%. The strain of flexure steel is lower than the yield strain for both design cases regardless of the pre-repair damage levels.

The CFRP strain is recorded as higher for beam B222d compared to beam B212d (1780 and 1020 μst). For beam B222d the higher strain is recorded at CFRP sheet which is close to the point of the applied load, while for beam B212d it is higher at the CFRP sheet nearest to the supports. The CFRP strain value is still small compared to the ultimate strain of the CFRP sheets. Such low strain values were observed by Triantafillou (1998) and Li et al. (2001), where Triantafillou (1998) concluded that the two-sided strengthening procedure using externally bonded FRP sheets delaminates before the loss of the aggregate interlock in the beam resulting in unusable strain, that is why the effective strain of the FRP sheets must be found.

The failure mode for both design cases is a combination of shear failure and CFRP debonding due to the progression of shear cracks into the adhesive layer. Such failure mode is in good agreement with the literature [El-Ghandour 2011, Pellegrino and Modena (2002)]. Both frequency based stiffness index and damping change show higher stiffness recovery for the design case with shear stirrups for cases when the beams are not allowed to fully fail at pre-repair damage stage. For the cases when the beam is fully failed at the pre-repair damage stage, the design case without shear stirrups has higher stiffness recovery value.

6.5 Effect of shear load location

This section has summarised the effect of the applied load location, either at quarter-span or at 1.5d from the support, on static and dynamic behaviour of the repaired beams. The internal shear stirrups show no contribution to the ultimate capacity for shear damage at 1.5d, while for shear damage at the quarter-span there is a contribution. The contribution from the CFRP sheets to the ultimate capacity depends on the pre-repair damage level for both shear damage locations, and the contribution for shear damage at 1.5d is higher for the case of high pre-repair damage level. Steel strain reaches rupture limit for shear damage at quarter-span, while it does not for shear damage at 1.5d. The CFRP strain is higher for damage at 1.5d compared to damage at quarter-span. The location where CFRP strain is highest depends on the pre-repair damage level for shear damage at quarter-span. It is at the CFRP sheet nearest to the point of the applied load for small pre-repair damage level and at the CFRP sheets located between the point of the applied load and the support in the case of high pre-repair damage level. For shear damage at 1.5d however, it depends on the concrete compressive strength from the support, where higher strain is located at the CFRP sheet

closest to the point of the applied load for higher compressive strength and is located at the CFRP sheets between the point of the applied load and the support for the case of smaller compressive strength.

The failure mode for shear damage at quarter-span is due to the progression of the pre-repair flexural cracks in the CFRP adhesive layer located at quarter-span which results in CFRP sheet delamination. For shear damage at 1.5d from the support, the failure mode is a combination of shear failure and CFRP debonding, where the shear cracks progress into the CFRP adhesive layer. Finally a combination of shear crack progression into the CFRP adhesive layer at the upper tip of the first CFRP sheet and the bottom tip of the second CFRP sheet results in CFRP debonding. The dynamic indicators for stiffness recovery, that is, frequency based stiffness index and damping change, have higher values for the shear damage at quarter-span compared to shear damage at 1.5d and for both cases the damping change shows a higher stiffness recovery than the frequency based stiffness index.

6.6 Code evaluation

The ACI Code is used through this study steps starting from the mix concrete design, the RC beams design in flexure and shear and repaired RC beams with CFRP sheets design in flexure and shear. After carrying out the static tests and obtaining the ultimate loads for the RC beams as unrepaired section and repaired sections, at flexure and shear, the last objective of this study is to evaluate the ACI Code equations for calculating the ultimate capacity. The evaluation covers the flexural design for both unrepaired RC beams and repaired RC beams with externally bonded CFRP sheets, and the shear design for both unrepaired RC beams and repaired RC beams with externally bonded CFRP sheets at different shear load locations. For the purpose of the evaluation and since the comparison

with the experimental results is based on the ultimate capacity, all the safety environmental factors are neglected from the ACI equations in order to find the actual ultimate capacity of the RC beams.

6.6.1 Flexural design

This section presents the flexural design when the load is applied as concentrated load at mid-span for the unrepaired beams with two flexural steel ratios. Moreover, it presents the flexural design of the repaired RC beams with externally bonded CFRP sheets at different pre-repair damage levels.

6.6.1.1 Unrepaired RC beams

Two beams are tested under flexural loading at mid-span (B111m and B121m), where one beam is designed using ρ_{max} and another using ρ_{min}. The cross-section and reinforcement detail for both beams is shown in Figure 4.2, and the material properties of the beams are shown in Table 4.3. The results for the first crack load, steel yield load, and the ultimate load based on both experimental and ACI 318 (2008) Code results for both beams, are shown in Table 6.37.

Table 6.37. Results for the unrepaired flexural beams

Beam	First Crack Load kN			Steel yield load kN			Ultimate Load kN		
	Exp.	ACI	Dif.%	Exp.	ACI	Dif.%	Exp.	ACI	Dif.%
B111m	10	9.4	-6	70	66.7	-4.7	107	103.4	-3.4
B121m	11	10.6	-3.6	56	50.5	-9.8	71	64	-9.8

The results show good agreement between experimental and ACI Code results in terms of first crack load, steel yield load and ultimate capacity for both flexural steel ratios. The ACI Code results are always smaller than the experimental results for the first crack load, steel yield load and the ultimate load capacity in the range of 3.4 to 9.8%. The difference between the ACI results at the first crack load is due to the fact that ACI indicates the actual

first crack which is at 9.4 and 10.6 kN for beam B111m and B121m respectively, while the experimental results indicate the first crack which can be detected by visual inspection of the beam which appears at a slightly higher load of 10 and 11 kN for beams B111m and B121m, respectively. The difference between ACI and experimental results is higher for the steel yield load and is due to the fact that the steel yield stress values used in the beam design calculation using ACI Code equations are obtained from the laboratory test on the steel bar samples which vary for different samples. The difference in the value of the ultimate capacity between experimental and ACI results is due to the properties of the actual beam material which can vary from the tested samples in the laboratory, and the assumption of the ACI Code that the ultimate strain of the concrete at compression is 3000 μst which is smaller than the actual concrete crushing strain.

6.6.1.2 Repaired RC beams

This section presents the comparison between experimental and ACI Code (ACI 440.2R 2002) results for the flexural repaired RC beams. The comparison covers both flexural reinforcement ratios, that is, ρ_{min} group (B122m, B123m and B124m) and ρ_{max} group (B112m, B113m, B114m). Beams B122m, B123m and B124m are designed using 12mm bar diameter, while beams B112m, B113m and B114m are designed using 16mm bar diameter. The material properties of all the beams are as shown in Table 4.3. The design of the repaired beams with externally bonded CFRP sheets is according to ACI 440.2R (2002) Code, where for ρ_{min} group beams, a CFRP sheet of 100mm width and 1.2mm thickness is used while for ρ_{max} group beams, a CFRP sheet of 50mm width and 1.2mm thickness is used. The CFRP properties are 2800 MPa for tensile stress and 165 GPa for elasticity modulus. The comparison highlights the values of the ultimate load capacity and CFRP debonding strain as shown in Table 6.38. The CFRP debonding strain is in better agreement

than the ultimate capacity results. For ρ_{min} group beams, the ACI Code results show a higher CFRP debonding strain compared to the experimental results with maximum difference of 11%, while for the ρ_{max} group beams the ACI results are smaller than the experimental results by a maximum difference of 8%. The difference in the CFRP debonding strain may be due to the accuracy of the strain gauges used to record the strain values during the experimental test. Another reason for the difference may be due to the difference between the material properties obtained from the laboratory testing on the material samples or from the manufacturer data sheets and the actual material properties in the beams under testing. The difference may also be due to the assumption of the ACI Code, that is, the stress distribution corresponding to the depth of the cross section.

Table 6.38. Results for the repaired flexural beams

Beam	Ultimate load capacity (kN)			CFRP debonding strain (μst)		
	Exp.	ACI	Dif.%	Exp.	ACI	Dif.%
B122m	131	103.4	-21.0	6100	6780	11.14
B123m	130.7	105.15	-19.54	5400	5900	9.25
B124m	128	101	-21.1	5890	5460	-7.3
B112m	120	104.2	-13.1	5550	5980	7.7
B113m	124.7	105.4	-15.5	5400	5150	-4.6
B114m	94.5	90	-4.8	4790	4400	-8.1

For the ultimate load capacity the ACI Code results show smaller values than the experimental results by approximately 20% for ρ_{min} group beams, and around 15% for ρ_{max} group beams B112m and B113m. They show good agreement with the difference of 4.8% which is observed for beam B114m. This difference is due to the difference in the material properties between the tested samples, that is, concrete, steel and the CFRP manufacturer data sheets as well as the actual material properties in the tested beams. The difference in the ultimate capacity may also be due to the ACI Code assumptions for the ultimate concrete crushing strain which is taken to be 3000 μst while the actual value can be higher.

The ACI Code advises not to consider the steel bars at the compression zone when calculating the ultimate capacity for the repaired section and this can be another reason behind the smaller ACI Code results compared to the experimental results. In the actual repaired RC beam the steel bars at the compression zone are still working and sharing the compression stresses. Therefore, considering the compression steel can reduce the difference between ACI Code and experimental results. Ultimate moment capacity of the repaired section according to the ACI Code is as in Equation 6.2:

$$Mu = A_{s1}.f_{s1}\left(d - B1.\frac{c}{2}\right) + A_f.f_f\ (h - B1.\frac{c}{2}) \quad (6.2)$$

where *Mu* is the ultimate moment capacity, A_{s1} is the cross section area of the main steel bars, f_{s1} is the ultimate stress of the main steel bars, *d* is the effective depth, *c* is the depth of the neutral axis, A_f is the CFRP cross section area, f_f is the CFRP ultimate stress, *h* is the beam depth, and

$$B1 = 0.85 - 0.008(f_c - 30)$$

where f_c is the concrete compressive strength.

In order to add-on the contribution of the steel bars at the compression zone, Equation 6.2 can be re-written in the following form:

$$Mu = (A_{S1} - A_{S2}).f_{s1}\left(d - B1.\frac{c}{2}\right) + A_f.f_f\ \left(h - B1.\frac{c}{2}\right) + A_{s2}.f_{s2}(d - d') \quad (6.3)$$

where A_{s2} is the cross section area of the compression steel bars, f_{s2} is the ultimate stress of the compression steel bars and d' is the effective depth of the compression steel bars. The ultimate load capacity based on the modified Equation (6.3) of the ACI Code gives the results which are shown in Table 6.39. The modified ACI equation provides closer results to the experimental data where the difference decreases to less than 6.87% for all the beams. The ACI Code results remain smaller than the experimental results for all the beams

except for beam B114m which shows that ACI Code values are higher than the experimental results by 1.58%.

Table 6.39.Ultimate capacity results for repaired flexural beam based on the modified ACI Code equation

Beam	Ultimate load capacity (kN)		
	Exp.	Modified ACI	Dif.%
B122m	131	122	-6.87
B123m	130.7	126	-3.6
B124m	128	120	-6.25
B112m	120	118.5	-1.25
B113m	124.7	116.7	-6.4
B114m	94.5	96	1.58

6.6.2 Shear at quarter-span

This section presents the comparison between ACI Code and experimental results for the shear scenarios when the load is applied at the quarter-span. The results for the unrepaired and repaired RC beams with CFRP sheets are presented. For the unrepaired case, beams B211q and B221q while for the repaired case, beams B211q, B212q, B221q and B222q are dealt with.

6.6.2.1 Unrepaired beams

For the unrepaired case, there are two design criteria to be investigated as shear beam with and without internal shear stirrups. Beam B211q is designed according to the ACI Code with shear stirrups, and beam B221q is designed without shear stirrups. The material properties for beams B211q and B221q are shown in Table 4.3. The comparison presents the ultimate capacity of the RC beams under a single concentrated load located at the quarter-span for both beams and as shown in Table 6.40.

Table 6.40. Results for unrepaired shear beams with load at quarter-span

Beam	Ultimate load capacity (kN)		
	Exp.	ACI	Dif.%
B211q	99	78	-21.2
B221q	90	44.5	-50.6

The results show a large difference between ACI and experimental results, with ACI results being much smaller than the experimental results. The higher difference is for beam B221q where the ultimate capacity entirely depends on the concrete shear component. The difference in the experimental results between beams B211q (with shear stirrups) and B221q (without shear stirrups) due to the presence of the shear stirrups is 9 kN. This is considered as a small contribution from the shear stirrups to the ultimate capacity of beam B211q even after taking into consideration the higher compressive strength of beam B221q. The expected difference between both beams is 22 kN. Thus, the shear stirrup contribution to the ultimate capacity must be revised where less contribution is experimentally observed. The contribution of the entire component to the ultimate capacity must be revised to reduce the difference between ACI Code and experimental results. The components which are taken into consideration for the calculation of the ultimate capacity based on the ACI Code are as shown in Figure 6.112 and Equation 6.4.

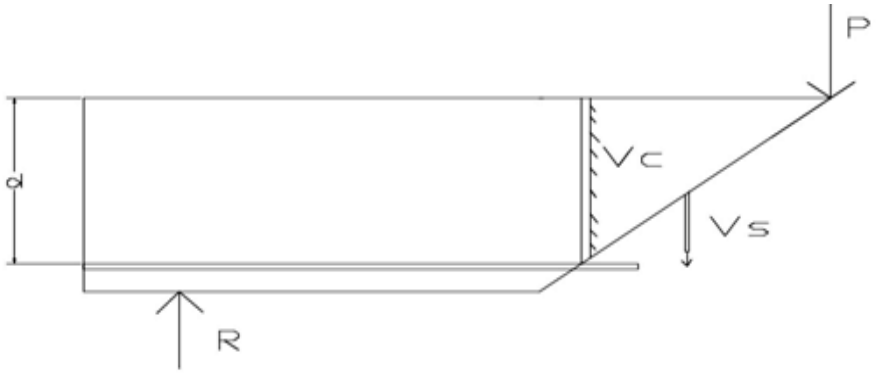

Figure 6.112 Ultimate shear capacity based on ACI Code

$$V = V_c + V_s \tag{6.4}$$

where

$$V_c = 0.17 \sqrt{f_c}\, b\, d \tag{6.5}$$

and

$$V_s = A_v . f_v . d/s \tag{6.6}$$

where f_c is the concrete compressive strength, b is the beam width, d is the effective depth, A_v is the cross section area of the stirrups bar, f_v is the yield stress of the vertical stirrups and s is the distance between the stirrups.

In reality when the beam is subjected to a point load applied at a distance from the support, the concrete contribution to the ultimate capacity is the resisting force by the inclined area of the beam cross section which is drawn with an angle of 45^0 (as average) from the support to the point of the applied load. The shear stirrups contribution to the ultimate capacity is equal to the component of the shear stirrups perpendicular to the inclined concrete surface. Figure 6.113 shows the contribution of the concrete and the shear stirrups to the ultimate capacity.

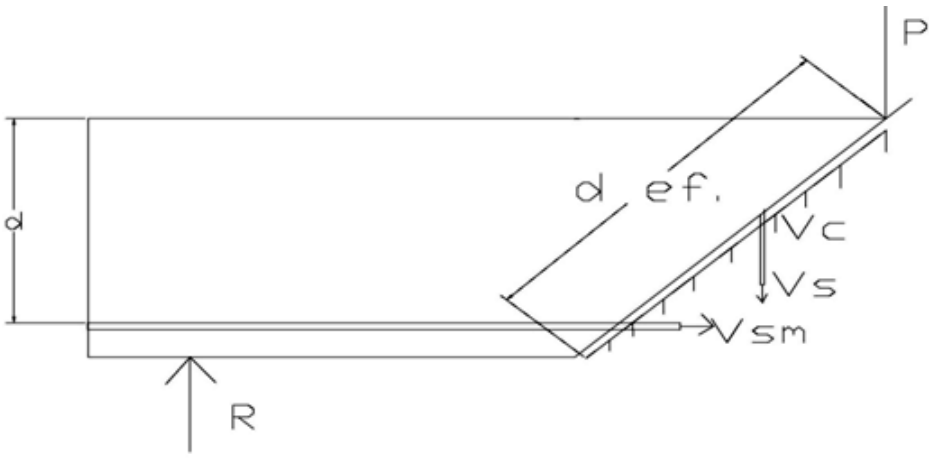

Figure 6.113. Modified contribution to the ultimate shear capacity of the RC beams

The modified contribution of both the concrete and shear stirrups to the ultimate shear capacity of the RC beams are as shown in Equations below:

$$V_c' = 0.24\, bh\sqrt{f_c} \tag{6.7}$$

and

$$V_s' = A_v.f_v.d.sin\,(45^0)/s \tag{6.8}$$

where V_c' and V_s' are the modified concrete and shear stirrups' contribution to the ultimate shear capacity and h is the beam depth.

According to the modified equation, the concrete contribution increases after considering the inclined effective depth, while the steel stirrups' contribution decreases after considering only the perpendicular component of the shear stirrups.

The flexural steel which crosses the inclined concrete surface makes a contribution to the ultimate shear capacity. In order to find the contribution of the flexural steel to the ultimate shear capacity, first the stress in the flexural steel bars must be established. The flexural steel stress can be calculated based on the moment of the beams at the section of the applied load. The total shear capacity of the beam at the section of the applied load and based on Equations 6.7 and 6.8 is as shown in the equations below:

$$V = 0.24\, bh\sqrt{f_c} + A_v.f_v.d.sin\,(45^0)/\mathrm{s} \tag{6.9}$$

For concentrated load located at quarter span (*L/4*) the moment at the applied load section is:

$$M = \frac{V*L}{4} \tag{6.10}$$

where *L* is the clear span length.

The stress at the flexural steel bars (f_s) can be found using trial and error procedure based on the following equations:

$$a = \frac{A_s \,.\, f_s}{0.85.\ f_c.\ b} \tag{6.11}$$

$$M = A_s.\ f_s.(d - a/2) \tag{6.12}$$

where A_s is the cross section area of the flexure bars and a is the depth of the concrete compressive stress.

After calculating the flexural steel stress (f_s), the force V_m which is shown in Figure 6.113 can be calculated as:

$$\mathrm{Vm} = \mathrm{As}.\,\mathrm{Fs} \tag{6.13}$$

The contribution of the flexural steel to the ultimate shear capacity of the RC beam is calculated based on the perpendicular component of force V_m to the inclined concrete surface. A contribution factor (*CF*) is used to indicate the amount of force shared that can be taken by the main flexural steel bars. The flexural contribution can be calculated as follows:

$$V'_M = CF_m.A_s.f_s.Sin\,(45^0) \tag{6.14}$$

Where V'_M is the flexural steel contribution to the ultimate shear capacity, CF_m is the contribution factor of the main steel with value of $0 \leq CF_m \leq 1.0$ which depends on the location of the applied load and the presence of the shear stirrups. The ultimate capacity based on the modified contribution of the concrete and shear stirrups and the contribution of the flexural steel is as follows:

$$V = \ 0.24\ bh\sqrt{f_c} + A_v.f_v.d.\frac{sin(45^0)}{s} + CF_m.A_s.f_s.sin\,(45^0) \tag{6.15}$$

Table 6.41 shows the results of the modified ACI equation. For beam B221q where there is no shear stirrup, the CF_m of 0.1 gives ultimate capacity of 89 kN which is very close to the experimental results of 90 kN. However, for beam B211q where there is a contribution

from the shear stirrups, the CF_m of 0.01 gives ultimate capacity of 97 kN which is also very close to the experimental results of 99 kN. The modified equation for the shear ultimate capacity based on the modified concrete and shear stirrups contribution and the extra contribution from the flexural steel, gives very good agreement between the modified ACI Code and experimental results with a difference of less than 2%.

Table 6.41. Ultimate capacity results for unrepaired shear beams at quarter-span based on the modified ACI Code equation

Beam	Ultimate load capacity (kN)		
	Exp.	Modified ACI	Dif.%
B211q	99	97	-2
B221q	90	89	-1.1

6.6.2.2 Repaired beams

For the repaired shear beam when the load is applied at quarter-span, four beams are tested in two groups. The first group is designed with the shear stirrups, that is, B211q and B212q, where beam B211q is damaged under the maximum load capacity at the pre-repair damage stage and beam B212q is damaged under the design limit load at the pre-repair damage stage. For both beams, the shear crack appears as an inclined line at the zone between the supports and the quarter-span. The second group is designed without the shear stirrups, that is, B221q and B222q, where beam B221q is damaged under the maximum capacity at the pre-repair damage stage while B222q is damaged under the design limit load at the pre-repair damage stage. For both beams the shear crack appears as an inclined line at the zone between the supports and the quarter-span. The cross section detail of beams B211q, B212q, B221q and B222q are as shown in Figure 4.3. The material properties of all the beams are as shown in Table 4.3.

Based on the ACI-440-2R Code equations and in order to calculate the ultimate capacity for the repaired beam (V_R), the contribution of the concrete and the shear stirrups is as shown in Equations 6.5 and 6.6. The extra contribution is from the fixed externally bonded CFRP sheets V_f as shown below.

$$V_f = \frac{A_f f_f (sin\,\alpha + cos\alpha).d_f}{S_f} \quad (6.16)$$

where A_f is the cross section of the CFRP sheet on both sides, f_f is the tensile stress of the CFRP sheet, α is the angle at which the CFRP sheet is placed to the side of the beam, d_f is the effective depth of the CFRP sheet on the beam side and S_f is the spacing between the CFRP sheets.

The ultimate repair capacity is as shown in the equation below:

$$V_R = V_c + V_s + V_f \quad (6.17)$$

The comparison is based on the ultimate repair capacity and the maximum CFRP sheet strain at failure for both ACI Code and experimental results, and the results are as shown in Table 6.42. The results show a very large difference between the ACI and experimental results in terms of ultimate shear capacity and the CFRP strain at failure. The difference in the CFRP strain is higher than the ultimate shear capacity. For both ultimate capacity and CFRP strain values, ACI Code results show much higher results than the experimental results which an overestimate of the shear capacity. The repaired beams after full damage at the pre-repair damage stage show a higher difference in terms of ultimate capacity, and the beams without stirrups show lower difference than the beams with stirrups. The significant difference between the ACI and the experimental may be due to the assumption of the ACI Code while calculating the contribution of the concert, steel and CFRP to the ultimate capacity.

Table 6.42. Comparison of ACI Code and experimental results for repair shear beam at quarter-span

Beam	Case	Ultimate load capacity (kN)			Max. CFRP strain (μst.)		
		Exp.	ACI	Dif.%	Exp.	ACI	Dif.%
B211q	Design load/with stirrups	120	178.5	48.75	660	1490	125.76
B222q	Design load / without stirrups	120	165.2	37.67	800	1750	118.75
B211q	Maximum load / with stirrups	107	176.4	64.86	695	1460	110.1
B222q	Maximum load / without stirrups	101	155.3	53.76	720	1630	126.4

The main considerations which can be taken into account in modifying the ACI Code equations are as follows:

- The ACI equations show no consideration for the pre-repair damage level on the calculation of the ultimate capacity in the repair stage.
- The contribution of the shear stirrups to the ultimate capacity is higher than the actual values, where beams with stirrups show higher difference.
- The CFRP contribution to the ultimate capacity is higher than the actual values, where the CFRP strain is much higher than the actual values.

The same modifications are applied to the ACI Code equations for calculating of the unrepaired beam capacity i.e. Equations 6.7, 6.8 & 6.15 are used. A reduction factor (RF_c) is applied to the concrete contribution which is based on the pre-repair damage level and will have a value of $0 \leq RF_c \leq 1.0$, where 0 for fully damaged beams at the pre-repair damage stage and 1.0 for undamaged beams. In reality, if the damage is induced in the shear zone, the contribution of the concrete is reduced based on the loss in the aggregate interlock at the shear crack zone. The contribution factor for the CFRP sheets to the ultimate repaired shear capacity (CF_f) is applied to the V_f part in Equation 6.17 of the ultimate repair capacity V_R.

The modified Equations 6.7 and 6.8 for the contribution of the concrete and shear stirrups to ultimate capacity are used. The contribution of the flexural steel to the shear capacity is considered and the same procedure in Equations 6.9 to 6.14 is used. The same CF_m values which are decided for both beams (B211q and B212q) for the unrepaired beams are used where CF_m of 0.1 is used for the beams without stirrups and CF_m of 0.01 is used for beams with stirrups. The modified equation of the repaired shear capacity can be written as follows:

$$V_R' = CF_f.V_f + RF_c.V_c' + V_s' + CF_m.V_m' \quad (6.18)$$

The comparison results based on the modified ACI Code equations are shown in Table 6.43. The modified ACI Code equation results show much better agreement with the experimental results in terms of ultimate capacity where the maximum difference is less than 3%. All the calculated ultimate capacity values from the modified ACI Code equation are smaller than the experimental results. The reduction factor for the concrete contribution (RF_c) is found to be equal to 0.15 for beams B212q and B222q which are subjected to the design limit load at the pre-repair damage stage, and 0 for beams B211q and B221q which are subjected to maximum load at the pre-repair damage stage where the concrete lost all of its stiffness. The CFRP contribution factor (CF_f) is found to equal 0.78 for all the pre-repair damage levels and for both design cases, that is, with and without the steel stirrups.

Table 6.43. Comparison of modified ACI Code and experimental results for repair shear beam at quarter-span

Beam	Case	Ultimate load capacity (kN)		
		Exp.	Modified ACI	Dif.%
B212q	Design load/with stirrups	120	116.4	-3
B222q	Design load / without stirrups	120	119.3	-0.6
B211q	Maximum load / with stirrups	107	105	-1.87
B221q	Maximum load / without stirrups	101	100.8	-0.2

6.6.3 Shear design at 1.5d

This section presents the results for the unrepaired and repaired RC beams with CFRP sheets for shear damage scenario with concentrated load applied at 1.5d from the support. For the unrepaired case, beams B211d, B212d, B221d and B222d are dealt with, and the same beams are used for the repaired case.

6.6.3.1 Unrepaired beams

For the unrepaired beams, two design criteria are investigated as the shear beam with and without the shear stirrups. Beams B211d and B212d are designed according to the ACI Code with shear stirrups as shown in Figure 4.3, and beams B221d and B222d are designed without shear stirrups as shown in Figure 4.3. The material properties of the beams are shown in Table 4.3. The comparison of the ultimate capacity of the RC beams under a single concentrated load located at the 1.5d from the support for all the beams obtained experimentally and from ACI Code is shown in Table 6.44.

Table 6.44. Unrepaired ultimate shear capacity for shear at 1.5d

Beam	Ultimate load capacity (kN)		
	Exp.	ACI	Dif.%
B211d	142.5	69.4	-51.3
B212d	126	67.7	-46.3
B221d	155	40.8	-73.7
B222d	155	39.8	-74.3

The results show a large difference between ACI and experimental results, with ACI results being much smaller than the experimental results. The higher difference is for the design case without shear stirrups and the ultimate capacity completely depends on the concrete shear component. The experimental results show less capacity for the beams with stirrups than the beams without stirrups by approximately 20 kN, which is considered as abnormal

behaviour even though the compressive strength of the beams without stirrups is higher which gives a higher concrete contribution of only 4 kN. Thus, the shear stirrup component in the ultimate capacity must be neglected for the case when the applied concentrated load is at a distance of 1.5d from the support. All the components of the ultimate capacity must be revised in order to reduce the difference between ACI and experimental results. The components which are taken into consideration for the calculation of the ultimate capacity based on the ACI Code are as shown in Figure 6.112 and Equation 6.4. The modified contribution of the concrete which is shown in Figure 6.113 and illustrated in Equation 6.7 is used.

The flexural steel contribution which can be calculated based on Equations 6.9 to 6.14 is considered. The contribution of the shear stirrups to the ultimate capacity is neglected. The value of the contribution factor (CF_m), as previously mentioned is based on the location of the applied load and the existence of the shear stirrups which are adjusted based on the experimental results. The ultimate capacity based on the contribution of the concrete and flexural steel for RC beams which is subjected to concentrated load at 1.5d can be calculated as follows:

$$V = 0.24\, bh\sqrt{f_c} + CF_m.A_s.f_s.sin\,(45^0) \qquad (6.19)$$

The comparison results of the modified ACI Code equation for the shear ultimate capacity of the RC beams subjected to concentrated load at 1.5d from the support and the experimental results are as shown in Table 6.45. The modified ACI Code equation for the shear ultimate capacity based on the modified concrete contribution and the extra contribution from the flexural steel give very good agreement with the experimental results with a difference of less than 10%. The CF_m value is found to be 1.0 for both the damage levels and design cases.

Table 6.45. Unrepaired capacity results for shear at 1.5d based on the modified ACI equation

Beam	Ultimate load capacity (kN)		
	Exp.	Modified ACI	Dif.%
B211d	142.5	131.5	-7.7
B212d	126	125.7	-0.3
B221d	155	142.5	-8
B222d	155	140	-9.7

6.6.3.2 Repaired beams

For the repaired shear beam when the load is applied at 1.5d from the supports, the same four beams which are used on the unrepaired group are used and are repaired after damage at the maximum load capacity. Beams B212d and B222d are subjected to the maximum load at the pre-repair damage stage without allowing them to fail fully, while beams B211d and B221d are subjected to the maximum load at the pre-repair damage stage and are subjected to full failure.

Beams B211d and B221d are repaired using two CFRP sheets with widths of 100mm and placed inclined at 45^0 on both sides of the RC beam between the applied load and the supports. In addition, beams B212d and B222d are repaired using three CFRP sheets (two with 100mm width and one with 50mm width) and placed vertically on both sides of the RC beam between the applied load and the supports.

The contribution of the added CFRP sheets to the ultimate shear capacity of the repaired RC beams based on the ACI Code is illustrated in Equation 6.16. The comparison is based on the ultimate repair capacity and the maximum CFRP sheet strain at failure for both ACI and experimental results, and the results are as shown in Table 6.46. The results show variation in the difference between ACI Code and experimental results in terms of ultimate shear capacity. For beam B211d, ACI Code results are higher by approximately 25%, and for beam B222d the ACI Code results are smaller by 4.4%. The difference in the CFRP

strain is higher than the ultimate shear capacity, and the ACI values are higher than the experimental results which indicate a smaller contribution from the CFRP sheets to the ultimate capacity. For the repaired beams with vertical CFRP sheets, the ACI Code results show much higher values than experimental in terms of CFRP strain, which indicates smaller contribution from the CFRP sheets. The significant difference between the ACI and the experimental can be due to the assumption of the ACI while calculating the contribution of the concert, steel and CFRP to the ultimate capacity.

Table 6.46. Comparison of ACI Code and experimental results for repair shear beam at 1.5d

Beam	Ultimate load capacity (kN)			Max. CFRP strain (μst.)		
	Exp.	ACI	Dif.%	Exp.	ACI	Dif.%
B211d	143	179.2	25.3	1000	1570	57
B212d	165	171.6	4	500	1490	198
B221d	155	162.5	4.8	1750	1750	0
B222d	165	157.8	-4.4	500	1690	238

The same considerations which have been taken into account to modify the ACI Code equations for the shear at quarter span are considered. The same modifications used for calculating the unrepaired beams capacity are considered, where shear stirrup contribution is neglected and the concrete contribution is calculated using Equation 6.7. A reduction factor (RF_c) is applied to the contribution of the concrete which is based on the pre-repair damage level and has a value of $0 \leq RF_c \leq 1.0$, where 0 is for fully damaged beams at the pre-repair damage stage and 1.0 for undamaged beams. The contribution of the flexural steel to the shear capacity is considered and the same procedure in Equations 6.9 to 6.14 is used. The same CF_m value which is decided for the unrepaired beams is used, where CF_m of 1.0 is used. The contribution from the shear stirrups is neglected.

The contribution factor for the CFRP sheets to the ultimate repaired shear capacity (CF_f) is applied to the V_f part in the equation of the ultimate repair capacity and its value is adjusted based on the experimental results. The modified ACI Code equation for repaired shear capacity is calculated using Equation 6.20.

$$V'_R = CF_f . V_f + RF_c . V'_c + CF_m . V'_m \quad (6.20)$$

The results of the comparison of the ultimate shear capacity between the modified ACI equations and the experimental results are as shown in Table 6.47. The modified ACI Code equations give better agreement with the experimental results for all the beams and the ACI Code results are smaller than the experimental. The reduction factor RF_c for the concrete contribution is chosen to be 0.0, where the concrete is presumed to lose all its stiffness at the pre-repair damage stage. The contribution factor for the CFRP CF_f is chosen to be 0.18 for the case of full failure at the pre-repair damage stage, that is, B211d and B221d where shear cracks and deformation influence the bond between the externally bonded CFRP sheets and the concrete surface. For the case where full failure is not allowed, that is, beams B212d and B222d, the CF_f values are chosen to be 0.3 with the shear cracks defect being smaller.

Table 6.47. Comparison of modified ACI Code equation and experimental results for repair shear beams at 1.5d

Beam	Case	Ultimate load capacity (kN)		
		Exp.	Modified ACI	Dif.%
B211d	With stirrups/full failure	143	143	0
B212d	With stirrups	165	153	-7.3
B221d	Without stirrups / full failure	155	154.8	-0.13
B222d	Without stirrups	165	165	0

6.7. Summary

This chapter covers the results related to use of modal testing to assess the effectiveness of CFRP sheet as flexural and shear repair systems. In the first section, the effectiveness of the CFRP sheets as flexural repair system with both designs limits i.e. ρ_{min} and ρ_{max} is presented. The results proved that the CFRP sheet as flexural repair system is able to recover the stiffness and increase the ultimate capacity regardless pre-repair damage level. The second section presents the effectiveness of CFRP sheets as shear repair system for both shear cases i.e. at quarter-span and at 1.5d, and for both design cases i.e. with and without shear stirrups. The results showed that the CFRP sheet is an effective repair system, where it was able to recover the stiffness and recover or increase the ultimate shear capacity regardless pre-repair damage level. In the third section, evaluation of the ACI Code for the flexural and shear design of RC beam with or without CFRP sheet is presented. Modification to the ACI Code equations is proposed, where modified equations results were in better agreement with experimental results than original ACI equations.

Chapter 7: Conclusions and Recommendations

7.1 Conclusions

The research findings of this study are presented in this chapter. These includes the findings related to the composite action phenomenon in RC beams, classification of the damage type, sensitivity of existing and developed dynamic damage severity algorithm and the static stiffness indicators, sensitivity of the modified and developed damage location algorithms, dynamic and static assessment of using CFRP sheets as flexural and shear repair system for damaged RC beams, repair composite action phenomenon of RC beams repaired with externally bonded CFRP sheets, adhesive setting time and evaluation of the ACI Code for flexural and shear design of RC beam with and without the externally bonded CFRP sheets.

7.1.1 Composite action phenomenon

Influence and effect of composite action, related to concrete softening in the tension, compression, and shear zones, and bond action between steel bars and surrounding concrete in the RC beams, with the changes in natural frequencies of the modes is evident from this investigation.

The presumption that bond affects the first bending frequency is apparent from the experimental results, thus making it a good indicator for the state of bond action in reinforced concrete beams. An increase in bond action will lead to an increase in the first bending frequency until yielding of the steel reinforcement is reached. Thus, first bending frequency seems to be the most appropriate and consistent indicator for the yielding of steel

in reinforced concrete beams in the case of flexural damage. The increase in the interaction stiffness caused by the tension bond action will have a smaller influence on the first bending frequency than the decrease of the concrete stiffness for the cases of shear damage. It is also apparent that the bond action and concrete softening has a dual effect on the natural frequency for the second bending mode, depending on the steel reinforcement ratio. For shear damage cases there is no effect from the bond action on the second bending mode. The bond action does not have any effect on the natural frequencies of the third and higher bending modes, and changes in the frequencies for these modes are mainly governed by concrete softening.

The main contribution of this objective is that the relationship of the natural frequencies at each specific mode is related to the overall stiffness component i.e. concrete stiffness, steel stiffness and bond action, and not to the change in overall stiffness.

7.1.2 Identification of damage type

This study investigated the ability for the classification of damage type either due to the support stiffness deterioration or the stiffness deterioration of the structural element itself using the modal parameters. Natural frequencies are sufficiently sensitive to detect the deterioration in the stiffness of the supports and the change in the trends are consistent for all the modes considered in this study except for the third bending mode which shows an abnormal trend. Natural frequency of the first bending mode has high sensitivity to support stiffness deterioration, which makes it the most promising for monitoring the changes in support stiffness. In contrast, although frequency of the third bending mode shows a different trend when compared to the other modes, it can be used as a tool to identify whether the frequency shifts are caused by changes in support stiffness or stiffness of the structural element itself. Deterioration of the stiffness of the supports shows an increase in

the third mode while deterioration in the structural element stiffness shows a decrease in the third bending frequency.

Modal Assurance Criteria (MAC) is a good indicator to classify the cause of deterioration, with the support stiffness deterioration of the first bending mode having higher change in MAC values, and higher modes having very small change, while for the structural element defect the higher modes will have higher change in MAC values, and the first mode will have very small change.

The main contribution of this objective is that the modal parameters are feasible and good indicators to classify the damage type either caused by changes in support stiffness or stiffness of the structural element itself.

7.1.3 Damage severity algorithms

The averaging of the existing algorithms based on the proposed weighting method shows an overall stiffness change pattern corresponding to each damage level and based on the set of the adopted modes. The weighted average using proposed weighting method helps to establish the trend with regards to the change in overall stiffness based on the effect of the change in the stiffness component on the modal parameters.

For the frequency based stiffness index, flexural damage shows the lowest effect on the stiffness deterioration, while the shear damage at quarter-span shows the highest influence on the stiffness. The nonlinear behaviour of the stiffness change is considered beyond a damage ratio of 0.56, 0.57 and 0.62 for flexural damage, shear damage at 1.5d from the supports and shear damage at quarter-span, respectively.

The general trend of the MAC based stiffness index shows very small stiffness deterioration at all the damage scenarios and levels until prior to failure, whereby the pattern of the modal assurance criteria shows a rapid decrease at failure.

The developed algorithm based on the combined modal parameter based stiffness index shows the highest sensitivity to the stiffness deterioration compared to existing algorithms at all the damage levels and scenarios. Based on the results of this study, it can be observed that the flexural damage scenario has the lowest influence on the stiffness deterioration, while the shear damage at 1.5d from the support has the highest effect on the stiffness deterioration based on the developed algorithm.

The flexural damage scenario shows the lowest stiffness deterioration based on the static test indicators, while both shear damage scenarios at 1.5d from the support and at quarter span indicate higher deterioration. Prior to 0.5 damage ratio, the shear damage at quarter-span induces the highest stiffness deterioration, while beyond 0.5 damage ratio, the shear damage at 1.5d from the support induces higher deterioration to the stiffness.

The main contribution of this objective is developing a new damage severity algorithm which increases the sensitivity of the existing algorithms at various damages levels and scenarios. It presents an averaging procedure which helps to establish the overall stiffness change based on the adopted set of modes. Finally, the indicator of stiffness change has been established based on the static test data, which show better sensitivity than the dynamic indices. However, static load test is time consuming, equipment and labour intensive and causes major disruptions to existing use of the structures. Thus, the use of the damage algorithms based on the modal testing are more suitable for exist structures with less time consuming and cost.

7.1.4 Damage location algorithms

Existing damage location algorithms (Curvature Damage Factor and Local Stiffness Indicator) show anomalies along the beam length for all of the adopted damage levels and scenarios, besides showing anomalies at the supports.

All of the adopted modes show anomalies along the beam length possibly as a result of the mathematical calculation of the damage location algorithm. Most of the algorithms are based on the calculation of the second or the fourth derivatives of mode vectors which results in very small values of the order of 10^{-8}. During multiplying or dividing, such values will show anomalies for the algorithm values along the beam length. A procedure to eliminate statistical anomalies is proposed and used in this study and helps to cut-off most of the anomalies along the beam length for each individual mode. The averaging of all the adopted modes using the proposed weighting method is applied to the algorithm values and indicates the appearance of some anomalies along the beam length. The statistical anomalies elimination procedure is further applied to help with cutting-off most of the anomalies along the beam length which result from the averaging procedure.

Modified algorithms show a much higher sensitivity than the original algorithms in localising single and multi cracks at different damage scenarios. Averaging using the results of the proposed weighting method, after performing the statistical anomalies elimination procedure, shows very good sensitivity of the modified algorithms in detecting cracks at various damage levels and scenarios.

The developed algorithm called stiffness reduction index, applied on flexural and shear damage scenarios and shows good sensitivity in detecting single and multi cracks and shows less peaks in the area around the actual cracks for the case of multi cracks.

Modified local stiffness index is not able to detect the first shear crack between the left support and 1.5d, while both modified curvature damage factors and developed stiffness reduction index are able to do so. Modified algorithms are not able to detect the first diagonal shear crack at the left support, while the developed algorithm is able to do so.

The contribution of this objective is modifying some of the existing damage location algorithms which results in enhancing their sensitivity. In addition, an elimination procedure which helps to cut-off the anomalies in the algorithms values along the beam length is presented. Also demonstrated is an averaging procedure which helps to draw the overall crack pattern based on the adopted set of modes. Finally, a new damage severity algorithm which shows higher sensitivity than existing and modified algorithms at various damage levels and scenarios is also presented.

7.1.5 Flexural CFRP repair assessment

The bending frequencies show an abnormal trend for the flexural repair with externally bonded CFRP sheets, where a decrease is seen after fixing the CFRP sheets instead of the expected increase due to overall stiffness increase.

The composite action phenomenon of flexural repaired RC beams with CFRP sheets is found to be the reason behind the abnormal trend, due to the laboratory repairing procedure which involves turning the beams over during repair. The dynamic indices which are based on the modal frequency and damping show good sensitivity for the repair effectiveness, and the modal damping shows the highest sensitivity.

The increase in the load capacity from 49% to 85% corresponding to the pre-repair damage level (design load to failure load) is found for the beams with minimum steel limit (ρ_{min})

and 15.3% to 28.4% for the beams with maximum steel limit (ρ_{max}). The failure mode is intermediate induced crack (IC) debonding due to existence of pre-repair flexural cracks.

The beams show an ability to withstand loads of close to the unrepaired capacity after the debonding of the CFRP sheets, which indicates the possibility of re-repair of the beams after the CFRP debonding.

The setting time of 15 days is proposed to be the maturation age of the CFRP adhesive material according to the dynamic test using the modal parameters, while the recommended maturation age by the adhesive material manufacturer is 7 days.

The main contribution of this objective is that the effectiveness of the repair using CFRP sheets decreases as the pre-repair damage level increases. Regardless of the pre-repair damage level and even at the failure level, repair with CFRP sheets helps to increase the load capacity. Dynamic indices based on the modal frequency and damping show promise as good indicators for the evaluation of the CFRP flexural repair system effectiveness and to estimate the repairing capacity.

7.1.6 Shear CFRP repair assessment

The results show that regardless of the pre-repair damage level, repair with CFRP sheets will recover the stiffness. Beams without shear stirrups indicate an increase in the capacity from 12.2% to 33.3% corresponding to pre-repair damage level (design load to failure load) while beams with stirrups show an increase from 8.1% to 21.2% for shear damage at quarter-span. The results show no contribution from the shear stirrups to the load capacity at the pre-repair phase for shear damage close to the support.

The dynamic indices for the stiffness recovery based on the modal frequency and damping show good sensitivity for the repair effectiveness, and the modal damping shows higher

sensitivity. The failure mode is a combination of flexural cracks and CFRP delamination of a concrete layer for shear damage at quarter-span and a combination of shear and CFRP debonding for shear damage close to the support.

The main contribution of this objective is that the CFRP sheets repair system is an effective technique regardless of the pre-repair damage level, shear damage location and existence of shear stirrups. Dynamic indices based on the modal frequency and damping show promise as good indicators for the evaluation of the CFRP shear repair system effectiveness and to estimate the repair capacity.

7.1.7 ACI Code evaluation

The results show good compatibility between ACI and experimental results for the un-repaired flexural beams, while for repaired beams the ACI results are smaller than the experimental results by about 20%. This is due to the fact that the ACI assumptions neglect the steel bars at the compression zone. For shear damage, the ACI results of the unrepaired beams are much lower than the experimental results. The proposed modification includes the following:

- Consideration of the concrete contribution based on the inclined area of the cross section which is drawn with an angle of 45^{o} (on average);
- The contribution of the flexural steel;
- Ignoring the shear stirrups contribution in the case of shear damage close to the support.

The modified ACI equation shows very good agreement with the experimental results. For the repaired RC beams, the ACI gives higher results than the experimental. This is because the ACI have no consideration for the pre-repair damage level for the calculation of the ultimate capacity for which the concrete contribution has to be multiplied by a reduction

factor, and the CFRP contribution must be reduced based on the pre-repair damage level. The modified ACI equation shows much better agreement with the experimental results.

The main contributions of this objective based on the experimental results of this study are the modified equations for concrete and shear stirrups contribution, contribution of the external CFRP sheets and the contribution of the flexural steel, which gives better agreement with the experimental results.

7.2 Recommendations

The study has achieved its objectives as mentioned in the contributions of each objective. The following recommendations for future research are made based on the findings of this study.

7.2.1 Future work direction

It could be very useful for future research work to proceed in the direction outlined below:

- Study the effect of the composite action phenomenon on the modal parameters for various steel bar surface conditions, since there is evidence of bond action effect.
- Study the classification of damage type for several support deterioration levels corresponding to several structural element stiffness defect levels, and for various integrity problems between the support and the girders for integral structures i.e. building, integral bridges.
- Develop a damage severity algorithm based on the combination of the dynamic and static data. Establish a modal testing procedure for detecting the damage location such as multi output/multi input systems.

- Study the ability for re-repair of repaired flexural beams after CFRP de-bonding, since repaired beams show an ability to withstand loading even after CFRP de-bonding. Study the effect of various concrete surface preparation procedures and conditions on the CFRP repair effectiveness, and the factors affecting the setting time of the CFRP adhesive material.
- Study the CFRP contribution to the shear ultimate capacity for shear repairing at various shear damage locations and at various shear stirrups provision. Study the contribution of the concrete and the shear stirrups to the shear ultimate capacity for RC beams subjected to various load locations from the supports and at various shear stirrups provision. Finally, evaluate the ACI code results based on more shear loading cases, various concrete properties and various shear stirrups provision.

7.2.2 Consideration for researchers

Since the present study is carried out using experimental work conducted on laboratory samples of RC beams, there are some recommendations which researchers must take into consideration. They are as follows:

- The modal testing must be carried out after 24 hours from the time of applying load into the beam, which is needed to give enough time for the RC beam material to recover, as the modal parameters are found to be influenced by the RC beam material recovery after releasing the load.
- When investigating the repair effectiveness of structures repaired in flexure with CFRP sheets, it is advised that the structure be exposed to a load within the design load limit prior to testing in order to activate the bond action in the CFRP adhesive layer.

Appendix A: Estimations of maximum deflection position

In order to place the displacement transducer to carry out the data of the maximum deflection for the shear group static load test, pre-test Finite Element model was build using DIANA TNO software. The modelling of the RC beam was done using the 20-node brick elements to represent the concrete. In addition, a 2-node embedded bar inside 3-D brick element was used to represent the reinforcement bars. Figure A.1 shows the FE modelling for the RC beam. For concrete linear elasticity behaviour it was modelled as isotropic material with a compressive strength of 30 MPa, modulus of elasticity of 26,000, poison ration of 0.3 (assumed), and mass density of 2350 Kg/m^3. Reinforcement steel bars were represented as bonded reinforcement with yeild stress of 420 MPa and modulus of elasticity of 200,000 MPa. The linear static analysis was carried out where the concentrated load was applied as a line load in to the top surface of the RC beam at two locations. First location is at 55 cm from the left support as the quarter-span and the second is at 1.5d from the left support (where it used to be 32 cm as mentioned in Section 4.3.2.1). The results shows that the maximum deflection for the shear loading at quarter-span is at 82 cm from the left support, while for shear damage at 1.5d it was at 70 cm from the left support.

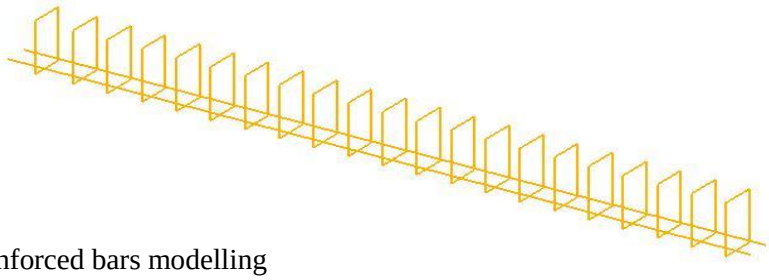

a- Reinforced bars modelling

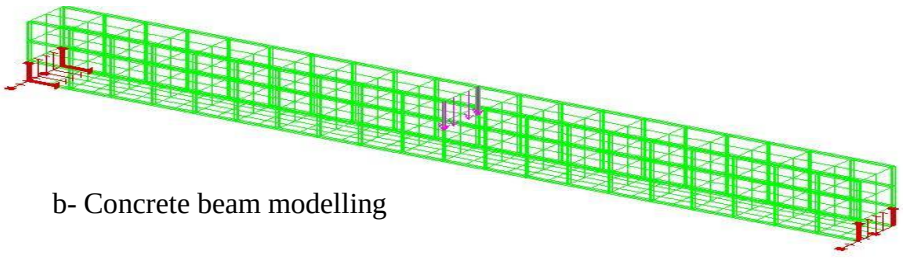

b- Concrete beam modelling

Figure A.1. Finite element model of reinforced concrete bridge girder

Appendix B: Crack Patterns

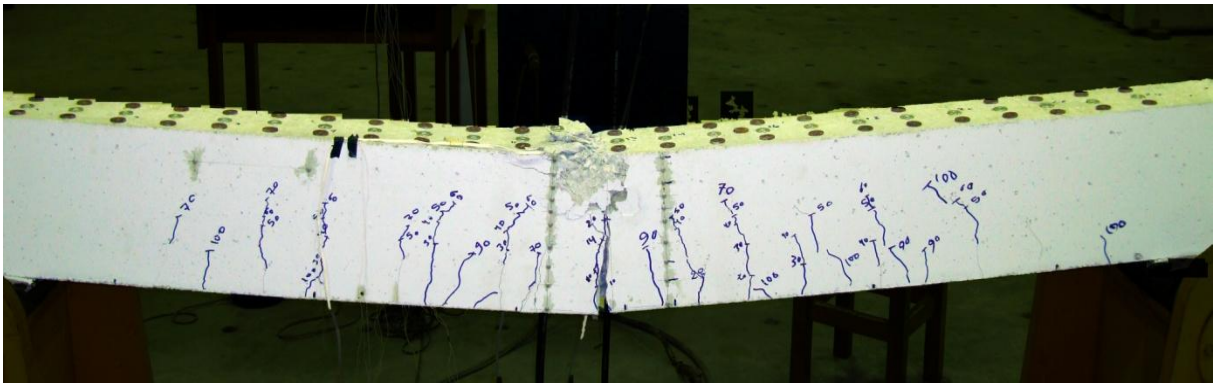

Figure B1. Crack patters of beam B111m

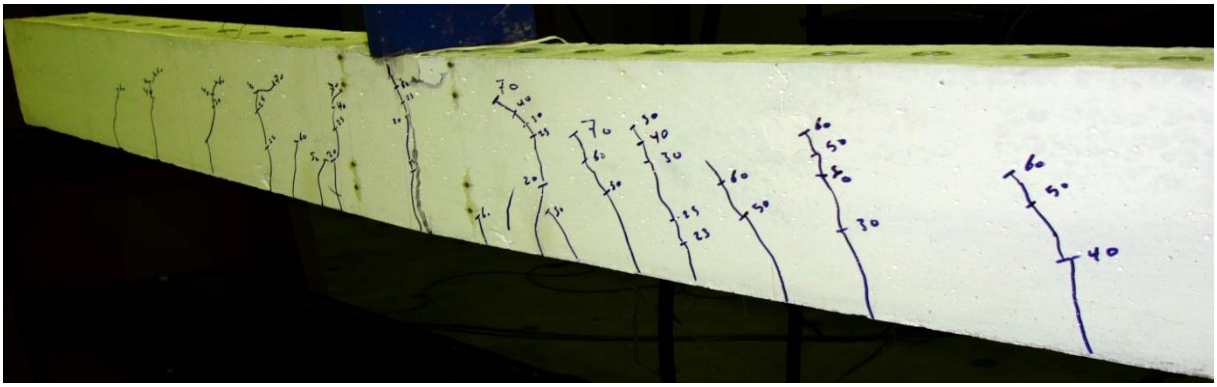

Figure B2. Crack patters of beam B121m

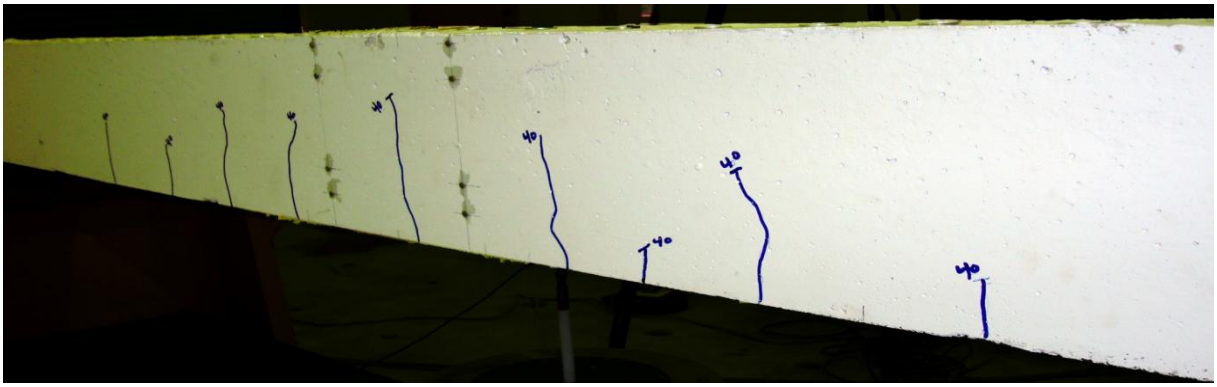

Figure B3. Crack patter of beam B112m prior to repair

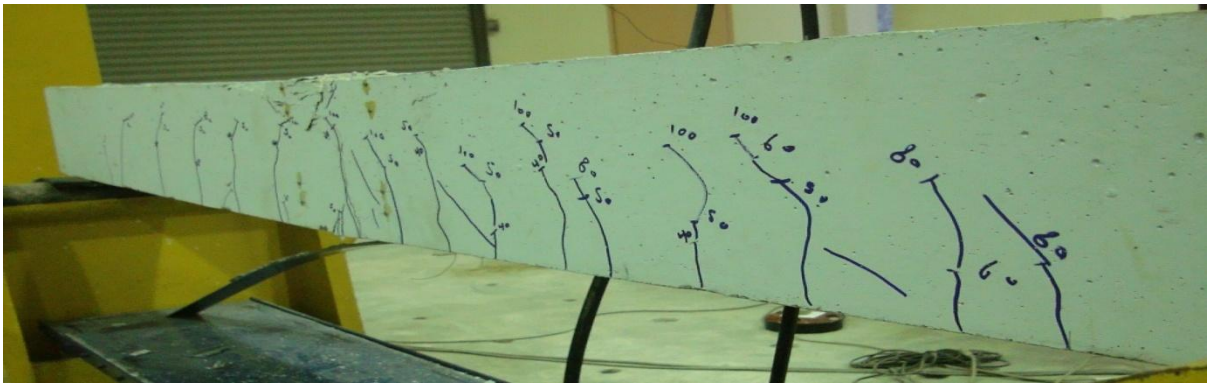

Figure B4. Crack patter of beam B112m at post repair

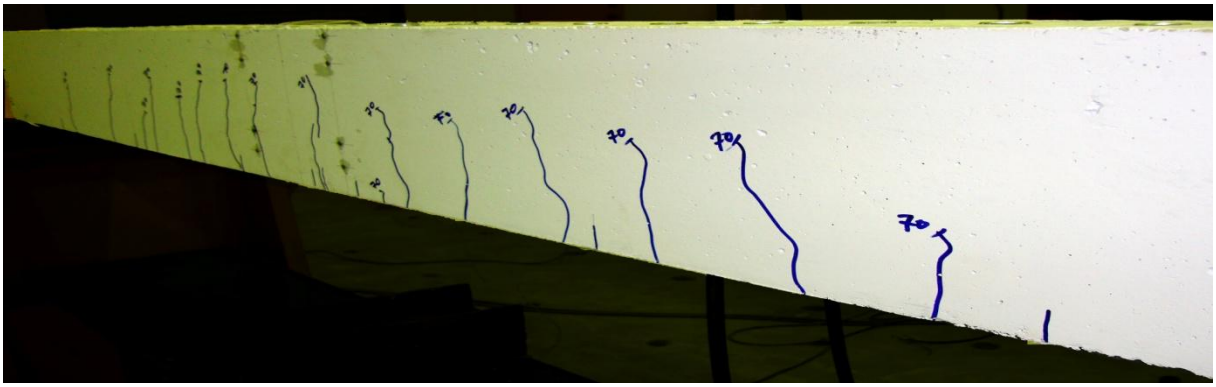

Figure B5. Crack patter of beam B113m prior to repair

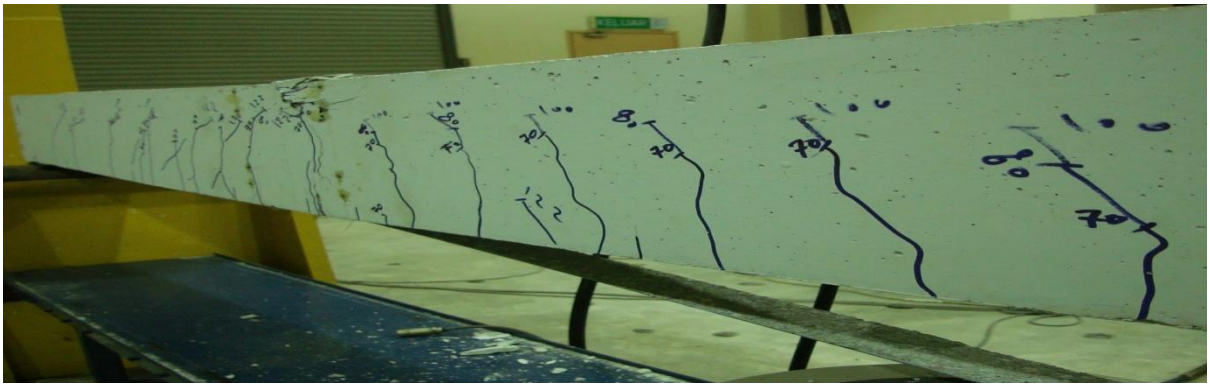

Figure B6. Crack patter of beam B113m at post repair

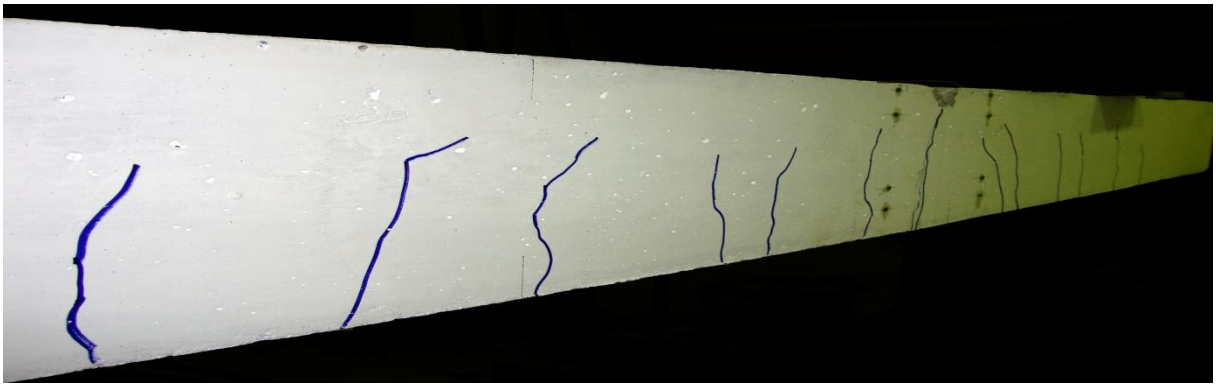

Figure B7. Crack patter of beam B114m prior to repair

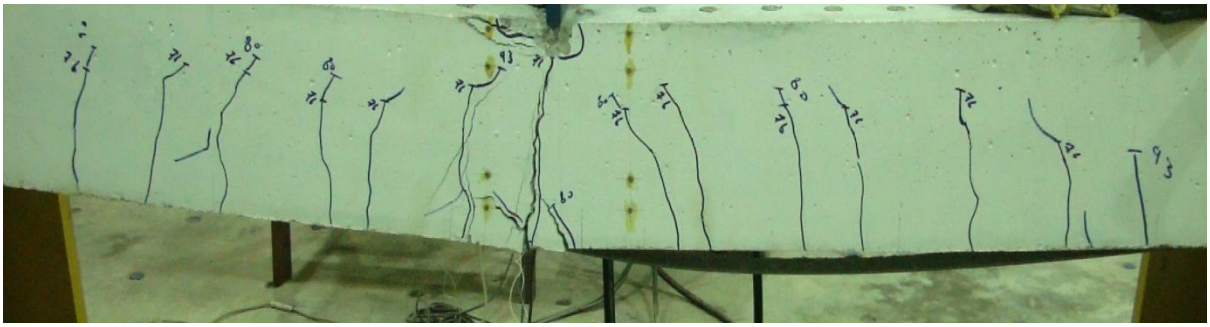

Figure B8. Crack patter of beam B114m at post repair

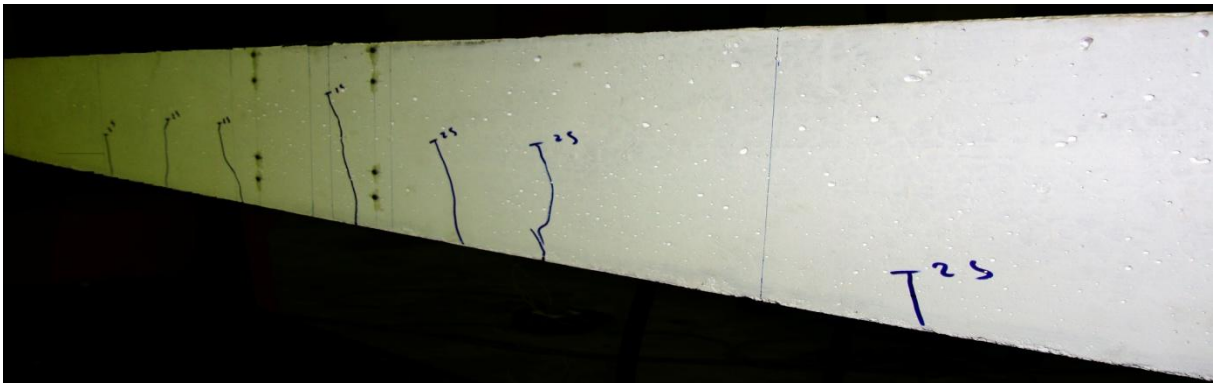

Figure B9. Crack patter of beam B122m prior to repair

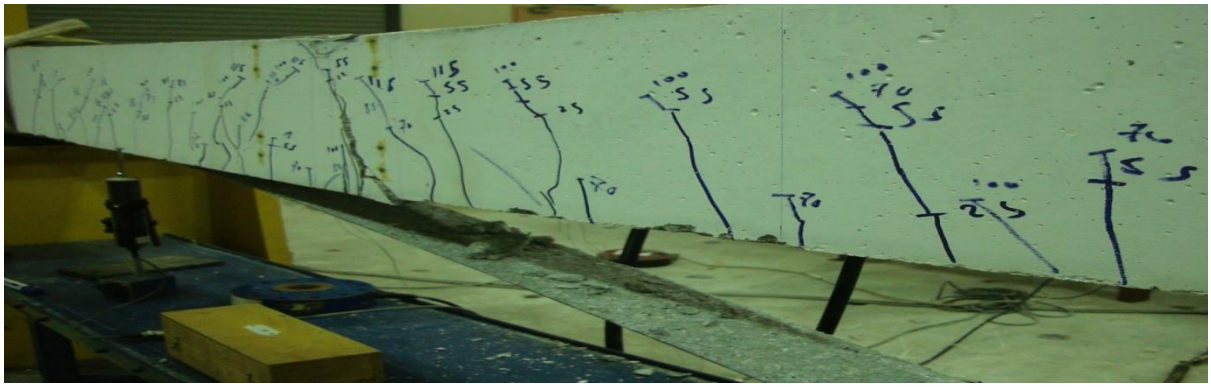

Figure B10. Crack patter of beam B122m at post repair

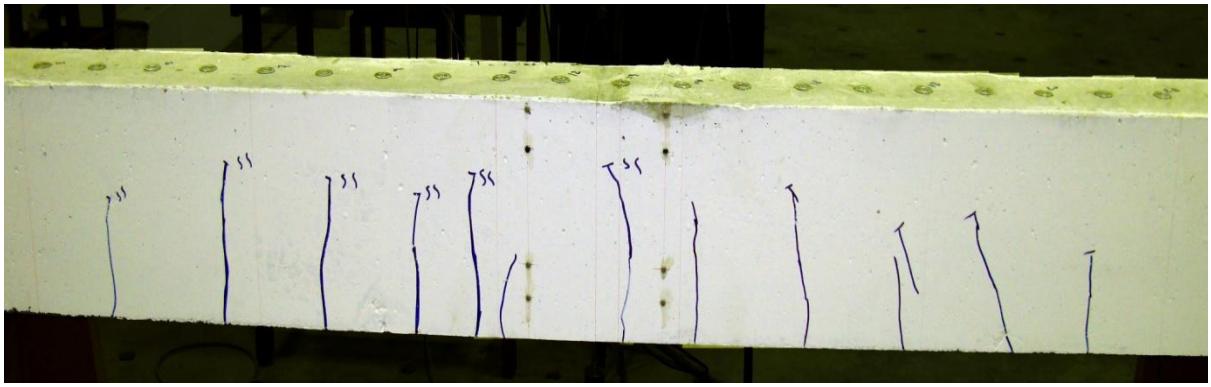

Figure B11. Crack patter of beam B123m prior to repair

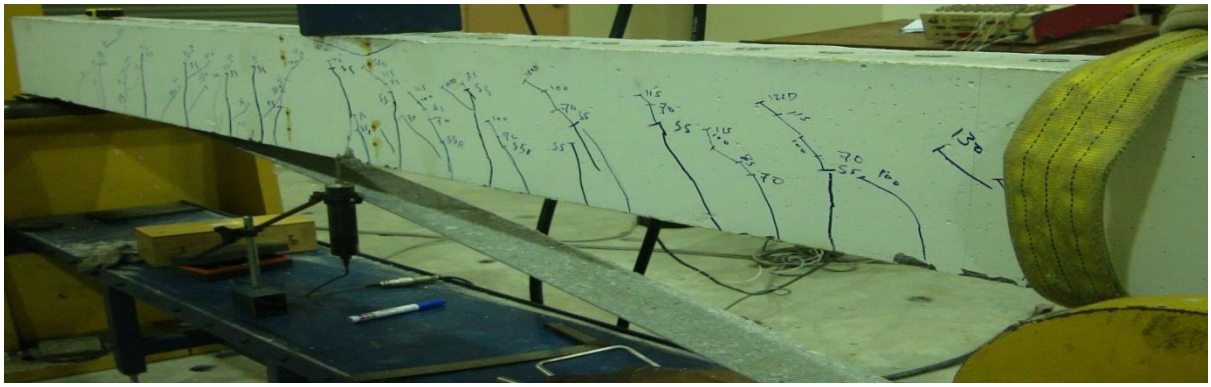

Figure B12. Crack patter of beam B123m at post repair

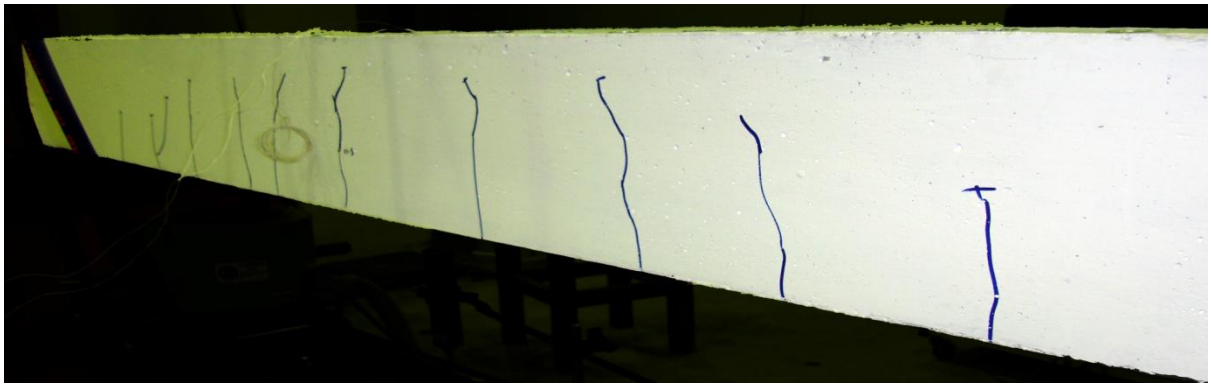

Figure B13. Crack patter of beam B124m prior to repair

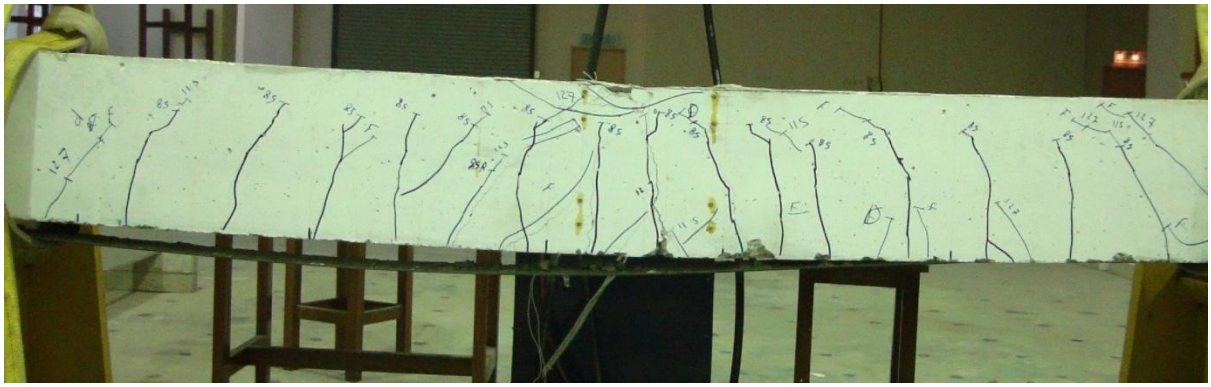

Figure B14. Crack patter of beam B124m at post repair

Figure B15. Crack patter of beam B211d prior to repair

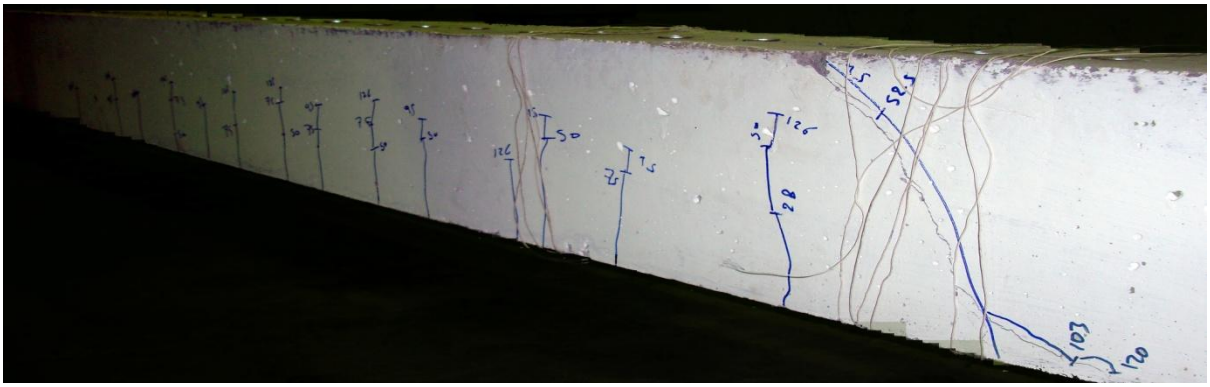

Figure B16. Crack patter of beam B212d prior to repair

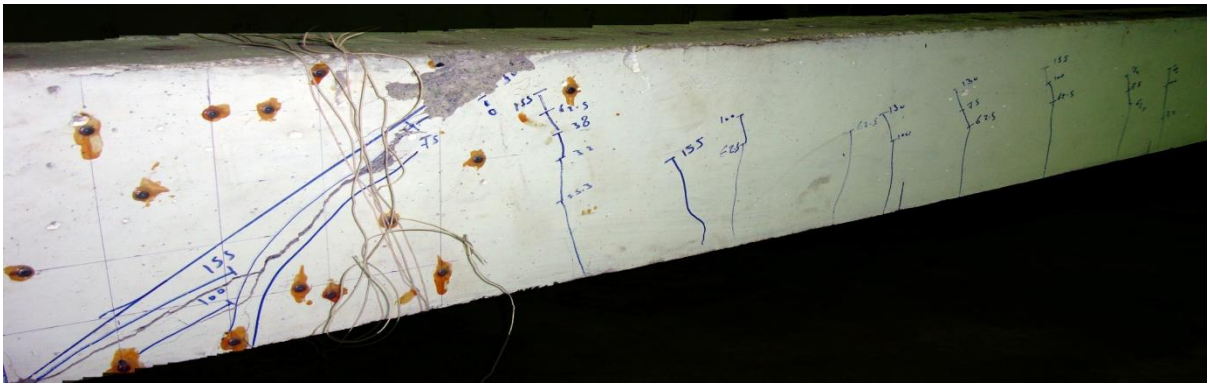

Figure B17. Crack patter of beam B221d prior to repair

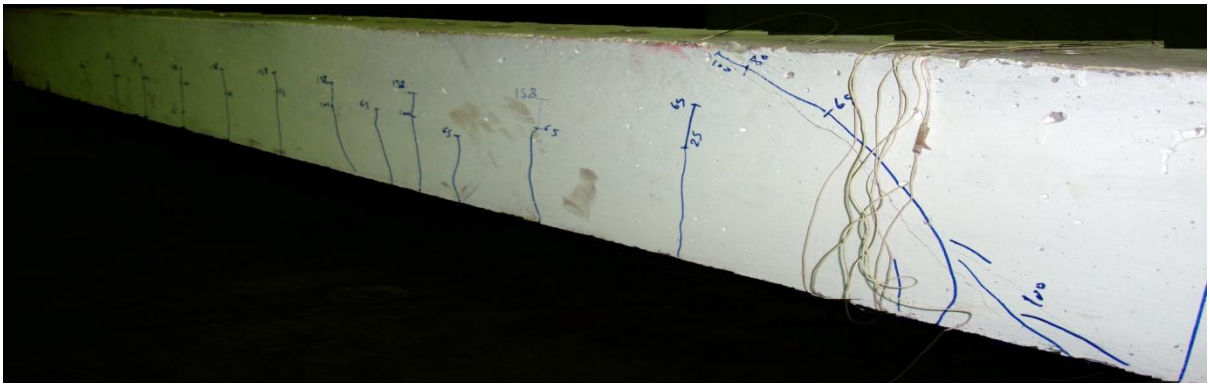

Figure B18. Crack patter of beam B222d prior to repair

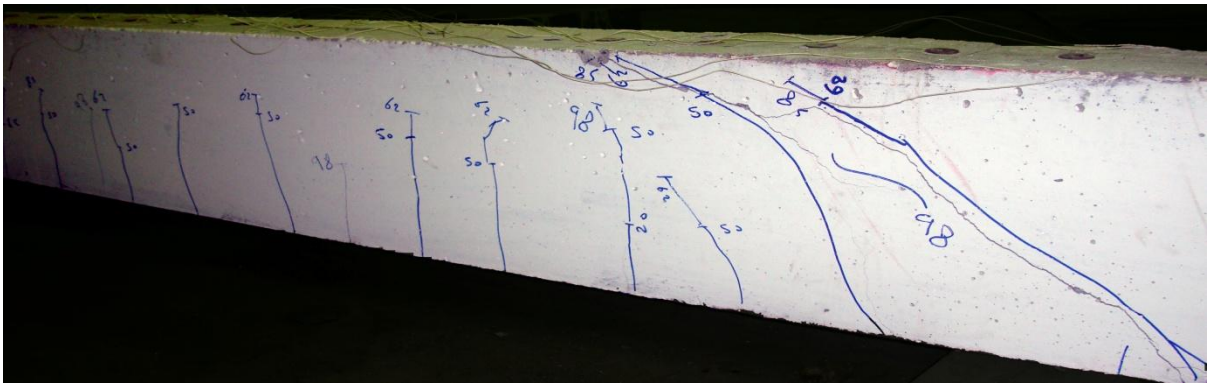

Figure B19. Crack patter of beam B211q prior to repair

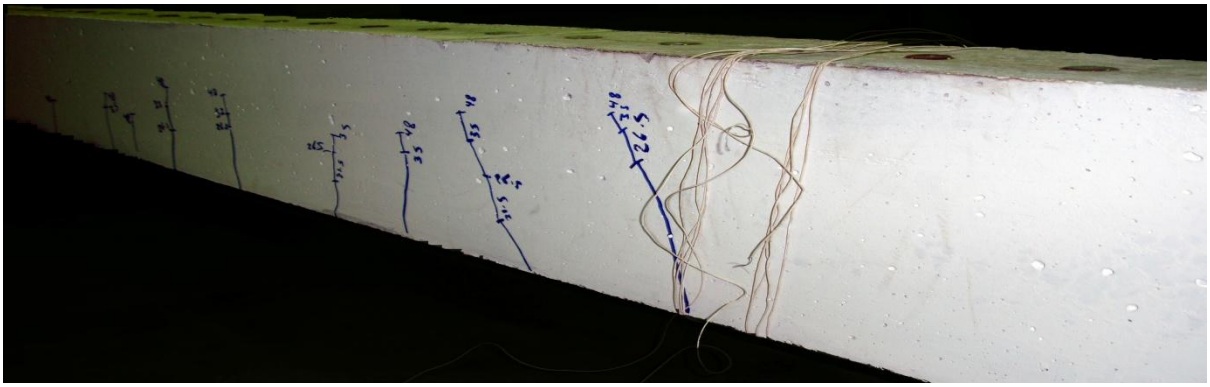

Figure B20. Crack patter of beam B212q prior to repair

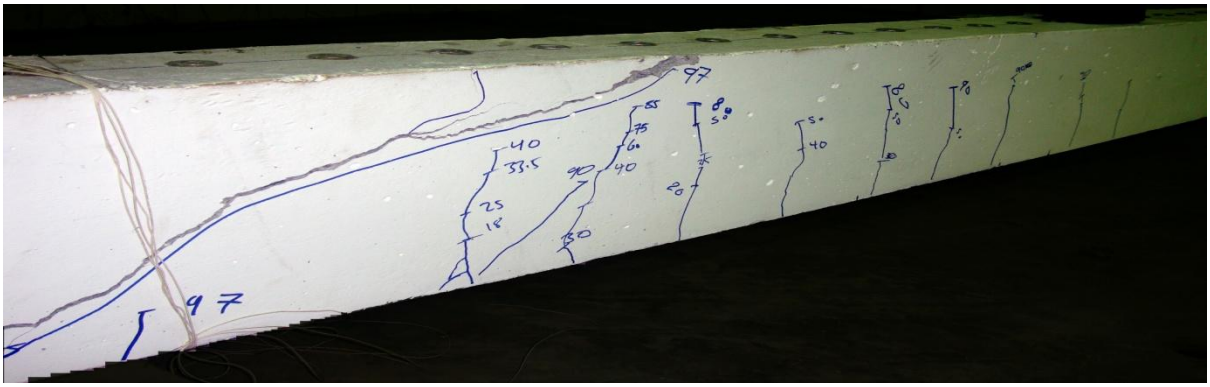

Figure B21. Crack patter of beam B221q prior to repair

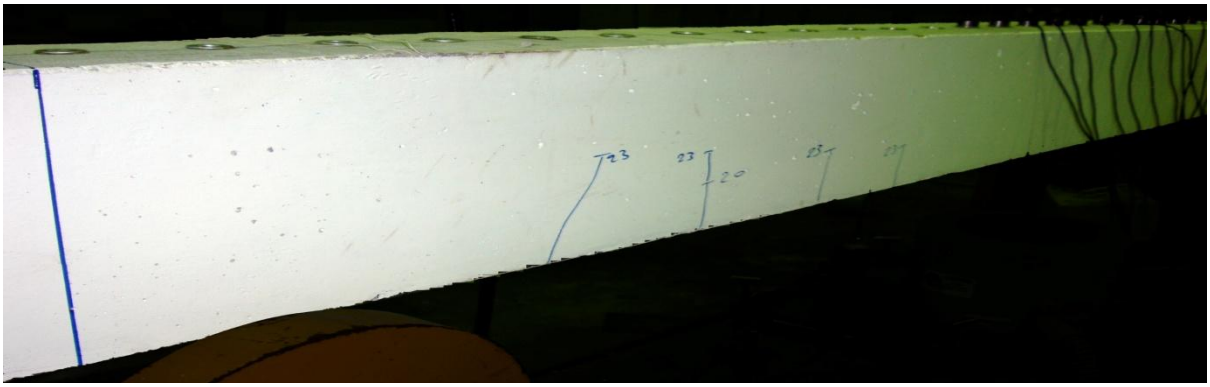

Figure B22. Crack patter of beam B222q prior to repair

Appendix C: Application of proposed weighting method

For the flexural damage scenario, Figure C1 shows the stiffness change results using frequency based stiffness index and corresponding to different damage levels for beam B121m. The weighted average using PWM approach is calculated and presented in Figure C1 as well, where the weighted of each mode as illustrated in Table 5.8. The variance in the stiffness changing corresponding to different modes shows the need to use an averaging procedure that is able to present the global stiffness changing due to the concrete stiffness deterioration, steel deterioration successive to yield, and the interaction stiffness changing. The weighted average (PWM) indicates deterioration in the global stiffness.

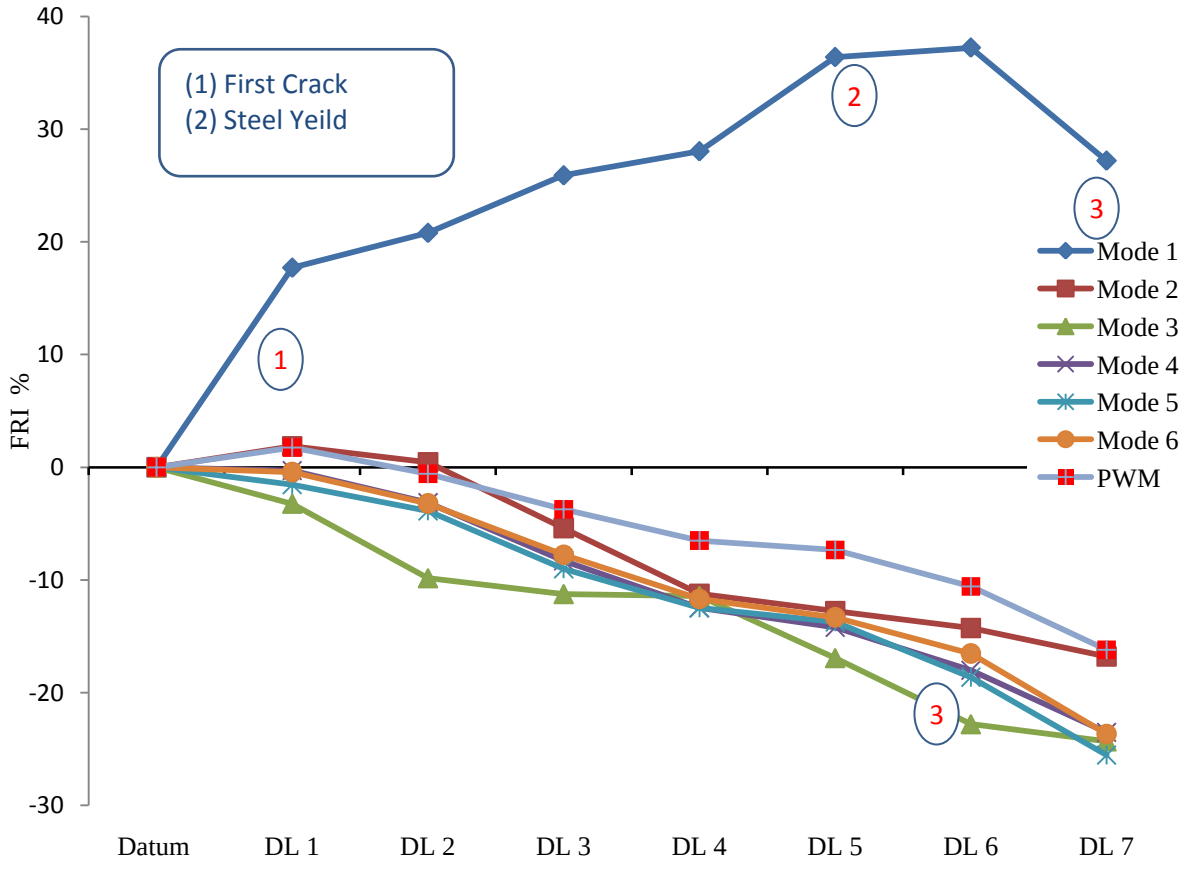

Figure C1. Frequency based stiffness index and weighted average (PWM) values for beam B121m

For the flexural damage scenario i.e. Beam B121m, Figure C2 presents the stiffness changing using MAC based stiffness index and corresponding to different damage levels. Since different modes showed different change in the MAC values, the weighted average using PWM approach is applied in order to highlight the global stiffness changing corresponding to the damage levels and influenced by the sensitivity of each specific mode. The weight of each mode are as illustrated in Table 5.8

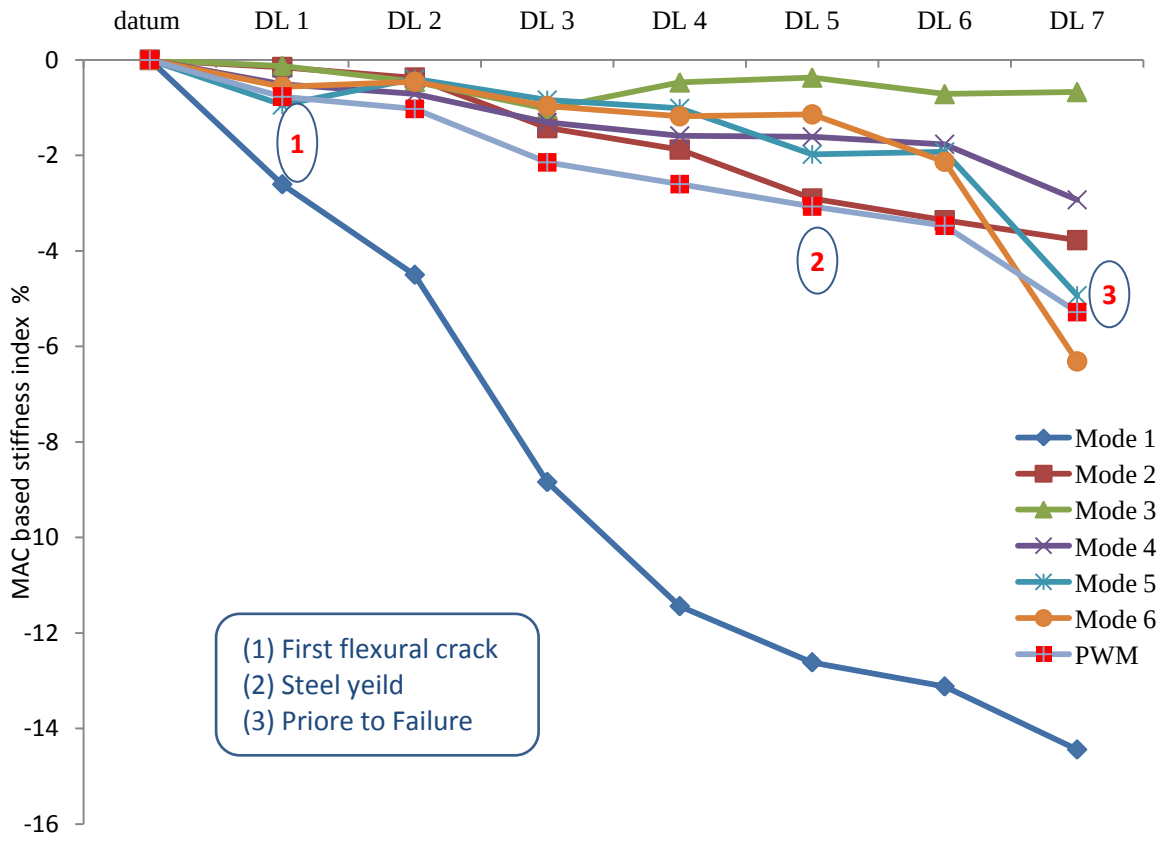

Figure C2. Change in stiffness based on MAC based stiffness index values for beam B121

Appendix D: Stiffness indicator based on static test data

D.1 Flexural damage scenario

For flexural damage scenarios, the flexural rigidity or the flexural stiffness is the governing stiffness for the status of the structure under different damage levels. Since the data carried out from the static test was the load vs. deflection, the relation of the stiffness will be based on the theoretical equation of the deflection calculation in the case of flexural stiffness. For a simply supported beam with a concentrated load at the mid-span, the deflection can be calculated as in Equation (D.1).

$$\delta = \frac{P\,L^3}{48\,EI} \tag{D.1}$$

The flexural stiffness (EI) can be calculated as in Equation (D.2).

$$EI = \frac{P}{\delta} * \frac{L^3}{48} \tag{D.2}$$

In order to calculate the flexural stiffness the secant modulus (Ks) of the load vs. deflection curve will be used to find the load over the deflection. The flexural stiffness for any RC beam will be affected by the applied load level, where with a load higher than the first crack load the stiffness will be influenced by the nonlinear behaviour of the RC beam. The flexural stiffness of the datum case of the RC beam can be found by applying a load on the mid-span of the beam and the secant modulus will be calculated based on the load over deflection of up to prior to the first crack load level to insure avoiding the nonlinear influence on the stiffness. The flexural stiffness of any load cycle that was induced at certain damage levels, its need is to apply a load again on the beam to carry out the load vs. deflection data, and the secant modulus (Ks) will be also calculated based on the load prior to the first crack limit. Figure D.1 shows graphically the calculation of the static flexural stiffness using the secant modulus (Ks) of the load vs. deflection curves and up to 10 kN, which is prior to the first crack level at 11 kN.

The flexural stiffness can be calculated mathematically as in Equations (D.3).

$$EI_{c,1^{st}d} = Ks_{c,1^{st}d} * \frac{L^3}{48} = \frac{\text{Load at 10 kN}_{c,1^{st}d}}{\text{Deflection at 10 kN}_{c,1^{st}d}} * \frac{L^3}{48} \quad \text{(D.3)}$$

where "c" indicates the datum case, and "1st d" indicates the first damage level.

The stiffness changing indicator based on the static test for flexural damage can be calculated as the difference between the flexural stiffness at any damage level and the datum stiffness.

$$\text{Stiffness chnage based on static data}_{\text{flexural}} = \frac{EI_d - EI_c}{EI_c} \quad \text{(D.4)}$$

where EI is the flexural stiffness , "d" indicates the damage cases, and "c" indicates the datum case.

Substituting Equation (D.2) into Equation (D.4) gives;

$$\text{Stiffness chnage based on static data}_{\text{flexural}} = \frac{(\frac{P}{\delta} * \frac{L^3}{48})_d - (\frac{P}{\delta} * \frac{L^3}{48})_c}{(\frac{P}{\delta} * \frac{L^3}{48})_c} \quad \text{(D.5)}$$

And since $(\frac{L^3}{48})$ for the datum and the damage will be same, then equation (D.5) can be rewritten as:

$$\text{Stiffness chnage based on static data}_{\text{flexural}} = \frac{(\frac{P}{\delta})_d - (\frac{P}{\delta})_c}{(\frac{P}{\delta})_c} \quad \text{(D.6)}$$

Where $(\frac{P}{\delta})$ is the secant modulus at prior to first crack load, "c" indicates the datum case, and "d" indicates the damage cases.

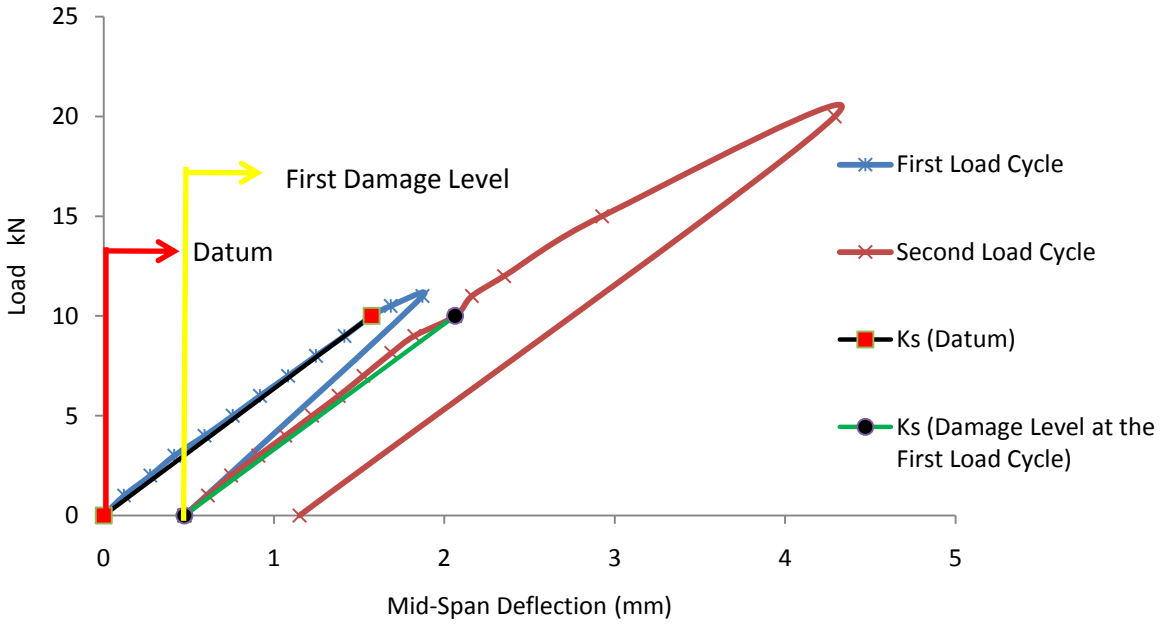

Figure D.1. Graphically calculating of the secant modulus

D.2 Shear damage scenario

The shear damage is different from the flexural damage, where the shear stiffness will be the governing stiffness of the global beam stiffness. In the shear stiffness the shear modulus (S) will be used, where to calculate the shear modulus (S), take a block with length L and cross sectional area A exposed to a force F, which is applied parallel to one of the vertical faces. The face will move a distance ΔX in the vertical direction and as shown in Figure D.2. The shear modulus will be the shear stresses divided by the shear strain, where the shear stress will equal the applied force F divided by the shear area A. The shear strain will be equal to the angle of rotation of the beam, which would be equal to the vertical movement of the shear face (ΔX) divided by the Length L. the shear modulus (S) can be calculated as in Equation (D.7).

$$S = \frac{\text{Shear Stress}}{\text{Shear Strain}} = \frac{F/A}{\Delta X/L} = \frac{F.L}{\Delta X.A} \qquad (D.7)$$

If this block is a part of a beam exposed to force at the shear zone as in Figure D.3, the force distance L will be the distance from the support to the applied load, and the area A will be the area of the cross-section, and the movement ΔX will be the deflection under the applied load δ.

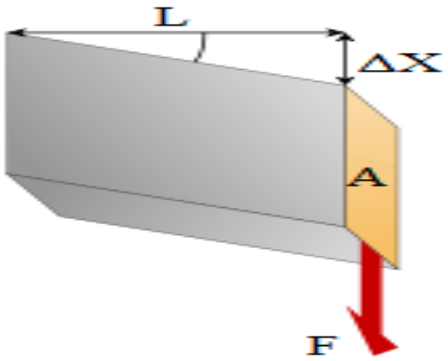

Figure D.2. Block with a shear force applied into the shear face

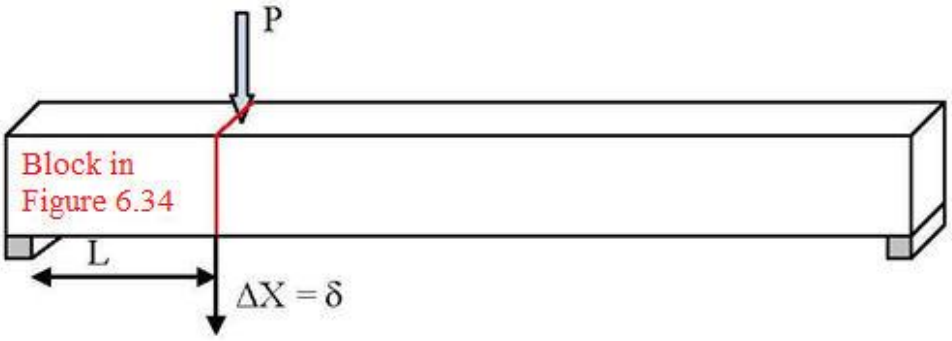

Figure D.3. General sketch for a beam under force applied at the shear zone

Equation (D.7) can be rewritten for the shear modulus of the beam subject to force at the shear zone and as following:

$$S = \frac{P.L}{\delta.A} = \frac{P}{\delta} * \frac{L}{A} \quad (D.8)$$

where $(\frac{P}{\delta})$ is the load divided by the deflection at the shear zone.

The proposed shear modulus calculation can be valid for the cases when the shear face remained as vertical plane, otherwise the calculated shear modulus will be influenced by the nonlinear behaviour. Thus, and to avoid the effect of the nonlinearity on the calculated shear modulus, the applied load shouldn't exceed the linearity limit of the RC beam, which can be achieved by an applied load less than the first crack limit. The $(\frac{P}{\delta})$ can be calculated using the secant modulus (Ks) of the load vs. deflection curves when the deflection is measured at the shear zone, and not at the mid-span as was used in the flexural cases. The graphical calculation of the secant modulus (Ks) can be performed as shown in Figure D.1, while changing the mid-span deflection to the defalcation at the shear zone and directly

under the applied shear force. The shear modulus (S) can be calculated mathematically as in Equation (D.9).

$$S_{c,1^{st}d} = Ks_{c,1^{st}d} * \frac{L}{A} = \frac{\text{Load at 10 kN}_{c,1^{st}d}}{\text{Deflection at 10 kN}_{c,1^{st}d}} * \frac{L}{A} \quad (D.9)$$

Where "c" indicates the datum case, and "1st d" indicates the first damage level.

The shear modulus of the datum case of the RC beam can be found by applying a load into the shear-span of the beam and the secant modulus will be calculated based on the load over deflection of up to prior the first crack load level to insure the avoiding of the nonlinear influence on the stiffness. The shear modulus of any load cycle that was induced to a certain damage level, its need is to apply a load again on the beam to carry out the load vs. deflection data, and the secant modulus (Ks) will be also calculated based on the load, which is prior to the first crack limit.

The stiffness changing indicator based on the static tests and for shear damage can be calculated as the difference between the shear modulus at any damage level and the datum.

$$\text{Stiffness chnage based on static data}_{\text{shear}} = \frac{S_d - S_c}{S_c} \quad (D.10)$$

where "d" indicates the damage cases, and "c" indicates the datum case.

Substituting Equation (D.8) into Equation (D.10) gives:

$$\text{Stiffness chnage based on static data}_{\text{shear}} = \frac{(\frac{P}{\delta} * \frac{L}{A})_d - (\frac{P}{\delta} * \frac{L}{A})_c}{(\frac{P}{\delta} * \frac{L}{A})_c} \quad (D.11)$$

And since $(\frac{L}{A})$ for the datum and the damage will be the same, then equation (D.11) can be rewritten as:

$$\text{Stiffness chnage based on static data}_{\text{shear}} = \frac{(\frac{P}{\delta})_d - (\frac{P}{\delta})_c}{(\frac{P}{\delta})_c} \quad (D.12)$$

where $(\frac{P}{\delta})$ is the secant modulus at prior to first crack load, "c" indicates the datum case, and "d" indicates the damage cases.

References

Abdessemed, M.; Kenai, S.; Bali, A. and Kibboua, A. **2011**. Dynamic analysis of a bridge repaired by CFRP: Experimental and numerical modelling, *Construction and Building Materials* 25:1270-1276.

Abdul Razak, H. and Choi, F. **2001**. The effect of corrosion on the natural frequency and modal damping of reinforced concrete beams, *Engineering Structures* 23:1126-1133.

Abdul Wahab, M.M. and De Roeck, G. **1999**. Damage Detection in Bridges Using Modal curvature: Application To A Real Damage Scenario, *Journal of Sound and Vibration* 226: 217-235.

Abe, M.; Fujino, Y. and Yoshida, J. **2000**. Dynamic behaviour and seismic performance of base-isolated bridges in observed seismic records, *In proc. of 12th World Conf. on Earthquake Engineering* Auckland, New Zealand, 30Jan-4Feb 2004.

ACI 211.1 **1991**. *Standard practice for selecting proportions for normal, heavyweight, and mass concrete,* American Concrete Institute, Farmington Hills, MI.

ACI 318 **2008**. *Building code requirements for structural concrete and commentary*, American Concrete Institute, Farmington Hills, MI.

ACI 440.1R **2006**. *Guide for the design and construction of structural concrete reinforced with FRP bars*, American Concrete Institute, Farmington Hills, MI.

ACI 440.2R **2000**. *Design guidance for strengthening concrete structures using fiber composite materials*, American Concrete Institute, Farmington Hills, MI.

ACI 440.2R **2002**. *Guide for the design and construction of externally bonded frp systems for strengthening concrete structures*, American Concrete Institute, Farmington Hills, MI.

ACI 440.2R **2008**. *Guide for the design and construction of externally bonded FRP systems for strengthening concrete structures*, American Concrete Institute, Farmington Hills, MI.

ACI 440.3R **2004**. *Guide for test methods for fiber reinforced polymers (FRP) for reinforcing and strengthening concrete structures,* American Concrete Institute, Farmington Hills, MI.

ACI 440.4R **2004**. *Prestressing concrete stuctures with FRP tendons*, American Concrete Institute, Farmington Hills, MI.

ACI 440.5 **2008**. *Specification for construction with fiber-reinforced polymer reinforcing bars*, American Concrete Institute, Farmington Hills, MI.

ACI 440.6 **2008**. *Specification for carbon and glass fiber-reinforced polymer bar materials for concrete reinforcement*, American Concrete Institute, Farmington Hills, MI.

ACI 440.7R **2010**. *Guide for the design and construction of externally bonded frp systems for strengthening unreinforced masonry structures*, American Concrete Institute, Farmington Hills, MI.

ACI 440.R **1996**. *State-of-the-art report on FRP for concrete structures, manual of concrete practice,* American Concrete Institute, Farmington Hills, MI.

ACI 440.R **2007**. *Report on fiber-reinforced polymer (FRP) reinforcement for concrete structures*, American Concrete Institute, Farmington Hills, MI.

Adachi, Y.; Kagayama, T.; Unjoh, S. and Kondoh, M. **2000**. Non-linear seismic response characteristics study of a RC bridge column with seismic isolators by a shaking table test, *in proc. of 12th World Conference on Earthquake Engineering* Auckland, New Zealand, 30Jan-4Feb 2004.

Alampalli, S. **2000**. Effect of Testing, Analysis, Damage, and Enviroment on Modal Parameters, *Mechanical System and Signal Processing* 14 (1): 63-74.

Alexander, J.G.S. and Cheng, J.J.R. **1996**. Shear strengthening of small scale concrete beams with carbon fibre reinforced plastic sheets, *Proceedings of the First Structural Speciality Conference*, Edmonton, Alberta, Canada, pp:167–77.

Almakt, M.M.; Balazs, G.L. and Pilakoutas, K. **1998**. Strengthening of RC elememts by CFRP plates local failure, *2nd International PhD Symposium in Civil Engineering*, Budapest.

Al-Saidy, A.H.; Al-Harthy, A.S.; Al-Jabri, K.S.; Abdul-Halim, M. and Al-Shidi, N.M. **2010**. Structural performance of corroded RC beams repaired with CFRP sheets, *Composite Structures* 92: 1931-1938.

AlShaarbaf, I. **1990**. *Three – dimensional nonlinear finite element analysis of reinforced concrete beams in torsion*, U.K.: Ph.D. Thesis, University of Bradford.

Al-Sulaimani, G.J.; Sharif, A.; Basunbul, I.A.; Baluch, M.H. and Ghaleb, B.N. **1994**. Shear repair for reinforced concrete by fiberglas plate bonding, *ACI Structural Journal* 91: 458-464.

An, W.; Saadatmanesh, H. and Ehsani, M.R. **1991**. RC beams strengthened with FRP plates. II: analysis and parametric study, *Journal of Structural Engineering-ASCE* 117: 3434-3455.

Ando, Y.; Sakakibara, M.; Yamandoe, S. and Ohbo, N. **1998**. Seismic evaluation of actual bridge with isolators by vibration tests, *in proc. of the Second World Conference on Structural Control*, Kyoto, Japan 28Jun-1July, 913-922..

Anil, Ö. **2006**. Improving shear capacity of RC T-beams using CFRP composites subjected to cyclic load, *Cement and Concrete Composites* 28: 638-649.

Araki, N.; Matsuzaki, Y.; Nakano, K.; Kataka, T. and Fukuyama, H. **1997**. Shear capacity of retrofitted RC members with continuous fibre sheets, *Non-metallic (FRP) reinforcement for concrete structures, Proceedings of the Third International Symposium*, Japan, 1: 512–522.

Arduini, M. and Nanni, A. **1997**. Behavior of precracked RC beams strengthened with carbon FRP sheets, *Journal of Composite for Construction-ASCE* 1: 63-70.

Arduini, M.; D'Ambrisi, A. and Di Tommaso, A. **1994**. Shear failure of concrete beams reinforced with FRP plates, *Proceedings, Infrastructure: New Materials and Methods of Repair Proceedings of the Materials Engineering Conference 804*, ASCE, New York (1994), pp. 123–130.

Badawi, M. and Soudki, K. **2009**. Flexural strengthening of RC beams with prestressed NSM CFRP rods – experimental and analytical investigation, *Construction and Building Materials* 23: 3292-3300.

Baghiee, N.; Esfahani, M.R. and Moslem, K. **2009**. Studies on damage and FRP strengthening of reinforced concrete beams by vibration monitoring, *Engineering Structures* 31: 875-893.

Bakis, C.E.; Bank, L.C.; Cosenza, E.; Davalos, J.F.; Lesko, J.J.; Machida, A., Rizkalla, S.H. and Triantafillou, T. **2002**. Fiber-reinforced polymer compositesfor construction- state o art review, *Journal of Composites for Construction- ASCE* 6:73-87.

Barros, J.A. and Fortes, A.S. **2005**. Flexural strengthening of concrete beams with CFRP laminates bonded into slits, *Cement and Concrete Composites* 27: 471-480.

Barros, J.A.O.; Ferreira, D.R.S.M.; Fortes, A.S. and Dias, S.J.E. **2006**. Assessing the effectiveness of embedding CFRP laminates in the near surface for structural strengthening, *Construction and Building Materials* 20: 478-491.

Begg, R.; Mackenzoland, A.; Dodds, C. and Loland, O. **1976**. Structural Integrity Monitoring Using Digital Processing of Vibration Signals, *in proc. of 8th Annual Offshore Tech. Conf.*, Houston, Texas, 305-311.

Benachour, A,; Tounsi, A. and Adda-Bedia, E.A. **2008**. Interfacial stress analysis of steel beams reinforced with bonded prestressed FRP plate, *Engineering Structures* 30: 3305-3315.

Bencardino, F.; Spadea, G. and Swamy, R.N. **2007**. The problem of shear in RC beams strengthened with CFRP laminates, *Construction and Building Materials* 21:1997-2006.

Benjeddou, O.; Ouezdou, M.B. and Bedday, A. **2007**. Damaged RC beams repaired by bonding of CFRP laminates, *Construction and Building Materials* 21:1301-1310.

Benrahou, K.H.; Adda-Bedia, E.A.; Benyoucef, S.; Tounsi, A. and Benguediab, M. **2006**. Interfacial stresses in damaged RC beams strengthened with externally bonded CFRP plate, *Materials Science and Engineering: A* 432: 12-19.

Berto, L.; Simioni, P. and Saetta, A. **2008**. Numerical modeling of bond behaviour in RC structures affected by reinforcement corrosion, *Engineering Structures* 30(5): 1375–1385.

Bonacci, J.F. and Maalej, M. **2000**. Externally bonded fiber reinforced polymer for rehabilitation of corrosion damaged concrete beams, *ACI Structural Journal* 97:703-711.

Bonfiglioli, B. and Pascale, G. **2006**. Dynamic assessment of reinforced concrete beams repaired with externally bonded FRP sheets, *Mechanics Of Composite Materials* 42: 1-12.

Buckle, I. and Mayes, R. **1990**. Seismic isolation: history, application and performance- a world overview, *Earthquake Spectra* 6:161-202.

Büyüköztürk, O. and Hearing, B.**1998**. Failure behavior of precracked concrete beams retrofitted with FRP, *Journal of Composites for Construction- ASCE*, 2:138-144.

Büyüköztürk, O. and Yu, T.Y. **2006**. Understanding and assessment of debonding failures in FRP-concrete systems, *Seventh International Congress on Advances in Civil Engineering*, Yildiz Technical University, Istanbul, Turkey, pp 1-19.

Cao, M.; Ye, L.; Zhou, L.; Su, Z. and Bai, R. **2011**. Sensitivity of fundamental mode shape and static deflection for damage identification in cantilever beams, *Mechanical Systems and Signal Processing* 25(2): 630-643.

Capozucca, R. **2009**. Static and dynamic response of damaged RC beams strengthened with NSM CFRP rods, *Composite Structures* 91: 237-248.

Capozucca, R. and Cerri, M.N. **2002**. Static and dynamic behaviour of RC beam model strengthened by CFRP-sheets, *Construction and Building Materials* 16:91-99.

Carne, T. and Dohrmam, C. **1998**. Support conditions, their effect on measured modal parameters, *in proc. of the 16th International Modal Analysis Conference*, 477-483.

Carne, T.; Griffith, D. and Casias, M. **2007**. Support Conditions for Experimental Modal Analysis, *Sound and Vibration Magazine* Issue of June.

Catbas, F.; Gul, M. and Burkett, J. **2008**. Conceptual Damage-Sensitive Features for Structural Health Monitoring: Laboratory and Field Demonstrations, *Mechanical Systems and Signal Processing* 22:1650-1669.

CEB-FIB-14 2002. *The international federation for structural concrete*, Technical Report Bulletin 14.

Chaallal, O.; Nollet, M.J. and Perraton, D. **1998**. Strengthening of reinforced concrete beams with externally bonded fiber-reinforced-plastic plates: Design guidelines for shear and flexure, *Canadian Journal of Civil Engineering* 25: 692-704.

Chaallal, O.; Nollet, M.J. and Perraton, D. **1998a**. Shear strengthening of RC beams by externally bonded side CFRP strips, *Journal of Composite for Construction-ASCE* 2: 111–114.

Chajes, M.J.; Finch W.W.; Jansuzka, T.F. and Thomosh, T.A. **1996**. Bond and force transfer of composite material plates bonded to concrete, *ACI Structural Journal* 93: 231-244.

Chajes, M.J.; Januszka, T.F.; Mertz, D.R.; Thomson Jr, T.A. and Finch Jr, W.W. **1995**. Shear strengthening of reinforced-concrete beams using externally applied composite fabrics, *ACI Structural Journal* 92: 295–303.

Chajes, M.J.; Thomson T.A.; Januszka, T.F. and Finch, W.W. **1994**. Flexural strengthening of concrete beams sing externally bonded compositew materials, *Construction and Building Materials* 8:191-201.

Chen, J.F. and Teng, J.G. **2001a**. Anchorage strength models for FRP and steel plates bonded to concrete , *Journal of Structural Engineering* 127: 784-791.

Chen, J.F. and Teng, J.G. **2001b**. Anchorage strength models for FRP and steel plates bonded to concrete, *Journal of Structural Engineering-ASCE* 127: 784-791.

Chen, J.F. and Teng, J.G. **2003a**. Shear capacity of fiber-reinforced polymer-strengthened reinforced concrete beams: fiber reinforced polymer rupture, *Journal of Structural Engineering-ASCE* 129: 615-626.

Chen, J.F. and Teng, J.G. **2003b**. Shear capacity of FRP-strengthened RC beams: FRP debonding, *Construction and Building Materials* 17: 27-41.

Chen, W.F. **1982**. *Plasticity in reinforced concrete*, New York: McGraw-Hill Book Company.

Choi, F.; Li, J.; Samali, B. and Crews, K. **2008**. Application of the Modified Damage Index Method to Timer Beams, *Engineering Structures* 30:1124-1145.

Choo, C.C.; Zhao, T. and Harik, I. **2007**. Flexural retrofit of a bridge subjected to overweight trucks using CFRP laminates, *Composites Part B: Engineering* 38: 732-738.

Choubey, A.; Sehgal, D. and Tandon, N. **2006**. Finite element analysis of vessels to study changes in natural frequencies due to cracks, *International Journal of Pressure Vessels and Piping* 83(3):181-187.

Colalillo, M.A. and Sheikh, S.A. **2011**. Seismic retrofit of shear-critical reinforced concrete beams using CFRP, *Construction and Building Materials* doi:10.1016/j.conbuildmat.2010.12.065.

Colotti, V. and Spadea, G. **2001**. Shear strength of rc beams strengthened with bonded steel or FRP plates, *Journal of Structural Engineering-ASCE* 127: 367-373.

Colotti, V. and Swamy, R.N. **2011**. Unified analytical approach for determining shear capacity of RC beams strengthened with FRP, *Engineering Structures* 33: 827-842.

Coppolino, R. and Rubin, S. **1980**. Detectability of Structural Failures in Offshore Platforms by Ambient Vibration Monitoring, *12th Annual Offshore Tech. Conf.*, 101-110.

Cromwell, J.R.; Harries, K.A. and Shahrooz, B.M. **2011**. Environmental durability of externally bonded FRP materials intended for repair of concrete structures , *Construction and Building Materials* 25: 2528-2539.

Dahou, Z.; Sbartai, Z.; Castel, A. and Ghomari, F. **2009**. Artificial neural network model for steel concrete bond prediction, *Engineering Structures* 31(8):1724-1733.

Dai, W.; Moroni, M.; Roesset, J. and Sarazin, M. **2006**. Effect of isolation pads and their stiffness on the dynamic characteristics of bridge, *Engineering Structures* 28:1298-1306.

Dawood, M.; Guddati, M. and Rizkalla, S. **2007**. Bond and splice behavior of a CFRP strengthening system for steel structures, *Asia-Pacific Conference on FRP in Structures*, Hong Kong, .

Decker, B.R. **2007**. *A methods of Strengthening monitored deficient bridges*. Master of Engineering Theses, Kansas State University.

Demeter, G. **1973**. *Free Vibration of Two-Degree Spring-Mass System,* Wiley-Interscience.

Dias, S.J.E. and Barros, J.A.O. **2010**. Performance of reinforced concrete T beams strengthened in shear with NSM CFRP laminates, *Engineering Structures* 32: 373-384.

Doebling, S.; Farrar, C. and Prime, M. **1998**. A summary review of vibration-based damage identification methods, *The Shock and Vibration Digest*, 30:91–105.

Douka, E.; Bamnios, G. and Trochidis, G. **2004**. A method for determining the location and depth of cracks in double-cracked beams, *Applied Acoustics* 65:997–1008.

Dutta, A. and Talukdar, S. **2004**. Damage Detection in Bridge Using Accurate Modal Parameters, *Finite Element in Analysis and Design* 40:287-304.

El-Ghandour, A.A. **2011**. Experimental and analytical investigation of CFRP flexural and shear strengthening efficiencies of RC beams, *Construction and Building Materials* 25: 1419-1429.

El-Mihilmy, M. and Tedesco, J.W. **2000**. Analysis of reinforced concrete beams strengthened with FRP laminates, *Journal of Structural Engineering-ASCE* 126: 684-691.

Erki, M.A. and Meier, U. **1999**. Impact loading of concrete beams externally strengthened with CFRP laminates, *Journal of Composites for Construction-ASCE* 3:117-124.

Etman, E.E. and Beeby, A.W. **2000**. Experimental programme and analytical study of bond stress distribution on a composite plate bonded to a reinforced concrete beam, *Cement & Concrete Composites* 22: 281-291.

Ewins, D.J. **2000**. *Modal Testing: Theory, Practice and Application,* Second Edition, Baldock, Hertfordshire, England. Research Studies Press Ltd.

Fam, A.; MacDougall, C. and Shaat, A. **2009**. Upgrading steel–concrete composite girders and repair of damaged steel beams using bonded CFRP laminates, *Thin-Walled Structures* 47:1122-1135.

Fang, C.; Gylltoft, K.; Lundgren, K. and Plos, M. **2006**. Effect of corrosion on bond in reinforced concrete under cyclic loading, *Cement and concrete research* 36:548-555.

Fanning, P. and Kelly, O. **1999**. Shear strengthening of reinforced concrete beams: an experimental study using CFRP plates, *Proceeding* of 8th *International Conference of structural Fault and Repair*, London.

Fanning, P.J. and Kelly, O. **2001**. Ultimate response of RC beams strengthened with CFRP plates, *Journal of Composites for Construction-ASCE* 5:122-127.

Ferracuti, B.; Savoia, M. and Mazzotti, C. **2007**. Interface law for FRP–concrete delamination, *Composite Structures* 80: 523–531.

Funakawa, I. **1997**. Experimental study of shear strengthening with continuos fiber reinforcement sheet and methyl metaacrylate resin. *Non-Metallic (FRP) Reinforcement for Concrete Structures, Proceedings of the Third Symposium*, Japan, pp. 465-482.

Garden, H.N. and Hollaway, L.C. **1998**. An expermintaoncrete beamsl study of the influnce of plate end anchorage of carbon fibre composite plates used to strengthen reinforced, *Composite Structures* 42:175-188.

Gergely, I.; Pantelides, C.P.; Nuismer, R.J. and Reaveley, L.D. **1998**. Bridge pier retrofit using fiber-reinforced plastic composites, *Journal of Composites for Construction-ASCE* 2: 165-174.

Ghosh, K.K. and Karbhari, V.M. **2007**. Evaluation of strengthening through laboratory testing of FRP rehabilitated bridge decks after in-service loading, *Composite Structures* 77: 206-222.

Guradelli, R.; Riera, J.; Ambrosini, D. and Amani, M. **2008**. Damage Detection by Means of Structural Damping Identification, *Engineering Structuers* 30: 3497-3504.

Hag-Elsafi, O.; Lund, R. and Alampalli, S. **2002**. Strengthening of a bridge pier capbeam using bonded FRP composite plates, *Composite Structures* 57: 393-403.

Haskett, M.; Oehlers, D. and Ali, M. **2008**. Local and global bond characteristics of steel reinforcing bars, *Engineering Structures* 30 (2), 376–383.

Heffernan, P.J. and Erik, M.A. **1996**. Equivalents capacity and efficiency of reinforced concrete beams strengthened with carbon fibre reinforced plastic sheets, *Canadian Journal of Civil Engineering* 23:21-29.

Heylen, W.; Lammens, S. and Sas, P. **1999**. *Modal Analysis Theory and Testing*, Katholieke Universiteit Leuven, Belgium.

Huang, H. and Chen, G. **2005**. Bonding and anchoring characterization between FRP sheets,concrete,and viscoelastic layers under static and dynamic loading, *Proceedings of the International Symposium on Bond Behaviour of FRP in Structures*, Hong Kong, China, pp. 489-494.

Hudson, J.L. and Darwin, D. **2005**. *Evaluation and repair of blast damaged reinforced concrete beams*. University of Kansas Center for Research.

Hughes, P. and Chapman, G. **1966**. The deformation of concrete and micro concrete in compression and tension with particular reference to aggregate size, *Magazine of Concrete Research* 18 (54): 19-24.

Hutchinson, R.L. **1999**. *The use of externally bonded CFRP sheets for shear strengthening of I-shaped prestressed concrete bridge girder*, PhD Theses, University of Manitoba.

Ichinose, T.; Kanayamab, Y.; Inouec, Y. and Bolander, J. **2004**. Size effect on bond strength of deformed bars, *Construction and Building Materials* 18 (7): 549-558.

Ismail, Z. **2005**. *Damage detection of reinforced concrete beams using modal testing,* Ph.D. Thesis, University of Malaya, Kuala Lumpur, Malaysia.

Ismail, Z.; Abdul Razak, H. and Abdul Rahman, A. **2006**. Determination of Damage Location in RC Beams Using Mode Shape Derivatives, *Engineering Structuers* 28:1566-1573.

Iwata, S. **2000**. Hybrid earthquake loading test (pseudo-dynamic test) of bi-directional base isolation bearing for a large pedestrian bridge, *12th World Conference on Earthquake Engineering.*

Jangid, R. **1996**. Seismic response of sliding structures to bi-directional earthquake excitations, *Earthquake Engineering and Structural Dynamics* 25: 1301-1306.

Jangid, R. and Datta, T. **1995**. Seismic behaviour of base-isolated buildings: a state-of-the-art review, *Structures and Buildings* 110: 186-202.

Johan, M. **2003**. *Damage Assessment of Civil Engineering Structures By Vibration Monitoring,* Katholieke University Leuven, Belgium.

Jumaat, M.Z. and Ashraful-Alam, M.D. **2006**. Problems associated with plate bonding methods of strengthening reinforced concrete beams, *Journal of Applied Sciences Research* 2: 703-708.

Kage, T.; Abe, M.; Lee, H.S. and Tomosawa, F. **1997**. Effect of CFRP sheets on shear strengthening of RC beams damaged by corrosion of stirrup, *Non-Metallic (FRP) Reinforcement for Concrete Structures, Proceedings of the Third Symposium,* Japan, pp. 443–450.

Kamiński, M.; Musiał, M. and Ubysz, A. **2011**. Eigenfrequencies of the reinforced concrete beams – methods of calculations, *Journal of Civil Engineering and Management* 17(2): 278-283.

Karbhari, V.M. and Zhao, L. **1998**. Issue related to composite plating and environmental exposure effects on composite-concrete interface in external strengthening, *Composite Structures* 40:293-304.

Karsan, I. and Jirsa, J. **1969**. Behavior of concrete under compressive loading, *Journal of the Structural Division, ASCE* 95: 2543-2563.

Kato, M. and Shimida, S. **1986**. Vibration of Bridge During the Failure Process, *Journal of Structural Engineering* ASCE 112 (7): 1692-1703.

Kelly, J. **1986**. Asesmic base isolation: A review and bibliography, *Soil Dynamics and Earthquake Engineering* 5: 202-216.

Kelly, J. **1997**. *Earthquake Design with Rubber,* Springer-Verlag, Inc, N.Y.

Kelly, T.; Jones, L. and Mayes, R. **1984**. Seismic retrofit of bridges utilising ductile base isolation concepts, *the 8th World Conf. on Earthquake Engineering, 1*, 651-658. New Jersey, California.

Khalfallah, S. **2008**. Tension stiffening bond modelling of cracked flexural reinforced concrete beams, *Journal of Civil Engineering and Management* 14(2):131-137.

Khalifa, A. and Nanni, A. **2000**. Improving shear capacity of existing RC T-section beams using CFRP composites, *Cement and Concrete Composite* 22: 165-174.

Khalifa, A.; De Lorenzis, L. and Nanni, A. **2000**. FRP composites for shear strengthneing of RC beams, *Proceeding of 3rd International Conference on Advanced Composites Materials in Bridges and Structures*, Ottawa, pp. 137–144.

Khalifa, A.; Gold, J.W.; Nanni, A. and Adbel-Aziz, M.I. **1998**. Contribution of externally bonded FRP to shear capacity of RC flexural members, *Journal of Composites for Construction-ASCE* 2: 195-203.

Khiem, N. And Lien, T. **2001**. A Simplified Method for Natural Equency Analysis of a Multiple Cracked Beam, *Journal of Sound and Vibration*, 245 (4): 737-751.

Kim, D. and Lee, S. **2010**. Structural Damage Identification of A Cantilever Beam Using Excitation Force Level Control, *Mechanical Systems and Signal Processing* , 24: 1814-1830.

Kim, J. and Stunns, N. **2002**. Improved Damage Identification Method Based on Modal Information, *Journal of Sound and Vibration* 252 (2): 223-238.

Kim, J.; Park, J. and Lee, B. **2007**. Vibration Based Damage Monitoring in Model Plate-Girder Bridge Under Uncertain Temprature Condations, *Engineering Structures* 29: 1354-1365.

Kim, J.; Ryu, Y.; Cho, H. and Stubbs, N. **2003**. Damage Identification in Beam-Type Structuers: Frequency-Based Method Vs. Mode Shape - Based Method, *Engineering Structures* 25: 57-67.

Kim, Y.J. and Brunell, G. **2011**. Interaction between CFRP-repair and initial damage of wide-flange steel beams subjected to flexure, *Composite Structures* 93: 1986-1996.

Kisaa, M. and Gurelb, M. **2007**. Free vibration analysis of uniform and stepped cracked beams with circular cross sections, *International Journal of Engineering Science* 45 (2-8): 364-380.

Klaiber, F.W.; Wipf, T.J. and Kempers, B.J. **2003**. *Repair of damaged prestressed concrete bridges using CFRP*, Mid-Continent Transportation Research Symposium, Ames, Iowa.

Kotsovos, M. and Newman, J. **1977**. Behavior of concrete under multiaxial stress, *ACI Journal, Proceeding* 74 (9): 443-446.

Kupfer, H.: Hilsdorf, H. and Rusch, H. **1969**. Behavior of concrete under biaxial stresses, *ACI Journal* 66 (8): 656-666.

Kutarba, M.P. **2004**. *Durability of carbon fiber reinforced polymer (CFRP) strengthening system used to repair corrosion damage in reinforced concrete,* Master of Engineering Theses, University of Florida.

Lam, L. and Teng, J.G. **2001**. Strength of RC cantilever slabs bonded with GFRP strips., *Journal of Composites for Construction-ASCE* 5: 221-227.

Law, S. And Lu, Z. **2005**. Crack Identification in Beam From Dynamic Response, *Journal of Sound and Vibration* 285: 967-987.

Lee, H.K.; Cheong, S.H.; Ha, S.K. and Lee, C.G. **2011**. Behavior and performance of RC T-section deep beams externally strengthened in shear with CFRP sheets, *Composite Structures* 93: 911-922.

Lee, L.K. and Al-Mahaidi, R. **2008**. An experimental investigation on shear behaviour of RC T-beams strengthened with CFRP using photogrammetry, *Composite Structures* 82: 185-193.

Lee, Y. and Chung, M. **2000**. A Study on Crack Detection Using Eignfrequency Test Data, *Computers and Structures* 77: 327-342.

Leung, C.K.Y. and Pan, J. **2005**. Effect of concrete composition on FRP/concrete bond capacity, *Proceedings of the International Symposium on Bond Behaviour of FRP in Structures*, Hong Kong, China, pp. 69-78.

Lewandowski, R and Grzymisławska, J. **2009**. Dynamic analysis of structures with multiple tuned mass dampers, *Journal of Civil Engineering and Management* 15(1): 77-86.

Li, A.; Assih, J. and Delmas, Y. **2001**. Shear strengthening of RC beams with externally bonded CRRP sheets, *Journal of Structural Engineering-ASCE* 127: 374-380.

Li, X. **1989**. Optimisation of the stochastic response of a bridge isolation system with hysteretic dampers, *Earthquake Engineering and Structural Dynamics* 18:951-964.

Limongelli, M. **2010**. Frequency Response Function Interpolation for Damage Detection Under Chnaging Enviroment, *Mechanical Systems and Signal Processing* 24: 2898-2913.

Lindorf, A.; Lemnitzer, L. and Curbach, M. **2009**. Experimental investigations on bond behaviour of reinforced concrete under transverse tension and repeated loading, *Engineering structures* 31: 469-1476.

Loutridis, S.; Douka, E. and Hadjileontiadisc, L. **2005**. Forced vibration behavior and crack detection of cracked beams using instantaneous frequency, *NDT&E International* 38:, 411–419.

Lu, X.Z.; Chen, J.F.; Ye, L.P.; Teng, J.G. and Rotter, J.M. **2009.** RC beams shear-strengthened with FRP: Stress distributions in the FRP reinforcement, *Construction and Building Materials* 23: 1544-1554.

Maeck, J. and De Roeck, G. **1999**. Dynamic Bending and Torsion Stiffness Derivation from Modal Curvature and Torsion Rates, *Journal of Sound and Vibration* 225 (1): 153-170.

Maeck, J.; Abdel Wahab, M.; Peeters, B.; De Roeck, G.; De Visscher, J. and De Wilde, W. **2000**. Damage Identification in Reinforced Concrete Structuers by Dynamic Stiffness Determination, *Engineering Structuers* 22: 1339-1349.

Maeda, T.; Asano, Y.; Ueda, T. and Kakuta, Y. **1997**. A study on bond mechanism of carbon fiber sheet, non-metallic (FRP) reinforcement for concrete structures, *Proceedings of the Third International Symposium*, Sapporo, Japan, pp. 279-286.

Maia, N.M.M.; Silva, E. and Julio, M. **1997**. *Theoretical and Experimental Modal Analysis*, New York, Research Studies Press Ltd. and John Wiley & Sons Inc.

Malek, A.M. and Patel, K. **2002**. Flexural strengthening of reinforced concrete flanged beams with composite laminates, *Journal of Composites for Construction-ASCE* 6: 97-103.

Malek, A.M. and Saadatmanesh, H. **1998**. Ultimate shear capacity of reinforced concrete beams strengthened with web-bonded fiber reinforced plastic plates, *ACI Structural Journal* 95: 391-399.

Marfia, S.; Rinaldi, Z. And Sacco, E. **2004**. Softening behavior of reinforced concrete beams under cyclic loading, *International Journal of Solids and Structures*, 41 (11-12): 3293-3316.

Masoud, S.; Soudki, K. and Topper, T. **2001**. CFRP-strengthened and corroded RC beams under monotonic and fatigue loads, *Journal of Composites for Construction- ASCE* 5: 228-236.

Meftah, S.A. and Tounsi, A. **2007**. Lateral stiffness and vibration characteristics of damaged RC coupled shear walls strengthened with thin composite plates, *Building and Environment* 42: 3596-3605.

Meftah, S.A.; Tounsi, A.; Megueni, A. and Adda-Bedia, E.A. **2006**. Lateral stiffness and vibration characteristics of RC shear walls bonded with thin composite plates, *Composite Structures* 73:110-119.

Meier, U. **1992**. Carbn fiber reinforced polymers: modern materials in bridge engineerig, *Structural Eineeering International* 2:7-12.

Meier, U. **1995**. Strengthening of structures using carbon fiber/epoxy composite, *Construction and Building Materials* 9:341-351.

Miller, A.D. **2006**. *Repair of impact-damaged prestressed concrete bridge girders using carbon fiber reinforced polymer (CFRP) materials*, Master of Engineering Theses, North Carolina State University.

Mohamed-Ali, M.S.; Oehlers, D.J. and Seracino, R. **2006**. Vertical shear interaction model between external FRP transverse plates and internal steel stirrups, *Engineering Structures* 28: 381-389.

Monti, G. and Liotta, M.A. **2007**. Tests and design equations for FRP-strengthening in shear, *Construction and Building Materials* 21: 799-809.

Naeim, F. and Kelly, J. **1999**. *Design of seismic isolated structures: from theory to practice.* New York: John Wiley & Sons.

Nahvi, H. and Jabbari, M. **2005**. Crack Detection in Beams Using Expermintal Modal Data and Finite Element Model, *International Journal of Mechanical Sciences* 47: 1477-1497.

Nanni, A.; Di-Ludovico, M. and Parretti, R. **2004**. Shear strengthening of a PC bridge girder with NSM CFRP rectangular bars, *Advance Structural Engineering* 7: 97–109.

Nanni, A.; Focacci, F. and Cobb, C.A. **1998**. Proposed procedure for the design of RC flexural members strengthened with FRP sheets, *Proceding of The Second International Conference on Composites in Infrastructure*, Tucson, Arizona, pp. 187-201.

Ndambi, J.; Vantomme, J. and Harri, K. **2002**. Damage Assessment in Reinforced Concrete Beams Using Eignfrequncies and Mode Shape Derivatives, *Engineering Structures* 24: 501-515.

Neville, A. and Brooks, J. **1987**. *Concrete technology.* New York: Harlow, Essex, UK : Longman Scientific & Technical ; New York : J. Wiley.

Newhook, J.; Ghali, A. and Tadros, G. **2002**. Cracking and deformability of concrete flexural sections, *Journal of Structural Engineering-ASCE* 128: 1195-1201.

Nezamian, A. and Setunge, S. **2004**. Comparison between ACI 440 and FIB 14 design Guidelines in using CFRP for strengthening of concrete bridge headstock, *Proceeding of 4th International Conference on Advanced Composite Materials in Bridges and Structures*, Calgary, Canada.

Nguyen, D.M.; Chan, T.K. and Cheong, H. **2001**. brittle failure and bond development length of CFRP-concrete beams, *Journal of Composites for Construction-ASCE* 5:12-17.

Niu, J. and Wu, Z. **2001**. Prediction of debonding failure load due to flexural cracks in concrete for FRP strengthened structures, *Proceeding of Non Metallic reinforcement for concrete structure FRPRCS-5*, Cambridge, pp. 361–370.

Obaidat, Y.T.; Heyden, S. and Dahlblom, O. **2010**. The effect of CFRP and CFRP/concrete interface models when modelling retrofitted RC beams with FEM, *Composite Structures* 92: 1391-1398.

Orhan, S. **2007**. Analysis of free and forced vibration of a cracked cantilever beam, *NDT & E International* 40(6): 443-450.

Pandey, A.; Biswas, M. and Samman, M. **1991**. Damage Detection From Change in Curvature Mode Shapes, *Journal of Sound and Vibration* 145(2): 321-332.

Park, S. and Kim, Y. **2002**. Nondestructive Damage Detection in Large Structuers Via Vibration Monitoring, *Electronic Journal of Structural Engineering* 2:59-75.

Patil, D. and Maiti, S. **2003**. Detection of Multiple Crcaks Using Frequency Measurements, *Engineering Fracture Mechanics* 70(12):1553-1572.

Patil, D. and Maiti, S. **2005**. Experimental verification of a method of detection of multiple cracks in beams based on frequency measurements, *Journal of Sound and Vibration* 281: 439–451.

Pellegrino, C. and Modena, C. **2002**. Fiber-reinforced polymer shear strengthening of reinforced concrete beams with transverse steel reinforcement, *Journal of Composites for Construction-ASCE* 6: 104-111.

Pellegrino, C.; Boschetto, G.; Tinazzi, D. and Modena, C. **2005**. Progress on understanding bond behaviour in RC elements strengthened with FRP, *Proceedings of the International Symposium on Bond Behaviour of FRP in Structures*, Hong Kong, China, pp. 63-68.

Perera, R.; Huerta, C. and Orqui´n, J. **2008**. Identification of damage in RC beams using indexes based on local modal stiffness, *Construction and Building Materials* 22 (8): 1656-1667.

Plevris, N. **1995**. Reliability of RC members strengthened with CFRP laminates, *Journal of Structural Engineering- ASCE* 121:1037-1044.

Qiao, P. and Chen, Y. **2008**. Cohesive fracture simulation and failure modes of FRP–concrete bonded interfaces, *Theoretical and Applied Fracture Mechanics* 49: 213-225.

Qu, Z.; Lu, X.Z. and Ye, L.P. **2005**. Size effect of shear contribution of externally bonded frp u-jackets for rc beams, *Proceeding of International Symposium on Bond Behaviour of FRP in Structures*, Hong Kong, China, pp. 371-380.

Quantrill, R.J.; Hollaway, L.C. and Thorne, A.M. **1996**. Experimental and analytical invetigation of FRP stregthened beam response: PartI. 177, *Magazine of Concrete Research* 48:331-342.

Radzieński, M.; Krawczuk, M. and Palacz, M. **2011**. Improvement of damage detection methods based on experimental modal parameters, *Mechanical Systems and Signal Processing* 25 (6): 2169-2190.

Rahimi, H. and Hutchinson, A. **2001**. Concrete beams strengthened with externally bonded FRP plates, *Journal of Composites for Construction- ASCE* 5:44-56.

Ratcliffe, C. **1997**. Damage Detection Using a Modified Laplacian Operator on Mode Shape Data, *Journal of Sound and Vibration* 204 (3): 505-517.

Rehm, G. **1961**. On the fundamentals of steel-concrete bond (in German), *Deutscher Ausschuss fur Stahlbeton* 138:1-59.

Reinhorn, A.; Simeonov, V.; DeRue, G. and Constantinou, M. **1998**. Sensitivity of response of isolated bridges to modelling and design parameters: a case study, *The U.S.-Italy Workshop on Seismic Protective Systems for Bridges.* MCEER, NY.

Renata, S. and Henriette, L. **2008**. An efficient tension-stiffening model for nonlinear analysis of reinforced concrete members, *Engineering Structures,* 30: 2069–2080.

Ritchie, P.A.; Thomas, D.A.; Lu, L.W. and Connely, G.M. **1991**. External reinforcement of concrete beams using fiber reinforced plastics, *ACI Structural Engineering*, 88:490-500.

Ross, C.A.; Jerome, D.M.; Tedesco, J.W. and Hughes, M.L. **1999**. Strengthening of reinforced concrete beams with externally bonded composite laminates, *ACI Structural Journal* 96:212-220.

Ruotolo, R. and Surace, C. **1997**. Damage Assessment of Multiple Crcaked Beams: Numerical Results and Expemrintal Validation, *Journal of Sound and Vibration* 206 (4): 567-588.

Rytter, A. **1993**. *Vibration Based Inspection of Civil Engineering Structures.* PhD Dissertation, Aalborg University, Denmark.

Saadatmanesh, H. and Ehsani, M.R. **1991**. RC beams stregthened with GFRP plates I:expermintal study, *Journal of structural engineering- ASCE* 117:3417-3433.

Saadatmanesh, H. and Malek, A.M. **1998**. Design guidelines for flexural strengthening of rc beams with FRP plates, *Journal of Composites for Construction-ASCE* 2: 158-164.

Saafan, M.A.A. **2006**. Shear strengthening of reinforced concrete beams using GFRP wraps, *Acta Polytechnica*, 46: 24-32.

Salawu, O. **1997**. Detection of Structural Damage Through Change in Frequency: Areview, *Engineering Structuers* 19: 718-723.

Salawu, O. and Williams, C. **1995**. Brudge Assessment Using Forced-Vibration Testing, *Journal of Structural Engineering ASCE* 121 (2): 161-173.

Sathishkumar, K. and Murthy, S. **2010**. Detection of Contiguous and Distributed Damage Through Contours of Equal Frequency Change, *Journal of Sound and Vibration* 329: 1310-1331.

Sato, Y.; Katsumata, H. and Kobatake, Y. **1997**. Shear strengthening of existing reinforced concrete beams by CFRP sheets, *Non-Metallic (FRP) Reinforcement for Concrete Structures, Proceedings of the Third Symposium*, Japan, pp. 507-514.

Scanlon, A. **1971**. *Time dependent deflections of reinforced concrete slabs*, Alberta, Canada: Ph.D. Thesis, University of Alberta Edmonton.

Sharif, A.; Al-Sulaimani, G.J.; Basunbul, I.A.; Baluch, M.H. and Ghaleb, B.N. **1994**. Strengthening of intially loaded reinforced concrete beams using FRP plates, *ACI Structural Journal* 91:160-168.

Sharma, S.K.; Mohamed-Ali, M.S.; Goldar, D. and Sikdar, P.K. **2006**. Plate–concrete interfacial bond strength of FRP and metallic plated concrete specimens, *Composites Part B: Engineering* 37: 54-63.

Shih, H.W.; Thambiratnam, D.P. ; Chan, T.H.T. **2009**. Vibration based structural damage detection in flexural members using multi-criteria approach. *Journal of Sound and Vibration* 323: 645–661.

Silva, M.A.G. and Biscaia, H. **2008**. Degradation of bond between FRP and RC beams, *Composite Structures* 85: 164–174.

Skinner, R.; Robinson, W. and McVerry, H. **1993**. *An introduction to seismic isolation,* Chichester (England): Wiley.

Souza, M. **1994**. The influence of changing support conditions on the vibration of buckled plates, *Thin-Walled Structures* 18 (2): 133-143.

Spadea, G.; Bencardino, F. and Swamy, R.N. **1998**. Structural behavior of composite RC beams with externally bonded CFRP, *Journal of Composites for Construction* 2:132-137.

Stallings, J.M.; Tedesco, J. W.; El-Mihilmy, M. and McCauley, M. **2000**. Field performance of FRP bridge repairs, *Journal of Bridge Engineering-ASCE* 5:107-113.

Stubbs, N. and Kim, J. **1996**. Damage Loclization in Structuers without baseline Modal Parameters, *AIAA Journal* 34 (8): 1644-1649.

Sugiyama, T. **2000**. Comparison of seismic response between bridge with sliding type base isolation system and that with laminated rubber bearing, *The Twelth World Conference WCEE.*

Swamy, R.N.; Jones, R. and Charif, A. **1986**. Shear adhesion properties of epoxy resin adhesives, *International Symposium on Adhesion between Polymers and Concrete: Aix-en-Provence,* Rilem, Chapman & Hall, London, pp. 741-755.

Täljsten, B. **1994**. *Plate bonding, strengthening of existing concrete structurers with epoxy bonded plates of steel or fibre reinforced plastics*, Doctoral Thesis , Luleå University of Technology.

Tan, K.H. **1999**. Towards a cost-effective application of frp reinforcement in structural rehabilitation, Proceeding og *7th East Asia-Pacific Conference on Structural Engineering & Construction*, Kochi, Japan, 1: 65-73.

Tasuji, M.; Slate, F. and Nelson, A. **1978**. Stress-strain response and fracture of concrete in biaxial loading, *ACI Journal* 75 (7): 306-312.

Teng, J.G.; Chen, J.F.; Smith, S.T. and Lam, L. **2000**. *RC structures strengthened with FRP composites*, Research Center for Advanced Technology in Structural Engineering, The Hong Kong Polytechnic University, Hong Kong, China.

Teng, J.G.**;** Chen, J.F.**;** Smith, S.T. and Lam, L. **2001.** *FRP-Strengthened RC Structures*, England : John Wiley & Sons Ltd.

Teng, J.G.; Yuan, H. and Chen, J.F. **2006**. FRP-to-concrete interfaces between two adjacent cracks: theoretical model for debonding failure, *International Journal of Solids and Structures* 43: 5750-5778.

Todorovska, M. and Trifunac, M. **2010**. Earthquake damage detection in the Imperial County Services Building II: Analysis of novelties via wavelets, *Structural Control and Health Monitoring* 17 (8):564-576.

Tomaszewska, A. **2010**. Influnce of Statistical Errors on Damage Setection Based on Structural Flexibility and Mode Shape Curvature, *Computer and Structures* 88: 154-164.

Tongaonkar, N. and Jangid, R. **1998**. Seismic response of bridges with sliding isolation devices, *ISET Journal of Earthquake Technology* 35: 9-27.

Tounsi, A. and Benyoucef, S. **2007**. Interfacial stresses in externally FRP-plated concrete beams, *International Journal of Adhesion & Adhesives* 27: 207–215.

Toutanji, H. and Ortiz, G. **2001**. The effect of surface preparation on the bond interface between FRP sheets and concrete members, *Composite Structures* 53: 457-462.

Triantafillou, T.C. **1998**. Shear strengthening of reinforced concrete beams using epoxy-bonded FRP composites, *ACI Structural Journal* 95:107-115.

Triantafillou, T.C. and Antonopoulos, C.P. **2000**. Design of concrete flexural members strengthened in shear with FRP, *Journal of Composites for Construction-ASCE* 4: 198-205.

Triantafillou, T.C. and Fardis, M.N. **1997**. Strengthening of historic masonry structures with composite materials, *Materials And Structures* 30: 486-496.

Triantafillou, T.C. and Plevris, N. **1992**.Strengthening of RC beams with epoxy-bonded fiber-composite materials, *Materials and Structures* 25:201-211.

Tsai, H. and Kelly, J. **1993**. Seismic response of heavily damped base isolated buildings, *Earthquake Engineering and Structural Dynamics* 22: 633-645.

Tsopelas, P.; Constantinou, M.; Kim, Y. and Okamoto, S. **1996**. Experimental study of FPS system in bridge seismic isolation, *Earthquake Engineering and Structural Dynamics* 25: 65-78.

Van Gemert, D. **1980**. Force transfer in epoxy-bonded steel-concrete joint, *International Journal of Adhesion and Adhesive* 1: 67-72.

Vandiver, J. **1975**. Detection of Structural Failure on Fixed Platforms by Measurment of Dynamic Response, *The 7th Annual Offshore Tech. Conf.*, 243-252.

Varastehpour, H. and Hamelin, P. **1997**. Strengthening of concrete beams using fiber reinforced plastics, *Materials and Structures* 30:160-166.

Viola, E. and Guidi, F. **2009**. Influence of the supporting braces on the dynamic control of buildings with added viscous dampers, *Structural Control and Health Monitoring* 16 (3): 267–286.

Wang, H. **2009**. An analytical study of bond strength associated with splitting of concrete cover, *Engineering Structures* 31 (4):968-975.

Wang, J. and Qiao, P. **2008**. On Irregularity-Based Damage Detection Method for Cracked Beams, *International Journal of Solid and Structures* 45:688-704.

Wang, J.**2006**. Debonding of FRP-plated reinforced concrete beam, a bond-slip analysis:I. theoretical formulation, *International Journal of Solids and Structures* 43: 6649-6664.

Wang, X. and Liu, X. **2003**. A strain – softening model for steel concrete bond, *Cement and concrete Research*, 33:1669-1673.

West, W. **1984**. Illustration of The Use of Modal Assurance Criterion to Detect Structural Changes in An Orbiter Test Soecimen, *Air Force Conference on Aircraft Structural Integrity*,1-6.

White, T.W.; Soudki, K.A. and Erki, M.A. **2001**. Response of RC beams strengthened with CFRP laminates and subjected to a high rate of loading, *Journal of Composites for Construction-ASCE* 5:153-162.

Wolf Jr, J. **1984**. *The influence of mounting stiffness on frequencies measured in a vibration test.* Society of Automotive Engineering.

Wu, Z.J. and Davies, J.M. **2003**. Mechanical analysis of a cracked beam reinforced with an external FRP plate, *Composite Structures* 62: 139-143.

Xia, Y.; Hoa, H. and Deeks, A. **2007**. Dynamic Assessment of Shear Connectors in Slab-Girder Bridges, *Engineering Structures* 29: 1475-1486.

Xiao, J.; Li, J. and Zha, Q. **2004**. Experimental study on bond behavior between FRP and concrete, *Construction and Building Materials* 18: 745-752.

Xue, W.; Zeng, L. and Tan, Y. **2008**. Experimental studies on bond behaviour of high strength CFRP plates, *Composites Part B: Engineering* 39: 592-603.

Yaun, H. and Wu, Z. **1999**. Interfacial fracture theory in structures strengthened with composite of continuous fibe, *Symposium of China and Japan Science and Technology of 21st Century*, Tokyo, Japan, pp. 142-155.

Yuan, H.; Wu, Z.S. and Yoshizawa, H. **2001**. Theoretical solutions on interfacial stress transfer of externally bonded steel/composite laminates, *Journal of Structural Mechanics and Earthquake Engineering* 675/1-55: 27-39.

Zhong, S. and Oyadiji, S. **2011**. Crack detection in simply supported beams using stationary wavelet transform of modal data, *Structural Control and Health Monitoring* 18 (2):169-190.

Zhua, H.; Lia, L. and Hec, X. **2011**. Damage detection method for shear buildings using the changes in the first mode shape slopes, *Computers & Structures* 89 (9-10): 733-743.

Zirab, Y.N.; Baluch, M.H.; Basunbul, I.A.; Azad, A.K.; Al-Sulaimani, G.J. and Sharif, A.M. **1995**. Combined experimental-numerical approach to characterization of steel-gle-concrete interface, *Materials and Structures* 28: 518 - 525.

Zonta, D.; Elgamal, A.; Fraser, M. and Priestley, M. **2008**. Analysis of change in dynamic properties of a frame –resistant test building, *Engineering Structures* 30: 183-196.